1-1-2011

An investigation of the biomechanical response from shock wave loading to the head

Alessandra Dal Cengio Leonardi
Wayne State University,

AN INVESTIGATION OF THE BIOMECHANICAL RESPONSE FROM SHOCK WAVE LOADING TO THE HEAD

by

ALESSANDRA DAL CENGIO LEONARDI

DISSERTATION

Submitted to the Graduate School

of Wayne State University

Detroit, Michigan

in partial fulfillment of the requirements

for the degree of

DOCTOR OF PHILOSOPHY

2011

MAJOR: BIOMEDICAL ENGINEERING

Approved by:

_____

Advisor Date

_____

Co-advisor Date

_____

Date

_____

Date

_____

Date

DEDICATION

To my wonderful children, Arianna, Erica, Marco, and Andre. You are the reason behind everything I do. I love you all very much and I am grateful for all the support you four gave me along the way.

To my one and only, my husband Franco. You did not realize what you signed up for at the beginning of this journey, but you patiently encouraged me through it all, and we finally reached the finish line together. This was such a joint effort; I could not have done it without you. I am so proud of our teamwork! Thank you for sharing your life with me, Amore mio.

To my amazing parents, my fearless mother, Iva, who led me by example and successfully pursued a second degree and career against all odds; and my supportive father, Pino, who is so incredibly proud of us both.

To my grandmother, Milena, who recognized the importance of giving her children a good education and dedicated her life to make sure that we all had a better chance than she had. Grazie nonna.

ACKNOWLEDGMENTS

First and foremost, I would like to acknowledge my PhD advisor, Dr. Pamela VandeVord, my co-advisor Dr. Cynthia Bir, and my dissertation committee members, Dr. Albert King and Dr. King Yang, for offering me the opportunity to start a new field of research at the Bioengineering Center at Wayne State University: the study of blast traumatic brain injury. Thanks to their amazing foresight, the BME department at WSU produced cutting edge blast research using both animals and post-mortem human subjects, ahead of other institutions. I am honored and proud of having been part of this effort from its beginning. A special thought goes to Pam: you were such a big presence in this journey we shared; you deserve everything you accomplished and I am delighted that you chose me to walk at your side. To Dave Ritzel, the external member of my dissertation committee, I will be forever grateful for your guidance and generosity in sharing your time and knowledge with me.

Furthermore, this project could not have been completed without the help of many people that were involved at one point or another, and I would like to thank everyone for their participation: Rick Bolander, Nate Dau, Srini Kallakuri, Nick Keane, Jim Kopacz, Blake Mathie and all my coworkers that helped during those long testing days. I would also like to convey my sincere thanks to Dr. Bulent Ozkan for his invaluable advise during statistical analysis, and to Dr. Warren Hardy for putting up with training me during his last days at WSU (Warren, it was a privilege to be your pest). Additionally I am extremely thankful to my all my lab group for their emotional support, especially my friend Evon Ereifej, who always put a smile on my face and food on my desk.

My heartfelt gratitude to all the sources of funding that supported in part this research: the Predoctoral Associated Health Research Fellowship offered by the Department of Veterans Affairs; the Anthony and Joyce Kales Scholarship for BME students at WSU; and the CDMRP grant # W81XWH-09-1-0498.

Finally, I want to take this moment to acknowledge the two wonderful people behind my successful outcome: my husband, Franco, and my friend, Susan Faulk. Franco, thank you for standing by my side through it all. It was challenging at best and it did require a lot of sacrifices, but we did it together as a family, and that, to me, was priceless. Sue, you were a dedicated friend to me, a second mother to my youngest child and a great help to my family; we would have gone crazy without you. My hope is that the fruits of this research will repay you by pay it forward to your "Army-family" and become an enabler for the development of better protective equipment for our Soldiers.

TABLE OF CONTENTS

LIST OF FIGURES

LIST OF TABLES

CHAPTER 1

1.1 Introduction of the problem

Traumatic brain injuries (TBI) caused by improvised explosive devices (IED) affect a significant percentage of soldiers wounded in Iraq and Afghanistan. In fact TBI has been called the signature wound for these wars (Gondusky and Reiter 2005; Hoge et al. 2008; Okie 2005; Warden 2006; Zoroya 2005). Primarily because of advancements in medicine and expedited medical evacuation, more soldiers are now surviving TBIs when in previous conflicts they would have died. The mortality rate in Vietnam from brain injuries was more than 75% (Okie 2006). Another important reason for the increased survivability of the Soldiers is the continuous improvements in personal protective equipment (PPE). Kevlar body armor and helmets contribute to saving lives by successfully protecting Soldiers from penetrating injuries to most of the body and skull. Unfortunately, with current equipment the face and forehead are still left unprotected; therefore, helmets cannot completely prevent penetrating brain injuries. Moreover in the recent conflicts closed brain injuries (often produced by blasts) have outnumbered penetrating ones (Okie 2005).

Although little is known about the mechanism of neurotrauma induced by blast waves, doctors are becoming more proficient at diagnosing blast related TBI problems. It is now known that blast related TBI can occur even without obvious external injuries, loss of consciousness, or visible findings from magnetic resonance imaging (Bhattacharjee, 2008; Cernak et al. 1999a; Guy et al. 2000; Irwin et al. 1997). Many of the TBI symptoms are cognitive: problems with memory, lack of concentration, increased anxiety and irritability, depression, and mood changes. These conditions can be associated with injuries that involve areas of the brain that control personality, emotional behavior, and intellectual abilities such as the frontal lobes or the regulator of the medial prefrontal cortex, the amygdala (Bryant 2008; Trudeau et al. 1998).

Presently there is a pressing need for a comprehensive explanation of the mechanism of brain injury after exposure to blast and several hypotheses have been suggested. Some have proposed that damage is due to transosteal propagation (Clemedson 1956a; Clemedson and Jonsson 1961a), or the shock wave entering the brain by propagating directly through the skull. Others contend that the skull remains effectively rigid and non-responsive, and that a hydrostatic pressure pulse is transmitted to the brain via blood vessels and possibly cerebrospinal fluid (Cernak et al. 2001; Courtney and Courtney 2009; Young 1945), or suggest that damage to the lungs can elicit a physiological response creating injury to the brain (Cernak et al. 1996). Still others propose that a pressure wave imparted to a different point in the body could have enough magnitude to be transmitted to the brain and cause histologically observable damage (Suneson et al. 1990).

Recently, two computational simulations using finite-element models that have not been validated by experimental results, have proposed different theories. Moss et al. (2009) have shown that skull flexure, primarily in the form of transverse "surface" waves across the skull, may be a mechanism of stress transfer and injury. In the computational model by Nyein et al. (2010), the blast wave was seen investing the face and entering the brain primarily through the soft tissues. In addition, using finite-element modeling, a different computational simulation that was validated against impact loadings of cadaveric specimens, predicted increasing ICP values, maximum shear stresses, and maximum principal strain within the brain during blast events with increased overpressure magnitudes (Chafi et al. 2010). Finally, preliminary studies conducted by our group have led us to hypothesize that a combination of several modes of skull flexure, including global compression, may contribute to generating injurious stress waves within the head (Dal Cengio Leonardi et al. 2009; Dal Cengio Leonardi et al. 2011).

1.2 Blast Review

1.2.1 Properties of the free-field blast wave

The classical free-field blast wave (sometimes described as the "Friedlander waveform") is a simplified representation of the open field blast wave hydrostatic pressure (also known as static or side-on pressure). It does not account for reflection against the ground or other natural occurring conditions. In general the classical free-field blast wave is characterized by a single high pressure pulse followed by a rapid decrease of the overpressure (positive phase) and terminating with a period of below ambient pressure (negative phase) before returning to ambient conditions. Figure 1 represents the variation through time of static pressure for a classical free field blast wave as would be measured at a fixed location passed by the blast.

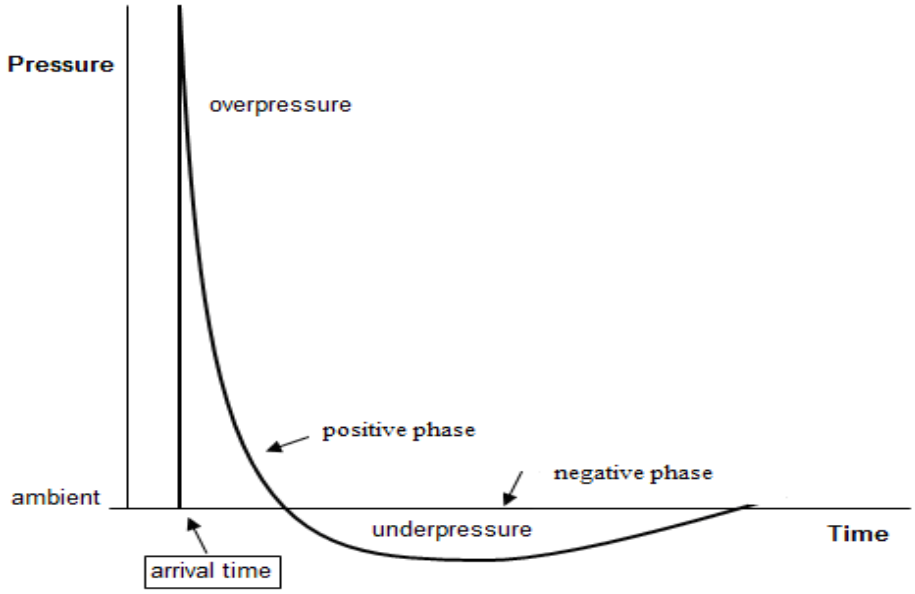

Figure 1: Friedlander wave, i.e. classical free field blast wave for hydrostatic pressure. Variation through time of static pressure for a classical free field blast wave as would be measured at a fixed location passed by the blast.

Associated with the sudden rise in pressure of the shock front there is also a blast wind (dynamic pressure) due to the kinetic energy transmitted to the air particles. Moreover, during the violent expansion of the gas caused by the explosion, inertial effects create overexpansion at the

epicenter, with a consequent reduction in pressure to below ambient levels for a period. This rarefaction wave is also associated with a reversal of the air-flow velocity meaning that air is slowly pulled back towards the source of the explosion (Figure 2).

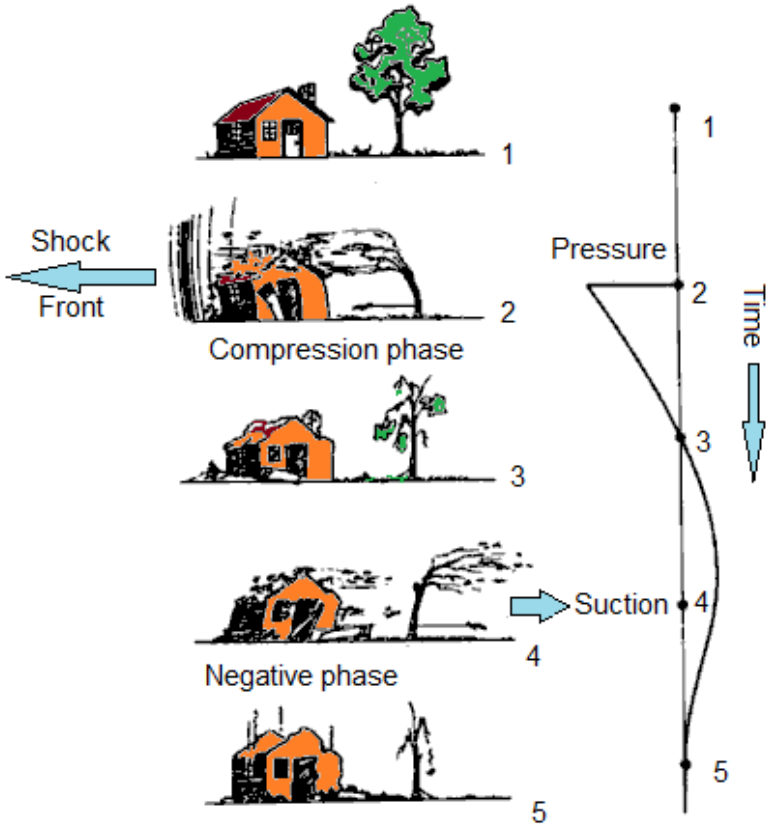

Figure 2: Variations of blast effects associated with positive and negative phase pressures with time.
Inertial effects create overexpansion at the epicenter, with a consequent reduction in pressure to below ambient levels for a period and a reversal of the air-flow velocity. **(**http://www.fas.org/nuke/intro/nuke/blast.htm**)**

With time and distance the peak pressure and velocity of the shock wave weakens while it propagates (Figure 3). Near the source of the explosion the overpressure decreases approximately with the cube of the distance from the epicenter, but at greater distance it attenuates more slowly until it decays as an acoustic wave inversely with distance as described by Iremonger (1997).

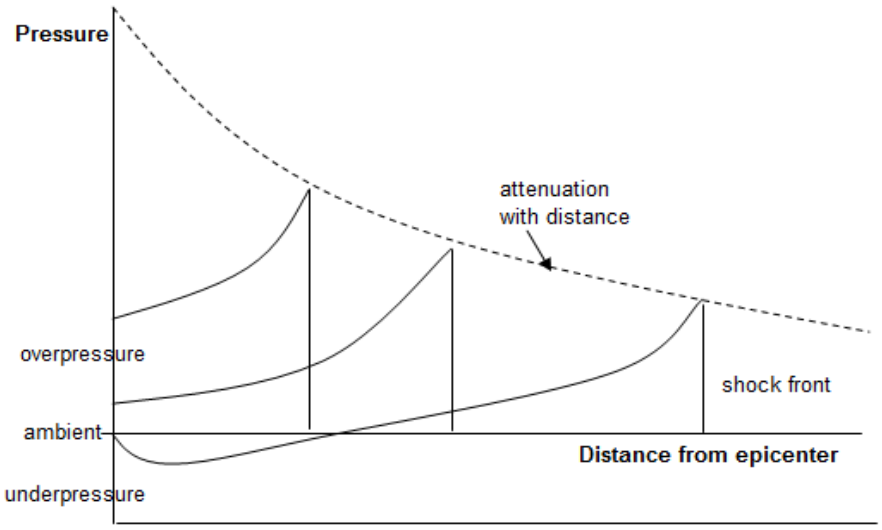

Figure 3: Blast wave profile at increasing distance from the epicenter of an explosion. Near the source of the explosion the overpressure decreases approximately with the cube of the distance from the epicenter, but at greater distance it attenuates more slowly until it decays as an acoustic wave inversely with distance

1.2.2 Biophysics of blast loading

When a blast wave encounters a structure, loading is imparted due to shock reflection and diffraction, much as a water wave crashing around a rock - as shown in Figure 4 - as well as aerodynamic forces from the blast wind. These external surface loads may cause surface deflections, damage, and global motion of the structure, and a stress-wave may be propagated into the material. In the case of humans, who often have 'compliant' surfaces, the aspects of stress-wave coupling as well as fluid-structure interaction (FSI) are critical to the problem of determining what is propagated as imparted loading.

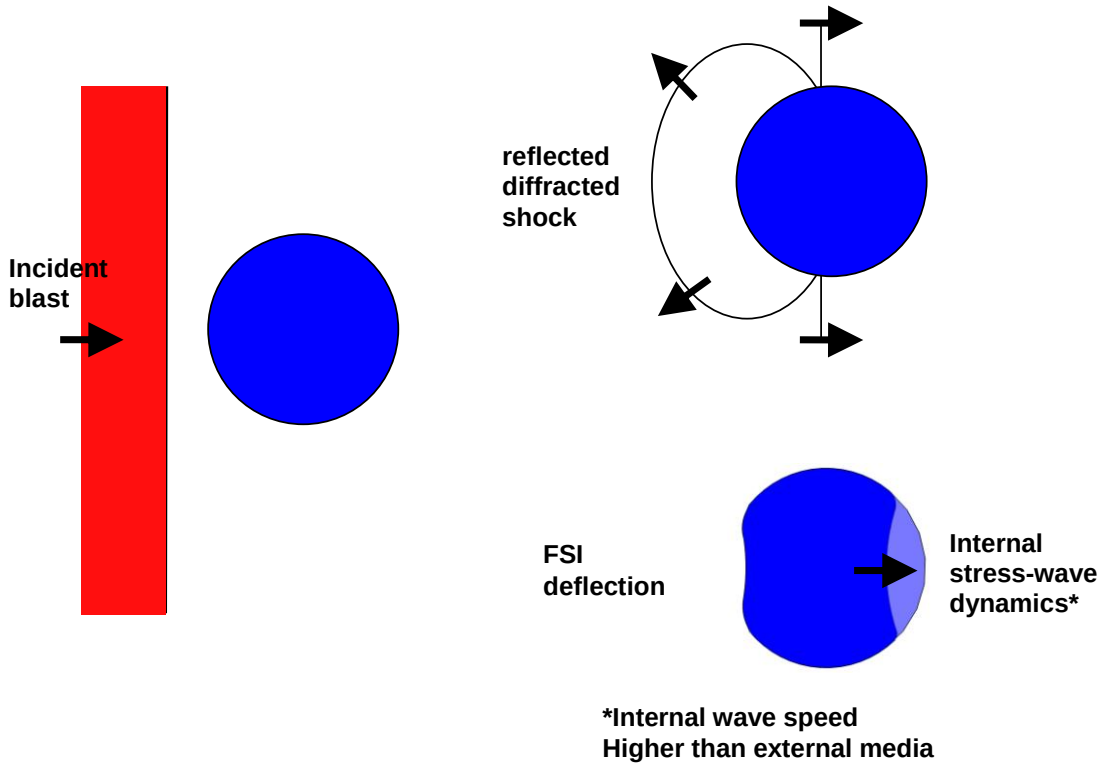

Figure 4: Depiction of blast loading of cylindrical or spherical structure showing external and internal wave dynamics.
(courtesy of Dave Ritzel)

As noted by Clemedson, various parts of the body surface react differently to the initial shock wave because of differences in their physical properties (Clemedson 1956b), giving different outcomes (Mayorga 1997). When placed into abrupt motion, oscillation will occur in a simple elastic system at its natural frequency (being the inverse of the natural period) according to the mechanical properties of the system. Then the system tends to return to rest following a damping pattern related to its mechanical properties. Classical thinking of a "single degree of freedom" model shows that the natural period of a system and its damping properties determine the general mechanical response of the structure. Simplistically, Clemedson and Criborn (1955) postulated that, if the natural period of the system was short compared to the duration of the shock wave, the peak overpressure was of main importance for blast injury, as the system would reach a damaging load before the overpressure had passed. On the other hand if the natural period

was long, then the impulse could be the main source of damage. A more thorough investigation reveals that the problem is more complex and that features like geometry of the structure, type of excitation, type of materials and their coupling, and internal wave dynamics, all play a role in blast injury.

In terms of physiological importance, the imparted loading is determined by the static P_s and dynamic P_d pressures of the blast wave and the structure's geometry during the reflection/diffraction phase. This loading will vary dramatically around the structure and through time. Therefore the combined static and dynamic pressure conditions through time are critical. Simplistically, the single best parameter to define the loading conditions imparted by a blast wave is the peak reflected pressure P_{refl}:

$$P_{refl} = 2P_s + 2.4P_d$$

as described by Iremonger (1997). Initially, the three parameters that were believed to be of primary importance were: peak overpressure, duration, and impulse, which is the area under the overpressure-time curve). The peak overpressure was defined as the maximum value of the positive phase; the duration also referred to the positive phase, and the impulse was the area under the positive phase of the overpressure-time curve (Celander et al. 1955b; Clemedson 1956b). However, critical features of the blast loading relevant to brain injuries still remain to be determined and in fact may relate foremost to the rate-of-change of loading. Chapter 2 provides more in-depth information regarding evidence of shock wave transmission to the brain, which is of particular interest here.

1.3 Hypotheses and specific aims

Presently there is a pressing need for a comprehensive explanation of the mechanism of brain injury after exposure to blast and several hypotheses have been suggested. This project was designed to investigate, at a basic level, one of the hypotheses for primary brain injury due to blast: multimodal skull flexure. The focus of this investigation was to establish the basic

phenomenology of shockwave interaction with the skull/brain system. Using a shockwave generator, two studies were pressed forward concurrently. One study explored the mechanical response of simplified head models of identical geometry that had differences in other characteristics (shell thickness, composition of the filling, and introduction of apertures). The other study examined the mechanical response of a few unembalmed human heads.

The **SPECIFIC AIMS** of this research were to:

1. map the transient responses of the simplified head model and of the skull/brain system during exposure to blast by monitoring the internal pressures in different regions,
2. compare pressure distribution patterns with surface strain data recorded concurrently for evaluation of gross deformations of the shell or skull in relation to internal pressure profiles,
3. determine the relationship between magnitude levels of incident pressure and values of internal pressure in different regions,
4. investigate the effects of specimen orientation on internal pressure in the same regions,
5. investigate the effects of apertures on internal pressures in the simplified head models
6. compare the mechanical responses in the cadaveric data to the mechanical responses in the simplified model data.

The **HYPOTHESES** of this study expect that:

1 the internal pressure profiles generated by shockwave exposure are imparted by a multimodal skull flexure that includes transverse surface waves and global compression coupled with the brain mass response;

2 these skull flexural modes have some similarities but important differences from those which are impact related;

3 head orientation and sample orientation relative to the blast have an effect on pressure transmission;

4 the mechanical response of a simplified head model can approximate the cadaveric behavior for transmission of pressure and strain;

5 when comparing head models, the presence of anatomical orifices in the shell increases the pressure transmitted to the filling;

6 the comparison of the collected cadaveric data to the simplified model data will help unravel the complexity of cadaveric mechanical response and help identify the primary aspects of such response.

CHAPTER 2

2.1 Properties of the shock wave produced by a shock tube

Within certain important limitations that will be discussed later, it is possible to simulate free-field blast wave conditions in the laboratory by means of a compressed-gas shock tube. A shock tube consists of two separate chambers: the driver section, where the pressure is created by means of an air compressor system or other gas, and the driven or test section, where the shock wave propagates (explained by Celander et al. 1955a). In the simplest shock tube operation, the driver section is separated from the driven section by a frangible membrane. The membrane ruptures at a particular pressure that is directly proportional to its thickness and allows the generation of the shock wave into the driven section. Because the wave is produced by compressed gas bursting a membrane instead of an actual chemical explosion, the term shock wave is used here instead of blast wave.

For all purposes of current interest, the test section contains air at ambient atmospheric pressure before the bursting of the diaphragm. If the diaphragm bursts ideally, a uniform shock front quickly develops and propagates down the test section. At the same time a rarefaction wave or pressure-relief wave, propagates in the opposite direction toward the closed end of the driver reducing the pressure in the driver section. Unlike the shock, this rarefaction is a distributed wave having flow properties changing gradually from ‘head’ to ‘tail’. A depiction of the spatial distribution of pressure in the tube moments after rupture of the diaphragm is shown in Figure 5.

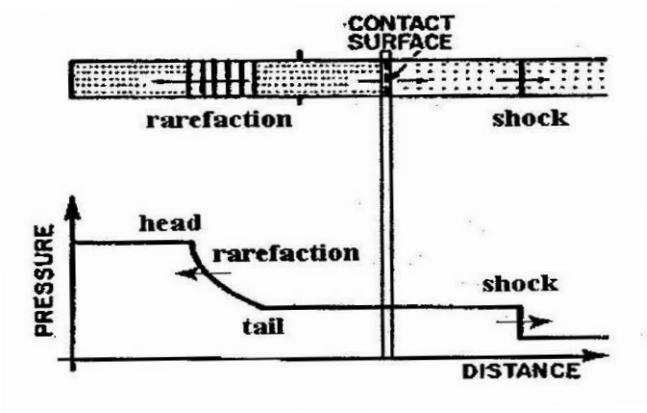

Figure 5: Propagation of the shock wave in a tube
A uniform shock front quickly develops and propagates. At the same time a rarefaction wave propagates in the opposite direction reducing the pressure in the driver section. (courtesy of Dave Ritzel)

Ahead of the shock front there is quiescent medium, not yet reached by the perturbation. Behind the shock front there is a region of heated and compressed driven gas that maintains the same flow properties (temperature, density, pressure and velocity) until the arrival of the contact surface. The contact surface is the boundary between the driven gas and the expanding driver gas and generally represents a discontinuity in temperature and density. Behind the contact surface the driver gas has been expanded and cooled by the rarefaction wave. This rarefaction wave will reflect from the closed end of the driver and propagate down the tube moving now in the same direction and, in fact, faster than the shock front. If the cross section of the shock tube is constant, the shock wave moves at constant speed unattenuated down the tube until the reflected rarefaction from the closed end of the driver overtakes it, or it diffracts from the open end of the tube. Prior to this overtaking, the shock waveform, as measured at any location within the test section, will feature a flat section after the peak. Subsequent to the overtaking, the pressure waveform will have a decaying profile similar to a blast wave, as shown in Figure 6.

Figure 6 presents two pressure profiles that were recorded with a Pitot-static probe, which is a device that has two separate gages to measure static pressure and stagnation or total pressure

(in case of Bernoulli flow the sum of the static and dynamic pressures is equal to total pressure). In this case the two gages are 5.5 inches apart, with the side-on gage (for static pressure) being the one downstream from the shock front, as it can be seen from the pressure profile in Figure 6. In this example the peak overpressure was around 13psi (pound per square inch), while stagnation pressure measured around 17 psi. The first spike in the record for stagnation reachess 30 psi, but it is in fact a brief artifact of the reflected pressure discussed previously. Table 1 shows static and dynamic pressure values for an ideal shock wave in air at sea level. The peak dynamic pressure value can be approximated in this case by subtracting the static peak from the stagnation peak giving a value about 4 psi. Extrapolating from the values provided in Table 1, the dynamic pressure component of the shock wave flow very closely matches that of free-field blast.

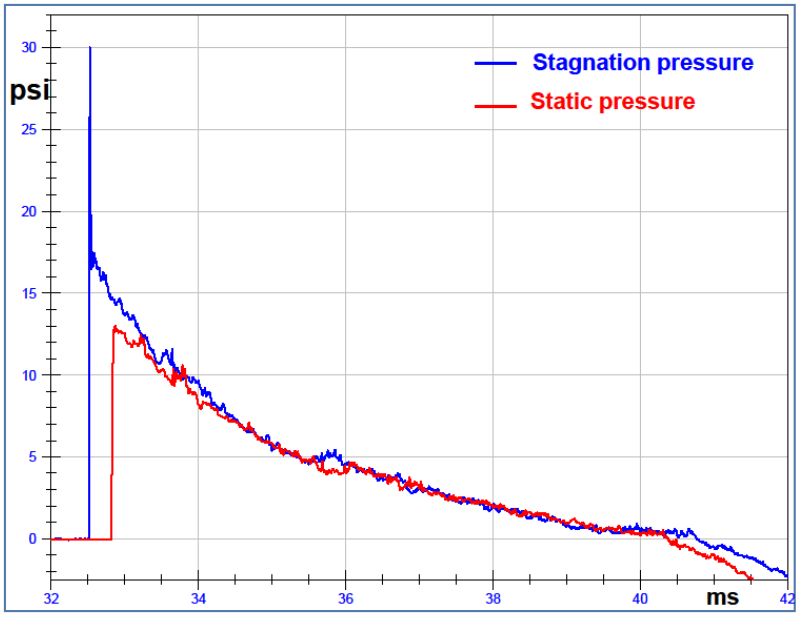

Figure 6: Real shock wave profiles obtained in the WSU tube expansion, which is the setup for larger specimens. Static pressure was measured at 49" from the open end; stagnation pressure was measured at 54.5" from the open end.

Table 1: Peak Overpressure and Dynamic Pressure and Maximum Wind Velocity in air at sea level calculated for an ideal shock front.
from The effect of nuclear weapons by S. Glasstone and P.J. Dolan, chapter 3, p. 82.

Peak overpressure (pounds per square inch)	Peak dynamic pressure (pounds per square inch)	Maximum wind velocity (miles per hour)
200	330	2,078
150	222	1,777
100	123	1,415
72	74	1,168
50	41	934
30	17	669
20	8.1	502
10	2.2	294
5	0.6	163
2	0.1	70

Any zone within the shock tube will eventually be affected by the arrival of disturbances and gas dynamic features entirely atypical of blast waves. Example of such anomalous disturbances might be the arrival of the contact surface with expanding driver gas, or the arrival of the strong rarefaction from the open end of the tube. At some locations within the tube, the effects of these anomalous flow features are exaggerated and will corrupt the experimental conditions much earlier. Extremely adverse effects will result from experiments staged with a specimen near the end of the tube where the end-rarefaction will quickly cause imbalance of high dynamic pressures yet reduced static pressure conditions. The target (specimen) in this regime would in fact be subjected to a nearly pure jet-stream outflow, exaggerated under-pressures or vacuum, or indeed a shock propagating upstream. Conditions external to the tube will be likened to a quasi-steady free-stream cold jet with negligible or very short static pressure content, as well as likely complex quasi-steady embedded shock structures (‘shock diamonds’ and Mach discs seen in jet engine exhaust).

These factors were taken into consideration when choosing the zone in the tube appropriate for blast simulation. The target needs to be placed at such a distance from the open

end of the expansion to optimize the shock wave pressure profile. This ideal position is dependent on the dimensions of the tube being used and needs to be evaluated as such.

2.2 Characterization of the shock wave produced by the WSU shock tubes

The shock wave generator (shock tube) used at WSU for small specimens is shown in Figure 7. The setup for small specimens consists of a steel section and a transparent, Lexan section (Figure 7A). The steel section contains the driver chamber and part of the driven chamber (Figure 7B). The Lexan section represents the final part of the driven chamber and its transparency provides video capability during the test for specimens placed within 48 inches from the muzzle (open end). A metal structure can be bolted in front of the open end of the tube for sensors and specimens to be inserted into the tube by means of a pole extension clamped to a trolley system (Figure 7A).

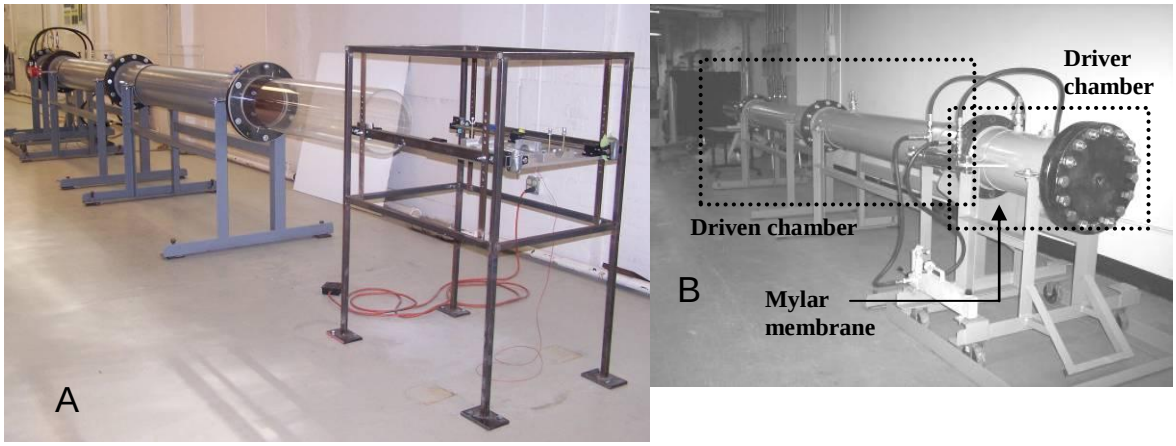

Figure 7: WSU shocktube.
A: Open-end view; B: Driver view.

The expansion section built to accommodate larger specimens is shown in Figure 8. The setup for larger animals consists of the same driver chamber and one section of the steel driven chamber, which is connected to a transition piece and the expansion. The transition piece (Figure 8, Insert A) gradually adjusts the internal surface from a cylinder to a cone, and a two-inch wooden spacer (Figure 8, Insert B), placed at 49 inches from the open end of the expansion,

allows insertion of gages and a suspension system for the specimen. These geometrical differences need to be considered when characterizing the shock wave delivered to the specimen in order to choose the zone appropriate for blast simulation for each configuration.

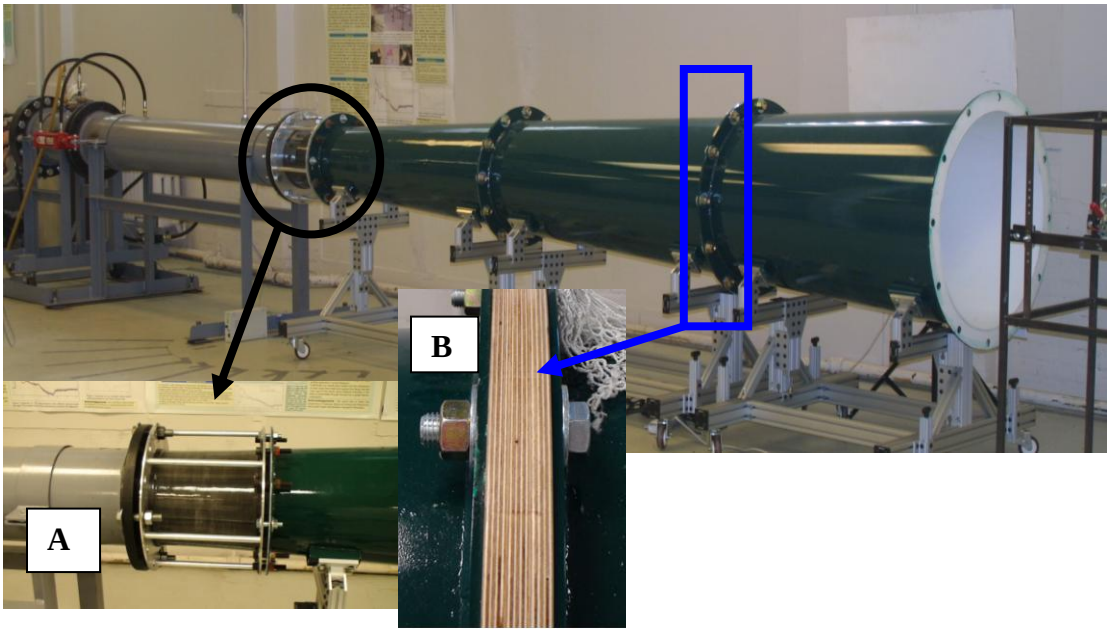

Figure 8: WSU shocktube with expansion.
The Lexan part and one of the steel chambers are removed and replaced by a transition part that leads to the expansion (in green). Insert A: transition. Insert B: 2 wooden spacer.

In characterizing the shock wave created by a shock tube several factors contribute to its qualities. First, a fundamental contributing factor is the maximum pressure the driver structure can achieve, because it determines the maximum peak pressure deliverable by the shock tube. The WSU shock tube has been designed for a working pressure of up to 300 psi in the driver section and a working pressure of up to 150 psi in the driven section (for closed end configuration). Presently, the major limitation to reaching higher driver pressures is the clamping system that holds the membrane, made of Mylar, between the driver and the driven sections.

Other fundamental contributing factors to the properties of the shock wave are the dimensions of the shock tube, because they affect the peak pressure, the duration of the peak plateau, the duration of the positive phase, and the impulse produced. The dimensions of the

cylindrical tube configuration are shown in Figure 9A, while Figure 9B shows the dimensions of the configuration with the expansion. In the cylindrical part, the pressure waveform propagating down the tube can be approximated to a steady wave with constant peak pressure, but not so in the expansion section. Because of its widening geometry, the peak pressure decreases while propagating down the expansion, similar to the quasi-spherical decay rate of actual blast waves. Thus more energy is required in the driver in order to provide an identical peak pressure for a specimen placed in the expansion section versus the cylindrical tube. As an example, to deliver 10 psi overpressure to a specimen in the tube, the driver needs to reach a pressure of approximately 25 psi; but for a specimen to be exposed to the same overpressure in the expansion section, the driver needs to be pressurized to approximately 65 psi.

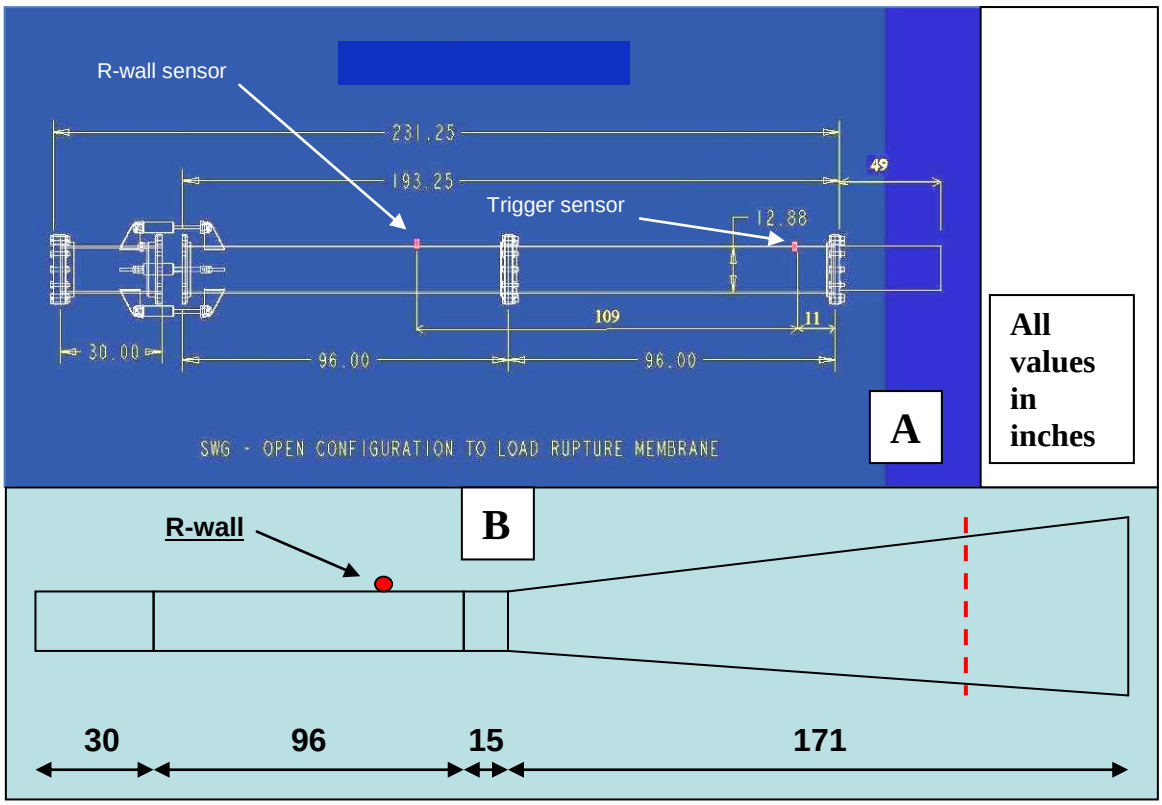

Figure 9 Configurations of the WSU shocktube
A: WSU small specimen shocktube. The inner diameter is 12 inches.
B: WSU tube with expansion. The open end of the conical part has a 36 inch diameter. The dotted red line marks the position of the wooden spacer (49 inches from the open end). Position of the pressure sensor installed in the tube wall is also marked (R-wall).

To control the pressurization of the driver, sheets of Mylar of different thicknesses are used. The mechanical properties of Mylar are such that the pressure required to rupture a Mylar sheet of a given thickness is very consistent. Figure 10 shows how Mylar thickness (1, 3, 5, 7, 10, and 20 mil) has a direct correlation the static peak pressure measured at the trigger sensor (position identified in Figure 9A). The example in Figure 10 was taken from calibration tests performed in the cylindrical tube. The impulse delivered to the specimen is defined as the area under the positive phase of the pressure profile and is directly connected to the peak overpressure value: when pressure increases impulse also increases, as shown in Figure 10.

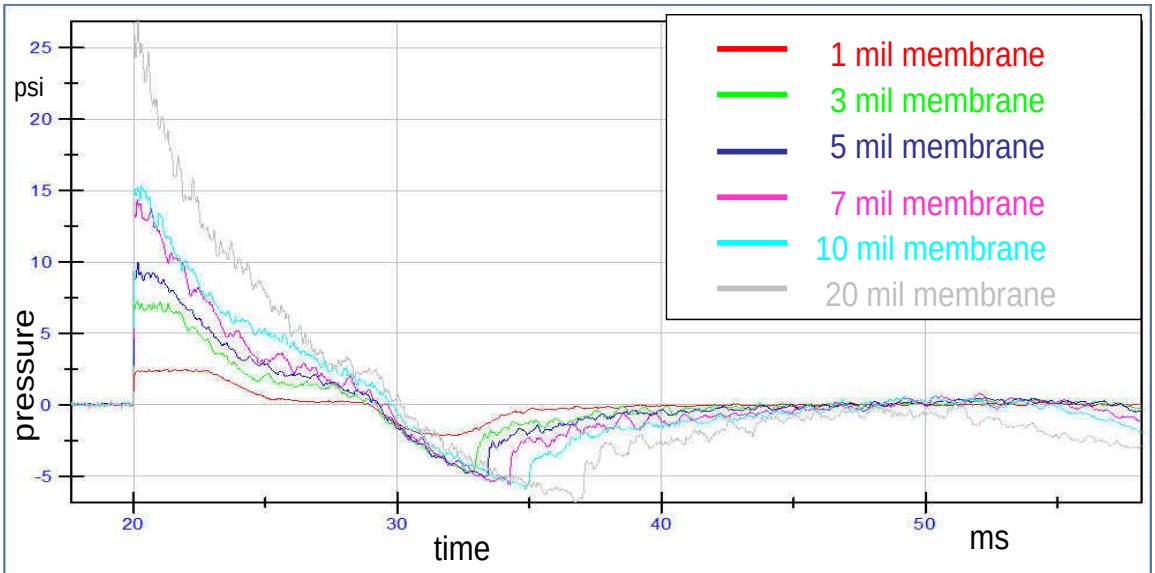

Figure 10: Shock waves with different peak pressures due to the thickness of the Mylar sheet used.
Measurements were taken at the trigger when Helium gas was used in the driver. All recordings were captured by a side-on pressure sensor.

Changing the length of the driver section also has affects the duration and impulse of the shock wave. The rarefaction wave that reflects from the closed end of the driver section propagates down the tube moving in the same direction and faster than the shock front. The shorter the driver section, the earlier the rarefaction wave catches up with the compression wave and reduces the duration of the plateau. In fact, if the driver section is short enough relative to the

position of the pressure sensor, the rarefaction wave may completely overtake the front of the plateau and then start decreasing the peak overpressure, as shown in Figure 11.

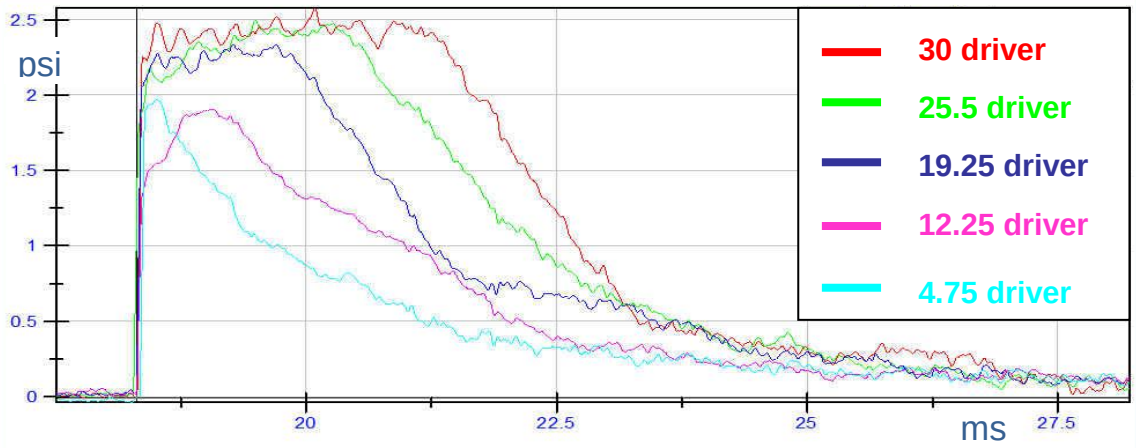

Figure 11: Shock wave profiles (trigger sensor) in the cylindrical shock tube caused by shocks of equal intensity
(1 mil Mylar, compressed He) when changing the length of the driver. The internal length of the driver is expressed in inches. All recordings were captured by a side-on pressure sensor.

Another contributing factor to the reduction of the impulse of the shock wave is the effect of the rarefaction wave generated by the shock front after reaching the open end of the tube. When the compression front reaches the open end of the driven section, the sudden change in geometry produces a rarefaction wave going in the opposite direction of the compression flow (therefore going back into the driven section) and this rarefaction affects the tail of the shock wave. This rarefaction wave coming from the open end of the driven section can be recognized as a change in the slope of the decaying shock wave profile. Figure 12 shows the wave diagram of a shock wave recorded at different location along the tube.

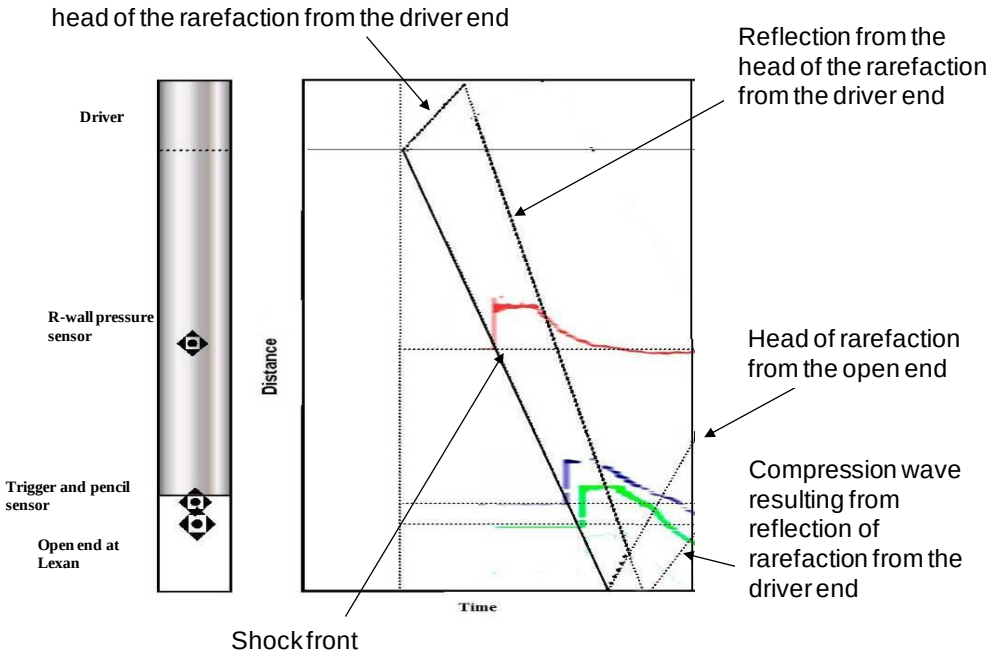

Figure 12: Wave Diagram obtained from one experiment using compressed air in the driver.
The effects on the pressure profiles created by the rarefaction waves from the driver section and from the open end of the tube are shown by the arrows. (courtesy of Dave Ritzel)

Figure 13 shows similar diagrams when helium gas was used in the driver section. Helium is a more efficient gas than air as a shock tube driver gas and provides a higher peak overpressure and shorter peak pressure plateau for the same driver pressure. The effects of the different rarefaction waves on the original compression wave are indicated by the arrows in both figures. The duration of the positive phase of the shock wave is related to sensor position inside the tube (Figure 13). The sensors in both figures are recording static pressure at fixed points along the tube: R-wall at 170 inches, trigger at 61 inches, and pencil at 45 inches with respect to the open end of the tube. Because the test was run in the cylindrical tube the peak overpressure remains quite constant along the three positions as it shows in each pressure profile. The duration of the positive phase, however, is affected by the arrival of the rarefaction wave from the open end of the tube. Since it is a wave travelling upstream with respect to the direction of the shock

front, it reaches each sensor in reverse order and causes a more noticeable decrease in positive phase to the one closer to the end, thereby reducing the impulse for locations closer to the end of the tube. This is one of the features that are entirely atypical of blast waves. In fact the closer the specimen is to the open end, the earlier the blast simulation event becomes atypical.

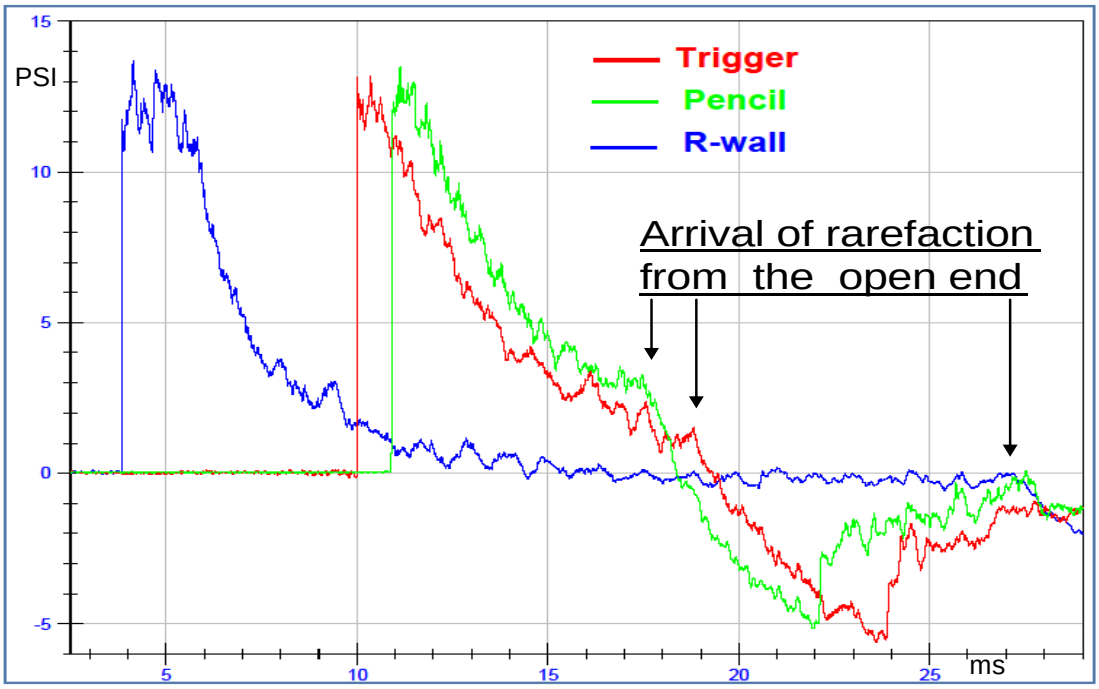

Figure 13: Shock wave profiles at different points along the tube.
Helium gas was used in the driver. All recordings were captured by side-on pressure sensors. Trigger is called the sensor at 61" from the open end of the tube (OET). The specimen position is called pencil in the figure and it is at 45" from OET. R-wall is the sensor at 170" from OET. This is an example of a single test using the tube, at driver pressurization of about 35 psi and at about 13 psi of peak overpressure delivered at the optimized specimen position.

Figure 14 illustrates this problem by providing examples of static pressure recordings for two positions near the end of the tube and one at 45 inches inside: the duration decreases as the distance decreases and even more dramatic is the reduction of impulse. Concurrently to the change in static pressure and impulse, there is a change in the dynamic pressure that cannot be shown by the static pressure sensor. The static and dynamic pressures are now unbalanced and are no longer at the ratio shown in Table 1, which indicates a correct balance for a shock wave. The dynamic pressure, which is associated with kinetic energy of the flow (movement of air particles),

quickly increases and that greatly exaggerates the effects of the blast wind. Meanwhile the static pressure, which is associated with air density, decreases causing the pressure in the environment to drop. In general, the effect of the dynamic pressure is to enhance acceleration-related injuries whereas the static component induces compression-related injuries. For the blast conditions and specimens considered here, there are relatively weak displacement forces. In summary, the specimen placed at the "end of the tube" is subjected to low static pressures and extremely high winds, representing a jet-stream outflow event, not simulating a free-field blast event.

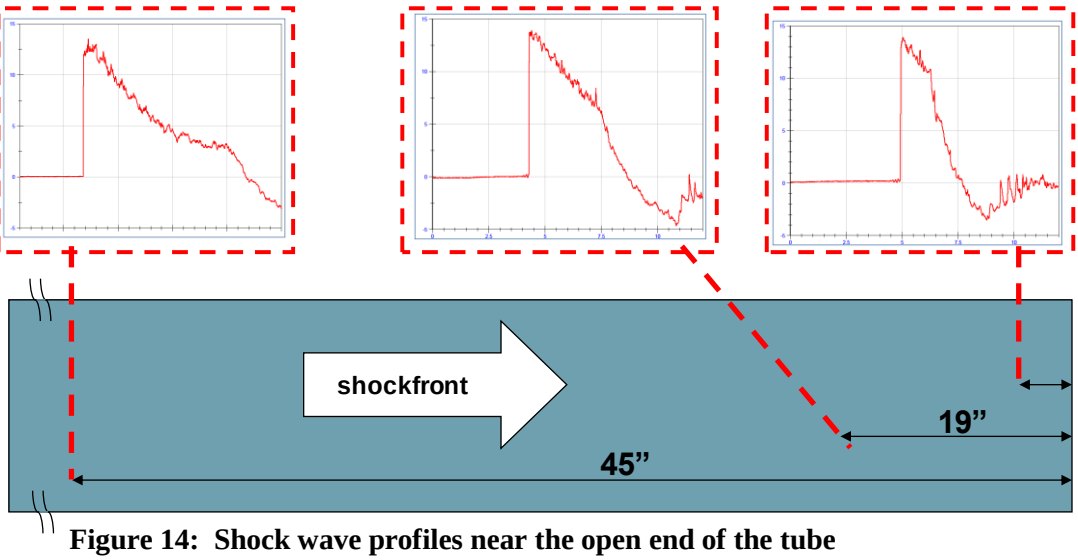

Figure 14: Shock wave profiles near the open end of the tube (7" and 19") and at the location where the specimen is actually placed (45" from the open end). The blue rectangle represents the Lexan portion of the tube.

Since the purpose of the shock tube is to simulate blast wave conditions from a free-field explosion, it is extremely important to consider all the qualities needed (peak overpressure, duration, and impulse) for each test. The location of the test station within the shock tube affects the particular waveform developed and hence the effectiveness of the blast simulation. Although computational fluid dynamics (CFD) was used to predict waveforms within the WSU shock tube, a PCB side-on pressure sensor (PCB Piezotronics Inc., model 137A) mounted on a pole extension was used to confirm the optimal location for the test station. The metal structure seen in Figure 8 in front of the open end of the expansion was used to hold the pole extension. This particular

sensor, called a pencil probe due to its shape, can be centered inside the shock tube as if it were suspended in air. This setup allows recording of the static shock wave profile that a specimen would experience at the chosen position. Figure 15 shows examples of the position of the monitoring station (pencil sensor). For the cylindrical tube configuration, a major concern was to ensure that the specimen could be placed into the Lexan portion of the driven section, to allow monitoring of the blast event. After conducting a series of tests at different pressures the results indicated the best location in the Lexan was 45 inches from the open end, when operating a full length driver (30 inches) and compressed Helium gas.

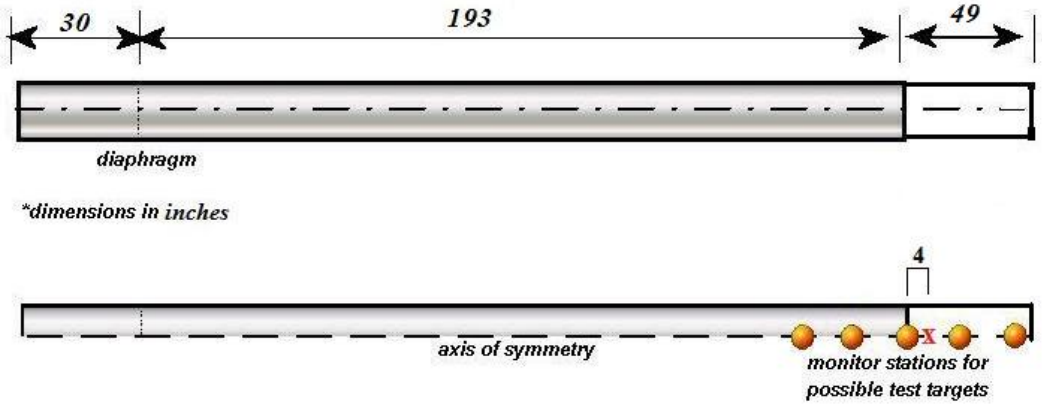

Figure 15: Placement of monitoring stations for evaluation of specimen positioning. The red X indicates the chosen location in the Lexan, 4 inches from the end of the steel tube. (courtesy of Dave Ritzel)

Similar positioning of the monitoring station indicated that the best specimen location for the expansion configuration was at 49 inches inside the expansion. Figure 16 and Figure 17 illustrate results for static and stagnation pressures at the chosen location: the slight increase in slope at the conclusion of the positive phase indicates the arrival of the rarefaction wave. For the expansion configuration, the specimen was located at the position of the wooden spacer (Figure 8 and 9) allowing convenient fixture points and ports for cabling. Figure 18 shows the pressure variations in the expansion due to positioning. The loss of pressure is not dramatic among the three positions and it justifies choosing the location that created the least concern (49 inches from the open end).

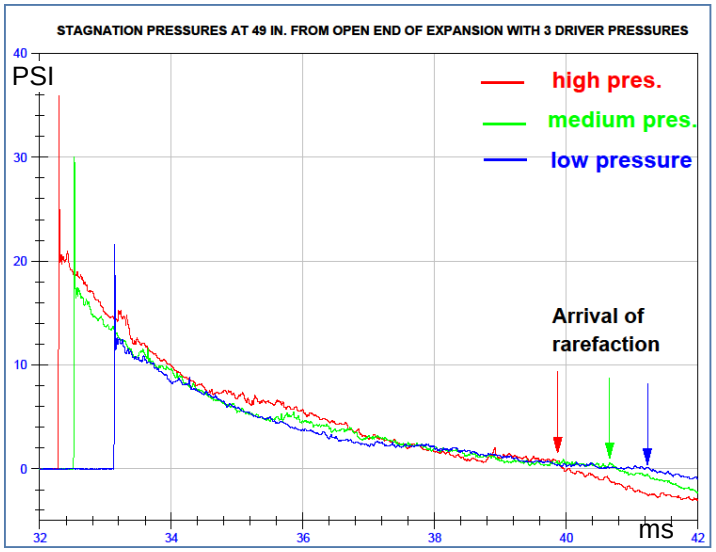

Figure 16: Stagnation pressure profiles at 49 inches from the open end of the expansion. The pressures delivered were around 20 psi for high, 17 psi for medium, and 12.5 psi for low. The frontal spike in each profile shows the reflected pressure value (loading).

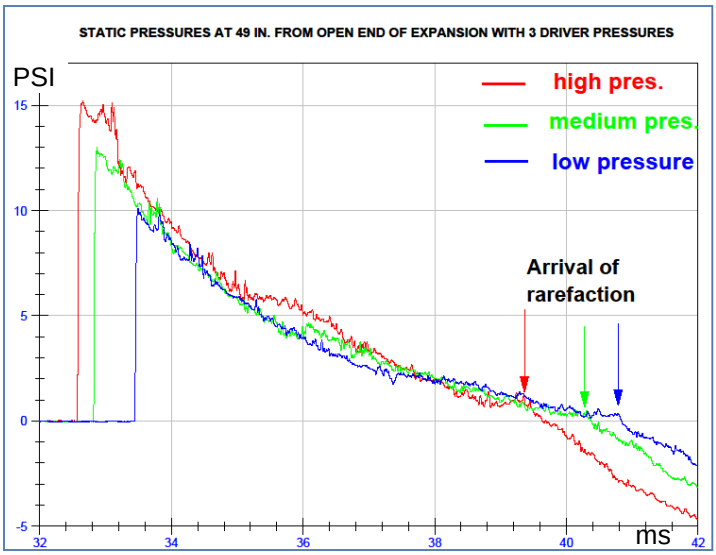

Figure 17: Static pressure profiles at 49 inches from the open end of expansion. The static pressures delivered were around 15 psi at high magnitude (stagnation pressure of 20 psi); 12 psi at medium magnitude (stagnation pressure of 17 psi); and 10 psi at low magnitude (stagnation pressure of 12.5 psi).

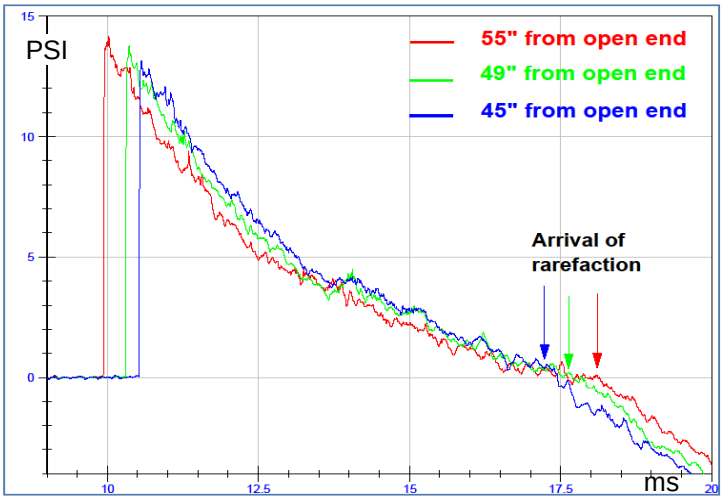

Figure 18: Static pressure profiles at three different locations inside the expansion for the same driver bursting pressure. Location 49" allows installing the specimen suspension system in the wooden spacer, while locations 55" and 45" would force drilling of the steel walls of the expansion. These results proved drilling unnecessary.

In conclusion, to avoid corrupting the experimental conditions, specimen location needs to be in a zone reasonably away from the open end such that the dynamic pressure component of the shock wave flow will be credibly similar to that of free-field blast. Furthermore, if the arrival of the rarefaction wave is near the ending of the shock wave's positive phase, then the pressure data acquired during the positive phase will be representative of a true blast event.

2.3 Testing in shock tube, blast tube, and free-field

A number of significant contributions to the study of shock wave interaction with biological systems have been made since the 1950s. Clemedson was one of the most prolific workers in this area; therefore the next several paragraphs will review his work with various collaborators.

Clemedson reported several experiments pertinent to shock wave transmission in bone and brain tissues using either a blast tube (detonation chamber) or a shock tube; results were also compared to free-field blast testing. By means of a small charge of explosive, a detonation chamber creates a blast wave that transmits inside a structure resembling a shock tube. This structure can be usually closed at both ends, producing a complex wave profile with multiple peaks due to the reflective nature of the apparatus. In 1955, Clemedson and Pettersson observed that shock waves are easily transmitted through bone (unpublished observations referenced in Clemedson (1956a)).

In 1956, Clemedson and Pettersson investigated the transmission of blast waves through different parts of a live rabbit body (skull, right thoracic cavity, abdomen, and femoral musculature). In one setup they introduced a pressure transducer in the brain of dead rabbits and exposed them to blast in a blasting range and in a detonation chamber. The transducer in the brain was inserted in one of two sites: either through the optic foramen or through the foramen magnum (in decapitated animals). The intracranial pressure (ICP) recordings in the brain did not differ significantly between the two insertion sites. In such experiments a pressure sensor was also

placed in the thorax of the rabbits and the recordings looked entirely different from the data recorded in the brain, with peak pressure attenuation of about 50% in the thorax compared to the incident wave and to the recording in the brain.

The authors believed that the incident shock wave energy was transmitted directly to the interior of the body and the shock wave was transformed into a pressure wave. The relative homogeneity of the brain tissue, according to their interpretation, did not significantly modify the pressure wave, while the inhomogeneous thoracic structure with its many air-filled regions, dramatically changed the wave in the lungs. They concluded that, regardless of the wave qualities, relative homogeneous tissue, such as the brain, only slightly modified the blast wave, while tissue with higher elastic and damping properties, such as the lungs, caused marked distortion of the blast wave (Clemedson and Pettersson 1956). In these experiments the animals were anesthetized and exposed to a blast wave either in a detonation chamber or in a blasting range (free-field blast). Recording of the blast waves, both in air and within the animal's body, was achieved by means of barium titanate pressure transducers (30 mm in length, 9 mm in diameter). Because of the size of the pressure transducer, recording in the brain had to be performed on dead animals.

Similar experiments with transducers in the brain of dead rabbits were conducted in 1956 by Clemedson to investigate the transmission of air blast waves to the central nervous system (Clemedson 1956a). The animals were placed in a detonation chamber that delivered a multiple peak wave, whose first peak was almost 20 psi and had a positive phase 5 ms long. The transducer was inserted into the brain through the optic foramen after removal of the eye. In order to evaluate the possible ways a blast wave may reach the brain, the animals were exposed to the blast in the following manners: whole body exposure; body exposure with head protected; head exposure with body protected; and whole body protected during blast (to test the effectiveness of the protections). When only the head was protected there was some pressure transmitted to the brain, although the pressure oscillations were much smaller than in air. Moreover some of the

experiments investigated possible shock wave transmission through the spinal column and through the blood vessels. By means of a rubber band, the blood vessel of the neck were compressed to interrupt vascular communication from the thorax to the brain. When these animals were subjected to shock waves the recordings in the brain did not differ significantly from the results obtained from animals that had intact vasculatures.

To explore the possibility of shock wave transmission through the spinal cord, a sensor was placed in the lumbar region and for comparison another one was placed in the abdominal cavity at the same levels. When the neck and trunk were protected during the blast the sensor in the abdominal cavity did not record any change in pressure, while the sensor connected to the spinal cord showed a small increase in pressure. This finding could only be explained by a pressure wave propagating from the brain down the spinal cord. In order to test if there could be transmission from the spinal cord up to the brain, some animals had the spinal column completely separated at the cervical level and they were tested with the head protected. A comparison between animals with an intact spine and this last group indicated that there was no significant pressure transmitted from the spine to the brain. The authors concluded that the main part of the shock wave pressure recorded in the brain was transmitted directly through skull exposure and only some insignificant contribution to the ICP was possibly coming from blood vessels and spinal cord.

In 1961, Clemedson and Jonsson investigated the transmission of elastic disturbances in different part of a living body (Clemedson and Jonsson 1961b). Anesthetized rabbits were exposed to blast in a detonation chamber left open on the opposite side of the charge; therefore the blast wave possessed only one peak. Small zirconate titanate pressure transducers (18.5 mm in length, 2.4 mm in diameter) were placed in several area of the body including in the skull, between the bone and the brain. Because of their smaller size, the transducers in the body were able to record the internal pressure with less distortion than in previous experiments and they revealed that the transmitted wave had a slower rise time and a lower peak overpressure value

than the incident wave. The authors suggested that the changes introduced in the original blast wave were mostly due to the inhomogeneous composition of the body. Also in 1961, Clemedson and Jonsson studied the propagation of the blast wave in bone and noted that the pressure wave undergoes a considerable change through reflection and scattering when propagated through bone tissue (Clemedson and Jonsson 1961a). The bone specimens came from an ox and a horse and samples were exposed to blast in a detonation chamber open at the distal end. The authors concluded that reflection of the shock wave was linked to the acoustical impedance of the medium (i.e. bone versus gelatin) and the amplitude of the transmitted wave was dependent on the physical properties of the medium and the size of the front surface.

In 1961, Romba and Martin studied the transmission of a shock wave into the skull and brain tissue of adolescent Rhesus monkeys. Dead monkeys were exposed to blast at an explosive test site. The authors investigated four conditions for exposure: (a) entire body exposed to the blast; (b) a portion of the head exposed to the blast (rest of the body is protected); (c) head only exposed to the blast; and (d) torso only exposed to the blast. Their study found that shock waves do propagate through the skull into the brain and, compared to the outside overpressure, they found amplification of peak ICPs in agreement with Clemedson's studies. They also found that some ICP was occurring when only the torso was exposed to the blast, although it was greatly reduced (Romba and Martin 1961).

In 1996, Cernak et al. studied the cerebral responses in live rabbits exposed to a focused shock overpressure causing moderate pulmonary shock injury. Rabbits were subjected to pulmonary deafferentation and then compared to a group whose nerves were left intact. The authors concluded that vagal afferent nerves play an important role in modification of the general and local responses that arise during a pulmonary shock injury. Moreover they suggested that the observed functional changes in the medulla oblongata may be the consequences of afferent neural impulses from the injured region (lungs) rather than consequences from ischemia, energy transfer to the brain, or both (Cernak et al. 1996).

In 2001 Cernak et al. investigated whether whole-body or local (chest) exposure to shock overpressure can induce ultrastructural, biochemical, and cognitive impairments in the brain of rats trained for an active avoidance test. They found that all rats revealed significant deficits at first (3 hours after blast), but only the rats subjected to whole-body shock wave had persistent deficits (5 days after injury) (Cernak et al. 2001). Strictly from the injuries observed in her studies without monitoring internal pressure in the blood vessels of the neck, Cernak revisited a theory first postulated in World War I. Cernak's hypothesis was that the shock wave transmits kinetic energy to the torso, causing ripple waves to reach the brain through the main blood vessels and leading to neurological damage as it was described by Bhattacharjee (2008).

In 2000 Axelsson et al. examined respiration, circulation, and brain activity in pigs exposed to a blast wave in a blasting range. The blast was moderate and exposure caused intestinal injuries, but no lung damage. There was a momentary depression of cortical activity (up to 15 seconds of transient flattening of the electroencephalogram) accompanied by short lasting apnea. These effects indicated that the blast wave affected the brainstem and/or a higher controlling center (Axelsson et al. 2000).

In 2000 Blix et al. presented a study on the effects of grenade harpoons on the killing of whales using a pig-model (Blix et al 2000). The authors concluded that the shock effect on the brain by the blast was relatively minor and that death was due to hemorrhaging. Their conclusion was later contradicted by another study on whales by Knudsen and Oen (2003). Knudsen and Oen examined the brains of 37 minke whales hunted using fire harpoons tipped with a grenade. They concluded that even if several vital organs were fatally injured, the neurotrauma induced by the blast waves was the primary cause for the rapid loss of consciousness and death (Knudsen and Oen 2003).

Using a shock tube, Chavko et al. (2007) investigated ICP changes in the brain of rats exposed to shock waves. Three days prior to testing a cannula was inserted in the brain of each rat (0.9 mm posterior from bregma and 1.5 mm lateral from midline) at 3.5 mm below the surface

(third cerebral ventricle). The day of the test, the rats were anesthetized with an intra-peritoneal injection of ketamine-xylazine and an optic pressure sensor (FOP-MIV, FISO technologies, Quebec, Canada) was placed in the cannula. The rats were exposed to a weak shock wave (about 6 psi) with positive phase duration of 4.5 ms. Two orientations were tested: head facing the shock wave, and right side exposed to the shock wave. The authors found that shock waves were transmitted inside the brain with negligible attenuation of the magnitude and that the wave profile depended on the animal orientation (Chavko et al. 2007). Unfortunately the authors did not provide details either on the location of the specimen in the tube, or the method used to mount and seal the ICP sensor in position on the rat's skull (problem known to affect measurements), or the number of animals used.

In a most recent study Chavko et al. (2011) investigated the relationship between the orientation of the blast and propagation of the shock wave inside the rat brain. The ICP sensor was placed into a lateral ventricle and each rat was exposed to low shock waves (about 4.5 psi) in three different orientations: head-on, side-on, and backward. The authors concluded that there are different patterns and durations of the pressure traces (profiles) inside the brain depending on the rat orientation to the blast, with frontal exposure providing the highest amplitudes and longest durations. The authors did supply the location of the animal holder (about 12 inches inside the tube), and unfortunately it is not in an appropriate zone to simulate free-field conditions due to end-wave effects. The authors also provided pictures that show the positioning of the rat's head in the three orientations, which seem to reveal a potential discrepancy in head location within the tube among the three orientations. Furthermore, the ICP profiles, provided as examples to confirm their conclusions, closely resemble the overpressures that would be measured in air at 6, 9, and 12 inches inside from the open end of the tube. These findings together with the fact that the authors make no mention of being aware of changing overpressure conditions at the end of the tube, suggest caution when comparing data results from this study.

Saljo et al. (2008) exposed pigs to blast overpressure in different scenarios: although the main purpose of the study was to investigate the effect on the brain of multiple blast exposures as they occur in soldiers operating howitzers, bazookas (recoilless rifles) and other weapons. Other experiments are also described that involved using a shock tube for exposing swine to localize shock wave insult and for whole body exposures in rats. Further, pigs were exposed in under-water blast experiments. In all these cases, ICPs were recorded using hydrophones in pigs and Samba optic sensors in rats. In pigs selected for local exposure tests, pressures in the abdomen, thorax and neck were also measured. The shock tube used was 8 inches in diameter, and the length of the driver and driven sections were 59 and 63 inches respectively. The placement of the animals with respect to the shock tube muzzle appears incorrect for both the local exposure in pigs and the body exposure in rats. For the size of the tube used, the rats were placed too close to the open end, at 25 cm (10 inches) inside the tube, with the body perpendicular to the arrival of the shock front and they were exposed to 10 or 25 kPa (1.45 or 3.63 psi). The pigs were placed outside the tube, with the abdomen at approximately 8 inches from the open end and then with the top of the head at 8 inches from the open end. The measured static air overpressure inside the tube was around 4.35psi and outside the tube on the side was about 2psi. The results of the ICP measurements suggested direct pressure transmission to the brain and discounted significant transmission within the body, and the authors concluded that their data corroborated results in other studies such as Clemedson (1956a) and Chavko et al. (2007). Adding to the incorrect placement of the animals, of scientific concern is the fact that the authors stated: "the results of Chavko et al. (2007) support the present results on brain air ratio for the maximal peak pressure and contradict the possibility of a pressure leakage around the implanted hydrophones".

Dal Cengio Leonardi et al. (2011) recorded ICPs in anesthetized rats during head-on exposure to blast. The rat's head was placed at 44 inches inside from the open end of the tube and an optic pressure sensor (FISO Technologies) was used for ICP recordings. Results demonstrated that proper sealing techniques led to a significant increase in ICP values, compared to the outside

overpressure. Further, these values seem to have a direct relation to a rat's size and age: heavier, older rats had the highest ICP readings. These findings suggest that a global flexure of the skull by the transient shock wave is an important mechanism of pressure transmission inside the brain. The authors explain that transosteal propagation should cause the thicker skulls to have lower ICP values; therefore the higher pressures should be seen in the younger rats. Instead, global flexure validates why the younger rats had lower ICP values. When pressure is exerted on the skull of a young rat, the more flexible, pliant structure is capable of deforming more easily than an older, more rigid skull. Since pressure is a force applied to a surface, the ability to increase even slightly the surface value due to a more flexible material (e.g., bones and suture lines), allows the younger rat to keep the ICP at a lower value. Thus, the deformation allows dissipation of some of the pressure that otherwise would build inside (Dal Cengio Leonardi et al. 2011).

CHAPTER 3

3.1 Introduction

Animal testing in the blast environment can provide important information on the response of biological systems after exposure to blast, and the acquired knowledge could ultimately be applied for the advancement of medical therapies for humans. However, it is important to understand that animals cannot offer a complete picture regarding the mechanism of brain injury due to blast. Although the biology of mammals is very similar, the anatomical structures of the human skull and brain are very different from other animals: for example in terms of thickness of the skull, shape of the skull and brain, and brain size in comparison to other body organs. All of these characteristics are important factors to consider when investigating how a blast wave affects the intracranial structures. Furthermore, very small animals such as rats and mice present a particular scaling challenge, as their size is a fraction of the human body; the scale of the head relative to the blast wave-length is likely of consequence. This problem justifies the search for better alternatives when attempting to unravel the complexity of the mechanical response of the skull/brain system to blast loading. This chapter presents some of the attempts made to help identify the primary components of such response through the use of surrogates of the human body and of computational models. However, to date, physical experiments have not yet validated either appropriate surrogates of the human skull/brain system for blast research nor computational models of skull/brain interaction during exposure to blast.

3.2 Anatomy of the human skull and brain

In order to understand blast wave interaction with the head it is important to know the basic anatomical properties of the human head. The scalp consists of skin and subcutaneous tissue that extend from the superior nuchal line on the occipital bone to the supraorbital margins of the frontal bone (Figure 19). It consists of 5 layers, three of which are bound together as a single unit and constitute the scalp proper (Moore and Agur 2002).

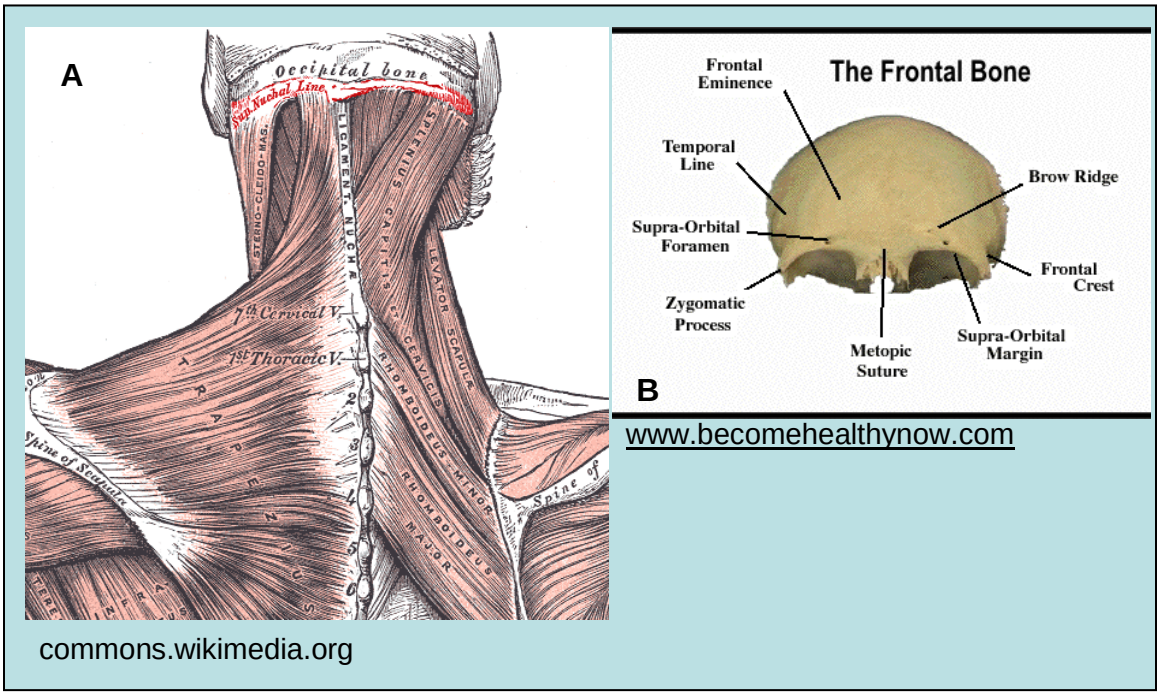

Figure 19: Scalp boundaries. A: Superior nuchal line; B: Supra-orbital margins.

The skull is a structure composed of many bones and divided into two parts: the cranium, which accommodates and protects the brain; and the face, which contains the orifices of the mouth, the nose, and the orbital cavities. The thickness of the different bones can vary from 5 mm to 8 mm with an average thickness of 6 mm. The cranium is mainly composed of flattened bones that are immovably joined together and create an effective shield that fully encloses the brain. However the superior orbital fissures and the optic foramen provide considerable frontal access to the brain directly through soft tissues (Figure 20).

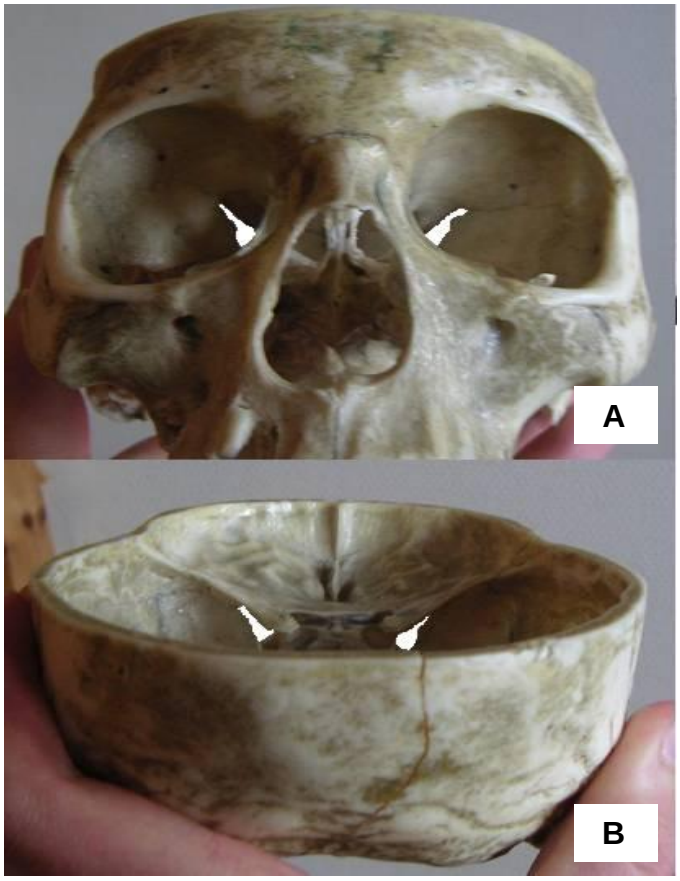

Figure 20: Superior Orbital Fissures (SOF).
A: Frontal view of SOF highlighted in white;
B: View from inside the cranium of SOF highlighted in white. (upload.wikimedia.org)

The superior orbital fissure is a cleft between the greater and the lesser wings of the sphenoid bone through which pass the lacrimal nerve, the frontal nerve, the trochlear nerve, the superior ophthalmic vein, the superior and inferior branches of the oculomotor nerve, the abducent nerve, and the nasociliary nerve. It measures about 18 mm in length and its width varies from about 2 mm to 10 mm, with the superior portion being narrower (Figure 20). The optic foramen is located in the lesser wing of the sphenoid; it conveys the optic nerve and the ophthalmic artery; in adults, it is about 6 mm in diameter.

Inside the cranium, the brain is surrounded by the cranial meninges, a group of three membranes layered together that contain the cerebrospinal fluid and form a supporting structure for the arteries, the veins, and the venous sinuses supplying the brain. Once the meninges are

removed, the cerebral cortex is exposed (Figure 21A). The cortex is the outer shell of the two hemispheres of the cerebrum, consisting of grey matter 2-4 mm thick. The cortex is divided in four lobes per hemisphere; each lobe is named after the skull bone covering it: frontal, parietal, temporal, and occipital (Figure 21B).

The frontal lobes occupy the front part of the brain behind the forehead and are associated with judgment and decision making skills. The frontal lobes are the portion of the brain more closely linked to control of conscious response and in the human species the frontal lobes account for 29% of the cerebral cortex, as opposed to only 3.5% in rats and 17% in chimpanzees. Below the cortex there is an inner layer composed of white matter, which makes up the bulk of the cerebrum and overlies another layer of grey matter cell clusters, called the subcortical nuclei (basal ganglia). The corpus callosum is also part of the cerebrum and consists of a thick bundle of nerve fibers that connects the two cerebral hemispheres. The diencephalon is located below the corpus callosum and above the brain stems; it surrounds the third ventricle and it is mostly composed of grey matter. The thalamus, the hypothalamus, and the optic tracts are parts of the diencephalon. Among other things the diencephalon controls emotional responses, sleep and wakefulness, and production of various hormones.

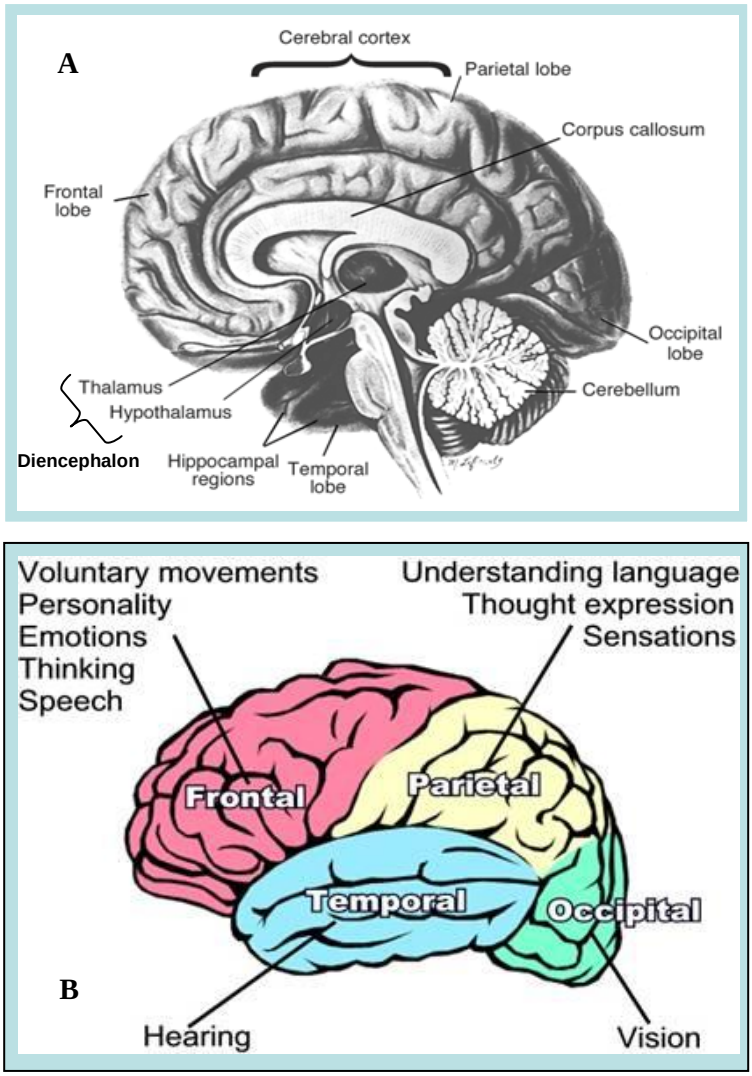

Figure 21: The brain.
A: Open view to show the brain structures (http://www.niaaa.nih.gov/NR);
B: Functional areas of the brain (http://www.agrabilityproject.org)

An adult human brain weighs about three pounds (1300-1400 grams), it occupies a volume of about 1400 ml, not including blood and cerebrospinal fluid, and its normal ICP is between 150 and 180 mm of water (between 0.213 psi and 0.256 psi). The total intracranial contents by volume are around 1700 ml, where roughly 80% is brain (1400ml), 10% is blood (150ml) and the other 10% is cerebrospinal fluid in the ventricular system (Blinkov and Glezer 1968; Renghachary and Ellenbogen 2005). The ventricular system of the human brain is mainly composed of four ventricles: two lateral ventricles and two midline ventricles (Figure 22). The

lateral ventricles (1st and 2nd ventricles) have a C-shape and wrap around the dorsal part of the basal ganglia within each cerebral hemisphere. The lateral ventricles communicate with the 3rd ventricle, located centrally below them, through the interventricular foramina. The 3rd ventricle is a slit-like cavity surrounded by the diencephalon; through the cerebral acqueduct, it connects inferoposteriorly to the 4th ventricle. Three apertures (foramina) connect the 4th ventricle to the subarachnoid space, permitting the circulation of the cerebrospinal fluid (CSF) to the brain stem, cerebellum, spinal cord, and cerebral cortex; in fact the function of the CSF is nutritive as well as protective, by cushioning the brain inside the cranium. In 2006 an imaging study by Zhu et al. determined that the average CSF volume contained in a normal adult's lateral ventricle is around 10 ml (Zhu et al. 2006); the ventricular system's internal pressure measures between 4.4 and 7.3 mmHg (between 0.085 psi and 0.141 psi).

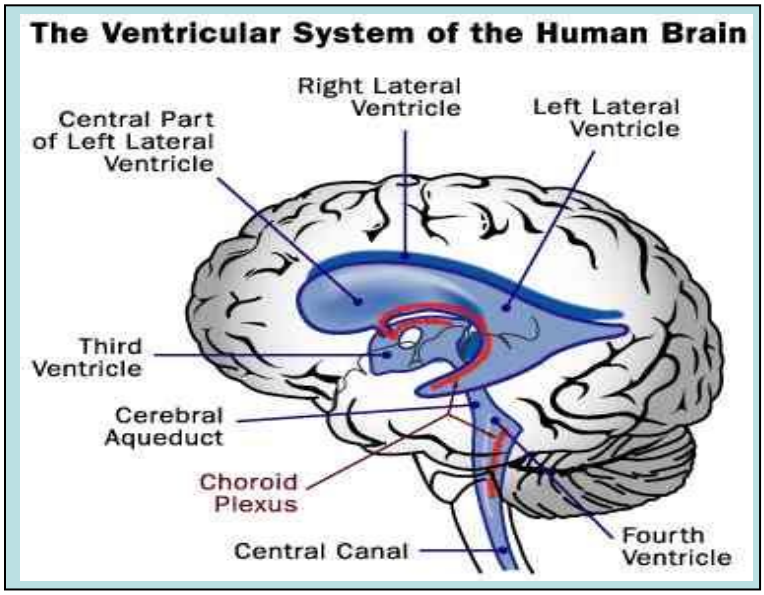

Figure 22: The ventricular system of the brain
http://www.solarnavigator.net/human_brain.htm

3.3 Brain and skull surrogates and models

While the evolution of car-crash research developed human surrogates, anthropomorphic test devices (ATDs) or "crash test dummies", to be used in car-crash testing after extensive testing with cadavers, blast research attempted to advance without the use of cadavers. ATDs developed for automotive testing were also recruited for blast testing. The major limitation of these dummies is the fact that they collect only acceleration measurements, not pressures or other values of relevance during a blast event. Therefore an attempt was made to create more appropriate surrogates for blast research following the example of physical model in other fields of study, mainly blunt trauma and ballistics. These models tried to reproduce the skull/brain system more closely and could also integrate pressure sensors, but the difference in materials used and degree of model-fidelity produced contradictory results. Recently computational modeling has offered a new approach to the study of blast injuries, but as all the other models, computational models lack one essential part: experimental validation. This section presents a brief summary on proposed models and some cadaveric results that may be relevant for blast testing. To our knowledge, the cadaver study presented in Chapter 6 is the only study of its kind for blast research and it will provide crucial information to validate physical and computational models in this field.

A few studies investigated the effect of blast using anthropomorphic test dummies. Dionne et al. (2004) used Hybrid II dummies instrumented with a tri-axial cluster of linear accelerometers in the head. Three different blast conditions were investigated at a blasting range: first, a 5.1 kg C4 charge located 1 m from ground level was detonated with the dummies standing 3 m from the charge; second, a 10 kg C4 charge located 1 m from ground level was detonated with the dummies standing 3 m from the charge; third, a 0.567 kg C4 charge placed at chest height (0.7 m) was detonated with the dummies kneeling at 0.6 m from the charge. This last situation was designed specifically to reproduce a close-range blast. Tests were carried out with dummies either unprotected or fully protected (wearing explosive ordnance disposal, EOD, suits). The authors evaluated the applicability of the Head Injury Criterion (HIC) for blast scenarios and

confirmed its validity for well-protected individual (average head acceleration was found more appropriate for the unprotected person) (Dionne et al. 2004).

In a follow-up study, a new correlation between blast impulse and blast-induced head acceleration was developed and subsequently used to generate charts on blast-induced head acceleration injury that considered the size of the explosive charge and the standoff distance and looked at the probabilities of survival (Dionne et al. 2006). Because the charts were expressed in terms of probabilities of survival, they allowed a direct comparison to the Bowen curves for chest overpressure injuries. The Bowen curves predict probability of survival for blast lung injury based on the peak side-on overpressure and the duration of the positive phase of the blast wave. Since peak overpressure and positive phase duration are functions of charge and distance, the Bowen curves can be expressed in terms of explosive charge and standoff distance. The two charts were merged and this approach revealed that head acceleration injuries would be dominant for a larger blast-induced impulse (larger explosive charges at larger standoff distances) as opposed to chest overpressure injuries being dominant for higher pressure peaks (lower explosive charges at lower standoff distances). The authors suggested scenarios where the slowly-decaying impulse loading may explain the current high occurrences of TBIs in the military. Due to the use of Hybrid-II dummies without advance simulation of neck articulation, and the unusual blast exposures from height-of-burst explosions, the conclusions from the Dionne's studies are limited.

In 2007, Mott et al. used Hybrid III dummies to evaluate the pressure fields surrounding the head when wearing a helmet (Mott et al. 2007). The sensors were placed along the forehead, the ear, rear, and at the crown of the head; in addition the dummy's head was instrumented with a tri-axial cluster of accelerometers. Tests showed that the greatest attenuation of pressure was noted at the rear sensor in back-facing trials and the authors concluded that a different mechanism other than direct transmission of the blast wave through the helmet was at play.

Currently the literature provides validated physical models for ballistic and blunt scenarios, but lacks information for blast. Thali et al. (2002) proposed a head physical model that

has been validated for both ballistics and blunt impact (Thali et al. 2002a; Thali et al. 2002b). The research was carried out to achieve a biofidelic response for blunt trauma and ballistics: it incorporated skin simulating material (a silicon cap containing synthetic fibers to simulate the collagen and fat of the scalp), artificial skull (a layered polyurethane sphere), and a surrogate brain material (ordnance gelatin, 10% at 4˚C). Morphological findings were comparable to real cases, but no biomechanical data were measured. The bone surrogate material described was made by Synbone AG (Neugutstrasse 4, CH- 7208 Malans, Switzerland), a company that manufactures surrogate bones from specially formulated polyurethane foam, comprising of a cancellous inner core and a harder outer shell simulating cortical bone. The company discloses that the surrogates do not possess all the same biomechanical properties of natural bone, although they have been successfully tested in ballistic experiments and have very favorable feedback from a number of biomechanical testing facilities that compare artificial bone with real bone. At the moment, Synbone spheres represents the best option for a simplified surrogate skull providing a generic hollow sphere, 190 mm in diameter and a choice of 5, 6, or 7 mm shell thickness.

Presently there are not many options for credible brain surrogate materials, as well. Ordnance gelatin is commonly used as a muscle simulant and some authors have used it as a brain surrogate. Brands et al. (1999) did not find it suitable as a brain material, suggesting that Sylgard 527 A&B was a better alternative in certain conditions.

To study the biomechanics of ballistic brain injury, Zhang et al. used Sylgard 527 A&B (mixed at a one to one ratio) in their trials and reported that it was an appropriate simulant for ballistics (Zhang et al. 2005). Zhang et al. also compared two head models made with an acrylic globe and filled either with 10% gelatin or Sylgard 527 A&B: they found Sylgard 527 A&B to be more appropriate to simulate ballistic injury (Zhang et al. 2007).

Ivarsson et al. (2000) created a more sophisticated head model for blunt trauma. It consisted of a non-homogeneous surrogate brain containing lateral ventricles: Sylgard 527 A&B was the brain simulant, while the ventricles were elliptical inclusions filled with liquid paraffin

(Ivarsson et al. 2000). The models, with and without ventricles, were exposed to angular acceleration and it was determined that the lateral ventricles played an important role as strain relievers, providing natural protection against brain injury during head rotation.

A review of headform development commissioned by Defense Research and Development Canada in 2007 suggested that presently Sylgard 527 A&B appears the best candidate to mimic brain matter (Fournier et al. 2007). Additionally, it was suggested that the cerebral vasculature may influence the deformation response of the brain, since blood vessels are more rigid than cerebral tissue and they are likely to stiffen the mechanical response of the brain.

Some studies have investigated the structural influence of the vasculature both in physical and computational models, with contradictory results (Ho and Kleiven 2007; Parnaik et al. 2004; Zhang et al. 2002). In 2004, Parnaik et al. compared the peak maximum principal strain (translational scenario) and the peak maximum shear stress (rotational scenario) for two physical models that used silicon gel as the brain simulant, an aluminum cylinder as skull simulant, and silicon tubing as blood vessels surrogate (for the model with vasculature). The model had limited biofidelity and results suggested that the structural influence of the vasculature was limited (Parnaik et al. 2004).

In 2002, Zhang et al. created some computational models that were more elaborate than Parnaik's physical model. The authors compared a finite element model that included the skull, dura mater, cerebrospinal fluid, tentorium, brain tissue, and the parasagittal bridging veins to one that also had the major branches of the cerebral arteries. The study compared the dynamic response of both brain models when subjected to anterior-posterior linear acceleration and a flexion-extension angular velocity pulse. The simulation results suggested that the vasculature should not be ignored in TBI modeling (Zhang et al. 2002). However, in 2007 Ho and Kleiven looked at the dynamic response of the brain with vasculature in a three-dimensional computational study. The head model included the scalp, skull, brain, meninges, cerebrospinal fluid, spinal cord, and major arteries and veins (for the models with vasculature); translational and

rotational loading scenarios were compared for a 3D model without vessels, for a 3D model with linear elastic vessels, and for a 3D model with non-linear elastic vessels. The simulation results indicated that the influence of the vasculature on the dynamic response of the brain is minimal and the authors suggested scaling the stiffness parameters in the composite properties of the brain tissue in order to include the small stiffness contribution of the blood vessels (Ho and Kleiven 2007).

As computational modeling showed the ability to increase the elaboration of computer-models to a greater degree than any physical model, the biofidelity of computer simulations needed to be improved by adopting more precise mechanical properties of the imitated tissues.

Several authors (Prange and Margulies 2002; Shuck and Advani 1972; Takhounts et al. 2003) looked at the mechanical properties of brain tissues and concluded that fresh human brain tissue is stiffer than porcine or bovine brain tissue in the same test conditions, but it is considerably less stiff than human brain tissue days after death.

Several studies in vivo and in physical and computational models looked at the dynamic characteristics of the human skull and brain as pertaining to the skull's natural frequencies (Franke 1956; Hakansson et al. 1993; Khalil et al. 1979; Ruan and Prasad 2001; Su 1981; Stalnaker et al. 1971). Franke measured the mechanical impedance of the human skull in dry skull, cadaver head, and living subjects (Franke 1956). The author looked at the mechanical impedance when a vibrating pistol was maintained in contact with the frontal bone and the occipital bone was mounted against a small rigid support. Franke reported that the lowest resonant frequency of the dry skull was approximately 800 Hz; when the skull was filled with gelatin the lowest frequency was reduced to 500 Hz. The cadaver head was tested after removing the skin and two frequencies were noticed: a highly damped lower frequency of 600 Hz and another frequency at approximately 900 Hz. For living subjects, the lowest frequency was approximately 600 Hz.

In a different study Stalnaker et al.(1971) used an electromagnetic shaker to determine the resonant frequencies of fresh non-embalmed cadaver heads and found a frequency at approximately 800 Hz. The shaker was attached to the parietal bone and the response was monitored at the opposite parietal bone. The authors reported that the removal of the scalp and the cranium contents did not significantly affect the resonant frequency.

Using a minicomputer-based laboratory equipment, Khalil et al. studied the vibrational characteristics of two human dry skulls: the first skull represented the 50^{th} percentile adult male, and the second the 5^{th} percentile adult female (Khalil et al. 1979). The lowest frequency of the first skull was 1385 Hz, and for the second skull the lowest frequency was 1641 Hz. The authors recognized that this was a limited study but suggested that the vibrational pattern of the human skull seem unique to the particular skull and was not influenced by sutures.

Hakansson et al. (1994) measured the resonant frequency of the human skull in living subjects. The in vivo study found that 972 Hz is the average lowest frequency and 1230 Hz is the second lowest frequency for the human skull. The authors could not find an obvious relation between skull size (width and circumference) and first resonance frequency. They concluded that it was probable that other properties, such as bone thickness and stiffness, as well as size, determine the resonance frequencies of the human skull.

In 2001, Ruan and Prasad measured the frontal bone thickness in 7 cadavers and created a computational model to look at the effects of skull thickness variations on the dynamic impact response of the human head. They found that increase thickness of the skull decreased skull deformation and there was a substantial reduction in shear stresses and coup pressures (pressures that occurs at the site of the initial loading) between the thickest and the thinnest skulls. However brain countercoup pressures (pressures that occur at the site opposite to the initial loading) increased as skull thickness increased.

Engin (1969) investigated the dynamic response of a fluid-filled spherical shell in a theoretical model. In his work, he described a mathematical simulation that only reproduced a

local loading pattern; however, he demonstrated the importance of accounting for coupling of the fluid with the shell and, secondly, the elasticity of the shell in the coupled response.

In 1981, Su studied the effects of viscosity on the free oscillations of fluid filled spherical shell and concluded that the natural frequencies of the shell decreases with higher viscosity values.

Moss et al. (2009) created a computational model of a simplified human head to compare the mechanical response of the brain either during impact (compatible with a motor vehicle accident) or blast (charge size and stand-off distance equivalent to a non-lethal exposure of 100kPa). The model has not been validated experimentally. The simulations indicate dramatically different loading modes in the two cases: even a low blast generates flexural ripples in the skull. From the blast simulation is skull flexure that produces most of the mechanical load in the brain, and not head acceleration (impact case). A simulation with increased skull stiffness reduces shear strains, pressure gradients, and peak pressure. Skull flexure persisted even after parameters were altered such as orientation of the blast, insertion of holes in the skull, and modified material and mechanical properties for the skull and brain.

In the computational model by Nyein et al. (2010), the effects on the brain of the Advanced Combat Helmet (ACH) and a conceptual face shield during a blast event were explored. The blast wave was seen investing the face and entering the brain primarily through the soft tissues and compared to the unprotected head the head with helmet experienced a slight mitigation of intracranial stresses. These results have not been validated experimentally.

Chafi et al. (2010) developed a computational model to assess the biomechanical response of human brain in the first 5 ms of exposure to blast wave (Chafi et al. 2010). Their model, which was validated only against impact loadings of cadaveric specimens, predicts that higher ICP will correspond to increase magnitude of explosion, when keeping the head stand-off distance constant. According to the model, peak positive ICP occurs at the coup site, while peak negative ICP occurs at the countercoup site, but both positive and negative pressures develop at

the impact site as well as at the opposite site, creating tension and compression phenomena at the sites. The authors state that the pressure gradient may play an important role in the causation of brain injury. Furthermore, the first peak is followed by lower peaks that the authors attribute to translational and rotational movements of the brain. The most important outcome revealed by the model is that the ICPs generated at the coup and countercoup are significantly higher (as much as double for the worst explosive scenario) than the air overpressure at the vicinity of the head. At the same time pressures in the corpus callosum and brain stem remain within a safe value. The authors looked also at shear strain and stress and concluded that the dynamic responses of these three measurements are consistent with each other, i.e. when one is increased the others are too.

In conclusions, all the studies presented highlight the need for experimental validation through cadaveric testing, as blast events appear to create experimental conditions that are fundamentally different from those which are impact related.

CHAPTER 4

4.1 Description and preparation of pressure sensors

Part of the challenge of this study was the development of the instrumentation that was used during testing. Firstly, the shock tube required careful work to learn the correct operational conditions, which were explained in Chapter 2. Secondly, some of the sensors employed during shock wave tests were not designed to operate in such harsh environment, hence special techniques were developed to improve the chances of sensor survival and these techniques are presented in this chapter.

4.1.1 Pressure sensors

Figure 23 shows an optic pressure sensor (FISO Technologies, FOP-MIV not coated model) and two static piezoelectric pressure sensors (PCB Piezotronics Inc, model 102A06 and model 137A22) used in this research project.

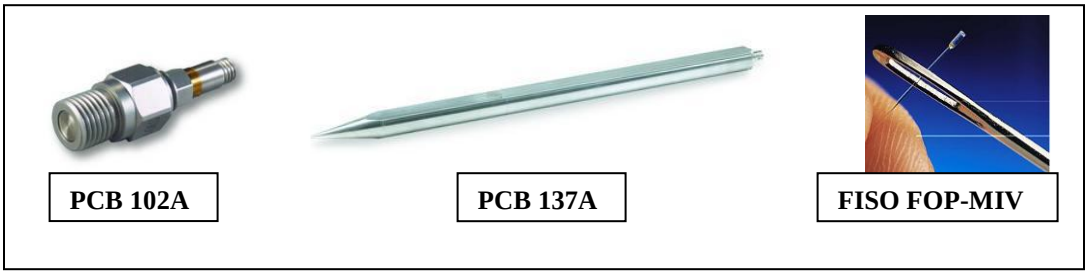

Figure 23: Pressure sensors used to record pressure profiles in the air (PCB) and inside fluids (FISO).
PCB 102A is commonly mounted on the wall of shock tubes in a side-on configuration (perpendicular to the direction of the shock front).
PCB 137A is used as a monitoring station and it is mounted so that the tip is facing the shock front and the long axis is parallel to the direction of the shock front. FISO FOP-MIV is a sensitive device used to measure blood pressure in animals. The picture shows the optic fiber passing through the eye of a needle and the sensing gage is at the tip. The optic fiber is usually coated with a blue plastic sheathing for common applications.

These sensors differ on a few levels: first, the mechanism for measuring pressure is distinct. The PCB sensors utilize an acceleration-compensated quartz piezoelectric element coupled to source follower type miniature electronics. The FISO sensors measure pressure by converting wavelength-modulated light into a voltage value. Additionally, the weight and size are different as the PCB sensor weighs around 13 g and measures 4 cm in length and 8 mm in diameter at the diaphragm, while the FISO optic sensor weighs 0.163 mg and the tip of the sensor, excluding the connecting optic fiber, measures around 0.5 mm both in diameter and in length.

Finally the PCB sensors are very robust as they were designed to work in a blast environment; therefore they do not require careful handling. On the other hand, FISO sensors are very delicate and special care is required to protect the optic fiber from tension or extreme bending. Furthermore, since the FISO sensors has been designed for medical use and not shock-related pressure variances, it does not have high frequency response (some estimated no higher than 15kHz).

On the other hand, one feature both FISO and PCB sensors have in common is that they are capable of measuring pressure below ambient (called gage-negative pressure as ambient is set at zero), but the precision of these relative values is not fully identified by the respective companies. FISO Technologies declares that the FOP-MIV sensor has a linear behavior between 300 mmHg absolute (-5.8 psi) and 7500 mmHg (145 psi); therefore for values below -5.8psi there will not be a reliable correspondence between the measured and the actual pressure value. By personal communication with FISO Technologies technical staff, it is known that a lower value will correspond to a bigger rarefaction, but the recorded number may not be physically correct. PCB Piezotronics declares that no calibration test is performed below ambient pressure; although they expect linear behavior to apply. This feature is less important for PCB sensors, since they are not placed in the specimens.

4.1.2 Preparation of the Intra-Cranial Pressure (ICP) sensors

Since the optic pressure sensors (FISO Technologies, FOP-MIV-PK, 150 psi) adopted for this study were not originally created to withstand a blast environment, a special technique was developed to improve the survivability of such sensors. Extensive testing in a previous analogous study (Dal Cengio Leonardi et al. 2011) that investigated ICP measurements in the brain of rats, had given the opportunity to optimize both sealing and cable-reinforcing techniques when using FISO optic sensors. The steps of the preparatory procedure, slightly modified to adapt to cadaver testing, are presented below:

Initially, the coated optic sensor cable was inserted in a 25 inch long thin plastic tubing (Biomedical Polyethylene Tubing #804000, A-M Systems, Inc., Carlsborg, WA), leaving a three-inch part near to the tip exposed. Then the sheath of the exposed part of the sensor was measured to mark the desired depth of penetration into the brain (or filling) with respect to the inner surface of the skull (or shell). A depth of 65 mm would represent an installation in the human ventricle; therefore the sensor was called ventricle. A depth of 30 mm would represent an installation in the cortex and therefore the sensors were called frontal, parietal and occipital, according to the surface location.

Fine sand paper was used to gently rub the sheath to create a rough surface around the area previously marked. A two-part epoxy glue (drying time 5 minutes) was applied to the area and a plastic cannula was inserted in position to bond at the marked position (Figure 24A). These cannulae usually come with a hallow steel stem inserted into the plastic part, therefore the stem needs to be removed .

The thin plastic tubing that was slid on at the beginning of the process, was put in contact with the cannula and glued in position; then a plastic ring was placed over the junction and filled with glue for reinforcement of the point of contact (Figure 24B). The prepared sensor was left to cure in horizontal position for one hour.

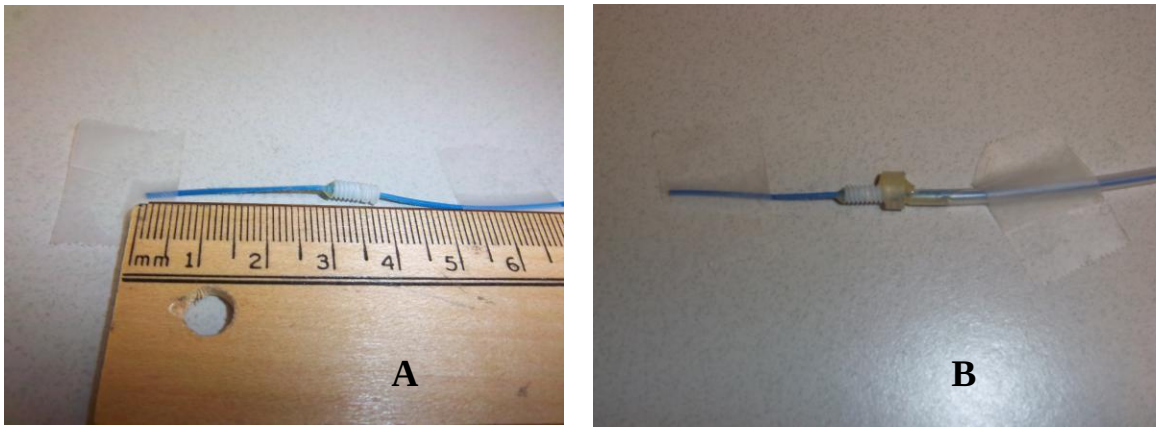

Figure 24: Preparation of optic sensor for cortex placement (30 mm).
A: Plastic cannula glued in position;
B: Plastic tubing and plastic ring added for ultimate protection of the optic fiber.

4.2 Preliminary studies

Tests were conducted to assess the effect of optic sensor orientation on pressure readings. Sensors were inserted in an oval form made of cured Sylgard 527 A&B, and they were placed either side-on or frontal to the shock front as shown in Figure 25. Blast simulations were run as the sensors were exposed in the different positions, and the results did not find consistent differences between any of the sensor positions.

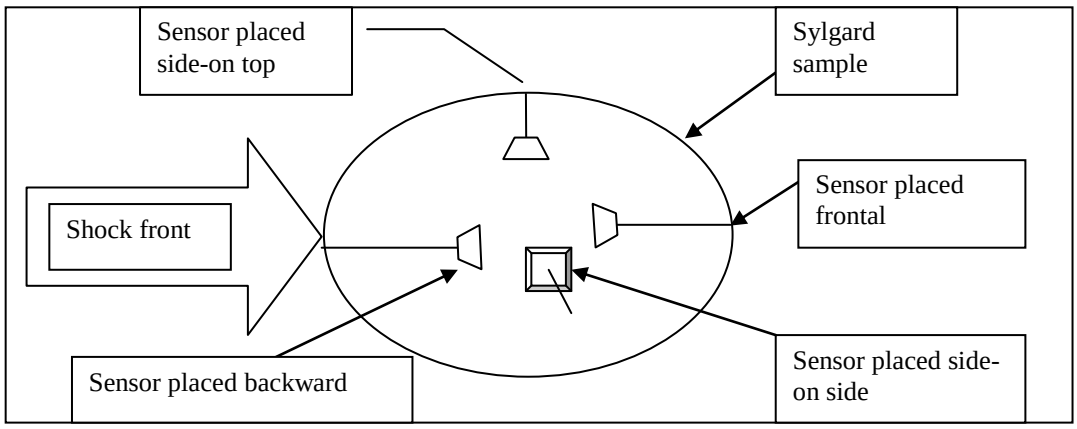

Figure 25: Possible positions assumed by the pressure sensors relative to the arrival of the shock front.

To investigate the effects of apertures in the transmission of a pressure wave inside a structure, we introduced a hole 5mm in diameter in an oval, hard plastic shell filled with Sylgard

(Figure 26). A bare optic sensor (no coating in the terminal 20 mm before the tip), was positioned side-on, and it was used to monitor the transmission of pressure within. The oval sample was exposed to simulated blasts and Figure 27 summarizes the results of various tests, in which the aperture was either facing the shock front or being opposite to the shock front.

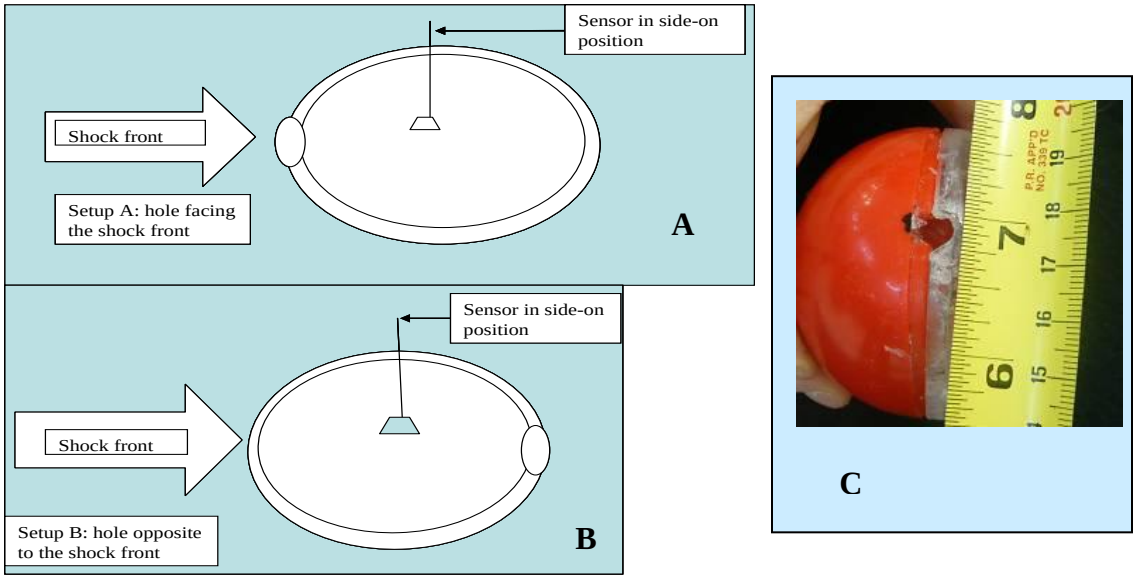

Figure 26: Example of the two different setups used to investigate the effect of apertures. A: hole facing the shock front; B: hole away from shock front; C: Actual hole created in the oval structure.

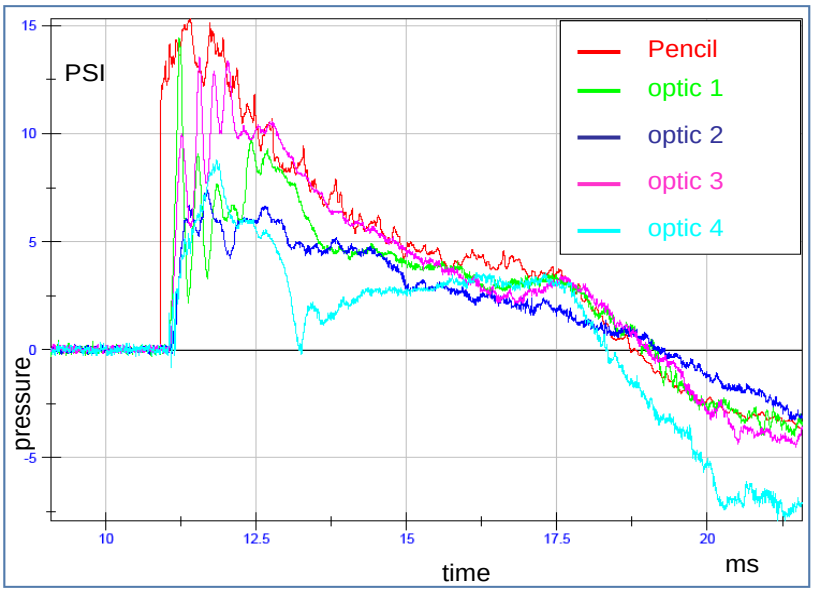

Figure 27: Summary of shock tests featuring a hard oval structure. The aperture is either opposite to the shock front or facing the shock front.
Optic 1 is placed side-on side with the hole facing the shock front. Optic 2 is side-on side with the hole opposite to the shock front. Optic 3 is placed side-on top with the hole facing the shock front. Optic 4 is side-on top with the hole opposite to the shock front. The red line is the pencil that records the shock wave in air (side-on).

As Figure 27 illustrates, there was a significant effect of the aperture's position on pressure transmission. The main distinguishing factor was the position of the aperture with respect to the shock front, although the particular position of the side-on sensor, whether top or side, did not appear of relevance. The red line in Figure 27 is the wave profile recorded by the pencil sensor in air just outside the oval structure, and it monitors the shock wave pressure changes. The pink and the green curves (optic 3 and optic 1) are plots of identical shock events collected by the optic sensor placed inside the structure when the aperture was facing the shock front; the two blue curves (optic 2 and optic 4) are plots of the same shock events when the aperture was opposite to the shock front. The peak ICP amplitudes for the case of the rear-facing apertures are clearly lower than for apertures forward-facing. However, it is not clear at this stage whether this effect is due to direct pressure ingress via the apertures or reduced shell stiffness and hence greater flexure.

To investigate the effect of shell hardness on the transmission of pressure, we compared tests that used different materials to shield a sensor immerged in cured Sylgard: a wrapping film, a thin elastic plastic shell, and a thicker stiff plastic shell (Figure 28). All tests had the sensor placed in a side-on position.

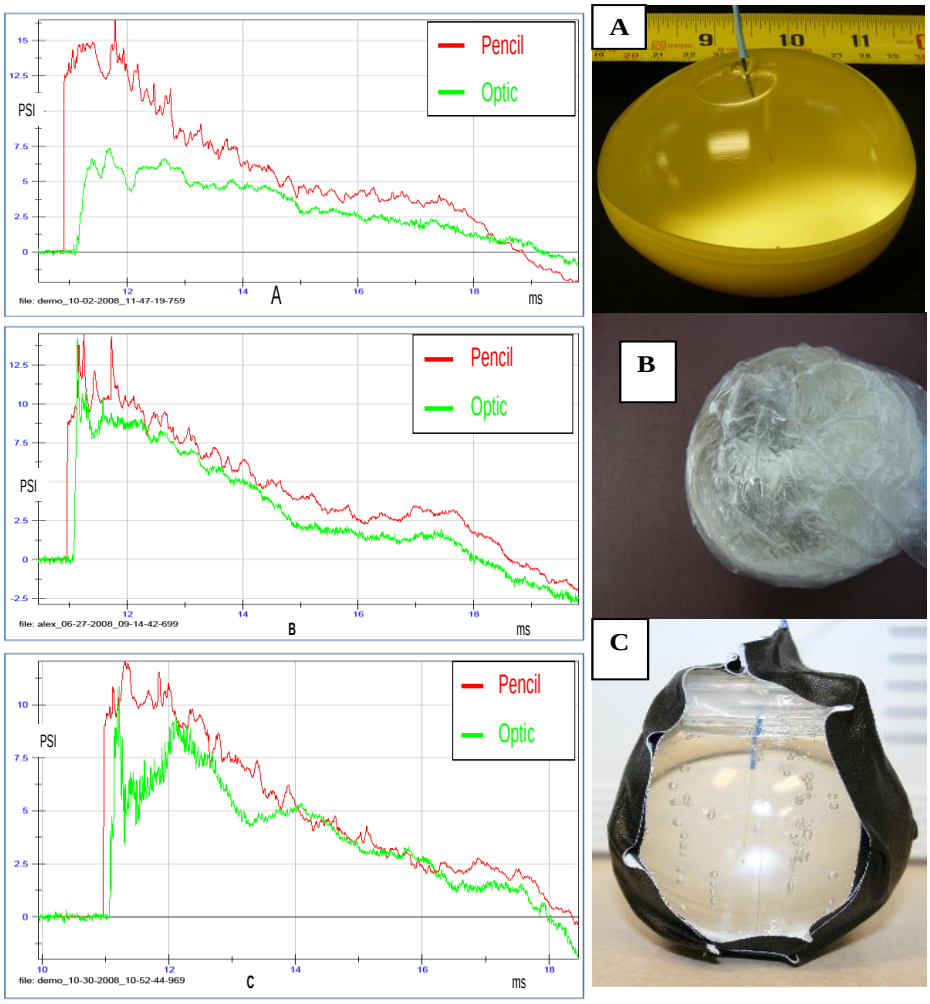

Figure 28: Graphs showing examples of testing with different shell hardness. Pictures of the 3 types of shells used: (A, right) Thicker, non bendable plastic shell; (B, right) Wrapping film; (C, right) Thin, bendable plastic shell. Pressure profiles: (A, left) Optic sensor pressure (green) inside a hard shell filled with Sylgard. (B, left) Optic sensor pressure (green) inside plain Sylgard surrounded by wrapping film; (C, left) Optic sensor pressure (green) inside a thin bendable plastic shell filled with Sylgard. When exposed to the blast, the optic sensor was placed in a side-on top positioning in all three tests. Red is the pencil sensor placed in air adjacent to the specimen in all three tests. The three tests were conducted at slightly different pressures.

Results showed that when the optic sensor in Sylgard was shielded by wrapping film there was almost no attenuation compared to the pressure recorded by the pencil sensor in air (Figure 28B). When the optic sensor was shielded by a thick, stiff plastic shell, there was noticeable attenuation (Figure 28A). In the case of the intermediate shell hardness, some attenuation of the shock wave could be detected (Figure 28C).

To test the effect of fillings with different material properties, we examined pressure transmission through either Sylgard or water in a thin, elastic plastic shell (Figure 29). Two optic sensors were placed side-on top in each material: one was submerged in Sylgard and the other was immersed in colored water.

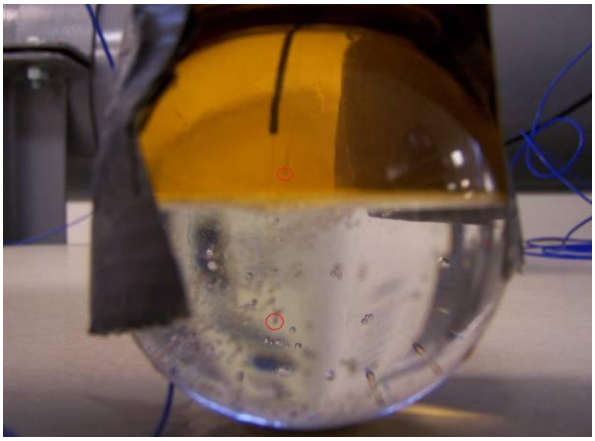

Figure 29: Thin, bendable clear plastic sphere containing two materials.
Sylgard 527 is at the bottom and colored water (yellow) on top. The optic sensor tips are circled in red.

Figure 30A shows an example of testing with the clear sphere containing the two different materials. The wave profiles show that the less viscous element (water) introduced oscillations into the system, and both sensors reflect that. The same sphere, when filled completely with Sylgard (Figure 28C), did not produce nearly any oscillation (Figure 30B).

These preliminary results suggested that the response of a heterogeneous system simulating a simplified human head will be dependent on the shell thickness, on the viscosity of the filling, and on the presence of apertures.

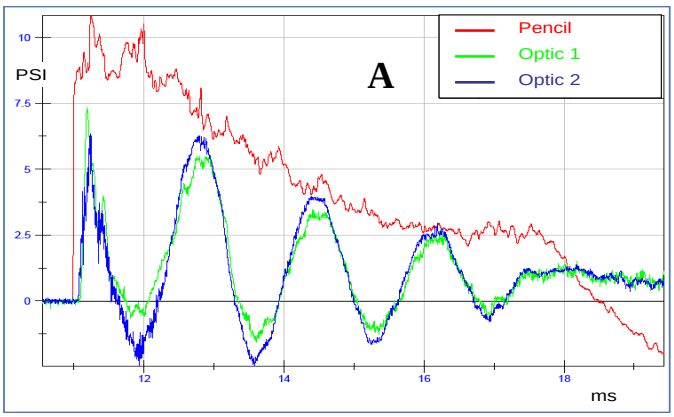

A: Graph depicts testing of 2 different materials enclosed inside the same shell. Optic 1 is the sensor in Sylgard and optic 2 is the sensor in water. Pencil shows the pressure recorded in a location in air adjacent to the specimen.

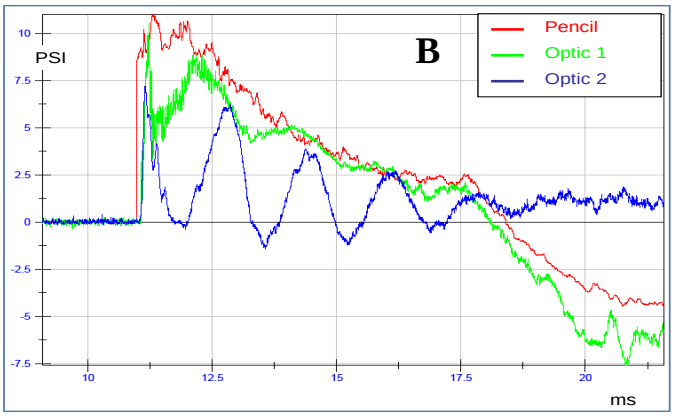

B: Graph depicts comparison of the wave-forms obtained from optic sensors placed in Sylgard. Optic 1 recorded when the whole structure was filled with only Sylgard and Optic 2 recorded when the same structure was filled with 2 different substances. Pencil shows the shock pressure in air.

Figure 30: Graphs showing examples of testing with different filling materials.

CHAPTER 5

5.1 Introduction

The goal of this research was to establish the basic phenomenology of shock wave interaction with a simplified model of skull/brain system. The preliminary studies of Chapter 4 provided some insight as to the basic phenomenology involved using very simple fluid-filled shells as well as allowing instrumentation development. This study explored the mechanical response of three simplified head models of identical geometry that had differences in key characteristics: shell thickness, composition of the filling, and introduction of apertures. Furthermore, the sensors used in this study were placed following an installation similar to the concurrent cadaveric study presented in the next chapter. This scheme was designed to allow for comparison of trends between the data collected from the physical models and the data collected from the cadaver study to help identify the primary components of the biomechanical response of the skull/brain system.

The specific aims of this study were to map the internal pressures in regions of the simplified models that mirrored the cadaveric study; to determine the relationship between magnitude levels of incident shock wave overpressure and values of internal pressures in the simplified models; to investigate the effects of orientation, shell thickness, and apertures on internal pressures in the same models; and to compare pressure distribution patterns with surface strain data recorded concurrently for evaluation of gross deformations of the models' shells in relation to internal pressure profiles. As determined by the shock tube analysis, the simplified models were placed at 49 inches from the open end of the expansion, and exposed to simulated blasts that varied in magnitude and orientation.

This research is significant because the resolution of the primary components of the mechanical response of the skull/brain systems during blast exposure is the first step in the understanding of the complete mechanism of brain injury. One of the main objectives from this

work will be to find out what material properties are important to replicate in order to improve the sophistication of the physical models. The ultimate goal is to make a contribution to the creation of a biofedelic head surrogate for blast testing.

5.2 Methods

When searching for a suitable physical model of human head for blast scenarios, it seems reasonable to start from models already accepted for blunt impact settings. Therefore, a layered polyurethane sphere filled with Sylgard 527 A&B was used as a starting point. However, polyurethane spheres and Sylgard 527 A&B have never been validated as head surrogate during blast exposure. At the moment, Synbone spheres represent the best option for a simplified physical model of the human skull and it was the only shell material used during testing. On the contrary, two materials with very different characteristics were tested as filling, and details are given in the following section.

5.2.1 Model preparation

The bone surrogate material used was made by Synbone AG (Neugutstrasse 4, CH- 7208 Malans, Switzerland), a company that manufactures surrogate bones from specially formulated polyurethane foam, comprising of a cancellous inner core and a harder outer shell simulating cortical bone. The company discloses that the surrogates do not possess all the same biomechanical properties of natural bone, although they have been successfully tested in ballistic experiments and have very favorable feedback from a number of biomechanical testing facilities that compare artificial bone with real bone. At the moment Synbone spheres represents the best option for a simplified surrogate skull providing a generic hollow sphere, 190 mm in diameter and a choice of 5, 6, or 7 mm shell thickness.

Three spheres were prepared, one for each thickness dimension. Three pressure sensors and four strain gages were mounted on each sphere. The three pressure sensors, called Frontal,

Ventricle and Occipital, were prepared in the same manner as explained in Chapter 4.1, and were installed on the shells at identical locations. Figure 31 shows the modified stereotaxic frame that was used to measure the locations where the pressure sensors were placed. The frame allowed very consistent positioning of the sensors.

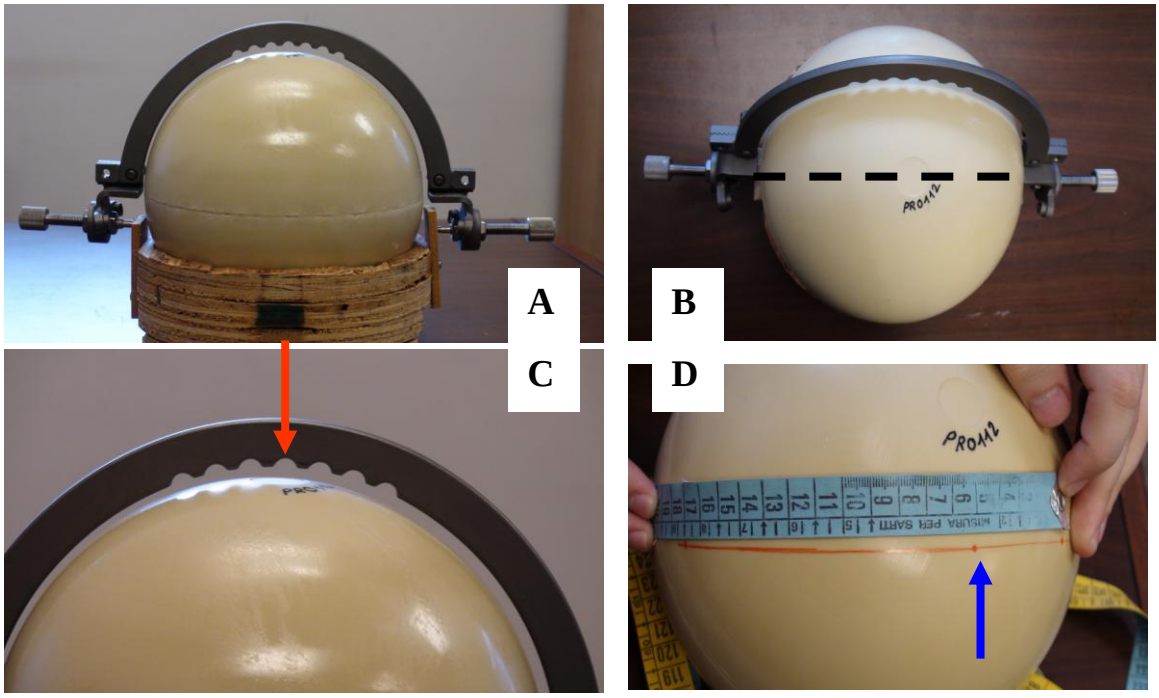

Figure 31: Modified stereotaxic frame.
A: sphere placed in position; B: steel arc tilted 25 degrees to mark the line for position of the pressure sensors; C: the central bump on the steel arc (red arrow) identifies the position of one of the pressure sensors (Ventricle) on the shell once the arc has been tilted; D: once the line is drawn and the position of the Ventricle sensor has been marked (blue arrow), the Frontal and Occipital sensor positions are measured on the line (Frontal is 50mm on one side of the Ventricle and Occipital is 120mm on the other side).

The steel arc in Figure 31B could tilt 25 degrees from midline (black dotted line in the picture) and an orange line was marked on the sphere (Figure 31D). A 25 degree inclination was chosen to place the sensors away from the midline and differentiate side exposure. The pressure sensor locations were determined to provide guidance for the pressure sensor installation on the cadaver specimens (on the anatomical right side of the skull). The central bump on the steel arc

identified where to mark the place for the sensor called Ventricle (red arrow Figure 31C). Once the location of the Ventricle sensor was determined (blue arrow in Figure 31D), the two other sensors, Frontal and Occipital, were marked on the orange line. Frontal was marked 50mm ahead of Ventricle, while Occipital was marked 120mm back from Ventricle. Holes were drilled on the shell at the marked locations and then a tap was used to create a thread in the shell (Figure 32A).

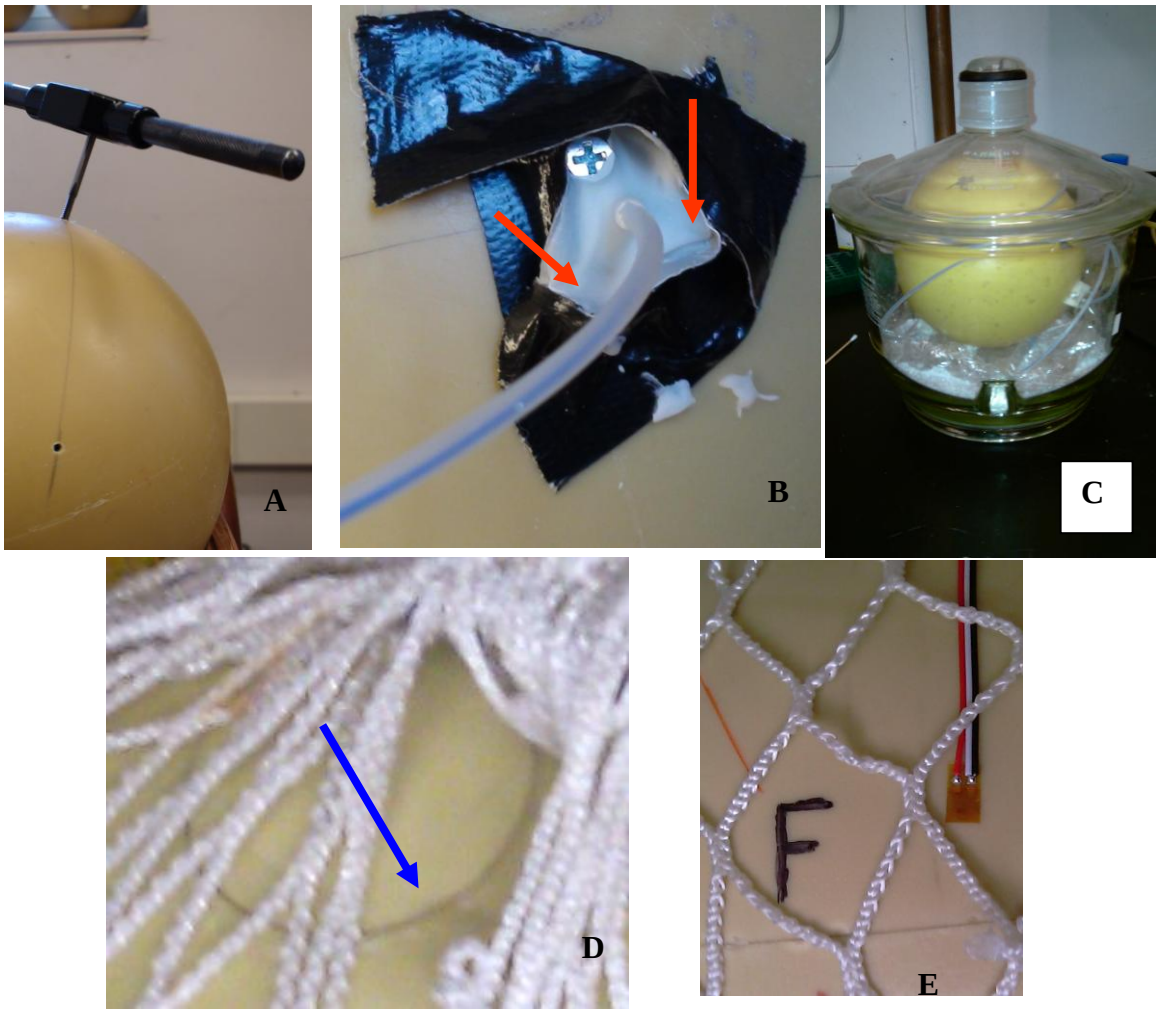

Figure 32: Preparation of the sphere in steps.
A: tapping the shell; B: cementing the pressure sensor to the shell; C: placement of the sphere in a vacuum; D: the cap (blue arrow) is glued in place sealing the sphere; E: strain gages are glued to the surface of the sphere.

After fastening of the pressure sensors, three screws were arranged in a triangular layout. Duct tape was wrapped around the outside of the triangle to create a supporting structure for the

bone cement (Figure 32B) that was poured in it. The bone cement was left to harden for 5 minutes and then the duct tape was removed. The bone cement together with the three screws created a protective cap for the optic sensor exiting the shell, and prevented the netting of the suspension system from sliding into the optic cable. The bone cement also provided a seal for the hole preventing leaks.

Once all sensors were anchored to the shell, the spheres were filled with brain simulant materials. In the case of the sphere that was 6mm thick, the brain surrogate used was Sylgard 527 A&B at the ratio of 1:1; while for the other two cases (5mm and 7mm thickness) the filling was aqueous glycerine at 40% weight. After the spheres were completely filled up, they were placed in a vacuum chamber for 2 minutes to de-gas (Figure 32C) in an attempt to remove most of the air bubbles formed during pouring of the filling. Because of the Sylgard curing requirements, the sphere filled with Sylgard was left undisturbed for 48 hours before sealing the big opening with a customized cap. For the other two spheres, the procedure was done immediately after degassing. The customized cap, which had the same external curvature as the rest of the sphere, was glued into place to seal the sample (Figure 32D).

Four strain gages were placed at the front, back, left and right side of the shell, as cardinal points of a compass. The sites were first sanded, cleaned, and then the gages were glued to the surface (Figure 32E). Because of limitations on the number of channels available in the data acquisition system, only one grid was used per site (each grid was extracted from a rosette, Vishay Micro-Measurements, General Purpose Strain Gages, item code 16793). The calculation of principal strain was beyond the scope of this study and the strain values were analyzed for evaluation of gross deformations of the skull in relation to internal pressure profiles.

Figure 33 shows how the sensors were installed on the shells and how the pressure sensors were positioned inside the spheres. Figure 34 illustrates the spherical coordinate system used to estimate the position of the tips of the pressure sensors in the spheres. The center of the sphere was chosen as the origin point; the zenith axis was positive toward the top of the sphere;

the azimuth axis was along the midline between the front and back hemisphere, positive toward the right side, and the azimuth angle was positive when going counterclockwise. By these conventions, the positions of the sensor tips in spherical coordinates are reported in Table 2.

Table 2: Spherical Coordinates of the pressure sensor locations for the 5mm thick sphere

	Radius [mm]	Inclination [degrees]	Azimuth [degrees]
Ventricle	25	25	0
Frontal	60	25	30
Occipital	60	25	-72.5

For the sphere that is 7 mm in thickness the inclination and azimuth angle remained the same, while the radius values were 2 mm smaller for each position (23 mm for ventricle; 58 mm for frontal; 58 mm for occipital).

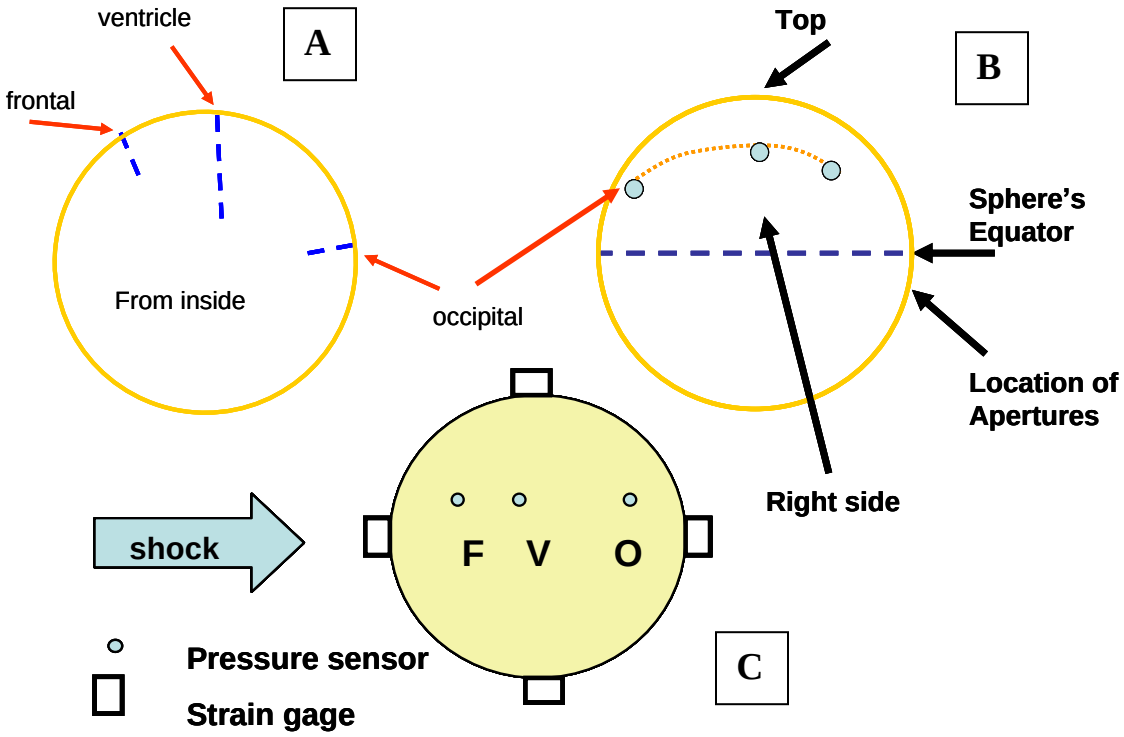

Figure 33: Positioning of gages and apertures.
A: Pressure sensor locations inside the sphere (Frontal and Occipital are 30mm from the inner surface, while Ventricle is 65mm from the inner surface); B: Positions of pressure gages and apertures on the sphere's surface (outside view from the right side); C: Strain gage locations on surface (view from the top).

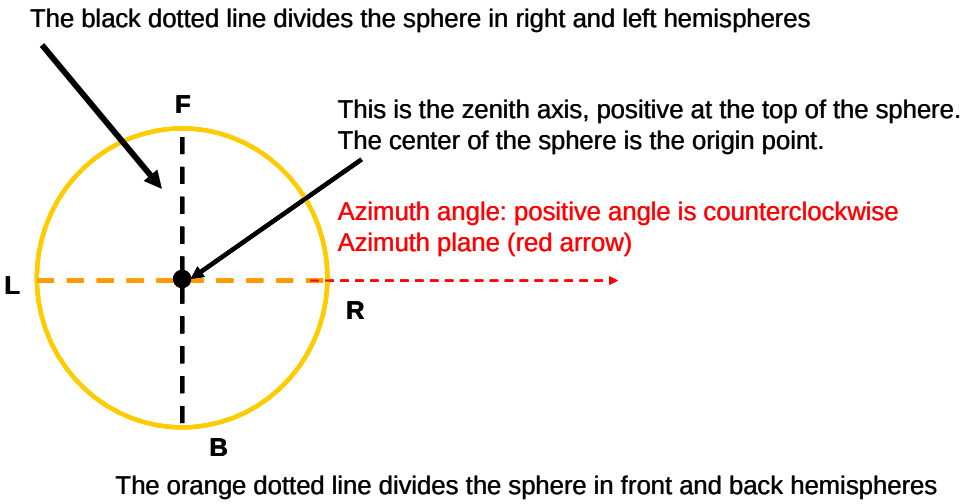

Figure 34: Spherical coordinate system for estimation of the location of the pressure tips in the sphere.
View from the top of the sphere: F= front; B= back; L= left; R= right.

Figure 33B indicates the positioning of the apertures on the shells in relation to the equatorial line. The apertures' sites were marked prior to testing, although the holes were introduced only in the second series of tests for each sphere. The intact spheres were exposed to the testing schedule in Table 3; then the holes were introduced and strain gages were replaced if needed; finally a second series of tests was conducted following the same schedule shown in Table 3.

Table 3 Testing conditions for spheres exposed to blast simulations in the shock expansion

Orientation	Static Pressure PSI	Stagnation Pressure PSI
Front	10	12.5
Right	10	12.5
Back	10	12.5
Left	10	12.5
Front	10	12.5
Front	12	15
Left	12	15
Back	12	15
Right	12	15
Front	12	15
Front	15	20
Right	15	20
Back	15	20
Left	15	20
Front	15	20

Figure 35 illustrates the steps required to properly insert apertures to the spheres. Initially, from a dry skull a template of the superior orbital fissures was made on a small plastic sheet. The template was then transferred to each sphere by marking the locations of the future apertures (Figure 35A). After the first series of tests was completed, the intact sphere was drilled at the marked locations (Figure 35B). In the case of the sphere containing cured Sylgard, there was no concern regarding the filling pouring out of the sphere; therefore the holes were left exposed (Figure 35C). On the contrary, in the spheres containing aqueous glycerine, once the holes were created they had to be sealed to avoid losing the liquid filling. A plastic adhesive patch (Vinyl Plastic Repair Patch, Union Laboratories, Inc., Flagstaff, Arizona) was placed onto the surface (Figure 35D). Prior to positioning the patch, more aqueous glycerine was added into each sphere up to their outer shell surface, to prevent including air pockets inside the sealed spheres.

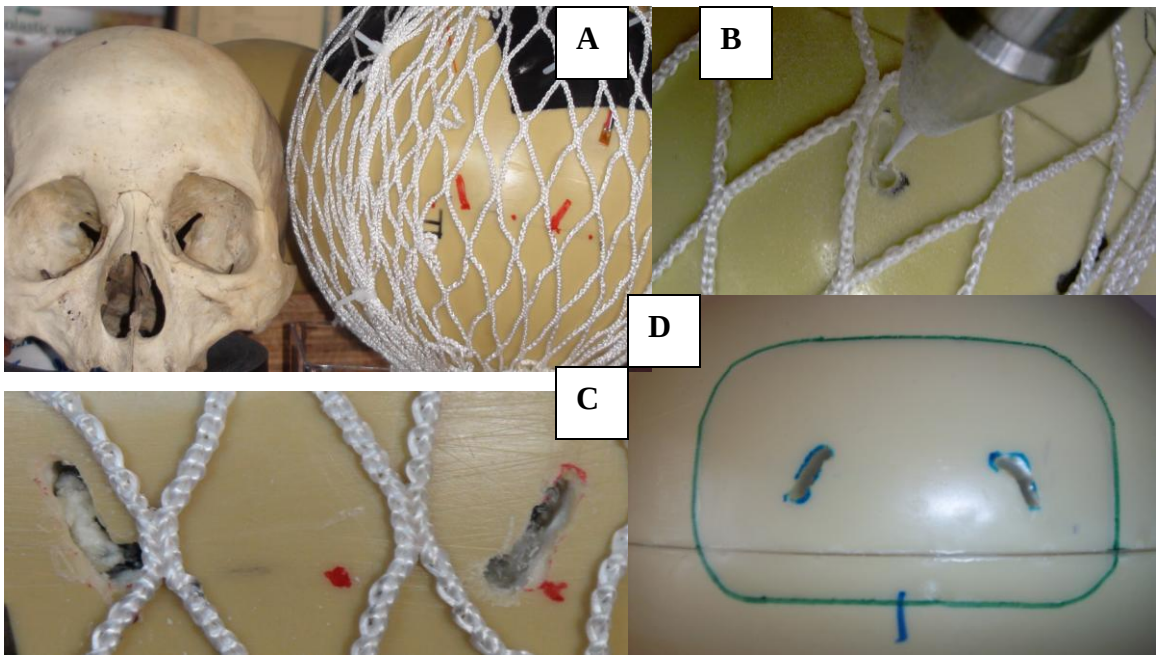

Figure 35: Preparation of the apertures in steps.
A: Superior orbital fissures are marked on the sphere; B: after the first series of tests the marked locations are drilled; C: the holes are completed and can remain open when Sylgard is the filling; D: the holes need to be sealed with a plastic patch (marked in green) when the filling is aqueous glycerin.

As mentioned previously, at the moment Synbone spheres represents the best option for a simplified surrogate skull; however two different filling materials were tested: Sylgard 527 A&B at the ration 1:1, which is a sticky, jello-like solid when it is cured; and aqueous glycerine at 40% weight, a liquid solution that has some physical properties that closely resembled those of the human blood and brain. Aqueous glycerine is a solution of water and glycerine that has specific properties according to the percentage of glycerine in the solution. Table 4 provides the viscosity of the aqueous solution in relation to ambient temperature and percentage of glycerine.

Table 4

Viscosity of Aqueous Glycerine Solutions in Centipoises/mPa s											
Glycerine Percent Weight	*Temperature (°C)*										
	0	10	20	30	40	50	60	70	80	90	100
0	1.792	1.308	1.005	0.8007	0.656	0.5494	0.4688	0.4061	0.3565	0.3165	0.2838
10	2.44	1.74	1.31	1.03	0.826	0.68	0.575	0.5	–	–	–
20	3.44	2.41	1.76	1.35	1.07	0.879	0.731	0.635	–	–	–
30	5.14	3.49	2.5	1.87	1.46	1.16	0.956	0.816	0.69	–	–
40	8.25	5.37	3.72	2.72	2.07	1.62	1.3	1.09	0.918	0.763	0.668
50	14.6	9.01	6	4.21	3.1	2.37	1.86	1.53	1.25	1.05	0.91
60	29.9	17.4	10.8	7.19	5.08	3.76	2.85	2.29	1.84	1.52	1.28
65	45.7	25.3	15.2	9.85	6.8	4.89	3.66	2.91	2.28	1.86	1.55
67	55.5	29.9	17.7	11.3	7.73	5.5	4.09	3.23	2.5	2.03	1.68
70	76	38.8	22.5	14.1	9.4	6.61	4.86	3.78	2.9	2.34	1.93
75	132	65.2	35.5	21.2	13.6	9.25	6.61	5.01	3.8	3	2.43
80	255	116	60.1	33.9	20.8	13.6	9.42	6.94	5.13	4.03	3.18
85	540	223	109	58	33.5	21.2	14.2	10	7.28	5.52	4.24
90	1310	498	219	109	60	35.5	22.5	15.5	11	7.93	6
91	1590	592	259	127	68.1	39.8	25.1	17.1	11.9	8.62	6.4
92	1950	729	310	147	78.3	44.8	28	19	13.1	9.46	6.82
93	2400	860	367	172	89	51.5	31.6	21.2	14.4	10.3	7.54
94	2930	1040	437	202	105	58.4	35.4	23.6	15.8	11.2	8.19
95	3690	1270	523	237	121	67	39.9	26.4	17.5	12.4	9.08
96	4600	1580	624	281	142	77.8	45.4	29.7	19.6	13.6	10.1
97	5770	1950	765	340	166	88.9	51.9	33.6	21.9	15.1	10.9
98	7370	2460	939	409	196	104	59.8	38.5	24.8	17	12.2
99	9420	3090	1150	500	235	122	69.1	43.6	27.8	19	13.3
100	12070	3900	1410	612	284	142	81.3	50.6	31.9	21.3	14.8

Viscosity of water taken from "Properties of Ordinary Water-Substance." N.E. Dorsey, p. 184. New York (1940)

Since data on the viscosity of the brain as a whole is not available and the blood capillary network in the brain is extensive, it seemed reasonable to look at the viscosity of blood instead. In comparison, the viscosity of human blood at 37˚C is between 3 and 4 mPa*s; in contrast, the viscosity of the Sylgard 527 mixture, after curing for 2 hours at room temperature, is about 900 mPa*s. Since the testing environment was kept at room temperature (between 20˚C and 30˚C) a solution of aqueous glycerine at 40% weight was the best match for the viscosity of blood (2.72 to 3.72 mPa*s).

Furthermore, blood, grey matter and white matter have a density of 1.06 g/cm^3 (Horgan and Gilchrist 2004), in contrast to the Sylgard mixture, which has a density of 0.97 g/cm^3. In comparison, a solution of aqueous glycerine at 40% weight has a density of 1.0888 g/cm^3, which is a better approximation of human brain.

The simplified human head model was placed in the expansion section of the shock tube, at the location previously determined to create the correct pressure wave. Details of the magnitudes and orientations were noted to allow for replication in the cadaveric study that followed.

5.2.2 Data acquisition, processing and analysis

Internal pressure measurements were obtained by three optic pressure sensors (presented in Chapter 4). The pressure sensors were connected to the conditioning unit, then low noise coaxial cables connected the conditioning unit to the Dash data acquisition system. The system was also used to capture the air overpressure in the tube (Rwall) and the four strain values on the sphere's surface. The sampling rate of the acquisition system was set to 250 kHz.

An anti-aliasing filter (2 pole Bessel at 200 kHz) was applied to the data during acquisition. This filter is an automatic settings of the Dash unit when sampling is above 200kHz. During post-processing, the pressure data was filtered with a low-pass second order Butterworth filter at 4 kHz to allow a leveled comparison of the sphere data to the cadaver data. Appendix B, C, and D present pressure profiles from each sphere before and after post-processing filtering. Strain values were not filtered, but were analyzed for evaluation of gross deformations of the skull in relation to internal pressure profiles. Appendix B, C, and D contain also the strain results associated with each test.

As explained in Chapter 2, the specimens were positioned so that the arrival of the rarefaction wave coming from the open end of the tube would coincide with the end of the positive phase. The arrival of the rarefaction wave marks the end of the time-window in which the simulated blast is appropriate. This arrival depends on the shock wave overpressure magnitude: the higher the overpressure, the narrower the window. Hence the time-window for the 10 psi and 12.5 psi static overpressure was approximately 7.5 ms for both, while for the 15 psi static overpressure the time-window was approximately 6.7 ms (not a linear behavior). Data

analysis was limited to the time-window appropriate for each magnitude. A practical window of 10 ms, 9 ms after arrival of the shock front at the specimen and 1 ms prior, is presented in the graphs. The acquisition system was triggered automatically by the rising edge of the pressure profile at the Rwall sensor. Since this sensor was positioned closer to the driver chamber, it met the shock wave sooner than the specimen, which was placed downstream (49 inches from the open end of the expansion). Therefore, in all the pressure and strain profiles, the time frame shown goes from 6 ms to 16 ms, as it takes about 7 ms for the shock wave to reach the specimen location from the Rwall.

A focal point of this study was the characterization of pressures imparted into the spheres; thus maximum and minimum internal pressures, pressure differential, and rate of change of pressure (pressure gradient) were determined for each sensor in each test (Figure 36).

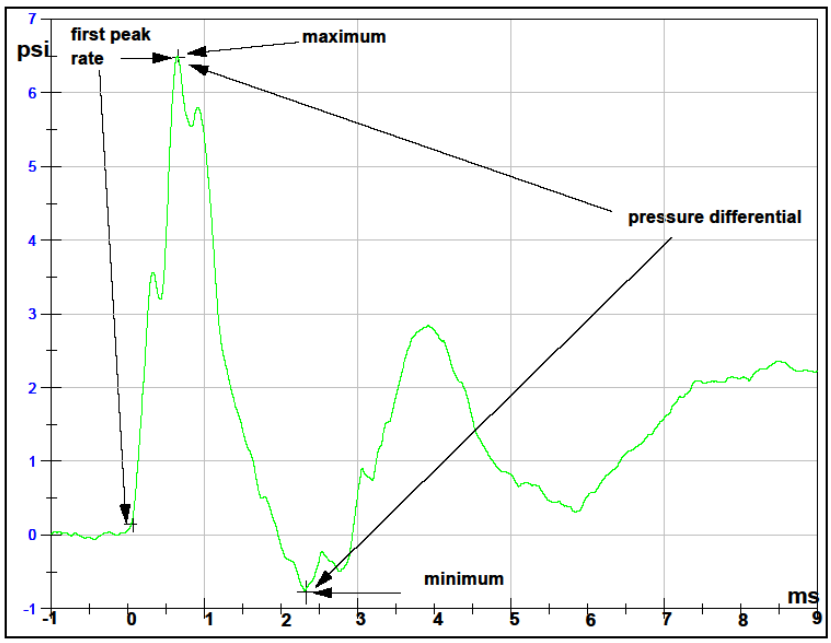

Figure 36: Values used in data analysis for each sensor.
Each point presented is used to calculate the indicated values for data analysis.

The pressure differential values were calculated by subtracting the minimum value from the maximum value. Time elapsed between these two values was also recorded (all records can be

found in Appendix B, C, and D). The pressure gradient was calculated at the initial loading as the pressure differential from inception of the shock front to the first peak (or valley in the case of a negative value) divided by the corresponding elapsed time). For convenience, the rate of change of pressure, or pressure gradient, was named 1st rate. Pressure gradients could be an important mechanism of injury and the sign associated with the value indicates increasing compression in the brain if the number is positive, and decreasing pressure (tensile stresses) if the number is negative.

To investigate the effect of apertures, the results from each sphere were also compared between the intact sample and the same sample after the introduction of holes. Then, to investigate the effect of different filling materials, the pressure results from the three spheres were examined. Finally, to investigate the effect of shell thickness, the results from the 5mm and 7mm thick spheres were compared.

5.3 Results

Three polyurethane spheres, used as simplified models of a human skull/brain system, were placed in an inverted position inside a shock tube expansion and were exposed to a first series of fifteen simulated blasts, changing pressure magnitudes and orientation of the sample. Then apertures were introduced in the spheres and a second series of fifteen simulated blasts was conducted, reproducing the same air overpressure magnitudes and orientation of the sample. Internal pressures in three regions of the simulated brain and strain values in four regions of the shell were collected.

5.3.1 Pressure results

Three pressure sensors were installed on the sphere to monitor pressure changes inside the sample. The sensor depths from the inner surface of the shell were 30 mm for Frontal and Occipital, and 65 mm for Ventricle. The sensor position inside the spheres was extensively

explained in section 2 of this chapter. To confirm reproducibility of results, the first front test was repeated at the end for each magnitude. Reproducibility was checked by visually comparing the first and last pressure profiles at each magnitude, for every sensor in all spheres. Figure 37 presents an example of reproducibility of data (for pressure profiles) between the first front orientation and the final front orientation at one magnitude for one sensor. Consistency of results is high and all cases can be found in Appendix B, C, and D.

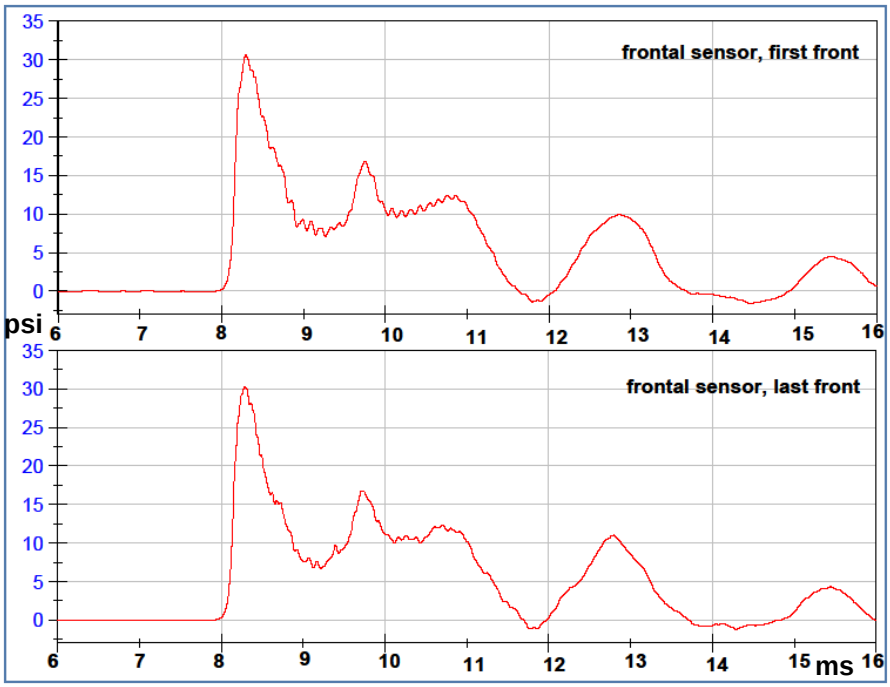

Figure 37: Comparison between first and last test at 10psi magnitude for frontal sensor in the intact sphere 5mm thick.
Reproducibility of results is high.

Figure 38 offers an example of pressure profiles for each of the three sensors in one single test.

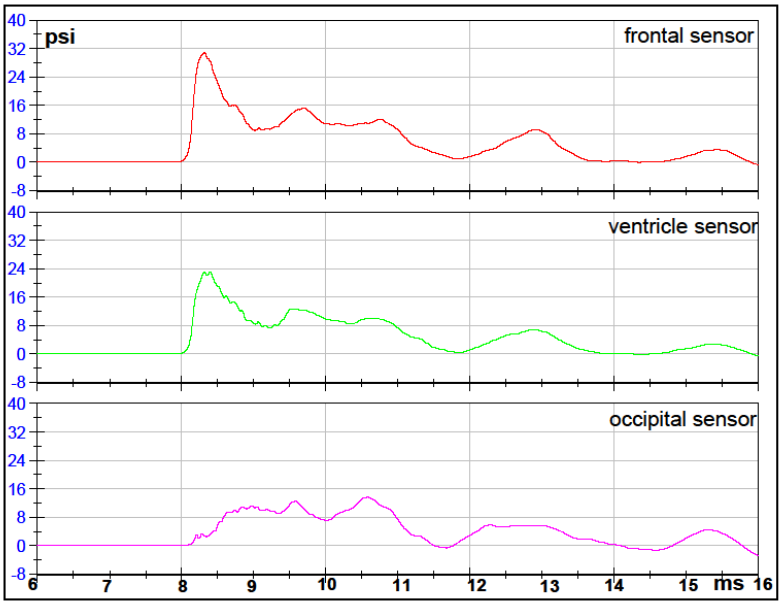

Figure 38: Pressure profiles of each sensor
for the first front exposure at 10 psi shock wave static overpressure for sphere 5mm thick with holes.

Figure 39 provides an example of pressure profiles for one sensor at the four different orientations for one magnitude of air overpressure. All records of pressure time history by sphere thickness can be found in Appendix B, C, and D.

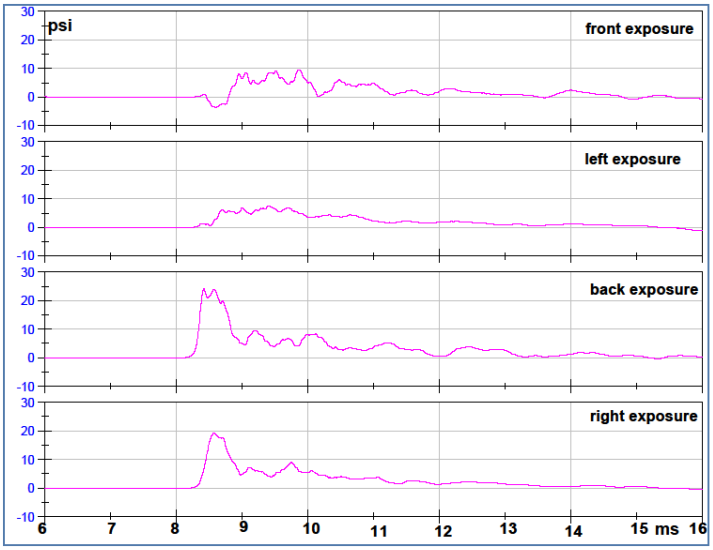

Figure 39: Occipital sensor pressure profiles for the four orientations
at 10 psi shock wave static overpressure exposure for 7mm-thick intact sphere.

When looking at the filtered pressure profiles in Appendix B, C, and D, some preliminary observations can be made on the response of the three sphere systems, which are quite similar:

- peak pressure is higher than shock wave overpressure in every test and for every sensor;
- occipital pressure profiles are very similar in every sphere for the corresponding orientations and specifically the back and right exposures consistently show similar peak-shaped profiles among the three spheres, while the other two orientations (left and front) have similar plateau shapes;
- frontal pressure profiles are very similar in every sphere for the corresponding orientations and specifically the front and right exposures consistently show similar peak-shaped profiles among the three spheres, while the other two orientations (left and back) have similar plateau shapes;
- ventricle pressure profiles are very similar in every sphere for the corresponding orientations and specifically the right exposure shows similar peak-shaped profiles with consistency among the three spheres, while the left orientation have similar plateau shapes;
- for every sensor in each sphere, the maximum peak pressure consistently increases with magnitude of shock wave overpressure at each orientation, contrary to minimum pressure values, which do not show a clear pattern;
- in every sensor the wave main component indicates a frequency of about 700Hz although damping is rapidly decreasing the oscillation;
- all sensors in the 6mm-thick sphere, which is filled with Sylgard 527 A&B, recorded a secondary oscillation (5.6 kHz) that rides on the main wave component. This secondary frequency is atypical of the other spheres.

Table 5 shows an example of results for maximum and minimum values collected for one sphere. Tables of results for each sphere are presented in Appendix B, C, and D. Figure 40 to Figure 45 summarize the same maximum and minimum results in graphical format for all cases.

Table 5: Pressure Extremes for intact sphere 5mm										
	Maximun Pressure					Minimum Pressure				
ventricle	front 1	right	back	left	front 2	front 1	right	back	left	front 2
10 psi air	**23.29**	**20.44**	**14.08**	**16.7**	**22.78**	**-1.80**	**-1.86**	**-2.35**	**-1.84**	**-1.30**
12 psi air	**25.55**	**21.88**	**15.43**	**18.4**	**25.74**	**-0.23**	**-0.96**	**-1.02**	**-1.26**	**-0.03**
15 psi air	**33.56**	**28.62**	**18.85**	**22.57**	**NA**	**0.21**	**-0.36**	**-0.79**	**0.19**	**NA**
frontal	front 1	right	back	left	front 2	front 1	right	back	left	front 2
10 psi air	**30.68**	**28.42**	**15.93**	**14.81**	**30.23**	**-1.62**	**-1.80**	**-3.07**	**-2.84**	**-1.15**
12 psi air	**32.92**	**29.69**	**16.73**	**17.5**	**33.59**	**-1.06**	**-1.02**	**-1.74**	**-2.35**	**-0.76**
15 psi air	**42.23**	**39.04**	**20.68**	**20.82**	**NA**	**-1.04**	**-0.74**	**-2.09**	**-0.37**	**NA**
occipital	front 1	right	back	left	front 2	front 1	right	back	left	front 2
10 psi air	**14.73**	**25.17**	**31.21**	**15.55**	**14.18**	**-3.26**	**-2.53**	**-3.22**	**-2.77**	**-2.41**
12 psi air	**15.75**	**26.06**	**35.68**	**16.99**	**14.95**	**-1.92**	**-1.74**	**-1.42**	**-1.73**	**-1.57**
15 psi air	**17.64**	**38.19**	**NA**	**NA**	**18.17**	**-0.88**	**0.14**	**NA**	**NA**	**-2.28**

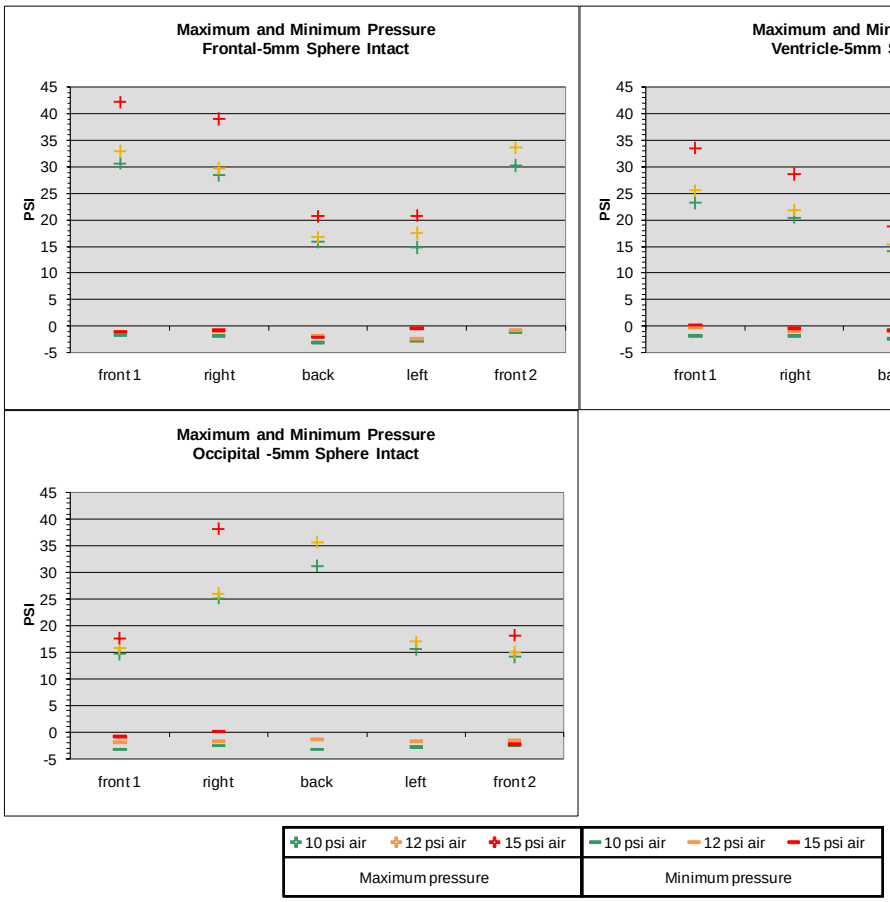

Figure 40: Graphs by sensor for maximum and minimum pressure values for the 5mm sphere (the results are color coded according to shockwave pressure).

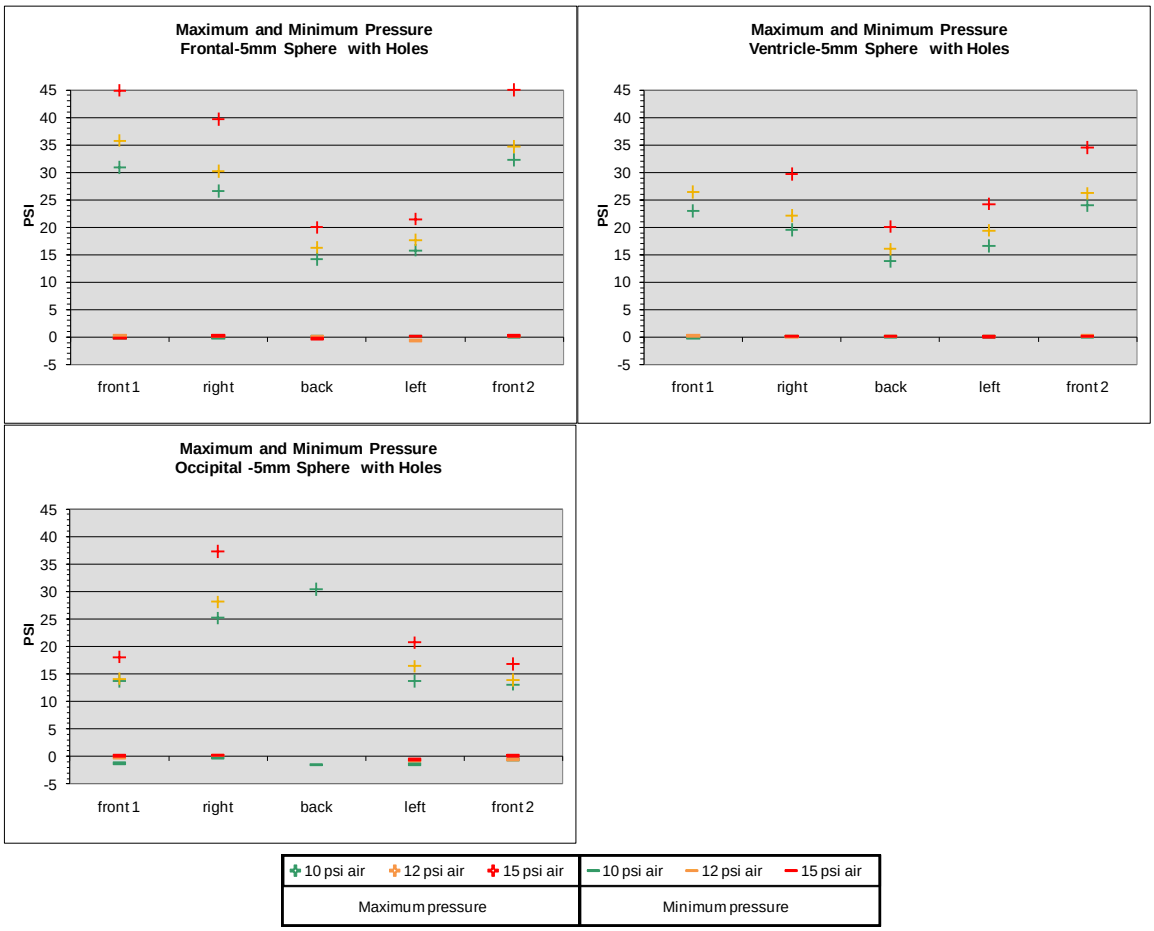

Figure 41: Graphs by sensor for maximum and minimum pressure values for the 5mm sphere with holes (the results are color coded according to shockwave pressure).

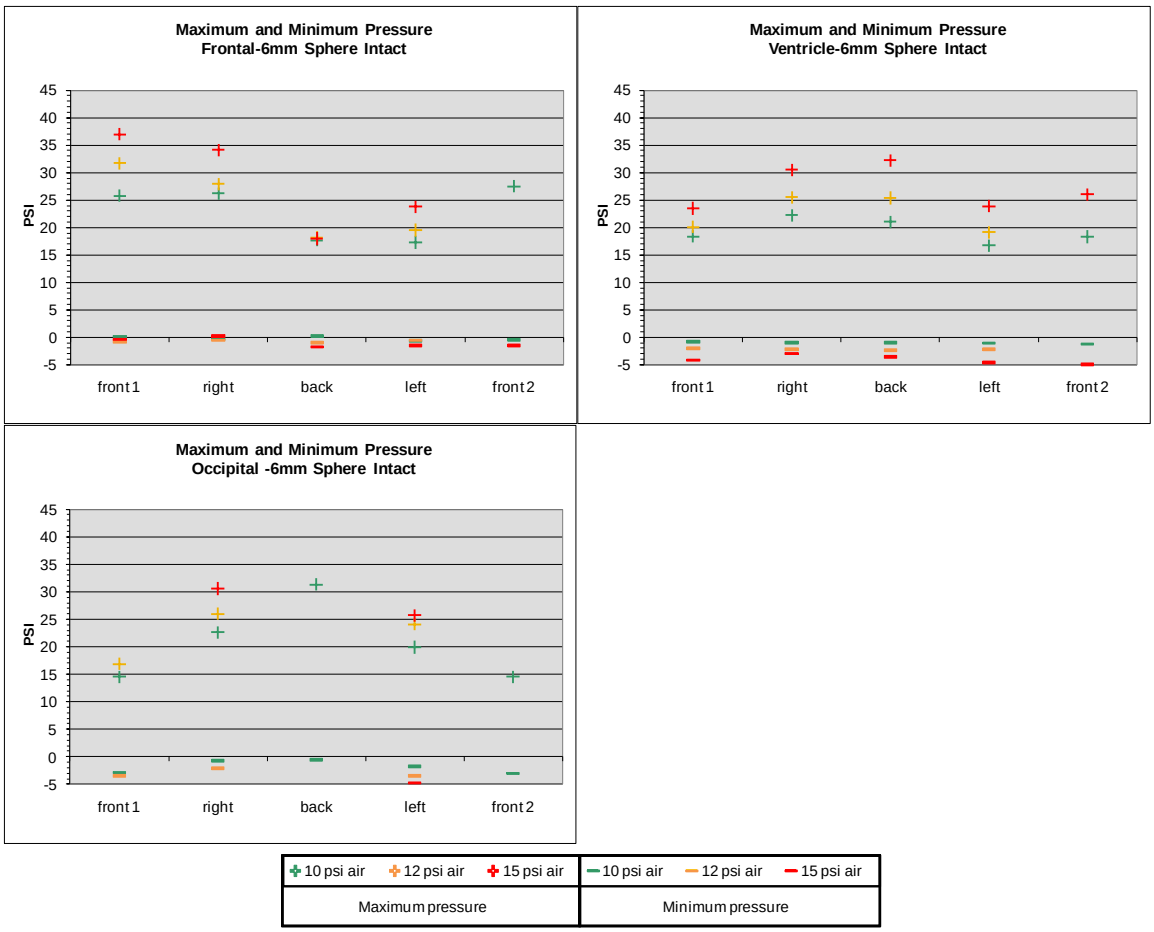

Figure 42: Graphs by sensor for maximum and minimum pressure values for the 6mm sphere (the results are color coded according to shockwave pressure).

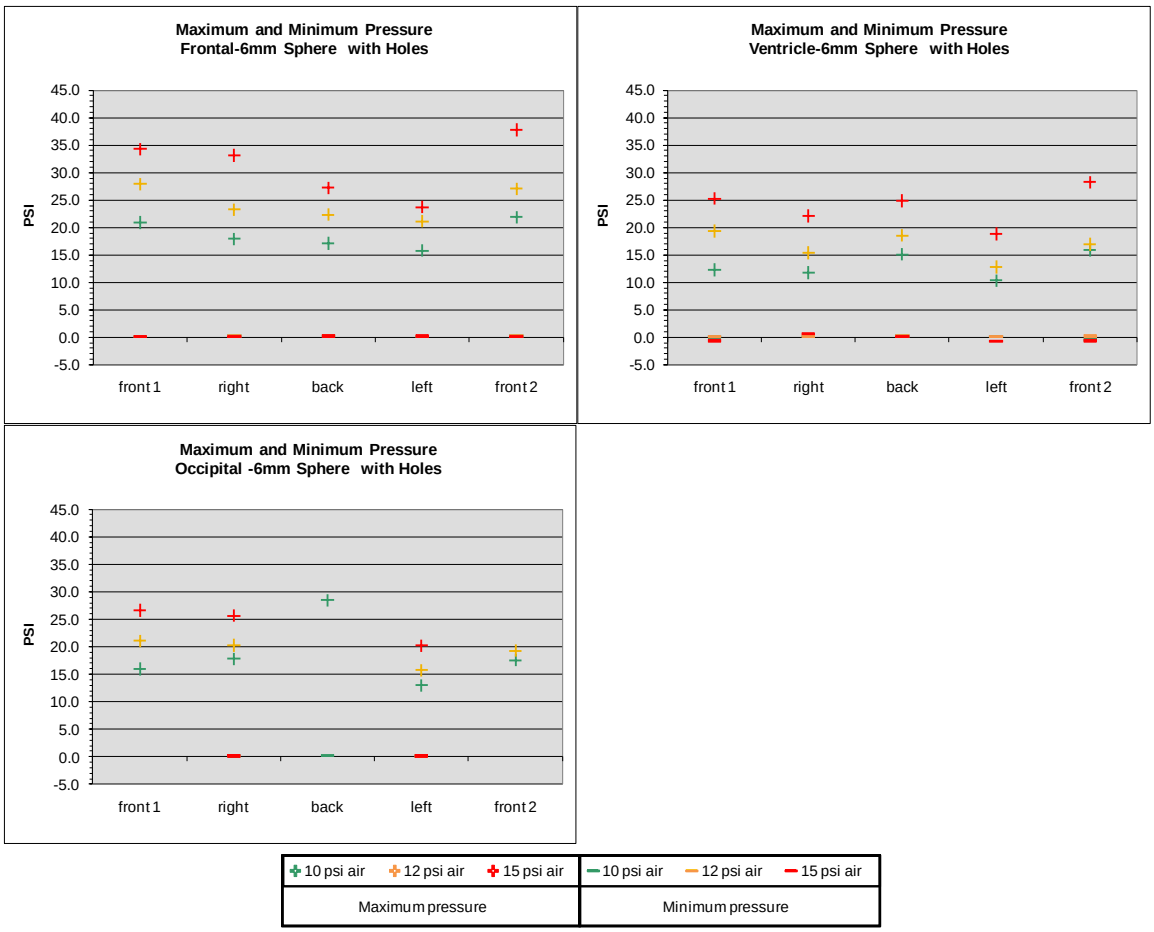

Figure 43: Graphs by sensor for maximum and minimum pressure values for the 6mm sphere with holes (the results are color coded according to shockwave pressure).

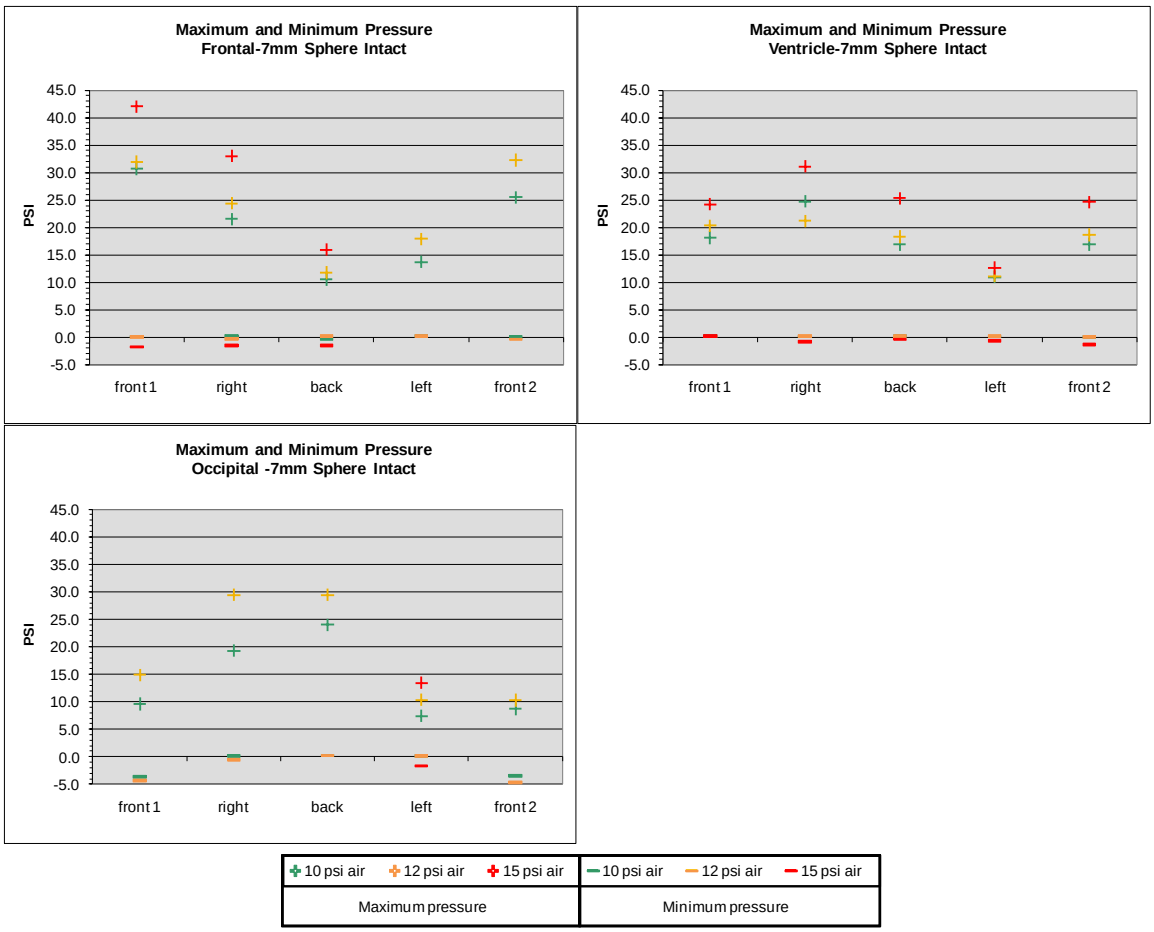

Figure 44: Graphs by sensor for maximum and minimum pressure values for the 7mm sphere (the results are color coded according to shockwave pressure).

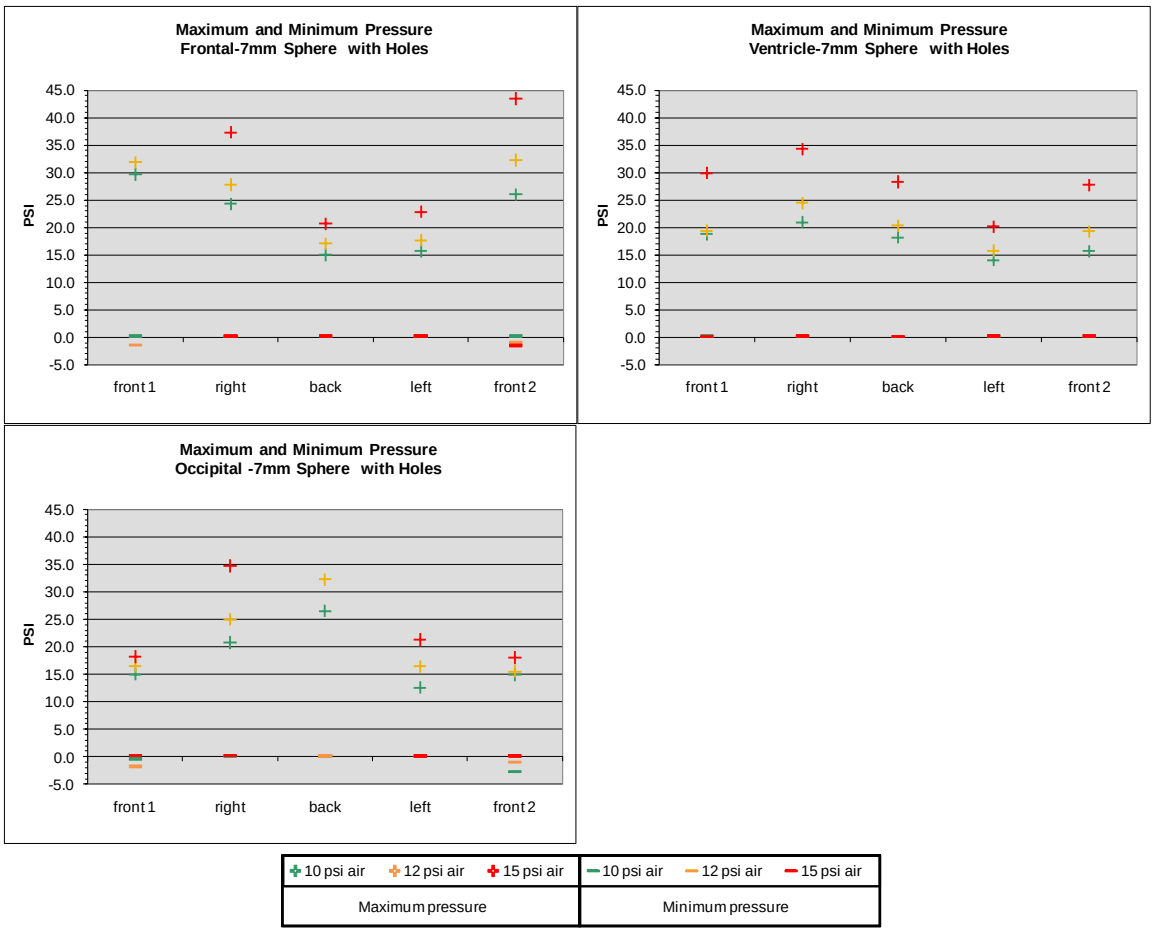

Figure 45: Graphs by sensor for maximum and minimum pressure values for the 7mm sphere with holes (the results are color coded according to shockwave pressure).

The graphical format permits to quickly identify the effects on peak pressure of increasing shock wave overpressure. Maximum pressure values increased in 98% of the cases. In fact, each case is a comparison of two values within the same orientation for each sensor and each sphere, for a total of 226 comparisons for all sensors and all spheres. By region, the effects of increased shock wave magnitude were: the ventricle sensor saw increased in maximum value 99% of the time; frontal increased 96% of the time; and occipital increased 100% of the time. In the same way, minimum values were compared to investigate the effects of increasing magnitude, but the results did not appear to be directly related to the shock wave overpressure. In general minimum values increased (i.e. had a greater negative value) in 51% of the cases (216 comparisons). By region the ventricle sensor had greater minimum values with increased

magnitude 52% of the time; frontal sensor 48% of the time; and occipital sensor 45% of the time. From the pressure results in the spheres, the minimum values did not appear to be directly related to the shock wave overpressure; consequently further analysis was focused only on the internal maximum pressure values collected in each sphere. Furthermore, because the minimum values had in general such a small variation, the pressure differential and maximum pressure results showed nearly identical behavior; therefore, there was no further use for pressure differentials in this study.

Table 6 shows an example of results for 1st rate values collected for one sphere. Tables of results for all spheres are provided in Appendix B, C, and D. Figure 46 to

Figure 51 summarize the same 1st rate results in graphical format for all cases. Similarly to the maximum pressure data, comparisons were performed to investigate the relationship between pressure gradients and increasing shock wave overpressure.

Table 6: 1st rate of change of pressure for 5mm-thick sphere.

1st rate (psi/ms)					
ventricle	front 1	right	back	left	front 2
10 psi air	**76.76**	**62.59**	**37.28**	**44.96**	**69.02**
12 psi air	**83.39**	**63.03**	**47.58**	**53.45**	**84.9**
15 psi air	**110.85**	**94.59**	**48.17**	**73.01**	**NA**
frontal	front 1	right	back	left	front 2
10 psi air	**97.81**	**89.52**	**29.17**	**33.94**	**100.1**
12 psi air	**107.4**	**90.06**	**37.76**	**37.59**	**117.07**
15 psi air	**140.1**	**124.2**	**44.14**	**46.9**	**NA**
occipital	front 1	right	back	left	front 2
10 psi air	**22.28**	**79.27**	**109.4**	**40.91**	**26.91**
12 psi air	**27.65**	**83.12**	**127.9**	**43.06**	**27.44**
15 psi air	**39.08**	**121.7**	**NA**	**NA**	**33.61**

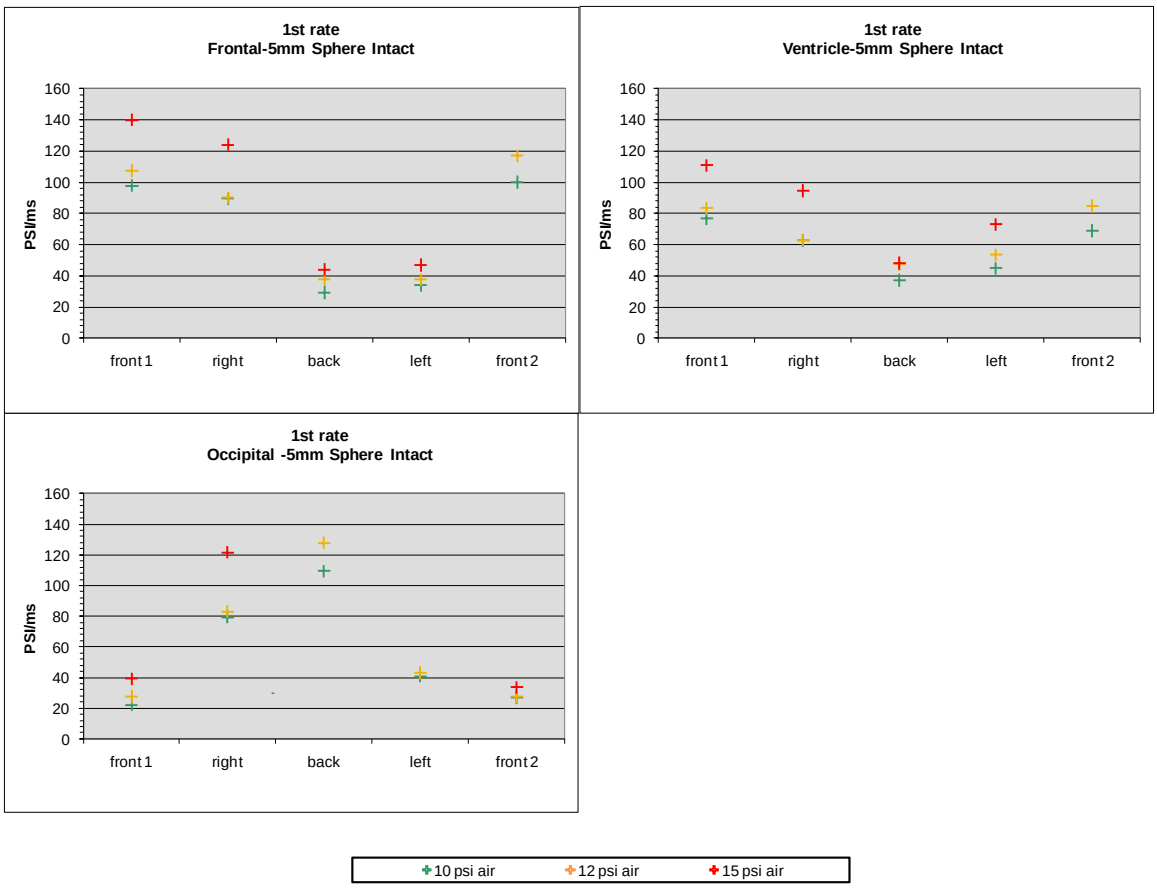

Figure 46: Graphs by sensor for 1st rate change of pressure values for the 5mm sphere (the results are color coded according to shockwave pressure).

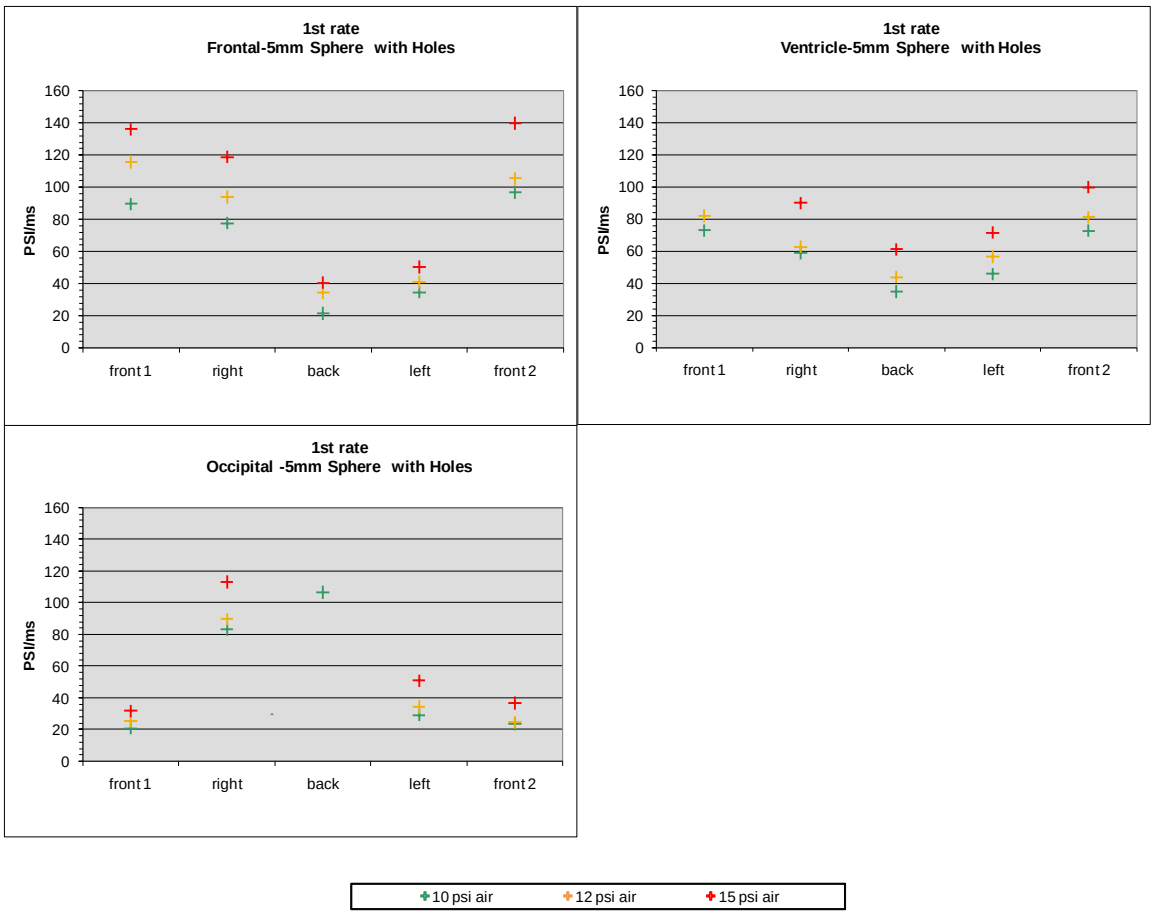

Figure 47: Graphs by sensor for 1st rate change of pressure values for the 5mm sphere with holes (the results are color coded according to shockwave pressure).

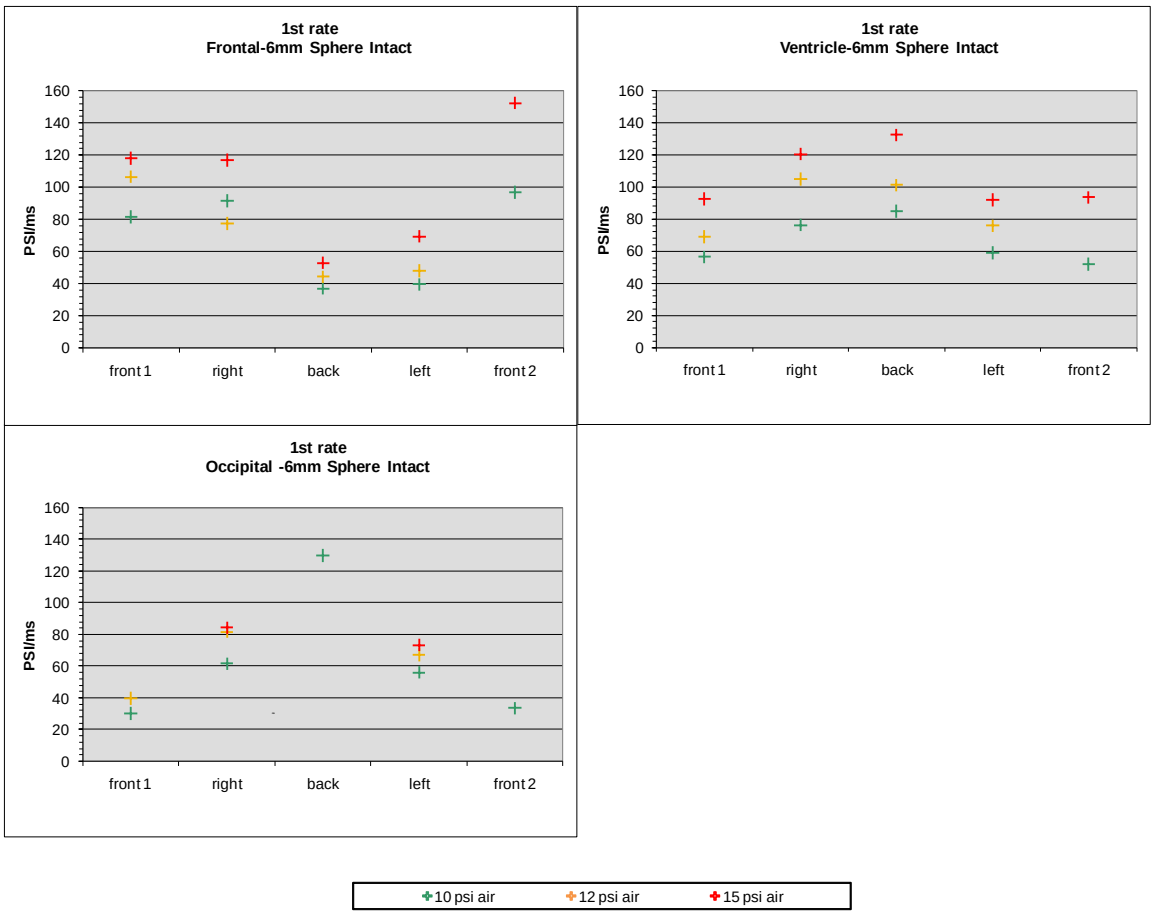

Figure 48: Graphs by sensor for 1st rate change of pressure values for the 6mm sphere (the results are color coded according to shockwave pressure).

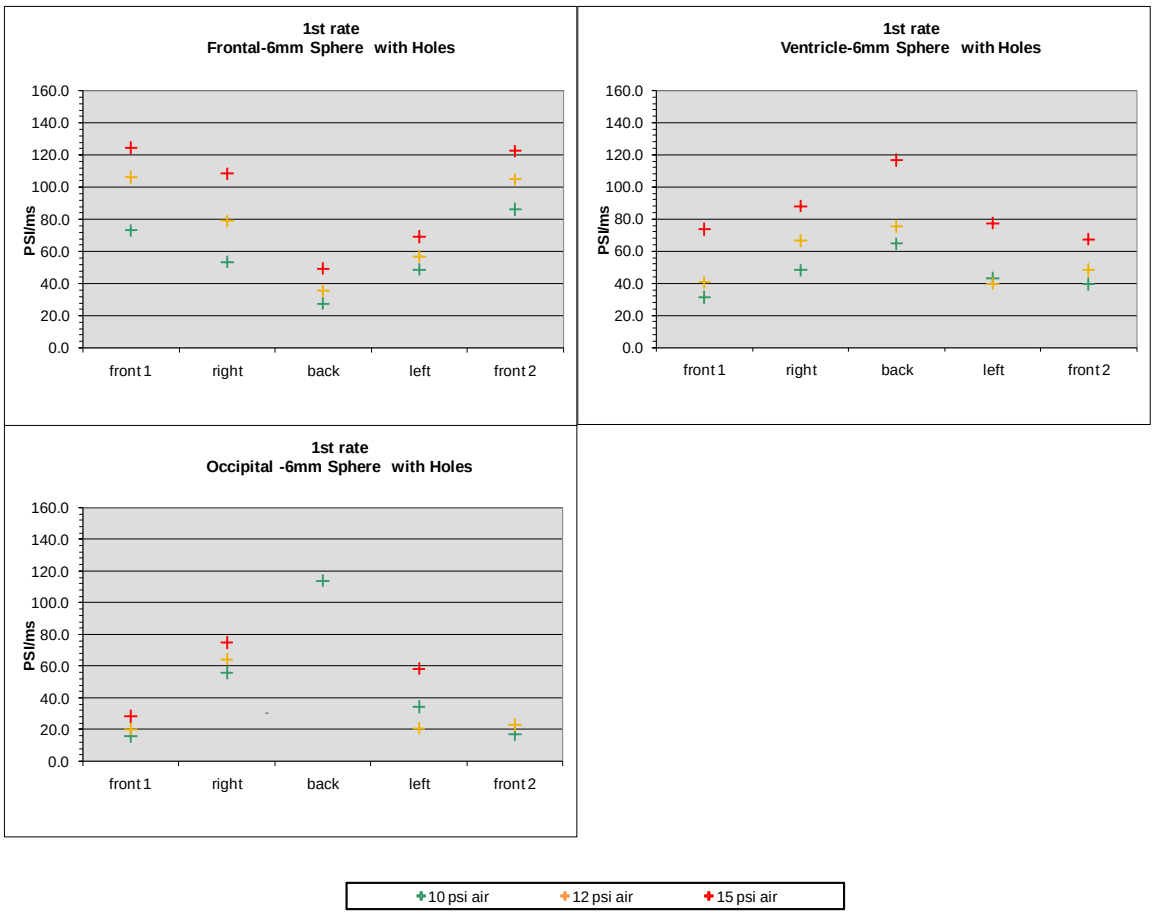

Figure 49: Graphs by sensor for 1st rate change of pressure values for the 6mm sphere with holes (the results are color coded according to shockwave pressure).

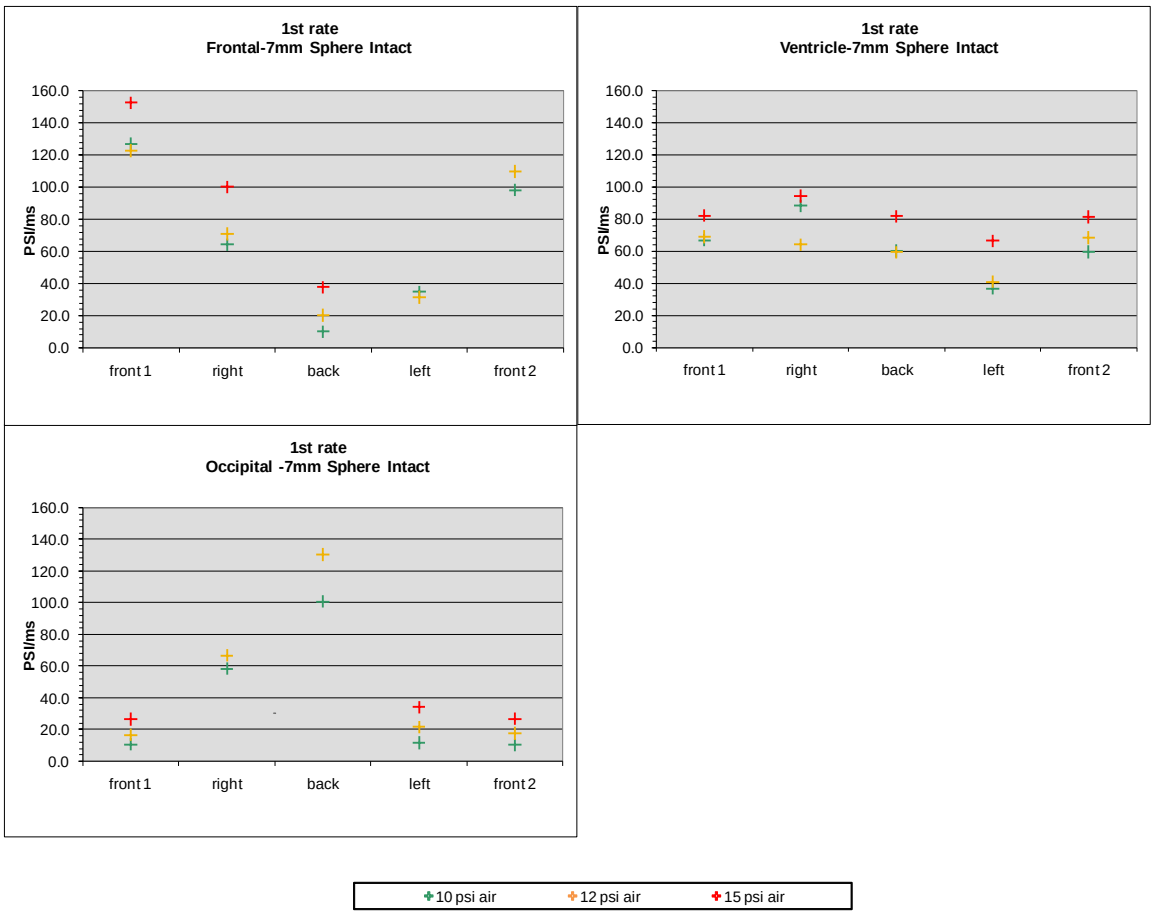

Figure 50: Graphs by sensor for 1st rate change of pressure values for the 7mm sphere (the results are color coded according to shockwave pressure).

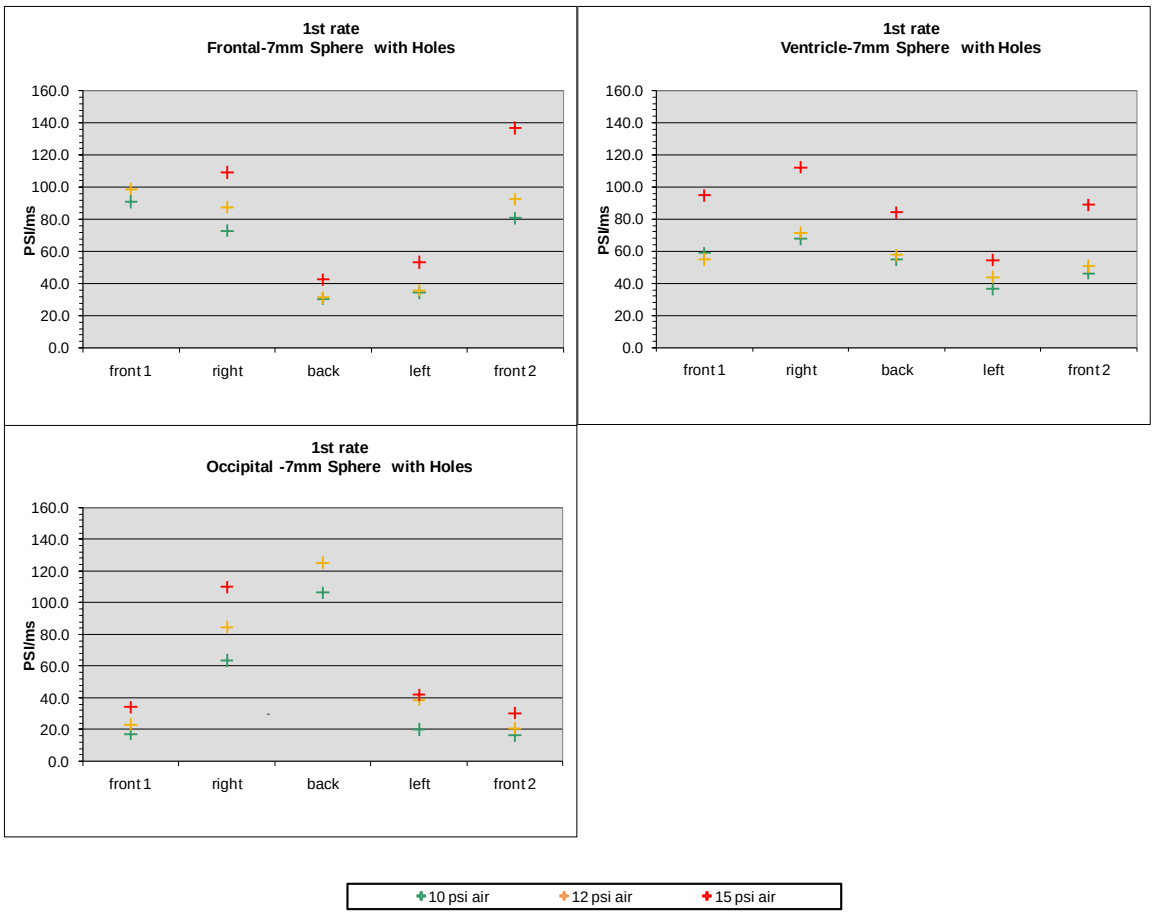

Figure 51: Graphs by sensor for 1st rate change of pressure values for the 7mm sphere with holes (the results are color coded according to shockwave pressure).

The graphical format permits to quickly identify the effects on 1st rate of increasing shock wave overpressure. As done for the peak pressure results, a total of 228 comparisons were performed for 1st rate. The 1st rate value increased with magnitude in 97% of the comparisons and by region the results were: ventricle 1st rate value increased 95% of the time; frontal 1st rate value increased 84% of the time; occipital 1st rate value increased 98% of the time.

To analyze if there were a direct proportion in the increase of internal pressure with increased shock wave magnitudes, percentages of peak internal pressure changes in each sphere were calculated normalizing for the corresponding pressure value at the 10 psi shock wave overpressure for each orientation (the overpressure increases from 10 psi to 12 psi and 15 psi are also presented as percentages in the tables). All tables are provided in Appendix B, C, and D. The

results confirmed that a higher shock wave overpressure (the 50% case in the tables) consistently corresponded to a higher percentage increase of peak pressure, but a more specific relationship could not be found. Similar results were obtained for 1st rate and the tables with values as percentages are provided in Appendix B, C, and D.

To investigate the effect of apertures on the samples, pressure results were compared between the intact sphere and the same sphere after holes were added. Tables of results are presented in Appendix B, C, and D and illustrate the comparisons as percentages of the peak pressure values in the intact spheres for each thickness. The comparisons between the tests in the intact sphere and the same tests in the sample with holes were obtained by subtracting the values of the latter tests (holes) from the values of the former tests (intact) and then dividing the result by the pressure values of the intact tests, to express the results as percentages of the peak pressure in the intact spheres. Therefore, in each table a positive value signifies higher internal pressure in the intact sphere compared to the same test once the apertures were introduced. For the 5mm-thick sphere, the differences in the maximum pressure values were rarely above 10% and this result is addressed in the discussion part of this chapter. In each table a value of "1" was given to each positive result and a value of "0" to each negative result (0% and NA were excluded); therefore for each table a respective matrix of 1 and 0 was created. Table 7 shows an example of this procedure for the case of the 5mm sphere.

Table 7: Matrix expressing maximum peak pressure increase in the 5mm-thick sphere with holes relative to the intact sphere when the value is "0".

	Maximun Pressure				
ventricle	front 1	right	back	left	front 2
10 psi air	1	1	1	1	0
12 psi air	0	0	0	0	0
15 psi air	NA	0	0	0	NA
frontal	front 1	right	back	left	front 2
10 psi air	0	1	1	0	0
12 psi air	0	0	1	0	0
15 psi air	0	0	1	0	NA
occipital	front 1	right	back	left	front 2
10 psi air	1	0	1	1	1
12 psi air	1	0	NA	1	1
15 psi air	0	1	NA	NA	1

From each matrix, percentages of 1 and 0 were calculated: the percentage of 0 was associated to the number of cases that the peak pressure was higher in the sphere with holes, while the percentage of 1 indicated the number of cases when the intact sphere had higher maximum pressure values. For the 5mm-thick sphere, when apertures were present, higher internal pressures were recorded in the frontal (71% of cases) and ventricle sensors (69%); while the occipital sensor (82%) measured higher pressures when the sphere was intact. For the 7mm-thick sphere, the matrix results revealed that higher internal pressures were recorded in all sensors when apertures were present: for frontal in 80% of the cases; for ventricle in 80% of the cases; and for occipital in 91% of the cases. On the contrary, the 6mm-thick sphere showed higher internal values occurring more frequently when the sphere was still intact: for frontal sensor in 77% of the cases; for ventricle in 86% of the cases; and for occipital in 70% of the cases. Figure 52 summarizes the results.

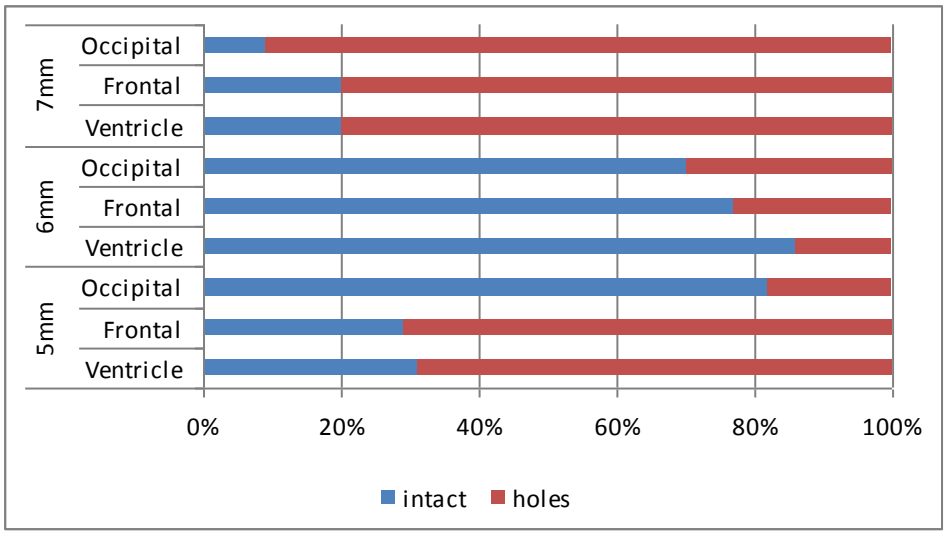

Figure 52: Summary of results in percentages of the number of cases the maximum peak pressure is higher in each sphere compared to the same sphere with apertures.
The value indicates percentage of cases when higher peak pressure was either in the intact sphere or in the sphere with holes for each sensor and for each shell thickness.

The 1st rate results were also examined when investigating the effect of apertures. The tables that illustrate the percentage of 1st rate variation before and after the introduction of apertures are presented in Appendix B, C, and D. Calculations were performed as for the maximum pressure values and similar matrices of 0 and 1 were created for each table. As before, from each matrix, percentages of 1 and 0 were calculated: the percentage of 0 was associated to the number of cases when 1st rate was higher in the sphere with holes, while the percentage of 1 indicated the number of cases when the intact sphere had higher 1st rate values.

For the 5mm-thick sphere, the calculated numbers revealed that higher 1st rate values were recorded more frequently in the intact sphere: frontal sensor in 64% of cases; ventricle sensor in 69% of cases, and occipital sensor in 75% of cases. Instead, for the 7mm-thick sphere, the 1st rate values were higher when apertures were present: in the frontal sensor 58% of the cases, in the occipital sensor 92% of the cases, and in the ventricle 43% of the cases. When the recorded data shows frequency of occurrence around 50%, it is safer to assume that we cannot recognize the presence of a definite trend. The 6mm-thick sphere showed higher 1st rate values

when the sphere was still intact: frontal sensor 67% of the cases; ventricle sensor 100% of the cases; and occipital sensor 100% of the cases. Figure 53 presents a summary of these results.

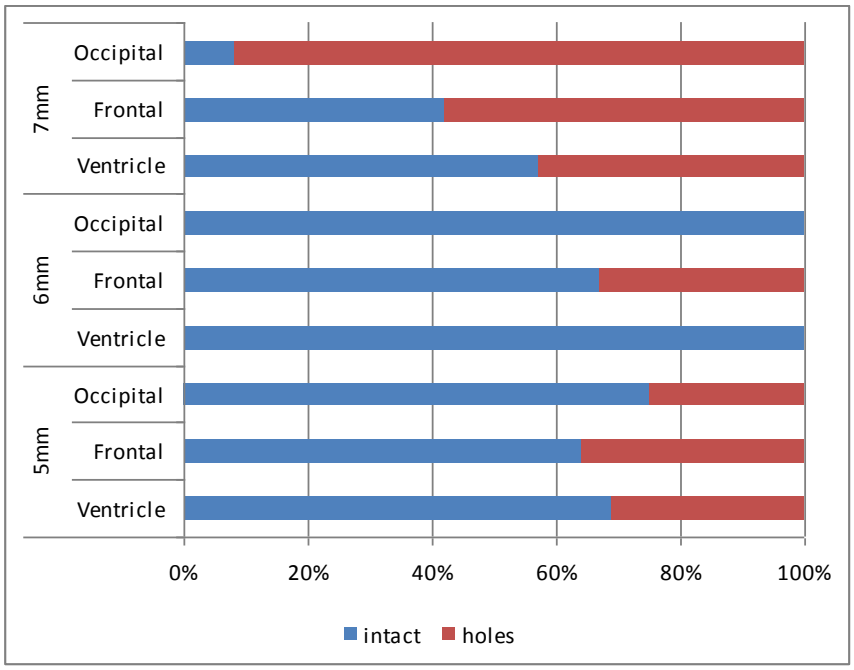

Figure 53: Summary of results in percentages for 1st rate in each sphere compared to the same sphere with apertures.
The value indicates percentage of higher rate in either the intact shells or the shells after the introduction of apertures.

To investigate the effect of shell thickness, a comparison of maximum peak values was carried out between the 5mm and 7mm thick spheres, which were filled with the same material (aqueous glycerin at 40% weight). Table 8 illustrates results of the comparisons between the tests in the intact 5mm-thick sphere and the same tests in the intact 7mm-thick sphere, and results of the comparisons between the tests in the 5mm-thick sphere with holes and the same tests in the 7mm-thick sphere with holes. The numbers are expressed in percentages of the thinner shell and they were obtained by subtracting the values of the 7mm-thick sphere tests from the values of the 5mm-thick sphere tests and then dividing the result by the pressure values of the 5mm-thick sphere tests. Therefore, in each table a positive value in the cell signifies higher internal pressure in the thinner sphere.

Table 8: Comparisons of blast test results using spheres at different shell thickness. The data is expressed in percentage of the thinner shell results. Positive numbers indicate higher pressure values in the thinner shell (5mm-thick sphere).

	Percentage of relative Maximum Peak Pressure Increase									
	7mm-sphere in respect to 5mm-sphere					**7mm-s with holes in respect to 5mm-s with holes**				
ventricle	front 1	right	back	left	front 2	front 1	right	back	left	front 2
10 psi air	**22%**	**-21%**	**-20%**	**34%**	**26%**	**18%**	**-7%**	**-32%**	**15%**	**35%**
12 psi air	**20%**	**3%**	**-19%**	**40%**	**27%**	**27%**	**-11%**	**-27%**	**19%**	**26%**
15 psi air	**28%**	**-9%**	**-34%**	**44%**	**NA**	**NA**	**-15%**	**-41%**	**17%**	**20%**
frontal	front 1	right	back	left	front 2	front 1	right	back	left	front 2
10 psi air	**0%**	**24%**	**34%**	**7%**	**16%**	**4%**	**9%**	**-6%**	**0%**	**20%**
12 psi air	**3%**	**18%**	**30%**	**-2%**	**4%**	**11%**	**8%**	**-5%**	**0%**	**7%**
15 psi air	**0%**	**15%**	**23%**	**NA**	**NA**	**NA**	**6%**	**-4%**	**-6%**	**3%**
occipital	front 1	right	back	left	front 2	front 1	right	back	left	front 2
10 psi air	**35%**	**23%**	**23%**	**52%**	**39%**	**-9%**	**18%**	**13%**	**8%**	**-14%**
12 psi air	**6%**	**-13%**	**17%**	**39%**	**31%**	**-17%**	**11%**	**NA**	**0%**	**-11%**
15 psi air	**NA**	**NA**	**NA**	**NA**	**NA**	**-1%**	**7%**	**NA**	**-3%**	**-7%**

As before, a value of 1 was given to each positive result and a value of 0 for each negative result (0% and NA were not included). This time the percentage of 0 indicated the number of cases when the thicker sphere had higher pressure, while the percentage of 1 indicated the number of cases when the thinner sphere had higher pressure. In the case of the intact spheres, a total of 36 comparisons were performed between the 5mm and 7mm data results for maximum value. The 5mm-thick sphere had higher peak internal pressure in 81% of the comparisons. By region, the 5mm-sphere peak pressure value was higher 64% of the time in the ventricle, 92% of the time in the frontal and 90% of the time in the occipital location. In the case of spheres with apertures, a total of 38 comparisons were performed for maximum value, and the 5mm thick sphere had a higher peak internal pressure in 55% of the comparisons. By region, the 5mm-sphere peak pressure value was higher than the 7mm-sphere peak pressure 57% of the time in the ventricle, 67% of the time in the frontal and 42% of the time in the occipital location. Figure 54

presents a summary of the results of different shell thickness for both cases of the intact spheres and of the spheres with apertures.

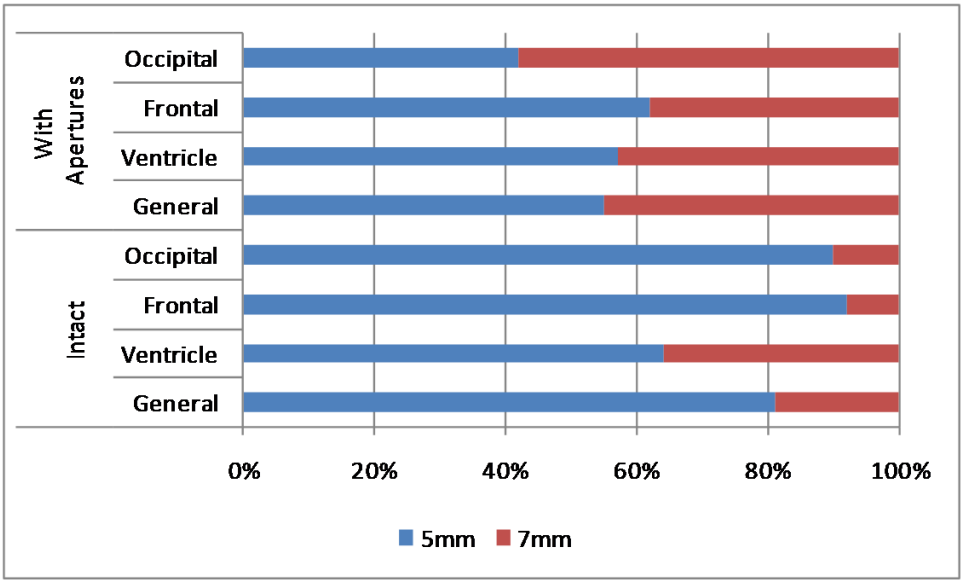

Figure 54: Percentages of peak pressure values that are higher in the 5mm-thick sphere compared to the 7mm-thick sphere.
Pressure results were compared for both the intact shells and the shells after the introduction of apertures. General groups all the sensors together.

Comparisons on the 1st rate values between the 5mm- and the 7mm-thick spheres (for both 'intact' and 'holes' cases) were also performed to investigate the effect of shell thickness on pressure gradients. In Appendix B, tables present the results of the comparisons in percentages of the thinner shell values. Calculations were similar to all the cases previously presented and, as before, a positive value signifies higher rate in the 5mm-thick sphere compared to the same test in the 7mm-thick sphere.

In the case of the intact spheres, 38 comparisons of 1st rate values were performed between the 5mm- and the 7mm- thick spheres. The results indicated that the thinner sphere presented higher rates than the thicker sphere 74% of the time. By region the results were: ventricle had higher 1st rate in the thinner shell in 62% of the cases, frontal in 69% of the cases, and occipital in 92% of the cases. After apertures were introduced, 40 comparisons of 1st rate

values were performed between the 5mm- and the 7mm- thick spheres with holes. The results indicated that the thinner sphere with holes presented higher rates than the thicker sphere with holes 70% of the time. By region the results were: ventricle had higher 1st rate in the thinner shell in 57% of the cases, frontal 71%, and occipital 83%. Figure 55 presents a summary of the results for both cases of the intact spheres and of the spheres with apertures.

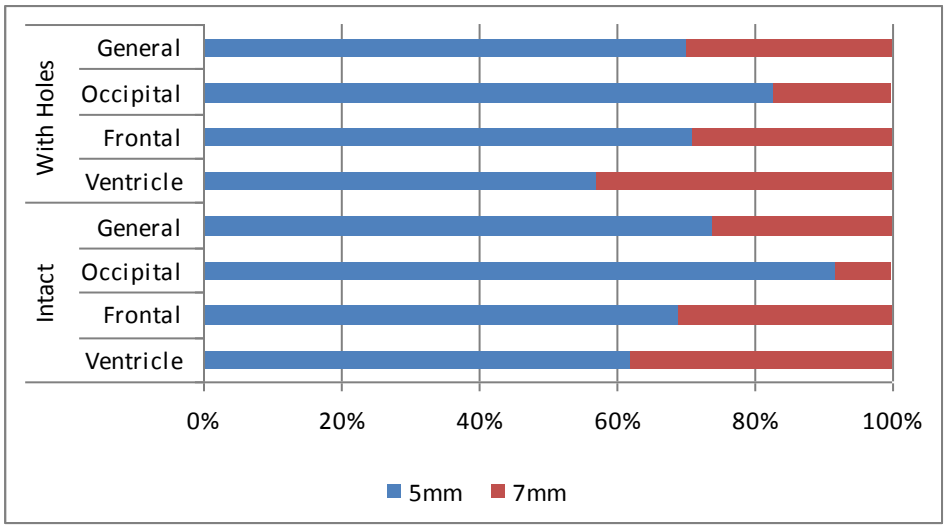

Figure 55: : Percentages of 1st rate of change of pressure values that are higher in the 5mm-thick sphere compared to the 7mm-thick sphere.
Pressure results were compared for both the intact shells and the shells after the introduction of apertures. General groups all the sensors together.

Finally, for each test that had a valid reading for all three sensor locations (regions), comparisons were performed among each of the pressure sensors data to determine which region possessed the highest peak pressure and 1st rate values in the spheres. For every test, among all three sensors the corresponding maximum peak values (and later 1st rate) were compared and the sensor associated with the highest value for that test was reported. Overall 58 tests could be used for comparisons for the maximum peak value and 59 for the 1st rate value. In the case of the 5mm-thick intact sphere, the frontal sensor had the highest maximum peak 60% of the time (ventricle 20% and occipital 20%); the highest 1st rate 60% of the time (ventricle 20% and occipital 20%). In the case of the 5mm-thick sphere with holes, the frontal sensor had the highest maximum peak 60% of the time (ventricle 30% and occipital 10%); the highest 1st rate 50% of

the time (ventricle 30% and occipital 20%). In the case of the 6mm-thick intact sphere, the frontal sensor had the highest maximum peak 56% of the time (ventricle 0% and occipital 44%); the highest 1st rate 33% of the time (ventricle 56% and occipital 11%). In the case of the 6mm-thick sphere with holes, the frontal sensor had the highest maximum peak 90% of the time (ventricle 0% and occipital 10%); the highest 1st rate 70% of the time (ventricle 10% and occipital 20%). In the case of the 7mm-thick intact sphere, the frontal sensor had the highest maximum peak 50% of the time (ventricle 13% and occipital 37%); the highest 1st rate 44% of the time (ventricle 33% and occipital 22%). Finally, in the case of the 7mm-thick sphere with holes, the frontal sensor had the highest maximum peak 82% of the time (ventricle 0% and occipital 18%); the highest 1st rate 45% of the time (ventricle 36% and occipital 18%). Figure 56 summarizes the results.

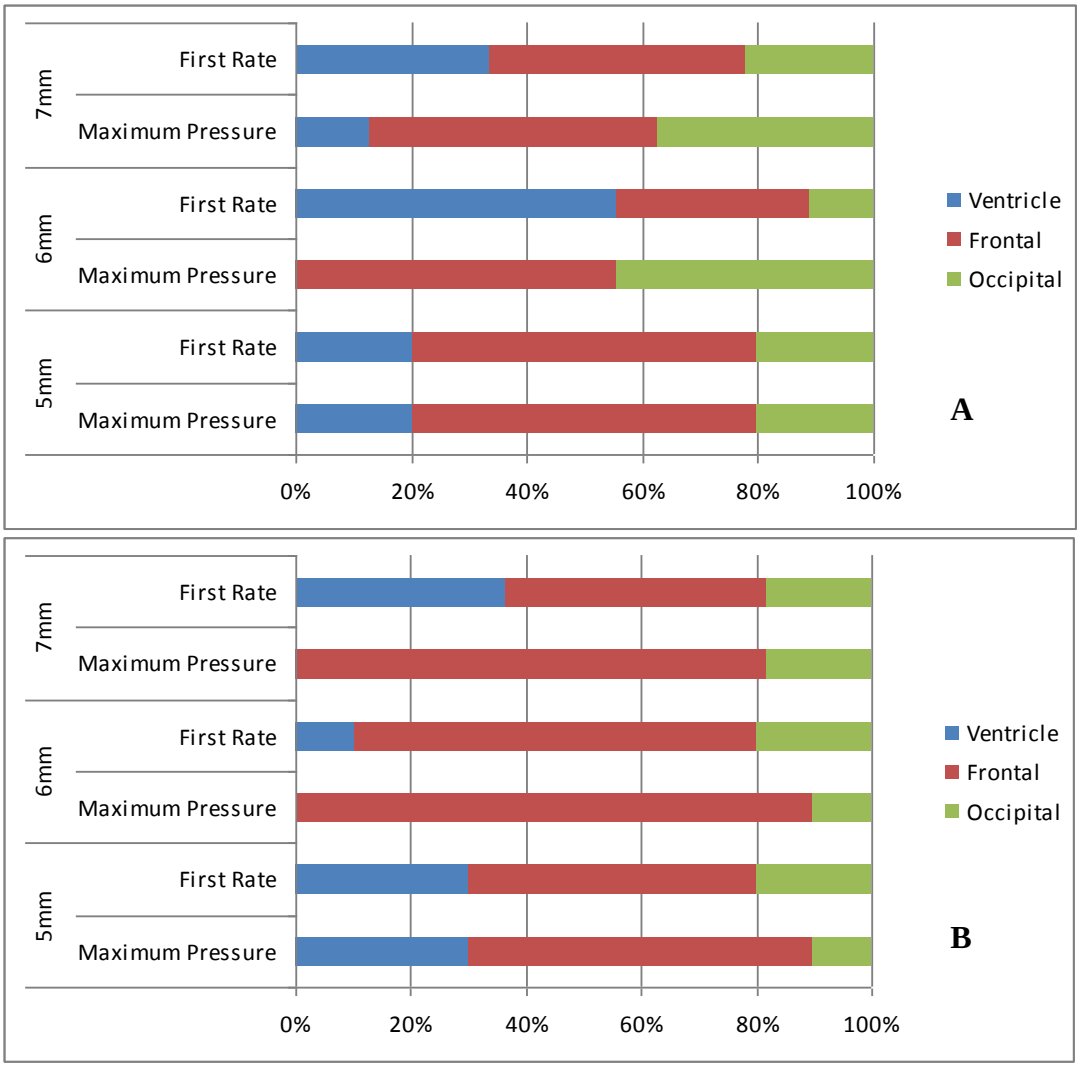

Figure 56: Percentage of tests in which each sensor had the highest value for peak pressure and 1st rate, in each sphere.
A: intact sphere; B: sphere with holes.

5.3.2 Strain results

Four strain gages were placed at the front, back, left and right side of the shell, as cardinal points of a compass (Figure 33). Although the harsh blast testing environment usually creates problems to the survivability of strain gages, their installation was quite successful in this study and seldom there was wiring damage or delamination. Tables in Appendix B, C, and D show the state of the gages during the blast simulation series. When a gage stopped working during the first

series, the series was first completed and then the gage was replaced for the second series. The gage was not replaced if it stopped working or malfunctioned in the second series.

During testing it was discovered that the glue amount on the gage was a concern: too much and the data would show time delays during blast loading (delays of microseconds are an issue in the blast environment); too little and the gage would start to delaminate from the surface affecting data collection. Both behaviors described above were experienced in this study, and the extent to which these behaviors reflected on the collected data is unknown. However, valuable observations regarding gross deformation of the shell could still be made from the strain results. Appendix B, C, and D provide strain gage time-traces in the same time-window as the pressure profiles concurrently recorded.

From strain data collected with all spheres, a first important observation could be made regarding the primary mode of deformation of the shell. Figure 57 presents an example of strain data: results are similar for every shell thickness.

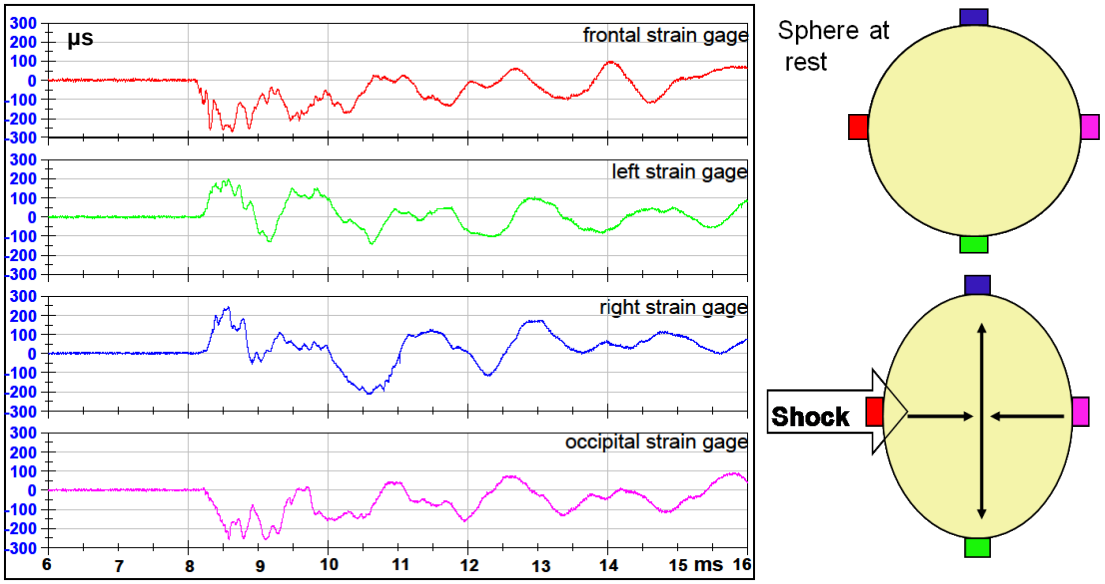

Figure 57 Example of strain time-traces that show deformation mode for the sphere. The strain traces are color-coded to identify the position of the sphere (cartoon on the right). For strain data, compression is negative on the diagrams and positive values indicate tension. The cartoon shows the sphere deformation (exaggerated) at the first moment of blast loading. These records come from test 1 for the intact 5mm-thick sphere.

The strain data presented in Figure 57 is an example of a consistent pattern seen in all spheres at each test during the first moment of blast loading. In the shell the coup (site of initial blast loading) and countercoup (location opposite to coup) would experience compression, while the sides would experience tension. Therefore, the initial deformation of the sphere is similar to what is shown in the cartoon in Figure 57. In addition, the strain data revealed that the response of the shell resulted in a prolonged pattern of mirrored areas of tension and compression, which created an asynchronous mode of deformation. First, the coup and countercoup experienced compression while the sides went into tension; then the stresses were reversed and the sides experienced compression while the coup and countercoup went into tension. The pattern continued on, although damping quickly decreased the amplitude of the oscillations. Furthermore, when orientation was changed and the gages on the sides were moved to coup/countercoup positions (90 degrees rotation), the strain data showed reciprocal behavior in the time-traces, as it would be expected due to the symmetry of the sphere (Figure 58).

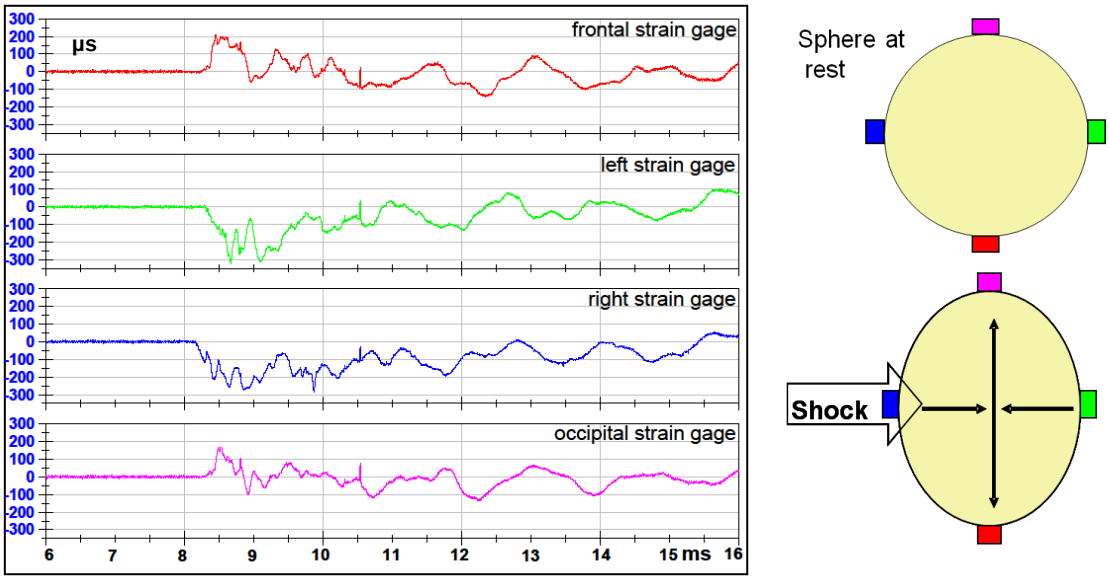

Figure 58: Example of strain data time-traces after a 90 degree rotation.
The coup site is at the right strain gage and the countercoup site is at the left gage.
The right and left strain gages experience a compression first (negative strains), while the other two experience tension (positive strains).
These records come from test 2 for the intact 5mm-thick sphere.

A second observation could be made regarding the interaction of the strain gages and the shock wave overpressure. Figure 59 compares the frontal strain recordings in a front orientation during blast exposure to the shock wave overpressure occurring around the sample during the simulated blast event. This example shows that the strain time-trace has a background quasi-static component that nearly tracks the external static pressure, as it would be expected when applying an external pressure to the strain gage. In fact, the two responses are overlapping: the shock front excites an oscillation on the shell, which is seen riding a decreasing compression because concurrently the external pressure, which also acts on the shell and strain gage, is decreasing as well. This behavior is present in every gage but it is more exaggerated in the gage at the coup site.

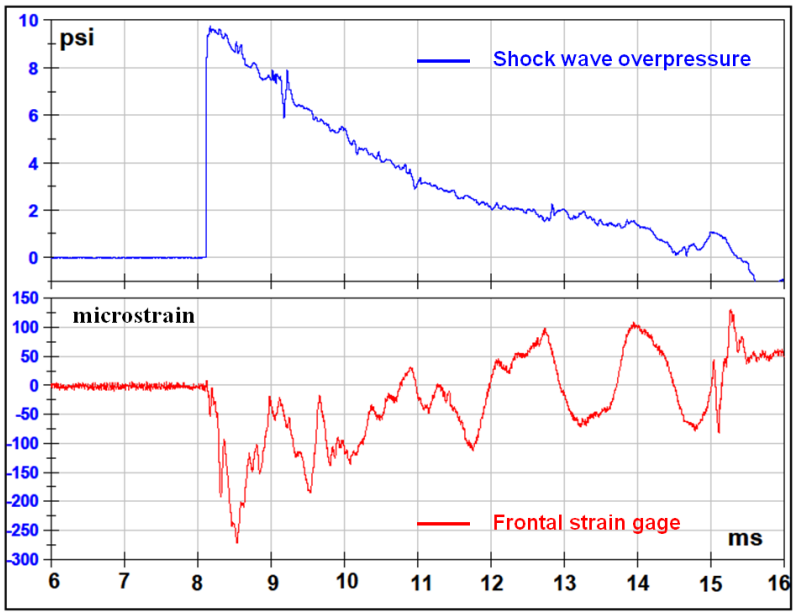

Figure 59: Example of frontal strain showing the background quasi-static component that nearly tracks the external static pressure.
This record comes from test 1 for the 5mm-thick sphere with apertures.

In addition, when comparing the strain and pressure profiles in terms of frequency response, strain data shows an oscillatory response close to that of the internal pressure data. The internal pressure data demonstrates a highly damped frequency around 700 Hz for each sphere, and a similar frequency was found for strain recordings. The presence of a similar oscillatory response in the two sets of gages indicates a close coupling of the shell/filling systems.

Interesting observations can also be made when looking at the data recordings beyond the time-window that appropriately simulates a free field blast. Figure 60 shows the strain records together with the shock wave overpressure measured in the proximity of the gages. The time-window spans 85ms, which allows for the development of pressure phenomena completely atypical of free-field blast physics and the consequences can be seen on the sample. The most dramatic effects are marked by line A and B in Figure 60. Line A shows the arrival of a compression wave coming from the open end of the expansion. This compression wave was described in Figure 12: it started as the rarefaction wave that reflected from the close end of the

driver, then traveled down the driven and after reflecting at the open end of the expansion has now become a compression wave. The effects of such compression are quite visible both in the air overpressure profile and in the strain gage time traces. In the air overpressure there is a sudden increase in pressure, as pointed out by the arrow of line A. Concurrently, in the strain gages this compression wave re-excites the oscillatory response that was dying down.

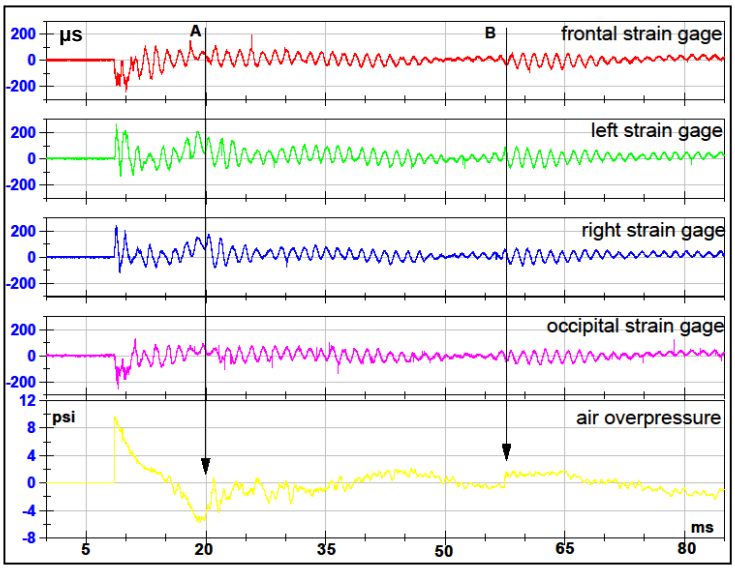

Figure 60: Strain data beyond the appropriate time-window.
These records are used to show some pressure phenomena completely atypical of free field blast that occur after the set time window. Line A shows a first reflected compression wave that hits the sample and can be detected in the strain records. Line B shows a second compression wave. Both compression waves re-excite an oscillatory mode that was almost dying down.

A later compression is shown by line B in Figure 60. This compression is also linked to the same rarefaction wave that started by reflecting at the driver end: after becoming a compression wave is seen moving upstream (towards the driver) into the expansion and interacting with the sample a first time at line A; then this wave continues on until it reflects at the close end of the driver and comes back again as a compression. This time it is moving downstream, interacting with the sample (and the strain gages) as a new compression at time-line B. The effects of such compression are also quite visible both in the shock wave overpressure profile and in the strain gage time-traces. In the shock wave overpressure profile there is again a

sudden increase in pressure, as pointed out by the arrow of line B. At the same time, in the strain gages this compression wave re-excites a new oscillatory response after damping had almost reduced the strain values to zero.

When considering the strain data recordings beyond the appropriate time-window, a final observation was made regarding the mechanical response of the sphere in connection to the different filling materials. Figure 61 shows examples of strain records for spheres of different thickness before and after the introduction of apertures. The time-window spans 85ms.

A

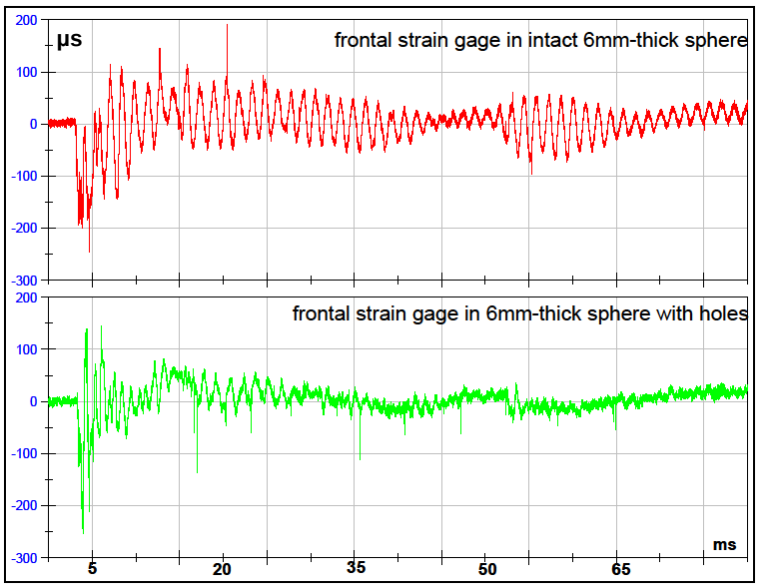

B

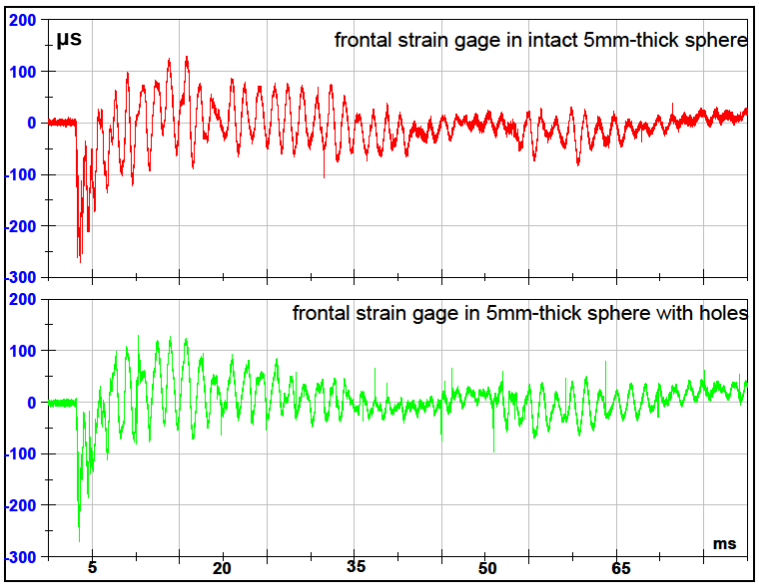

Figure 61: Examples of strain data before and after the introduction of holes in the shells.
The spheres contained different filling material: Sylgard in A and aqueous glycerine in B. Both tests show the first front orientation at 10psi overpressure. In both graphs the timeline has been shifted to eliminate some unnecessary zero-data at the beginning of the recordings. Therefore time is only indicating correct elapsed time.

As it can be noticed in Figure 61, the strain data before and after the introduction of apertures is quite similar in the first few milliseconds of blast loading for both spheres. However, the general behavior changed when a larger time-window was considered. In the sample

containing aqueous glycerine (5mm-thick sphere), the strain data does not look very different when visually comparing the two cases (no holes versus holes). On the contrary, in the sample containing Sylgard 527 (6mm-thick sphere), the strain data has clearly fewer oscillations after the apertures were introduced. It appears that damping was affected quite dramatically in the Sylgard experiments after holes were drilled.

5.4 Discussion

This study sought to establish the basic phenomenology of shock wave interaction with a simplified model of skull/brain system. The effects of the incident shock wave pressure on waveform shape and magnitude for the internal pressure were explored. The relationship between magnitude levels of incident pressure and values of internal pressure in spheres of different thicknesses, using two different filling materials, and also introducing holes in the shells were examined. Different regions of the spheres were monitored to investigate the effects of orientation on internal pressures, and to compare pressure distribution patterns with surface strain data recorded concurrently. Three polyurethane spheres were tested inside a shock tube expansion: they were exposed to fifteen simulated blasts, changing pressure magnitudes and orientation of the sample; then apertures were added and a second series of tests was conducted as before. Internal pressures with three sensors, and strain values with four gages were collected.

For each test, the pressure data was filtered, then maximum and minimum pressures were recorded and pressure differential and 1^{st} rate of change of internal pressure were calculated. Because the minimum values had in general a small variation, the pressure differential and maximum pressure results showed nearly identical behavior. Therefore, no further reference was made to minimum values and pressure differential values in this study. Of the remaining processed data (maximum pressure and 1^{st} rate), the most reliable values belonged to the maximum pressure tables, as the attainment of such values was more straight forward and requires almost no manual procedure. On the contrary, rate values were manually calculated and

therefore subjected to human error (the operator had to pick the two points on the curve that would provide the rate value). It would have been preferable to have derivatives, but a more sophisticated filtering process must be developed first. Therefore, outcomes from 1st rate analysis were presented with the understanding that this is a limitation of the current study.

Another limitation of the study was the use of strain gages. Strain gages were a crude way to investigate shell/skull flexure, because they only presented measurements for isolated points on the surface, and it is difficult to infer the global behavior from a few points. In this case the geometrical symmetry of the samples helped when analyzing deformation patterns, and the information gathered was adequate for the basic level of the study. A final limitation of this study was the restricted range of shock wave overpressure values provided during testing. As mentioned in Chapter 2, presently, the major limitation to reaching higher driver pressures is the clamping system that holds the membrane.

A first observation that has validity for every sphere (intact or with holes) is that the measured internal peak pressures were higher than shock wave overpressure in every test and for every sensor. This is likely due to the fact that the sphere systems were practically sealed with no air inside, therefore a small decrease in volume could cause great pressure increase. The fundamental event is a global compression experienced by the shell as shown by the strain gages. Also comparisons of data showed that maximum pressure and 1st rate directly increased with higher magnitudes of air overpressure. This direct relation is due to the fact that the samples tested had a simplified geometry.

A second observation that has general validity is that, when comparing the strain and pressure profiles in terms of frequency response, strain data showed an oscillatory response close to that of the internal pressure data. The internal pressure data demonstrates a highly damped frequency around 700 Hz for each sphere, and a similar frequency was found for strain recordings. The presence of a similar oscillatory response in the two sets of sensors provides evidence of a close coupling of the filling/shell systems for the simple physical model.

To investigate the effect of shell thickness, two spheres of identical external dimension and identical filling material were tested and the results compared. Increasing the thickness of the shell generally reduced the maximum pressure value, although the effect was more noticeable when the spheres were intact (Figure 54). Once apertures were introduced, the maximum pressure values in each sphere increased when compared to the intact case (Figure 52). However, the maximum pressure differences between the 5mm-thick sphere and the 7mm-thick sphere were reduced to the point of becoming nearly insignificant as the energy from the shock had a direct path to the inside and less protection was provided by the added thickness (Figure 54), in fact the thinner sphere recorded higher values in approximately one half of the tests. The fact that a wider thickness range was not available for the Synbone spheres was a limitation of this study.

To investigate the effect of apertures, each sphere was tested before and after the introduction of holes that simulated superior orbital fissures. Figure 52 summarizes the differences in maximum pressure between the two cases (intact vs. holes) for each sphere, expressed as percentages of the intact sphere. The results of Figure 52 appear to indicate that the maximum pressure increased when holes were present for the 5mm-thick sphere and the 7mm-thick sphere, while pressures were higher for the intact 6mm-thick sphere. However, when considering the actual percentages presented in tables (Appendix B, C, and D), this observation needs to be further discussed. When examining the tables for the 6mm-thick and 7mm-thick spheres, most of the percentages are above or near 10%, while most of the percentages for the 5mm-thick sphere are below that threshold. The low percentages would indicate that the results for the 5mm-thick spheres are quite close to each other and, in many cases, within the precision of the data acquisition system. In the end, it seems more appropriate to conclude that there was no significant difference in maximum pressure transmission in the two cases of the thinnest sphere, while the thickest sphere clearly showed maximum pressure increase after holes were introduced. Since the aperture size was the same in both cases, this observation supports the interpretation

that the increase in peak ICP was likely related to the relative decrease in local shell stiffness versus the direct pressure ingress.

Regarding the medium-thickness sphere, it measured higher maximum pressures when still intact. This sphere was filled with Sylgard, a material having great adhesion to the internal surface of the shell as well as greater shear stiffness properties. This is an important detail that can explain the decrease in pressure when the apertures were introduced, especially after considering that the holes in this sphere were left open. When cured Sylgard is exposed to increased pressure, it tends to change shape similarly to a balloon full of water. We suggest that in the presence of open holes, Sylgard would dissipate some of the blast energy that is experienced as shell compression by changing shape and temporarily protruding through these holes. This very small deformation is not possible while the sphere is still intact. Therefore, pressure does not increase as much as in the intact sphere, because more energy is actually dissipated by the deformation of the filling. Moreover, this phenomenon is also seen by the strain data, which recorded a faster damping of the shell oscillations in the 6mm-thick sphere with holes (Figure 61).

In preliminary observations it was pointed out that each pressure sensor demonstrated consistency of pressure profiles at each orientation during exposure to shock waves of increasing magnitude. More specifically, the occipital sensors showed peak-shaped pressure profiles at back and right orientations; the frontal sensors presented peak-shaped pressure profiles at front and right orientations; and the ventricle sensors showed peak-shaped profiles at right orientation. These findings were also confirmed when looking at the maximum peak pressure values in the graphs summarizing each sensor (Figure 40 to Figure 45). In every sphere, at every magnitude, each sensor consistently showed the highest peak pressure values at a precise orientation. For each sensor, this orientation matched the position where the sensor-tip was the closest to the coup site during exposure to the simulated blast. Therefore, for each test the peak internal pressure decreased rapidly with distance from the coup site, as it would be expected in the case of a

simplified geometry. The current data demonstrated that the highest pressures were at front orientation for the frontal sensors, at back orientation for the occipital sensors, and at right or front orientation for the ventricle sensor.

This behavior could be used as evidence of transosteal propagation if no other data on the event were concurrently available. Fortunately the frontal and occipital sensors were installed in such a way to be able to monitor the coup and countercoup sites in some of the shock tests. Therefore especially during front exposures, the occipital sensor that monitored the region close to the countercoup site was able to provide evidence of a different behavior. As shown in Figure 39 the occipital sensor experienced tensile stress (reduction in pressure) during the first moments of the front exposure, while the occipital strain gage was concurrently recording compression of the shell. If the mechanism of energy transmission were purely transosteal, the two gages would be showing the same type of stress. The fact that a compression value was collected in the shell while a tensile value was collected in the filling supports the idea that the mechanism of energy transmission is not transosteal but rather a "multimodal flexure" mechanism.

The tensile stress is easier to detect at the countercoup site with increasing stiffness of the shell, and the 7mm-thick intact sphere presents the best examples in our study. The thinner the sphere the less stiff the shell, and the introduction of holes decreases the stiffness of a sphere. The observed phenomena can be explain by considering that the stiffer the shell the sooner the deformation/loading is propagated along the shell. A sudden and very small relative motion is created between the filling on the inside and the shell, because the filling cannot react as quickly as the shell. As the result of this temporary small although sudden separation between filling and shell, a compression can be seen at the coup site, while a tensile stress is developed at the countercoup site. In the meanwhile, the shock front is progressing on the outside of the shell and a global compression is imparted to the structure. Similar behavior was described by Engin (1969) in computational simulations of fluid-filled spherical shells.

Finally, for each test, comparisons of pressure data were performed among each of the pressure sensors to determine which sensor possessed the highest peak pressure values at any magnitude. Results unveiled that the frontal sensor was consistently linked to the highest values, especially after apertures were introduced (Figure 56). This result is a consequence of the proximity of the frontal sensor to the apertures. More energy from the blast is transmitted through the holes and is recorded at the nearest sensor, which happens to be the frontal sensor.

Although as previously explained, there is a need to be cautious when examining the pressure gradient results, some rates had consistent trends and suggested a particular mechanical response of the sphere systems. It appears that the 1st rate values are associated with energy that reaches the filling inside: more specifically higher rates correspond to greater energy exchange. When comparing the effect of shell thickness, Figure 55 shows the percentages of 1st rate cases that were higher in the 5mm-thick spheres compared to the 7mm-thick spheres. At the moment of blast loading, when the spheres were intact, more energy was reflected by the stiffer shell and less was imparted to the filling inside. On the contrary the thinner shell being less stiff reflected less energy; therefore, an initial steeper 1st rate is seen in the thinner sphere (5mm-thick). After apertures were introduced, the 1st rate values increased in the 7mm-thick sphere (Figure 53) as the stiffness of the shell decreased and more energy reached the filling. In the same figure, it appears that the 5mm-thick and the 6mm-thick spheres present a behavior opposite to the one just described, but both cases can be explained. In the case of the 6mm-thick sphere, it was already established how the presence of holes actually allows the filling to dissipate more energy; therefore to lower energy corresponded lower 1st rate values. In the case of the 5mm-thick sphere, the actual percentage need to be examined (table in Appendix B) to realize that most percentages are below 10%. That would indicate that there is not much difference in 1st rate values before and after the introduction of apertures, as explained previously when commenting on maximum values for the 5mm spheres. These results would indicate that pressure gradient values recorded in the filling are linked to the stiffness of the shell.

5.5 Conclusion

The main goal of this research was to establish the fundamental phenomenology of shock wave interaction with a simplified brain/skull system. Results proved the credibility of the multimodal skull flexure model. The results of this study demonstrated that:

1. the shock wave caused deformation of solid structures;
2. significant internal pressure values were recorded in the physical models and their distribution could be explained by the multimodal skull flexure theory;
3. the peak internal pressure and the pressure gradient increased with increased shock wave overpressure;
4. the mechanical response of the fluid/shell configuration showed coupling of these two systems when comparing the frequency response.

In conclusion, our data suggest that internal pressure is linked to the mechanical response of the coupled shell/fluid system, similar to previously published data (Dal Cengio Leonardi et al. 2010). Among the primary variables affecting shell dynamics were factors such as peak ambient overpressure and material properties such as viscosity of the filling. This study also revealed that the presence of apertures may allow for some release of the pressure building up internally, substantiating previous findings that points of access to the brain in the skull could be a means for pressure not just to enter but also to escape (Clemedson 1956a).

5.6 Acknowledgements

This research project was partially funded by a Predoctoral Associated Health Research Fellowship managed by the *John D. Dingell Medical Center, Detroit MI* for the Department of Veterans Affairs.

CHAPTER 6

6.1 Introduction

Blast TBI research is a relatively young field and, to our knowledge, cadaveric data have not been collected and/or published yet and are greatly needed. The goal of this research effort with unembalmed human heads was the determination of the transient responses of the skull-brain system during exposure to blast to help identify the primary mechanism of blast TBI. The specific aims of this study are to:

1. ascertain the relationship between magnitude levels of incident pressure and values of ICP in different regions of the brain,
2. to investigate the effects of orientation on ICP in the same regions,
3. to compare pressure distribution patterns with surface strain data recorded concurrently and
4. to compare the mechanical responses in the cadaveric data to the mechanical responses obtained in the simplified head models.

Clearly we cannot obtain injury response data from cadavers, but by studying the mechanical response of the brain we aim to contribute to the understanding of the mechanism of injury during exposure to blast. The focus of this research is to investigate one of the hypotheses for primary brain injury due to blast: multimodal skull flexure.

In order to conduct our study in a laboratory setting, a shock tube was utilized. Because of the human head standard dimensions, an expansion of the shock tube was needed to be used to avoid blocking more than 15% of the area available at the location where the specimen was positioned. A description of the expansion section and the characterization of the shock wave provided by it are in Chapter 2.2. All specimens were handled and prepared per guidelines outlined by Wayne State University School of Medicine Willed Body Program and the Human Investigation Committee.

The significance of this research is twofold. First, resolution of the mode of energy transfer and of the induced stresses within the skull/brain system will allow for creation of mitigation/protective techniques/equipment, as well as design of experiments investigating live-cell response using more reliable physical models. Second, the data obtained experimentally will be available to validate computational models already developed, as well as future blast injury models.

6.2 METHODS

6.2.1 Proof of concept: cadaver 1

In our proof-of-concept study we employed an unembalmed post-mortem-human-subject (PMHS) head without a neck, which had been frozen. Specimens that have been frozen are not ideal for this type of test, because material properties of the brain change after freezing and thawing, but, due to availability restrictions, unfrozen specimens have been proven difficult to acquire. This was a major distinction between cadaver 1 and all the others, and the reason that its recorded data could not be part of the study.

The head of cadaver 1 was received frozen and left to thaw at controlled temperature (38˚ F) for three days. On the day of specimen preparation, inspection of the inner brain revealed that some areas of the core were still frozen. Preparation continued as scheduled and testing was carried out the next day. Because the specimen lacked the neck, there was no convenient access to straight sections of the major blood vessels irrigating the brain. Therefore attachment of compression fittings as described in Hardy et al. 2007 was foregone; as a result the head of this cadaver was not perfused before testing. This was a second major distinction between this specimen and the others.

Furthermore, the focus of this training exercise was to investigate installation and testing problems in order to optimize sensor installation for data collection. Three pressure sensors instead of four were used in this specimen, as the installation was relatively easy. On the other

hand, strain gages were placed in very diverse locations (in terms of bone characteristics); therefore all five positions were tested.

Finally, a triax of 7264 accelerometers was installed on the maxilla, right below the nose, to monitor acceleration of the global system during the blast event. Acceleration results demonstrated that there was no global motion at the initial loading and limited motion was seen as the shock wave progressed due to blast wind.

Cadaver 1 was exposed to the full testing schedule to assess survivability of the gages, especially at the highest pressure magnitudes, when the dynamic pressure delivers higher winds. The installation of the pressure sensors was a success: only one sensor failed and data showed excellent reproducibility of results. The severity of the tests resulted in the loss of three of the five strain gages during the test series. Post test inspection identified inherently problematic locations for wires to be damaged and, to improve data collection for the subsequent specimens, additional strain relief was added to the sensor wires both at the sensor attachment point and at various locations along the wire.

6.2.2 Specimen preparation

A total of four unembalmed cadavers were used for this study. The specimen characteristics are listed in Table 9. The average age, mass, and stature were 75 $\pm$ 16.5 years, 63 $\pm$ 10.9 kg, and 160 $\pm$ 5.46 cm, respectively.

Table 9: Specimen characteristics.
The head circumference, width and length were measured after the specimen's scalp was removed at post-test inspection.

Cadaver #	WSU 5092	WSU 5103	UM 336524	UM336555	Average	Standard Deviation
Age	52	87	73	87	74.8	16.5
Gender	M	F	F	F		
Mass (kg)	63.5	49.9	76.6	63.5	63.4	10.9
Stature (cm)	162.6	160	152.4	165	160	5.5
Head Width (cm)	14.4	14.5	15.2	15	14.8	0.3
Head Length (cm)	16.5	16.8	16.2	16.5	16.5	0.2
Head Circum. (cm)	51.1	51.5	52.4	52.0	51.8	0.5

The specimen's head was disarticulated from the body between the sixth and seventh cervical vertebrae with the exception of cadaver 2. Upon disarticulating the head, careful attention was given to preserving the carotid arteries and jugular veins, where quick disconnect fittings were installed to facilitate perfusion of the cerebral vasculature (prior to testing, the specimens were repressurized using artificial cerebral spinal fluid, following a procedure similar to the one described by Hardy et al. in 2007).

In cadavers 2 and 3, the spinal cord was also fitted with a quick disconnect (Figure 62). Because of damage to the spinal dura, the vertebrae of cadaver 2 were completely removed and the compression fitting was installed just outside the foramen magnum (Figure 62). In cadaver 3 the fifth and sixth cervical vertebrae were removed to expose the spinal dura and the fitting was installed just outside the fifth vertebra. The severity of the test environment in combination with the compression fitting being close to the spinal canal, caused the spinal dura to chafe and tear against the vertebral rough surfaces unless the entire neck was removed. Therefore, in the last two

specimens the spinal cord was tied off with a string to prevent leaking of the pressurized system, while maintaining the integrity of the head-neck system.

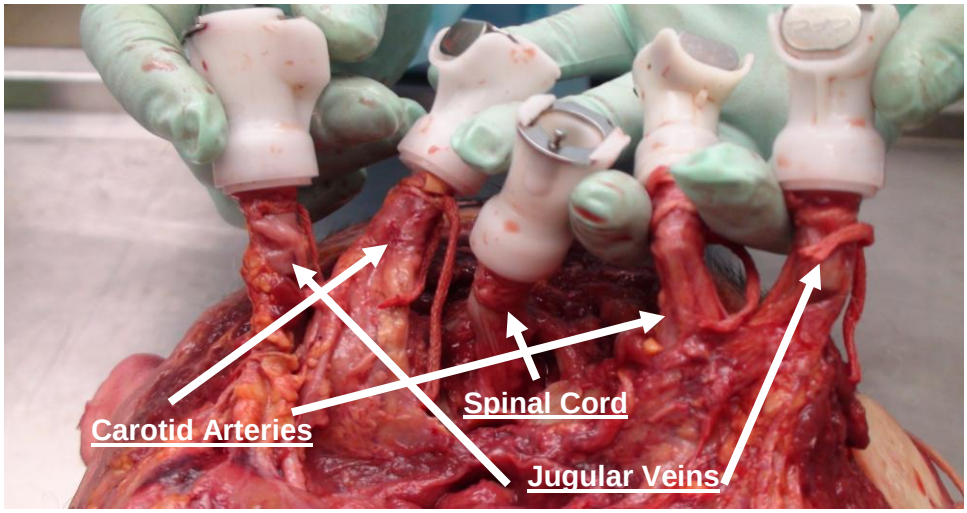

Figure 62: Installation of the quick-disconnect fittings for pressurization of the brain.

The head was shaved prior to installation of pressure sensors and strain gages. For determining ICP values, four FISO optic sensors were implanted in the right side of the skull at the locations described in Table 10. All the ICP sensors were placed on the right side of the skull, while the strain gages were placed on the left side. As mentioned in Chapter CHAPTER 4**,** the depths of the ICP sensors in the brain, with respect to the inner surface of the skull, were 65 mm for the sensor called ventricle and 30 mm for sensors called frontal, parietal and occipital.

Table 10: Positions of the ICP access ports following human skull landmarks.

ICP sensor	Measurements for Location
frontal	10 mm away from midline; 70 mm from nasion going towards the back of the skull
ventricle	20 mm away from midline; 50 mm from frontal going towards the back of the skull; usually on coronal suture line
parietal	10 mm away from midline; 70 mm from ventricle going towards the back of the skull
occipital	10mm away from midline; 50 mm from parietal going towards the back of the skull

A small square portion of the skin was removed at the ICP sensor site (2.25 cm^2). The optic sensors were prepared 2 days prior to testing as described in Chapter 4**.** A Dremel rotary tool was utilized to drill three holes into the skull (d=1.2mm), which were tapped to produce a 6-32 thread to which the cannula glued to the pressure sensor would be fastened into position. Pressure sensors were inserted into the brain by means of steel guides that placed them in a radial configuration (Figure 63).

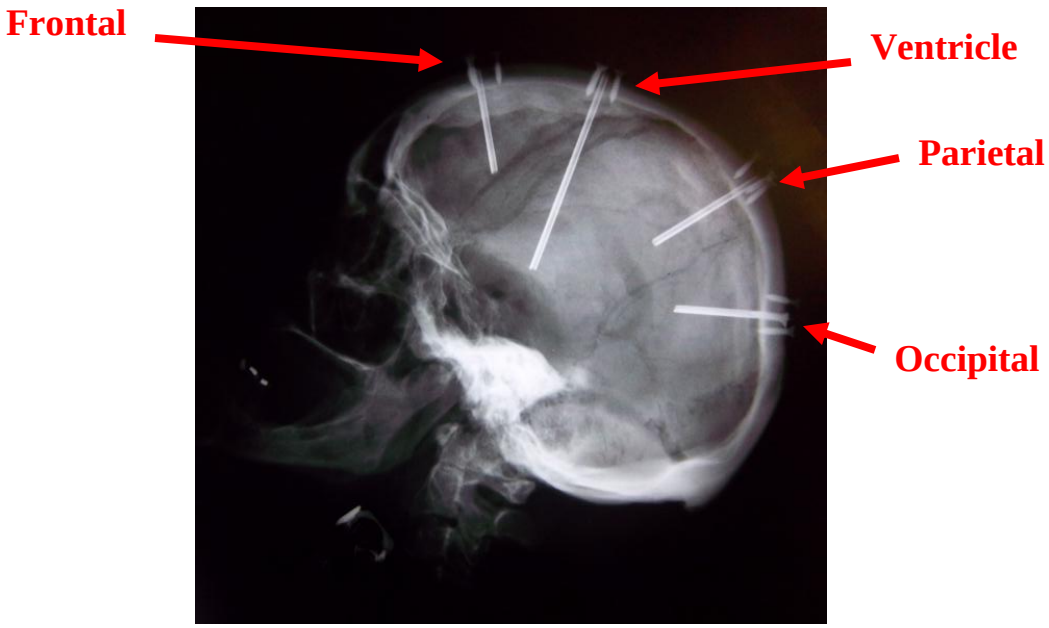

Figure 63: X-rays of cadaver-4 with guides in the brain.
The guides are used to insert the sensors in position and then they are removed.

After fastening of the ICP sensor, three screws were arranged in a triangular layout as shown in Figure 64A. Duct tape was wrapped around the outside of the triangle to create a supporting structure for the bone cement (Surgical Simplex P, Radiopaque bone cement, Howmedica Osteonics, Stryker, New Jersey) that was poured in it. The bone cement was left to harden for 5 minutes and then the duct tape was removed. The bone cement together with the three screws created a protective cap for the optic sensor exiting the skull, and prevented the netting of the suspension system from sliding into the optic cable (Figure 64B). Moreover the bone cement helped reinforcing the anchoring site while increasing sealing of the hole.

In cadaver 2 an attempt was made to avoid adding material around the optic sensor access port, but results were catastrophic for the integrity of the sensors, which all failed after completing only half of the testing series.

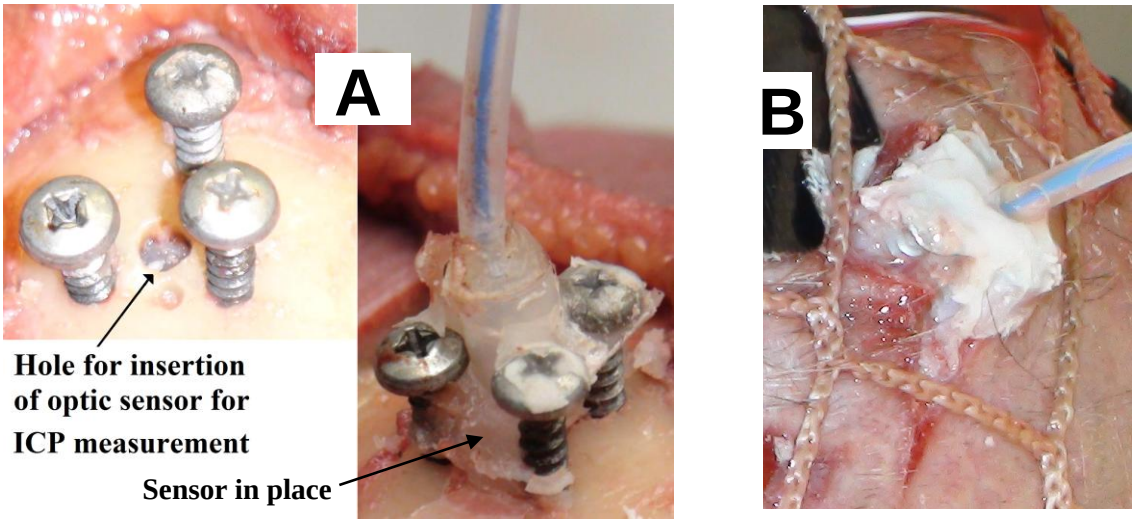

Figure 64: Placement of a FISO optic sensor on the skull of one of the specimens.
A: Hole for insertion of optic sensor with the supporting screw triangular structure; also showing after the bone cement has hardened.
B: Netting of the suspension system surrounds the optic pressure sensor anchoring site.

The strain gage sites were prepared a day prior to testing, to allow the bone to dry as much as possible before placement of the strain gages. This procedure increased adherence between the gage and the skull. A 2x2 cm^2 section of the skin was removed and underlying tissue was scraped with a scalpel. Acetone was used to clean the bone and increase the site's dryness. The next day, five rosettes (Vishay Micro-Measurements, General Purpose Strain Gages, item code 16793) were glued to the skull on the left zygomatic, temporal, parietal bones and the left side of the frontal and occipital bones (20mm on the left side of the midline). The glue adopted was a two part compound: one part was placed on the surface of the skull and the second part was placed on the rosette (M Bond 200, Micro-Measurements). Once the two parts were pressed together a chemical bond was formed that provided strong adhesion. A sealant was also applied on the rosette's grid to avoid contact with bodily fluids that may have altered strain results (M Coat A, Micro-Measurements). At 10 mm from the grid, the wires were also glued to the bone and then skin was sutured on top of them to prevent further movement as shown in Figure 65. This configuration provided the greatest survivability of the strain gages.

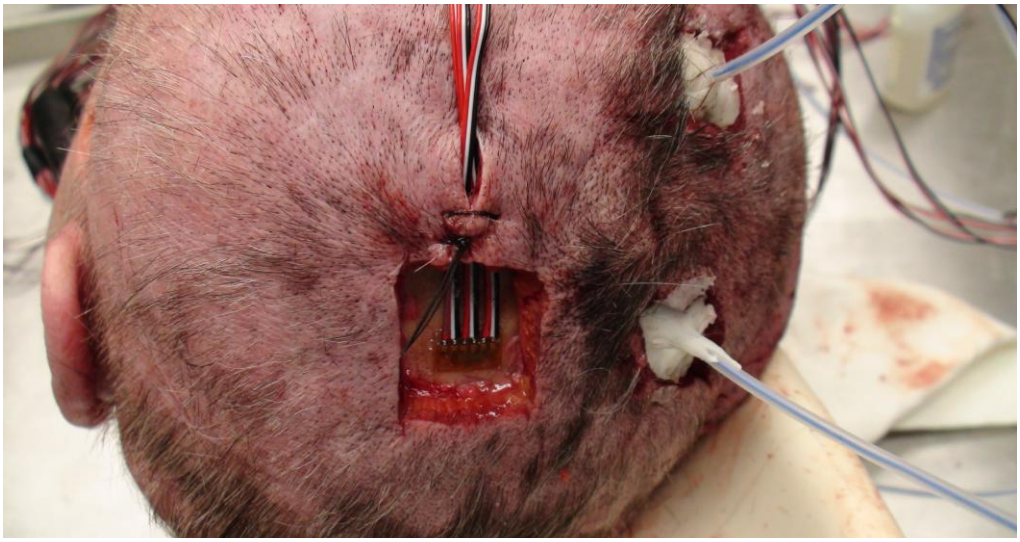

Figure 65: Example of strain gage installation for the occipital strain gage.

Also careful attention was given to the placement of the instrumented head into the netting of the suspension system to avoid stressing the wires and optic cables during testing. The suspension system was composed of three separate parts: a nylon net that wrapped around the specimen and two metal chains that were used to hold the net from the top and bottom of the wooden spacer inside the expansion (Figure 66). The head was placed in an inverted configuration, with the head's center of gravity at around 49 inches from the open end. ICP optic cables and strain gage wires were taped separately to the bottom chain as an ultimate protective measure against the blast wind (Polyken 219, Berry Plastics Corporation and Subsidiaries). The ICP optic cables were then inserted through a hole at the bottom of the spacer, while the strain gage wires were run along the bottom of the expansion tube and held in place with black tape (Polyken 219, Berry Plastics Corporation and Subsidiaries).

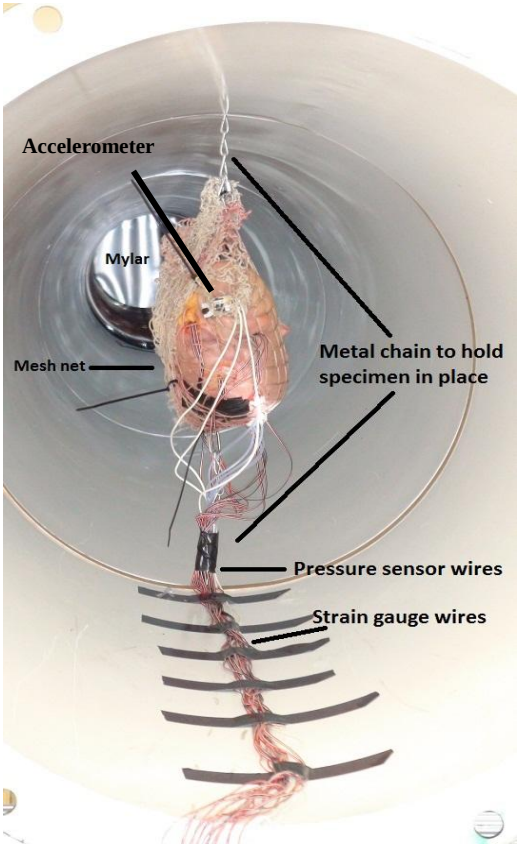

Figure 66: An inverted head specimen placed in the suspension system composed of a mesh Nylon net and two metal chains at the top and bottom of the wooden spacer inside the expansion. ICP optic cables and strain gage wires were taped to the bottom chain as an ultimate protective measure against the blast wind. The ICP optic cables were inserted through a hole at the bottom of the spacer, to be connected to a conditioning system. The strain gage wires were run along the bottom of the expansion tube and held in place with black Polyken tape. This specimen also had an accelerometer mounted on the maxilla, right below the nose as shown by the arrow.

Each specimen was subjected to a series of 15 simulated blasts, except cadaver 4 on whom 16 tests were performed (one test was repeated at the end). Table 11 shows the testing conditions: four different orientations and three different magnitudes were tested. The term orientation is relative to the side the shock front strikes first: front is the face; right is the anatomical right, which was the side where the pressure sensors were mounted; back is the occipital bone; left is the anatomical left. To confirm reproducibility of results the front test was repeated at the end of each magnitude cycle. The three static pressure magnitudes used in this study were 10, 12, and 15 psi (69, 83, and 104 kPa), which are linked to the respective peak stagnation pressures of 12.5, 15, and 20 psi (86, 104, and 138 kPa). Immediately prior to testing, the specimen was placed in an inverted position and repressurized using artificial spinal fluid (aCSF). This position facilitates the evacuation of gases introduced during the installation of the

pressure sensors (Hardy et al. 2007). The applied perfusion pressure was 77 mmHg, which approximates the mean arterial and venous blood return pressure for humans.

Table 11: Testing conditions for head blast simulations in the shock expansion

Orientation	Static Pressure PSI	Stagnation Pressure PSI
Front	10	12.5
Right	10	12.5
Back	10	12.5
Left	10	12.5
Front	10	12.5
Front	12	15
Left	12	15
Back	12	15
Right	12	15
Front	12	15
Front	15	20
Right	15	20
Back	15	20
Left	15	20
Front	15	20

Post-test examination of each specimen followed testing. Strain gage sensors were inspected to record any wiring damage or delamination from the skull. The scalp was removed from the specimen calvaria to inspect sensor placement in relation to skull landmarks and suture lines. The left portion of the calvaria was removed to expose the brain underneath. Brain tissue was carefully removed to confirm ICP sensor placement (radial position and insertion in the ventricle when applicable). Small layers of brain tissue were taken out repeatedly until the ICP sensors were exposed in the right hemisphere. Figure 67 shows a frontal sensor from the inside.

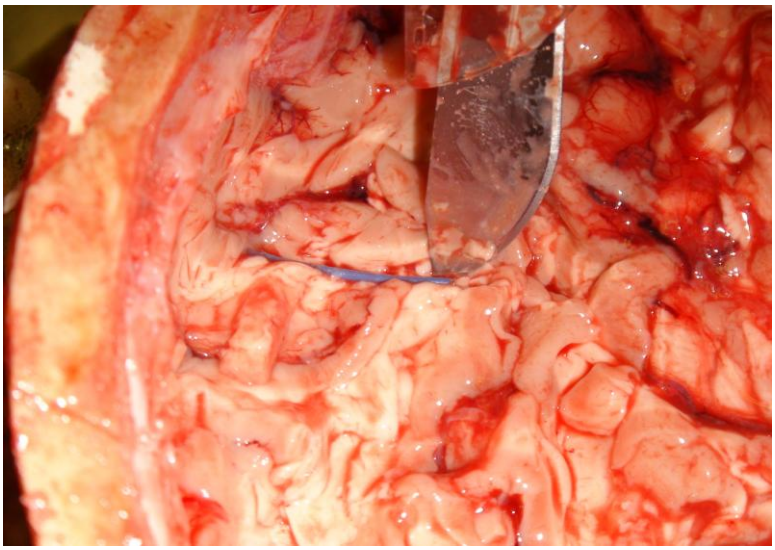

Figure 67: A frontal pressure sensor placement from the inside.
The scalpel points to the tip of the sensor.

In two cadavers the post-test examination revealed that internal conditions were different than intended at installation. In cadaver 3 we attempted to place a sensor in the corpus callosum, but inspection revealed that the tip was inserted in the ventricle instead; therefore the data from that sensor is highlighted in the result tables. The new location was near the original ventricle installation, at 10 mm from midline and 20 mm toward the back of the skull from the previous ventricle sensor, which broke prior to testing.

In cadaver 5 post test inspection revealed that the tip of the sensor was in contact with the tentorium cerebelli (Figure 68). Our intention was to place the occipital sensor in a region closer to coup-countercoup site, but unfortunately the interference of such fibrous tissue in the pressure data recording was conspicuous.

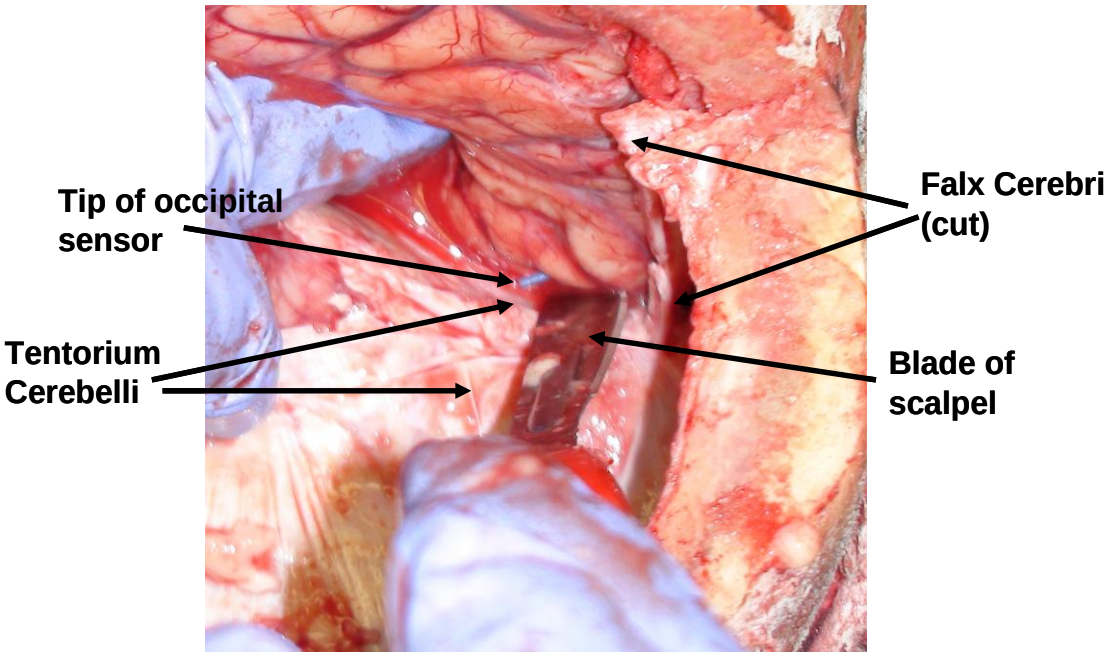

Figure 68: Location of the occipital sensor for cadaver 5. Because of the proximity of the sensor tip to the tentorium cerebelli, occipital data was very different than expected.

6.2.3 Data acquisition, processing and analysis

ICP measurements were obtained by optic pressure sensors (FISO Technologies, Model FOP-MIV-PK, range 150 psi). The ICP sensors were connected to a signal conditioning unit (FISO Veloce-50 System). Low noise coaxial cables connected the signal conditioning unit to a data acquisition system (Dash 8HF, Astro Med). The same system was also used to capture the air overpressure in the tube (Rwall) and in the driver. The sampling rate of this system was set at 250 kHz.

Strain measurements were obtained using five general purpose rosettes (Vishay Micro-Measurements, General Purpose strain Gages, item code 16793) connected to a second data acquisition system (TDAS PRO, Diversified Technical System, Inc.). To confirm data synchronization, the air overpressure sensor (Rwall) was also connected to this second system. The sampling rate of the second data acquisition system was 100 kHz.

In cadaver 2 and 3, a triax of 7264 accelerometers was installed on the maxilla, as in cadaver 1, to monitor acceleration of the global system during the blast event. Acceleration results demonstrated that there was no global motion at the initial loading and limited motion was seen as the shock wave progressed due to blast wind.

To initiate both acquisition systems simultaneously, a manual trigger was used.

An anti-aliasing filter (2 pole Bessel at 200 kHz) was applied to the data during acquisition. This filter is an automatic settings of the Dash unit when sampling is above 200kHz. During post-processing, the two sets of data coming from the acquisition systems were synchronized and the pressure offsets removed. Then the pressure data was filtered with a low-pass second order Butterworth filter at 4 kHz to remove the high frequency noise from the signal. Appendix A presents each pressure profile before and after filtering. Although rosettes were used, the calculation of principal strain is beyond the scope of this study. Strain values were analyzed for evaluation of gross deformations of the skull in relation to ICP profiles.

As explained in Chapter 2, the specimen was positioned so that the arrival of the rarefaction wave would coincide with the end of the shock wave's positive phase. The arrival of the rarefaction wave which marks the end of the time-window in which the simulated blast is appropriate, is dependent on the overpressure magnitude: the higher the overpressure, the narrower the window. Hence the time-window for the 10 psi and 12.5 psi static overpressure magnitude was approximately 7.5 ms for both (not a linear increase), while for the 15 psi static overpressure magnitude the time-window was approximately 6.7 ms. Data analysis was limited to the time window appropriate for each magnitude. A practical time-window of 10 ms, 9 ms after arrival of the shock front and 1 ms prior, is presented in the graphs. The arrival of the shock front was set to time zero based on the sensor closest to the shock front by orientation. In each graph, time zero referred to one particular sensor and time zero started when the ICP value had increased or decreased more than 0.2 psi. In most cases, all the five measurements of interest in this study were recorded in the first 5 ms from arrival of the shock front. As far as the convention used for

the pressure readings, the sensors were zeroed at the ambient internal pressure prior to the blast; therefore, negative pressure refers to the sensors reading below the ambient pressure. As explained in Chapter 4, the optic sensors have a linear behavior between 300 mmHg (-5.8 psi) and 7500 mmHg (145 psi); therefore values below -5.8 psi do not have a reliable correspondence between the measured and the actual pressure value. A lower value corresponds to a bigger rarefaction, although the recorded number will not be physically correct. This particular detail was kept in mind when evaluating results.

The focal point of this study was the characterization of pressures transmitted into the brain; thus maximum and minimum ICP, pressure differential, and rate of change of pressure (pressure gradient) were determined for each sensor in each test. The pressure differential values were calculated by subtracting the minimum value from the maximum value. Time elapsed between these two values was also recorded. The rate of change of pressure (Figure 69) was calculated by dividing the pressure differential from inception of the shock front to the first peak by the corresponding elapsed time (1^{st} rate). Pressure gradients could be an important mechanism of injury and the sign associated with the value indicates increasing compression in the brain when the number is positive and decreasing pressure when negative.

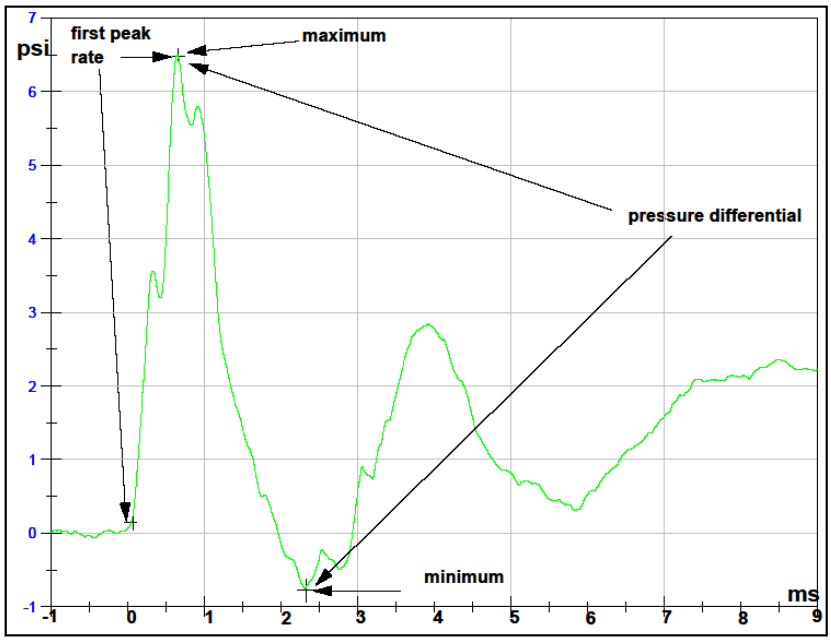

Figure 69: Values used in data analysis for one sensor.
Each point presented is used to calculate the indicated values for data analysis. Time zero is set once the ICP has crossed the 0.2 psi threshold.

6.3 RESULTS

Four unembalmed cadaver heads were placed in an inverted position inside a shock tube expansion and were exposed to fifteen simulated blasts, changing pressure magnitudes and orientation of the head. ICPs in four regions of the brain and strain values in five regions of the skull were collected.

Before presenting the results, a small digression needs to be made to emphasize the uniqueness of each specimen when dealing with post-mortem human subjects. Firstly, as donations of human bodies are extremely short in supply, it was not possible to introduce any additional requirement that could have made the group more homogeneous in terms of scalp thickness, or bone density, or other physical features that could have simplified gage installation. Moreover, each cadaver had abnormalities (Table 12) that presented unique challenges during testing, and the acquired data may have reflected these abnormalities in the pressure profiles. A

greater number of specimens would need to be investigated to truly determine how significantly these abnormalities affected pressure data.

Table 12: Abnormalities in the four specimens.

	Abnormalities
Cadaver 2 (WSU 509)	neck completely removed including atlas
Cadaver 3 (WSU 510)	tear in the spinal cord; ventricle sensor at different location
Cadaver 4 (UM33652)	eyes removed prior to testing
Cadaver 5 (UM33655)	occipital sensor at different location; left artery was blocked by coagulated blood

Finally, one characteristic that was common to all four cadavers was the fact that each head was not a perfectly sealed system. The harvested heads had the major blood vessels and spinal cord clipped, but it would have been impossible to close every capillary vessel in the time frame of the testing schedule. Dal Cengio Leonardi et al. 2011 demonstrated that proper sealing techniques lead to a significant increase in ICP values. Therefore, it seems realistic to expect that in the actual live scenario (Soldiers exposed to blast) the ICP values would be higher than the pressure values acquired in this study.

Although each specimen presented unique characteristics, the data collected revealed that a consistent set of observations could be made, especially when looking at data obtained from the last three cadavers. Unfortunately cadaver 2 did not provide many data points; however some observations that are true for cadaver 3, 4, and 5 still hold true for cadaver 2. The results are presented in the next section.

6.3.1 Pressure results

Four pressure sensors were installed in the brain, to monitor pressure changes in the frontal, parietal and occipital cortex and in the ventricle. The respective depths from the inner surface of the skull were 30 mm, 30 mm, 30 mm, and 65 mm. Figure 70 presents an example of reproducibility of data (pressure profiles) between the first front orientation and the final front orientation at one shock wave overpressure magnitude for one sensor. Reproducibility was checked by visually comparing the first and last pressure profile, for every sensor at each orientation in all cadavers. Results show very high reproducibility of pressure profiles and all cases can be found in Appendix A.

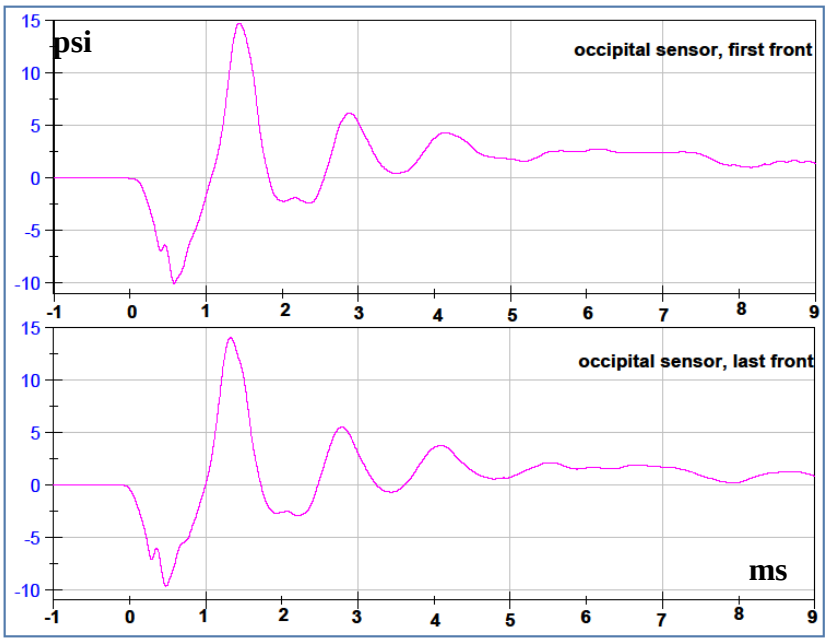

Figure 70: Comparison between first and last test at 12psi magnitude for occipital sensor in cadaver-3.
Reproducibility of results is very high..

Figure 71 offers an example of pressure profiles for each of the four sensors in one single test. Figure 72 provides an example of pressure profiles for one sensor at the four different orientations for one magnitude of air overpressure. All records of pressure time history by test subject can be found in Appendix A.

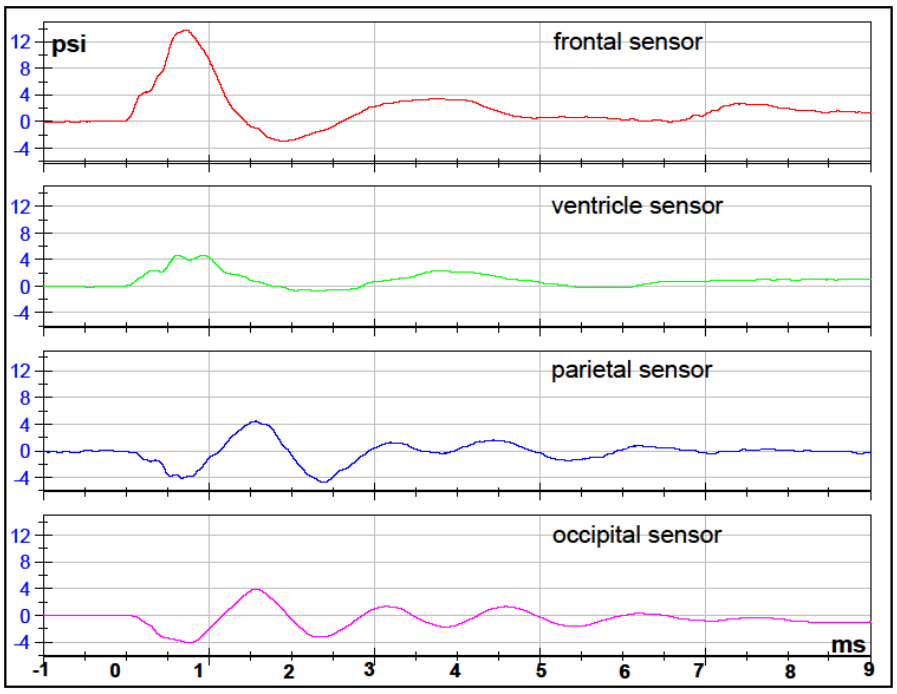

Figure 71: Pressure profiles of each sensor for the first front exposure at 12 psi overpressure for cadaver 4.

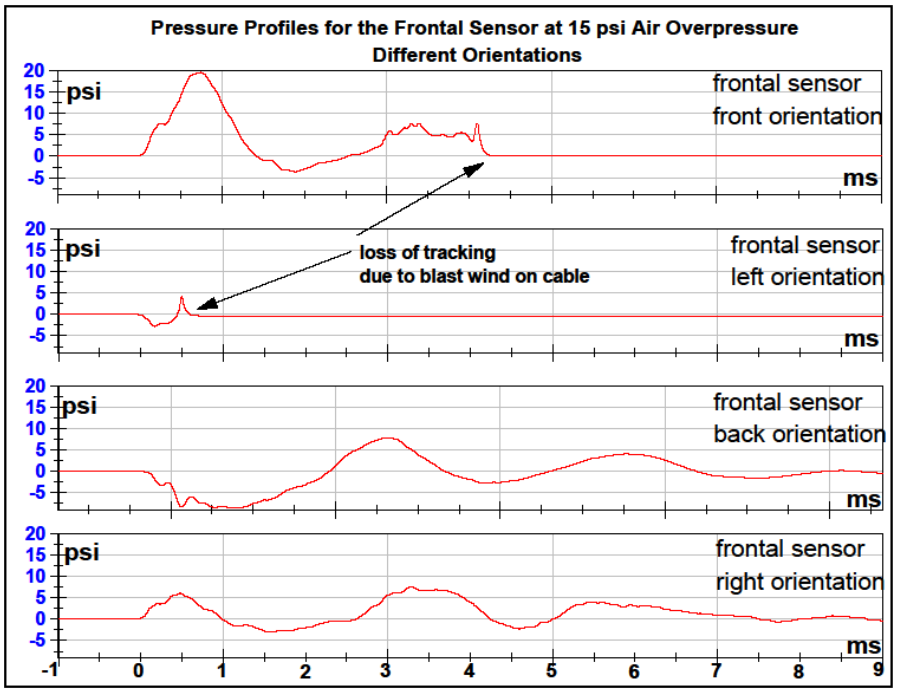

Figure 72: Frontal sensor pressure profiles for the four orientations at 15 psi overpressure exposure for cadaver 4.

The mechanical response of the system is similar of that predicted by Chafi et al. (2010), although damping is rapidly decreasing the oscillation magnitudes. There are both positive and negative pressures in each profile. Appendix A provides tables that show maximum and minimum values by cadaver, occurring within the appropriate time-window in each test. As a general reminder, all tables presented in this study were based on filtered data. However, as the high frequency noise intrinsic with the data was filtered out, the pressure values collected were also slightly reduced. This occurrence did not affect the general behavior when analyzing the data. The only time when this fact appeared to create an inconsistency was when looking at the data for maximum peak pressure of the frontal sensor at front orientation in every cadaver. In all the cadavers, 100% of the raw data established that the frontal sensor recorded ICP values higher than the shock wave overpressure. However this statement is no longer true when examining the filtered data, where it still holds true for 14 out of 16 cases (87.5%). Currently we are not aware of any other instance in which filtered data were diverging from raw data.

Table 13 shows pressure results for cadaver 2, which did not provide many data points. Figure 73 to Figure 75 summarize the maximum and minimum results in graphical format for cadaver 3, 4, and 5.

Table 13: Pressure Extremes for cadaver 2.
Sensor failure occurrence was very high for this specimen. 83% of the cells in this table had no pressure results in each category.

Pressure Extremes for cadaver -2 (psi)										
	Maximum Pressure					Minimum Pressure				
ventricle	front 1	right	back	left	front 2	front 1	right	back	left	front 2
10 psi air	**6.47**	**5.96**	**5.55**	**4.36**	**5.66**	**-1.61**	**-2.54**	**-4.1**	**-0.848**	**-1.49**
12 psi air	**7.39**	**4.52**	**6.82**	**NA**	**NA**	**-2.36**	**-1.8**	**-3.81**	**NA**	**NA**
15 psi air	**NA**	**NA**	**NA**	**NA**	**NA**	**NA**	**NA**	**NA**	**NA**	**NA**
frontal	front 1	right	back	left	front 2	front 1	right	back	left	front 2
10 psi air	**19.22**	**NA**	**NA**	**NA**	**NA**	**-4.67**	**NA**	**NA**	**NA**	**NA**
12 psi air	**NA**	**NA**	**NA**	**NA**	**NA**	**NA**	**NA**	**NA**	**NA**	**NA**
15 psi air	**NA**	**NA**	**NA**	**NA**	**NA**	**NA**	**NA**	**NA**	**NA**	**NA**
parietal	front 1	right	back	left	front 2	front 1	right	back	left	front 2
10 psi air	**NA**	**NA**	**NA**	**NA**	**NA**	**NA**	**NA**	**NA**	**NA**	**NA**
12 psi air	**NA**	**NA**	**NA**	**NA**	**NA**	**NA**	**NA**	**NA**	**NA**	**NA**
15 psi air	**NA**	**NA**	**NA**	**NA**	**NA**	**NA**	**NA**	**NA**	**NA**	**NA**
occipital	front 1	right	back	left	front 2	front 1	right	back	left	front 2
10 psi air	**NA**	**NA**	**NA**	**NA**	**NA**	**NA**	**NA**	**NA**	**NA**	**NA**
12 psi air	**NA**	**NA**	**NA**	**NA**	**NA**	**NA**	**NA**	**NA**	**NA**	**NA**
15 psi air	**NA**	**NA**	**NA**	**NA**	**NA**	**NA**	**NA**	**NA**	**NA**	**NA**

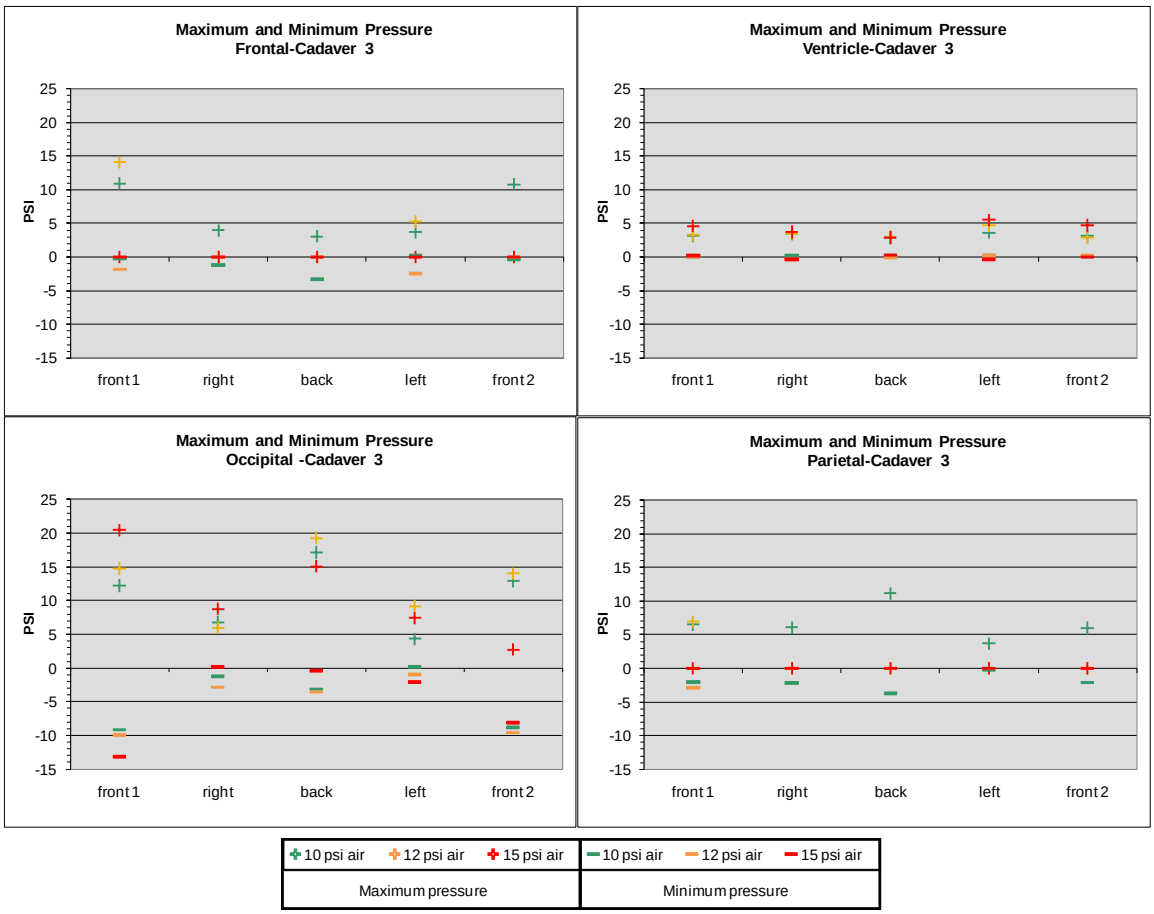

Figure 73: Graphs by sensor for maximum and minimum pressure values for cadaver 3 (the results are color coded according to the shock wave pressure).

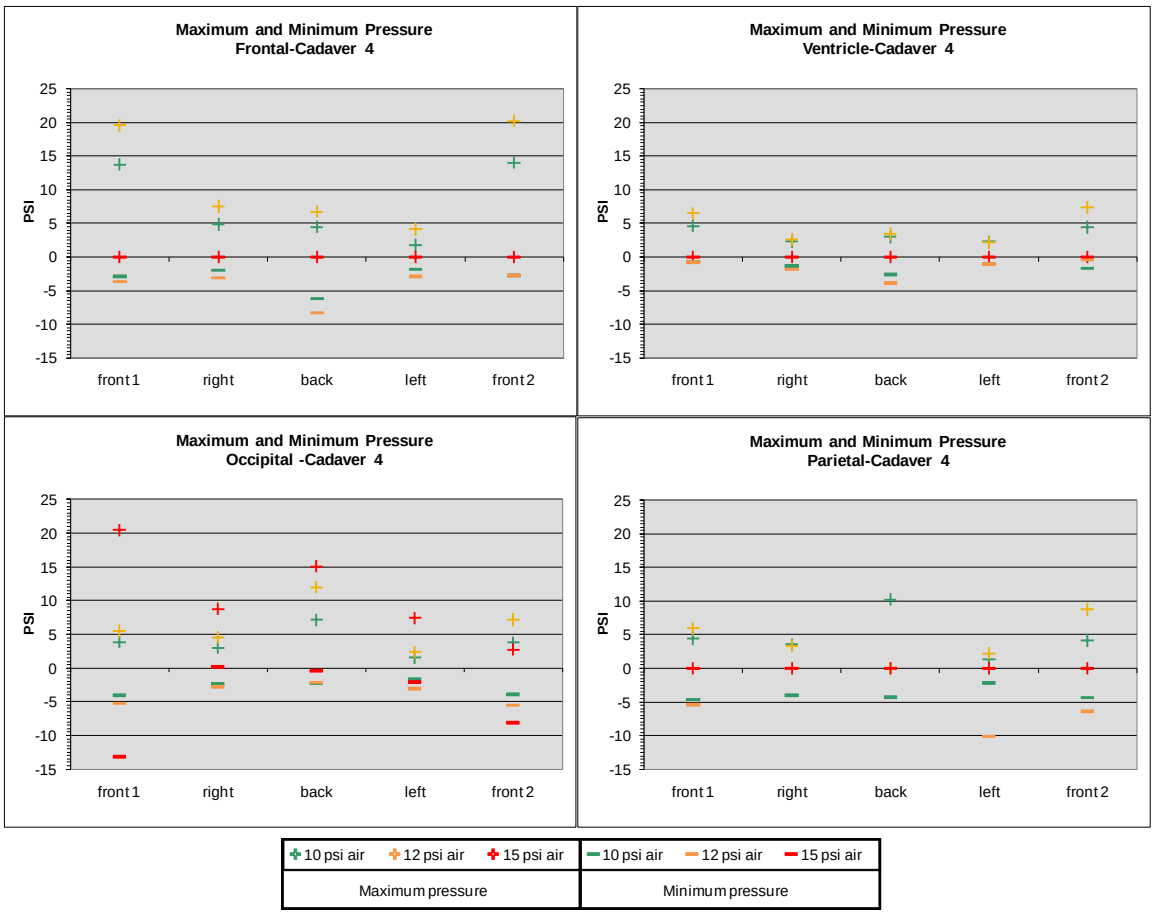

Figure 74: Graphs by sensor for maximum and minimum pressure values for cadaver 4 (the results are color coded according to the shock wave pressure).

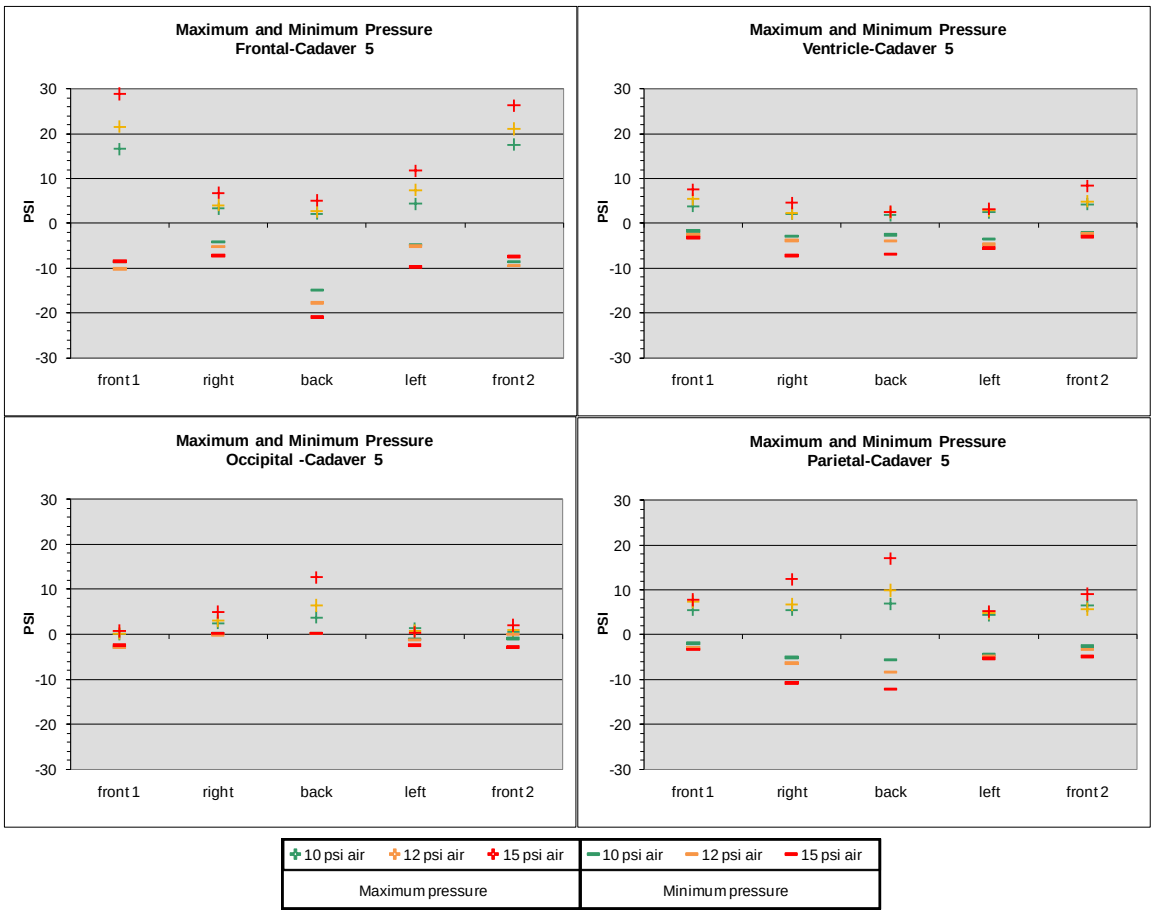

Figure 75: Graphs by sensor for maximum and minimum pressure values for cadaver 5 (the results are color coded according to the shock wave pressure).

By looking at the profiles of Figure 71 and Figure 72 and all other figures in Appendix A, and looking at the graphs in Figure 73 to Figure 75, preliminary observations reveal:

a) The recorded ICP profiles are different for each region of the brain, either in magnitude or shape of the profile, for each test;

b) At front and back orientations, the initial response of frontal and ventricle sensors is similar, as well as the initial response of parietal and occipital sensors;

c) Orientation affects the ICP magnitude and shape of the profile for each sensor;

d) ICP values usually increase with increased air overpressure.

Appendix A provides tables that show pressure differential values for each cadaver. In the same tables, the time elapsed between the maximum and minimum values, used to calculate the differential, is also presented. Figure 76 to

Figure 78 summarize the pressure differential tables in graphical format for cadaver 3, 4, and 5.

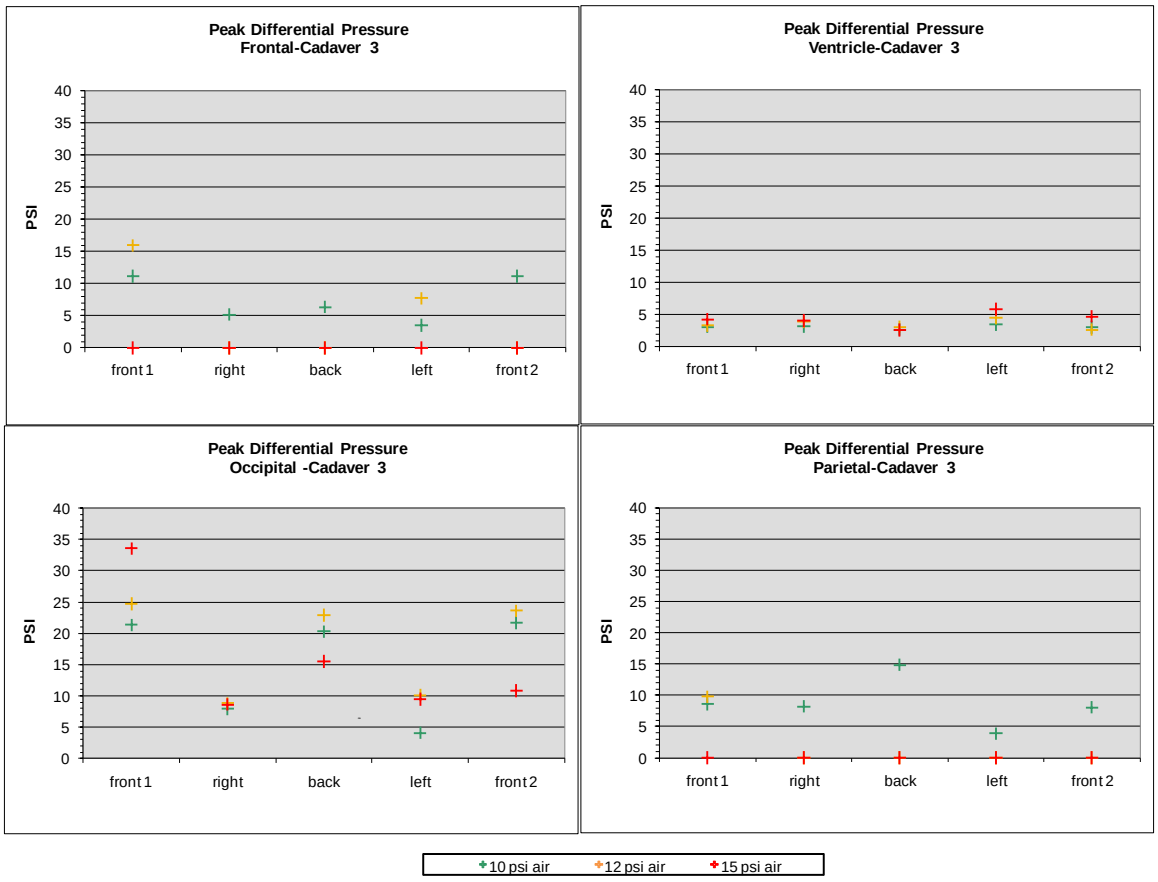

Figure 76: Graphs by sensor for pressure differential values for cadaver 3 (the results are color coded according to the shock wave pressure).

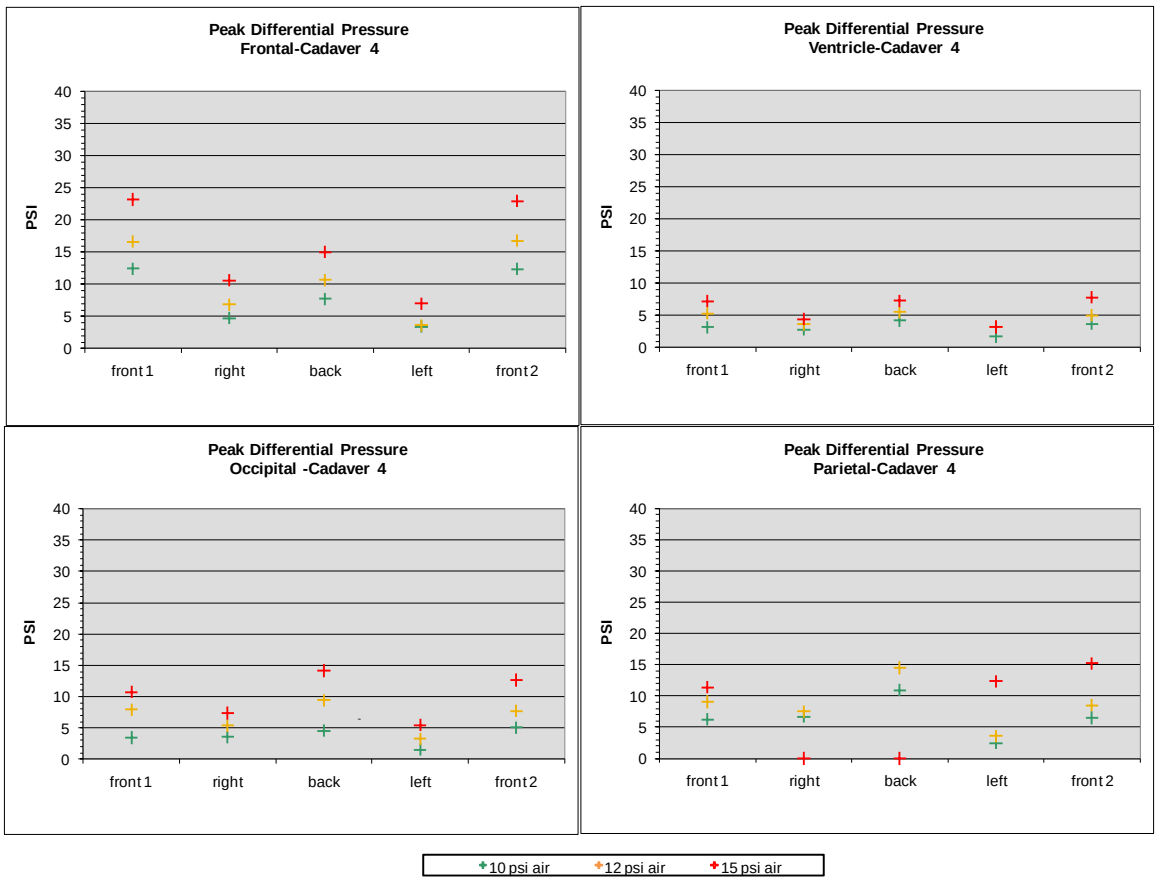

Figure 77: Graphs by sensor for pressure differential values for cadaver 4 (the results are color coded according to the shock wave pressure).

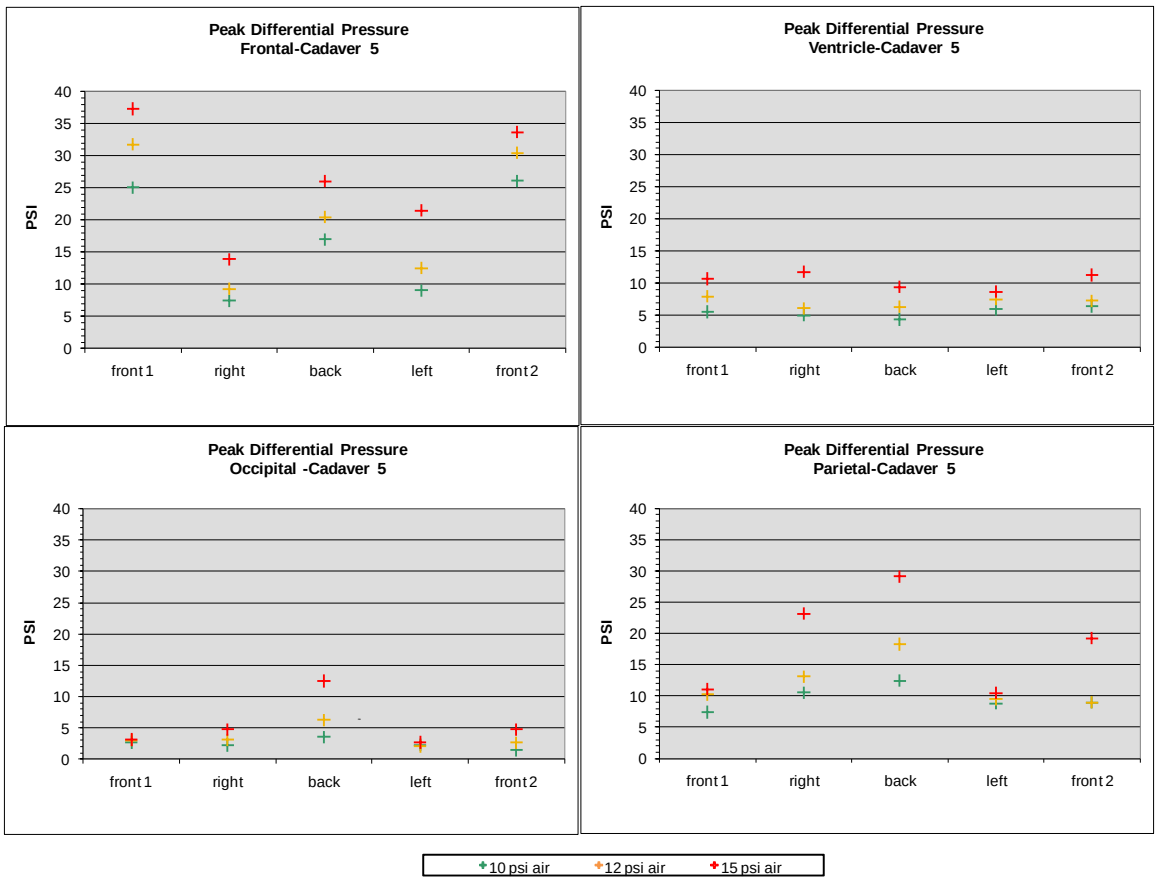

Figure 78: Graphs by sensor for pressure differential values for cadaver 5 (the results are color coded according to the shock wave pressure).

The graphical format permits to quickly identify the effects on pressure values of increasing shock wave overpressure. Maximum and minimum ICP values and the corresponding pressure differentials were compared within the same cadaver, for the same sensor, at the same orientation. The independent variable was shock wave overpressure, and the dependent variables were minimum and maximum ICP values and pressure differential values. For the pressure differential and the ICP maximum values the numbers were compared at increased shock wave overpressure and a value of 1 was given to each comparison that found an increased value, while a value of 0 was associated with decreased value at higher shock wave magnitude. If values were missing the comparison was skipped. For example, for any sensor, the value corresponding to a certain orientation at 10 psi magnitude was compared with the value of the same sensor, at the

same orientation but at the 12 psi magnitude. A 1 or a 0 were assigned. Then the value at the 12 psi magnitude was compared to the one at the 15 psi magnitude and a 1 or a 0 were assigned. Finally, the value at the 10 psi magnitude was compared to the value at the 15 psi magnitude and a value of 1 or 0 was assigned. Therefore, a table of 1 and 0 was created similar to the table shown for the spheres. For the minimum values the comparisons looked for decreasing values that moved towards greater negative numbers, when assigning a 1 to the table.

The percentage of assigned 1 (increased value with increased magnitude) to the total amount of comparisons was calculated. Cadaver 2 was not included in these comparisons. When gathering the results of these comparisons for the three cadavers, a total of 155 comparisons were performed for maximum, and 151 for minimum. Maximum value increased in 89% of the cases; minimum value increased in 82% of the cases. By region the results were: ventricle maximum value increased 93% of the time; ventricle minimum value increased (in absolute value) 83% of the time; frontal maximum value increased 97% of the time; frontal minimum values increased (in absolute value) 85% of the time; parietal maximum value increased 87% of the time; parietal minimum values increased (in absolute value) 100% of the time; occipital maximum value increased 80% of the time; and occipital minimum values increased (in absolute value) 68% of the time. Examining the pressure differential, the values are more consistent: for ventricle there was increase in the differential pressure value 91% of the time; frontal 100% of the time; parietal 96%; and occipital 85%. In general, pressure differential increased with magnitude 92% of the time in 153 comparisons. Figure 79 presents a summary of these results.

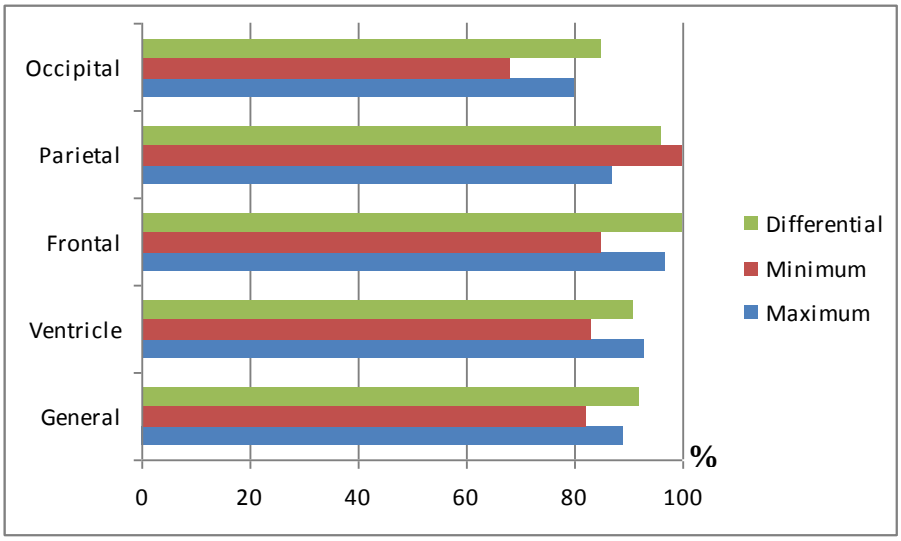

Figure 79: Percentage of pressure readings that recorded higher values for increased shock wave overpressure.
The data is presented by sensor location and also grouping all sensor results (general).

Further analysis of cadaver 3, 4 and 5 examined the percentage of actual change in internal pressure for each sensor at every orientation in relation to shock wave magnitude percentage increase. Tables with the percentage results are shown in Appendix A. No apparent relation could be found among these percentages.

Furthermore, for each test, comparisons of data were performed between the differential pressure values of each pressure sensor placed in the cortex (frontal, parietal and occipital), and the one in the ventricle (deeper region of the brain). The differential pressure values were chosen because capable of summarizing the extreme conditions experienced by each region. Results unveiled that in cadaver 3 the ventricle experienced differential pressure values lower than the other regions in 100% of the cases. For cadaver 4, in general, the ventricle experienced differential pressure values lower than the other regions in 95% of the cases. In particular, the frontal sensor had greater values than the ventricle 100% of the time; the parietal sensor had greater values than the ventricle 100% of the time; and the occipital sensor had greater values than the ventricle 87% of the time. Finally, for cadaver 5, in general, the ventricle experienced differential pressure values lower than the other regions in 66% of the cases. In particular, the

frontal sensor had greater values than the ventricle 93% of the time; the parietal sensor had greater values than the ventricle 100% of the time; and the occipital sensor had greater values than the ventricle 7% of the time. The occipital results need a further explanation for cadaver 5: as mentioned previously in this chapter, post testing inspection revealed that the tip of the sensor was placed in touch with the tentorium cerebelli (Figure 68). Our intention was to place the occipital sensor in a region that would have given true coup-countercoup data, but unfortunately the interference of such fibrous tissue in the recording of the pressure is striking. When excluding the occipital values for cadaver 5, the general results for cadaver 5 unveiled that the ventricle region experienced differential pressure values lower than the other regions in 97% of the cases (Figure 80 presents a summary of these results). These findings confirm another prediction by Chafi et al. (2010) that found that pressure values in deeper regions of the brain (cerebellum, brain stem, and corpus callosum) were lower.

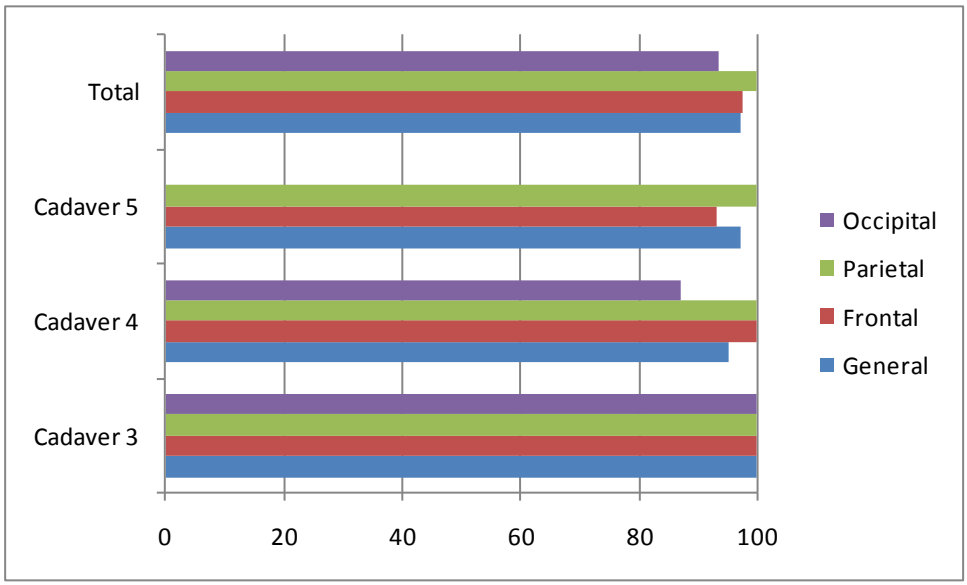

Figure 80: Comparisons expressed in percentages for differential pressure values higher than ventricle differential pressure values, for the same test sorted for regions of the brain and summarized in general.
'Total' groups all cadaver comparisons together, while 'General' groups the frontal, parietal and occipital sensor comparisons all together in each cadaver.

Presently it is unknown how the rate of change of the ICP can affect the brain cells, but it is becoming increasingly accepted that pressure gradients could be an important mechanism of injury. Consequently, data analysis also focused on the calculation of one pressure gradient, 1st rate, as it was previously described in this chapter. Tables with results are presented in Appendix A for each cadaver: as the rate represents the slope of a line, the sign of the rate indicates increasing compression when the number is positive and decreasing pressure when negative. Figure 81 to

Figure 83 summarize the results in graphical format for each cadaver and each sensor.

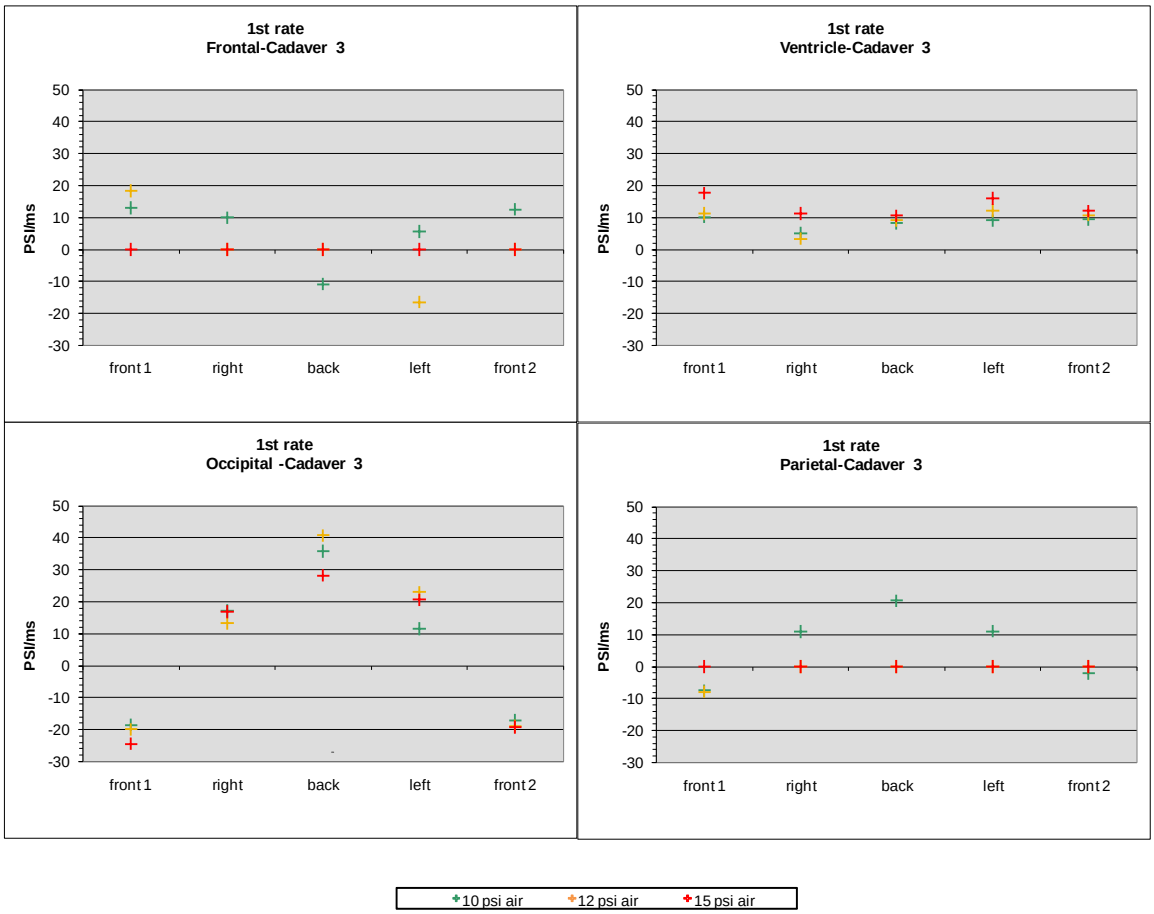

Figure 81: Graphs by sensor for 1st rate values for cadaver 3 (the results are color coded according to the shock wave pressure).

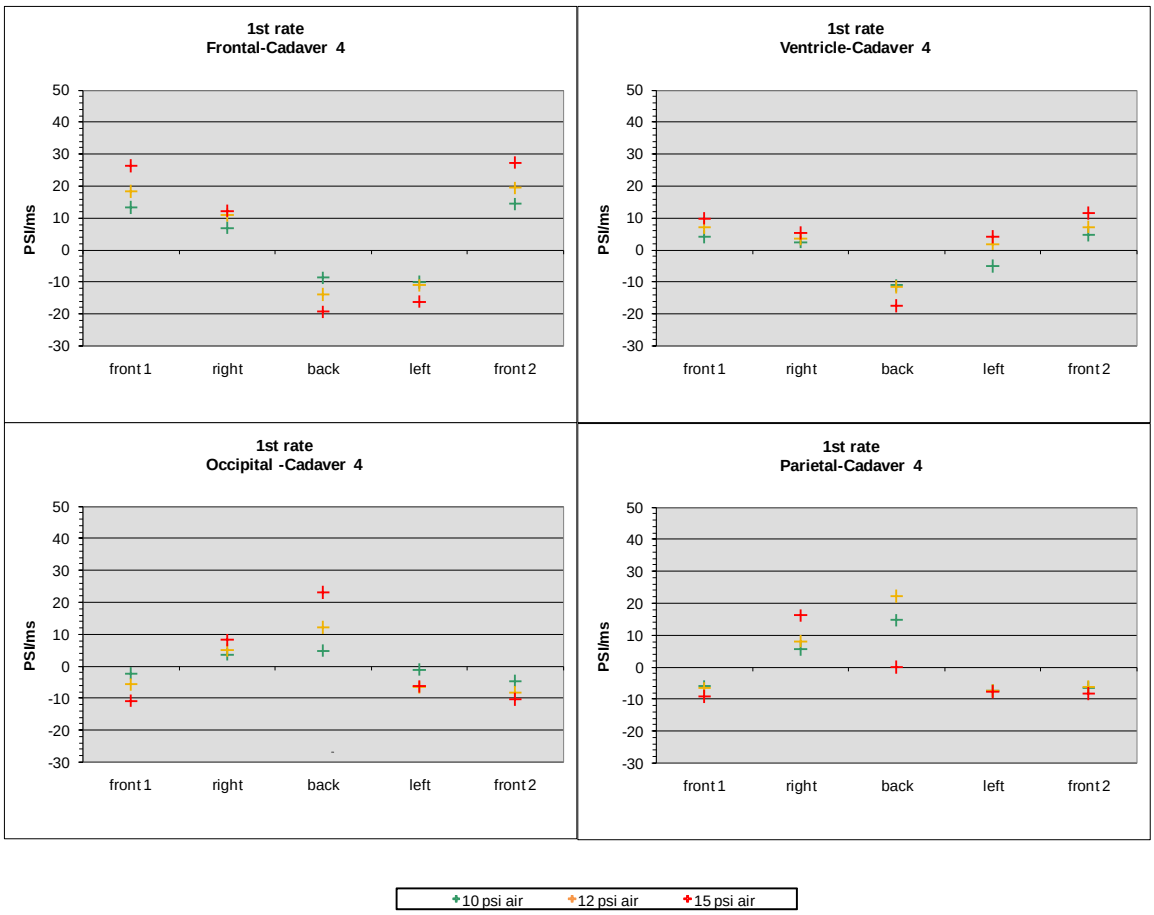

Figure 82: Graphs by sensor for 1st rate values for cadaver 4 (the results are color coded according to the shock wave pressure).

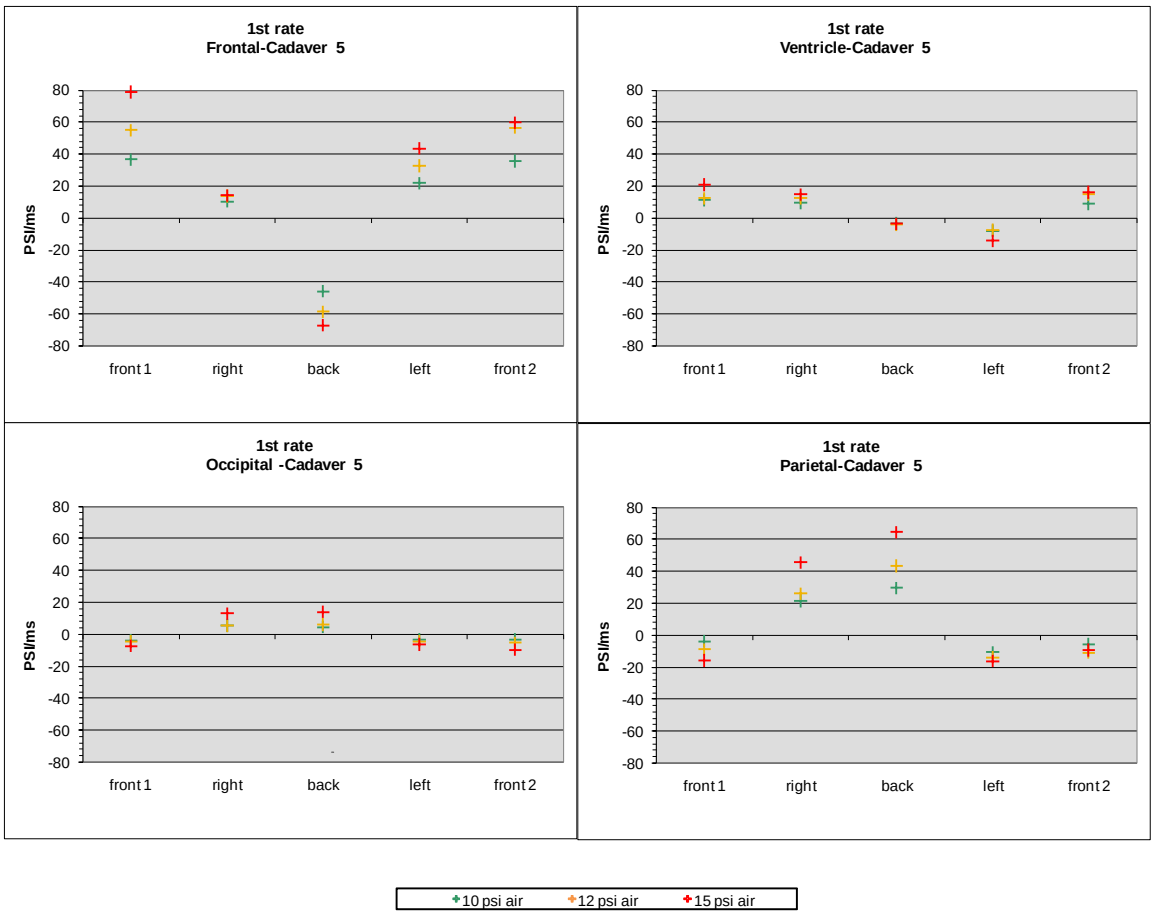

Figure 83: Graphs by sensor for 1st rate values for cadaver 5 (the results are color coded according to the shock wave pressure).

Analysis of the pressure gradient values was performed to investigate the response of 1st rate to increases in shock wave overpressure. The procedure was similar to the one previously described in this chapter for maximum values. When gathering the results of the 1st rate comparisons for the three cadavers, a total of 155 comparisons were performed. Results revealed that in general the 1st rate of change of ICP increased in 91% of the cases. By region the results were: ventricle 1st rate increased 93% of the time; frontal 1st rate increased 100% of the time; parietal 1st rate increased 93% of the time; and occipital 1st rate 80% of the time. Figure 84 presents a summary of these results.

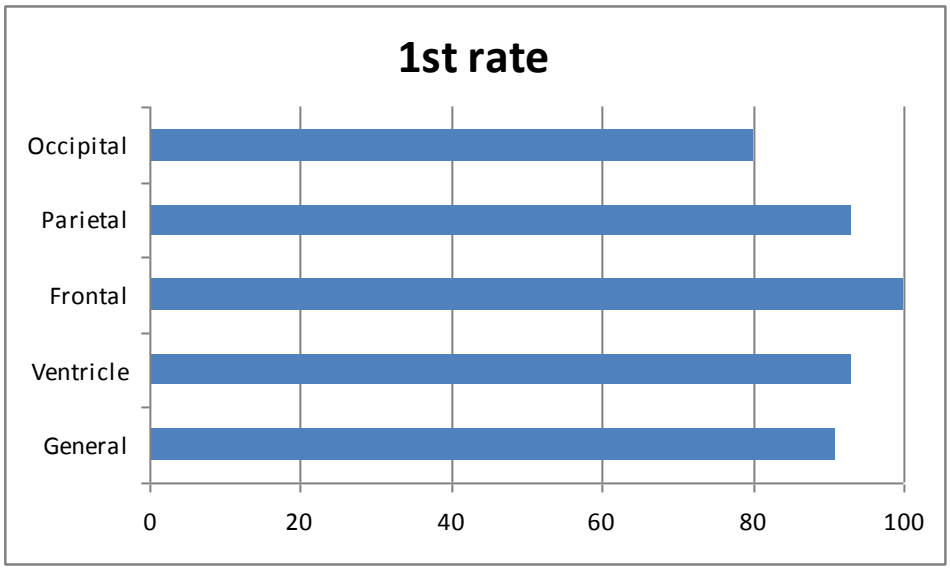

Figure 84: Comparisons expressed in percentages for 1st rate values in cadaver 3, 4, and 5 combined together, in relation to increasing shock wave overpressure.

Further analysis of cadavers 3, 4, and 5 examined the percentage of rate increase in relation to the rate value at the lowest shock wave overpressure magnitude, for each sensor at every orientation. Tables of results for the calculated percentages (calculation as previously done for maximum, minimum, and differential pressures) are shown in Appendix A. As for the pressure values, no apparent relation could be found among these percentages.

6.3.2 Strain results

Five strain gages were installed onto the skull to measure deformations in the left part of the frontal bone, left parietal bone, left temporal bone, left zygomatic bone, and left part of the occipital bone. The harsh testing environment created numerous survivability problems for the strain gages. Furthermore, because of each cadaver's own peculiarities in skull surface at the installation site (bumpy instead of flat), installation of gages sometimes had to rely heavily on adhesive. This probably had an effect on the collected data, the extent of which is unknown. Therefore, complete data for even one region of the skull are quite rare, and when present, they need to be reviewed with caution. Tables in Appendix A show the progressive damage sustained by the gages in each specimen. As previously mentioned, the calculation of principal strain was

beyond the scope of the study. When possible, strain values were analyzed only for evaluation of gross deformations of the skull in relation to ICP profiles.

Figure 85 shows an example of data collected simultaneously for the parietal pressure sensor and the parietal strain gage of cadaver 3. The pressure sensor is anchored to the right parietal bone, while the strain gage is anchored to the left parietal bone. Because gages and bones are coupled together, even small stresses to the bones can be recorded by the gages. In the case of Figure 85, the specimen was exposed to a front orientation. In relation to the initial loading the two parietal gages were placed towards the opposite side and closer to countercoup position. This example seem to show evidence of surface ripples traveling along the skull. At this orientation, the shock wave hits the frontal bone first, initiating surface ripples that quickly propagate to the adjacent parietal bones ahead of the shock front in air. Since the pressure wave transmits faster in the skull than in air, these surface ripples can be detected in the data recordings before the arrival of the global compression. The pressure and the stress profiles in Figure 85 show the same event as indicated by the arrows. The illustrations in Figure 85 explain the individual responses. The strain gage is compressed at the arrival of the surface wave (in this study, the sign convention adopted for stresses relates negative values to compression and positive values to tension). The ICP sensor is lifted by the surface wave and therefore a tensile stress is seen in the recordings (in this study, the sign convention adopted for ICP pressures relates positive values to compression and negative values to tension). At the arrival of the shock wave, global compression takes over (the small delay for compression in the pressure sensor is to be expected since the sensor is not at the surface), followed by decreasing values for pressure and stress.

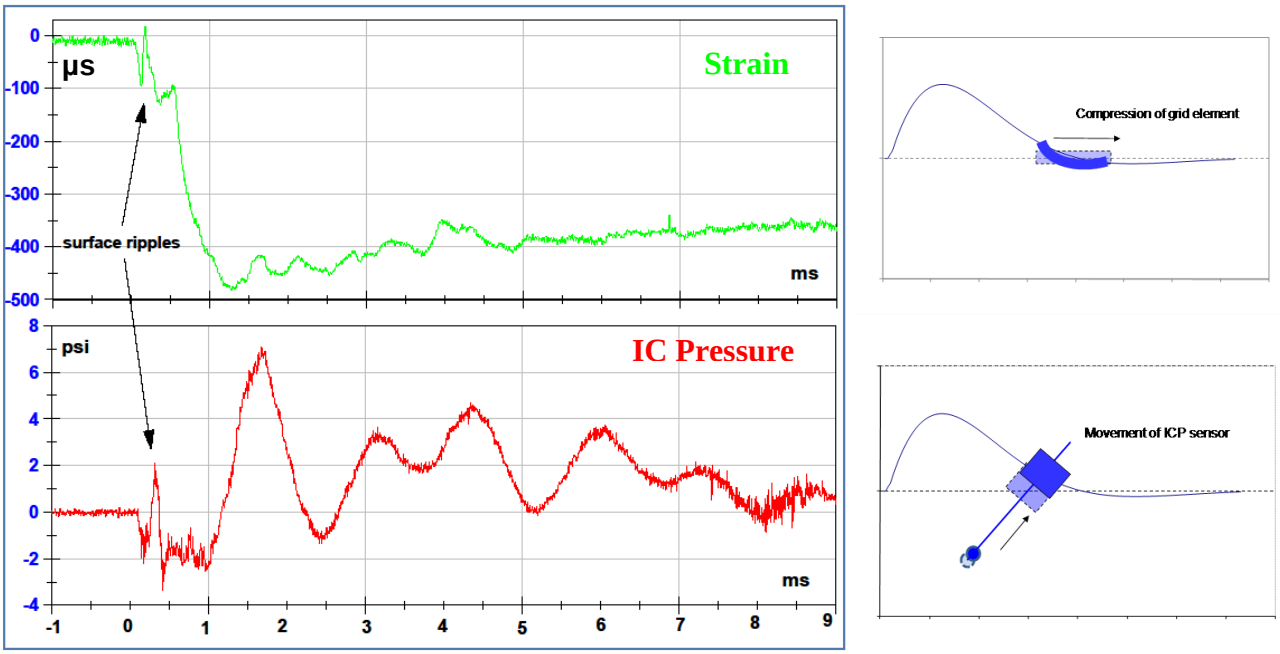

Figure 85: Parietal strain gage and parietal pressure sensor in cadaver 3 for front orientation at 10 psi overpressure.
The presence of surface ripples is noted in the recordings and the illustrations explain the compression in the surface strain gage and the tensile stress in the ICP sensor.

In contrast with the previous figure, Figure 86 shows the response for strain and pressure when the respective gages are located near the coup site. Figure 86 presents frontal strain and frontal pressure data for cadaver 5 for front orientation. Because of the proximity of the pressure sensor to the coup, no surface ripples are present before gross compression at the initial loading. When comparing the strain and pressure profiles, a second observation is made on the fact that strain data shows an oscillatory response with nearly double the frequency of the ICP data in the initial 3 ms from the shock arrival. Then the two recordings seem to reach a similar frequency after the 3 ms mark. The presence of these oscillatory responses in both recordings indicates a coupling of the skull/brain systems, with complex interaction due to the heterogeneity of the two structures. The ICP data demonstrates a highly damped frequency of 600 Hz for our specimens, confirming measurements acquired in previous studies (Franke 1956).

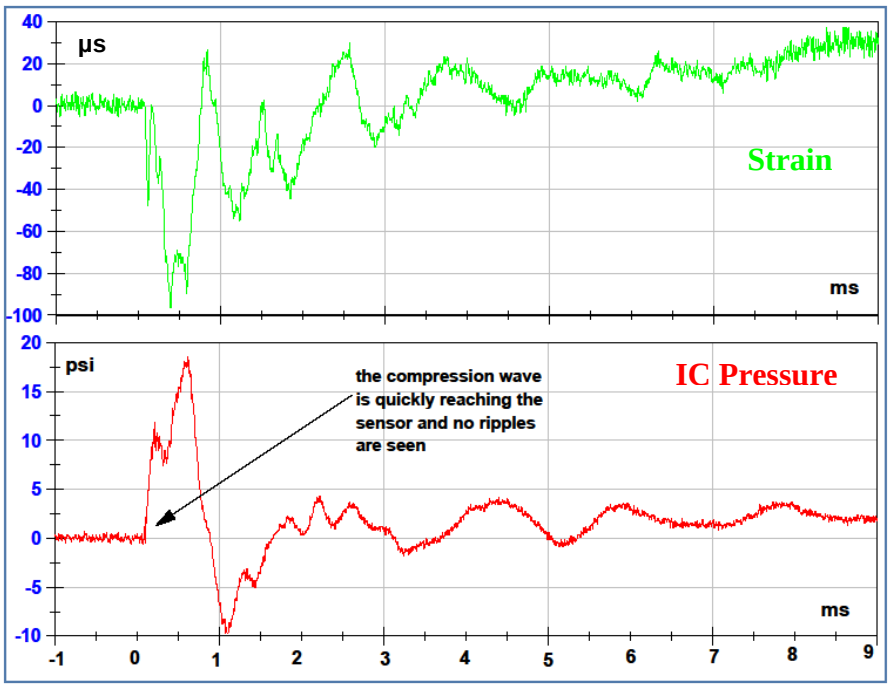

Figure 86: Frontal strain gage and frontal pressure sensor in cadaver 5 for front orientation at 10 psi overpressure.

Figure 87 compares the strain recordings already presented in Figure 86 to the shock wave overpressure occurring around the specimen during the simulated blast event. This example quite clearly shows that the strain recordings has a background quasi-static component that nearly tracks the external static pressure, as it would be expected when applying a force to the strain gage. The shock front creates an oscillation, which is seen riding a decreasing compression because the external decreasing pressure is also applied to the gage.

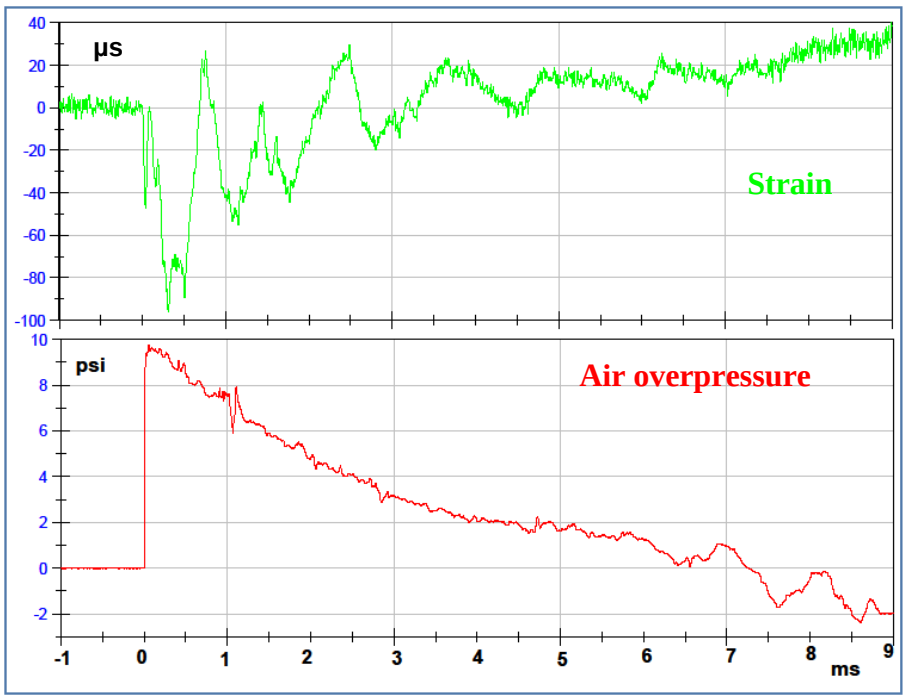

Figure 87: Frontal strain gage stress profile of cadaver 5 for front orientation at 10 psi overpressure and the shock wave overpressure profile around the specimen.

6.4 DISCUSSION

The main goal of this research was to establish the fundamental phenomenology of shock wave interaction with the skull/brain system. This study sought to explore the relationship between magnitude levels of incident pressure and values of ICP in different regions of the brain, to investigate the effects of orientation on ICP in the same regions, to compare pressure distribution patterns with surface strain data recorded concurrently, and also to compare the mechanical responses in the cadaveric data to the mechanical responses obtained in the simplified head models. Four unembalmed cadaver heads were placed in an inverted position inside a shock tube expansion section and were exposed to fifteen simulated blasts, changing pressure magnitudes and orientation of the head. ICPs in four regions of the brain and strain values in five regions of the skull were collected.

As for the simplified models presented in Chapter 5, the cadaveric ICP data was filtered, then maximum and minimum pressures were recorded and pressure differential and 1st rate of change of internal pressure were calculated. Of all the processed data, the least reliable values belonged to the pressure gradient tables, as the rate values were manually calculated and, therefore, subjected to human error (the operator had to pick the two points on the curve that would provide the rate value). It would have been preferable to have derivatives, but a more sophisticated filtering process must be developed first. Therefore, outcomes from 1st rate analysis were presented with the understanding that this is a limitation of the current study.

Another limitation of the study was the use of strain gages. Strain gages were a crude way to investigate skull flexure, because they only presented measurements for isolated points on the surface and it is hard to infer the global behavior from a few points especially in the presence of suture lines that could introduce unexpected variations to the deformation patterns. However, we believe the information gathered was adequate to establish the basic phenomenology, which was the goal of this study. A final limitation of this study was the restricted range of shock wave overpressure values provided during testing. As mentioned in Chapter 2, presently, the major limitation to reaching higher driver pressures is the clamping system that holds the membrane.

In preliminary observations it was noticed that, during front and back orientations, the pressure profiles of the frontal and ventricle sensors were similar, as well as the pressure profiles of the parietal and occipital sensors. When mounting the four pressure sensors, the location of frontal and ventricle was in the anterior part of the skull, while the location of parietal and occipital was towards the posterior part. Therefore, during front exposure, the frontal and ventricle sensors were both in the proximity of the coup site, while the parietal and occipital sensors were closer to the countercoup site. Vice versa, during back exposure, the frontal and ventricle were in proximity of the countercoup site and the parietal and occipital were closer to the coup site. This explains why their profiles were consistently similar.

When examining Figure 73 to Figure 75, the graphical format allows to easily identify that, for every sensor, the orientation that put the sensor in closer proximity to the cou site was linked to the greatest maximum pressures, and the orientation that put the sensor in closer proximity to the countercoup site was linked to the greater (in absolute value) minimum pressures. Furthermore, the countercoup site recorded negative ICP values, showing a behavior similar to that noticed in the spheres (Chapter 5). As seen in Figure 73 to Figure 75, in the case of the skull/brain system, the recorded negative pressure values at the countercoup site were greater than in the sphere models and indicated a direct relationship to increasing shock wave magnitudes (Figure 79).

In addition, the results from all the pressure profiles presented in Appendix A indicated that, during a blast event, at each region, the brain experienced variations of pressure in time, which we called pressure differentials. Also, when comparing different regions at the same moment in time, there were differences in pressure from one location to another. Not only did the ICP in the brain vary in time at each region, but also, from one region to another, the brain was simultaneously experiencing different pressures. The presence of these delta pressures (i.e. pressures that are either position-related or time-related) was undoubtedly creating stresses in the brain tissue, and it is reasonable to suspect that these stresses could be a primary source of injury.

We suggest that the main reason for these delta pressures is that the human skull has a finite stiffness, and that the encounter with the shock front causes the skull to partially deform but also rapidly move relative to the brain. Proof of this deformation is given by the response of the strain gages, which experience the global compression applied to the skull by the shock wave, but also endure the tension of the skull structure reacting to it as surface ripples. On the other hand, proof of the skull movement relative to the brain can be found in the pressure data when looking at the response of the brain (ICP values) at the coup and countercoup sites, particularly for front and back orientations (these orientations are more inclined to prove this behavior due to the inherited elliptical geometry of the human skull). When examining the maximum peak pressure

values across the four orientations, for frontal and ventricle sensors in cadaver 4 and cadaver 5 (complete data), front exposure was consistently recording the highest values. Similarly back exposure was recording the highest values for parietal and occipital. For minimum peak pressure values, the roles were reversed: frontal and ventricle presented the greatest values at back orientation, while occipital has the greatest values for front orientation. The parietal data was found less consistent for minimum values, but, since its location was really close to the anterior-posterior midline, mixed results are not inexplicable. This trend of peak positive pressures occurring at the coup site and greatest negative pressures occurring at the countercoup site were also predicted by Chafi et al. (2010). When the skull is invested by a shock front, as any stiff structure, it reflects the greatest part of the wave with little deformation. We propose that, when reflection occurs, the stiffer skull rapidly propagates the pressure wave through its structure and moves as a whole, while the softer brain lags behind, compressing at the coup site and experiencing tensile stress at the countercoup site.

Chafi et al. (2010) reported that their model generated significant levels of pressure in the brain before any overall motion of the head occurred. Acceleration results in cadaver 2 and 3 demonstrated that there was no global motion at the initial loading and limited motion was seen as the shock wave progressed due to blast wind. Moss et al. (2009) and Taylor and Ford (2009) also reported insignificant gross motion during the initial loading in their computational models.

We believe that the relative movement is very small, but very rapid, and this relative motion is what causes great positive and negative pressure values. Proof of the relative rapidity of this movement is linked to the results of the 1st rate of pressure change: comparing across the four orientations, for cadaver 4 and cadaver 5, all pressure sensors had consistently the highest 1st rate values at front or back exposure, which indicates that the pressure gradient was the highest when the sensors were either in a coup or countercoup position. In our proposed model the faster the skull moves relative to the brain, the faster the compression/tension occurs in the brain, which leads to greater pressure values, both positive and negative. Furthermore, as shown in Figure 84,

the 1st rate value consistently increased with increased magnitude (91% of cases). Increased shock wave overpressure magnitudes would translate into greater forces reflected by the skull, which, in turn, would create a more rapid motion of the skull relative to the brain. A faster motion would lead to higher pressure gradients in the deforming brain, and greater pressure values. However, we do not expect this relationship to be linear, as the skull also exhibits a deformation response that could conceivably increase further with increased shock wave overpressures.

Additionally, it was noted that in all front orientations the frontal sensors recorded ICPs (raw values) that were higher than the external overpressure environment. As we explained at the beginning of this section, the frontal sensor is near the coup site at front orientation, and the occipital sensor is at the coup site during back orientation. Although not entirely shown by our data, we predict that the coup sites, both frontal and occipital, would deliver higher ICPs than the air overpressure. In each cadaver, the frontal sensor was installed in a very consistent location, contrary to the occipital pressure sensor installation. Table 14 presents a summary of the post-test measurements for the location of each sensor relative to skull landmarks once the scalp was removed.

Table 14: Post test specimen measurements.
The highlighted cells indicate sensors that were moved from the original position. In cadaver-3 the ventricle was moved, therefore its measurements from midline and relative to the other sensors were different. In cadaver-5 the occipital sensor position was changed.

CADAVER NUMBER	WSU 5092	WSU 5103	UM 336524	UM 336555
Nasion to Frontal P.S. [mm]	50	70	70	67
Frontal to Ventricle [mm]	45	70	50	50
Ventricle to Parietal [mm]	65	45	55	67
Parietal to Occipital [mm]	50	60	45	120
Frontal P.S. from midline [mm]	10	20	10	10
Ventricle P.S. from midline [mm]	22.5	10	20	20
Parietal P.S. from midline [mm]	X	15	25	10
Occipital P.S. from midline [mm]	10	15	25	5

X = parietal sensor was not installed

The occipital sensor installation was fairly consistent in cadavers 2 and 3; then, due to an unusual skull geometry, it was moved more off midline in cadaver 4; and in cadaver 5, an unsuccessful attempt was made to place the occipital sensor closer to coup/countercoup position, as explained previously in this chapter. In cadaver 2 the occipital sensor failed before the beginning of testing. In cadaver 4 the occipital sensor distance from midline was 75% more than it should have been. It is reasonable to suspect that the pressure data for cadaver 4 is low because the sensor was away from coup position. The only installation that did not present abnormalities was the one for cadaver 3, which showed maximum pressure values that were consistently higher than the shock wave overpressure, both in coup and countercoup position (back and front orientations respectively). More specimens would be needed to test the validity of this prediction.

Furthermore, analysis of the cadaver data consistently indicates that ICP values tend to increase with increased shock wave overpressure, and that regions of the brain that are closer to the skull reach pressures that are higher than deeper regions of the brain. However, the increase

did not appear directly proportional. If the relation were linear, a higher increase in shock wave overpressure would cause an increase in every piece of data collected, but that was not the case. The apparent lack of any kind of proportional relationship could be partially due to the fact that the orientation of the specimen was rotated before increasing the overpressure magnitude. Therefore, matching exactly the same position for each orientation could not be ensured. Slight changes in skull orientation may result in a change in the energy imparted to the area monitored by the sensor. Finally, we suspect that geometrical and other characteristics of the bones (thickness, curvature etc.) could cause distinctive responses for each region, and that, possibly, an additional contribution to peculiar data values could be created by the way sutures interact during blast loading.

6.5 CONCLUSION

The main goal of this investigation was to establish the fundamental phenomenology of shock wave interaction with the skull/brain system. By studying the mechanical response of the skull/brain system at a fundamental level, we aim to contribute to the understanding of the mechanism of brain injury during exposure to blast.

The focus of this research was to examine one of the hypotheses for primary brain injury due to blast: multimodal skull flexure. Multimodal skull flexure hypothesizes that, when a shock wave interacts with the skull/brain system, it creates ICPs in the brain by producing skull deformation, surface ripples, relative motion between the skull and brain, and a global skull compression.

The data results of this study confirm that:

- significant ICP values are recorded even in the absence of a fully functioning vasculature and/or an intact body, refuting previous studies that uphold the thoracic mechanism as a primary mechanism of brain injury during exposure to blast,

- there is a direct interaction between the external overpressure, the pressures developing in the brain, and the strains recorded on the skull,
- the mechanical response of the fluid/structure (brain/skull) configuration is essentially based on the coupling of these two systems,
- the fluid/structure interaction between the stiffer skull and the compliant brain explains the distribution of ICPs, especially at coup/countercoup positions,
- deeper regions of the brain experienced lower pressure differentials than the cortex.

The results of this study led us to conclude that the proposed mechanism of brain injury by multimodal skull flexure is supported by our data. The presence of the spacial and temporal pressure distributions caused by the multimodal skull flexure is undoubtedly creating stresses in the brain tissue, and it is reasonable to suspect that these stresses could be a primary source of injury.

6.6 ACKNOWLEDGEMENTS

This research project was partially funded by ***CDMRP grant # W81XWH-09-1-0498.***

CHAPTER 7

7.1 CONCLUSIONS

The ultimate goal of this study was to help unravel the complexity of the mechanical response of the skull/brain system to blast loading and help identify the primary components of such response.

Cadaveric data and data from simplified models of a skull/brain system were analyzed to establish the basic phenomenology of shock wave interaction during a simulated free-field blast. The analysis showed that there were similarities in the mechanical responses of these two systems (cadavers and spheres). Based on the results of both systems the following observations can be made:

1. Significant ICP values were recorded even in the absence of a fully functioning vasculature and/or an intact body, refuting previous studies that uphold the thoracic mechanism as a primary mechanism of brain injury during exposure to blast.
2. The shock wave investing and surrounding the skull (or the spheres) produced fluid/structure interactions that could be explained by the multimodal skull flexure theory. This theory suggests that a shock wave interacting with a skull/brain system would create ICPs in the brain by producing skull deformation, surface ripples, relative motion between the skull and brain, and a global skull compression. The distribution of the ICP values, especially at the coup/countercoup positions, was consistent with the multimodal flexure theory. Finally, the frequency response of strain and ICP data showed evidence of the coupling of the skull (or shell) with the brain (or filling).
3. Comparison of internal pressures in the two studies, suggests a link between the mechanical response of the skull/brain system and its geometrical features. Results obtained in the simplified head systems showed similar patterns, even though key characteristics were modified among the models. High ICPs developed at the coup site,

and were recorded even by sensors that monitored regions deeper inside the filling. In comparison, the negative ICPs at the countercoup site seemed to have lower values and a much shorter range. On the other hand, the cadaver study showed significant negative pressure at the countercoup site and these values became greater with increased shock wave overpressure. It is practical to notice that the human skull geometry is more complex than the simplified fluid-filled sphere and that those geometrical features could be among the main reasons for the differences in the mechanical response of the two systems.

4. Since liquids are almost incompressible, in a sealed system very high pressures can be produced by very small deformations. By design, the simplified models had a better seal than cadavers and showed peak internal pressures higher than the peak shock wave overpressure in every test. The harvested heads had the major blood vessels and spinal cord clipped, but it would have been impossible to close every capillary vessel in the time frame of the testing schedule. Dal Cengio Leonardi et al. (2011) demonstrated that proper sealing techniques lead to a significant increase in ICP values. A living skull/brain system is not as perfectly sealed as the simplified models we tested. It seems realistic to expect that, in the actual live scenario, the ICP values would measure lower than in the spheres, but higher than the pressure values recorded in the cadaveric study. How much higher is still an open question, but these findings already have implications both in the design of protective gear and in the medical treatment provided to humans after exposure to blast.
5. The presence of apertures can cause an increase in ICP values, as demonstrated by the spheres. Holes in the skull, especially the superior orbital fissures (SOFs), are potential ports that could allow more energy from the shock wave to reach the brain. The SOFs have a funnel-shaped structure, called the orbit (the socket of the eye), right before them, which could amplify the amount of energy entering the brain. This funnel-shaped structure was not modeled in the spheres. It is reasonable to predict that higher ICP could

be measured in the spheres if we increased the sophistication of the models. However, further considerations need to be made regarding skull apertures. Soft tissue fills some openings in the skull, while fluids flow through other openings. In 1956, Clemedson investigated the possibility of shock wave transmission through the spinal column in rats, and found that a pressure wave was propagating from the brain down the spinal cord (Clemedson 1956a). The foramen magnum, filled with soft tissues and fluid, served as a portal for the internal pressure to vent out. A similar behavior was seen in the 6mm-thick sphere filled with Sylgard 527, once apertures were introduced. The results showed decreased internal pressure as the Sylgard was believed to protrude through the holes during shock exposure. Clemedson's report and our own results suggest potential dichotomic behavior of skull apertures. On one hand, these access ports could facilitate and increase energy transmission into the brain; on the other hand, the apertures could also serve as release valves. Stress would be caused to neurons and other tissues during each event.

6. When examining pressure and strain data, the frequency responses of the shell and filling material were much closer in value than those of the brain and skull. Because of the simplified materials and geometry, the physical models had better coupling than the skull/brain system. The brain has several layers of different tissues that can modify the frequency response between the skull and brain. In the case of polyurethane spheres filled with aqueous glycerine, the main frequency response was similar to cadaveric data. However, in the polyurethane sphere filled with Sylgard 527, the pressure sensors showed a consistent secondary oscillation (5.6 kHz) riding on the main wave component. This secondary frequency is atypical of the other spheres and also of the results in the cadaver study. This characteristic oscillation seemed attributable to the material properties of cured Sylgard 527, which has great adhesion and shear stiffness, and this

behavior needs to be considered when using this material as a brain surrogate for blast models.

In conclusion, the results of this research show that the proposed mechanism of brain injury by multimodal skull flexure is supported by our data. The presence of spacial and temporal pressure distributions, caused by the multimodal skull flexure, is undoubtedly creating stresses in the brain tissue,and it is reasonable to suspect that these stresses could be a primary source of injury. In addition, we suggest that the human skull geometry could play a strong role in the development of of stresses in the brain tissue, especially for tensile stresses. However, other factors, such as peak internal pressure and, possibly, energy acquired and/or released from apertures in the skull, could also contribute to exacerbate brain injury. It is reasonable to suspect that most of these stresses could be a primary source of injury at different brain locations.

Presently, it is unknown how the rate of change of the ICP can affect brain cells, but it is becoming increasingly evident that the rate of change of pressure could be an important mechanism of injury. Consequently, we suggest that, in the design of new PPE, attempts should be made to reduce both the peak internal pressure value and the rate of change of internal pressure.

CHAPTER 8

8.1 FUTURE WORKS

The results of this multi-study project suggest possible directions for future investigations.

- The present study utilized a simplified geometry as a surrogate of the skull/brain system. We now suggest that the human skull geometry plays a strong role in the development of some stresses in the brain tissue. To test our hypothesis we will need to develop a model that more closely resemble the skull geometry. By maintaining the same filling (aqueous glycerine at 40% weight) and varying only the shell shape, new information could be collected on the real contribution of the skull geometry.
- The effects of suture lines have not been investigated in this study, but animal studies have proved that sutures deserve investigation (Adams et al. 1992). Samples with simplified geometry, such as the spheres in this study, should be modified to include coronal and sagittal sutures. New information could be collected on the effect of sutures.
- The present study did not attempt to validate a surrogate for human head, but simply explored the mechanical response of three simplified head models of identical geometry that had differences in key characteristics: shell thickness, composition of the filling, and introduction of apertures. It is obvious that skull/brain models still need to improve before approaching surrogate-status. Blast research needs a better brain simulant. A starting point could be the addition of a binding agent to the aqueous glycerine solution utilized in this study, in an

effort to modify the simulant shear module value to one closer to the brain's shear module. Test with identical spheres, as the ones already used, could identify the effects of the modified simulants on the mechanical and frequency responses.

- In both the surrogate study and the cadaver study, the glue amount on the strain gages was a concern; therefore strain trends could be analyzed but magnitudes could not be trusted, because the effect of the glue on the collected data was unknown. In the future, the relationship between shock wave overpressure magnitudes and strain values needs to be investigated. Strain gages can help evaluate the deformation of the system. By knowing actual measurements of shell strain we could better infer the relation between overpressure and deformation values. A more reliable gage installation is necessary for the next blast testing series.
- Initially two rates of change of pressure values were calculated for both studies: one was 1st rate, the other was called peak to peak rate and it was calculated as the pressure differential between two consecutive opposite extremes divided by the corresponding elapsed time. The reason behind calculating a second rate was that the 1st rate value represents the first change of pressure, but it does not necessarily provide the highest pressure gradient that the brain region will endure during the event. However, when reviewing the processed data, we realized that the peak-to-peak rate values were highly subjective, as gradients were highly sensitive to the points chosen by the operator. Therefore, these values were dismissed until a more automated, less arbitrary process could be developed. Once objective data can be calculated, we expect to discover a relation between

the rates of change of pressure and the energy absorbed by the skull/brain surrogate system. 1st rate values seem to show a direct proportion to the energy that is absorbed by the filling. We hypothesize that the peak-to-peak rate may show a direct relation to the energy that is absorbed by the shell.

- A primary goal of this work is to translate the lessons learned so far into immediate improvements of military protective equipment. We believe that efforts should be concentrated into helmet design and we wish to develop a new product that will integrate with current standard equipment. By applying lessons learned in the sphere study, we suggest to dissipate as much energy as possible through deformation of protective materials before it reaches the skull and brain.

APPENDIX A

CADAVER 2 DATA

Test 1 Front 1 Orientation Cadaver-2

FILTERED DATA

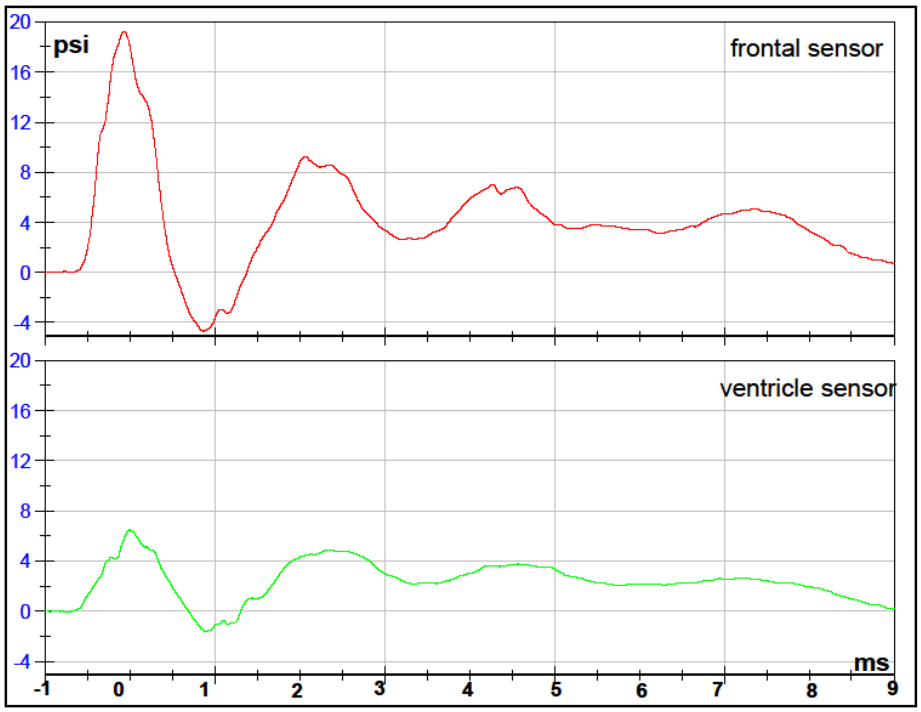

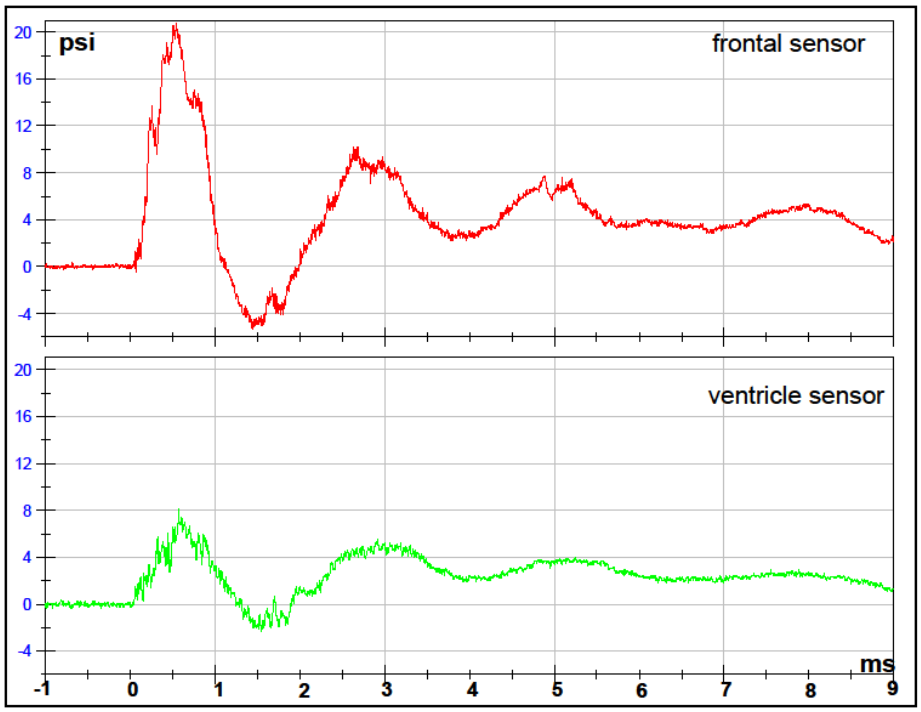

RAW DATA

Test 2 Left Orientation Cadaver-2

FILTERED and RAW DATA

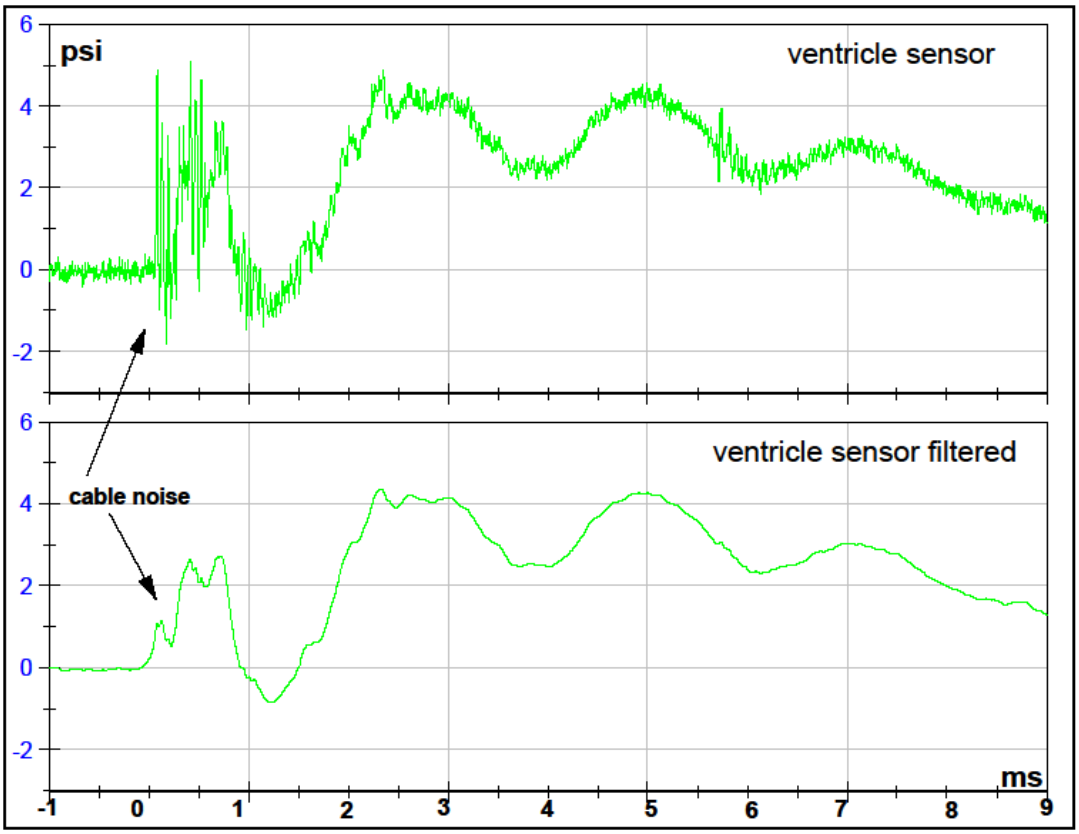

Test 3 Back Orientation Cadaver-2

FILTERED and RAW DATA

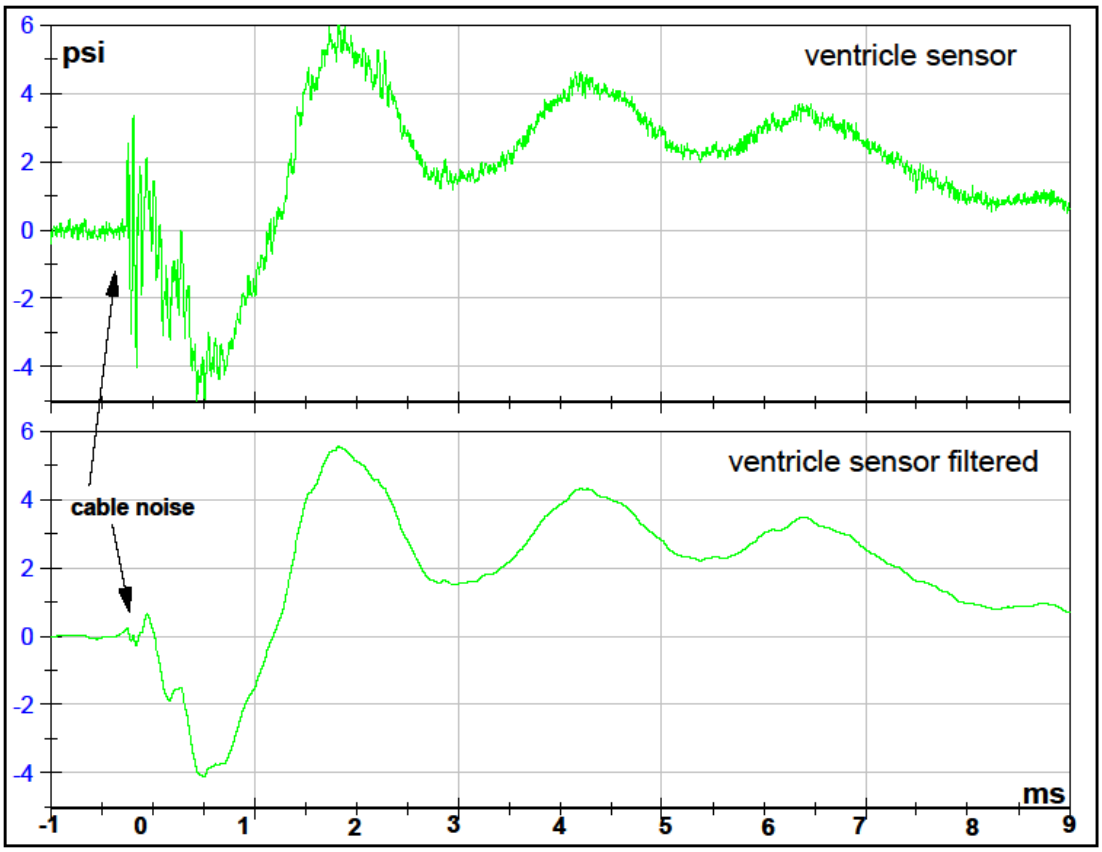

Test 4 Right Orientation Cadaver-2

FILTERED and RAW DATA

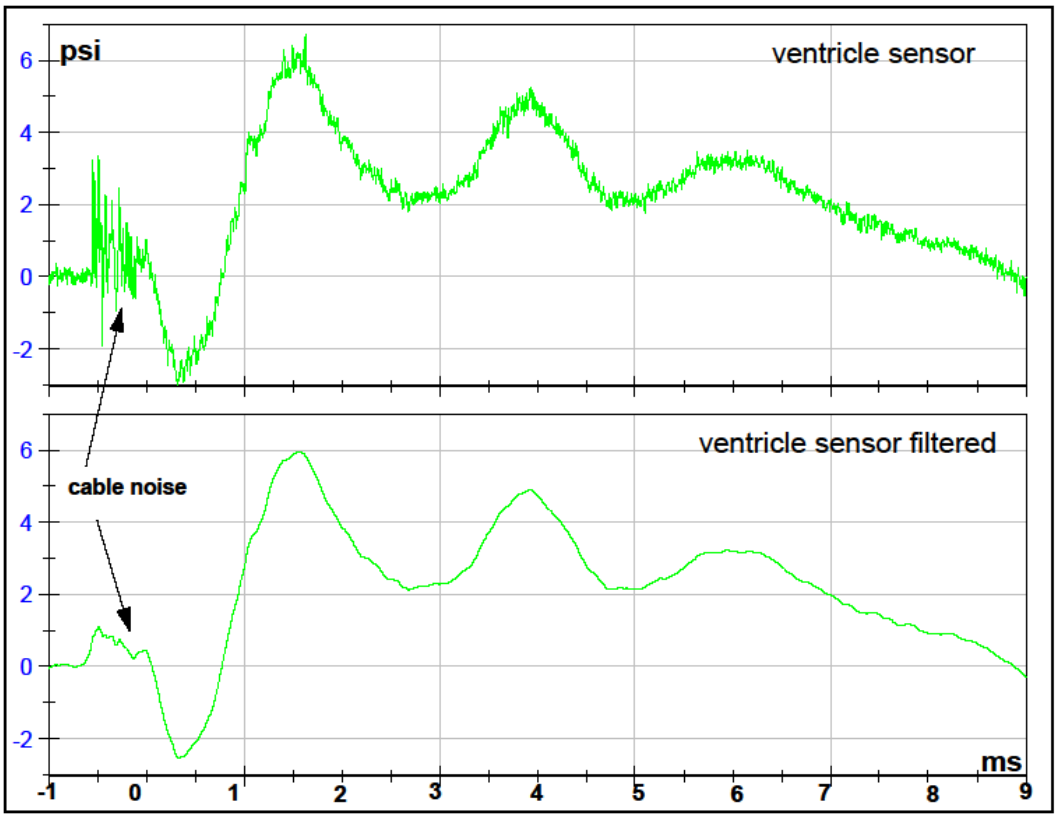

Test 5 Front 2 Orientation Cadaver-2

FILTERED and RAW DATA

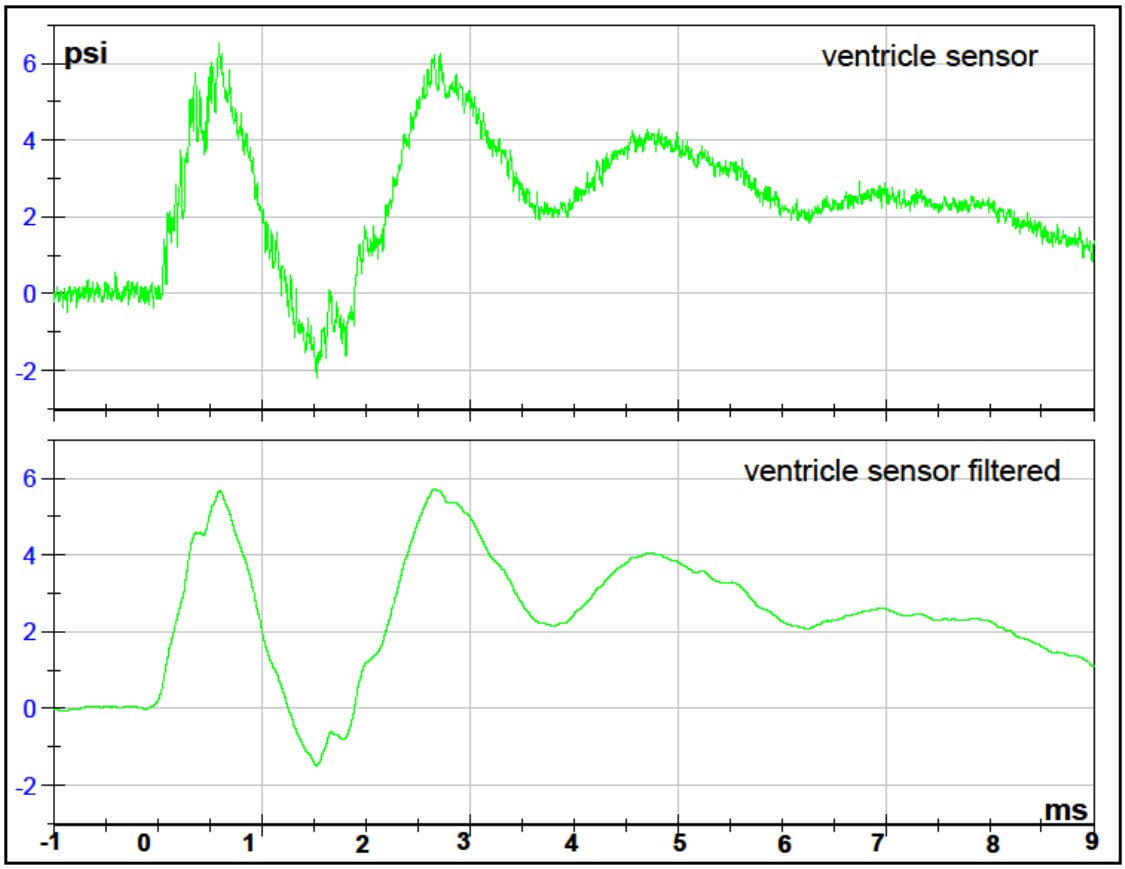

Test 6 Front 1 Orientation Cadaver-2

FILTERED and RAW DATA

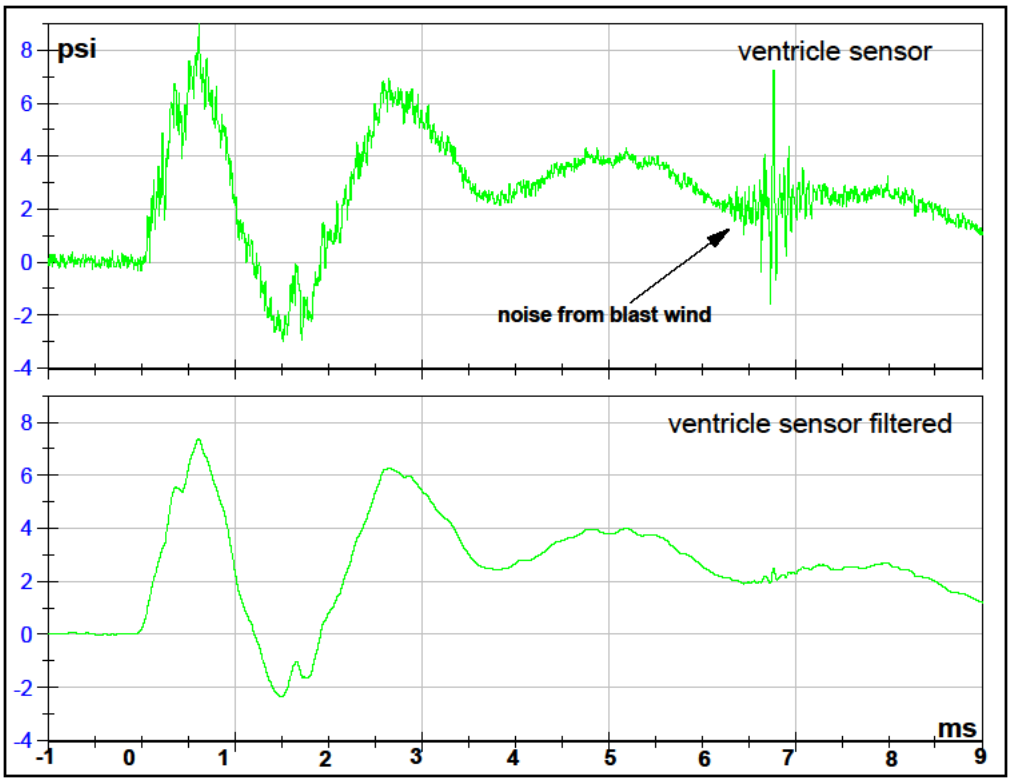

Test 7 Right Orientation Cadaver-2

FILTERED and RAW DATA

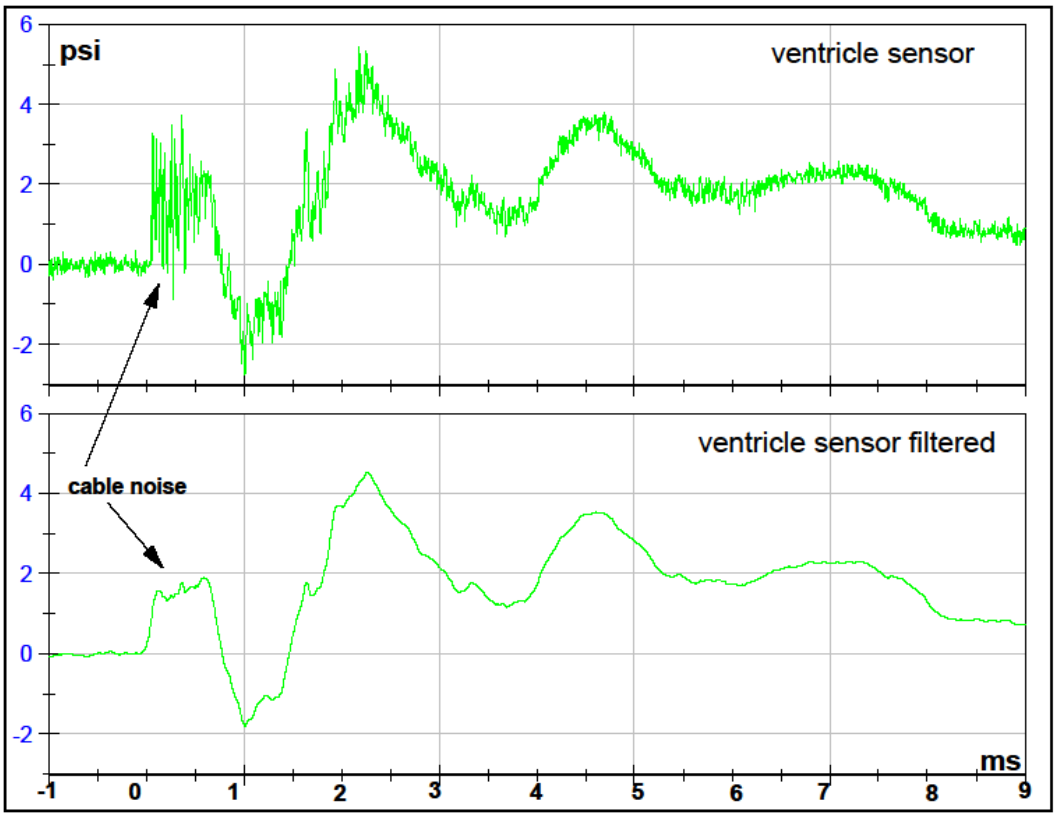

Test 8 Back Orientation Cadaver-2

FILTERED and RAW DATA

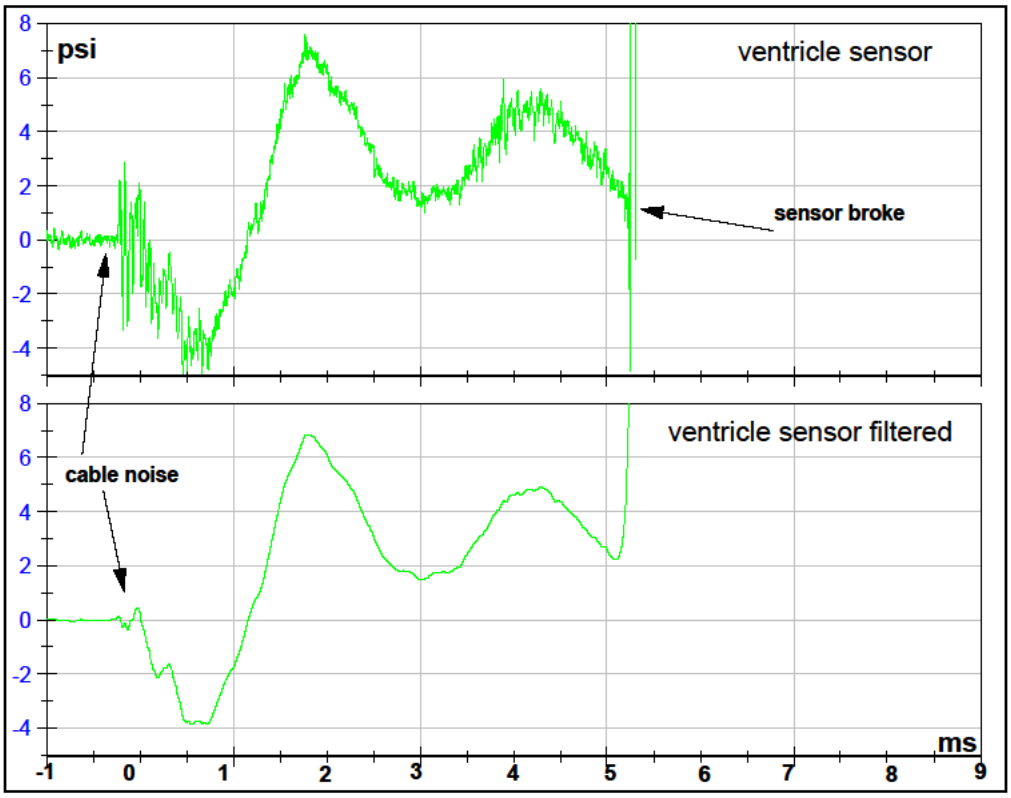

Comparison for reproducibility of each pressure sensor in Front Orientations at 10psi Cadaver-2

VENTRICLE FILTERED DATA

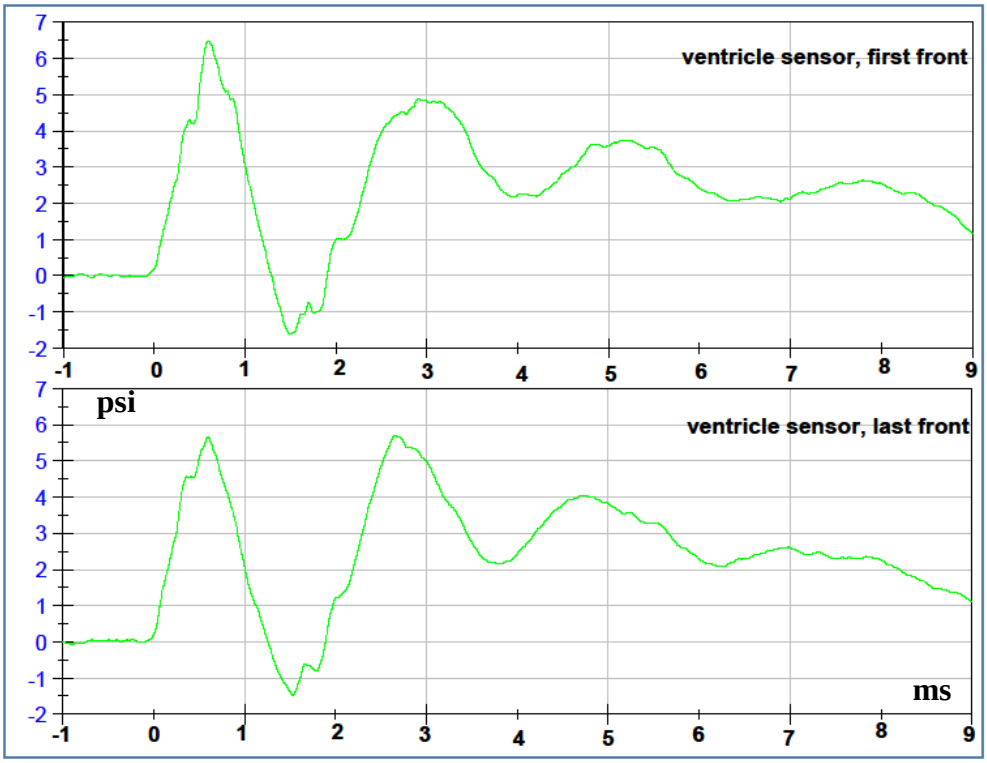

Pressure Extremes for cadaver-2.

Sensor failure occurrence was very high for this specimen. 83% of the table cells had no pressure results in each category.

Pressure Extremes for cadaver-2 (psi)										
	Maximun Pressure					Minimum Pressure				
ventricle	front 1	right	back	left	front 2	front 1	right	back	left	front 2
10 psi air	**6.47**	**5.96**	**5.55**	**4.36**	**5.66**	**-1.61**	**-2.54**	**-4.1**	**-0.848**	**-1.49**
12 psi air	**7.39**	**4.52**	**6.82**	**NA**	**NA**	**-2.36**	**-1.8**	**-3.81**	**NA**	**NA**
15 psi air	**NA**	**NA**	**NA**	**NA**	**NA**	**NA**	**NA**	**NA**	**NA**	**NA**
frontal	front 1	right	back	left	front 2	front 1	right	back	left	front 2
10 psi air	**19.22**	**NA**	**NA**	**NA**	**NA**	**-4.67**	**NA**	**NA**	**NA**	**NA**
12 psi air	**NA**	**NA**	**NA**	**NA**	**NA**	**NA**	**NA**	**NA**	**NA**	**NA**
15 psi air	**NA**	**NA**	**NA**	**NA**	**NA**	**NA**	**NA**	**NA**	**NA**	**NA**
parietal	front 1	right	back	left	front 2	front 1	right	back	left	front 2
10 psi air	**NA**	**NA**	**NA**	**NA**	**NA**	**NA**	**NA**	**NA**	**NA**	**NA**
12 psi air	**NA**	**NA**	**NA**	**NA**	**NA**	**NA**	**NA**	**NA**	**NA**	**NA**
15 psi air	**NA**	**NA**	**NA**	**NA**	**NA**	**NA**	**NA**	**NA**	**NA**	**NA**
occipital	front 1	right	back	left	front 2	front 1	right	back	left	front 2
10 psi air	**NA**	**NA**	**NA**	**NA**	**NA**	**NA**	**NA**	**NA**	**NA**	**NA**
12 psi air	**NA**	**NA**	**NA**	**NA**	**NA**	**NA**	**NA**	**NA**	**NA**	**NA**
15 psi air	**NA**	**NA**	**NA**	**NA**	**NA**	**NA**	**NA**	**NA**	**NA**	**NA**

Pressure differentials for cadaver-2.

Values were calculated by subtracting the peak negative (minimum) value from the peak positive (maximum).

Differential for cadaver-2										
	peak differential pressure (psi)					time elapsed between peaks (ms)				
ventricle	front 1	right	back	left	front 2	front 1	right	back	left	front 2
10 psi air	**8.08**	**8.5**	**9.64**	**5.21**	**7.15**	**0.896**	**1.22**	**1.33**	**1.11**	**0.936**
12 psi air	**9.75**	**6.32**	**10.64**	**NA**	**NA**	**0.892**	**1.25**	**1.14**	**NA**	**NA**
15 psi air	**NA**	**NA**	**NA**	**NA**	**NA**	**NA**	**NA**	**NA**	**NA**	**NA**
frontal	front 1	right	back	left	front 2	front 1	right	back	left	front 2
10 psi air	**23.89**	**NA**	**NA**	**NA**	**NA**	**0.928**	**NA**	**NA**	**NA**	**NA**
12 psi air	**NA**	**NA**	**NA**	**NA**	**NA**	**NA**	**NA**	**NA**	**NA**	**NA**
15 psi air	**NA**	**NA**	**NA**	**NA**	**NA**	**NA**	**NA**	**NA**	**NA**	**NA**
parietal	front 1	right	back	left	front 2	front 1	right	back	left	front 2
10 psi air	**NA**	**NA**	**NA**	**NA**	**NA**	**NA**	**NA**	**NA**	**NA**	**NA**
12 psi air	**NA**	**NA**	**NA**	**NA**	**NA**	**NA**	**NA**	**NA**	**NA**	**NA**
15 psi air	**NA**	**NA**	**NA**	**NA**	**NA**	**NA**	**NA**	**NA**	**NA**	**NA**
occipital	front 1	right	back	left	front 2	front 1	right	back	left	front 2
10 psi air	**NA**	**NA**	**NA**	**NA**	**NA**	**NA**	**NA**	**NA**	**NA**	**NA**
12 psi air	**NA**	**NA**	**NA**	**NA**	**NA**	**NA**	**NA**	**NA**	**NA**	**NA**
15 psi air	**NA**	**NA**	**NA**	**NA**	**NA**	**NA**	**NA**	**NA**	**NA**	**NA**

Pressure rate of change for cadaver-2.

	1st rate (psi/ms)				
ventricle	front 1	right	back	left	front 2
10 psi air	**10.57**	**-8.59**	**-8.53**	**5.91**	**9.15**
12 psi air	**11.83**	**2.45**	**-8.01**	**NA**	**NA**
15 psi air	**NA**	**NA**	**NA**	**NA**	**NA**
frontal	front 1	right	back	left	front 2
10 psi air	**35.72**	**NA**	**NA**	**NA**	**NA**
12 psi air	**NA**	**NA**	**NA**	**NA**	**NA**
15 psi air	**NA**	**NA**	**NA**	**NA**	**NA**
parietal	front 1	right	back	left	front 2
10 psi air	**NA**	**NA**	**NA**	**NA**	**NA**
12 psi air	**NA**	**NA**	**NA**	**NA**	**NA**
15 psi air	**NA**	**NA**	**NA**	**NA**	**NA**
occipital	front 1	right	back	left	front 2
10 psi air	**NA**	**NA**	**NA**	**NA**	**NA**
12 psi air	**NA**	**NA**	**NA**	**NA**	**NA**
15 psi air	**NA**	**NA**	**NA**	**NA**	**NA**

Strain gages status during testing of cadaver-2.

Rosettes were used to measure strain; therefore for complete data, three grids needed to be working.

Strain gages status for cadaver-2					
10psi	front 1	right	back	left	front 2
Frontal S.G.	3	3	0	3	3
Zygomatic S.G.	0	0	0	0	0
Temporal S.G.	0	0	0	0	0
Parietal S.G.	1	1	0	1	1
Occipital S.G.	3	3	0	3	3
12psi	front 1	right	back	left	front 2
Frontal S.G.	3	3	3	3	3
Zygomatic S.G.	0	0	0	0	0
Temporal S.G.	0	0	0	0	0
Parietal S.G.	1	1	1	1	1
Occipital S.G.	3	3	3	3	3
15psi	front 1	right	back	left	front 2
Frontal S.G.	3	1	0	0	0
Zygomatic S.G.	0	0	0	0	0
Temporal S.G.	0	0	0	0	0
Parietal S.G.	1	1	1	1	1
Occipital S.G.	3	3	3	2	2

0	0 grids working
1	1 grid working
2	2 grids working
3	3 grids working

CADAVER 3 DATA

Test 1 Front 1 Orientation Cadaver-3

FILTERED DATA

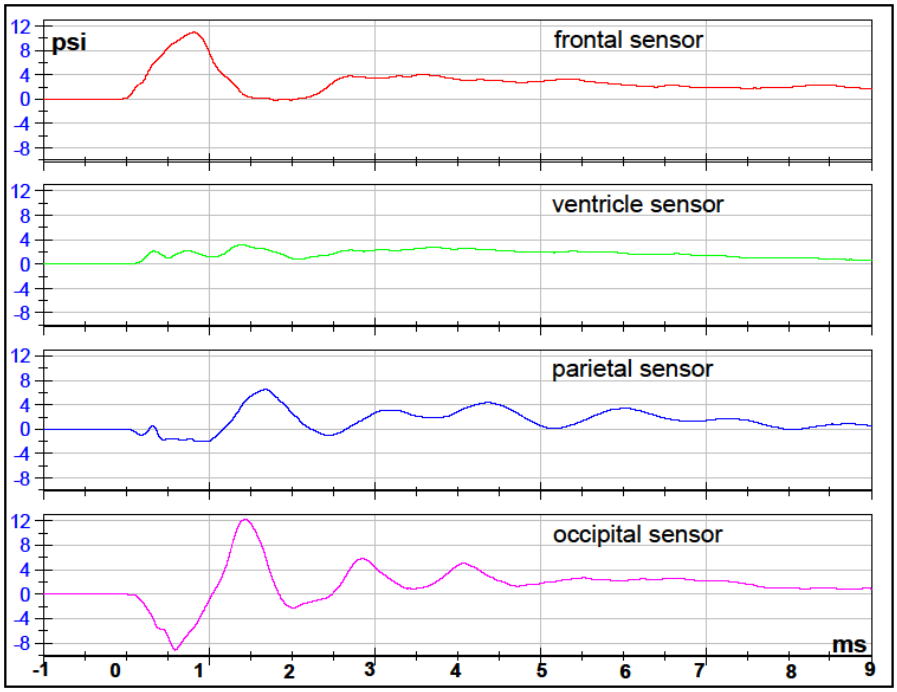

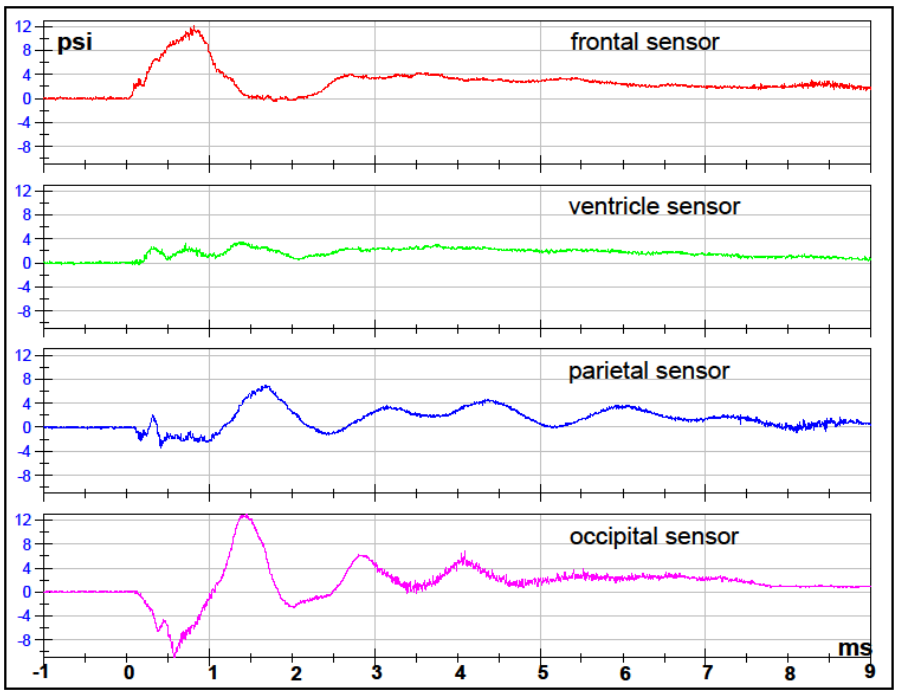

RAW DATA

Test 2 Left Orientation Cadaver-3

FILTERED DATA

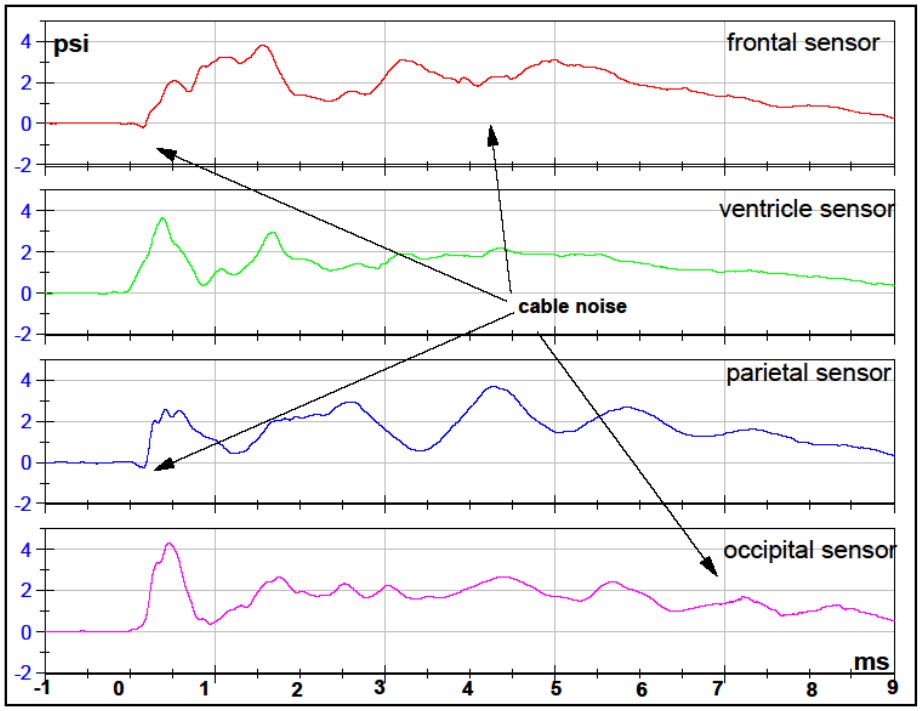

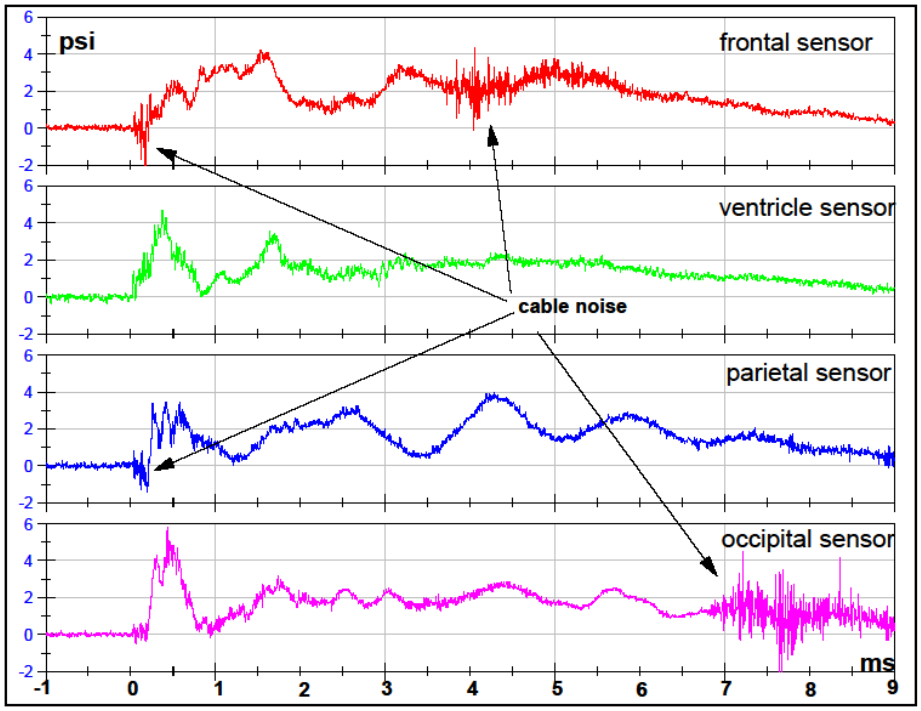

RAW DATA

Test 3 Back Orientation Cadaver-3

FILTERED DATA

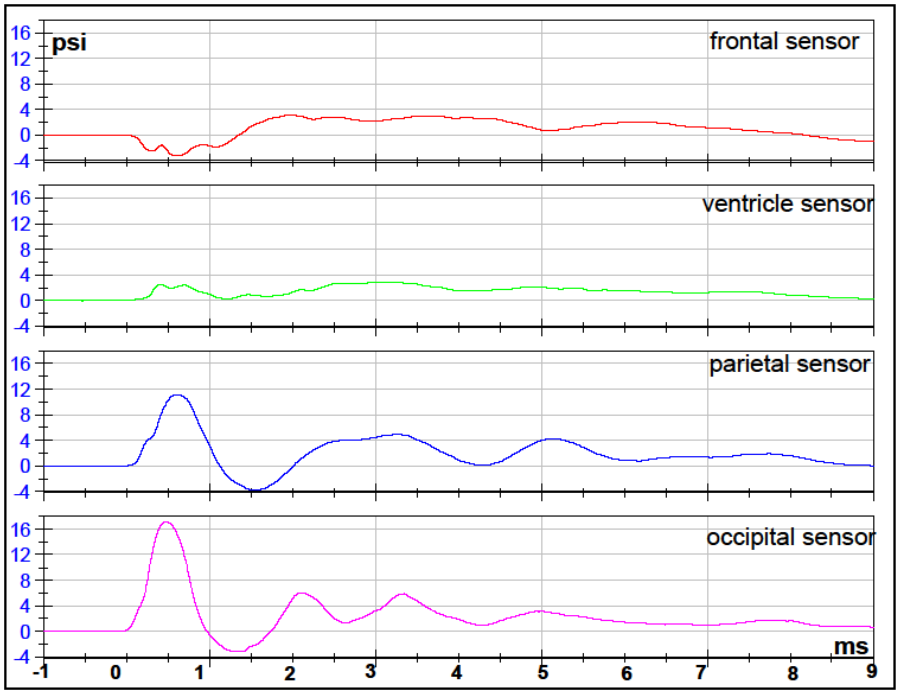

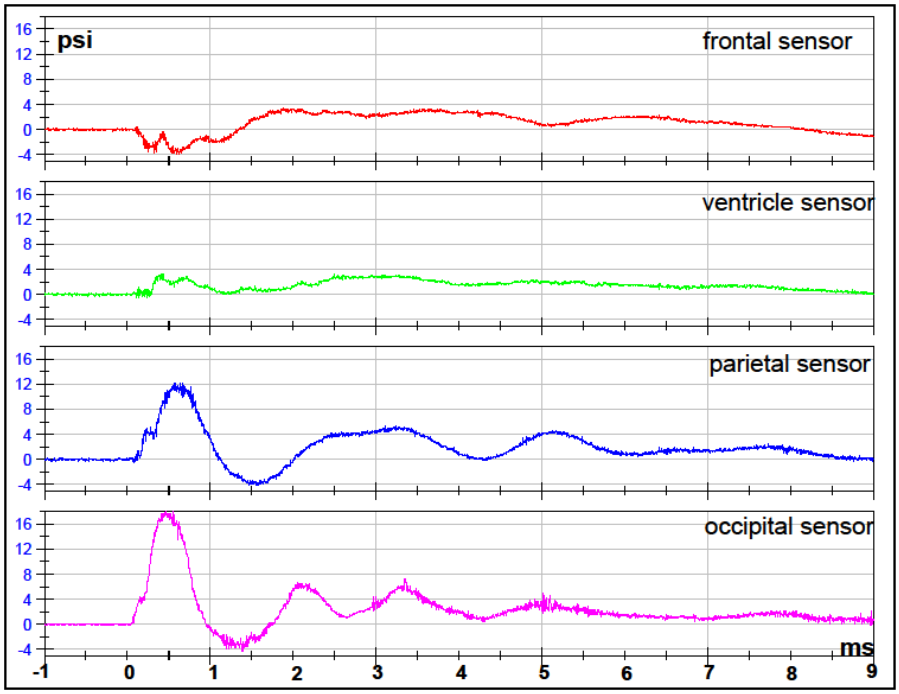

RAW DATA

Test 4 Right Orientation Cadaver-3

FILTERED DATA

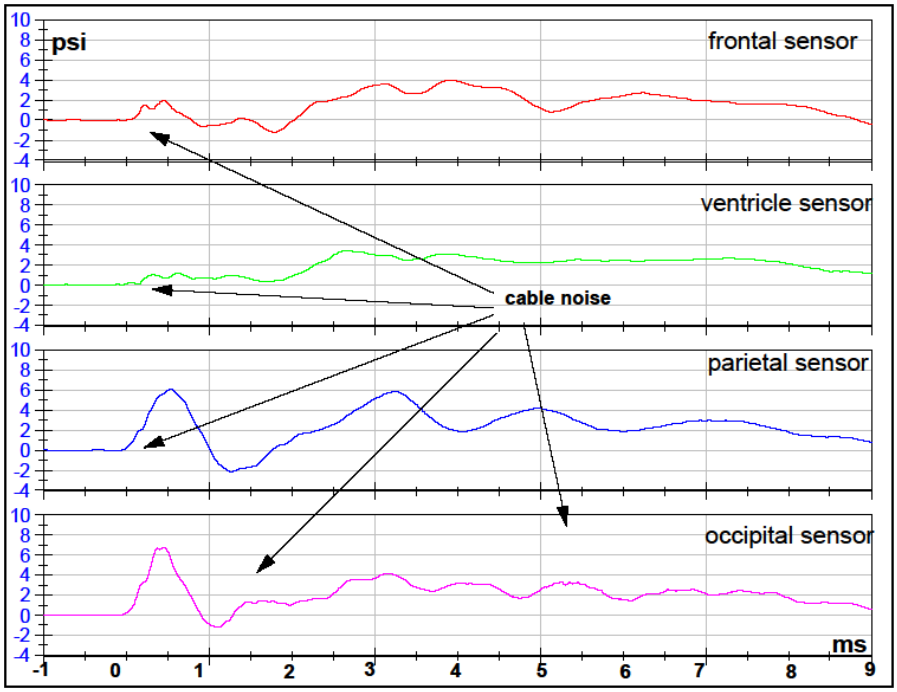

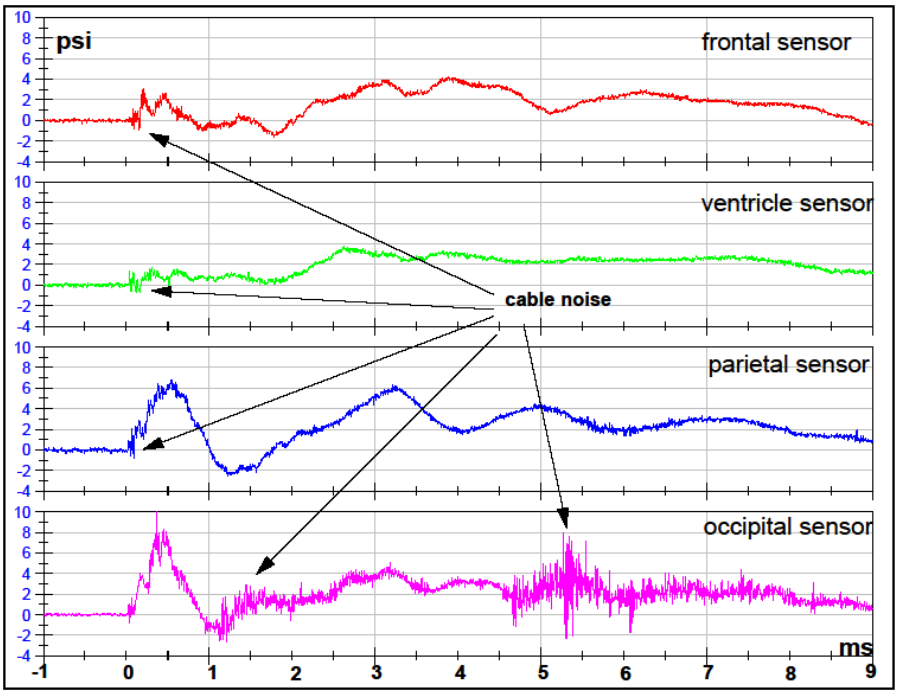

RAW DATA

Test 5 Front 2 Orientation Cadaver-3

FILTERED DATA

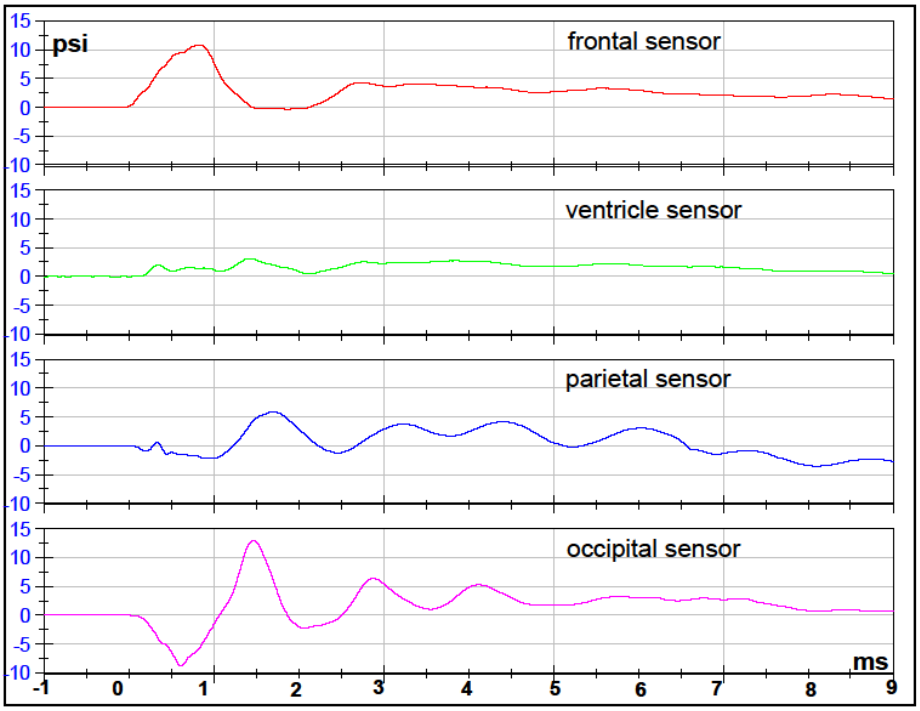

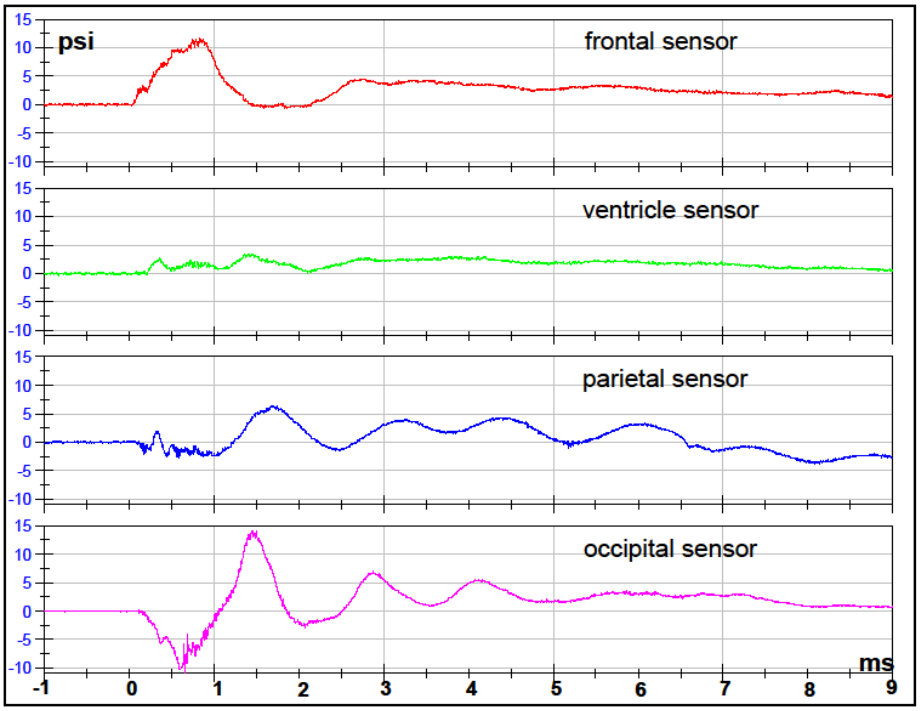

RAW DATA

Test 6 Front 1 Orientation Cadaver-3

FILTERED DATA

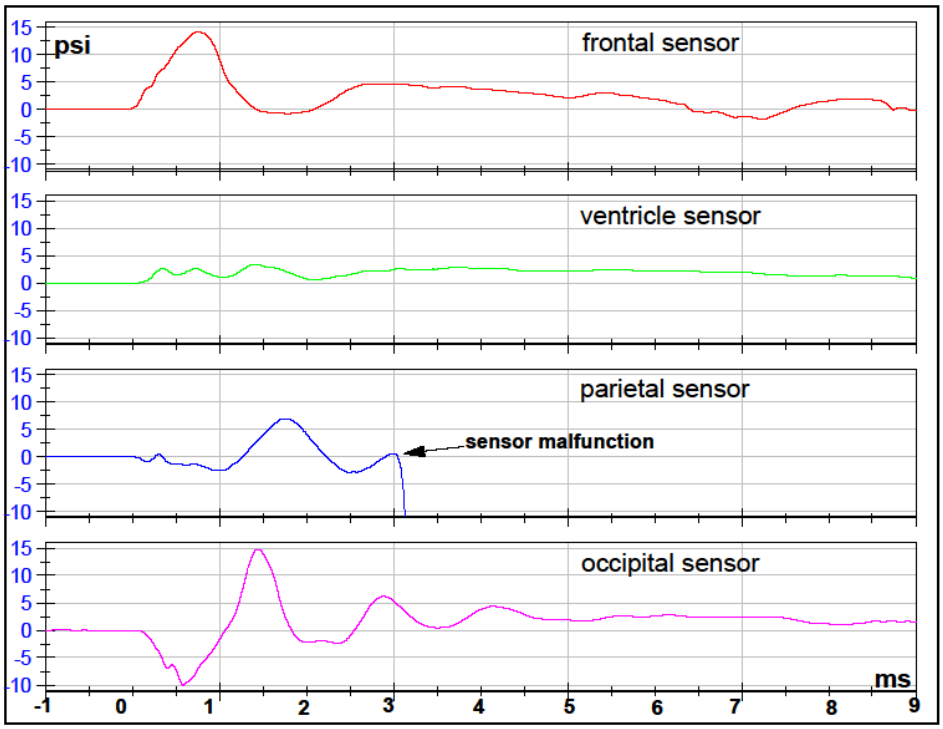

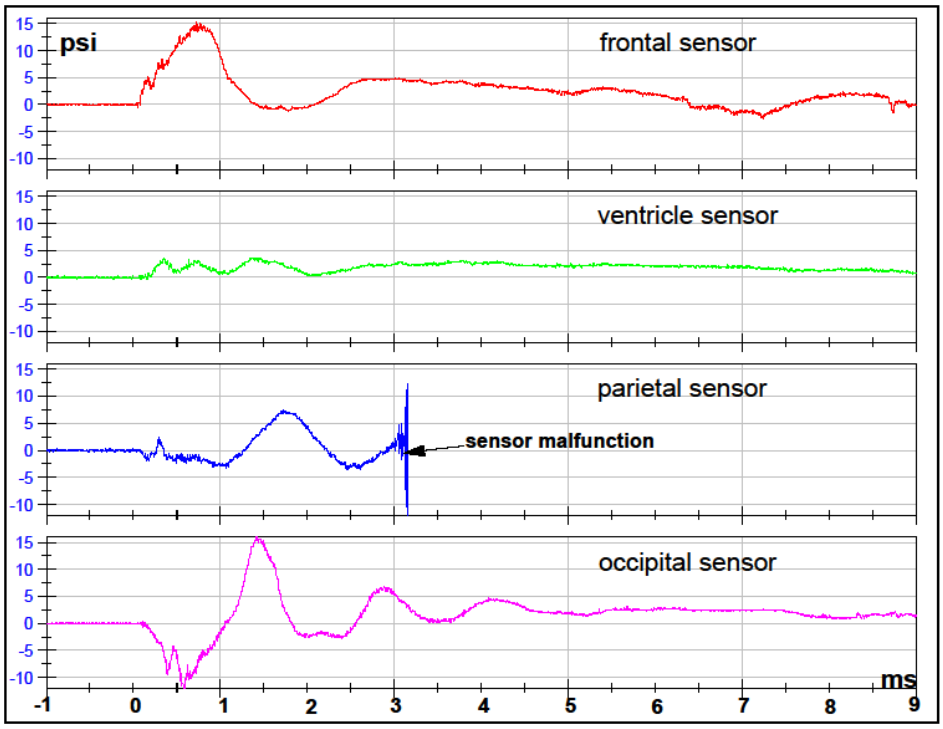

RAW DATA

Test 7 Left Orientation Cadaver-3

FILTERED DATA

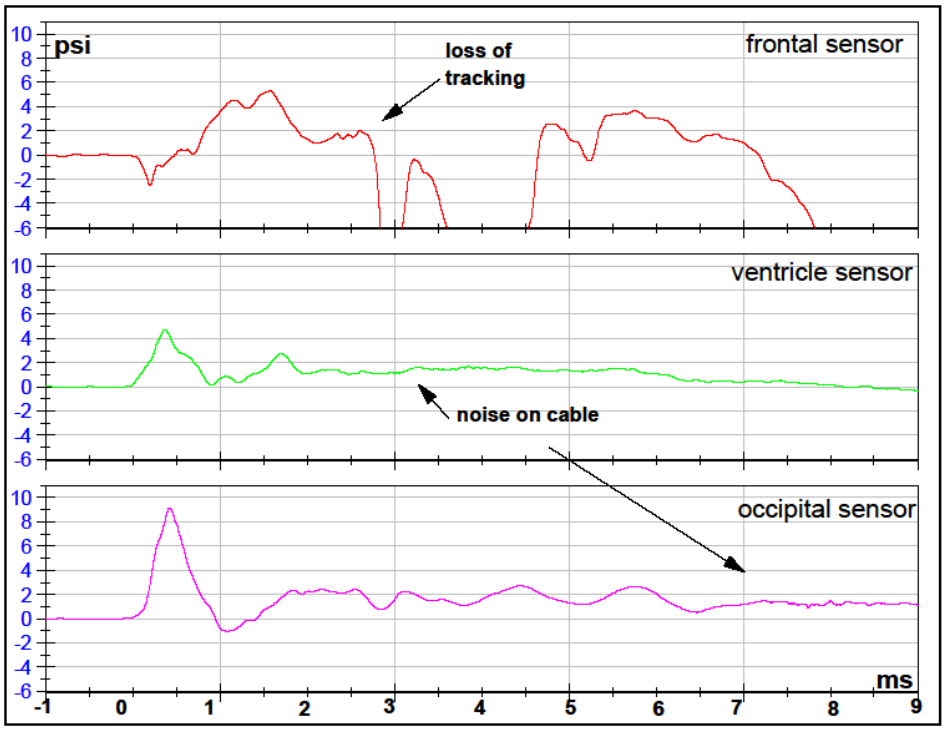

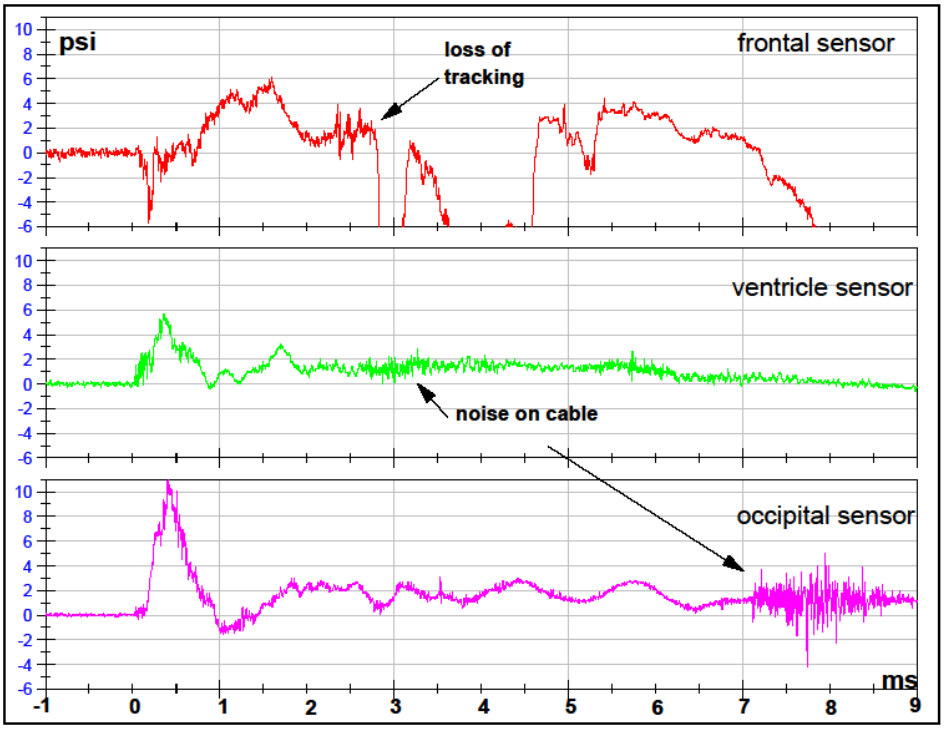

RAW DATA

Test 8 Back Orientation Cadaver-3

FILTERED DATA

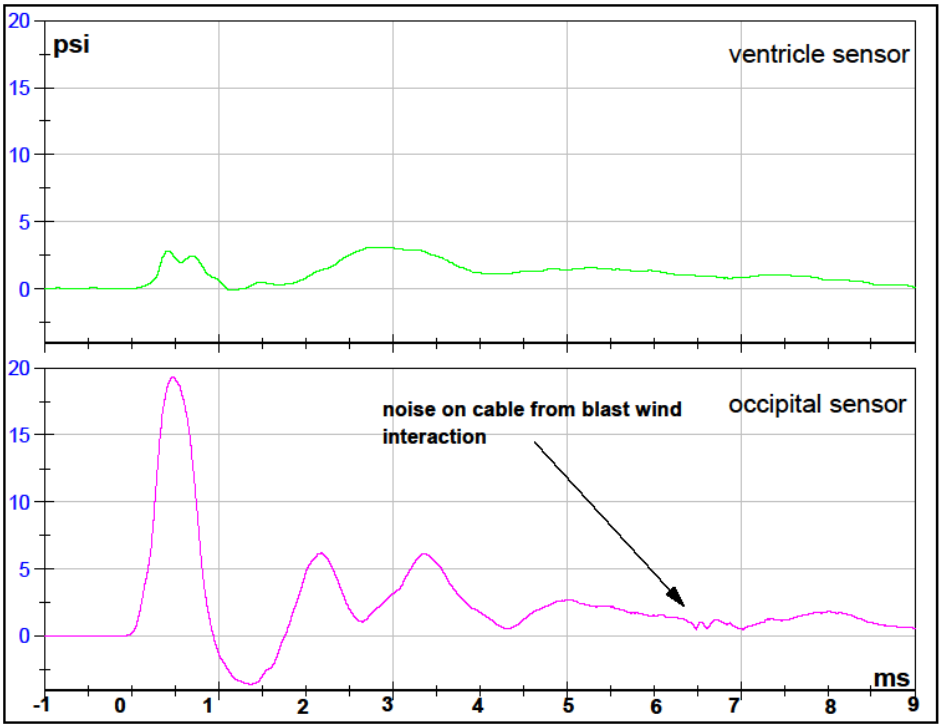

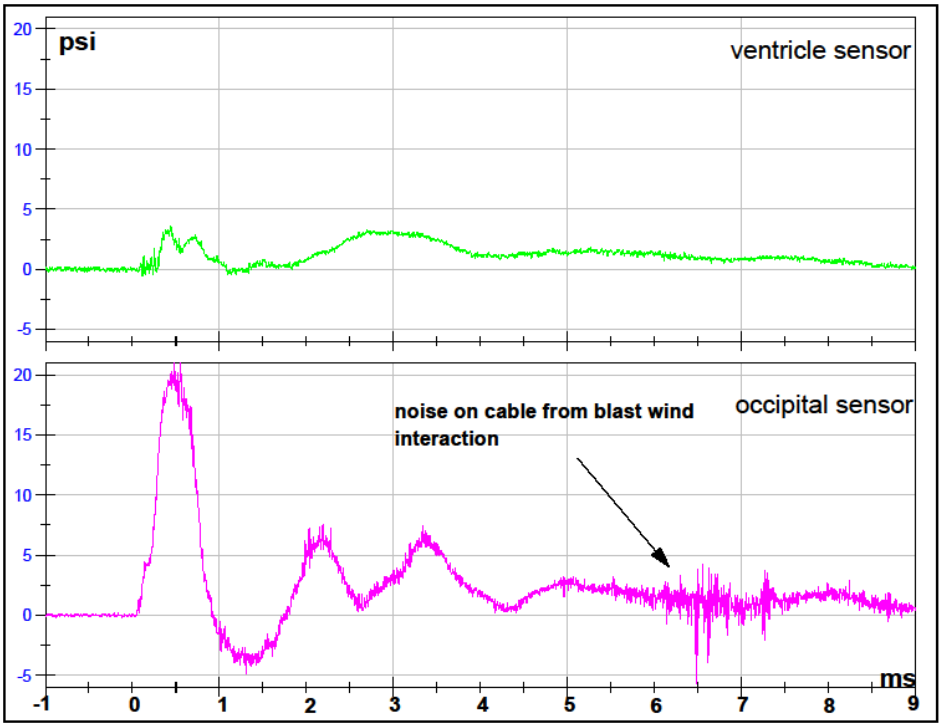

RAW DATA

Test 9 Right Orientation Cadaver-3

FILTERED DATA

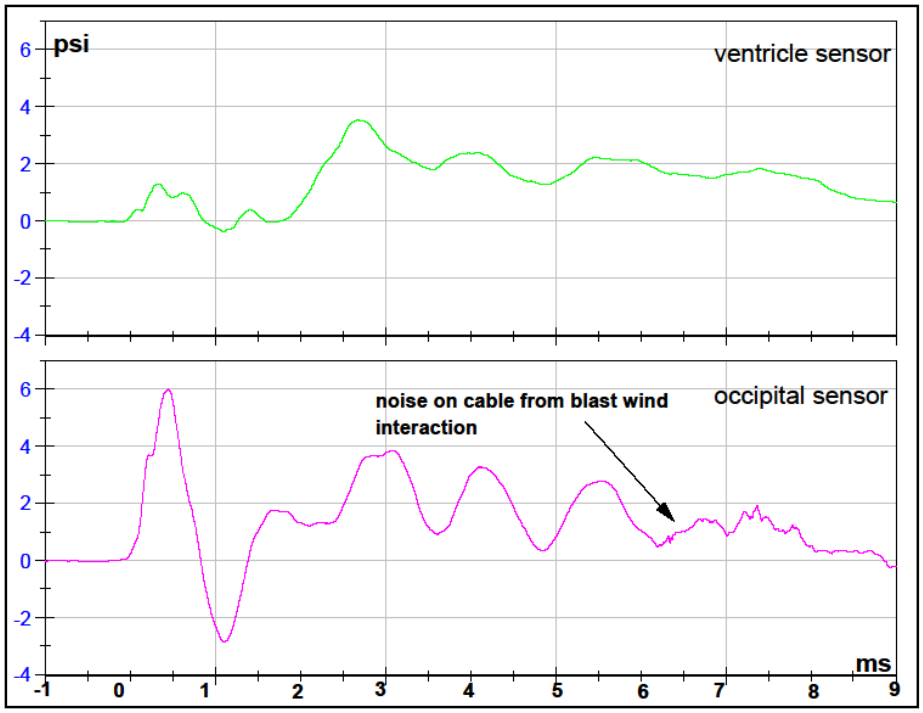

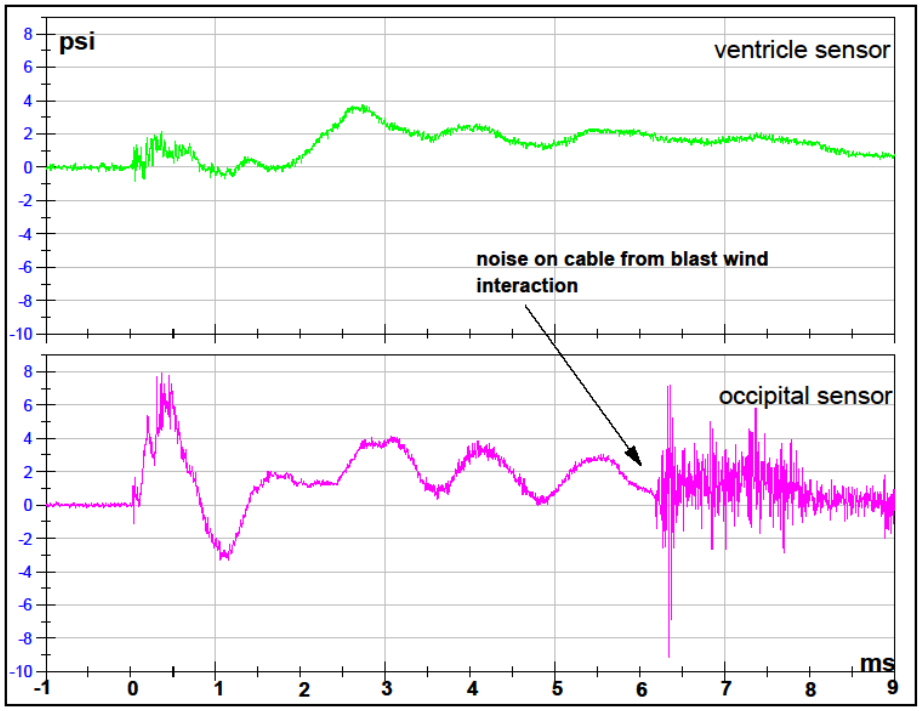

RAW DATA

Test 10 Front 2 Orientation Cadaver-3

FILTERED DATA

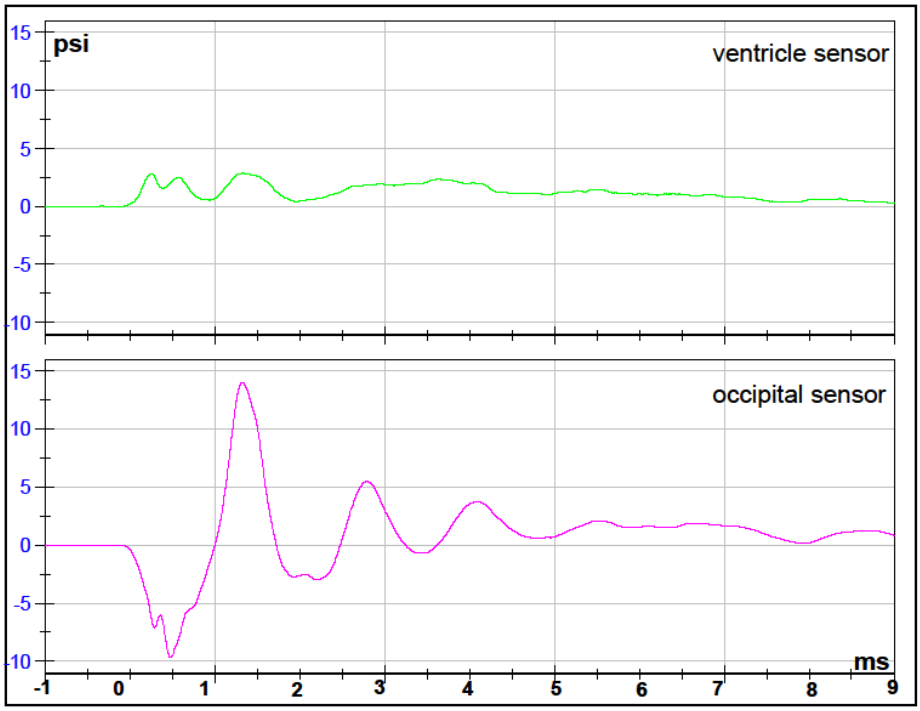

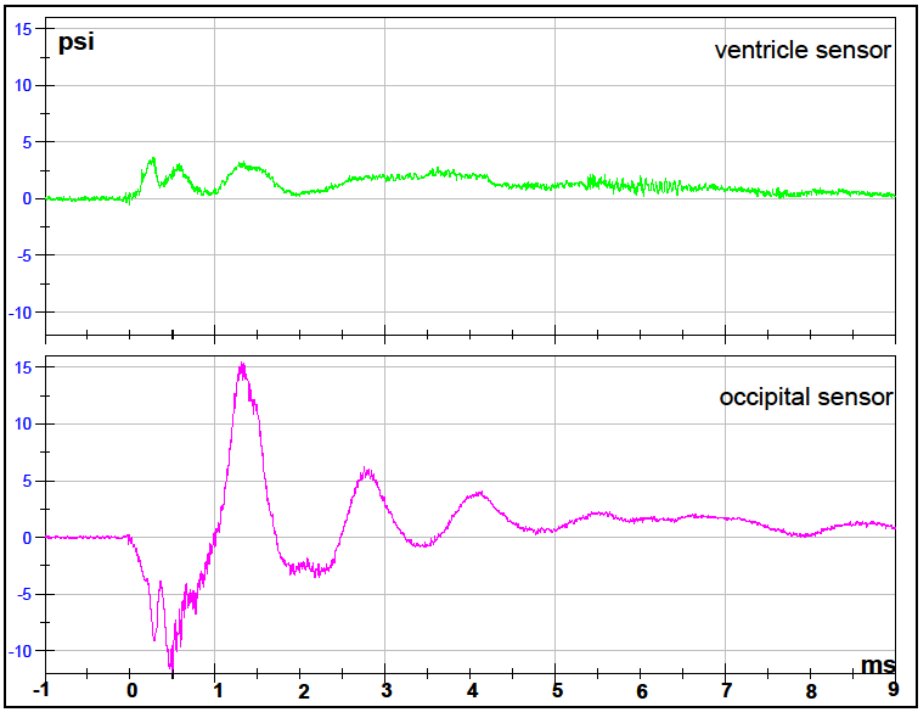

RAW DATA

Test 11 Front 1 Orientation Cadaver-3

FILTERED DATA

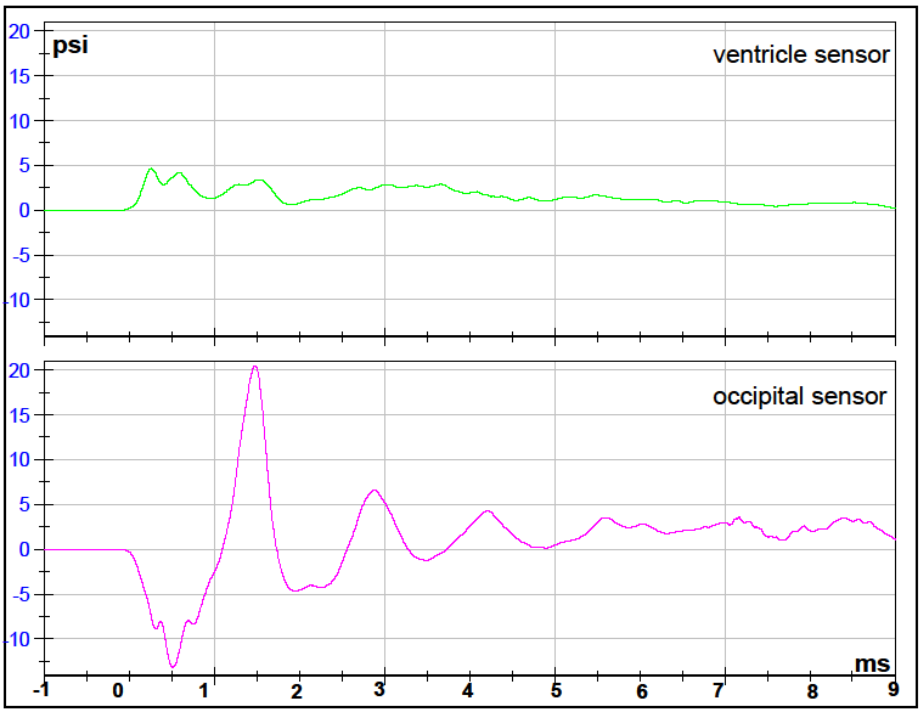

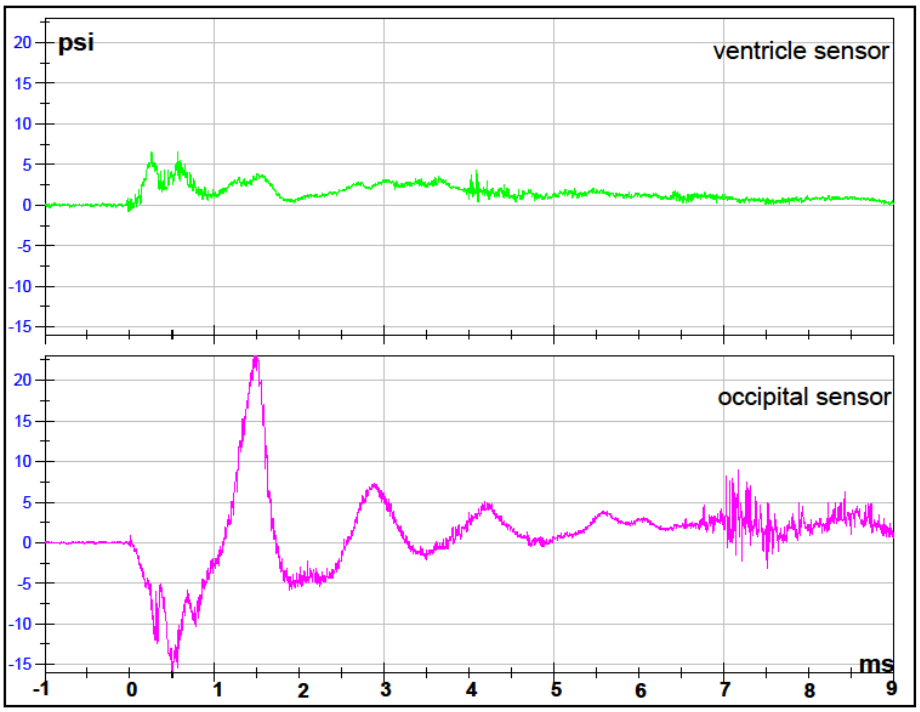

RAW DATA

Test 12 Left Orientation Cadaver-3

FILTERED DATA

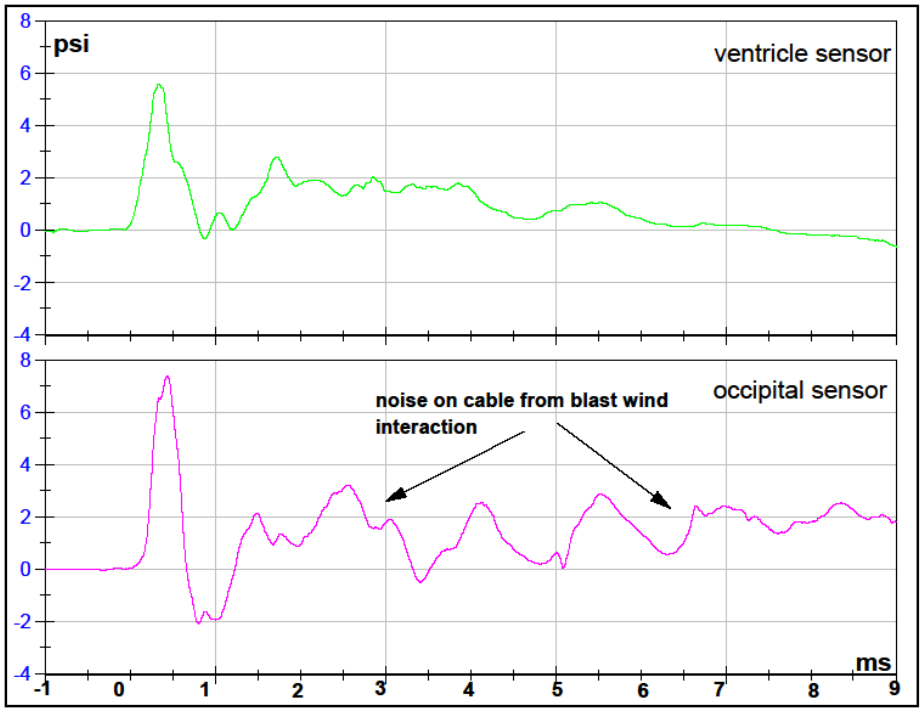

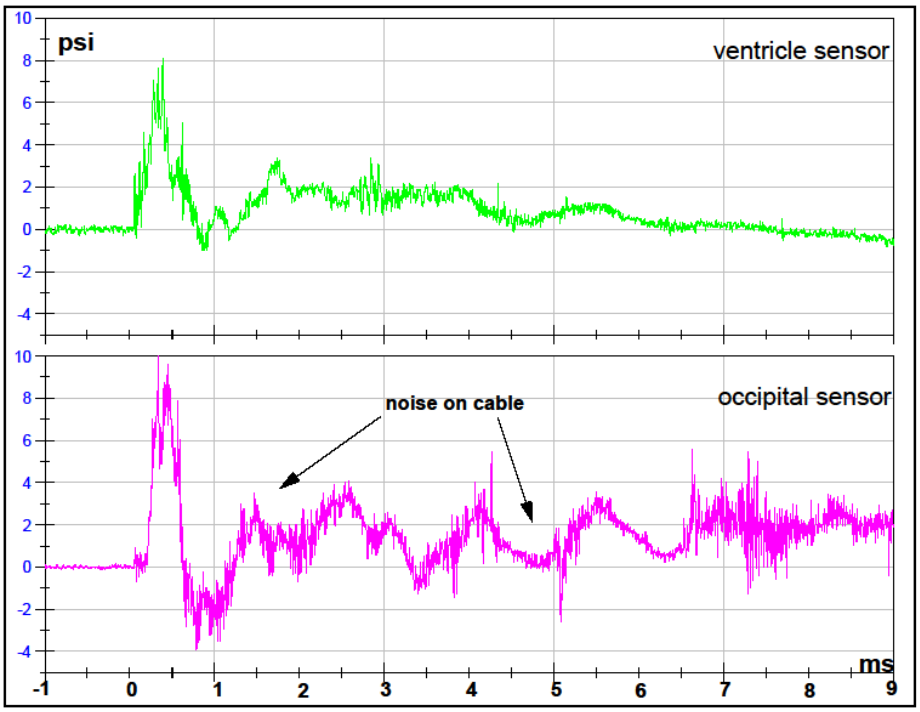

RAW DATA

Test 13 Back Orientation Cadaver-3

FILTERED DATA

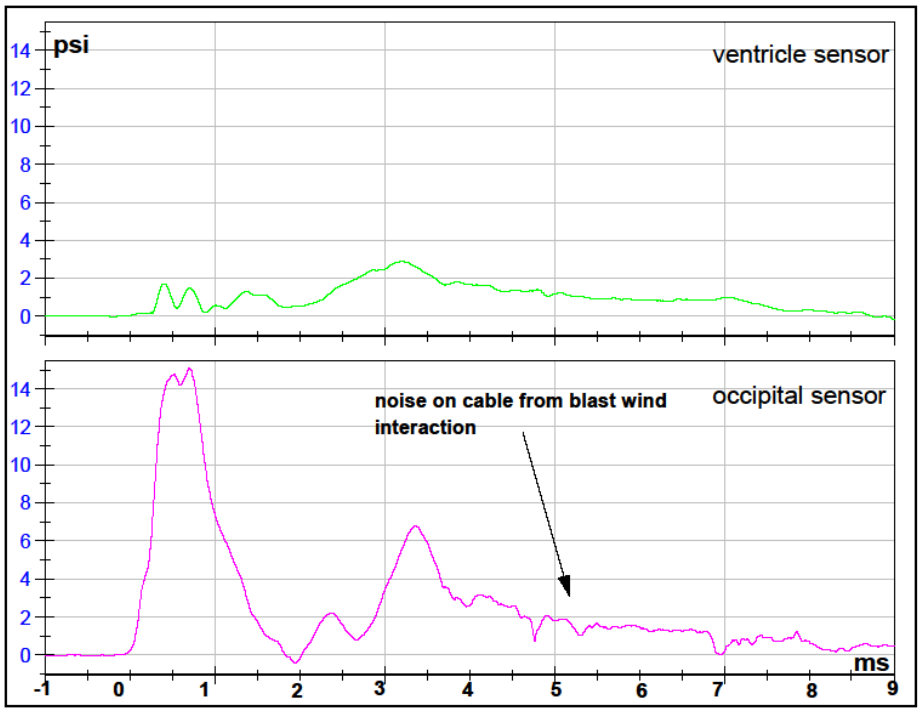

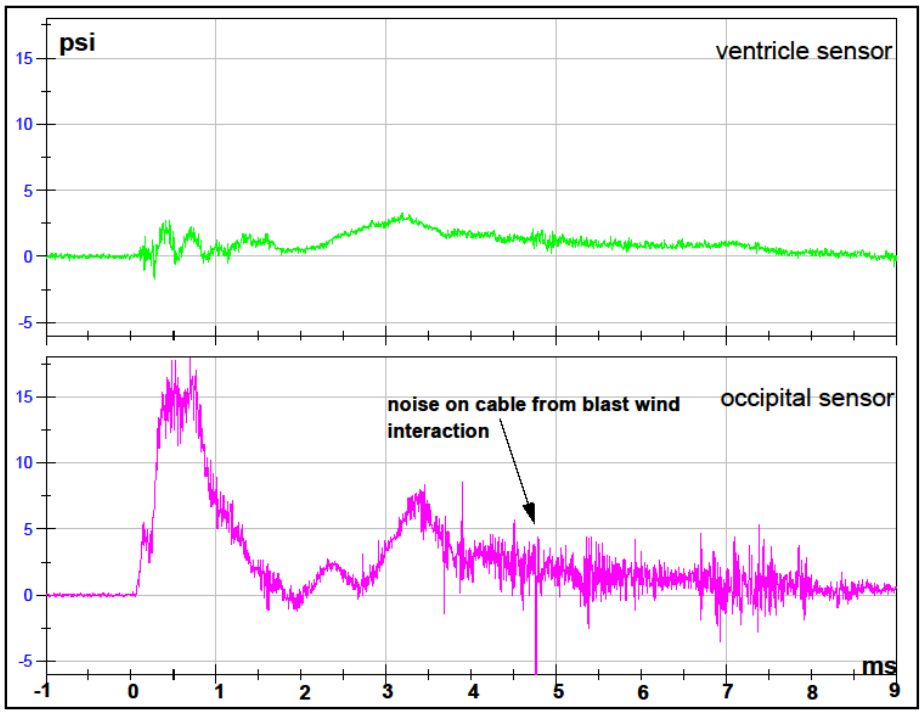

RAW DATA

Test 14 Right Orientation Cadaver-3

FILTERED DATA

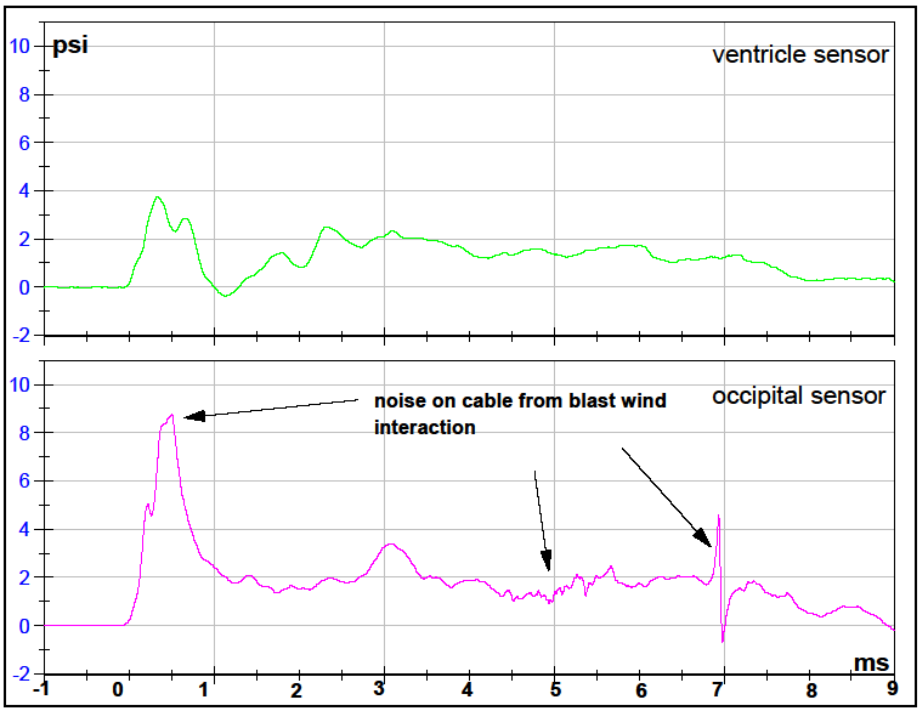

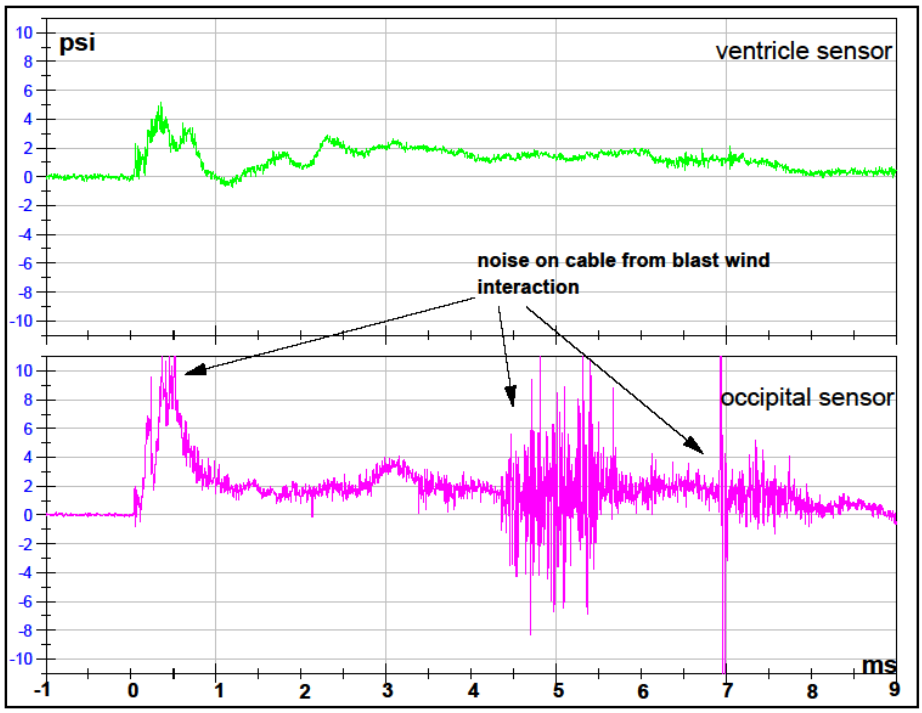

RAW DATA

Test 15 Front 2 Orientation Cadaver-3

FILTERED DATA

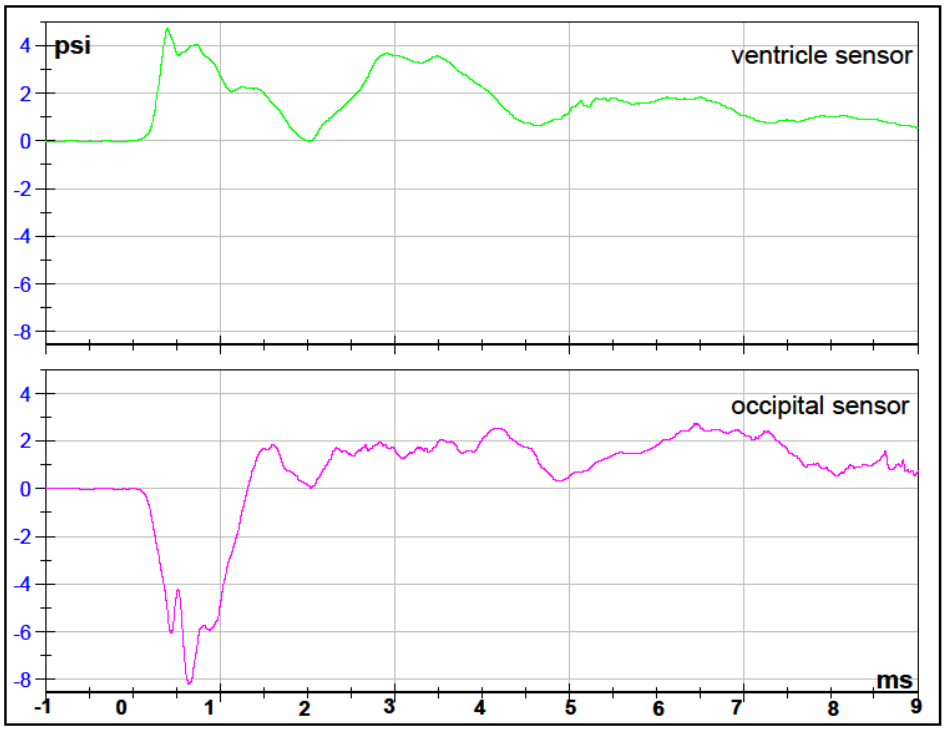

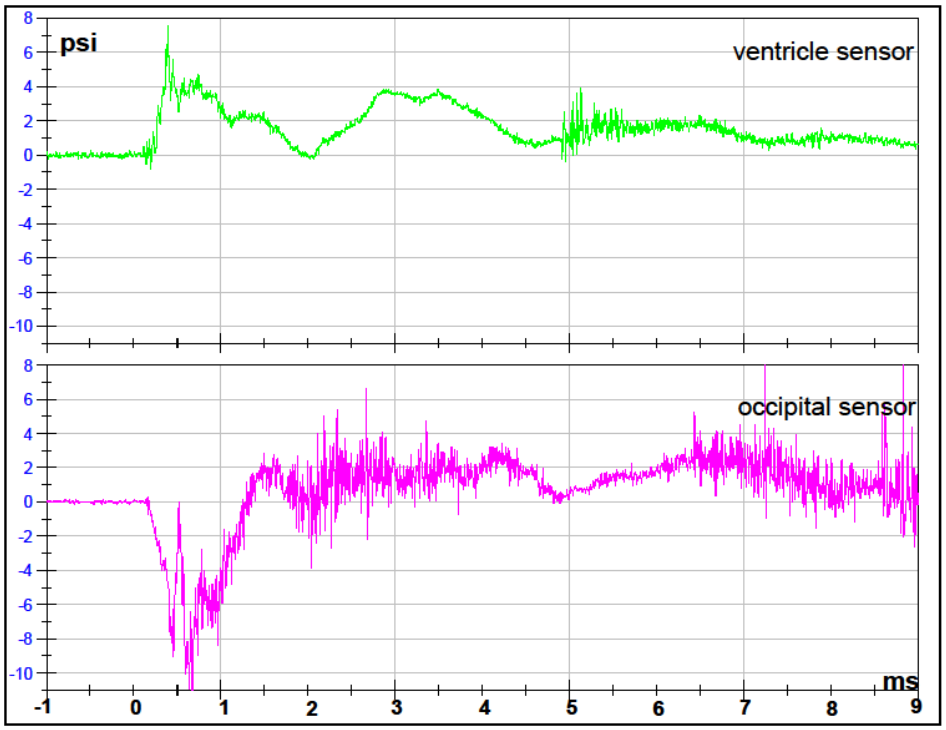

RAW DATA

Comparison for reproducibility of each pressure sensor in Front Orientations at 10psi Cadaver-3

VENTRICLE FILTERED DATA

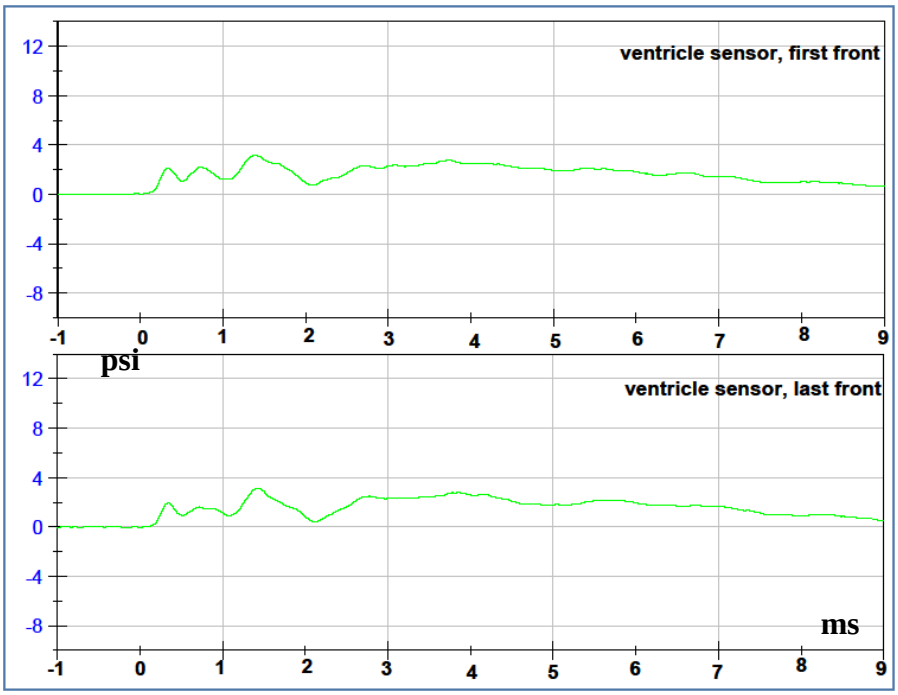

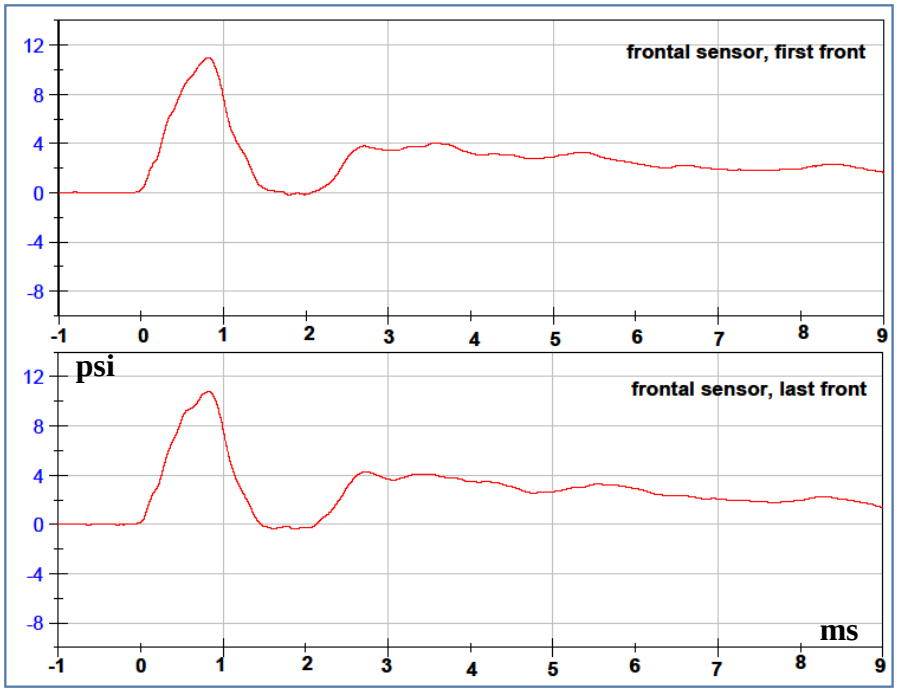

FRONTAL FILTERED DATA

Comparison for reproducibility of each pressure sensor in Front Orientations at 10psi Cadaver-3

PARIETAL FILTERED DATA

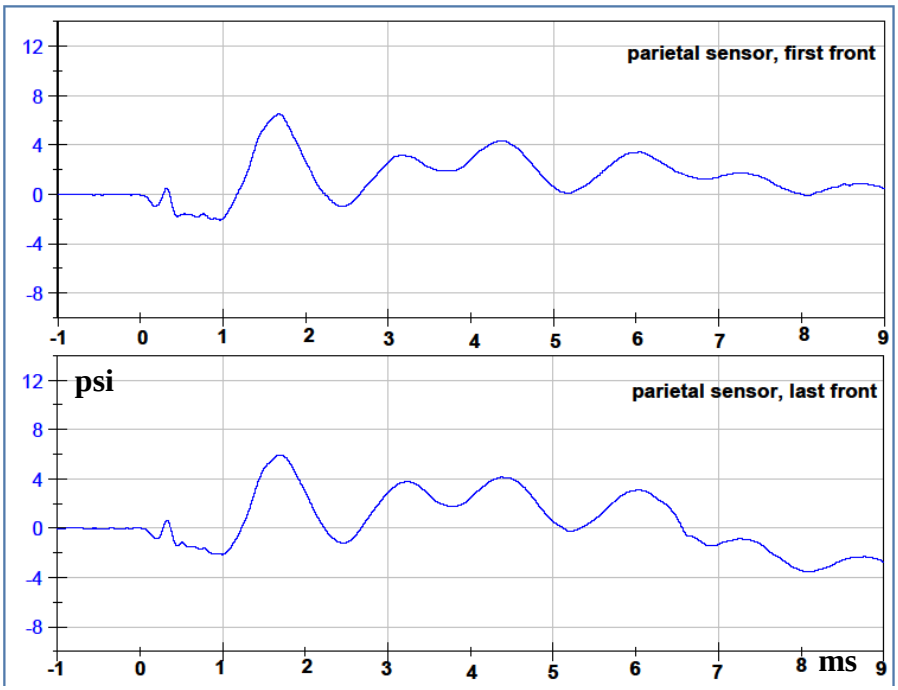

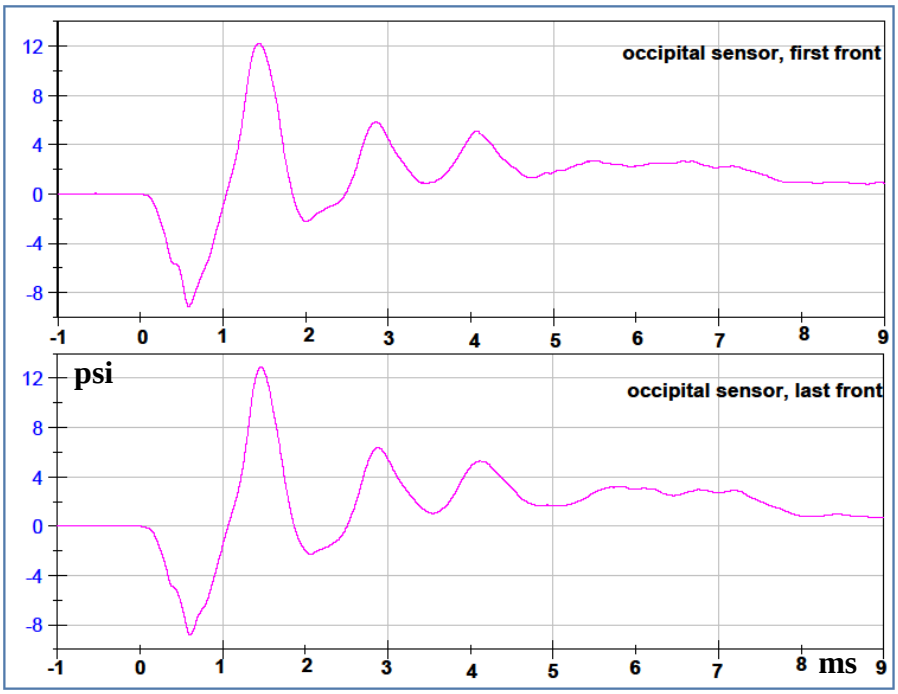

OCCIPITAL FILTERED DATA

Comparison for reproducibility of each pressure sensor in Front Orientations at 12psi Cadaver-3

VENTRICLE FILTERED DATA

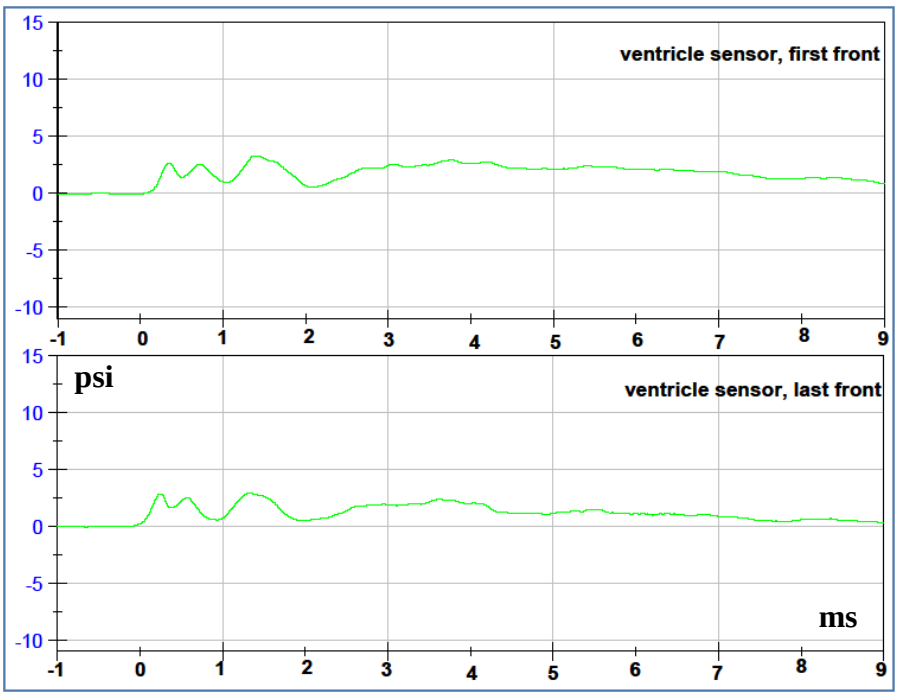

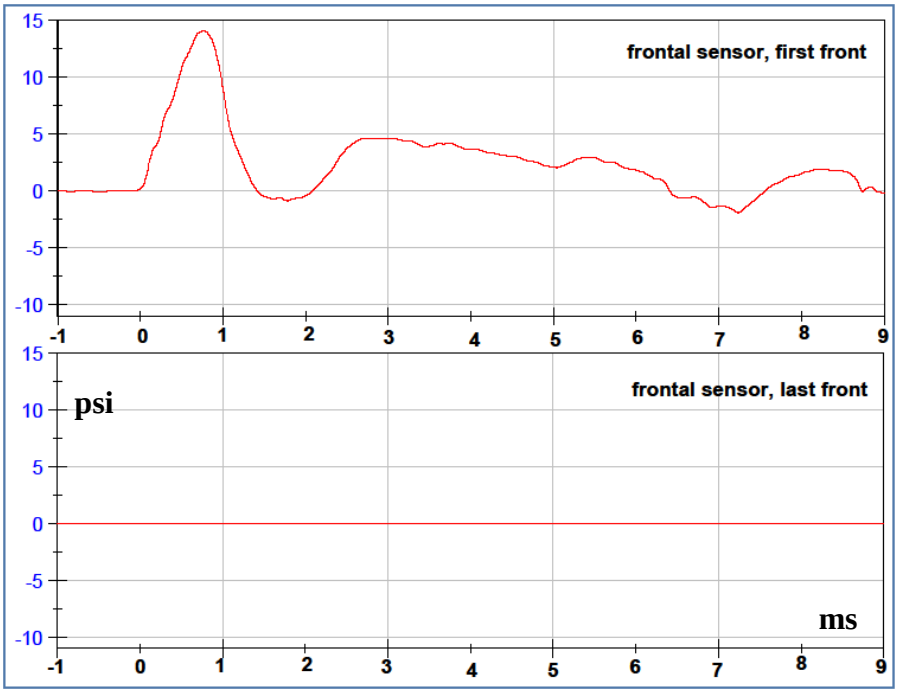

FRONTAL FILTERED DATA

Comparison for reproducibility of each pressure sensor in Front Orientations at 12psi Cadaver-3

PARIETAL FILTERED DATA

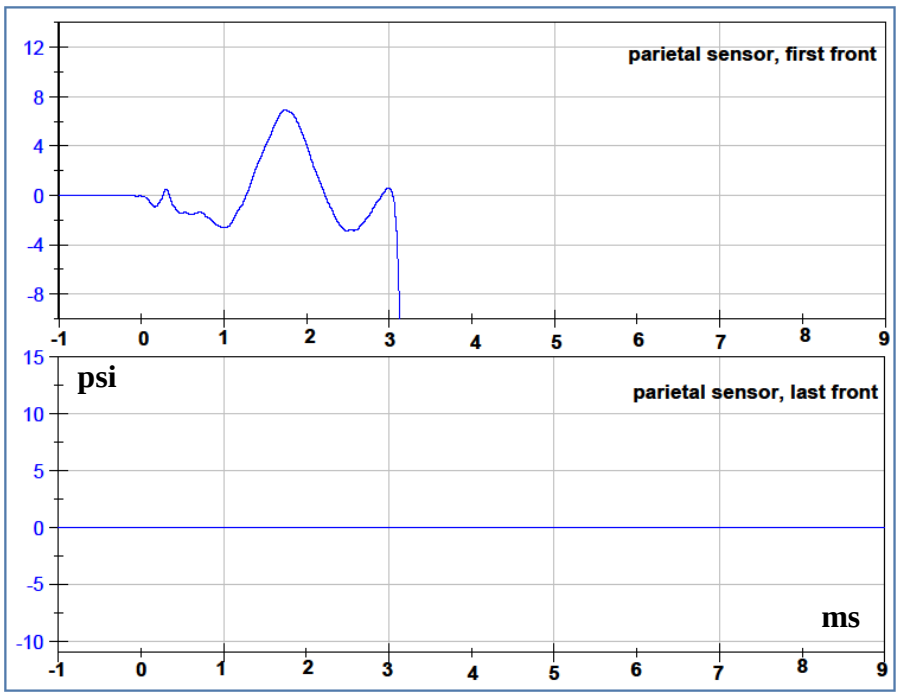

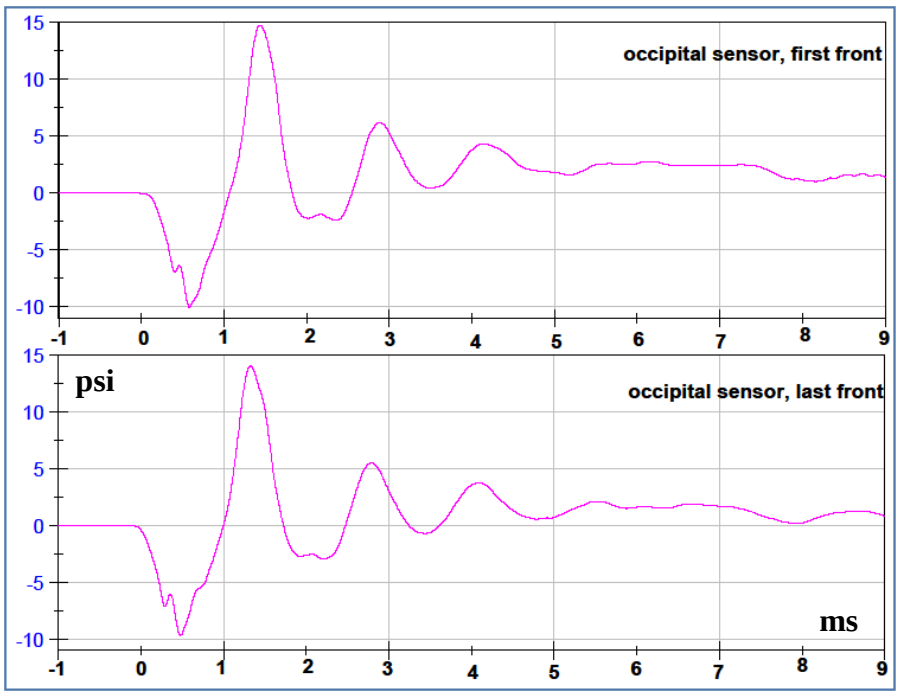

OCCIPITAL FILTERED DATA

Comparison for reproducibility of each pressure sensor in Front Orientations at 15psi Cadaver-3

VENTRICLE FILTERED DATA

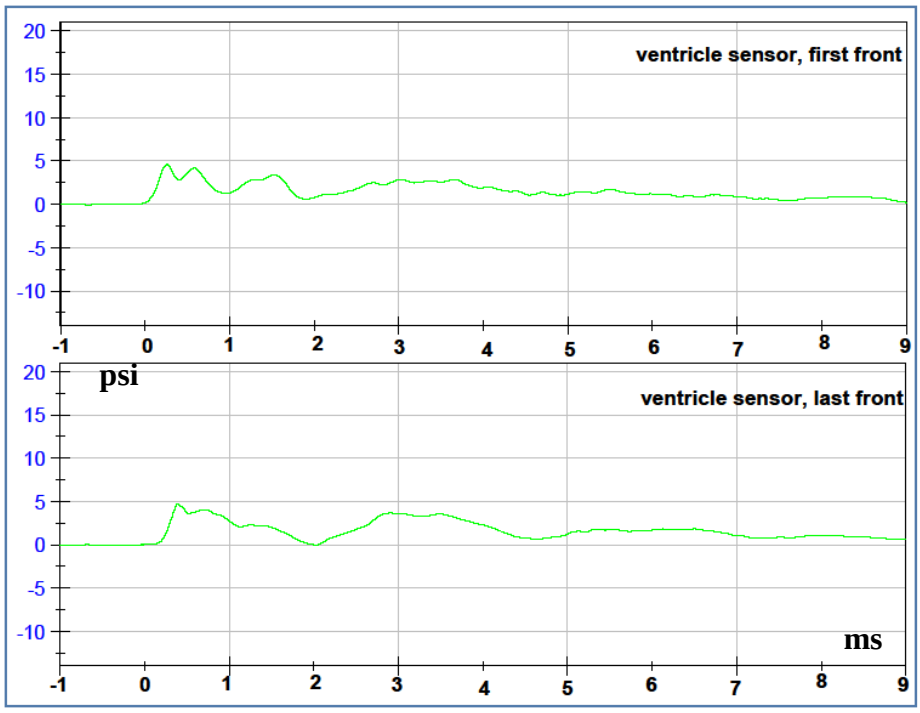

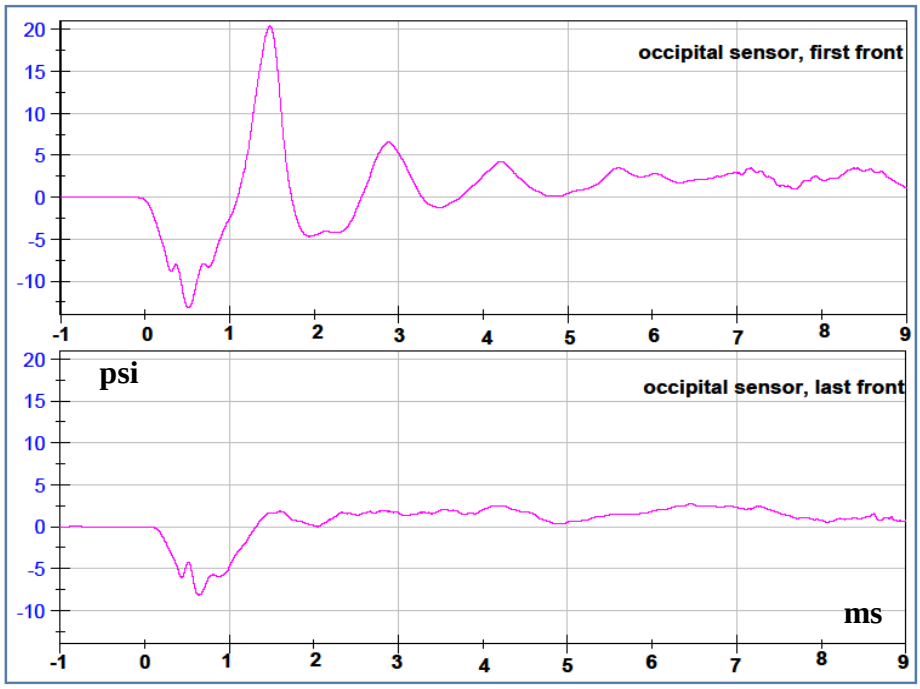

PARIETAL FILTERED DATA

Pressure Extremes for cadaver-3.

The ventricle values are highlighted because the sensor was placed at a different location: 10mm from midline and 20mm toward the back from the previous ventricle sensor.

Pressure Extremes for cadaver-3 (psi)										
	Maximun Pressure					Minimum Pressure				
ventricle	front 1	right	back	left	front 2	front 1	right	back	left	front 2
10 psi air	**3.16**	**3.44**	**2.87**	**3.65**	**3.12**	**0.0352**	**0.222**	**0.203**	**0.2**	**0.0715**
12 psi air	**3.32**	**3.51**	**3.06**	**4.71**	**2.87**	**0.0185**	**-0.364**	**-0.0894**	**0.2**	**0.2**
15 psi air	**4.61**	**3.74**	**2.9**	**5.51**	**4.73**	**0.2**	**-0.376**	**0.287**	**-0.35**	**-0.006**
frontal	front 1	right	back	left	front 2	front 1	right	back	left	front 2
10 psi air	**10.97**	**3.98**	**3.06**	**3.75**	**10.79**	**-0.183**	**-1.22**	**-3.28**	**0.228**	**-0.366**
12 psi air	**14.09**	**NA**	**NA**	**5.26**	**NA**	**-1.84**	**NA**	**NA**	**-2.45**	**NA**
15 psi air	**NA**	**NA**	**NA**	**NA**	**NA**	**NA**	**NA**	**NA**	**NA**	**NA**
parietal	front 1	right	back	left	front 2	front 1	right	back	left	front 2
10 psi air	**6.51**	**6.07**	**11.13**	**3.68**	**5.96**	**-2.05**	**-2.13**	**-3.72**	**-0.208**	**-2.11**
12 psi air	**6.91**	**NA**	**NA**	**NA**	**NA**	**-2.88**	**NA**	**NA**	**NA**	**NA**
15 psi air	**NA**	**NA**	**NA**	**NA**	**NA**	**NA**	**NA**	**NA**	**NA**	**NA**
occipital	front 1	right	back	left	front 2	front 1	right	back	left	front 2
10 psi air	**12.21**	**6.78**	**17.14**	**4.32**	**12.9**	**-9.16**	**-1.20**	**-3.14**	**0.207**	**-8.81**
12 psi air	**14.76**	**5.96**	**19.3**	**9.13**	**13.98**	**-9.92**	**-2.84**	**-3.57**	**-0.996**	**-9.61**
15 psi air	**20.44**	**8.75**	**15.09**	**7.39**	**2.72**	**-13.12**	**0.2**	**-0.431**	**-2.08**	**-8.13**

Pressure differentials for cadaver-3.

The ventricle values are highlighted because the sensor was placed at a different location: 10mm from midline and 20mm toward the back from the previous ventricle sensor.

Differential for cadaver-3										
	peak differential pressure (psi)					time elapsed between peaks (ms)				
ventricle	front 1	right	back	left	front 2	front 1	right	back	left	front 2
10 psi air	**3.12**	**3.21**	**2.67**	**3.45**	**3.05**	**1.39**	**2.48**	**3.11**	**0.38**	**1.3**
12 psi air	**3.3**	**3.88**	**3.14**	**4.49**	**2.66**	**1.36**	**1.6**	**1.62**	**0.368**	**1.33**
15 psi air	**4.31**	**4.11**	**2.62**	**5.86**	**4.72**	**0.244**	**0.808**	**2.91**	**0.54**	**1.63**
frontal	front 1	right	back	left	front 2	front 1	right	back	left	front 2
10 psi air	**11.16**	**5.19**	**6.34**	**3.52**	**11.16**	**0.976**	**2.12**	**1.33**	**1.35**	**1.03**
12 psi air	**15.93**	**NA**	**NA**	**7.72**	**NA**	**6.5**	**NA**	**NA**	**1.37**	**NA**
15 psi air	**NA**	**NA**	**NA**	**NA**	**NA**	**NA**	**NA**	**NA**	**NA**	**NA**
parietal	front 1	right	back	left	front 2	front 1	right	back	left	front 2
10 psi air	**8.56**	**8.2**	**14.85**	**3.88**	**8.07**	**0.732**	**0.748**	**0.952**	**4.096**	**0.696**
12 psi air	**9.79**	**NA**	**NA**	**NA**	**NA**	**0.74**	**NA**	**NA**	**NA**	**NA**
15 psi air	**NA**	**NA**	**NA**	**NA**	**NA**	**NA**	**NA**	**NA**	**NA**	**NA**
occipital	front 1	right	back	left	front 2	front 1	right	back	left	front 2
10 psi air	**21.36**	**7.98**	**20.28**	**4.12**	**21.71**	**0.852**	**0.67**	**0.844**	**0.356**	**0.844**
12 psi air	**24.68**	**8.81**	**22.87**	**10.13**	**23.59**	**0.836**	**0.668**	**0.852**	**0.704**	**0.86**
15 psi air	**33.56**	**8.61**	**15.52**	**9.47**	**10.85**	**0.968**	**0.52**	**1.25**	**0.372**	**5.82**

Percentage of change for maximum, minimum and differential pressure for cadaver-3.

The increase of pressure measured by the sensors is compared with the increase in the blast intensity (overpressure). The 10psi test was used as reference.

PERCENTAGES for CADAVER-3						
	AIR	Percentage Increase in Maximun Peak Pressure				
	Overpressure	front 1	right	back	left	front 2
ventricle	20%	5	2	7	29	-8
ventricle	50%	46	9	1	51	52
frontal	20%	28	NA	NA	40	NA
frontal	50%	NA	NA	NA	NA	NA
parietal	20%	6	NA	NA	NA	NA
parietal	50%	NA	NA	NA	NA	NA
occipital	20%	21	-12	13	111	8
occipital	50%	67	29	-12	71	-79
	AIR	Percentage Increase in Minimum Peak Pressure				
	Overpressure	front 1	right	back	left	front 2
ventricle	20%	-47	-264	-144	0	180
ventricle	50%	468	-269	41	-275	-108
frontal	20%	905	NA	NA	-1175	NA
frontal	50%	NA	NA	NA	NA	NA
parietal	20%	40	NA	NA	NA	NA
parietal	50%	NA	NA	NA	NA	NA
occipital	20%	8	137	14	-581	9
occipital	50%	43	-117	-86	-1105	-8
	AIR	Percentage Increase in Pressure Differential				
	Overpressure	front 1	right	back	left	front 2
ventricle	20%	6	21	18	30	-13
ventricle	50%	38	28	-2	70	55
frontal	20%	43	NA	NA	119	NA
frontal	50%	NA	NA	NA	NA	NA
parietal	20%	14	NA	NA	NA	NA
parietal	50%	NA	NA	NA	NA	NA
occipital	20%	16	10	13	146	9
occipital	50%	57	8	-23	130	-50

Percentage of change for 1st rate for cadaver-3

	AIR	Percentage 1st Rate Pressure Change				
	Overpressure	front 1	right	back	left	front 2
ventricle	20%	11	-33	10	34	15
ventricle	50%	74	122	28	76	29
frontal	20%	41	NA	NA	-392	NA
frontal	50%	NA	NA	NA	NA	NA
parietal	20%	5	NA	NA	NA	NA
parietal	50%	NA	NA	NA	NA	NA
occipital	20%	8	-23	14	99	11
occipital	50%	32	-1	-21	79	12

Pressure rate of change for cadaver-3.

	1st rate (psi/ms)				
ventricle	front 1	right	back	left	front 2
10 psi air	10.14	5.06	8.28	9.1	9.4
12 psi air	11.24	3.4	9.11	12.19	10.8
15 psi air	17.65	11.22	10.59	16	12.09
frontal	front 1	right	back	left	front 2
10 psi air	13	10.01	-10.83	5.65	12.55
12 psi air	18.35	NA	NA	-16.47	NA
15 psi air	NA	NA	NA	NA	NA
parietal	front 1	right	back	left	front 2
10 psi air	-7.5	11.01	20.67	11.06	-2.09
12 psi air	-7.91	NA	NA	NA	NA
15 psi air	NA	NA	NA	NA	NA
occipital	front 1	right	back	left	front 2
10 psi air	-18.5	17.15	35.86	11.56	-17.08
12 psi air	-19.94	13.2	40.8	23.01	-18.94
15 psi air	-24.45	16.92	28.2	20.64	-19.2

Strain gages status during testing of cadaver-3.

Rosettes were used to measure strain; therefore for complete data, three grids needed to be working.

Strain gages status for cadaver-3					
10psi	front 1	right	back	left	front 2
Frontal S.G.	3	3	3	3	3
Zygomatic S.G.	3	3	3	3	3
Temporal S.G.	3	3	2	2	1
Parietal S.G.	2	2	3	3	3
Occipital S.G.	2	2	2	2	2
12psi	front 1	right	back	left	front 2
Frontal S.G.	3	3	3	3	3
Zygomatic S.G.	3	3	3	3	3
Temporal S.G.	1	1	1	1	1
Parietal S.G.	3	3	2	2	2
Occipital S.G.	2	2	1	1	1
15psi	front 1	right	back	left	front 2
Frontal S.G.	3	3	3	3	3
Zygomatic S.G.	3	3	3	3	3
Temporal S.G.	1	1	1	1	1
Parietal S.G.	2	3	2	2	3
Occipital S.G.	1	1	1	1	1

0	0 grids working
1	1 grid working
2	2 grids working
3	3 grids working

CADAVER 4 DATA

Test 1 Front 1 Orientation Cadaver-4

FILTERED DATA

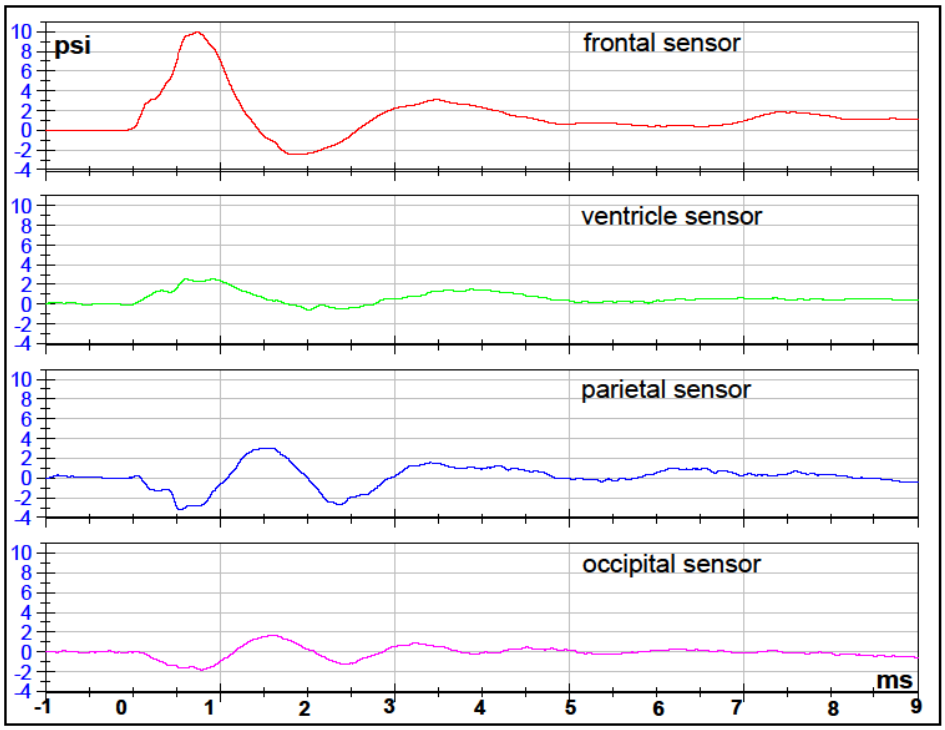

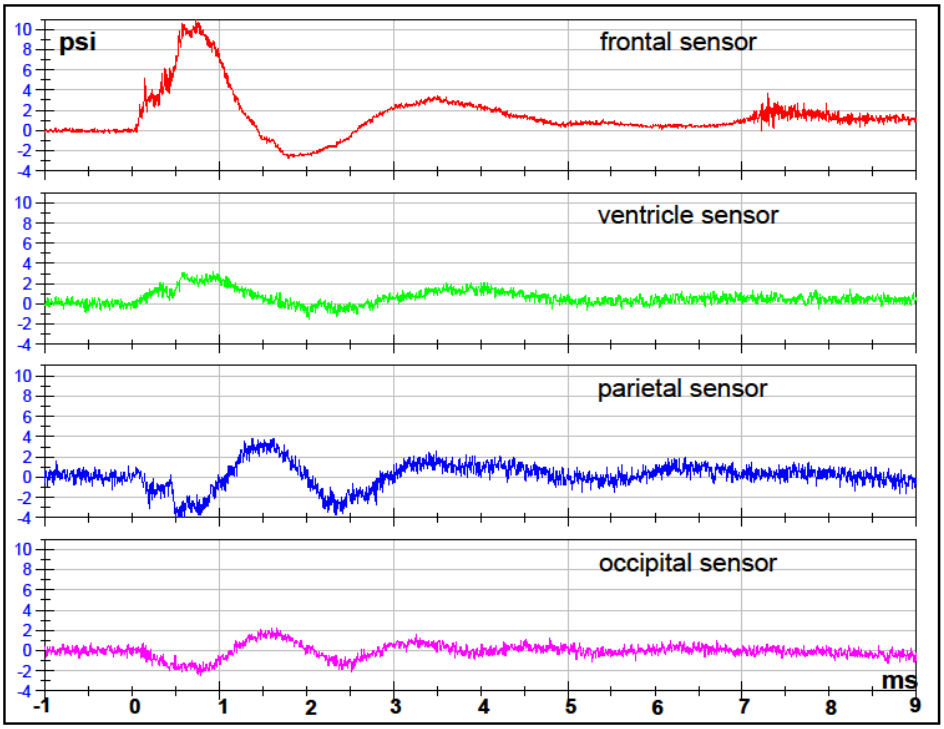

RAW DATA

Test 2 Left Orientation Cadaver-4

FILTERED DATA

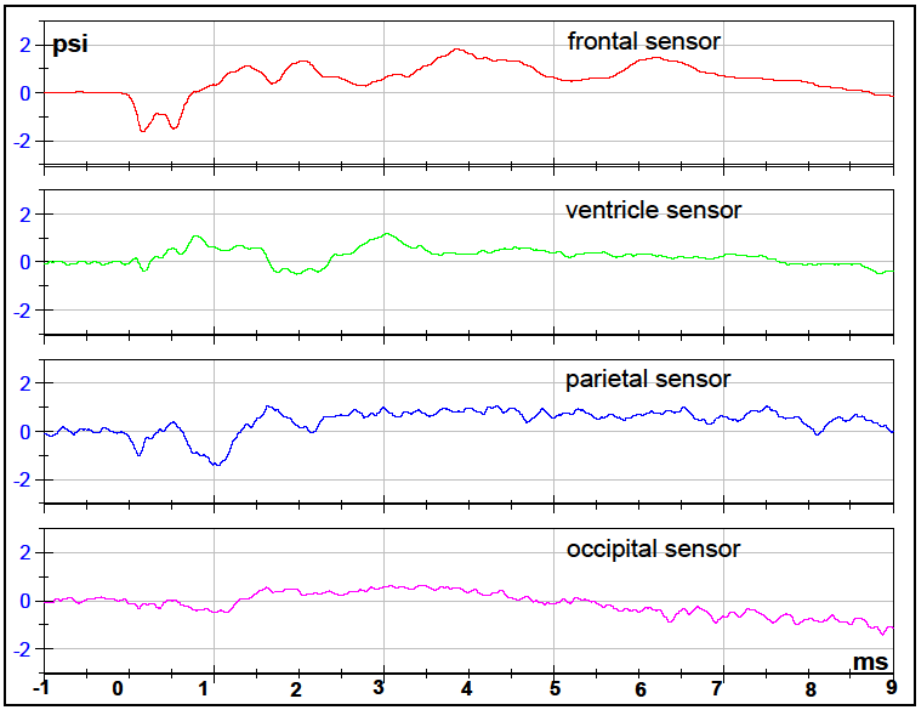

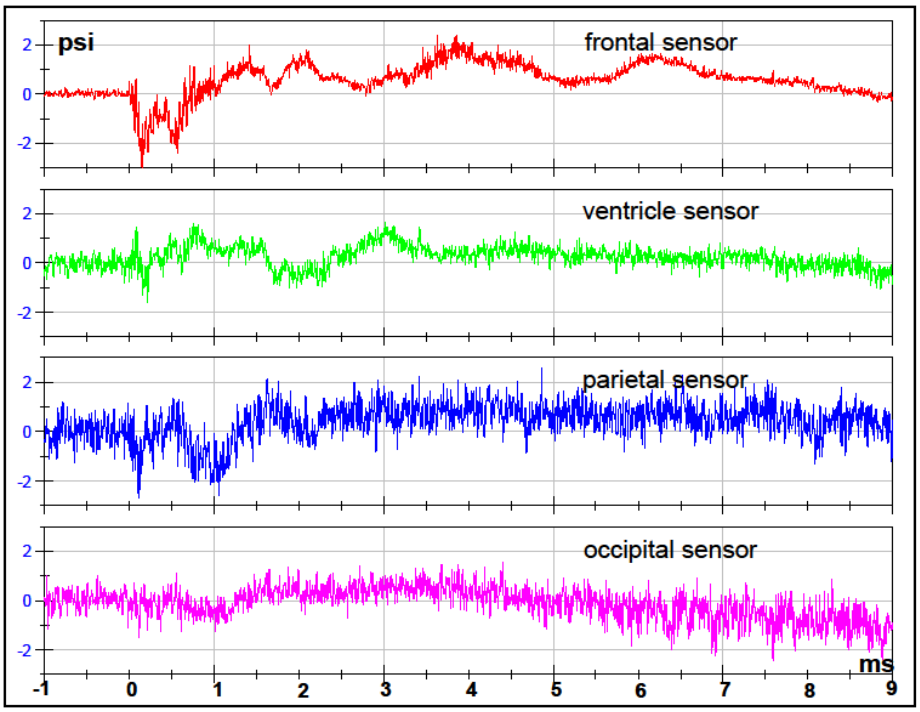

RAW DATA

Test 3 Back Orientation Cadaver-4

FILTERED DATA

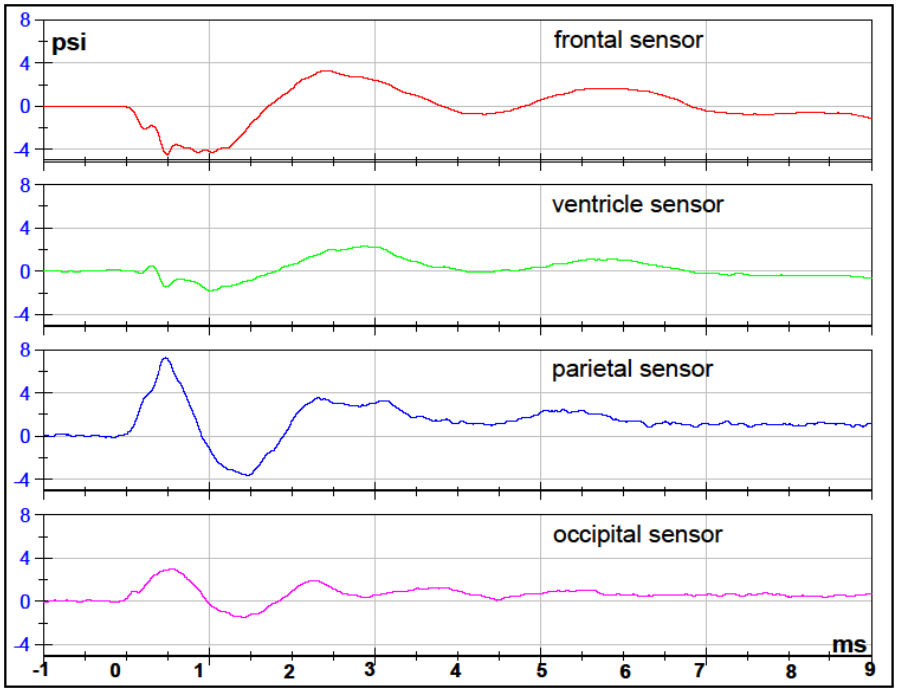

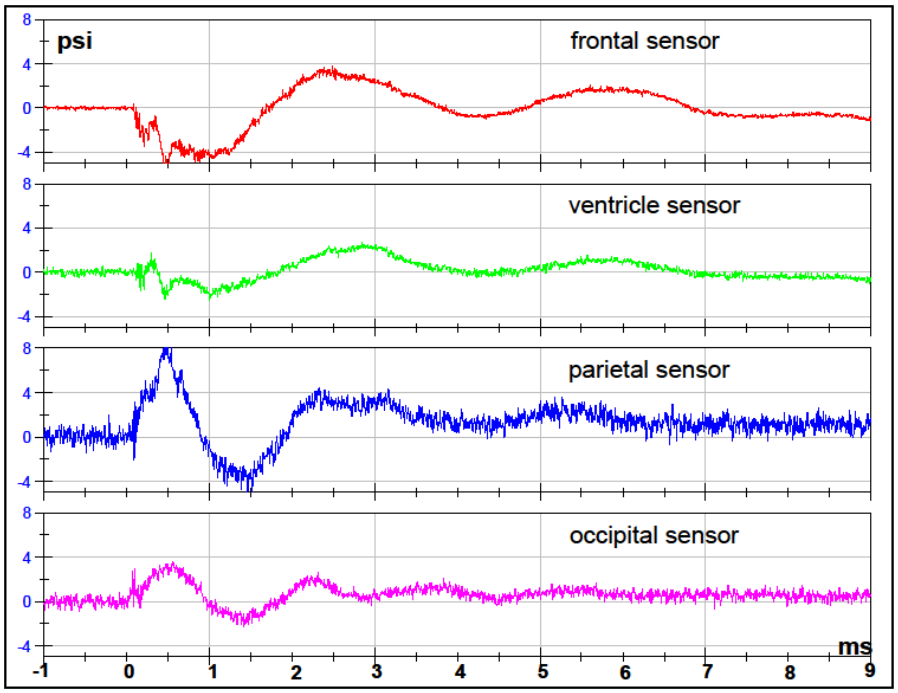

RAW DATA

Test 4 Right Orientation Cadaver-4

FILTERED DATA

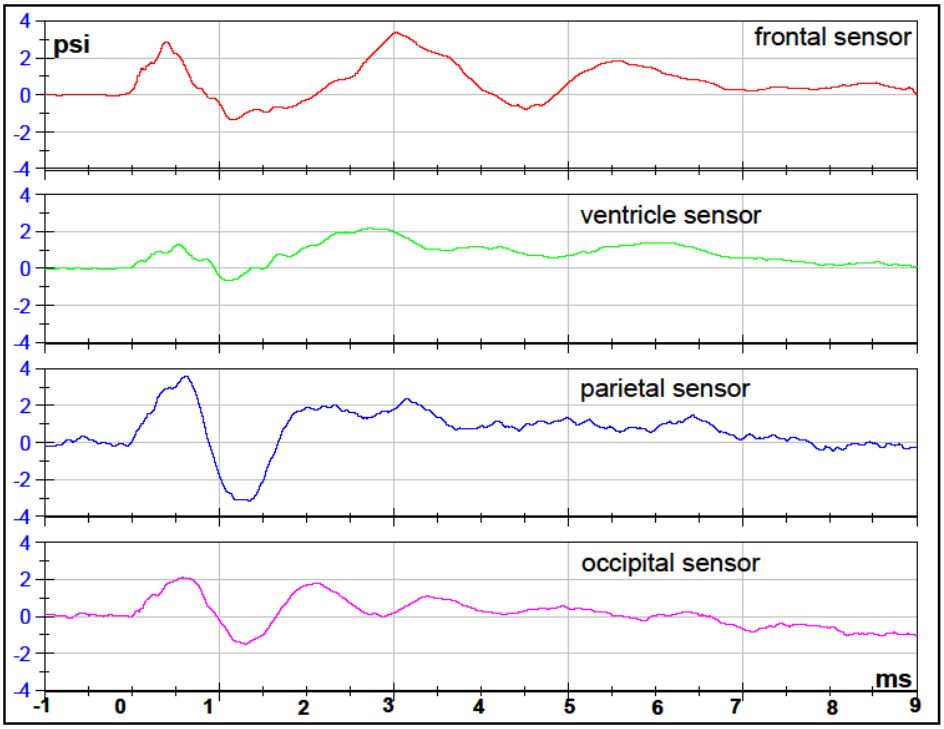

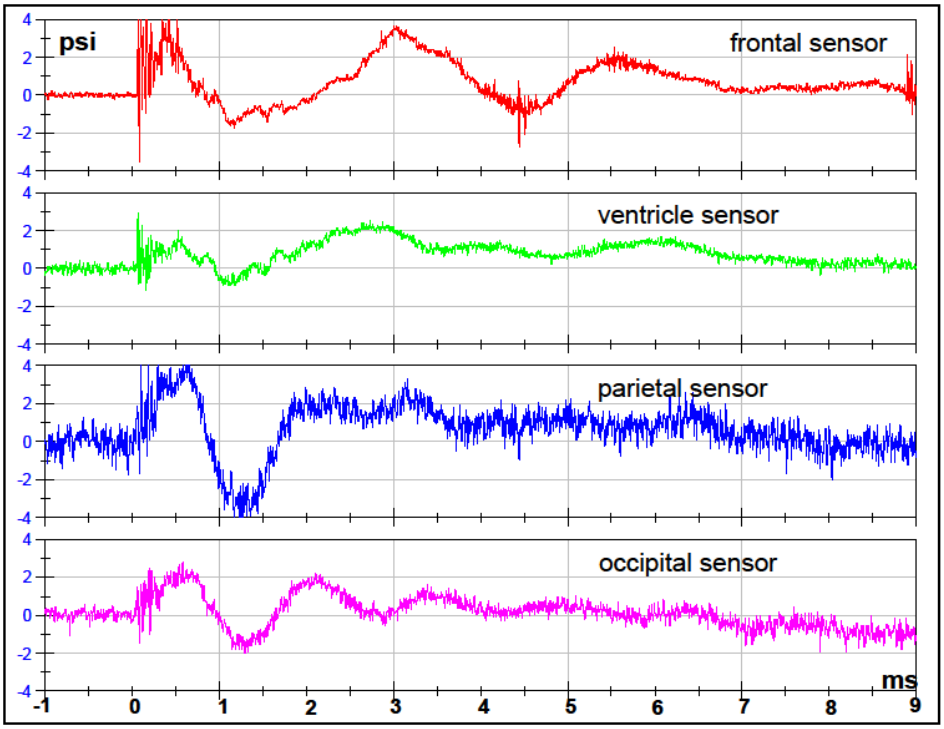

RAW DATA

Test 5 Front 2 Orientation Cadaver-4

FILTERED DATA

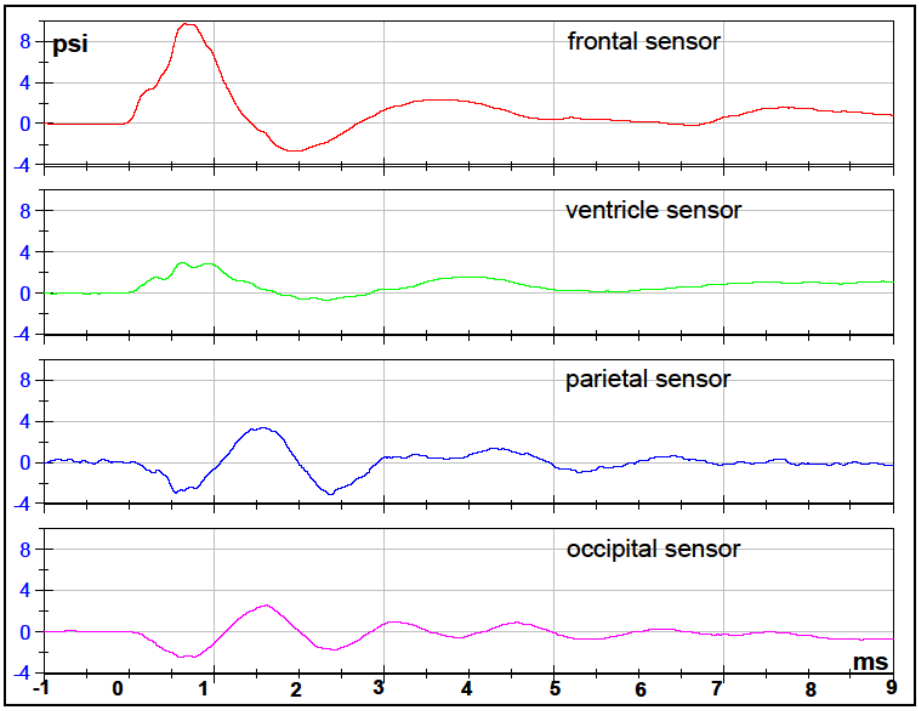

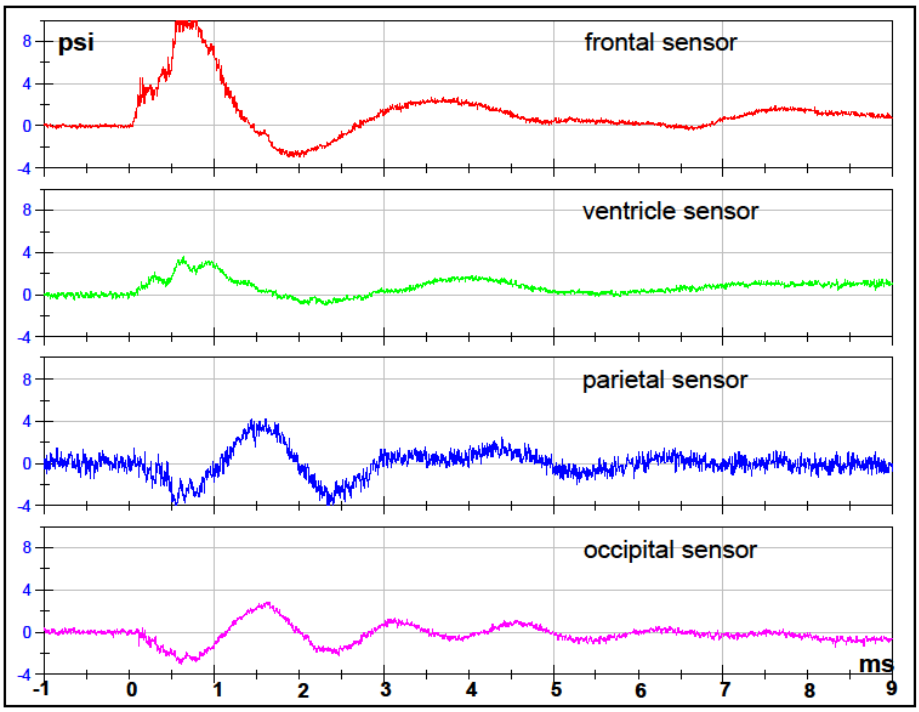

RAW DATA

Test 6 Front 1 Orientation Cadaver-4

FILTERED DATA

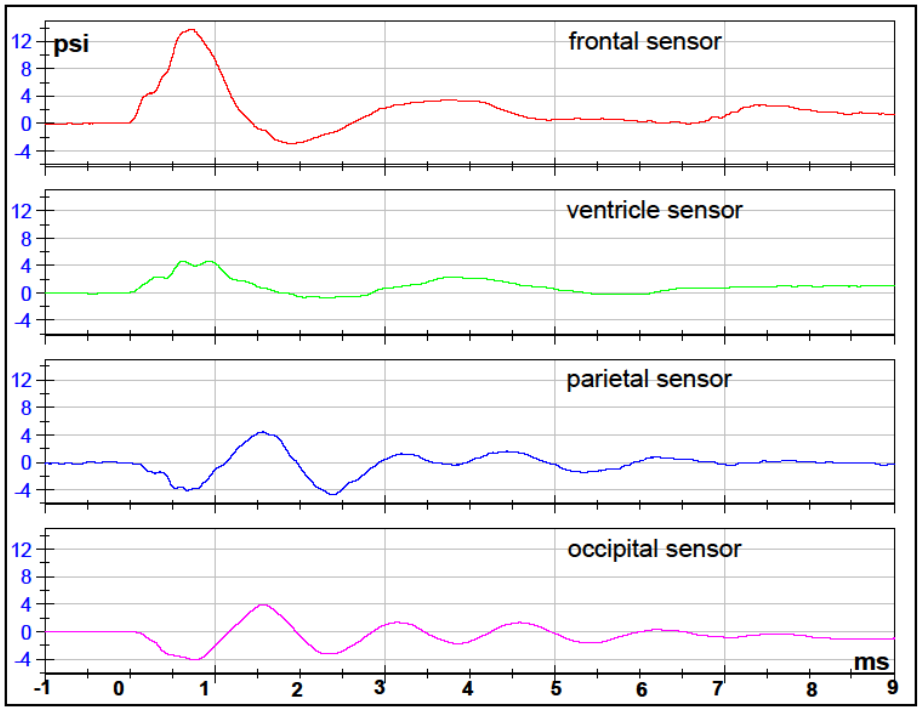

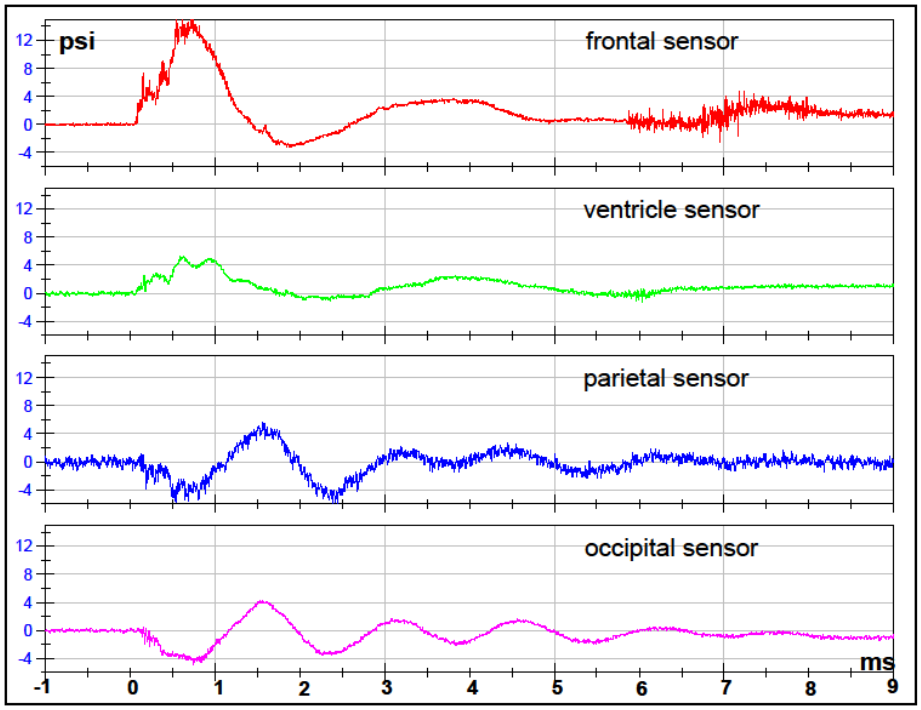

RAW DATA

Test 7 Right Orientation Cadaver-4

FILTERED DATA

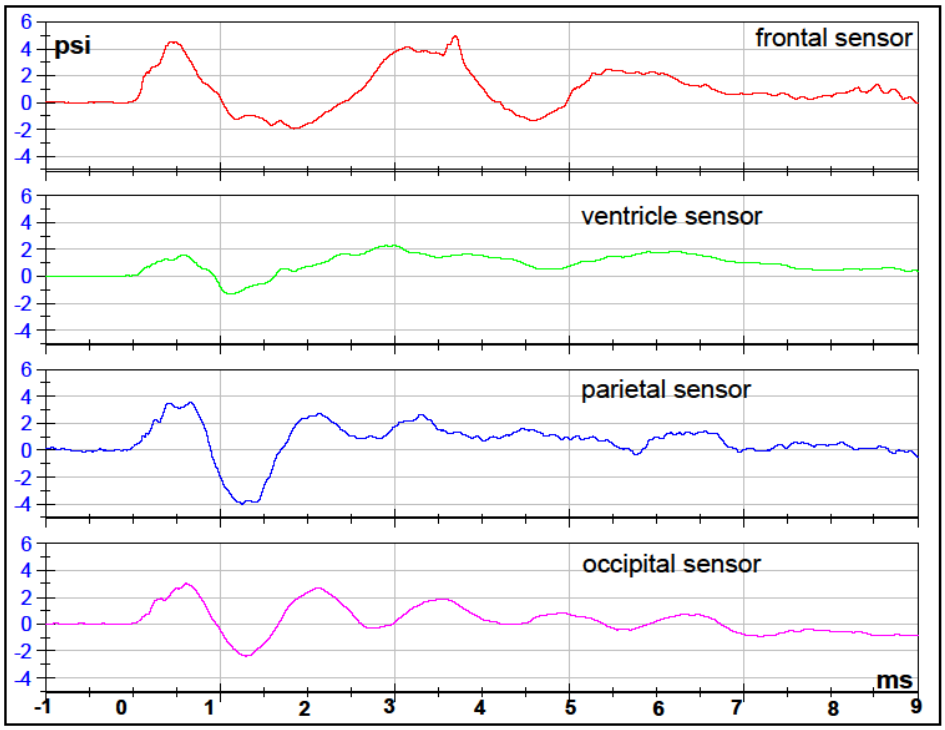

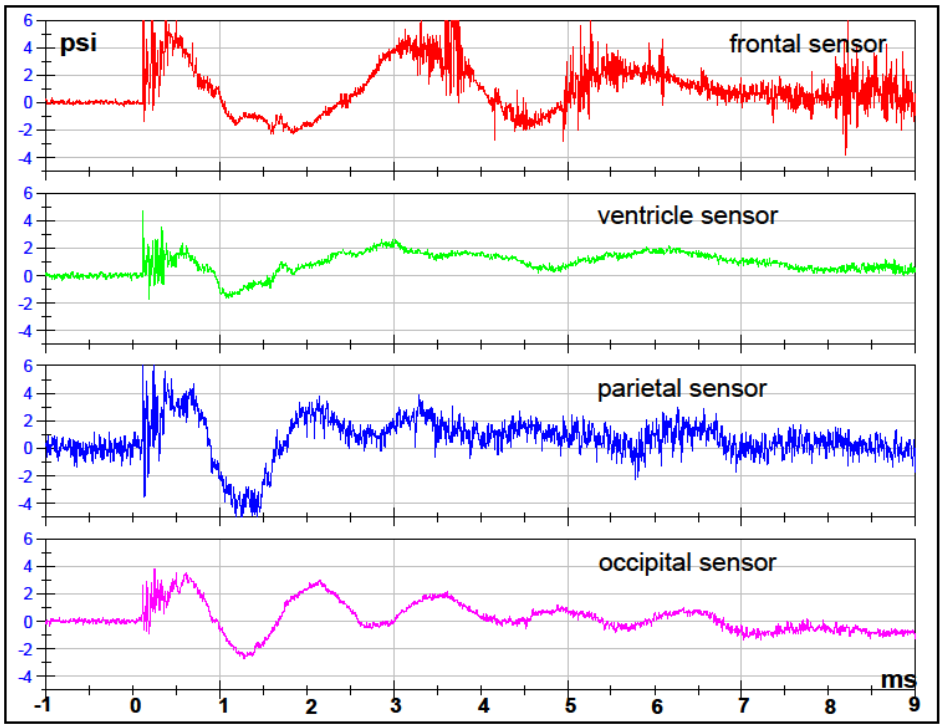

RAW DATA

Test 8 Back Orientation Cadaver-4

FILTERED DATA

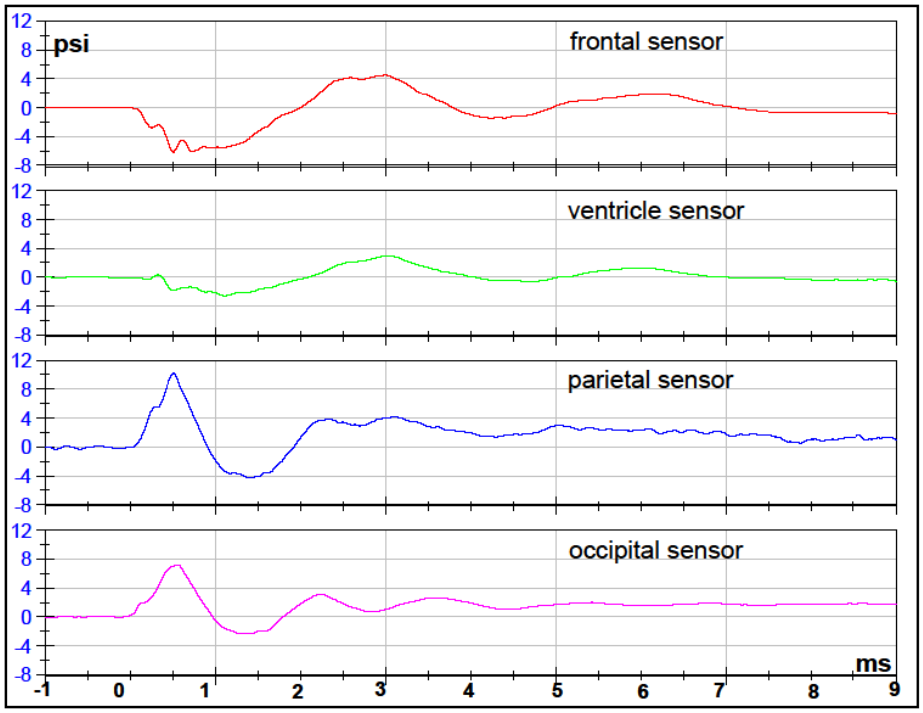

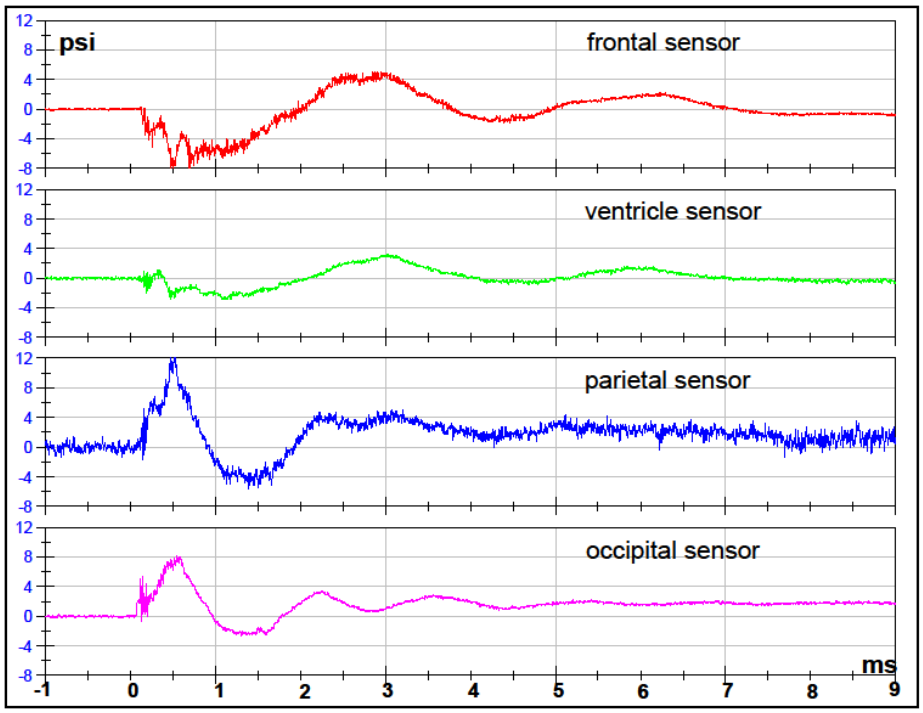

RAW DATA

Test 9 Left Orientation Cadaver-4

FILTERED DATA

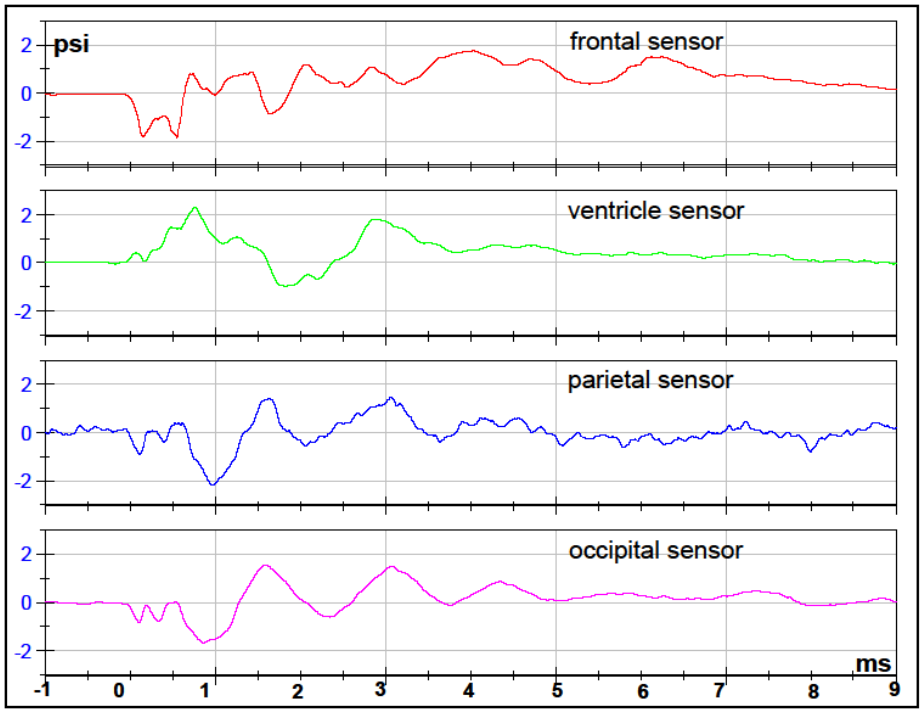

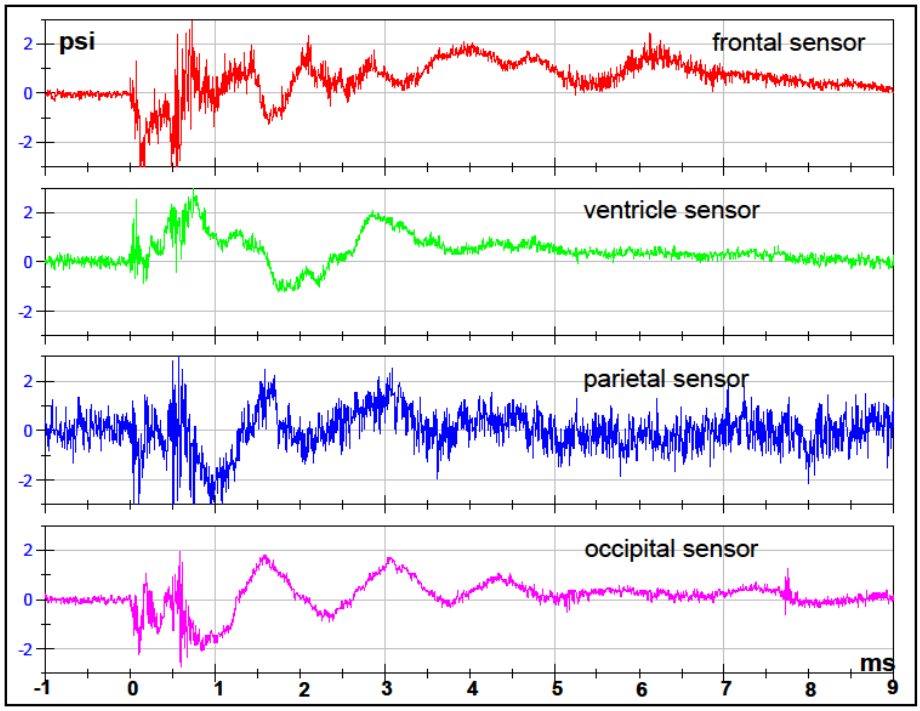

RAW DATA

Test 10 Front 2 Orientation Cadaver-4

FILTERED DATA

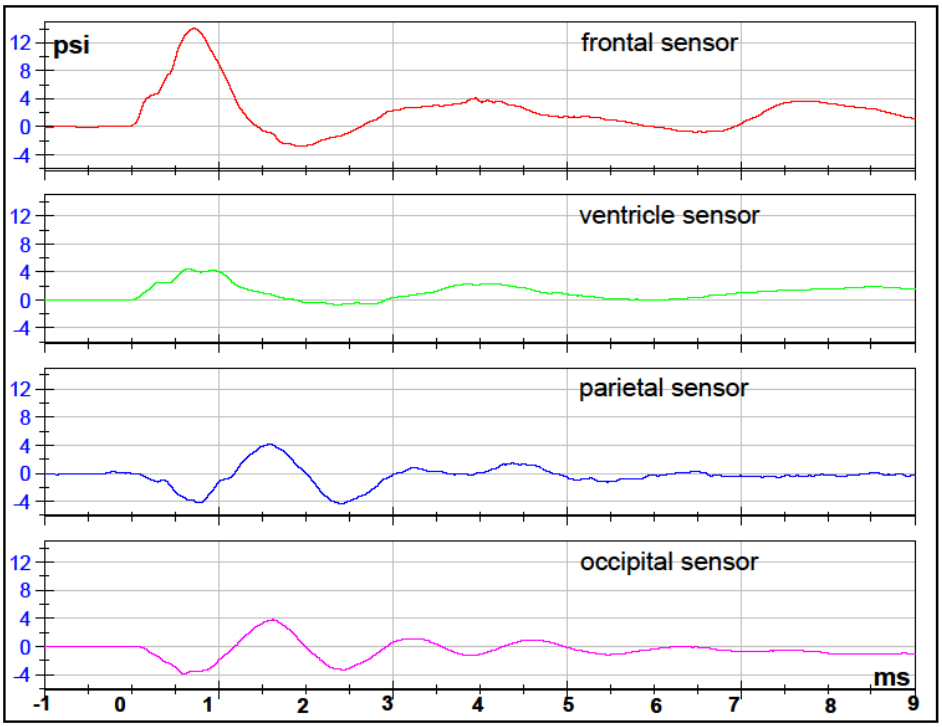

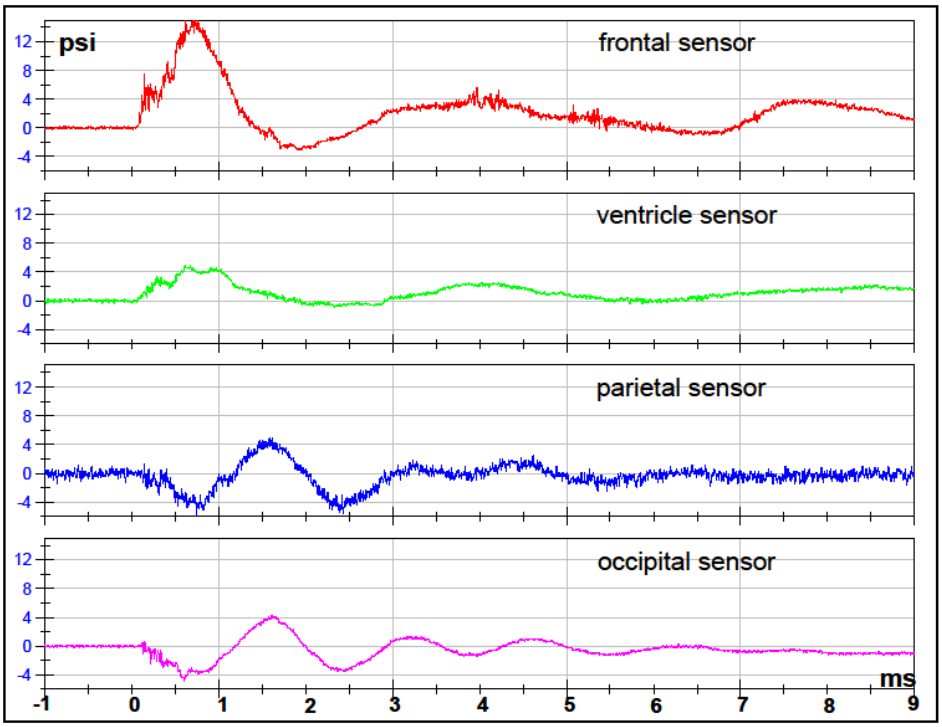

RAW DATA

Test 11 Front 1 Orientation Cadaver-4

FILTERED DATA

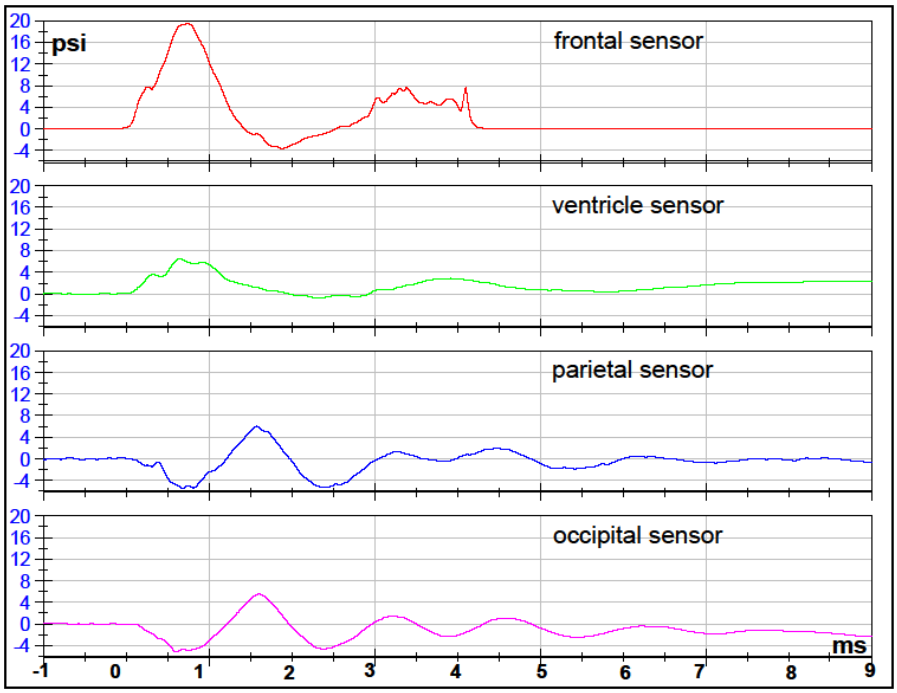

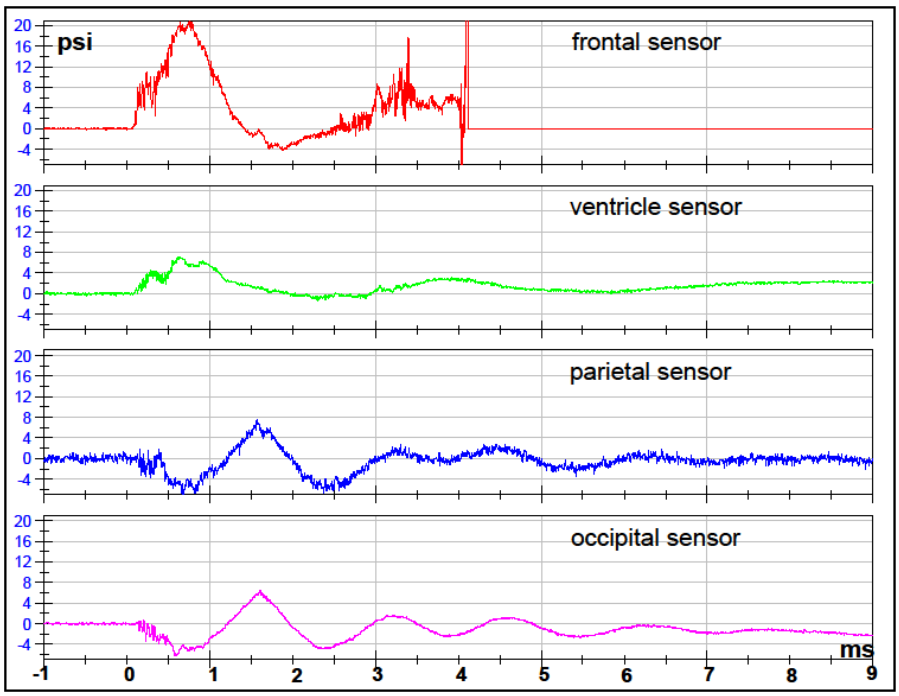

RAW DATA

Test 12 Left Orientation Cadaver-4

FILTERED DATA

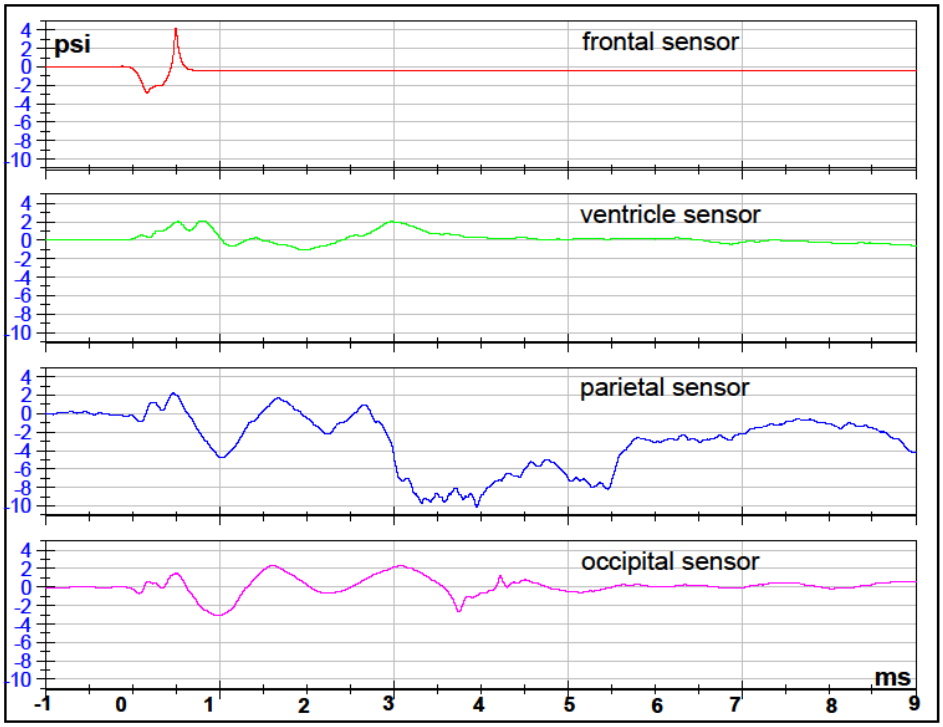

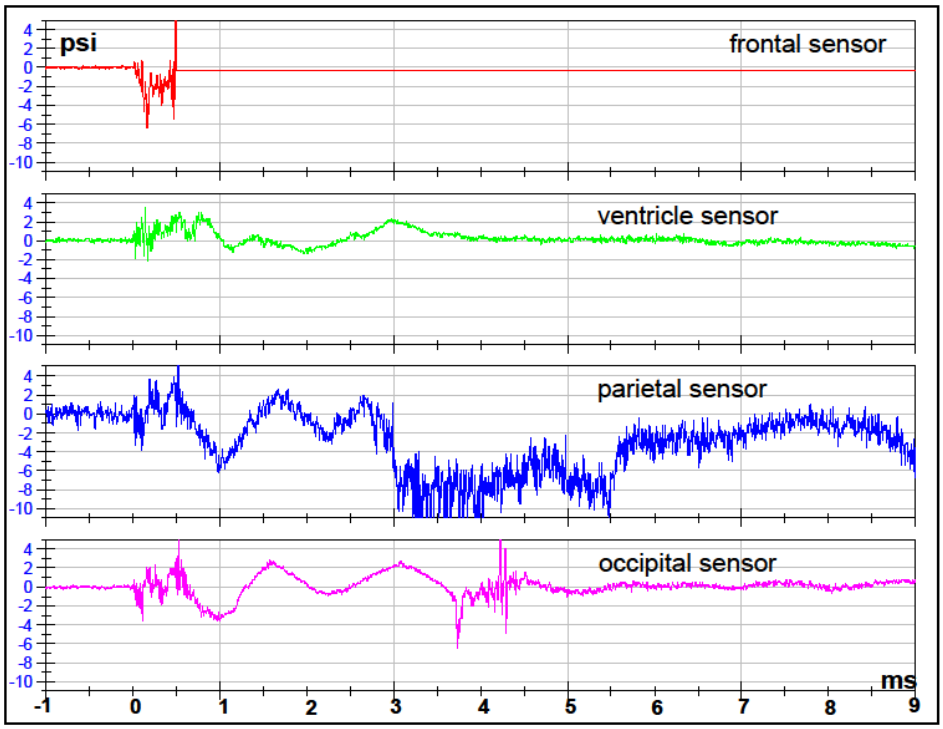

RAW DATA

Test 13 Back 1 Orientation Cadaver-4

FILTERED DATA

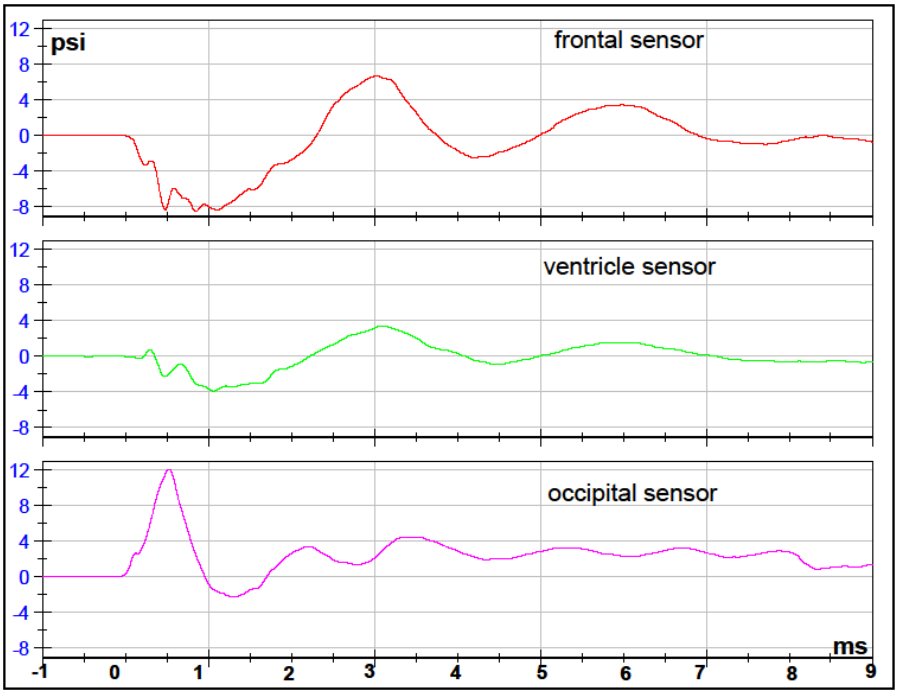

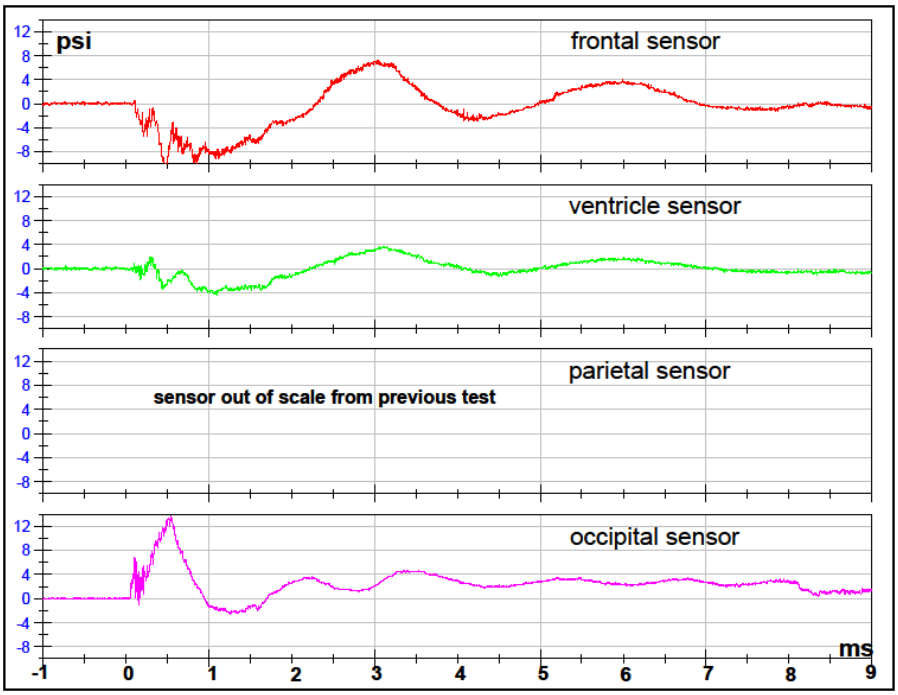

RAW DATA

Test 14 Right Orientation Cadaver-4

FILTERED DATA

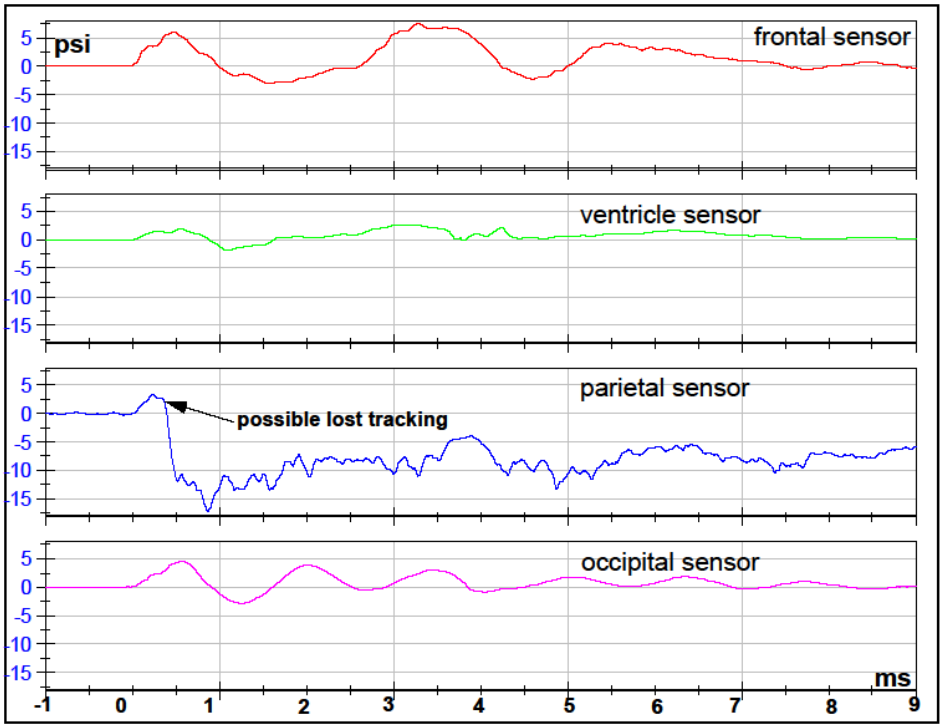

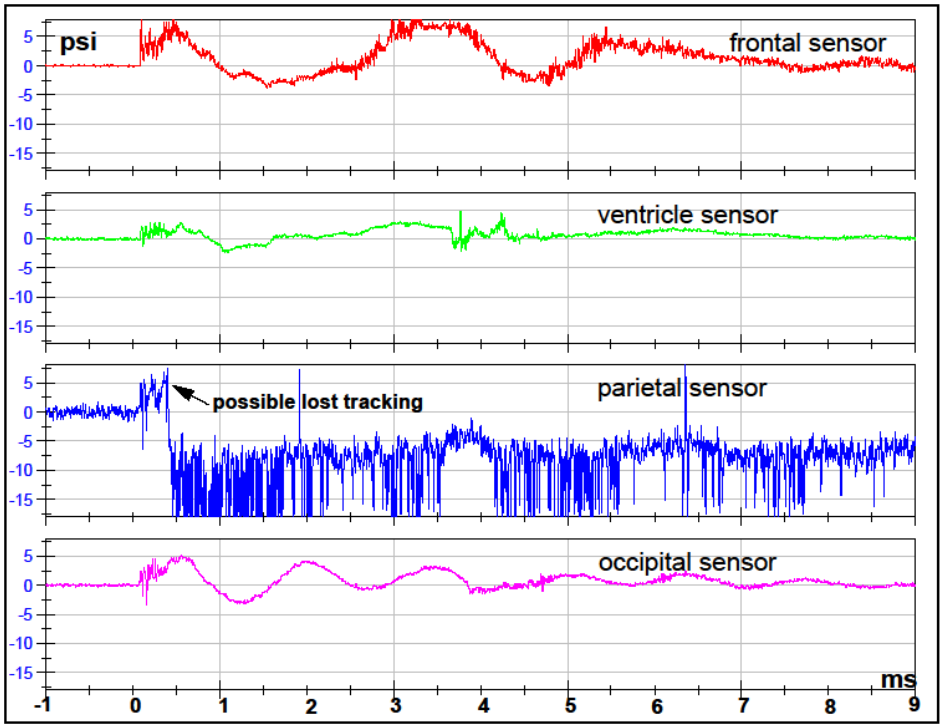

RAW DATA

Test 15 Front 2 Orientation Cadaver-4

FILTERED DATA

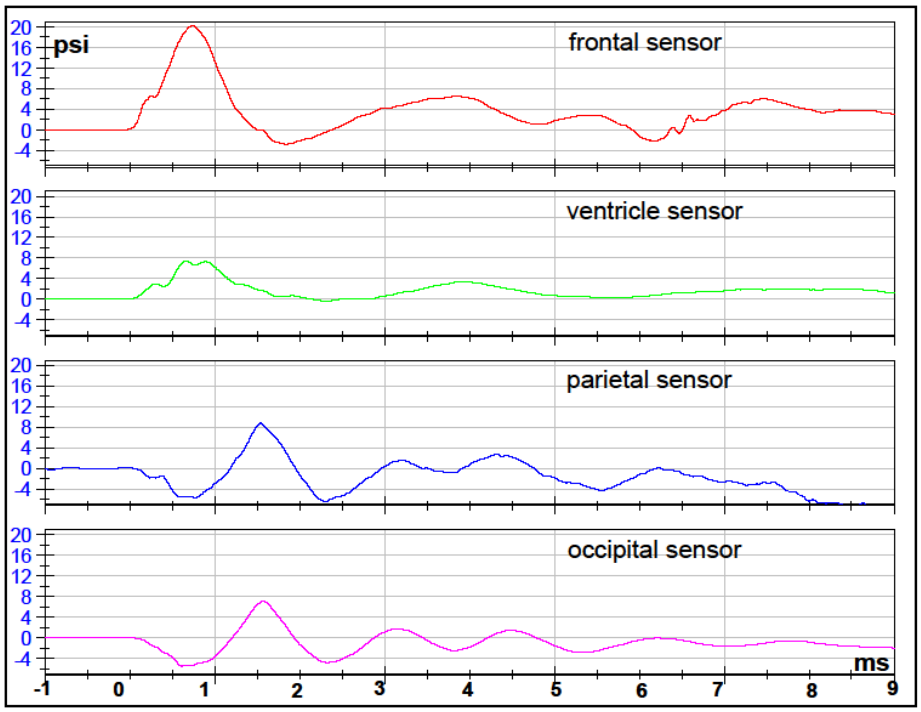

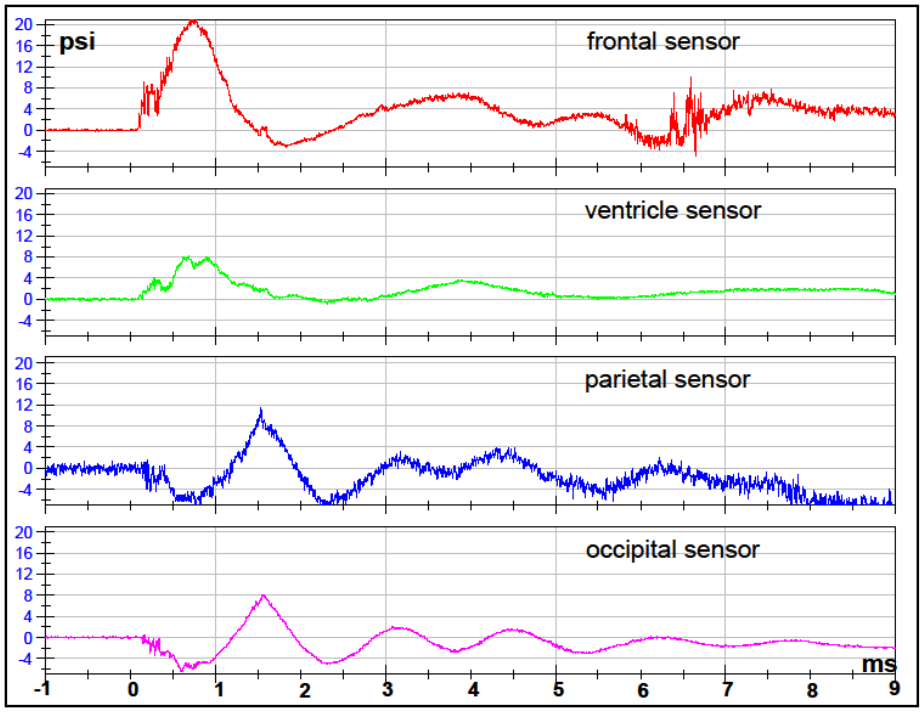

RAW DATA

Test 16 Back 2 Orientation Cadaver-4

FILTERED DATA

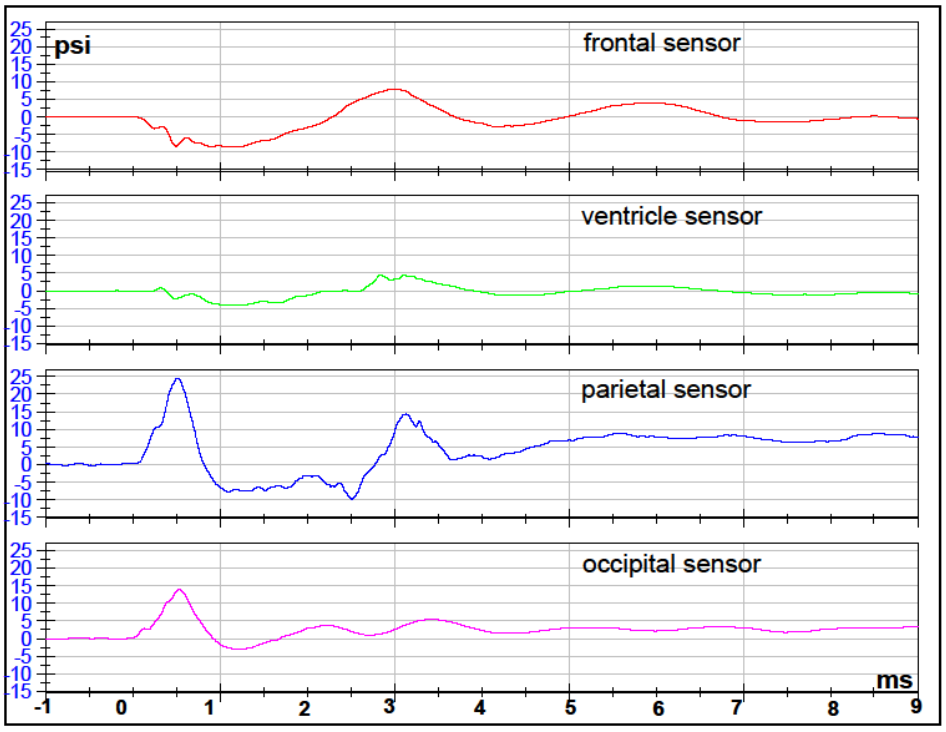

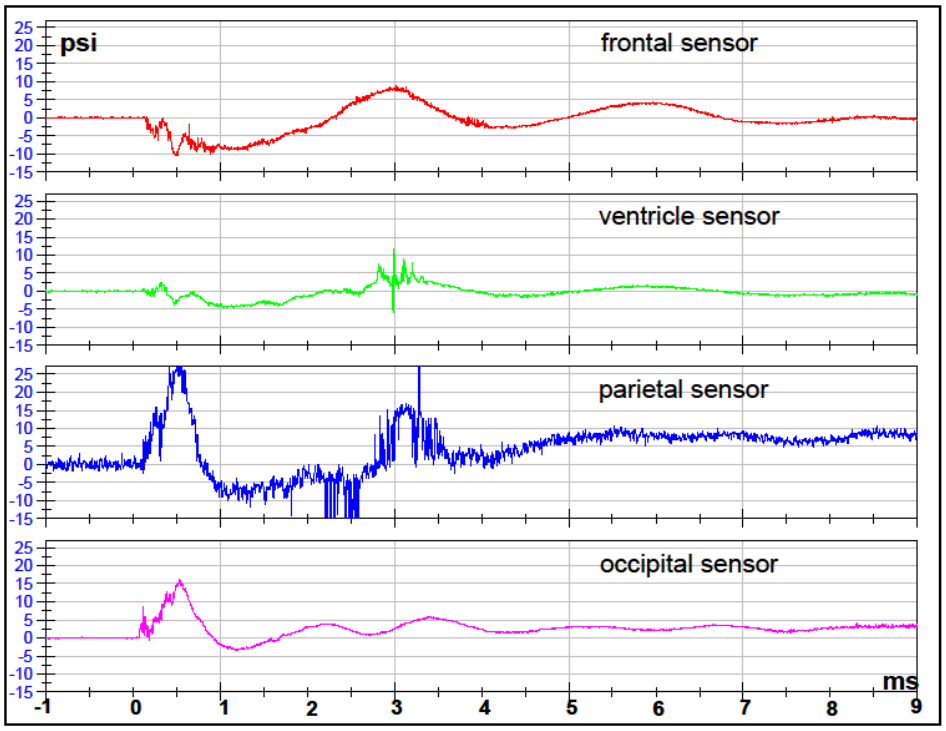

RAW DATA

Comparison for reproducibility of each pressure sensor in Front Orientations at 10psi Cadaver-4

VENTRICLE FILTERED DATA

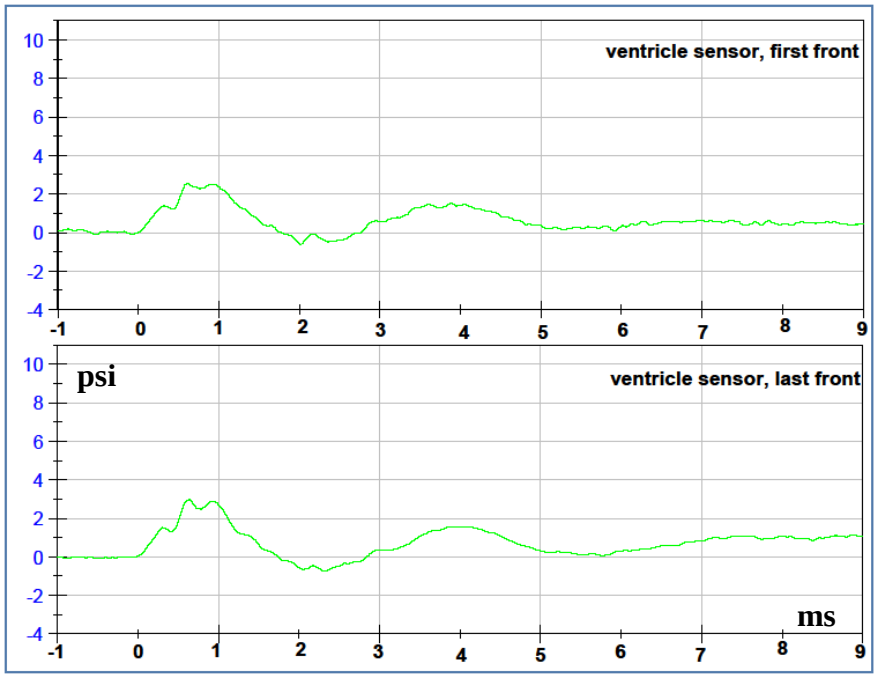

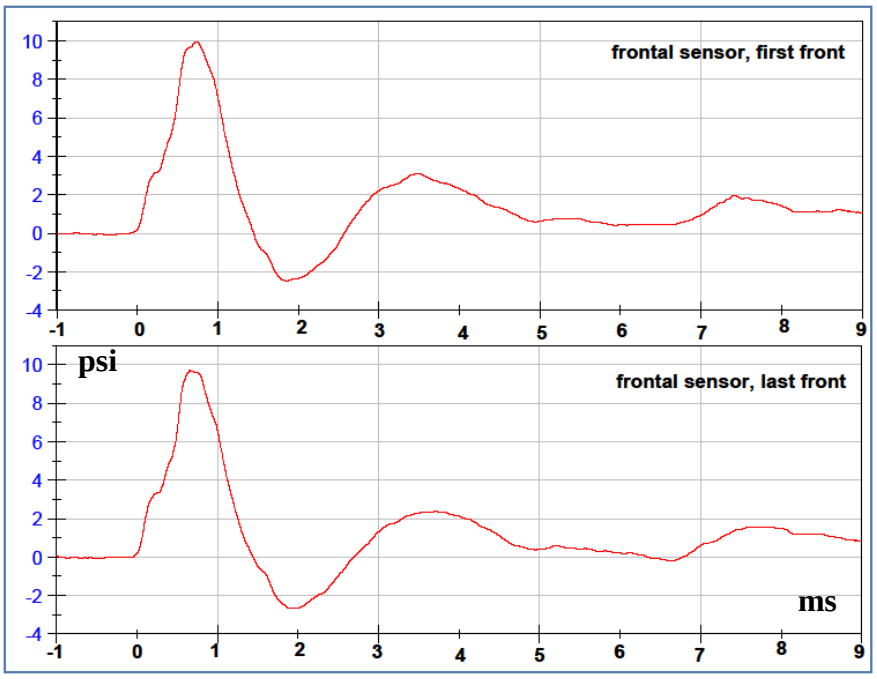

FRONTAL FILTERED DATA

Comparison for reproducibility of each pressure sensor in Front Orientations at 10psi Cadaver-4

PARIETAL FILTERED DATA

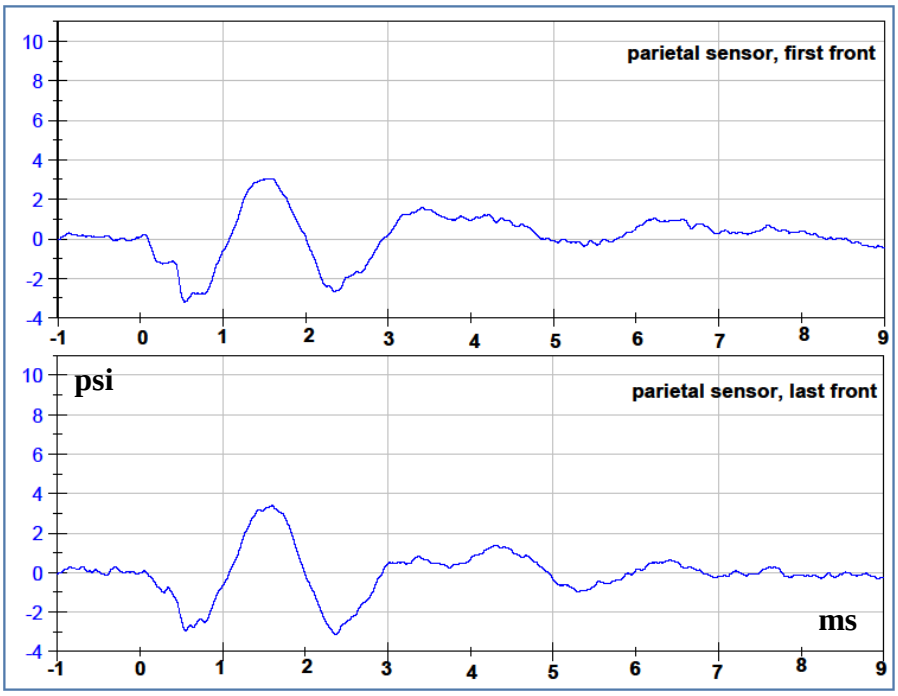

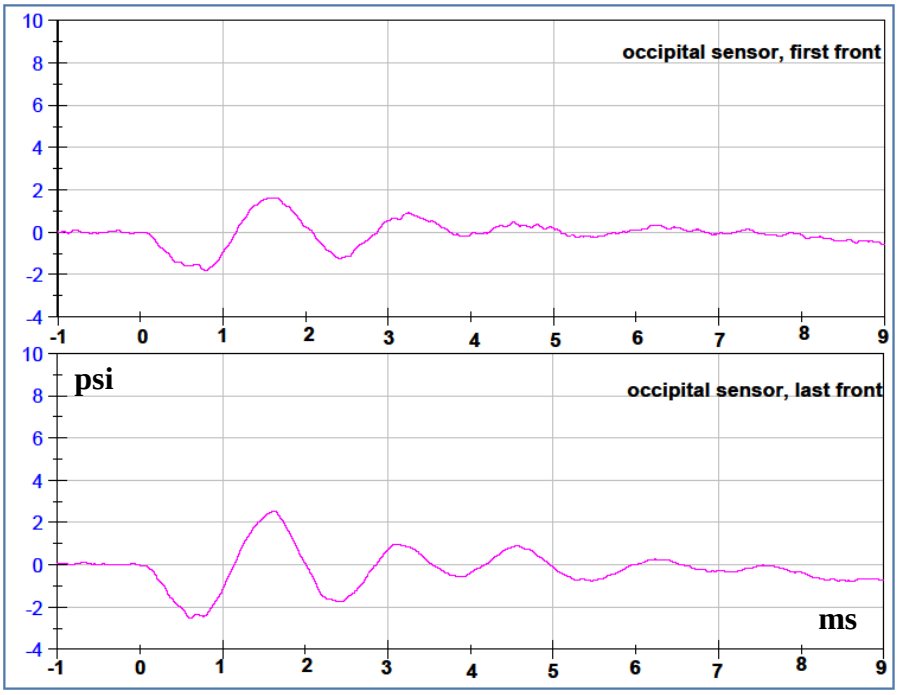

OCCIPITAL FILTERED DATA

Comparison for reproducibility of each pressure sensor in Front Orientations at 12psi Cadaver-4

VENTRICLE FILTERED DATA

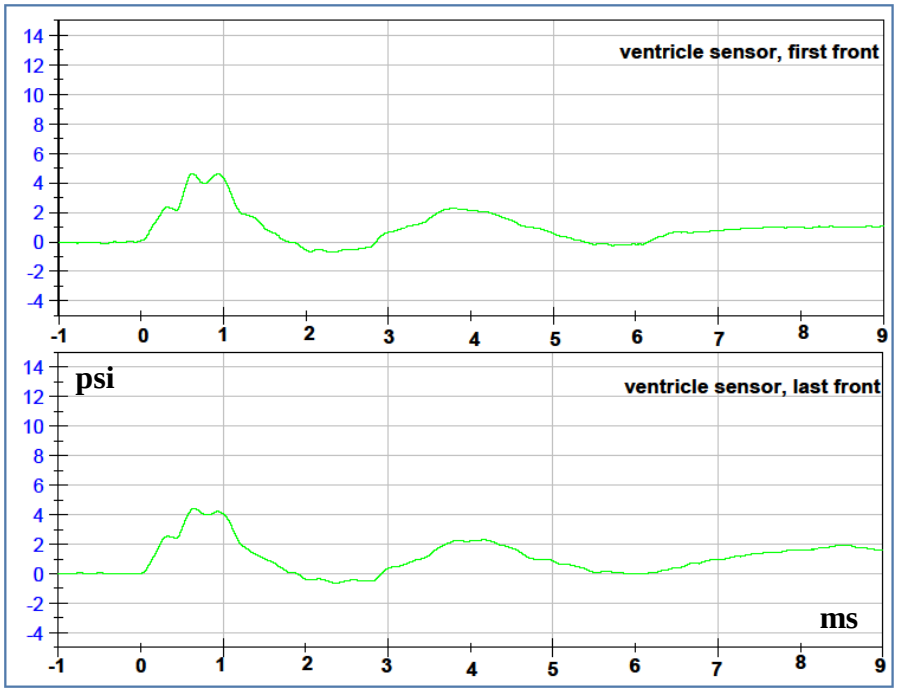

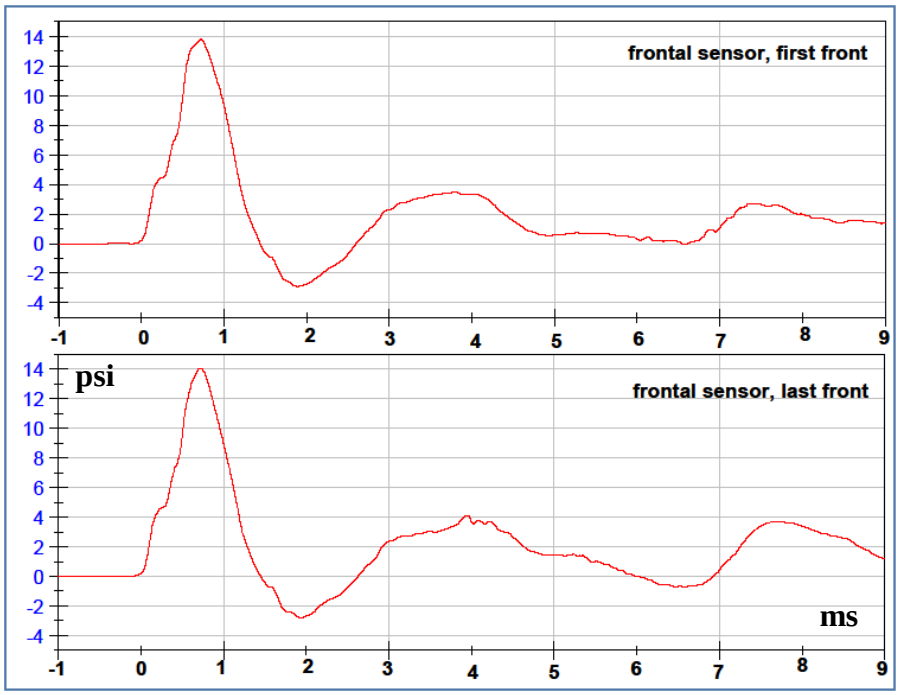

FRONTAL FILTERED DATA

Comparison for reproducibility of each pressure sensor in Front Orientations at 12psi Cadaver-4

PARIETAL FILTERED DATA

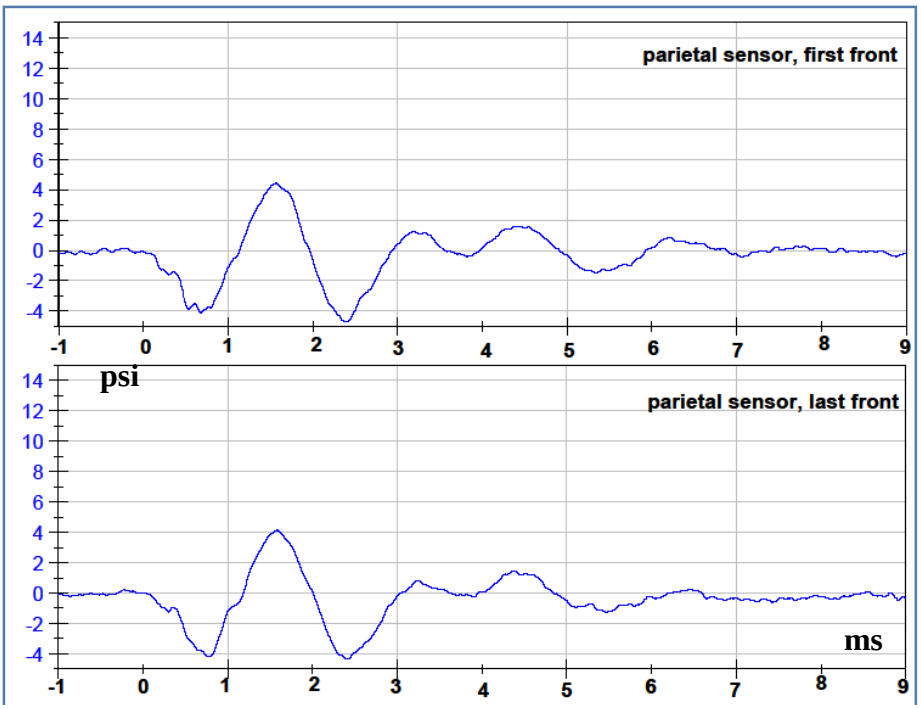

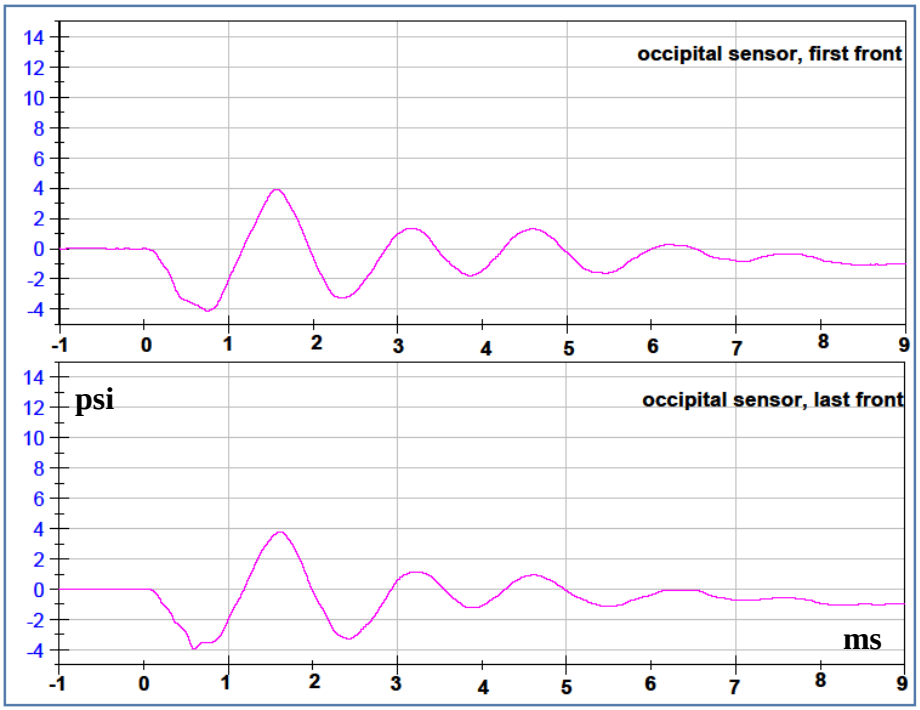

OCCIPITAL FILTERED DATA

Comparison for reproducibility of each pressure sensor in Front Orientations at 15psi Cadaver-4

VENTRICLE FILTERED DATA

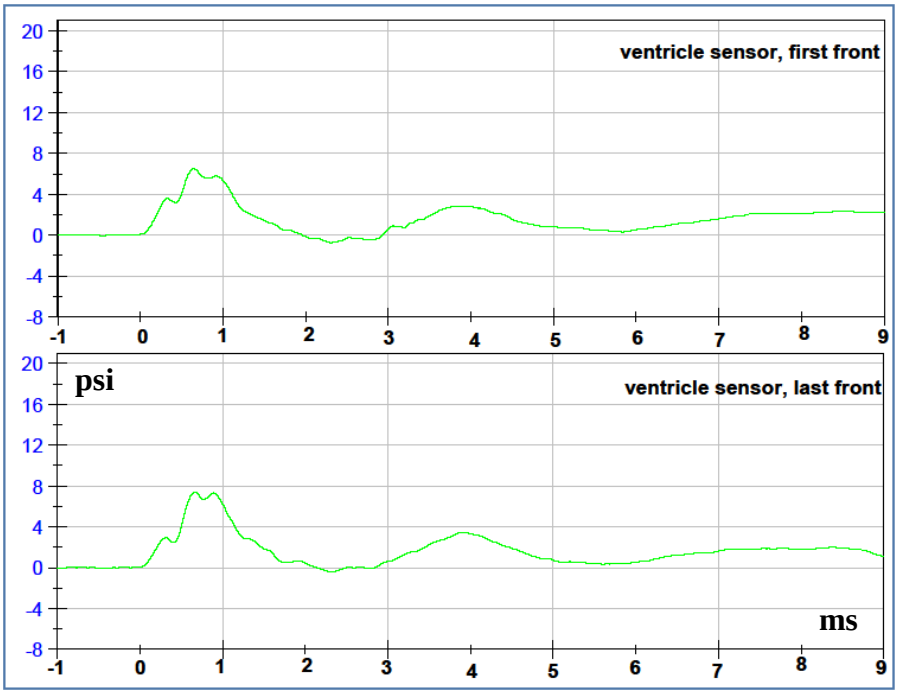

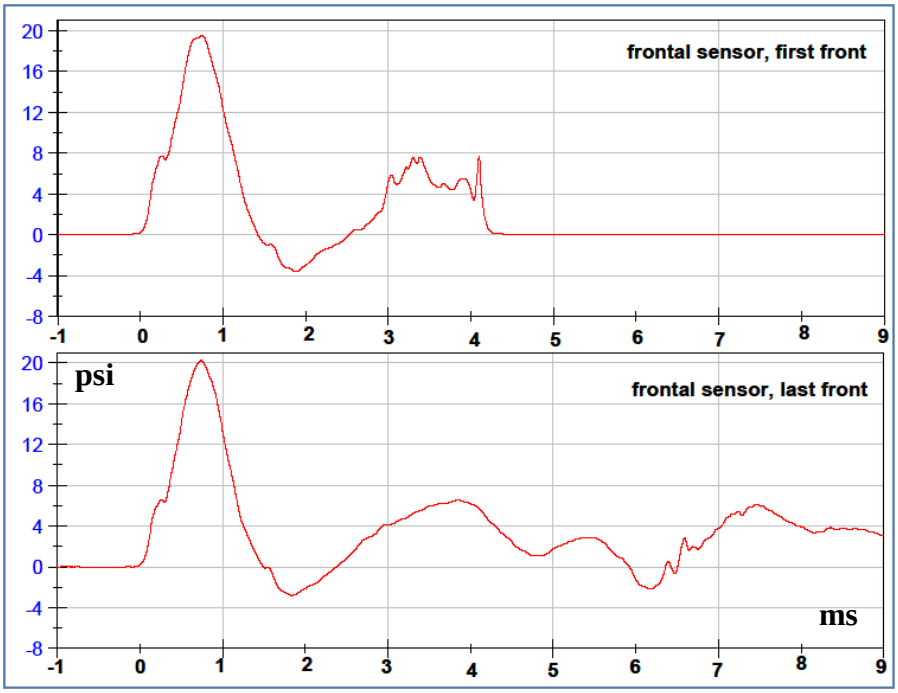

FRONTAL FILTERED DATA

Comparison for reproducibility of each pressure sensor in Front Orientations at 15psi Cadaver-4

PARIETAL FILTERED DATA

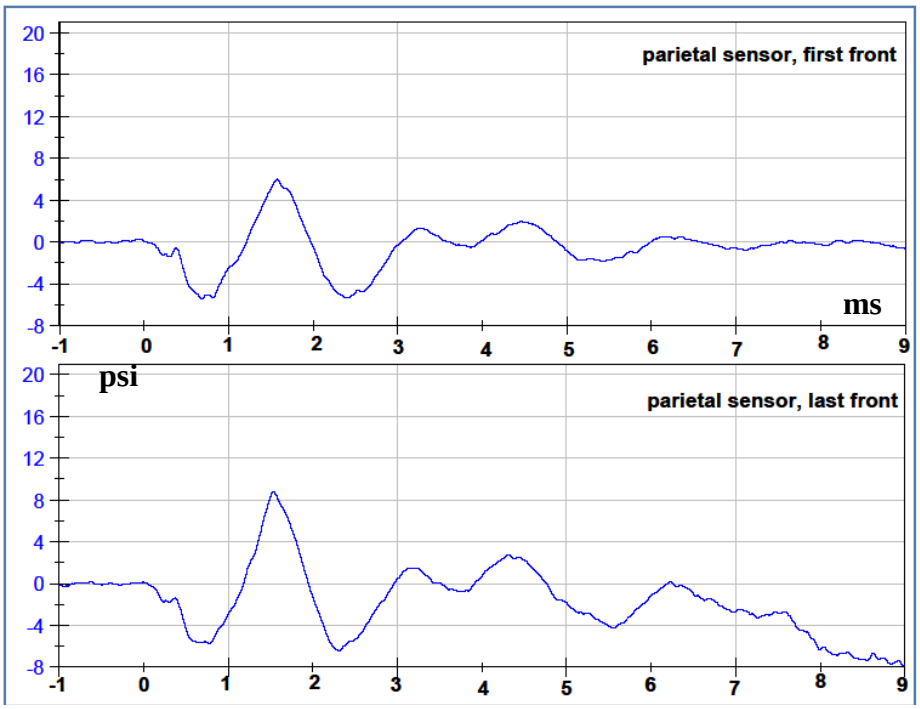

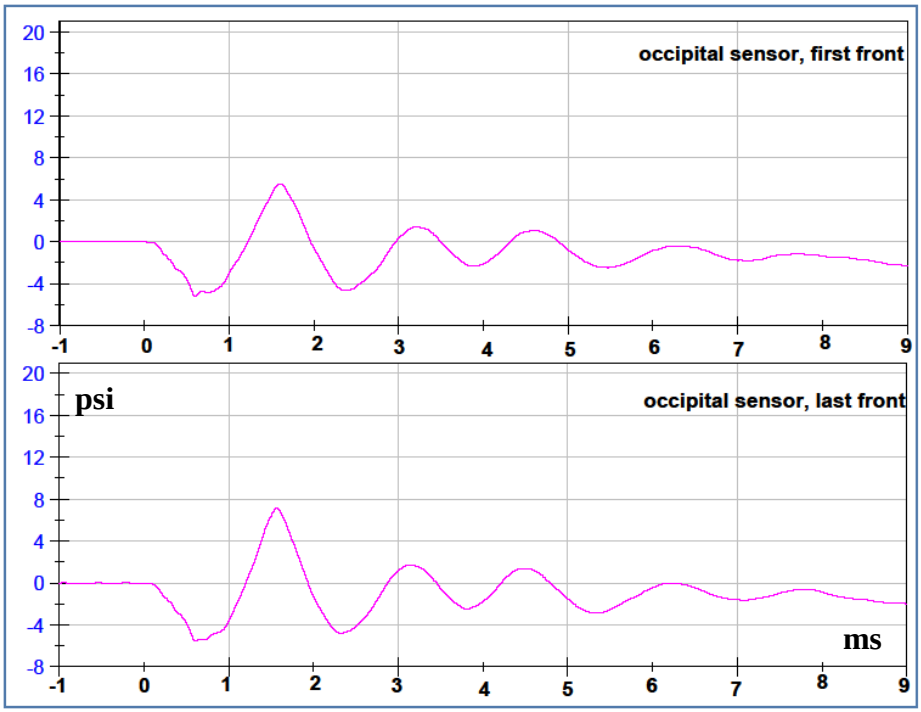

OCCIPITAL FILTERED DATA

Pressure Extremes for cadaver-4.

This test subject has one extra test. It was exposed to a second simulated blast for back orientation at high pressure (15psi).

Pressure Extremes for cadaver-4 (psi)												
	Maximun Pressure						Minimum Pressure					
ventricle	front 1	right	back	left	front 2	back 2	front 1	right	back	left	front 2	back 2
10 psi air	**2.54**	**2.19**	**2.33**	**1.19**	**2.96**		**-0.6**	**-0.627**	**-1.85**	**-0.499**	**-0.731**	
12 psi air	**4.63**	**2.28**	**2.97**	**2.29**	**4.42**		**-0.7**	**-1.33**	**-2.55**	**-0.975**	**-1.69**	
15 psi air	**6.49**	**2.63**	**3.43**	**2.13**	**7.41**	**4.54**	**-0.735**	**-1.82**	**-3.87**	**-1.06**	**-0.427**	**-4.14**
frontal	front 1	right	back	left	front 2	back 2	front 1	right	back	left	front 2	back 2
10 psi air	**9.94**	**3.35**	**3.25**	**1.81**	**9.7**		**-2.47**	**-1.36**	**-4.46**	**-1.62**	**-2.66**	
12 psi air	**13.76**	**4.87**	**4.5**	**1.74**	**14.03**		**-2.89**	**-1.95**	**-6.16**	**-1.84**	**-2.76**	
15 psi air	**19.56**	**7.52**	**6.72**	**4.16**	**20.24**	**7.84**	**-3.64**	**-3.09**	**-8.31**	**-2.85**	**-2.7**	**-8.47**
parietal	front 1	right	back	left	front 2	back 2	front 1	right	back	left	front 2	back 2
10 psi air	**3.05**	**3.59**	**7.25**	**1.07**	**3.39**		**-3.21**	**-3.13**	**-3.67**	**-1.43**	**-3.12**	
12 psi air	**4.42**	**3.53**	**10.23**	**1.41**	**4.14**		**-4.64**	**-3.97**	**-4.26**	**-2.18**	**-4.36**	
15 psi air	**5.94**	**3.36**	**NA**	**2.22**	**8.79**	**24.42**	**-5.45**	***-17.10**	**NA**	**-10.11**	**-6.41**	**-9.8**
occipital	front 1	right	back	left	front 2	back 2	front 1	right	back	left	front 2	back 2
10 psi air	**1.63**	**2.08**	**2.99**	**0.657**	**2.52**		**-1.8**	**-1.48**	**-1.53**	**-0.89**	**-2.52**	
12 psi air	**3.85**	**3**	**7.14**	**1.56**	**3.76**		**-4.07**	**-2.36**	**-2.27**	**-1.68**	**-3.94**	
15 psi air	**5.49**	**4.56**	**12.01**	**2.37**	**7.17**	**13.95**	**-5.22**	**-2.79**	**-2.15**	**-3.09**	**-5.5**	**-3**
							* means that there was an issue with possible loss of tracking					

Pressure differentials for cadaver-4.

This test subject has one extra test. It was exposed to a second simulated blast for back orientation at high pressure (15psi).

Differential for cadaver-4												
	peak differential pressure (psi)						time elapsed between peaks (ms)					
ventricle	front 1	right	back	left	front 2	back 2	front 1	right	back	left	front 2	back 2
10 psi air	**3.15**	**2.82**	**4.18**	**1.68**	**3.69**		**1.4**	**1.64**	**1.85**	**1.06**	**1.67**	
12 psi air	**5.33**	**3.61**	**5.52**	**3.26**	**5.03**		**1.7**	**1.88**	**1.91**	**1.072**	**2.98**	
15 psi air	**7.22**	**4.44**	**7.3**	**3.19**	**7.83**	**8.68**	**1.64**	**1.98**	**2.01**	**1.18**	**1.64**	**1.73**
frontal	front 1	right	back	left	front 2	back 2	front 1	right	back	left	front 2	back 2
10 psi air	**12.41**	**4.71**	**7.71**	**3.43**	**12.36**		**1.09**	**1.90**	**1.928**	**3.72**	**1.26**	
12 psi air	**16.65**	**6.82**	**10.66**	**3.59**	**16.79**		**1.15**	**1.88**	**2.49**	**3.452**	**1.19**	
15 psi air	**23.2**	**10.6**	**15.01**	**7.01**	**22.94**	**16.31**	**1.14**	**1.73**	**1.92**	**0.328**	**1.072**	**1.8**
parietal	front 1	right	back	left	front 2	back 2	front 1	right	back	left	front 2	back 2
10 psi air	**6.26**	**6.71**	**10.92**	**2.5**	**6.51**		**1.06**	**0.64**	**0.988**	**0.584**	**0.756**	
12 psi air	**9.06**	**7.5**	**14.49**	**3.59**	**8.5**		**0.808**	**0.576**	**0.88**	**0.68**	**0.8**	
15 psi air	**11.39**	***20.44**	**NA**	**12.33**	**15.2**	**34.22**	**0.888**	***0.628**	**NA**	**3.49**	**0.78**	**2.01**
occipital	front 1	right	back	left	front 2	back 2	front 1	right	back	left	front 2	back 2
10 psi air	**3.43**	**3.56**	**4.55**	**1.55**	**5.05**		**0.764**	**0.74**	**0.84**	**2.92**	**0.984**	
12 psi air	**7.93**	**5.36**	**9.41**	**3.24**	**7.7**		**0.8**	**0.68**	**0.768**	**0.732**	**1.01**	
15 psi air	**10.71**	**7.35**	**14.17**	**5.45**	**12.65**	**16.95**	**0.988**	**0.664**	**0.708**	**0.632**	**0.94**	**0.632**
							* means that there was an issue with possible loss of tracking					

Pressure rates of change for cadaver-4.

	1st rate (psi/ms)					
ventricle	front 1	right	back	left	front 2	back 2
10 psi air	**4.19**	**2.53**	**-11.07**	**-5.06**	**4.76**	
12 psi air	**7.15**	**3.54**	**-11.52**	**1.86**	**7.24**	
15 psi air	**9.93**	**5.38**	**-17.4**	**4.12**	**11.61**	**-19.09**
frontal	front 1	right	back	left	front 2	back 2
10 psi air	**13.3**	**6.94**	**-8.66**	**-10.09**	**14.4**	
12 psi air	**18.4**	**10.95**	**-13.9**	**-11.01**	**19.42**	
15 psi air	**26.38**	**12.3**	**-19.29**	**-16.13**	**27.36**	**-19.65**
parietal	front 1	right	back	left	front 2	back 2
10 psi air	**-5.99**	**5.64**	**14.69**	**-7.35**	**-6.44**	
12 psi air	**-6.64**	**8.1**	**22.2**	**-7.39**	**-6.08**	
15 psi air	**-9.16**	**16.16**	**NA**	**-7.69**	**-8.23**	**47.28**
occipital	front 1	right	back	left	front 2	back 2
10 psi air	**-2.26**	**3.66**	**4.87**	**-1.08**	**-4.63**	
12 psi air	**-5.68**	**5.03**	**12.12**	**-6.64**	**-8.13**	
15 psi air	**-10.86**	**8.17**	**23.14**	**-6.33**	**-10.3**	**25.41**

Percentage of change for 1st for cadaver-4

	AIR	Percentage 1st Rate Pressure Change				
	Overpressure	front 1	right	back	left	front 2
ventricle	20%	**70.64**	**39.92**	**4.07**	**-136.76**	**52.10**
ventricle	50%	**136.99**	**112.65**	**57.18**	**-181.42**	**143.91**
frontal	20%	**38.35**	**57.78**	**60.51**	**9.12**	**34.86**
frontal	50%	**98.35**	**77.23**	**122.75**	**59.86**	**90.00**
parietal	20%	**10.85**	**43.62**	**51.12**	**0.54**	**-5.59**
parietal	50%	**52.92**	**186.52**	**NA**	**4.63**	**27.80**
occipital	20%	**151.33**	**37.43**	**148.87**	**514.81**	**75.59**
occipital	50%	**380.53**	**123.22**	**375.15**	**486.11**	**122.46**

Percentage of change for maximum, minimum and differential pressure for cadaver-4.

The increase of pressure measured by the sensors is compared with the increase in the blast intensity (overpressure). The 10psi test was used as reference.

PERCENTAGES for CADAVER-4						
	AIR	**Percentage Increase in Maximun Peak Pressure**				
	Overpressure	front 1	right	back	left	front 2
ventricle	20%	**82**	**4**	**27**	**92**	**49**
ventricle	50%	**156**	**20**	**47**	**79**	**150**
frontal	20%	**38**	**45**	**38**	**-4**	**45**
frontal	50%	**97**	**124**	**107**	**130**	**109**
parietal	20%	**45**	**-2**	**41**	**32**	**22**
parietal	50%	**95**	**-6**	**NA**	**107**	**159**
occipital	20%	**136**	**44**	**139**	**137**	**49**
occipital	50%	**237**	**119**	**302**	**261**	**185**
	AIR	**Percentage Increase in Minimum Peak Pressure**				
	Overpressure	front 1	right	back	left	front 2
ventricle	20%	**17**	**112**	**38**	**95**	**131**
ventricle	50%	**23**	**190**	**109**	**112**	**-42**
frontal	20%	**17**	**43**	**38**	**14**	**4**
frontal	50%	**47**	**127**	**86**	**76**	**2**
parietal	20%	**45**	**27**	**16**	**52**	**40**
parietal	50%	**70**	**446**	**NA**	**607**	**105**
occipital	20%	**126**	**59**	**48**	**89**	**56**
occipital	50%	**190**	**89**	**41**	**247**	**118**
	AIR	**Percentage Increase in Pressure Differential**				
	Overpressure	front 1	right	back	left	front 2
ventricle	20%	**69**	**28**	**32**	**94**	**36**
ventricle	50%	**129**	**57**	**75**	**90**	**112**
frontal	20%	**34**	**45**	**38**	**5**	**36**
frontal	50%	**87**	**125**	**95**	**104**	**86**
parietal	20%	**45**	**12**	**33**	**44**	**31**
parietal	50%	**82**	**205**	**NA**	**393**	**133**
occipital	20%	**131**	**51**	**107**	**109**	**52**
occipital	50%	**212**	**106**	**211**	**252**	**150**

Strain gages status during testing of cadaver-4.

Rosettes were used to measure strain; therefore for complete data, three grids needed to be working.

Strain gages status for cadaver-4						
10psi	front 1	right	back	left	front 2	
Frontal S.G.	2	1	1	1	1	
Zygomatic S.G.	2	3	2	2	2	
Temporal S.G.	3	3	3	3	3	
Parietal S.G.	3	3	3	3	3	
Occipital S.G.	3	3	3	3	3	
12psi	front 1	right	back	left	front 2	
Frontal S.G.	1	2	2	1	1	
Zygomatic S.G.	2	2	2	3	1	
Temporal S.G.	3	3	3	3	3	
Parietal S.G.	3	3	3	3	3	
Occipital S.G.	3	3	3	3	3	
15psi	front 1	right	back	left	front 2	back 2
Frontal S.G.	2	2	3	2	1	3
Zygomatic S.G.	1	1	1	1	1	1
Temporal S.G.	3	3	3	3	3	3
Parietal S.G.	3	3	3	3	3	3
Occipital S.G.	3	3	3	3	3	3

0	0 grids working
1	1 grid working
2	2 grids working
3	3 grids working

CADAVER 5 DATA

Test 1 Front 1 Orientation Cadaver-5

FILTERED DATA

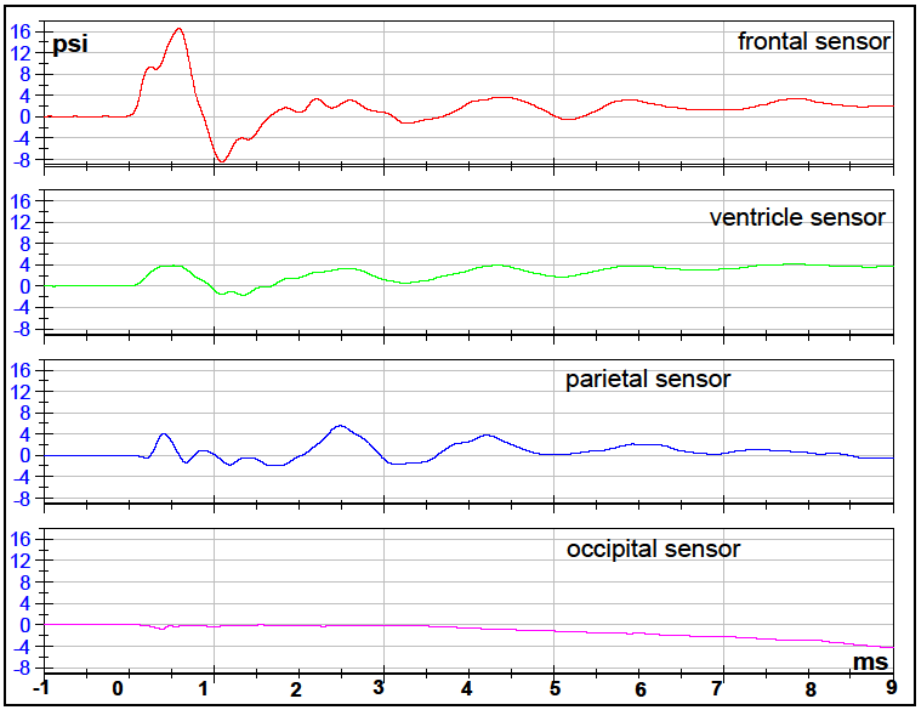

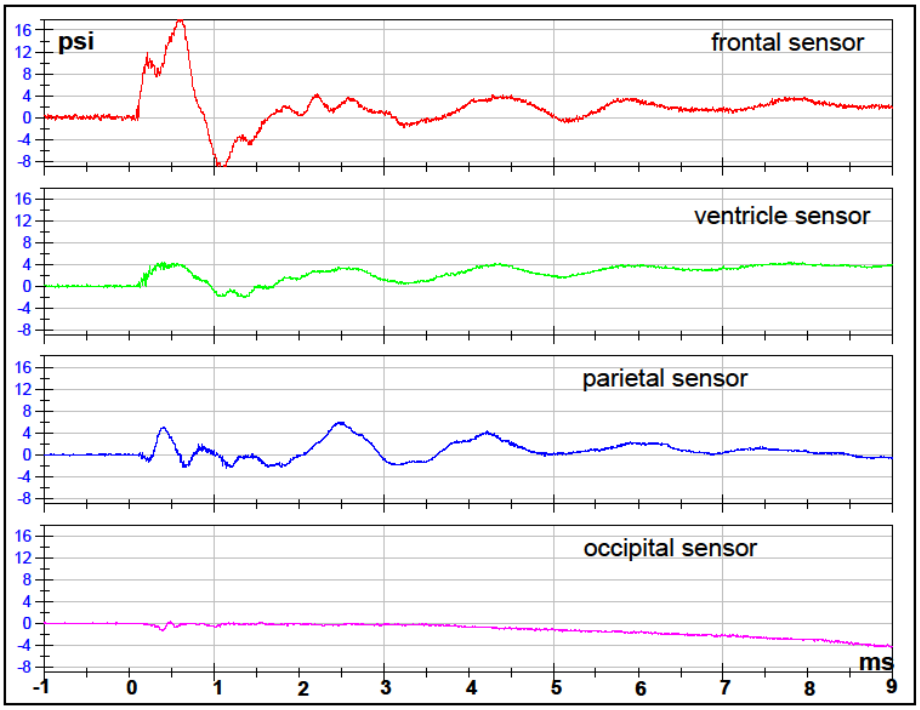

RAW DATA

Test 2 Left Orientation Cadaver-5

FILTERED DATA

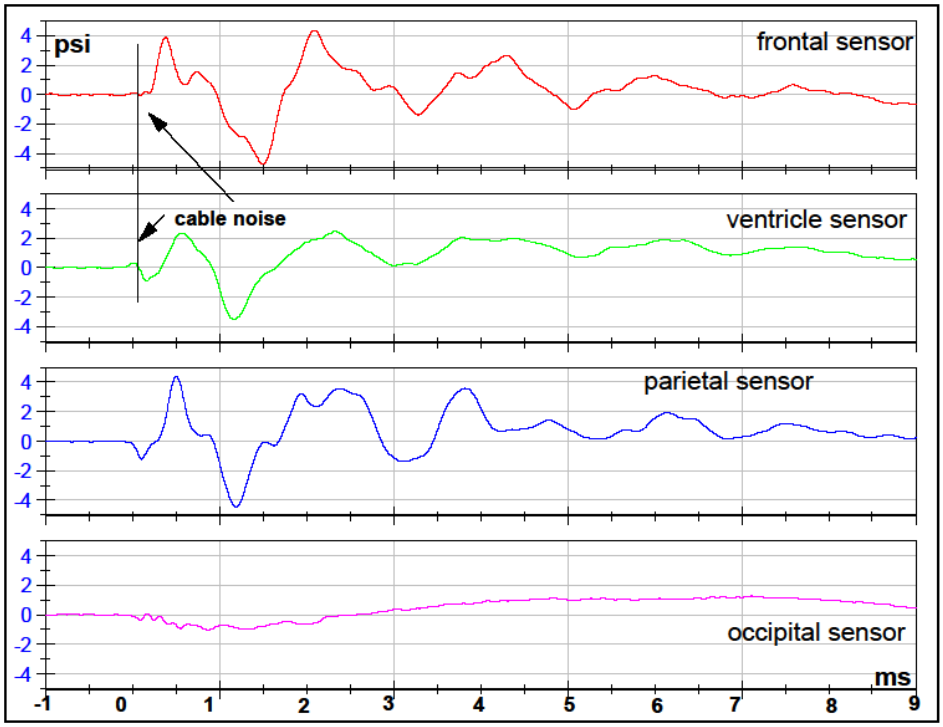

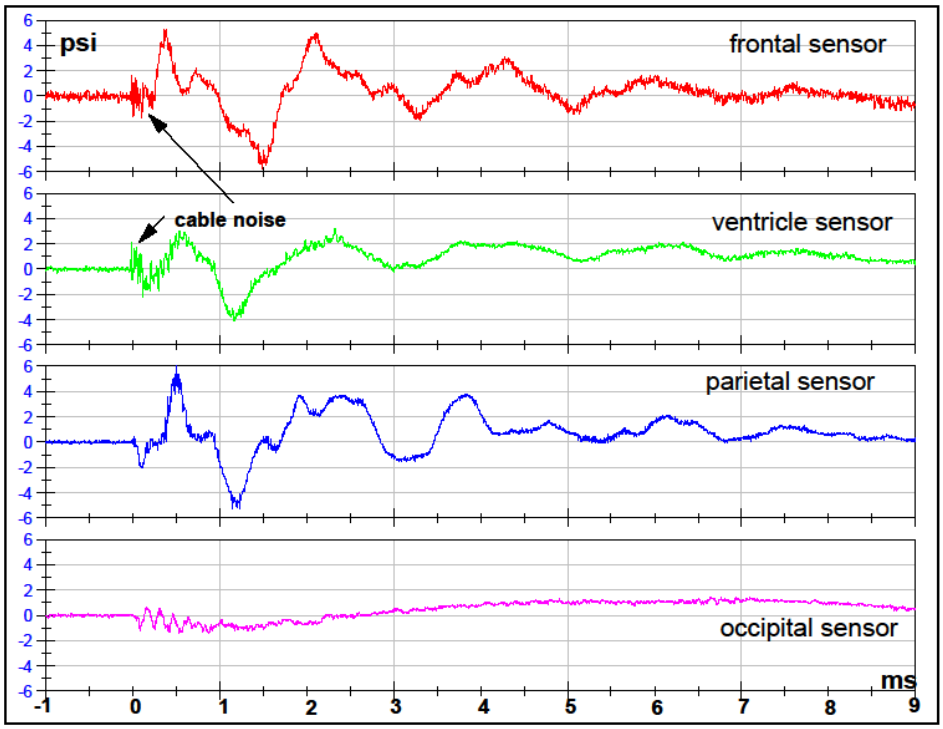

RAW DATA

Test 3 Back Orientation Cadaver-5

FILTERED DATA

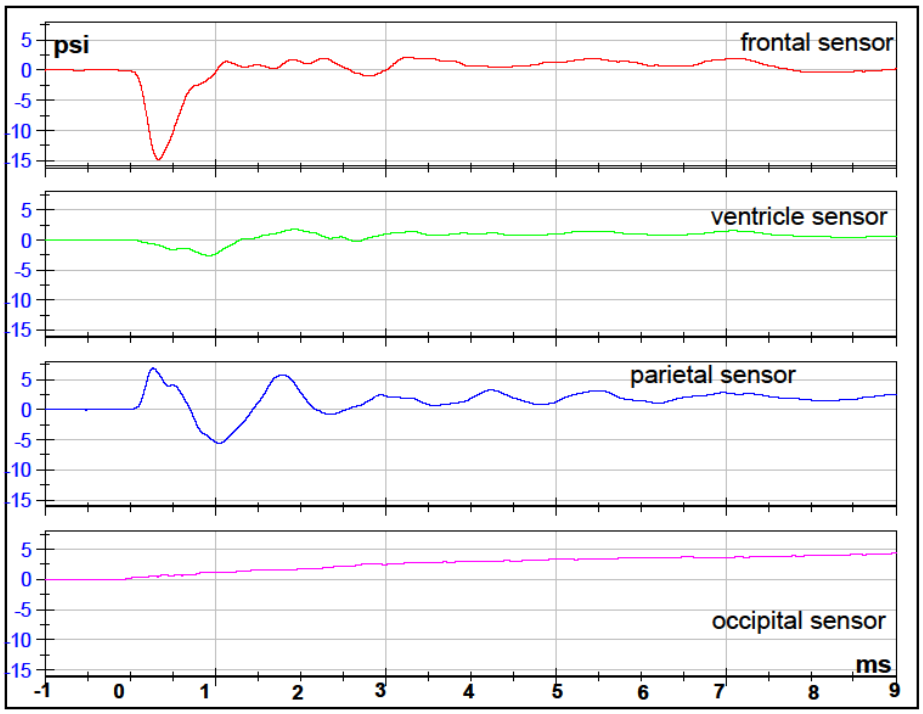

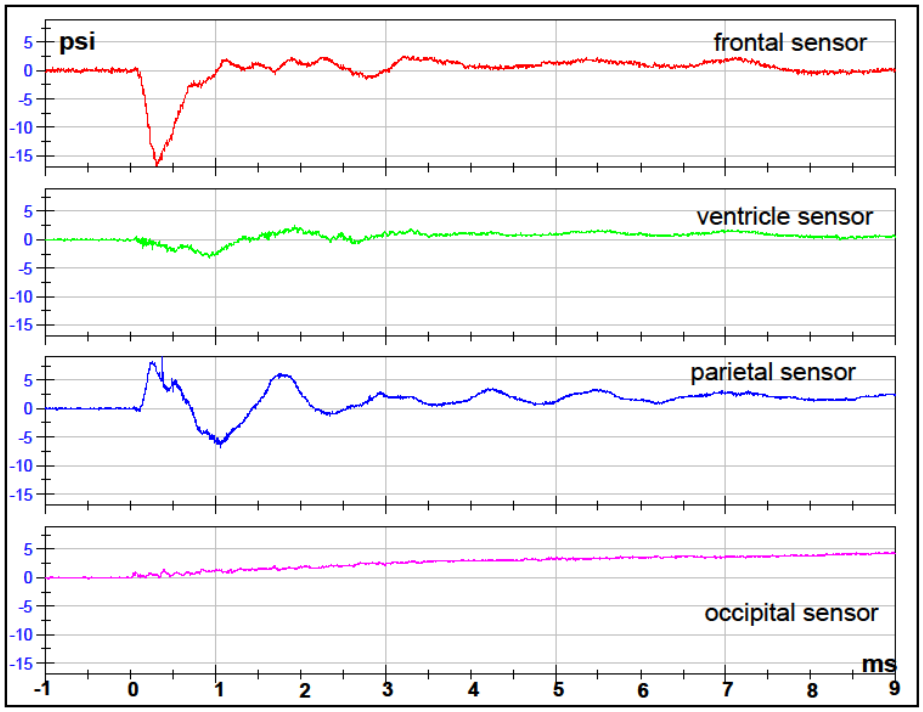

RAW DATA

Test 4 Right Orientation Cadaver-5

FILTERED DATA

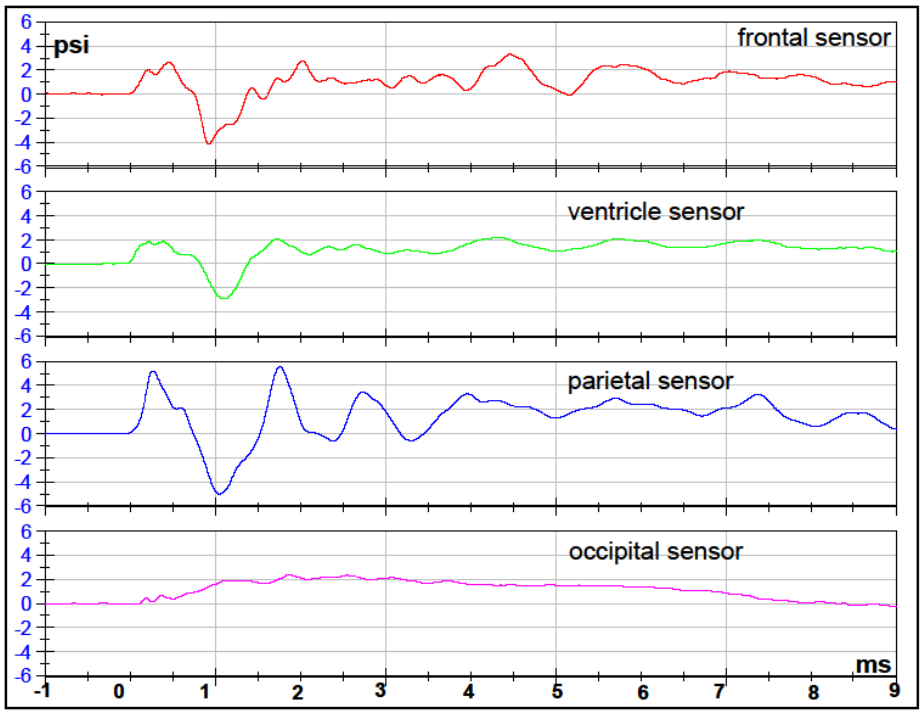

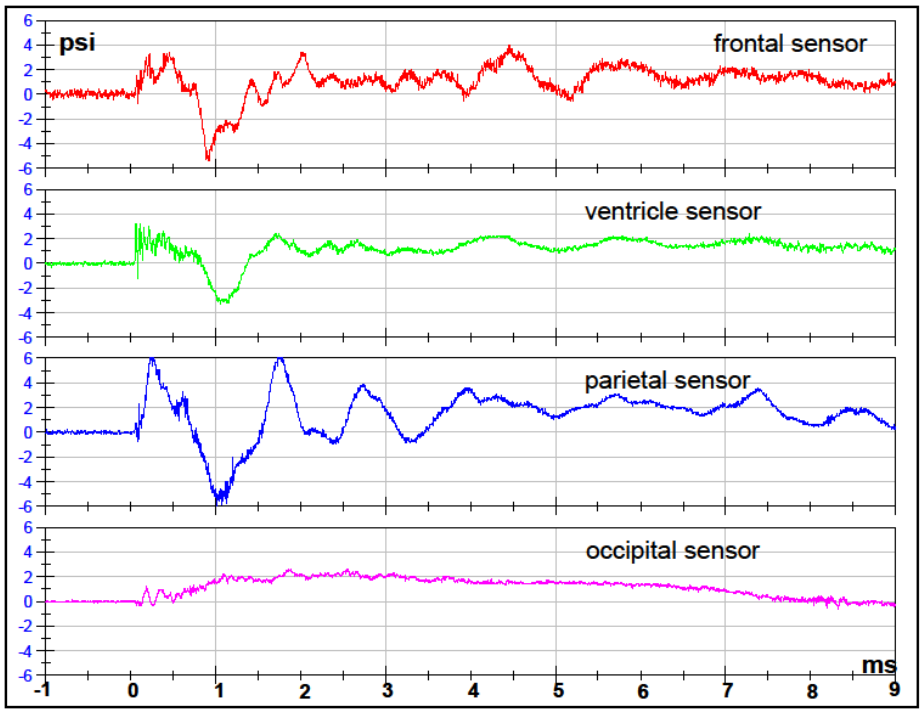

RAW DATA

Test 5 Front 2 Orientation Cadaver-5

FILTERED DATA

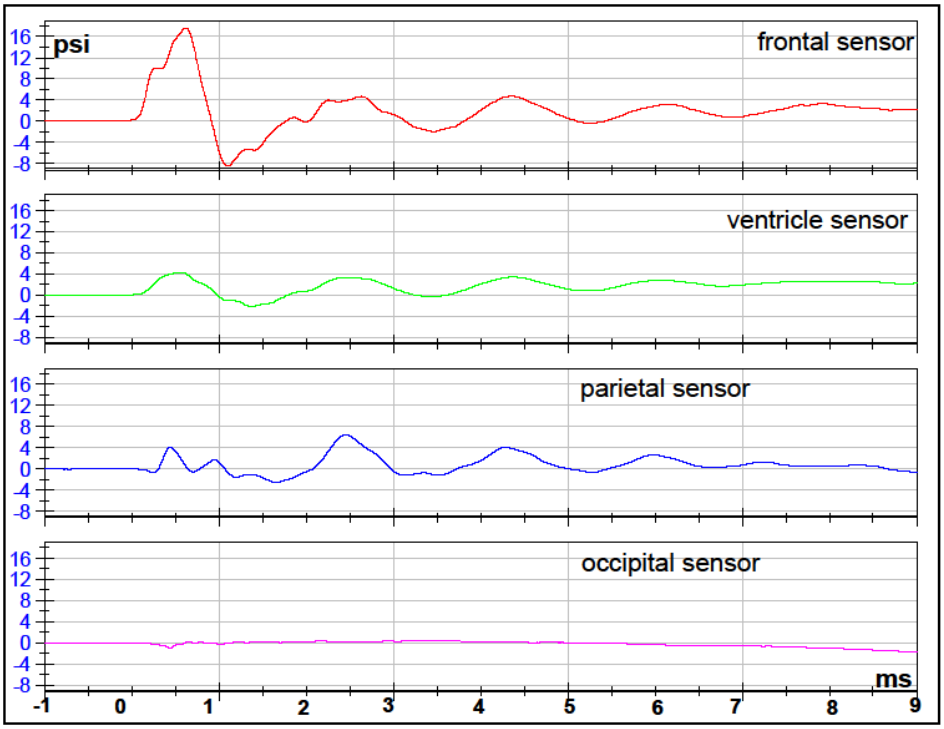

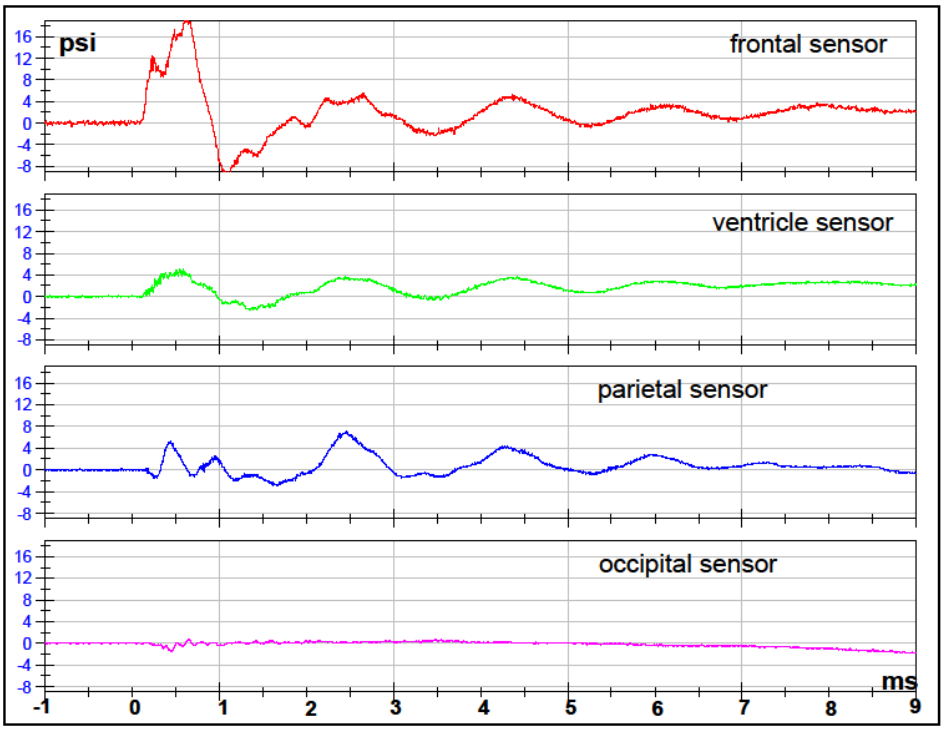

RAW DATA

Test 6 Front 1Orientation Cadaver-5

FILTERED DATA

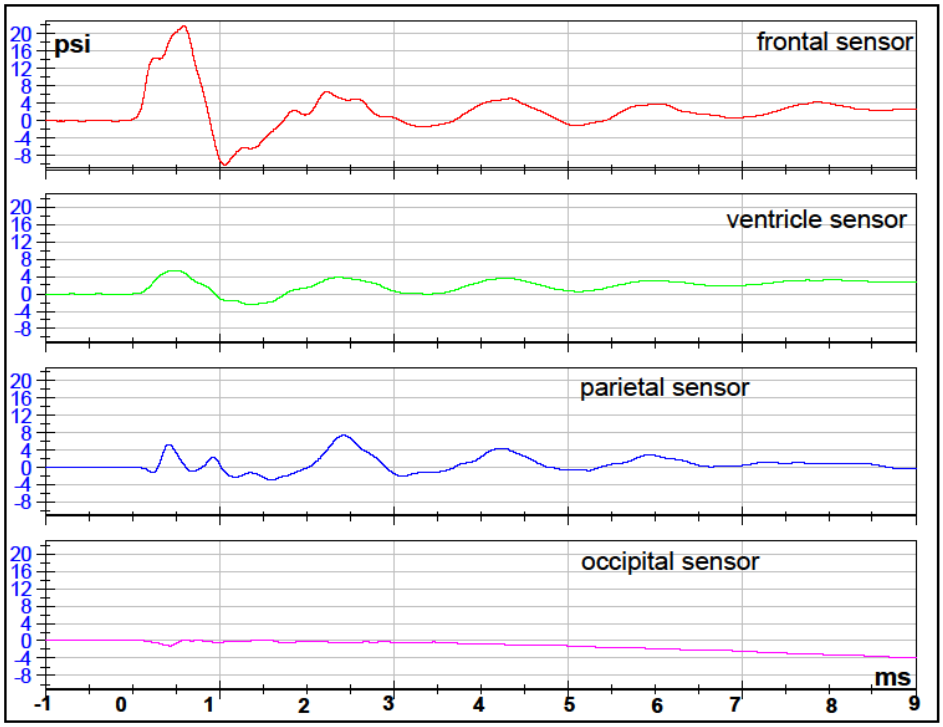

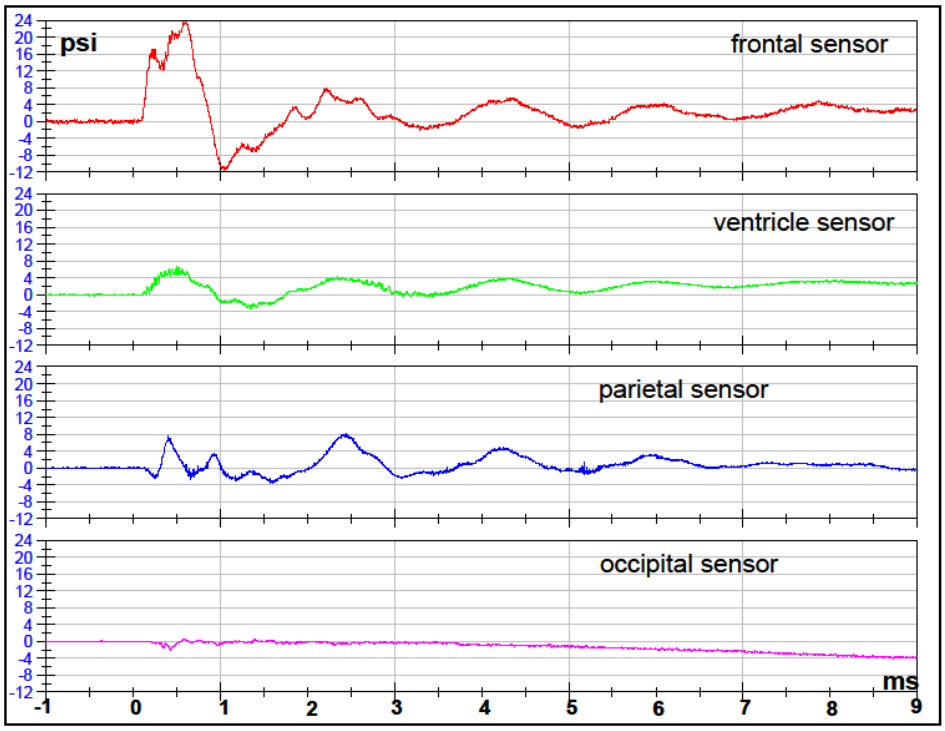

RAW DATA

Test 7 Right Orientation Cadaver-5

FILTERED DATA

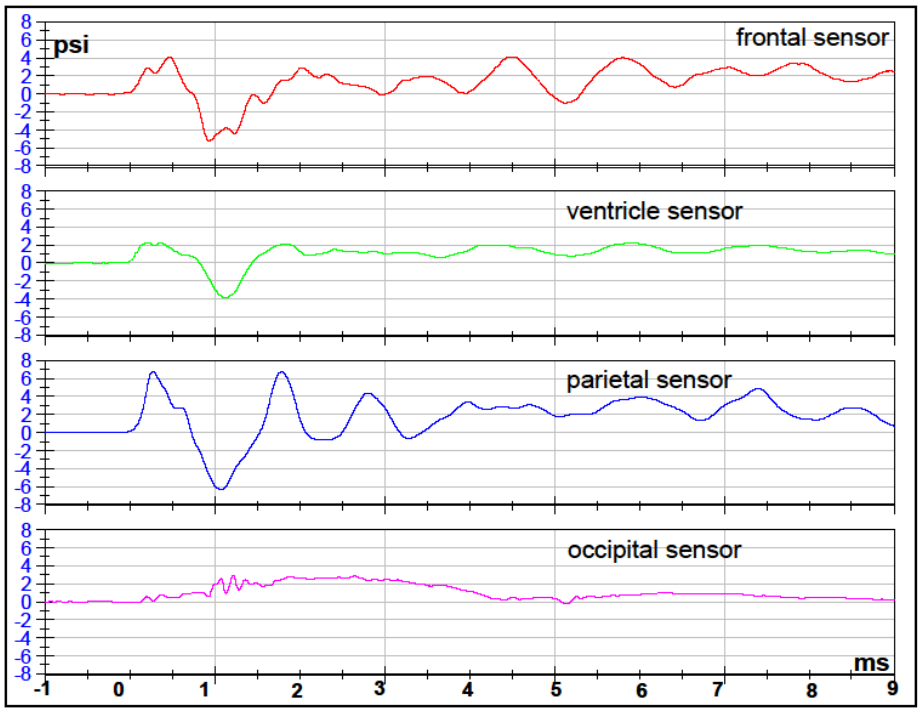

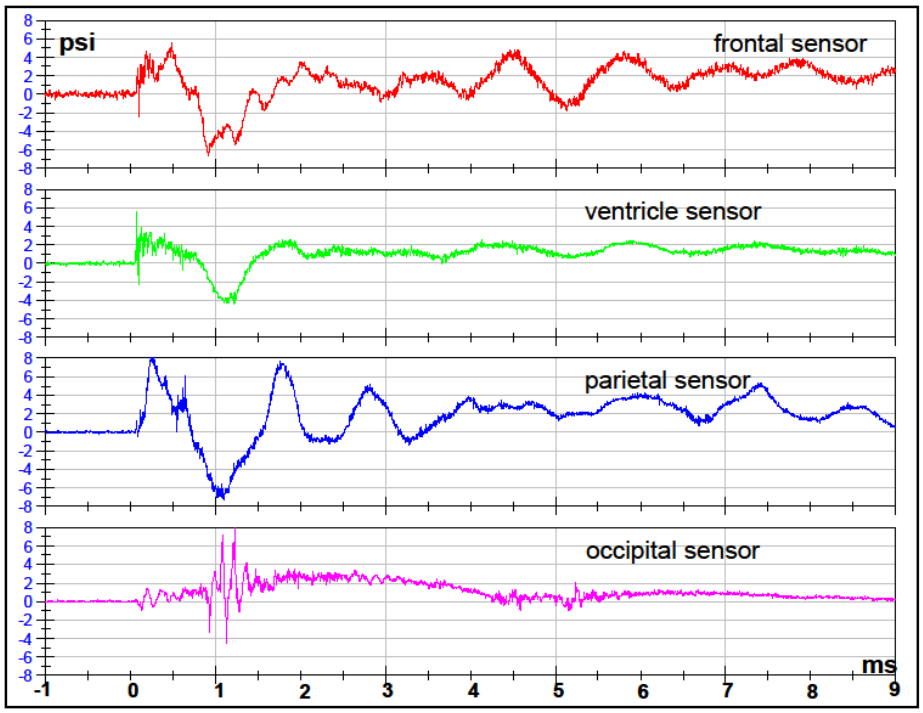

RAW DATA

Test 8 Back Orientation Cadaver-5

FILTERED DATA

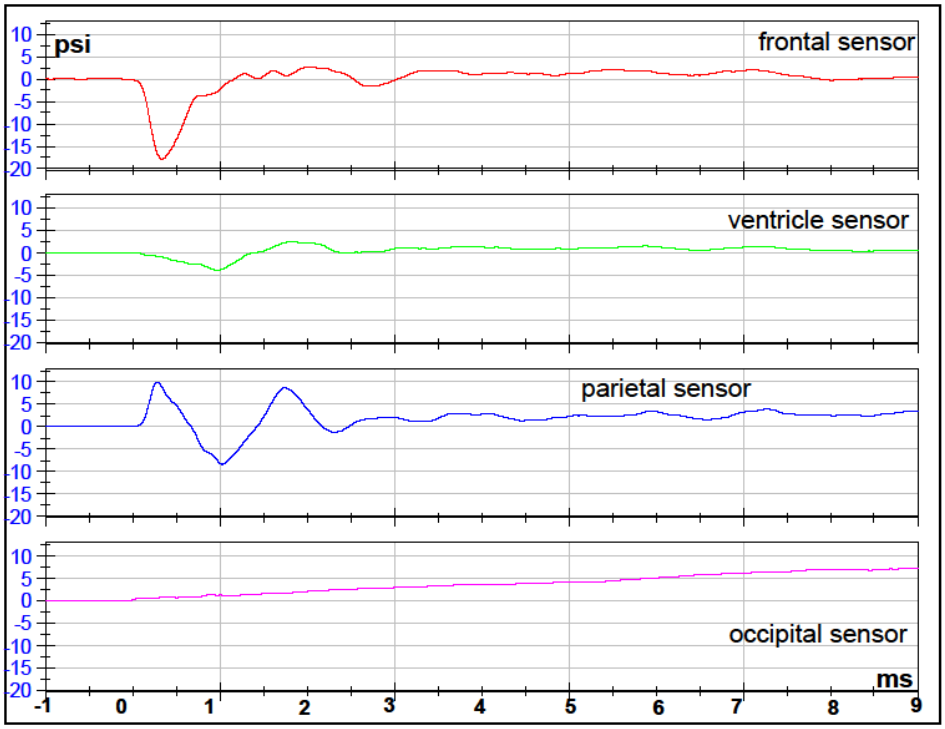

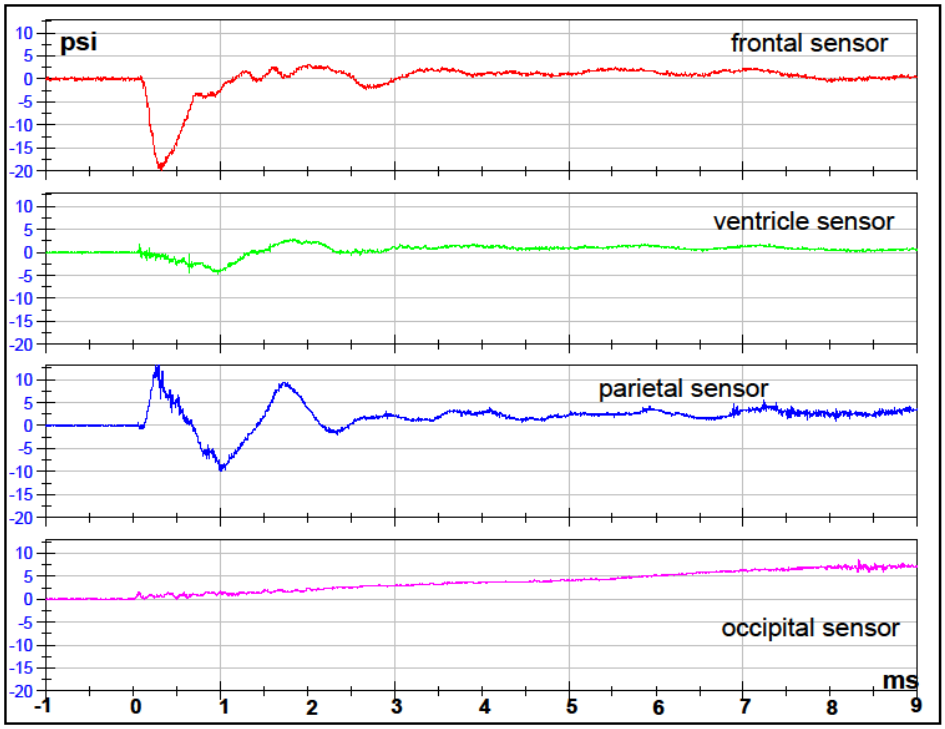

RAW DATA

Test 9 Left Orientation Cadaver-5

FILTERED DATA

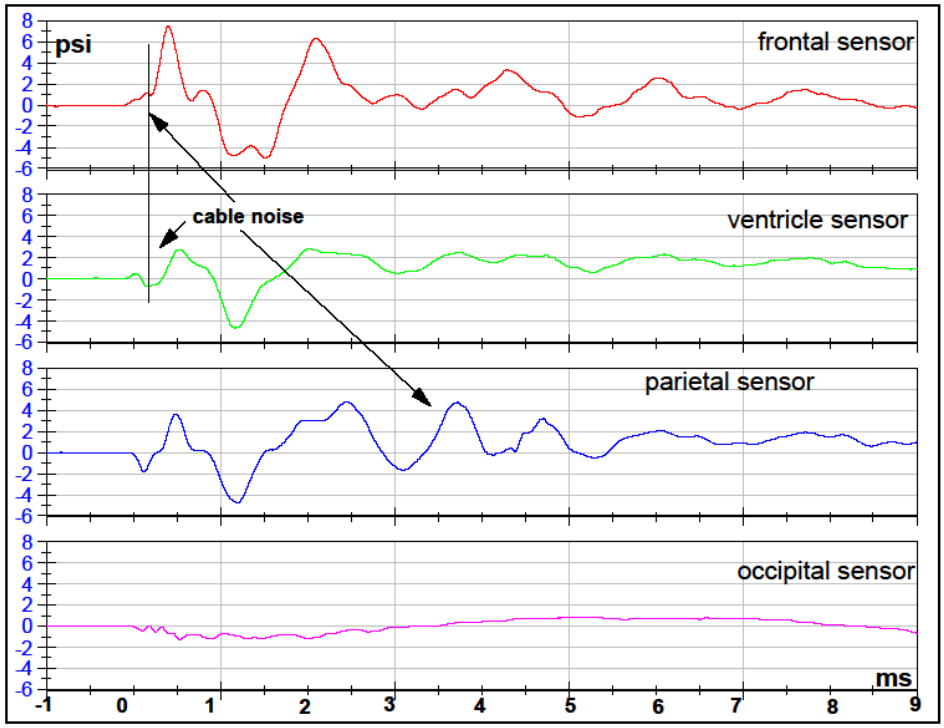

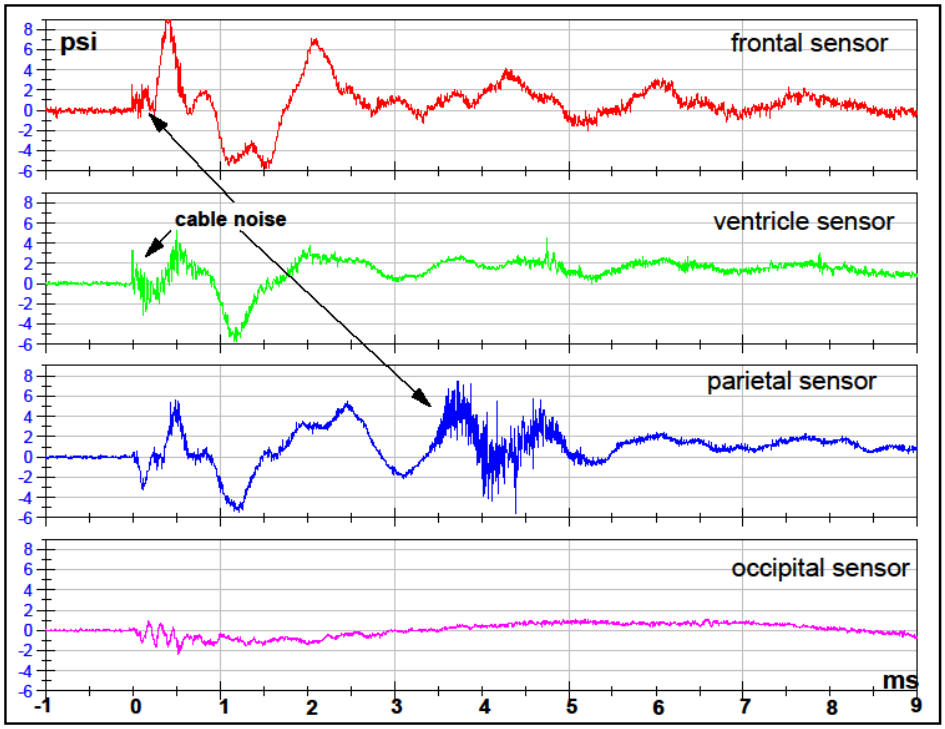

RAW DATA

Test 10 Front 2 Orientation Cadaver-5

FILTERED DATA

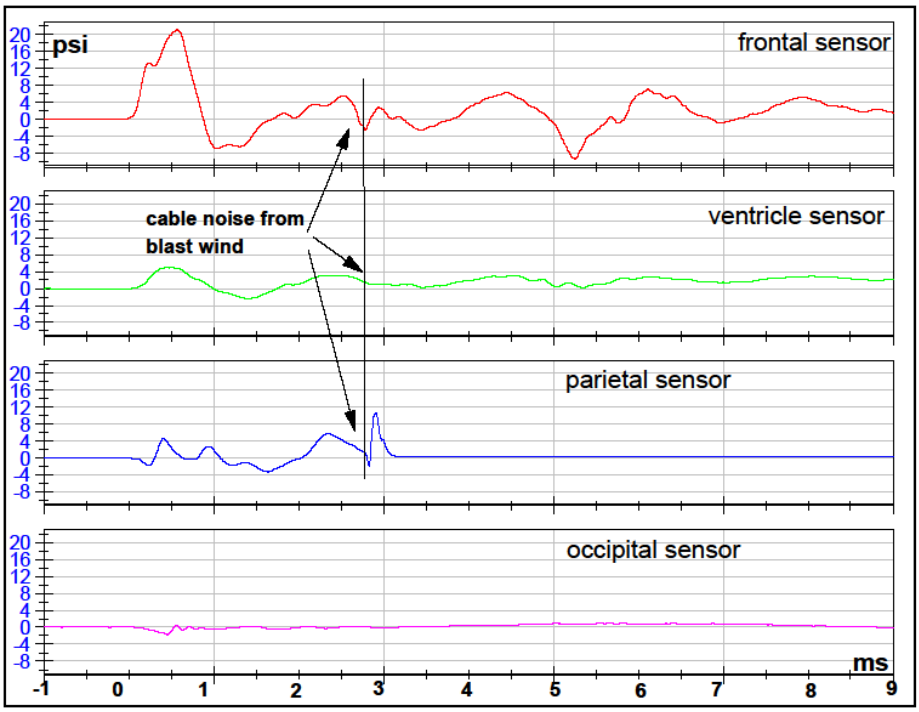

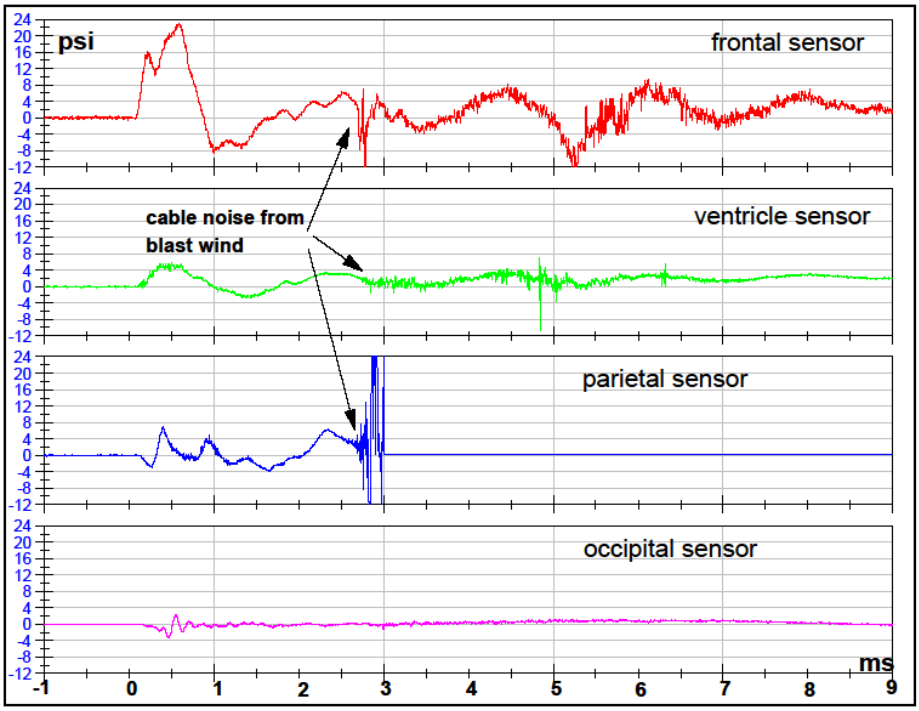

RAW DATA

Test 11 Front 1 Orientation Cadaver-5

FILTERED DATA

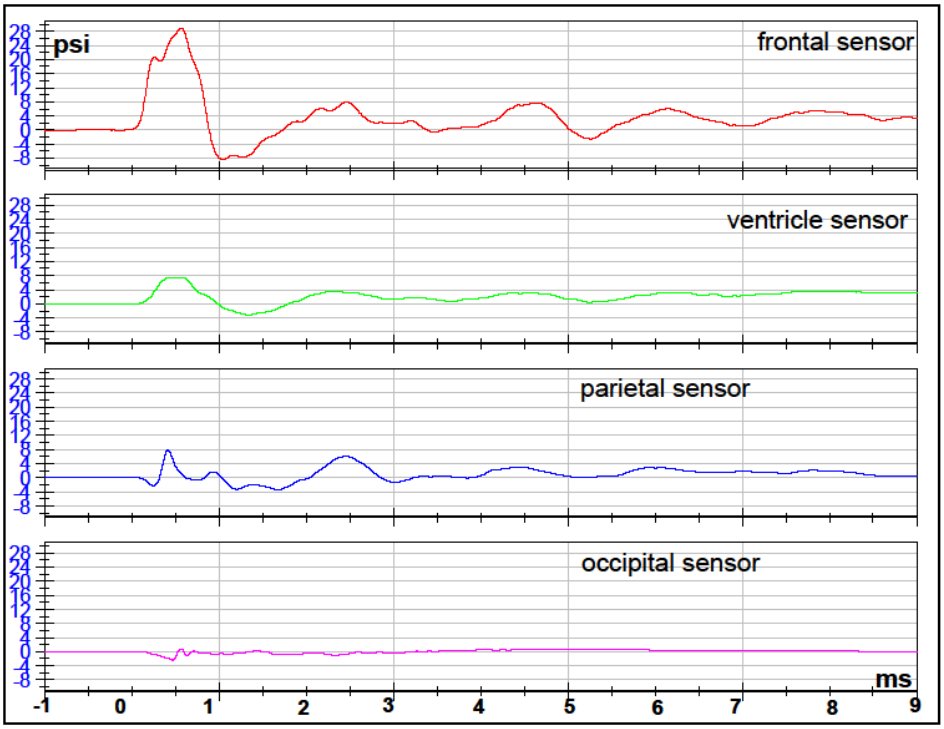

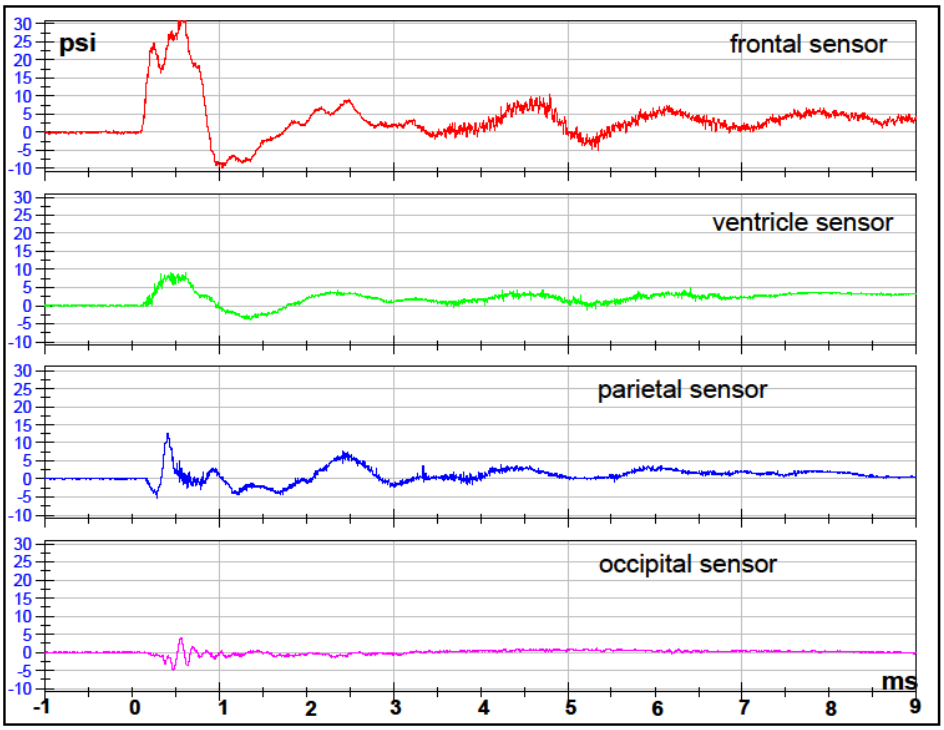

RAW DATA

Test 12 Left Orientation Cadaver-5

FILTERED DATA

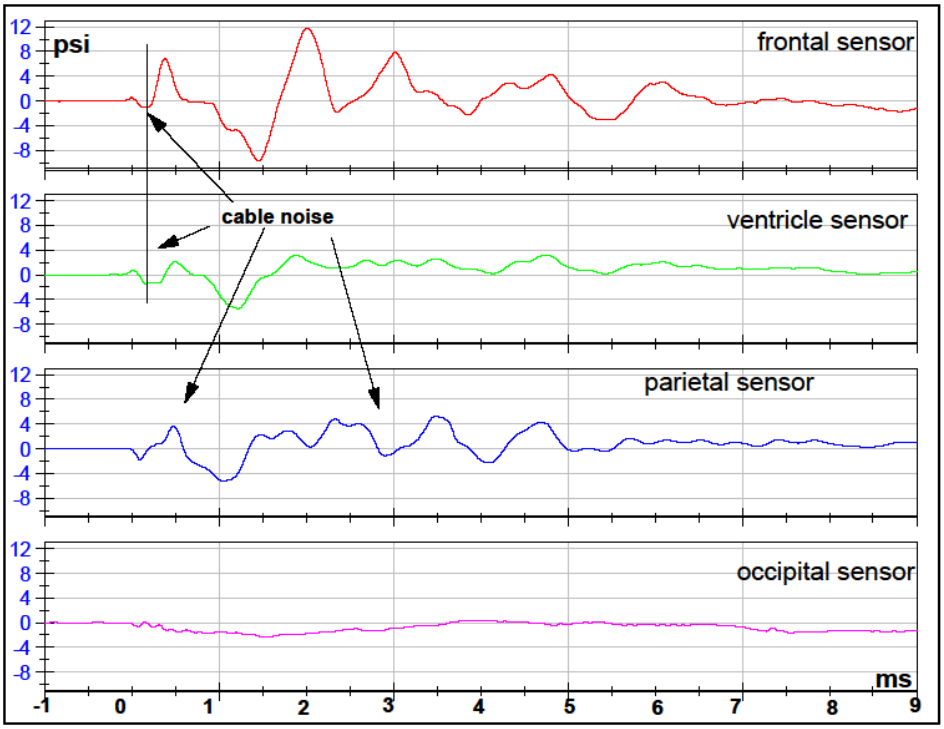

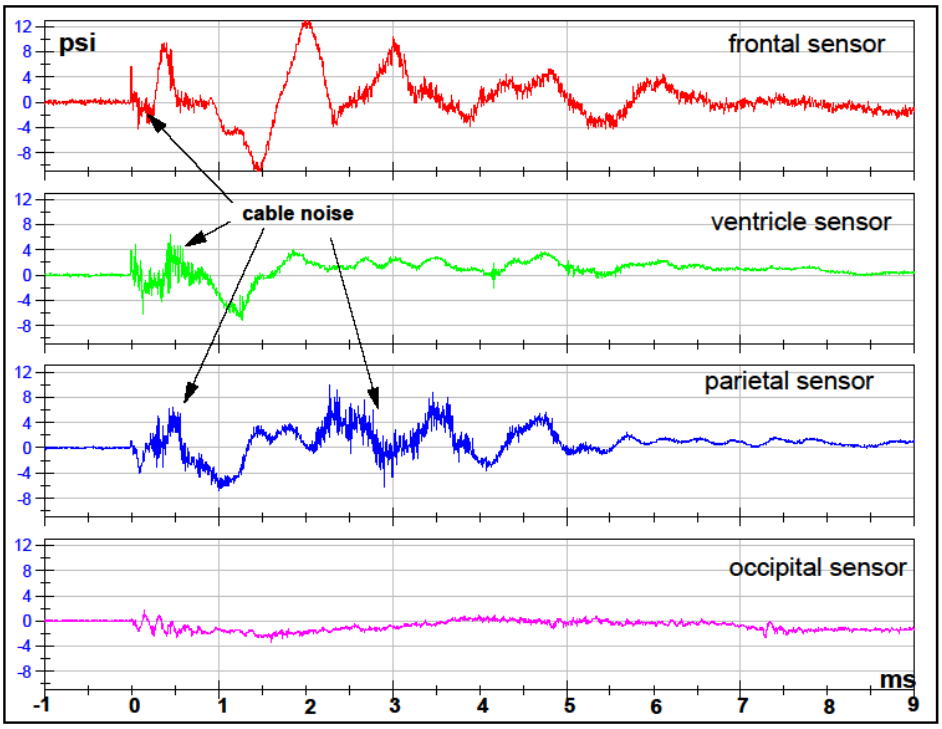

RAW DATA

Test 13 Back Orientation Cadaver-5

FILTERED DATA

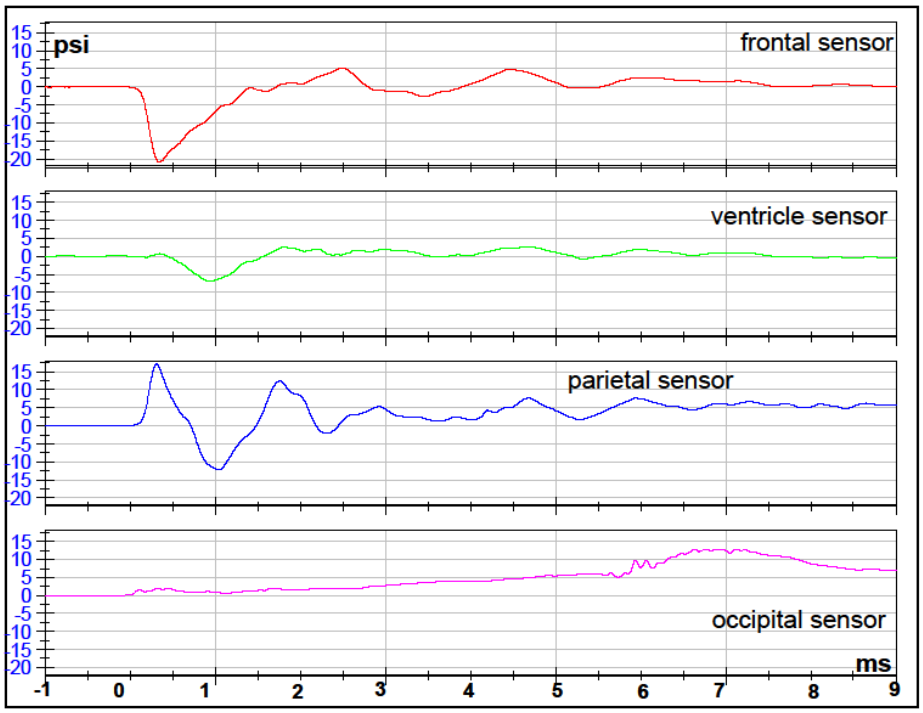

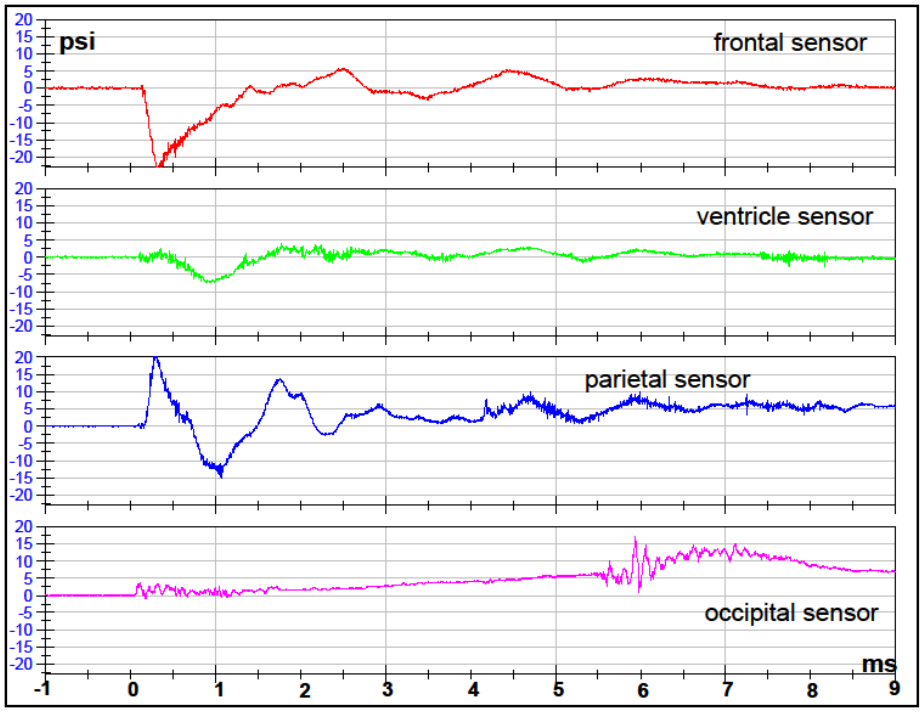

RAW DATA

Test 14 Right Orientation Cadaver-5

FILTERED DATA

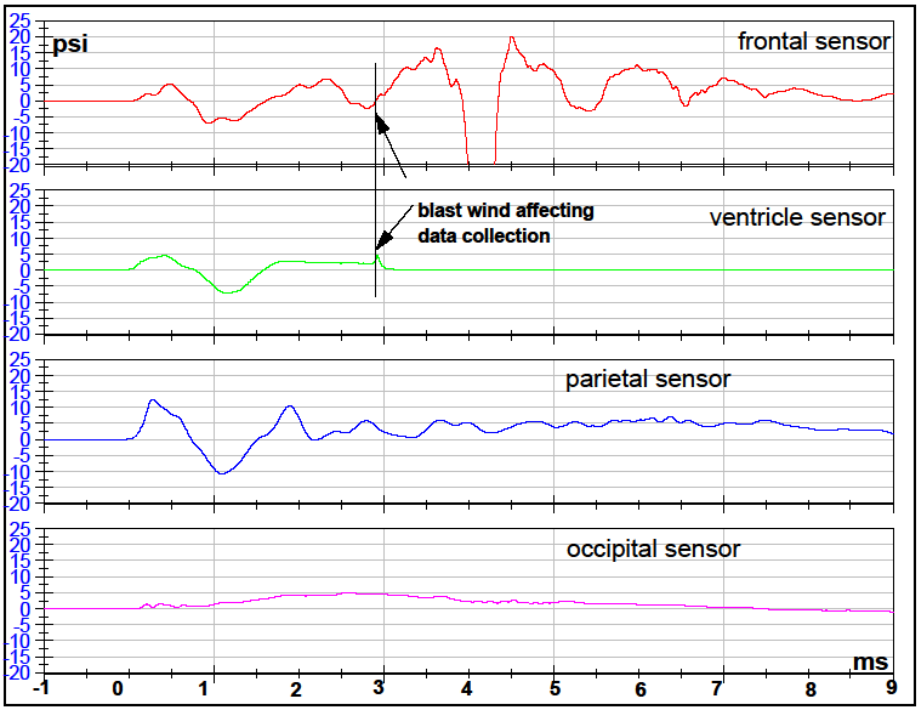

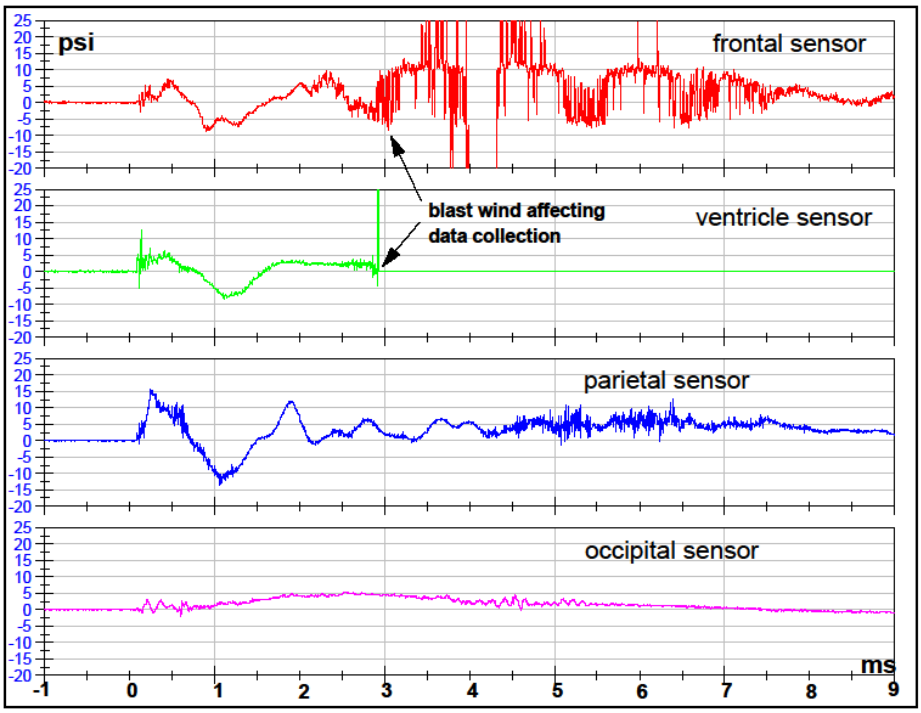

RAW DATA

Test 15 Front Orientation Cadaver-5

FILTERED DATA

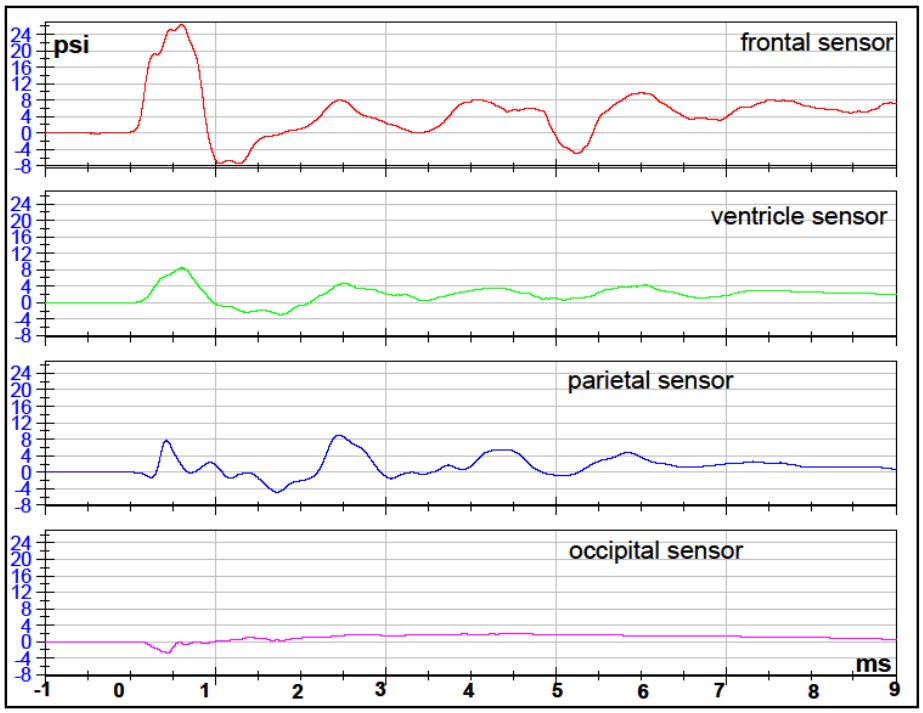

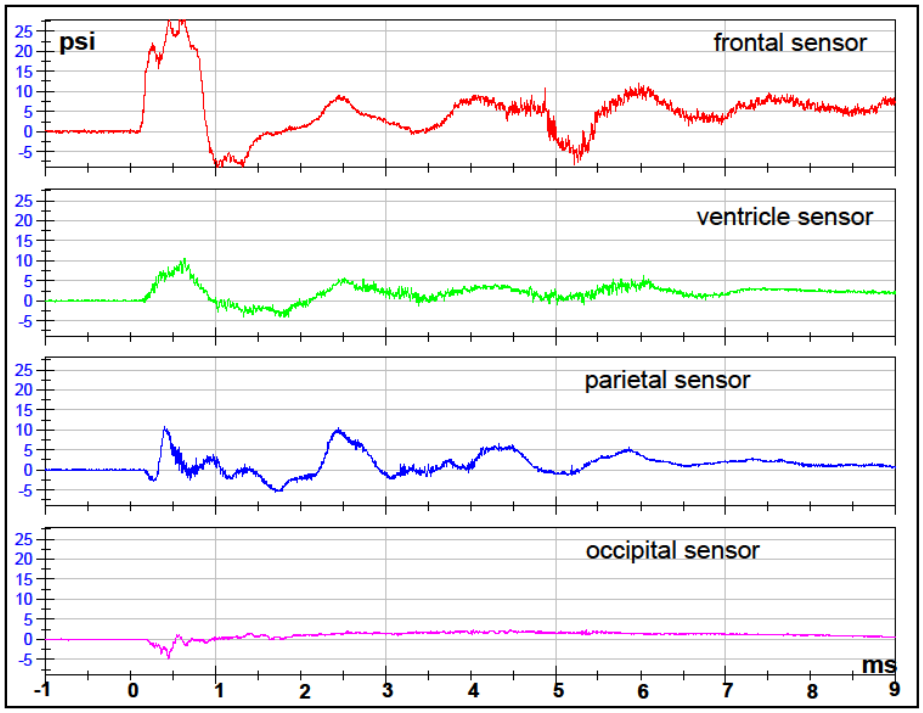

RAW DATA

Comparison for reproducibility of each pressure sensor in Front Orientations at 10psi Cadaver-5

VENTRICLE FILTERED DATA

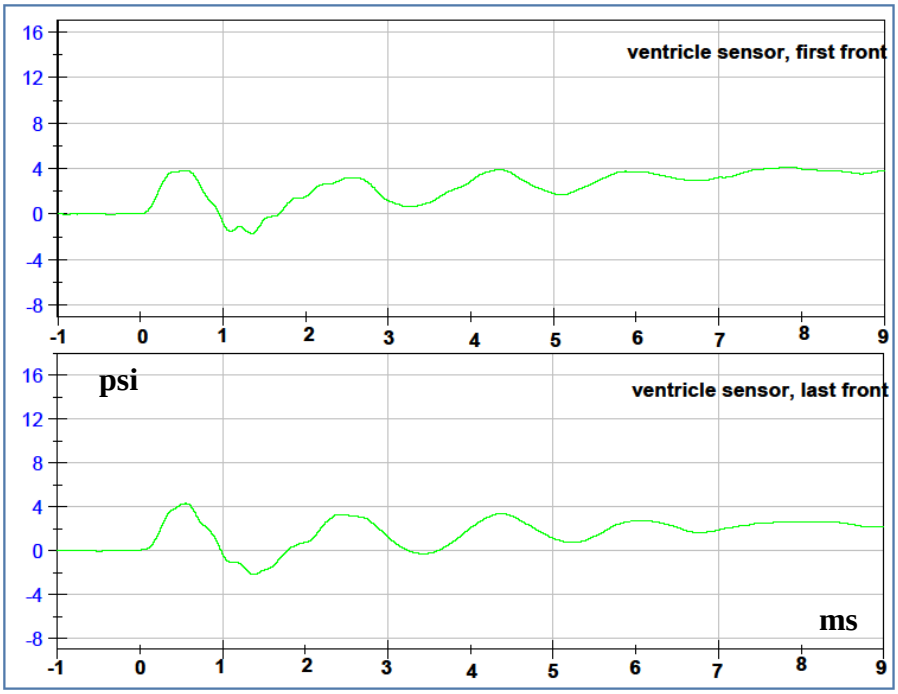

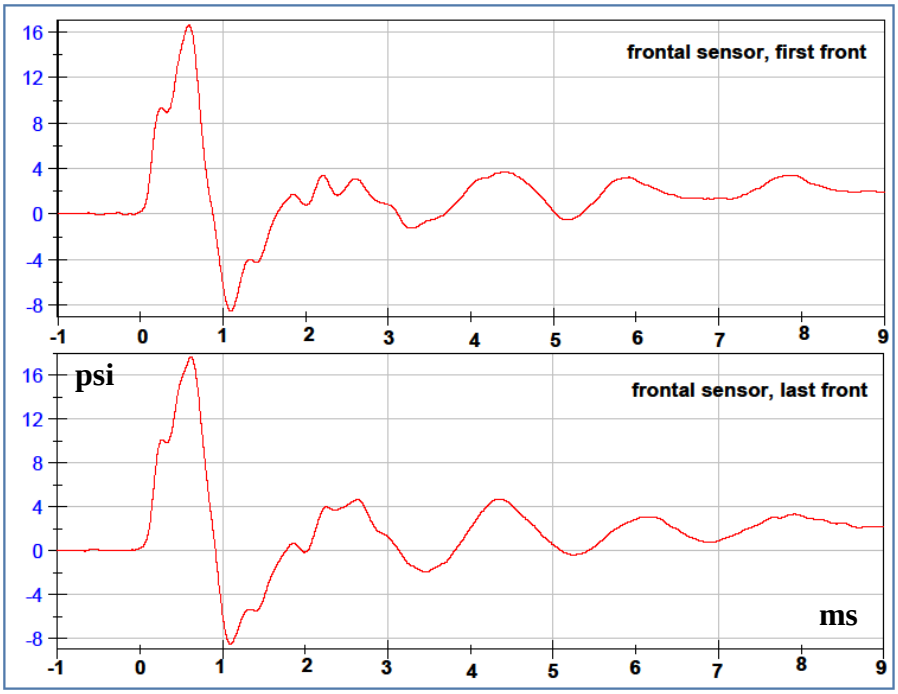

FRONTAL FILTERED DATA

Comparison for reproducibility of each pressure sensor in Front Orientations at 10psi Cadaver-5

PARIETAL FILTERED DATA

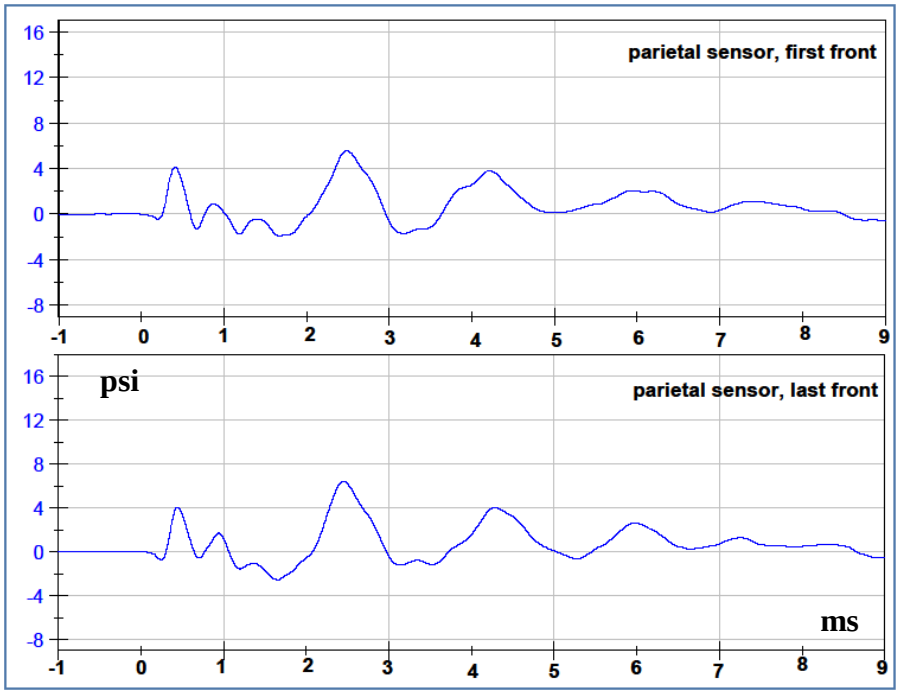

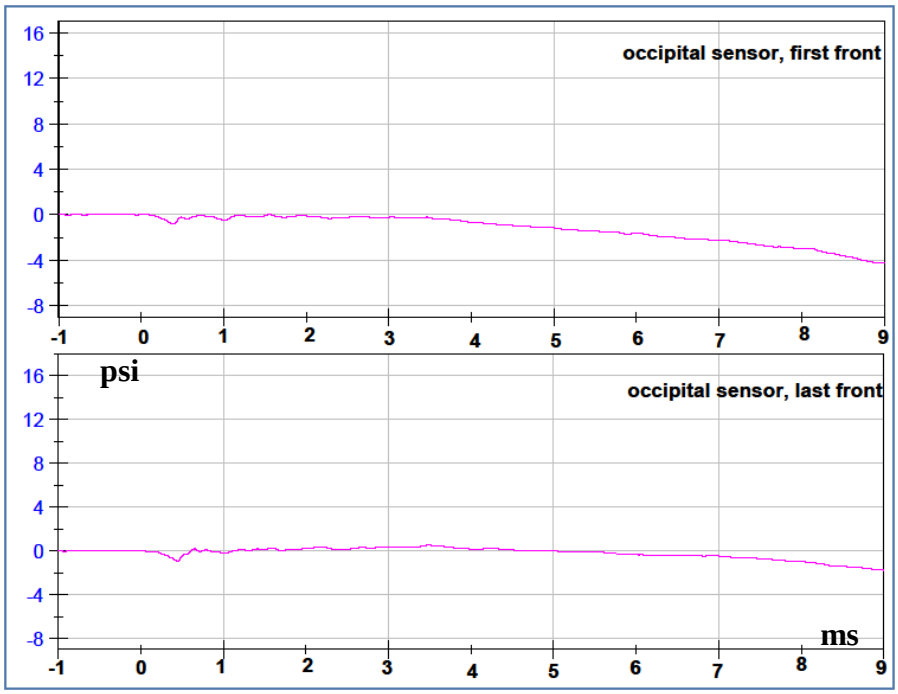

OCCIPITAL FILTERED DATA

Comparison for reproducibility of each pressure sensor in Front Orientations at 12psi Cadaver-5

VENTRICLE FILTERED DATA

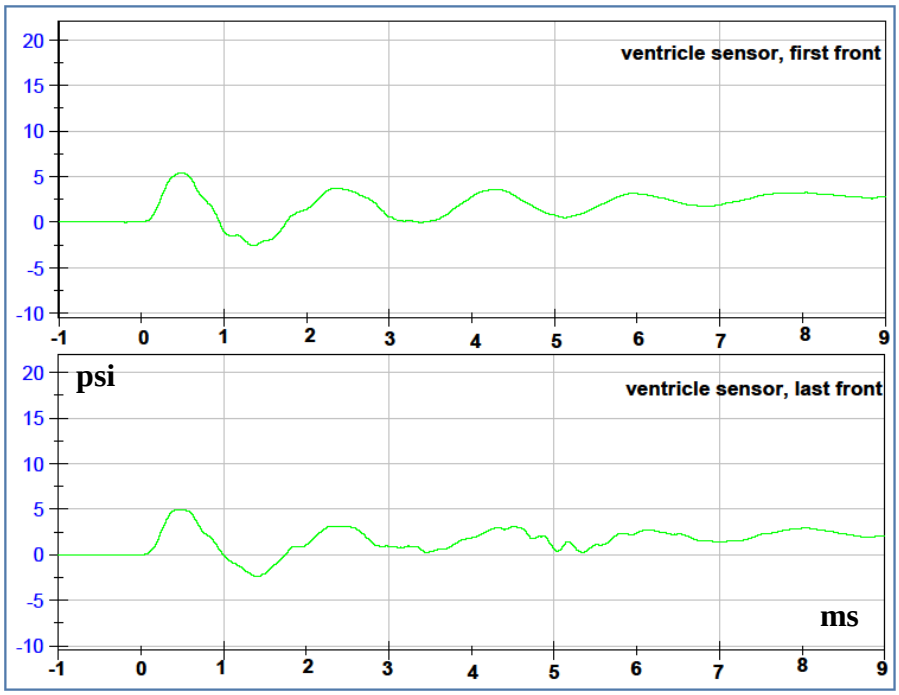

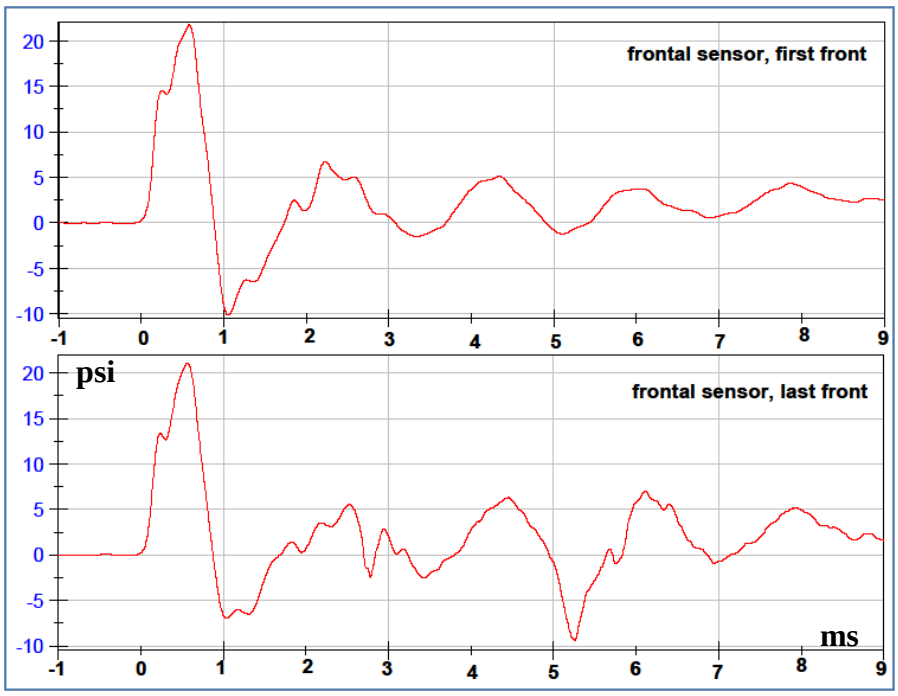

FRONTAL FILTERED DATA

Comparison for reproducibility of each pressure sensor in Front Orientations at 12psi Cadaver-5

PARIETAL FILTERED DATA

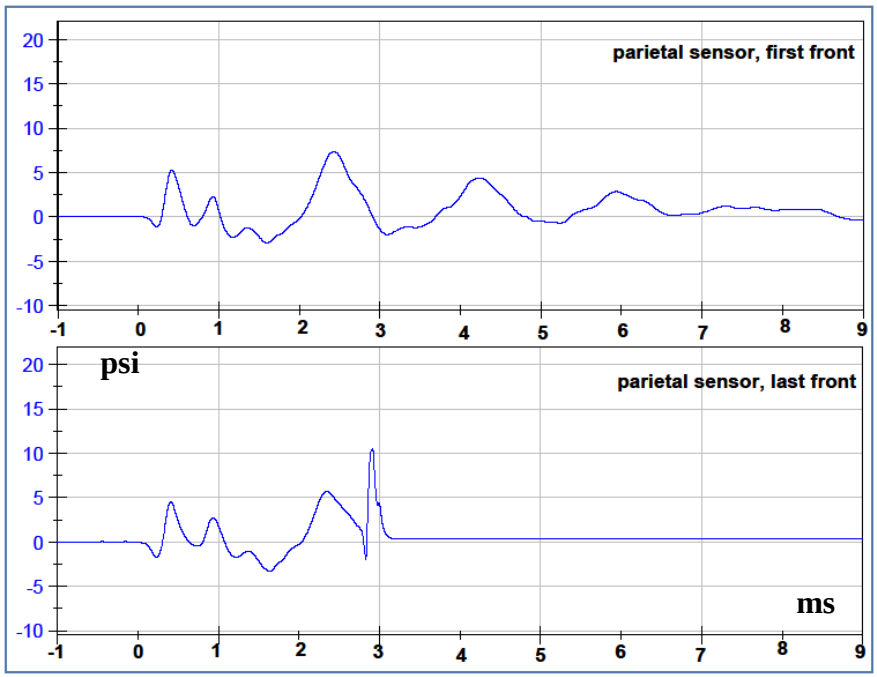

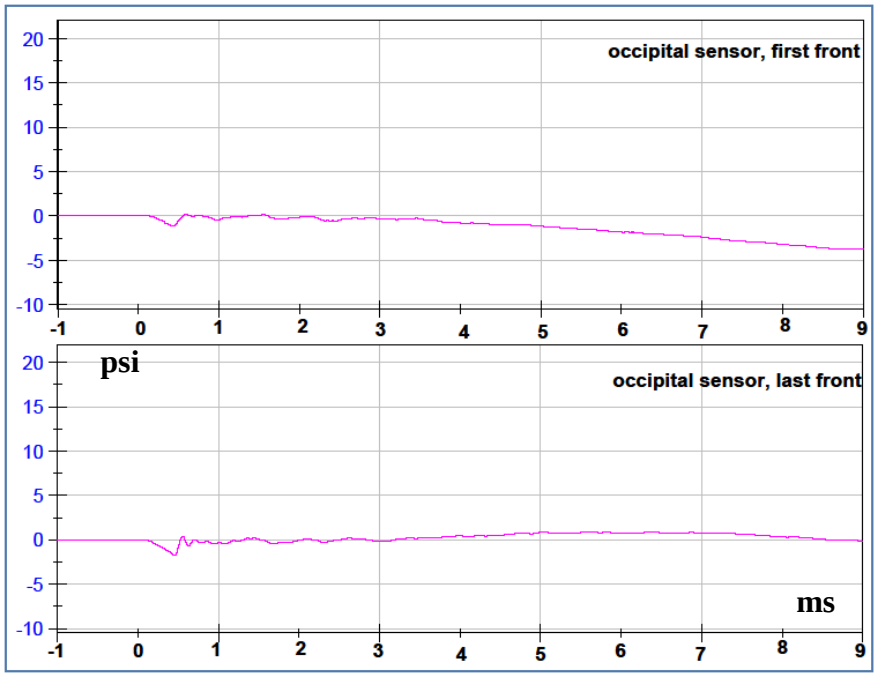

OCCIPITAL FILTERED DATA

Comparison for reproducibility of each pressure sensor in Front Orientations at 15psi Cadaver-5

VENTRICLE FILTERED DATA

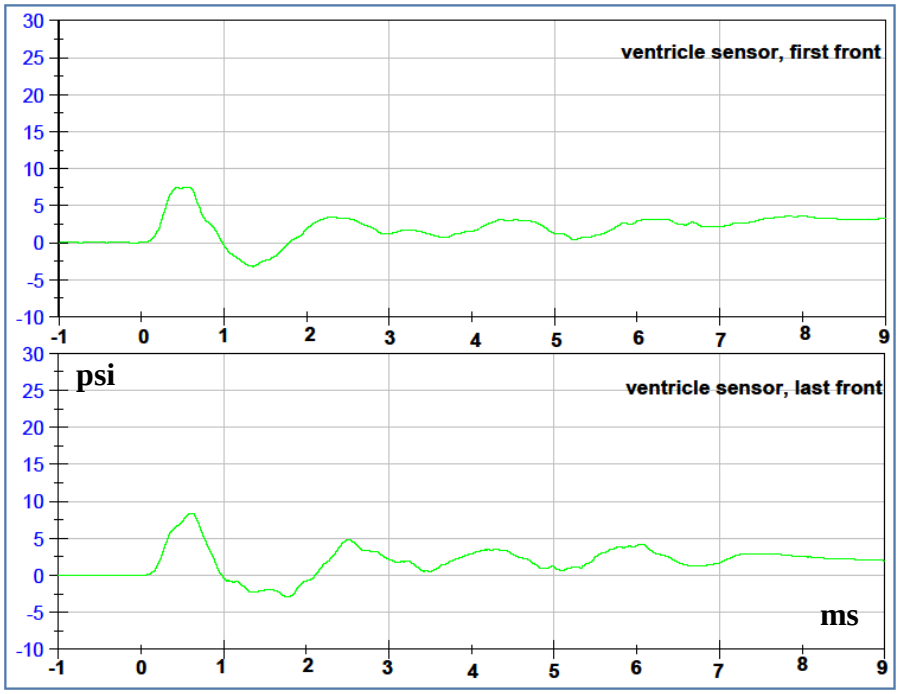

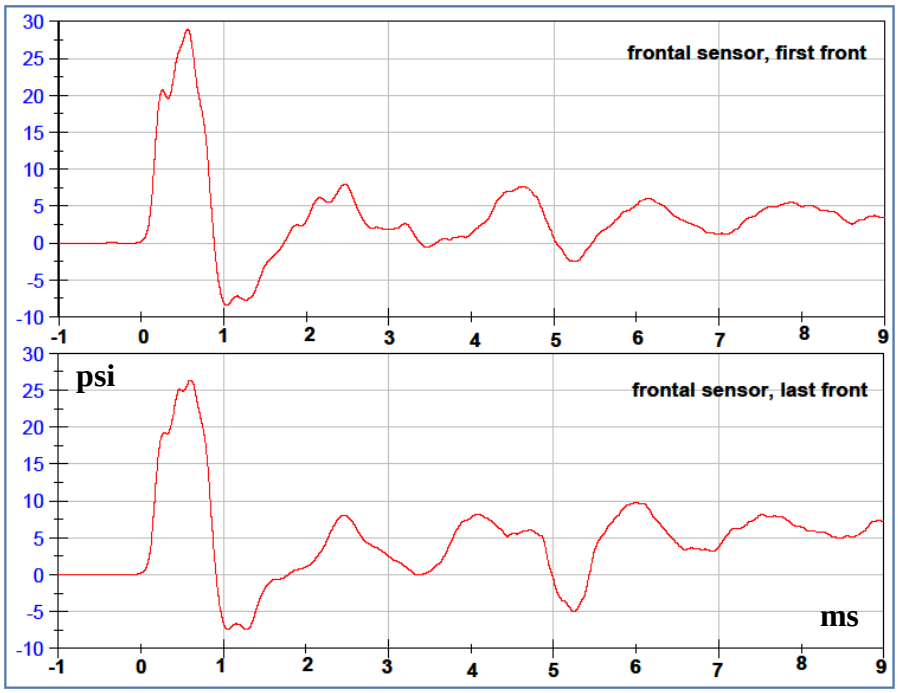

FRONTAL FILTERED DATA

Comparison for reproducibility of each pressure sensor in Front Orientations at 15psi Cadaver-5

PARIETAL FILTERED DATA

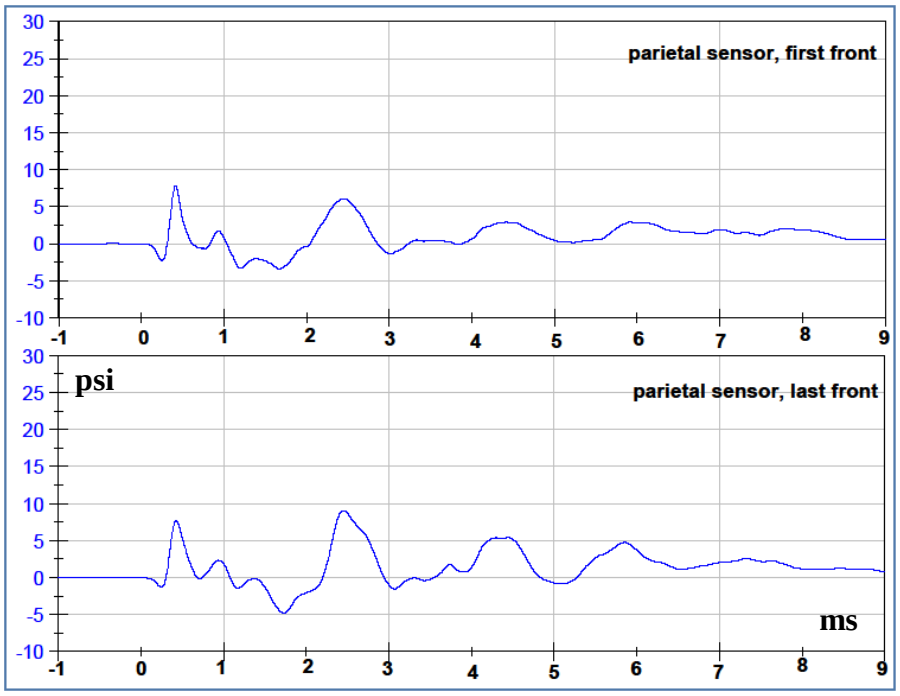

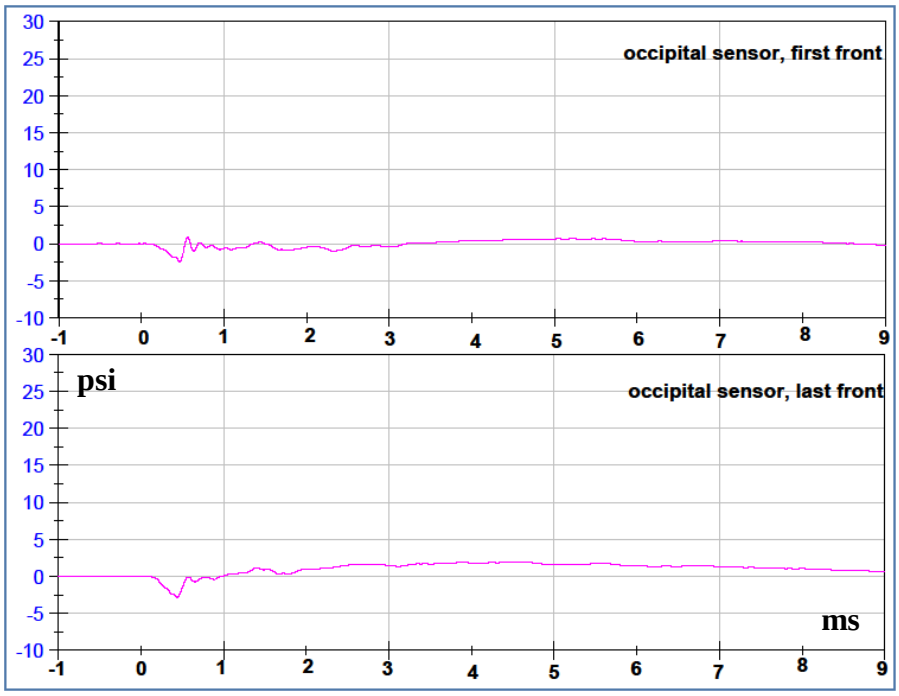

OCCIPITAL FILTERED DATA

Pressure extremes for cadaver-5.

The occipital values are highlighted because the sensor was placed at a different location: 10 mm from midline and 120 mm toward the back from the parietal sensor.

Pressure Extremes for cadaver-5 (psi)										
	Maximun Pressure					Minimum Pressure				
ventricle	front 1	right	back	left	front 2	front 1	right	back	left	front 2
10 psi air	**3.85**	**2.17**	**1.79**	**2.51**	**4.31**	**-1.7**	**-2.87**	**-2.6**	**-3.5**	**-2.12**
12 psi air	**5.39**	**2.28**	**2.48**	**2.87**	**4.94**	**-2.59**	**-3.81**	**-3.88**	**-4.67**	**-2.33**
15 psi air	**7.53**	**4.56**	**2.58**	**3.21**	**8.39**	**-3.18**	**-7.21**	**-6.85**	**-5.52**	**-2.92**
frontal	front 1	right	back	left	front 2	front 1	right	back	left	front 2
10 psi air	**16.58**	**3.29**	**2.14**	**4.32**	**17.56**	**-8.52**	**-4.15**	**-14.85**	**-4.75**	**-8.54**
12 psi air	**21.6**	**4.08**	**2.7**	**7.47**	**21.08**	**-10.17**	**-5.19**	**-17.78**	**-5.05**	**-9.37**
15 psi air	**28.91**	**6.78**	**5.16**	**11.73**	**26.29**	**-8.38**	**-7.11**	**-20.91**	**-9.75**	**-7.41**
parietal	front 1	right	back	left	front 2	front 1	right	back	left	front 2
10 psi air	**5.54**	**5.52**	**6.85**	**4.4**	**6.43**	**-1.89**	**-5.00**	**-5.62**	**-4.44**	**-2.54**
12 psi air	**7.37**	**6.76**	**9.94**	**4.77**	**5.68**	**-2.9**	**-6.32**	**-8.34**	**-4.73**	**-3.28**
15 psi air	**7.81**	**12.37**	**17.02**	**5.21**	**9.04**	**-3.29**	**-10.83**	**-12.11**	**-5.25**	**-4.8**
occipital	front 1	right	back	left	front 2	front 1	right	back	left	front 2
10 psi air	**0.02**	**2.49**	**3.73**	**1.27**	**0.533**	**-2.8**	**0.20**	**0.2**	**-1.04**	**-0.923**
12 psi air	**0.152**	**2.95**	**6.41**	**0.842**	**0.896**	**-2.89**	**-0.167**	**0.2**	**-1.25**	***-1.73**
15 psi air	**0.729**	**4.97**	**12.69**	**0.358**	**1.97**	**-2.42**	**0.2**	**0.2**	**-2.36**	**-2.8**

Pressure differentials for cadaver-5.

The occipital values are highlighted because the sensor was placed at a different location: 10 mm from midline and 120 mm toward the back from the parietal sensor.

Differential for cadaver-5										
	peak differential pressure (psi)					time elapsed between peaks (ms)				
ventricle	front 1	right	back	left	front 2	front 1	right	back	left	front 2
10 psi air	**5.55**	**5.04**	**4.39**	**6.01**	**6.43**	**0.788**	**3.24**	**1.02**	**1.15**	**0.816**
12 psi air	**7.99**	**6.09**	**6.36**	**7.54**	**7.27**	**0.852**	**0.888**	**0.864**	**0.844**	**0.896**
15 psi air	**10.71**	**11.77**	**9.43**	**8.72**	**11.31**	**0.76**	**0.744**	**3.72**	**3.54**	**1.14**
frontal	front 1	right	back	left	front 2	front 1	right	back	left	front 2
10 psi air	**25.09**	**7.44**	**16.99**	**9.06**	**26.11**	**0.5**	**3.52**	**2.93**	**0.616**	**0.492**
12 psi air	**31.77**	**9.27**	**20.48**	**12.52**	**30.45**	**0.488**	**0.472**	**1.71**	**1.12**	**4.68**
15 psi air	**37.3**	**13.89**	**26.07**	**21.48**	**33.7**	**0.484**	**1.35**	**2.15**	**0.556**	**0.664**
parietal	front 1	right	back	left	front 2	front 1	right	back	left	front 2
10 psi air	**7.43**	**10.52**	**12.47**	**8.84**	**8.97**	**0.82**	**0.72**	**0.78**	**0.688**	**0.8**
12 psi air	**10.27**	**13.08**	**18.29**	**9.5**	**8.96**	**0.84**	**0.808**	**0.744**	**1.26**	**0.696**
15 psi air	**11.11**	**23.2**	**29.13**	**10.46**	**19.23**	**0.8**	**0.792**	**0.716**	**2.464**	**0.72**
occipital	front 1	right	back	left	front 2	front 1	right	back	left	front 2
10 psi air	**2.72**	**2.25**	**3.53**	**2.31**	**1.46**	**6.12**	**1.74**	**7.48**	**6.24**	**3.04**
12 psi air	**3.04**	**3.12**	**6.24**	**2.09**	**2.62**	**6.98**	**3.92**	**7.44**	**4.548**	**5.36**
15 psi air	**3.14**	**4.76**	**12.49**	**2.72**	**4.77**	**4.74**	**2.45**	**6.63**	**2.476**	**4.04**

Percentage of change for 1st for cadaver-5

	AIR	Percentage 1st Rate Pressure Change				
	Overpressure	front 1	right	back	left	front 2
ventricle	20%	**11**	**28**	**22**	**NA**	**65**
ventricle	50%	**88**	**51**	**7**	**NA**	**78**
frontal	20%	**50**	**32**	**28**	**50**	**59**
frontal	50%	**116**	**37**	**47**	**100**	**67**
parietal	20%	**130**	**21**	**47**	**29**	**94**
parietal	50%	**307**	**112**	**118**	**51**	**68**
occipital	20%	**17**	**-4**	**33**	**25**	**56**
occipital	50%	**98**	**137**	**207**	**86**	**185**

Pressure rate of change for cadaver-5.

	1st rate (psi/ms)				
ventricle	front 1	right	back	left	front 2
10 psi air	**11.18**	**9.7**	**-3.44**	**˜ -7.97**	**9.13**
12 psi air	**12.43**	**12.44**	**-4.21**	**˜ -7.62**	**15.04**
15 psi air	**20.98**	**14.67**	**-3.67**	**˜ -14.28**	**16.23**
frontal	front 1	right	back	left	front 2
10 psi air	**36.63**	**10.37**	**-45.76**	**21.8**	**35.64**
12 psi air	**55.06**	**13.72**	**-58.59**	**32.69**	**56.61**
15 psi air	**78.98**	**14.16**	**-67.18**	**43.57**	**59.67**
parietal	front 1	right	back	left	front 2
10 psi air	**-3.87**	**21.48**	**29.66**	**-10.69**	**-5.59**
12 psi air	**-8.91**	**25.97**	**43.46**	**-13.78**	**-10.82**
15 psi air	**-15.75**	**45.48**	**64.55**	**-16.14**	**-9.39**
occipital	front 1	right	back	left	front 2
10 psi air	**-3.73**	**5.49**	**4.58**	**-3.45**	**-3.4**
12 psi air	**-4.37**	**5.29**	**6.1**	**-4.3**	**-5.29**
15 psi air	**-7.38**	**13.01**	**14.06**	**-6.4**	**-9.69**

˜ cable noise that could also be surface-ripples

Percentage of change for maximum, minimum and differential pressure for cadaver-5.

The increase of pressure measured by the sensors is compared with the increase in the blast intensity (overpressure). The 10psi test was used as reference.

PERCENTAGES for CADAVER-5						
	AIR	**Percentage Increase in Maximun Peak Pressure**				
	Overpressure	front 1	right	back	left	front 2
ventricle	20%	**40**	**5**	**39**	**14**	**15**
ventricle	50%	**96**	**110**	**44**	**28**	**95**
frontal	20%	**30**	**24**	**26**	**73**	**20**
frontal	50%	**74**	**106**	**141**	**172**	**50**
parietal	20%	**33**	**22**	**45**	**8**	**-12**
parietal	50%	**41**	**124**	**148**	**18**	**41**
occipital	20%	**660**	**18**	**72**	**-34**	**68**
occipital	50%	**3545**	**100**	**240**	**-72**	**270**
	AIR	**Percentage Increase in Minimum Peak Pressure**				
	Overpressure	front 1	right	back	left	front 2
ventricle	20%	**52**	**33**	**49**	**33**	**10**
ventricle	50%	**87**	**151**	**163**	**58**	**38**
frontal	20%	**19**	**25**	**20**	**6**	**10**
frontal	50%	**-2**	**71**	**41**	**105**	**-13**
parietal	20%	**53**	**26**	**48**	**7**	**29**
parietal	50%	**74**	**117**	**115**	**18**	**89**
occipital	20%	**3**	**-184**	**0**	**20**	**87**
occipital	50%	**-14**	**0**	**0**	**127**	**203**
	AIR	**Percentage Increase in Pressure Differential**				
	Overpressure	front 1	right	back	left	front 2
ventricle	20%	**44**	**21**	**45**	**25**	**13**
ventricle	50%	**93**	**134**	**115**	**45**	**76**
frontal	20%	**27**	**25**	**21**	**38**	**17**
frontal	50%	**49**	**87**	**53**	**137**	**29**
parietal	20%	**38**	**24**	**47**	**7**	**0**
parietal	50%	**50**	**121**	**134**	**18**	**114**
occipital	20%	**12**	**39**	**77**	**-10**	**79**
occipital	50%	**15**	**112**	**254**	**18**	**227**

Strain gages status during testing of cadaver-5.

Rosettes were used to measure strain; therefore for complete data, three grids needed to be working.

Strain gages status for cadaver-5					
10psi	front 1	right	back	left	front 2
Frontal S.G.	3	3	3	3	3
Zygomatic S.G.	1	0	0	0	0
Temporal S.G.	2	2	1	2	2
Parietal S.G.	3	3	3	3	1
Occipital S.G.	3	3	2	1	3
12psi	front 1	right	back	left	front 2
Frontal S.G.	2	3	3	3	3
Zygomatic S.G.	0	0	0	0	0
Temporal S.G.	2	2	0	1	2
Parietal S.G.	1	1	0	0	0
Occipital S.G.	1	0	0	0	0
15psi	front 1	right	back	left	front 2
Frontal S.G.	3	3	3	3	3
Zygomatic S.G.	0	0	0	0	0
Temporal S.G.	2	3	1	1	3
Parietal S.G.	0	1	0	1	1
Occipital S.G.	0	1	0	0	1

0	0 grids working
1	1 grid working
2	2 grids working
3	3 grids working

APPENDIX B

SPHERE 5 MM THICK DATA

Test 1 Front 1 Orientation 5mm Intact Sphere

FILTERED DATA

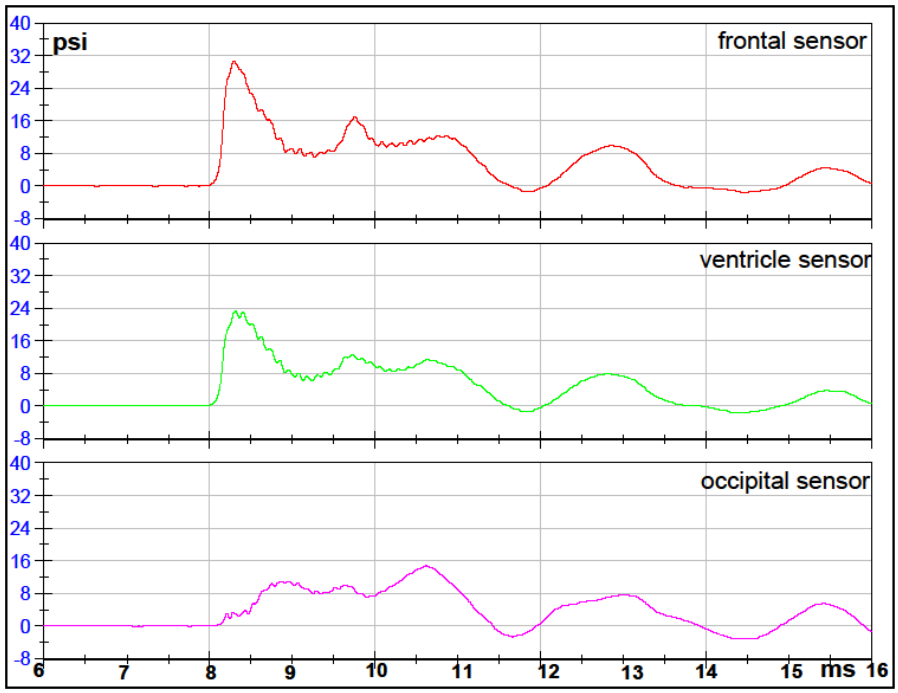

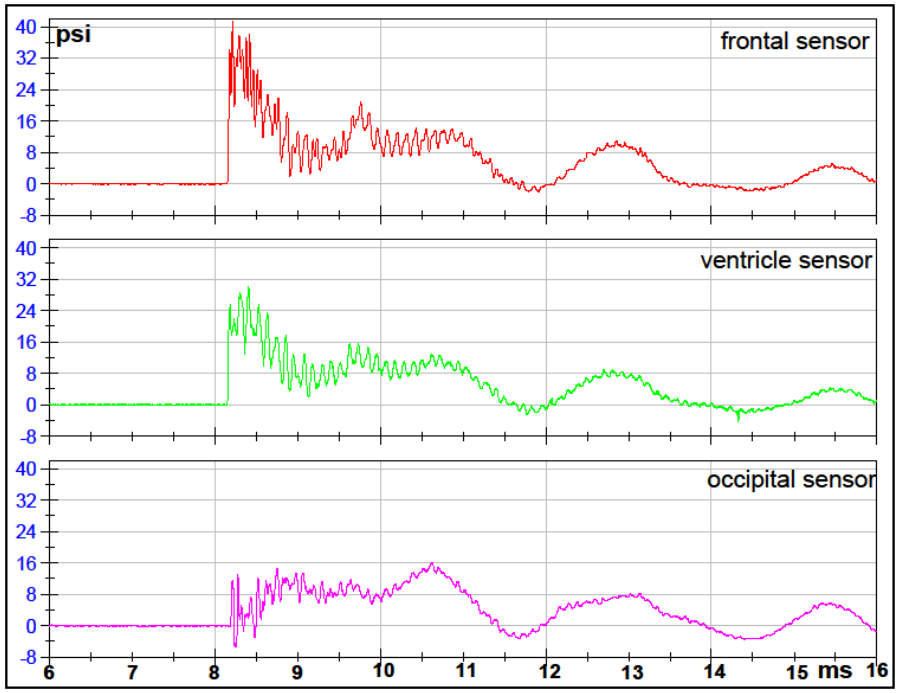

RAW DATA

Test 2 Right Orientation 5mm Intact Sphere

FILTERED DATA

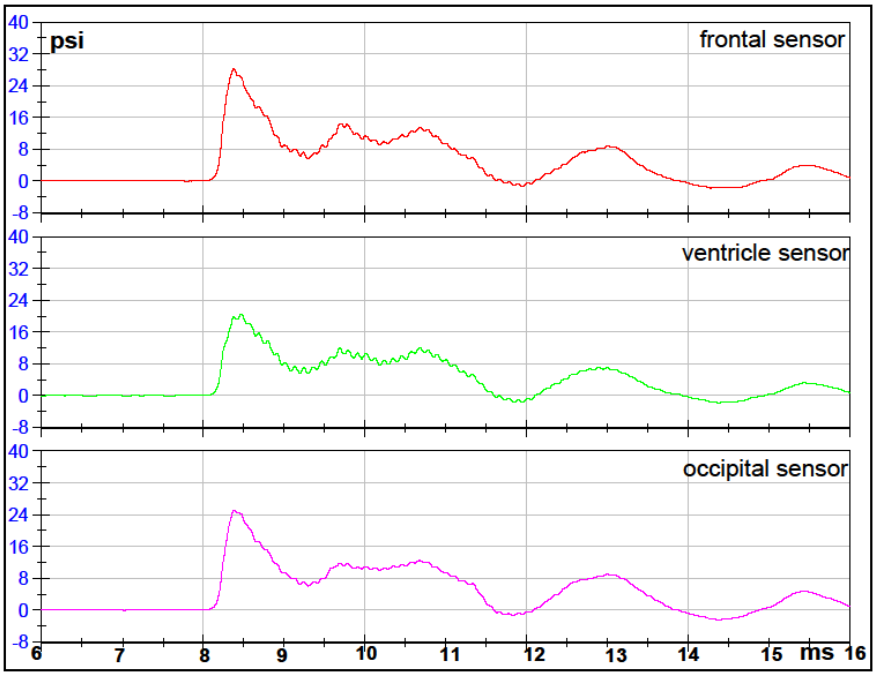

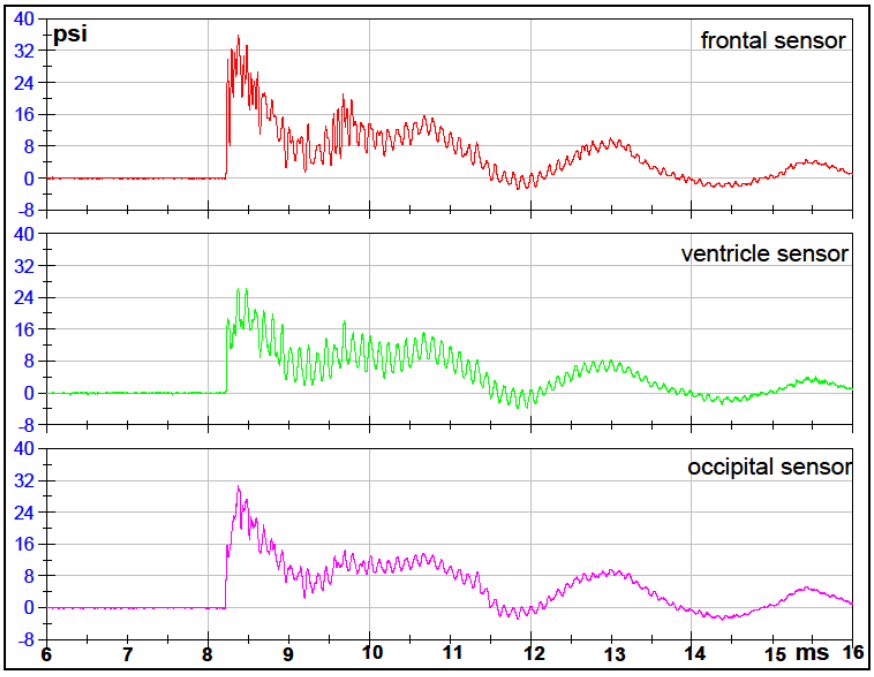

RAW DATA

Test 3 Back Orientation 5mm Intact Sphere

FILTERED DATA

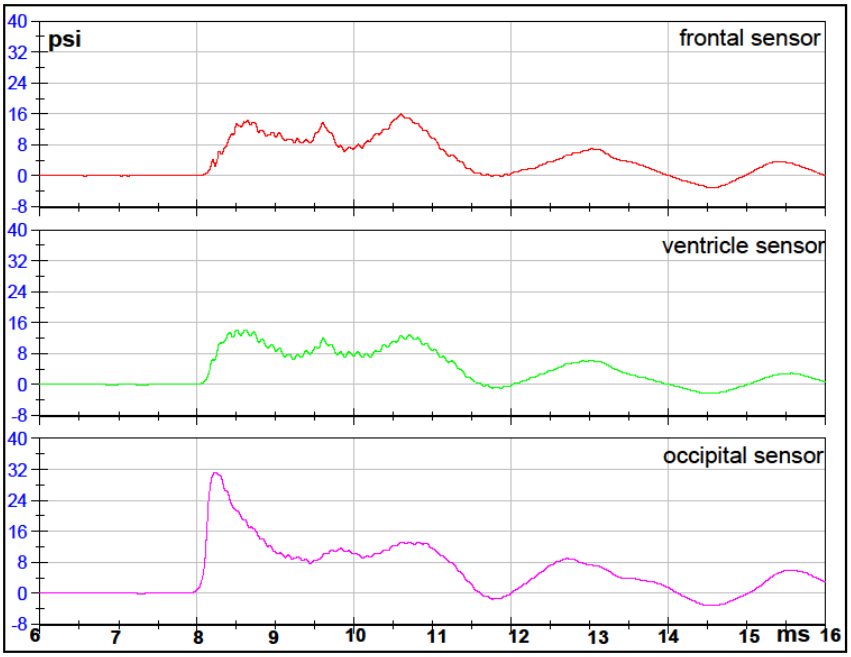

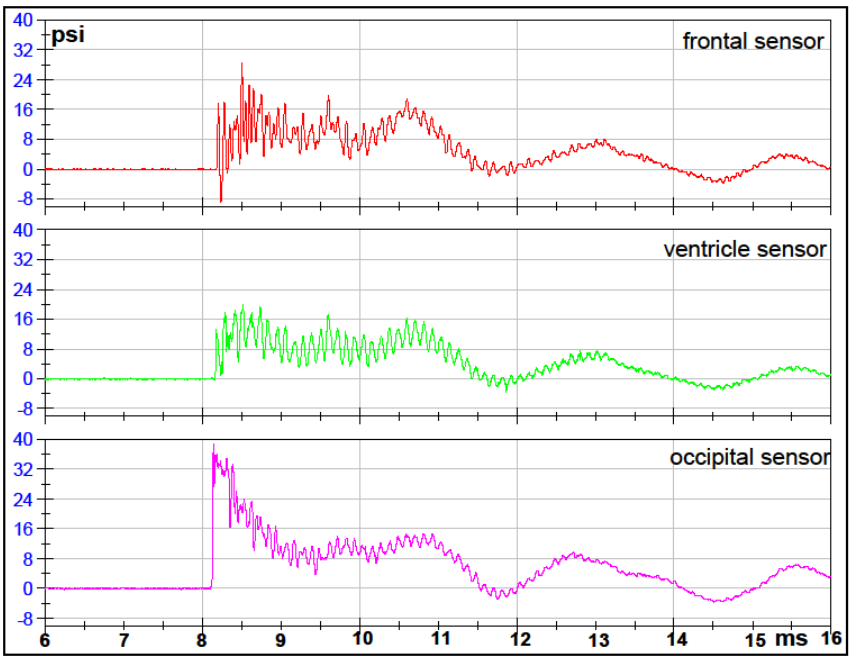

RAW DATA

Test 4 Left Orientation 5mm Intact Sphere

FILTERED DATA

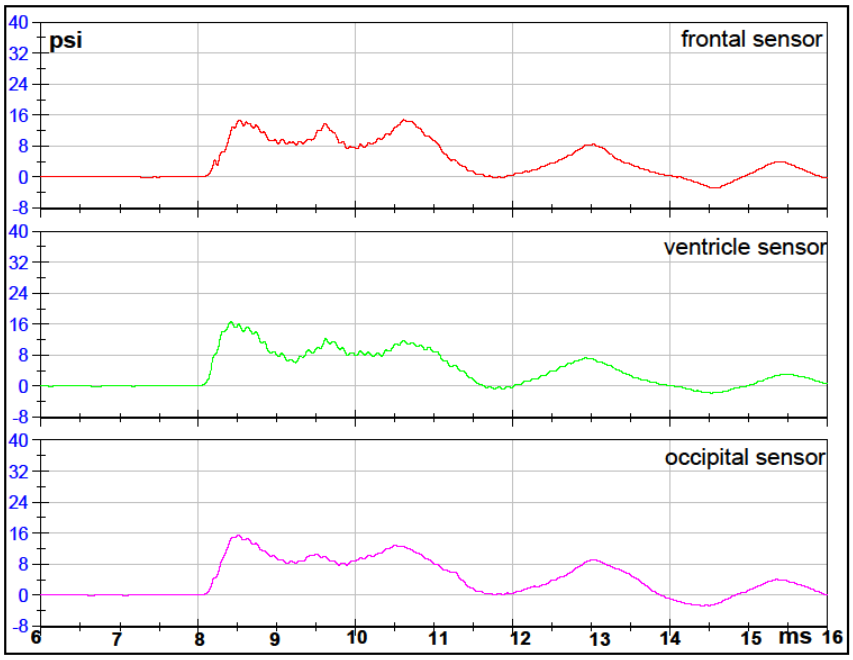

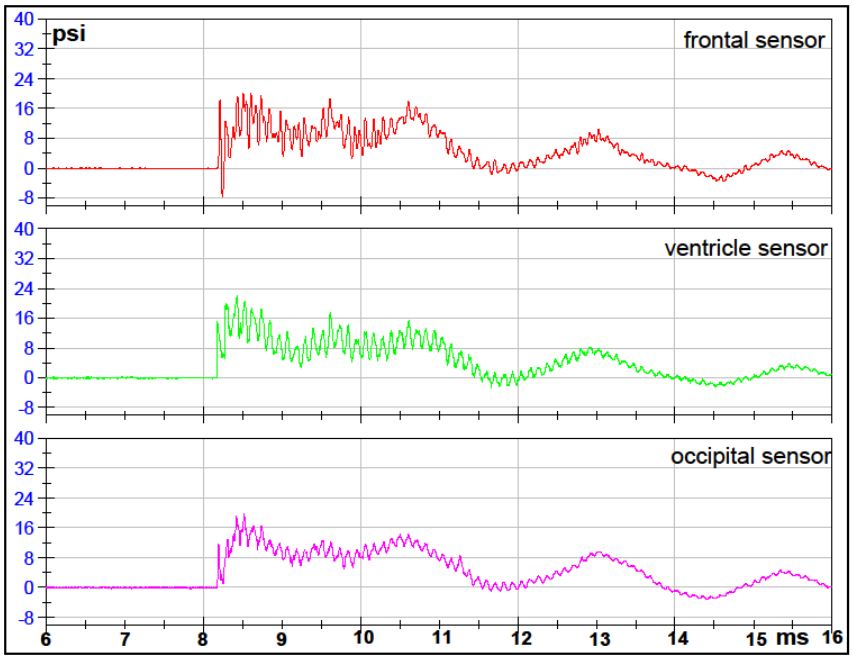

RAW DATA

Test 5 Front 2 Orientation 5mm Intact Sphere

FILTERED DATA

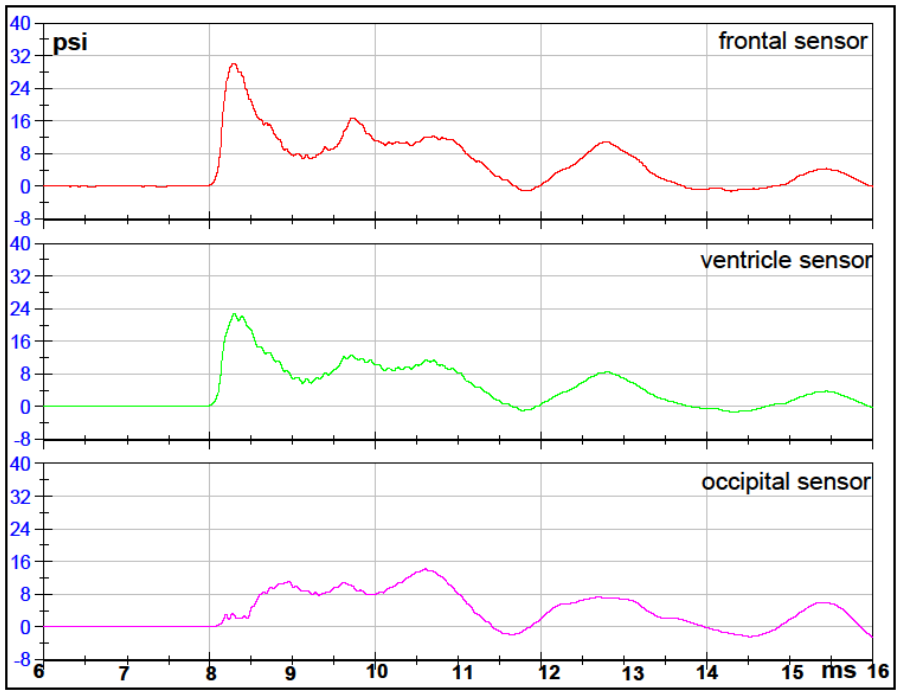

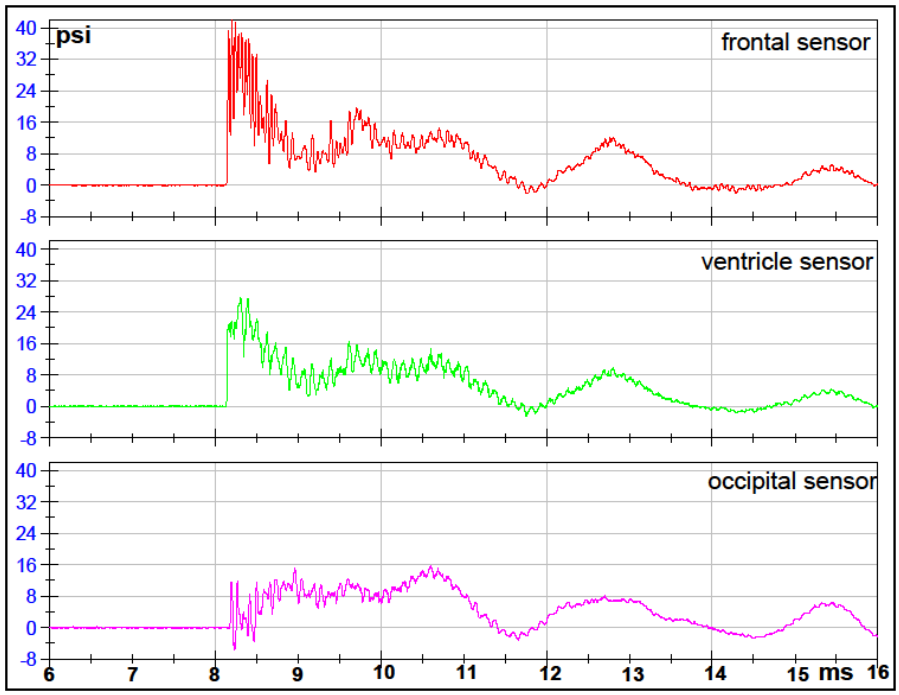

RAW DATA

Test 6 Front 1 Orientation 5mm Intact Sphere

FILTERED DATA

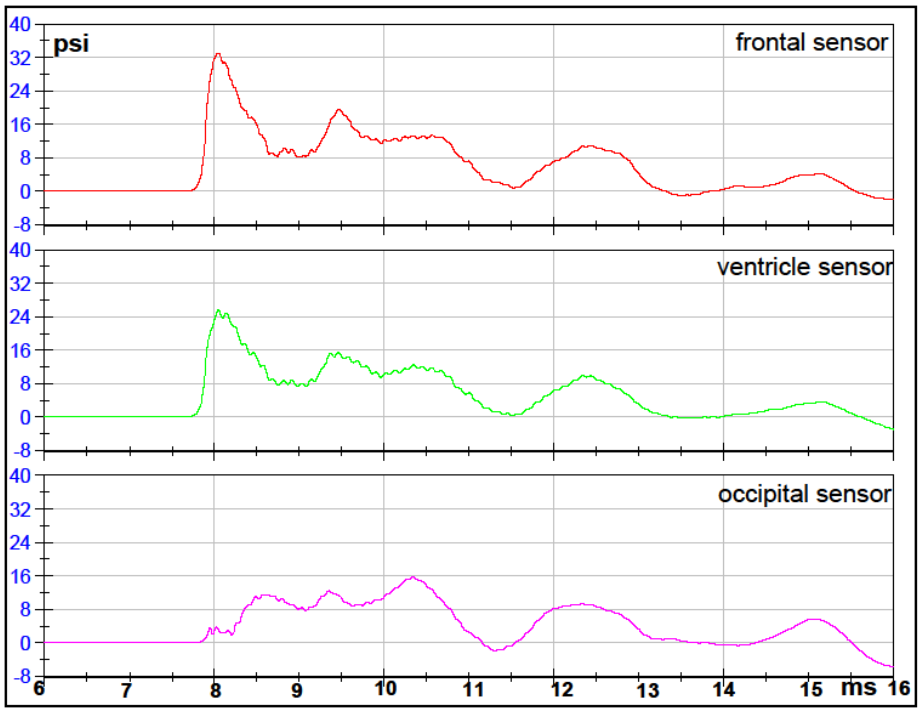

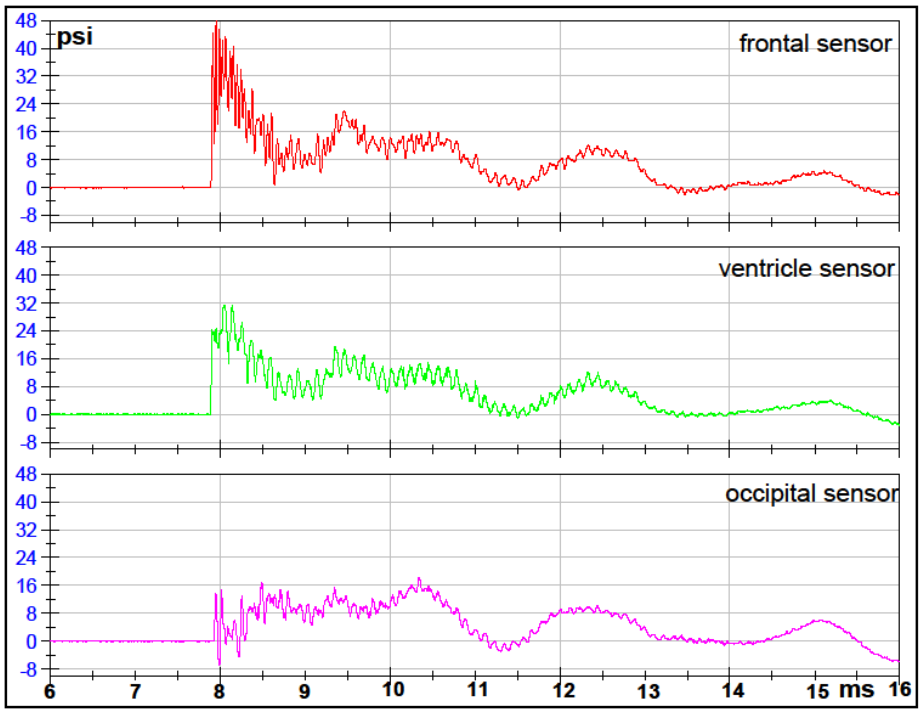

RAW DATA

Test 7 Left Orientation 5mm Intact Sphere

FILTERED DATA

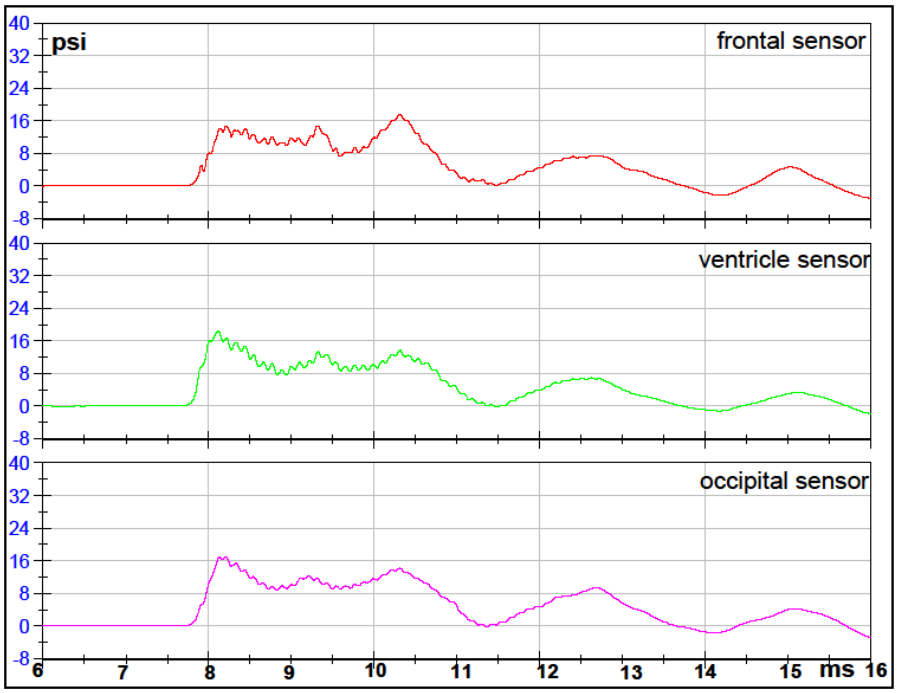

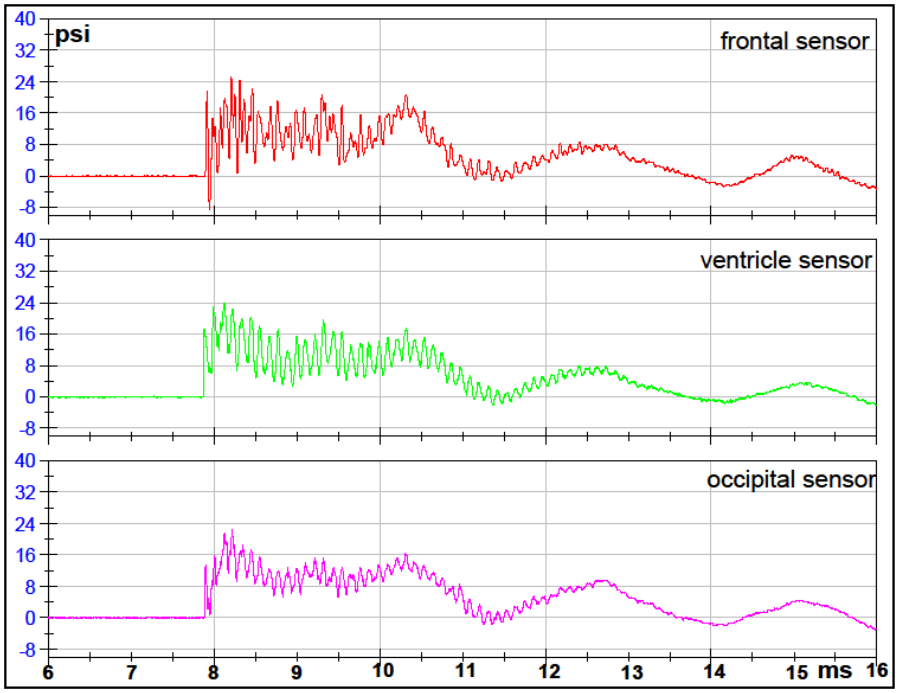

RAW DATA

Test 8 Back Orientation 5mm Intact Sphere

FILTERED DATA

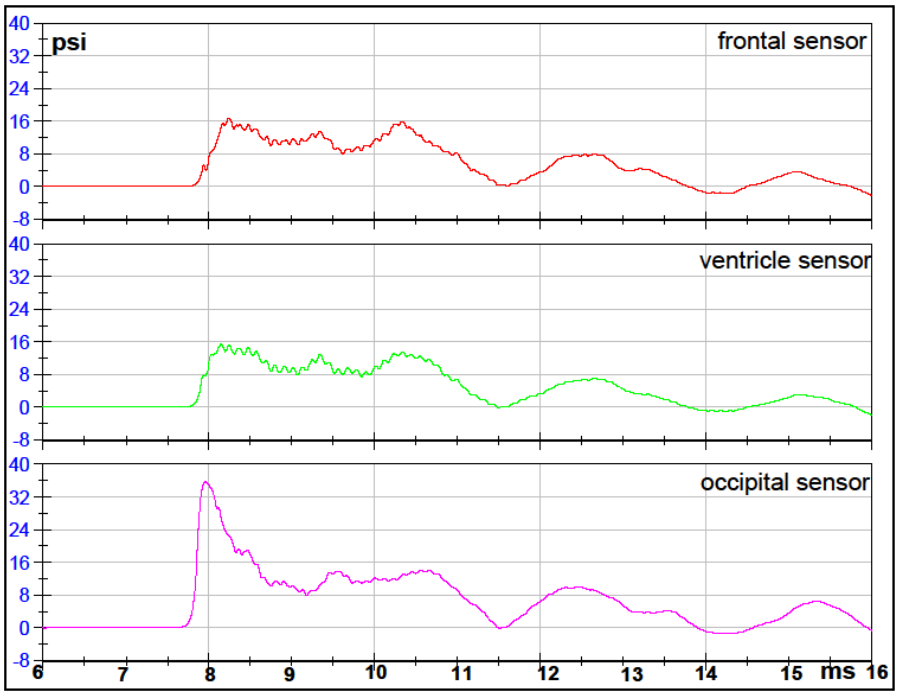

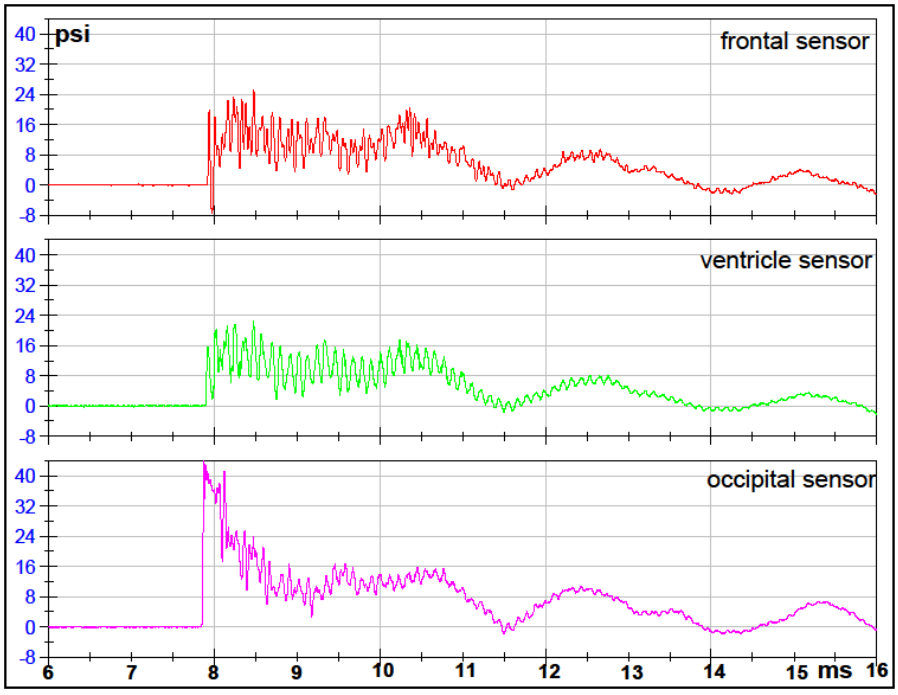

RAW DATA

Test 9 Right Orientation 5mm Intact Sphere

FILTERED DATA

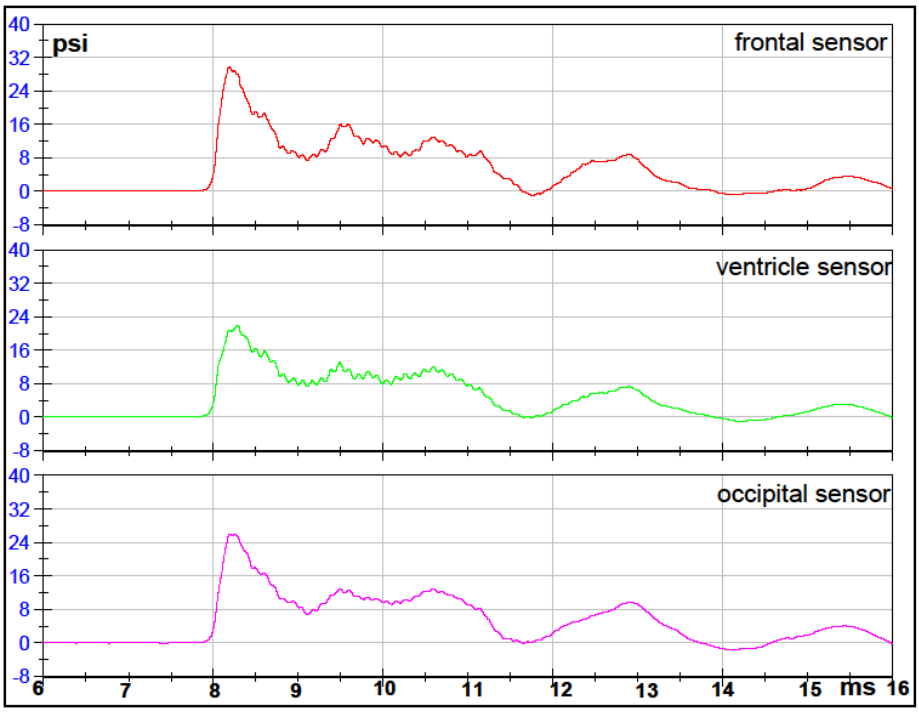

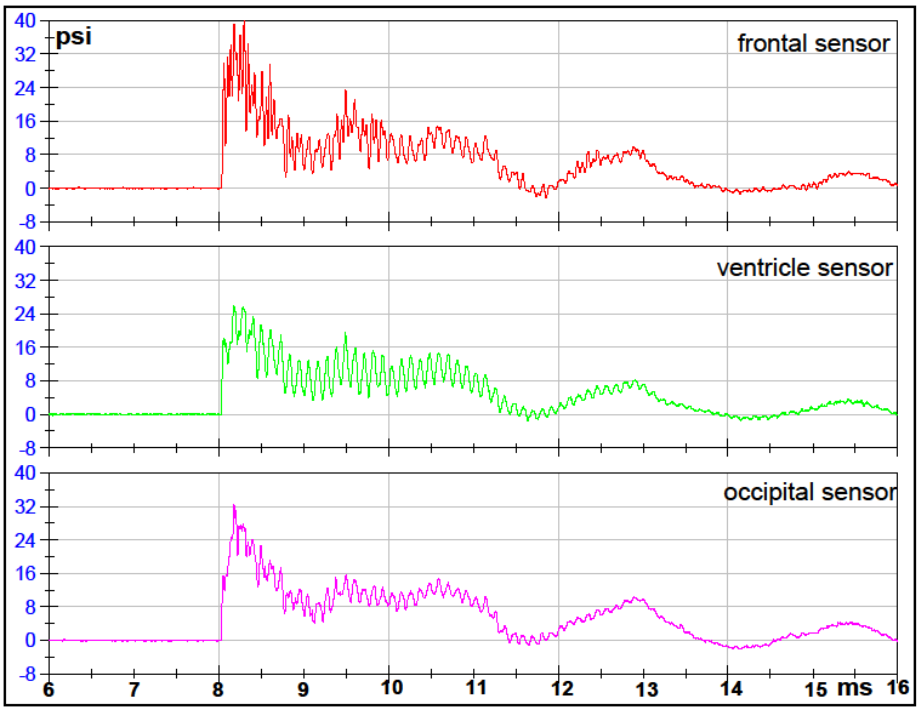

RAW DATA

Test 10 Front 2 Orientation 5mm Intact Sphere

FILTERED DATA

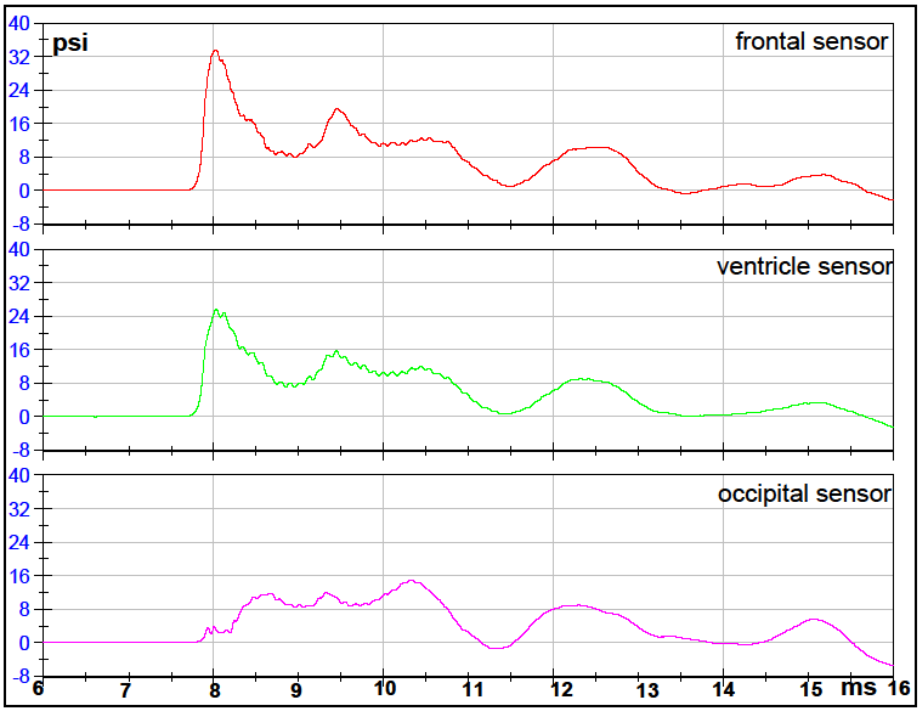

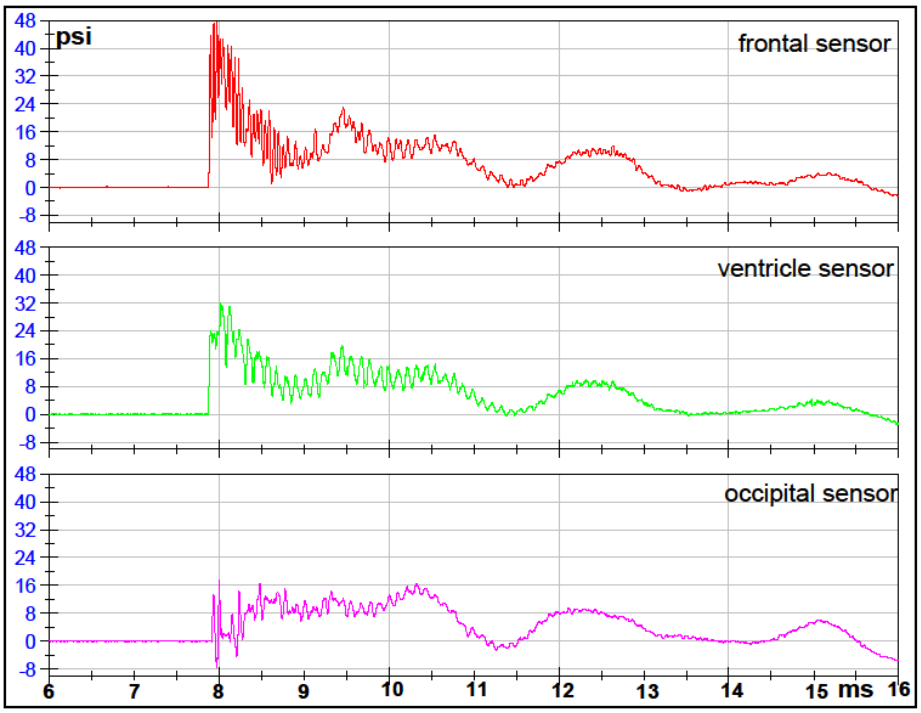

RAW DATA

Test 11 Front 1 Orientation 5mm Intact Sphere

FILTERED DATA

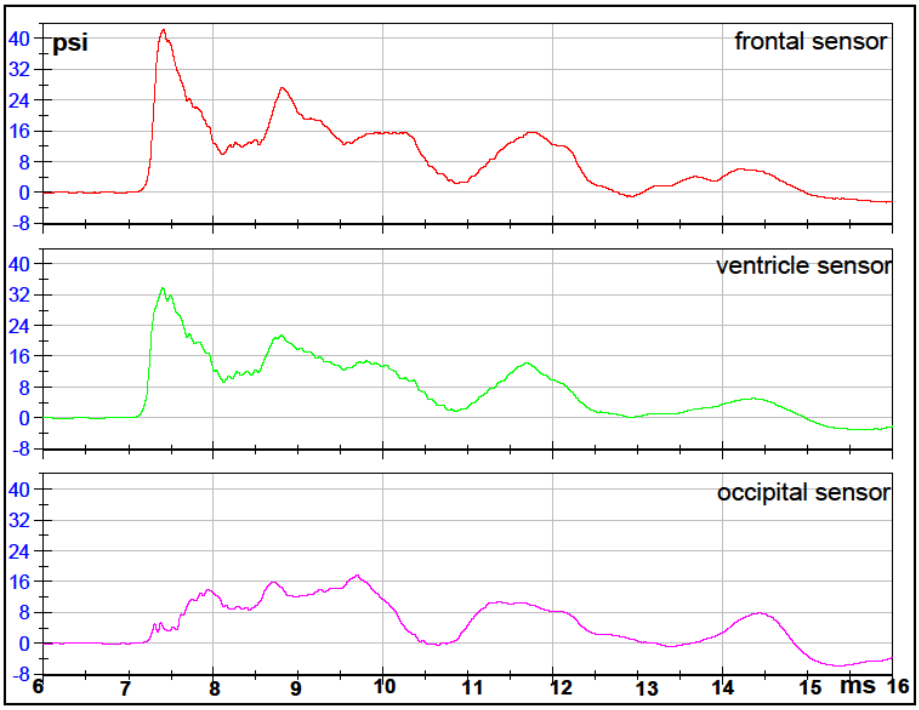

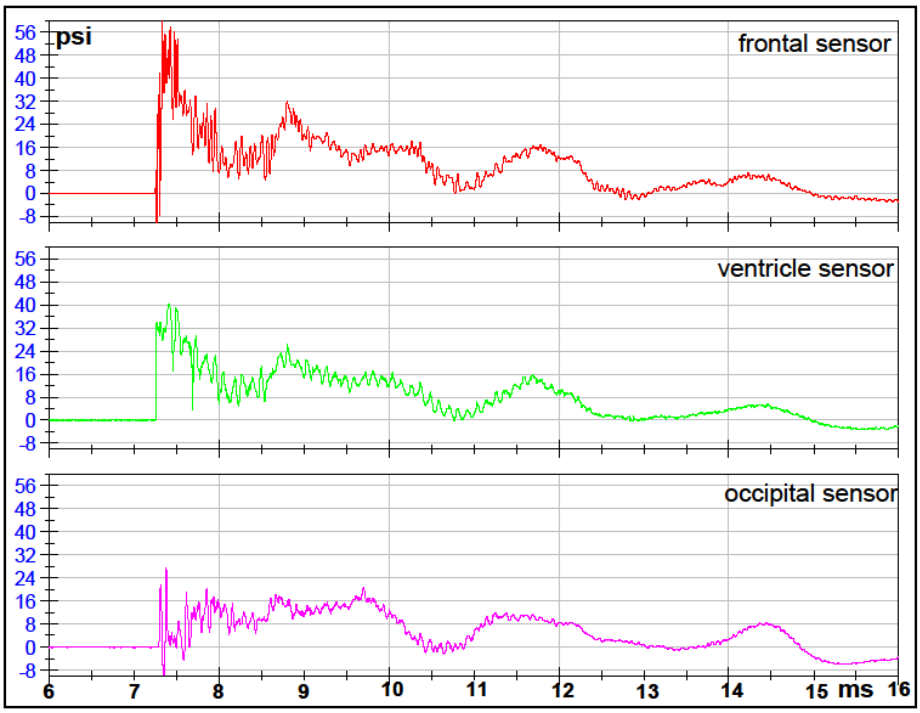

RAW DATA

Test 12 Right Orientation 5mm Intact Sphere

FILTERED DATA

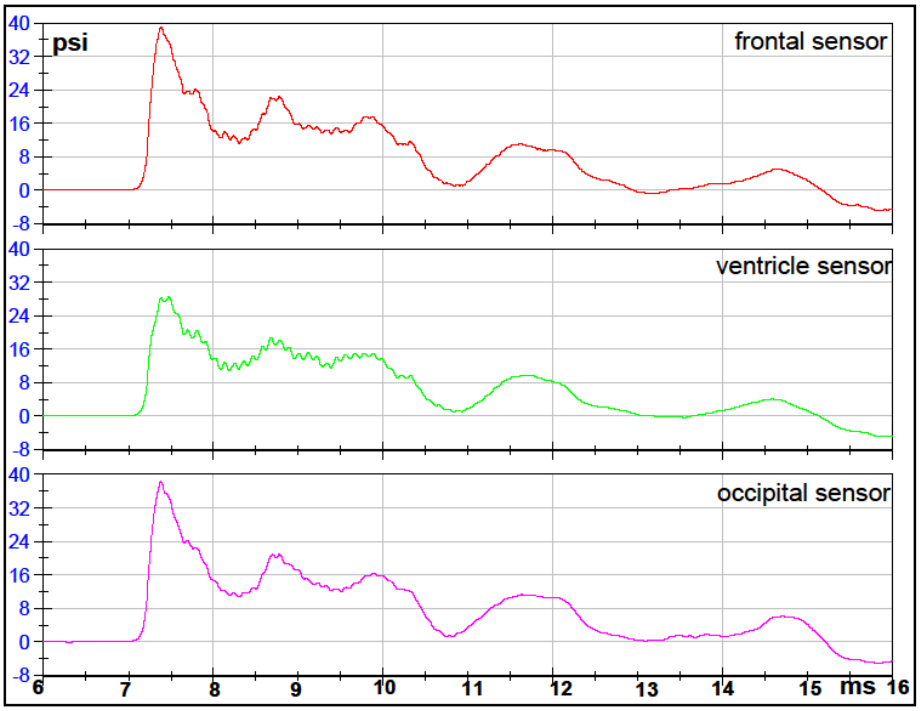

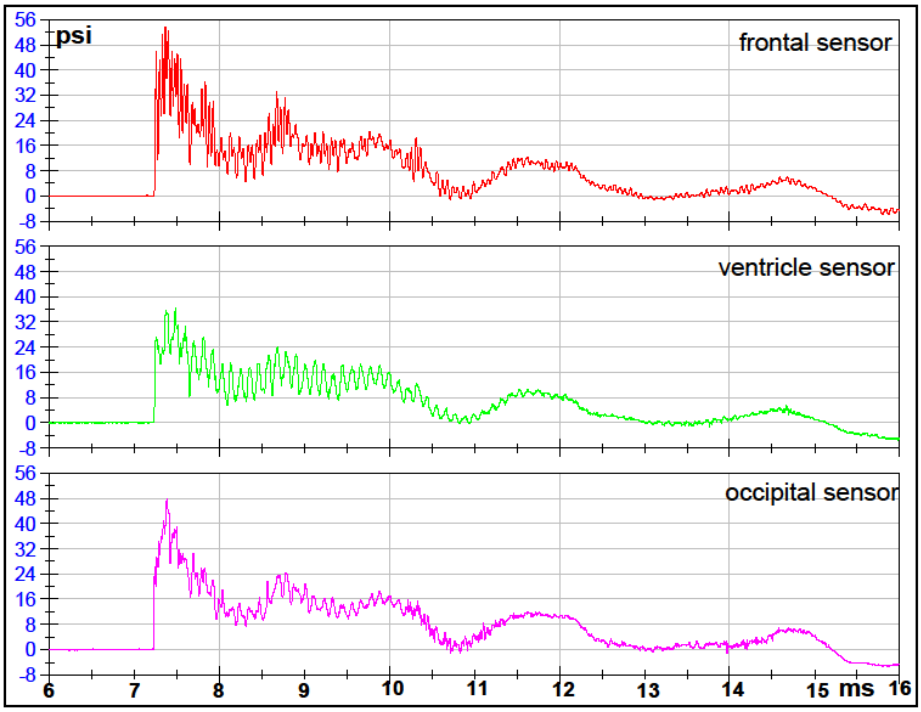

RAW DATA

Test 13 Back Orientation 5mm Intact Sphere

FILTERED DATA

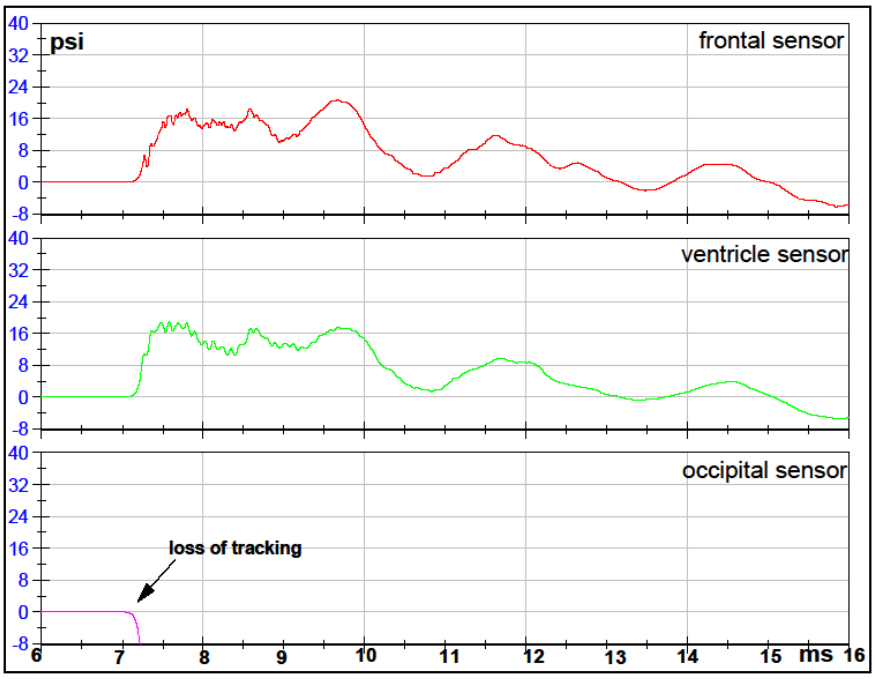

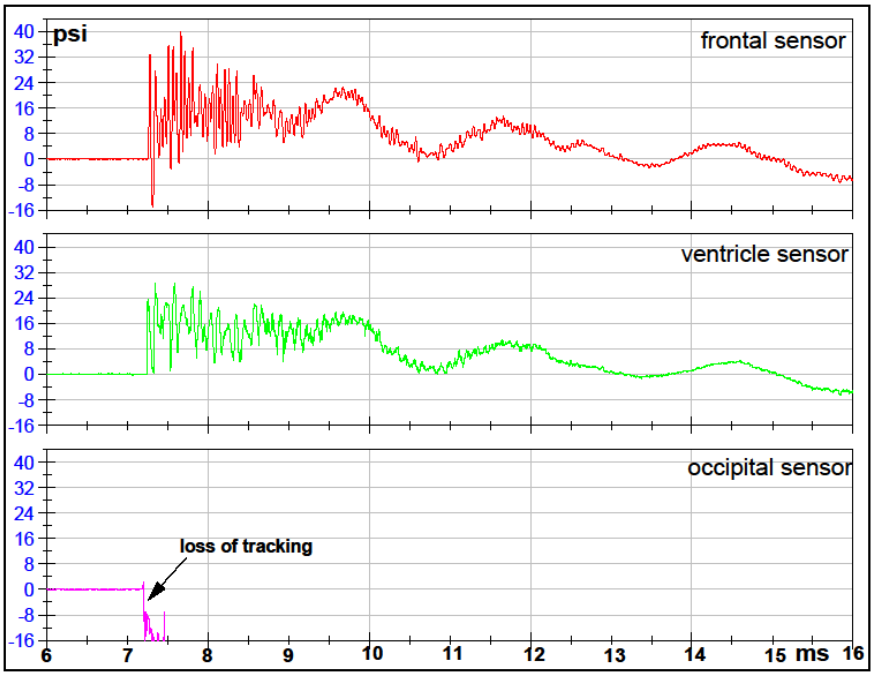

RAW DATA

Test 14 Left Orientation 5mm Intact Sphere

FILTERED DATA

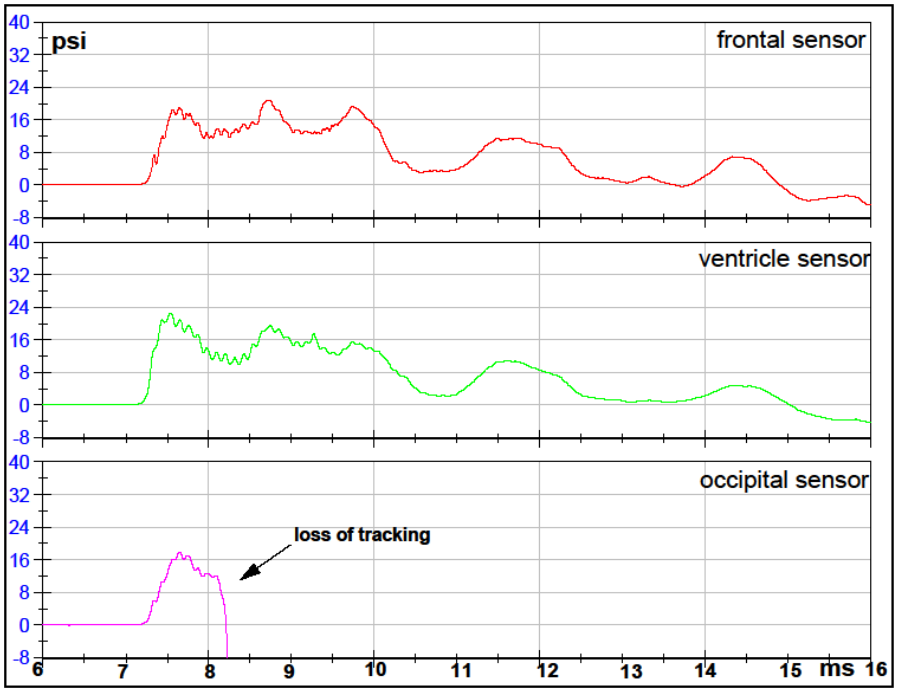

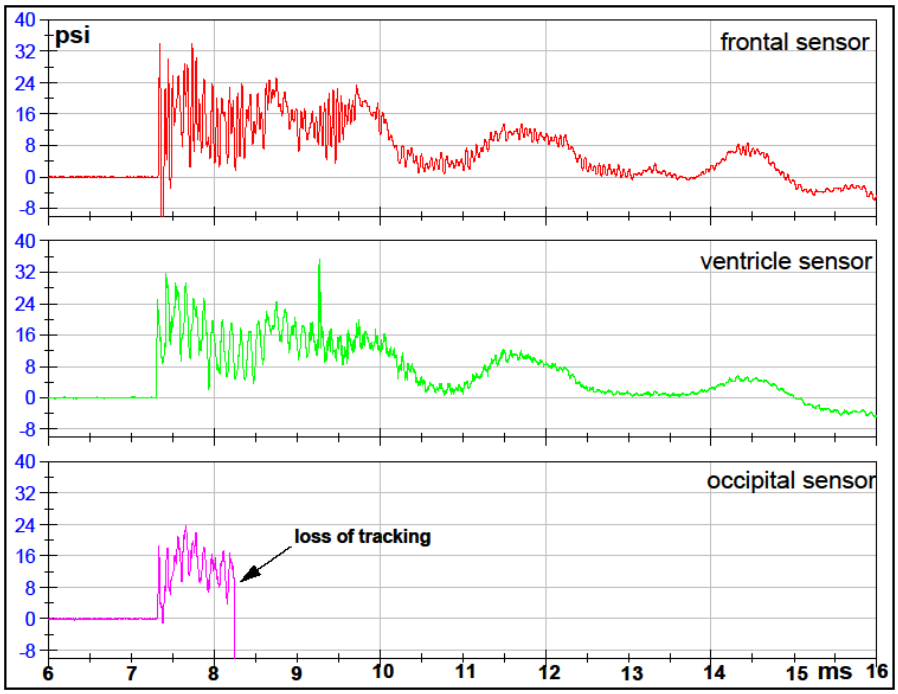

RAW DATA

Test 15 Front 2 Orientation 5mm Intact Sphere

FILTERED DATA

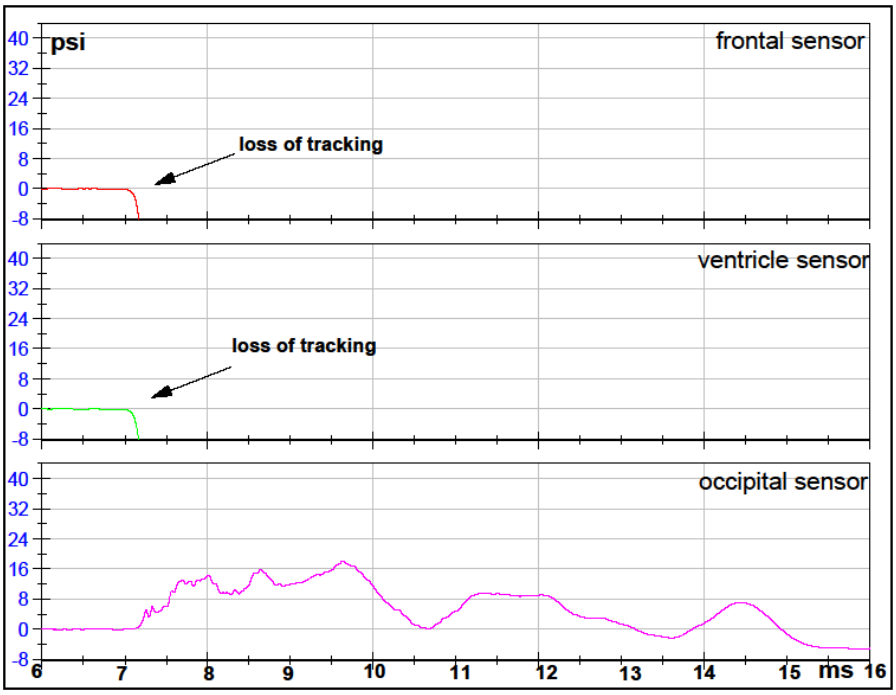

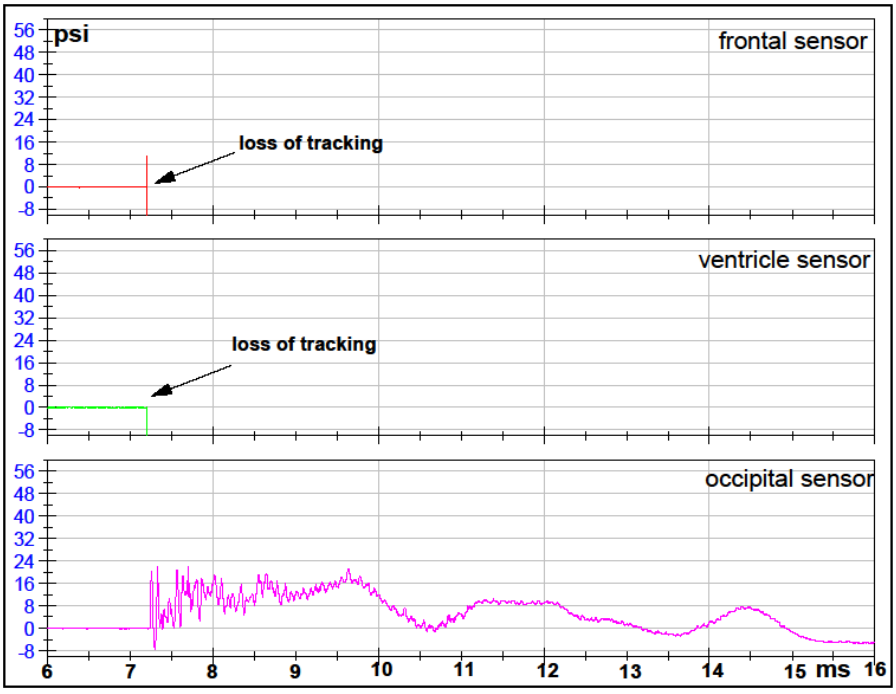

RAW DATA

Comparison for reproducibility of each pressure sensor in Front Orientation at 10psi 5mm Intact Sphere

VENTRICLE FILTERED DATA

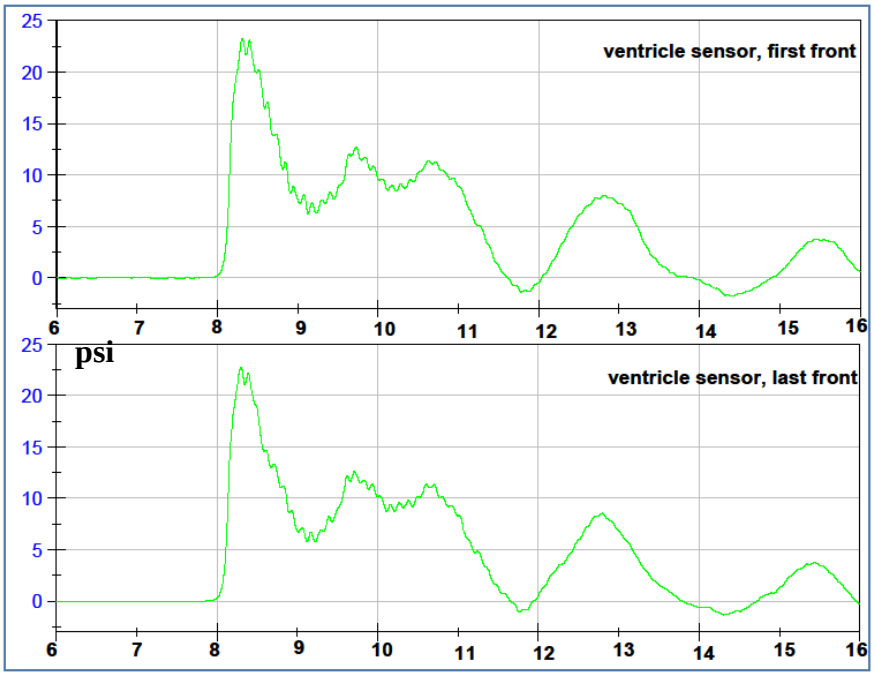

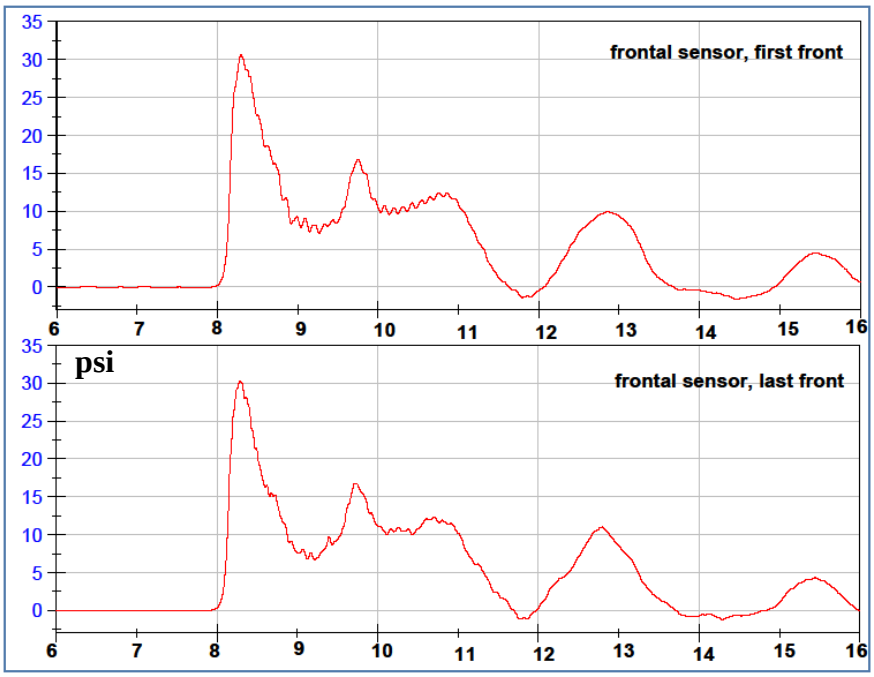

FRONTAL FILTERED DATA

Comparison for reproducibility of each pressure sensor in Front Orientation at 10psi 5mm Intact Sphere

OCCIPITAL FILTERED DATA

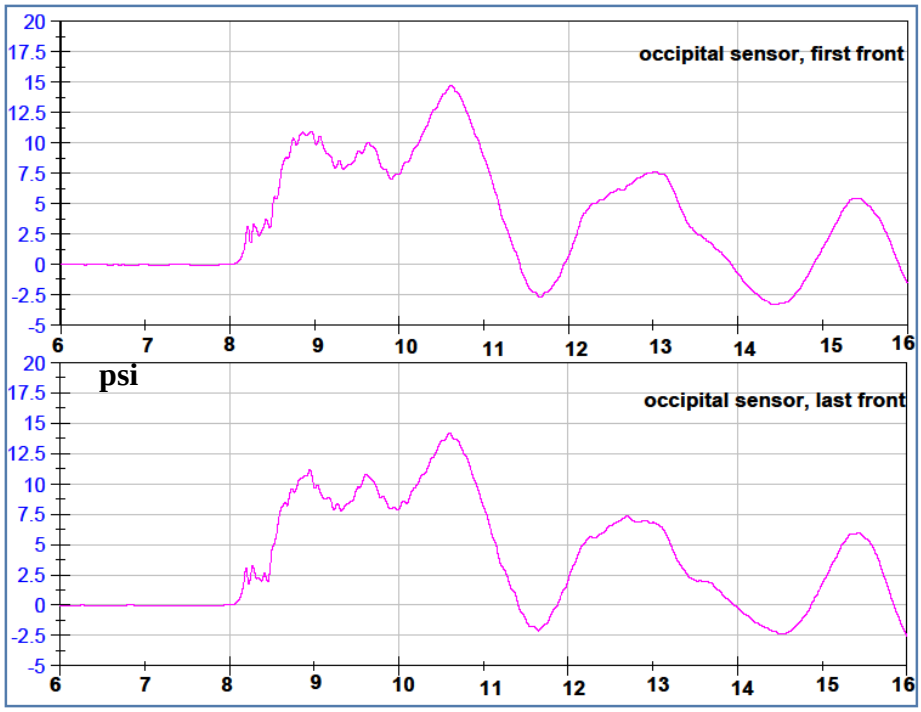

Comparison for reproducibility of each pressure sensor in Front Orientation at 12psi 5mm Intact Sphere

VENTRICLE FILTERED DATA

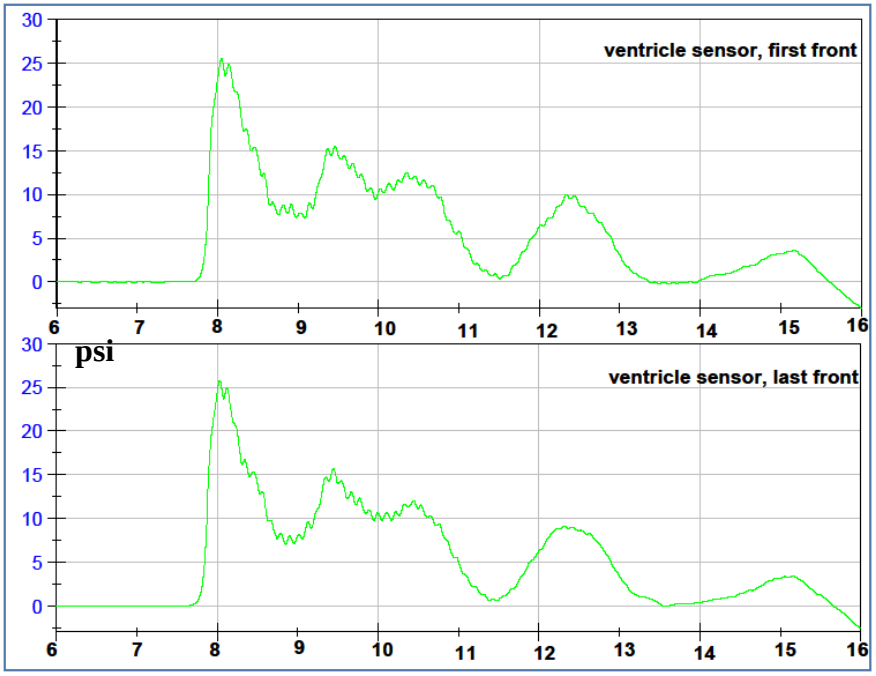

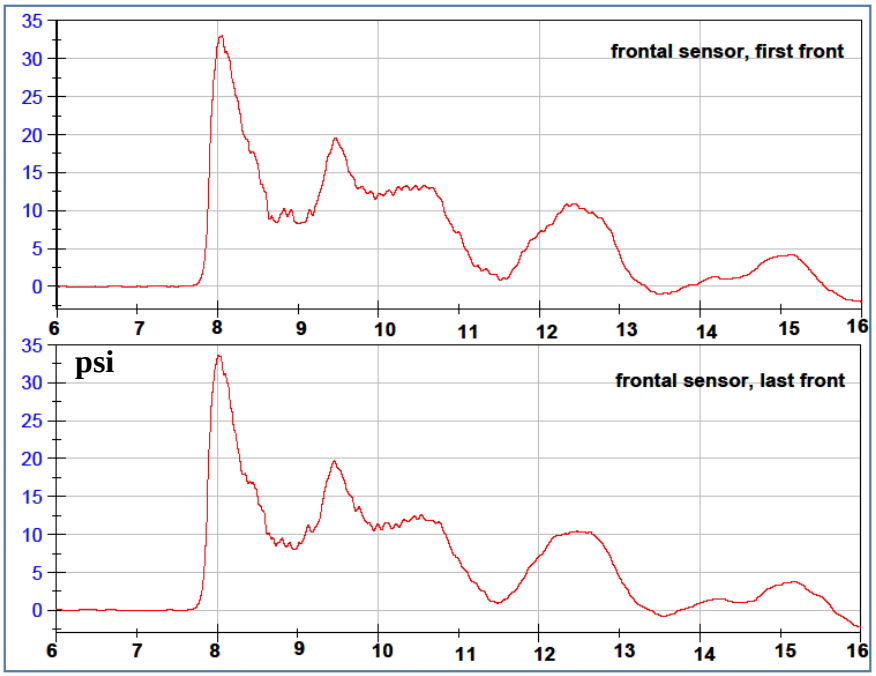

FRONTAL FILTERED DATA

Comparison for reproducibility of each pressure sensor in Front Orientation at 12psi 5mm Intact Sphere

OCCIPITAL FILTERED DATA

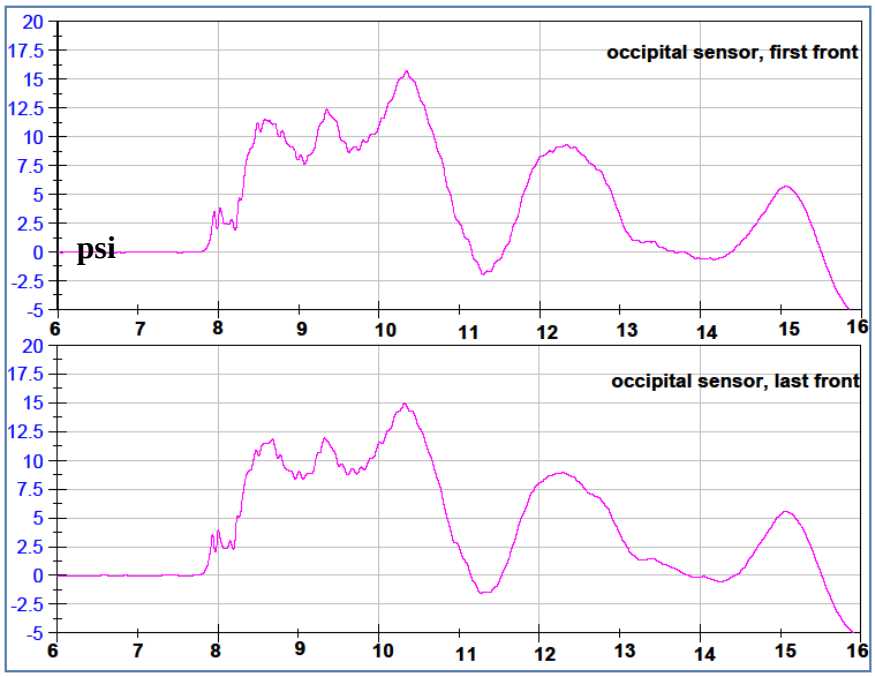

Comparison for reproducibility of each pressure sensor in Front Orientation at 15psi 5mm Intact Sphere

VENTRICLE FILTERED DATA

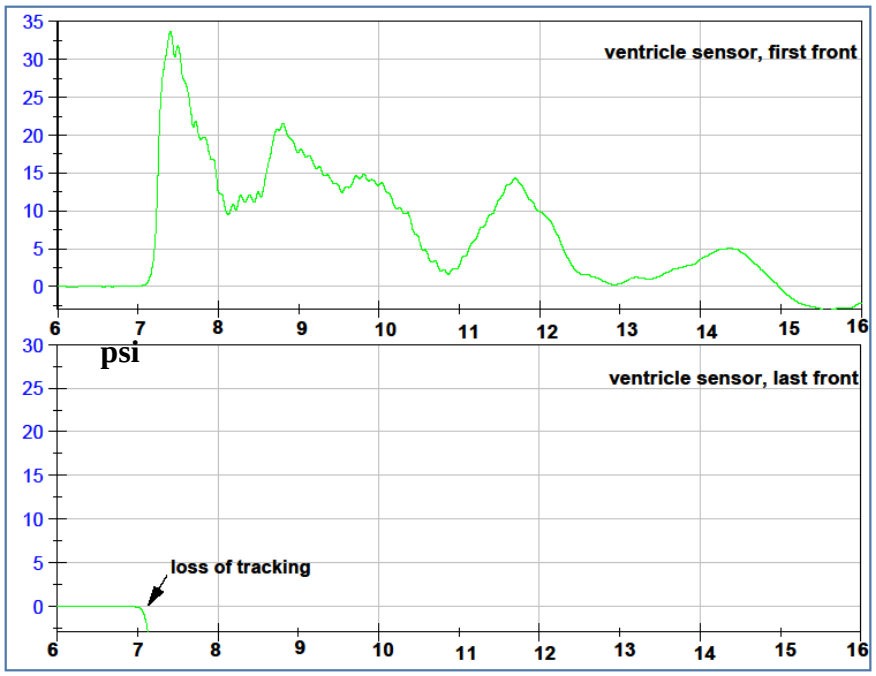

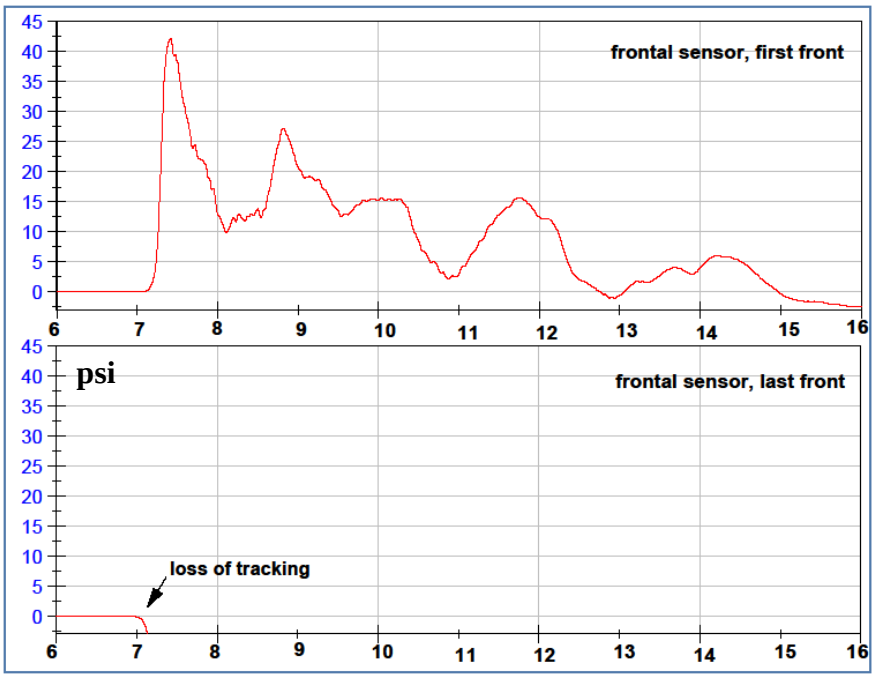

FRONTAL FILTERED DATA

Comparison for reproducibility of each pressure sensor in Front Orientation at 15psi 5mm Intact Sphere

OCCIPITAL FILTERED DATA

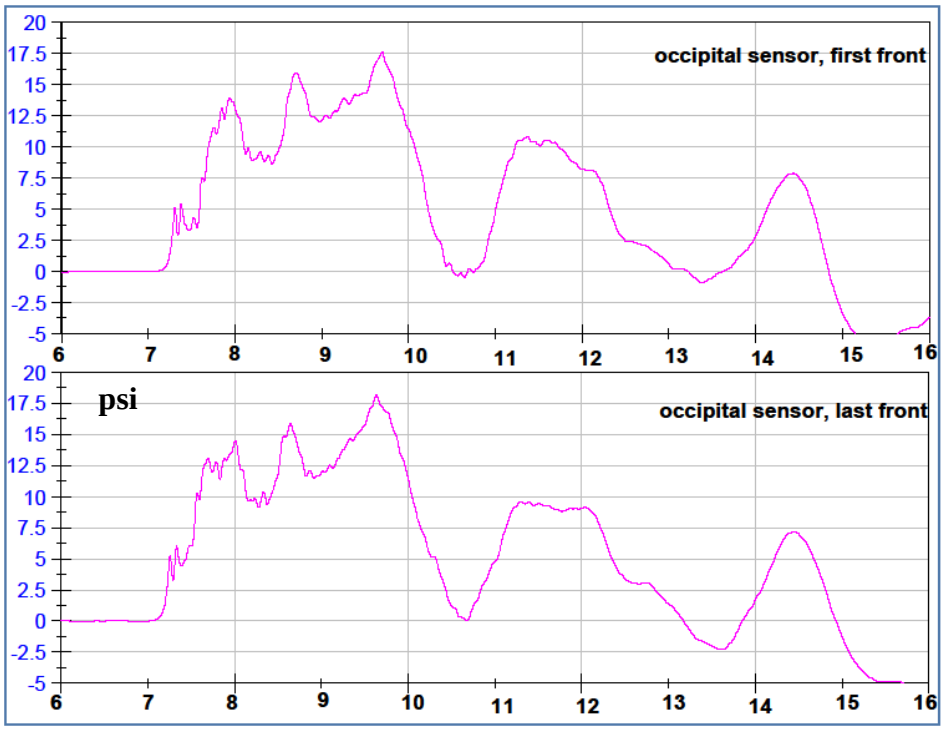

Frontal Sensor, 4 Orientations, Filtered Data, 5mm Intact Sphere

10 PSI

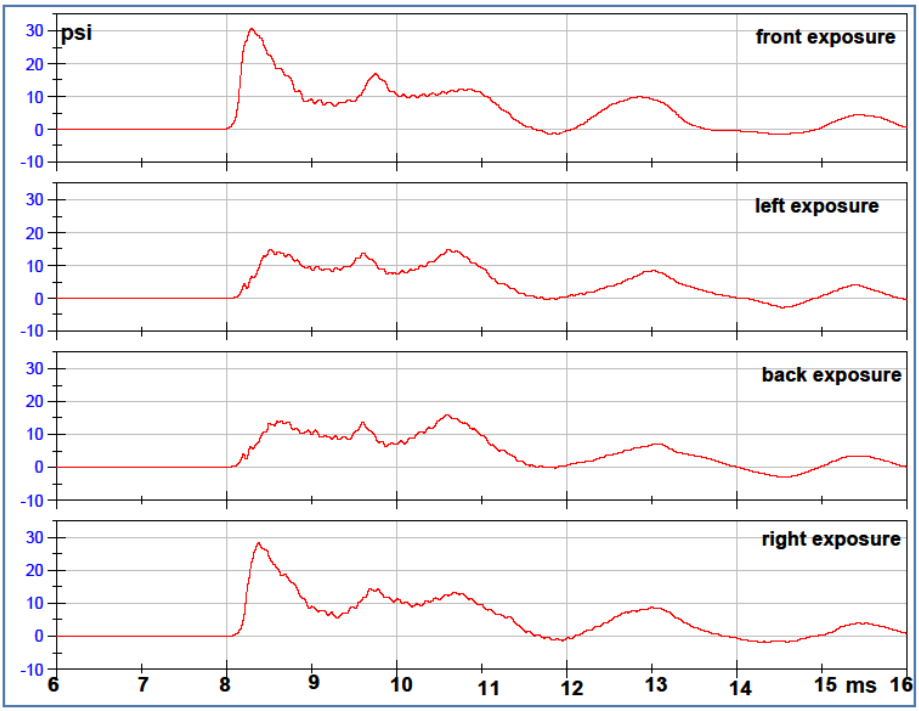

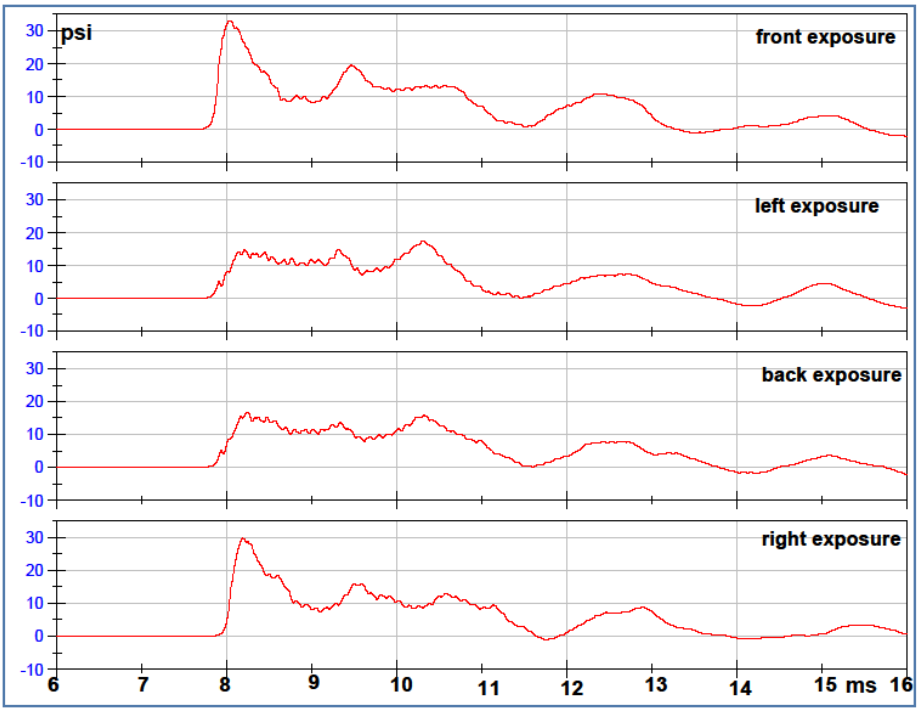

12 PSI

Frontal Sensor, 4 Orientations, Filtered Data, 5mm Intact Sphere

15 PSI

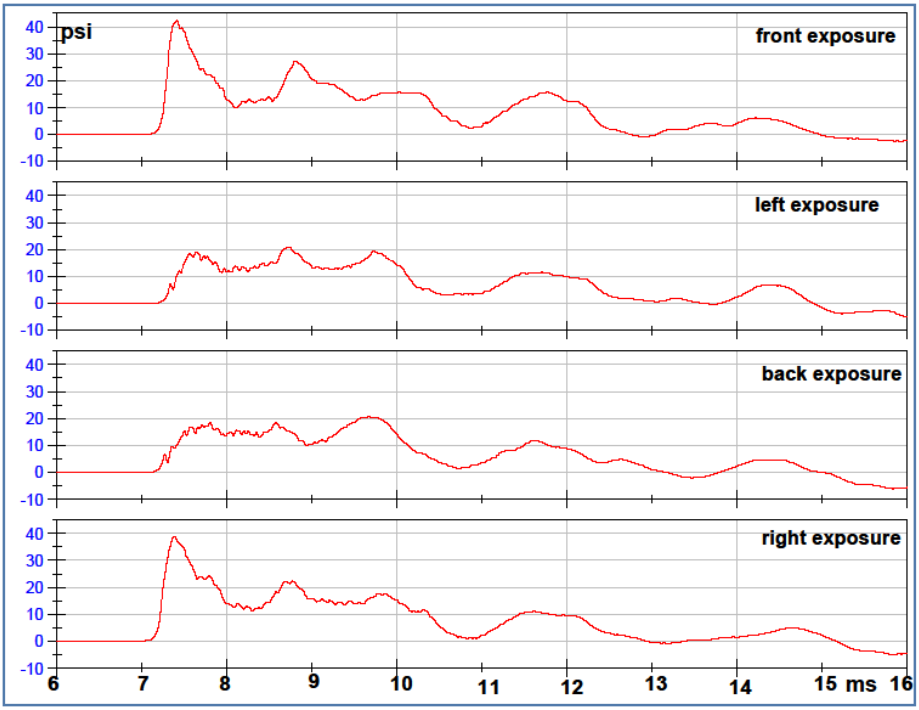

Ventricle Sensor, 4 Orientations, Filtered Data, 5mm Intact Sphere

10 PSI

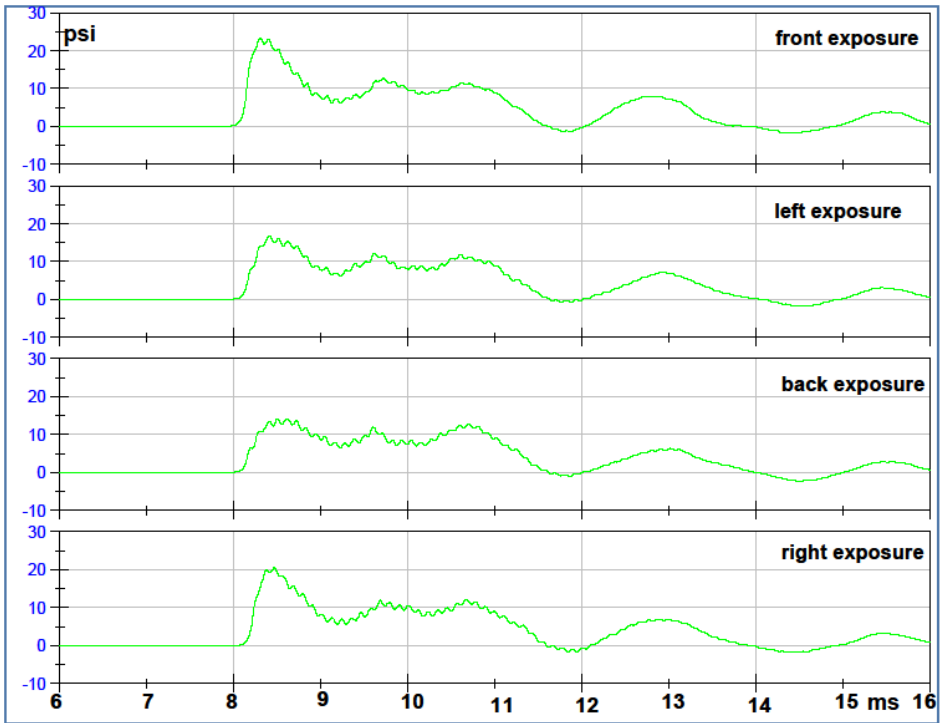

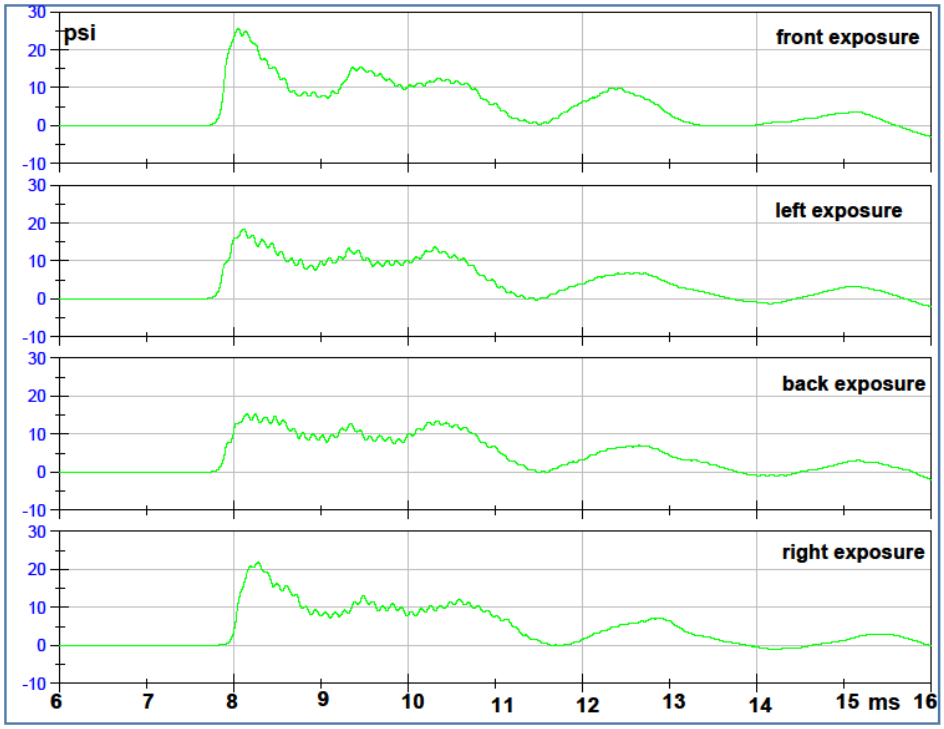

12 PSI

Ventricle Sensor, 4 Orientations, Filtered Data, 5mm Intact Sphere

15 PSI

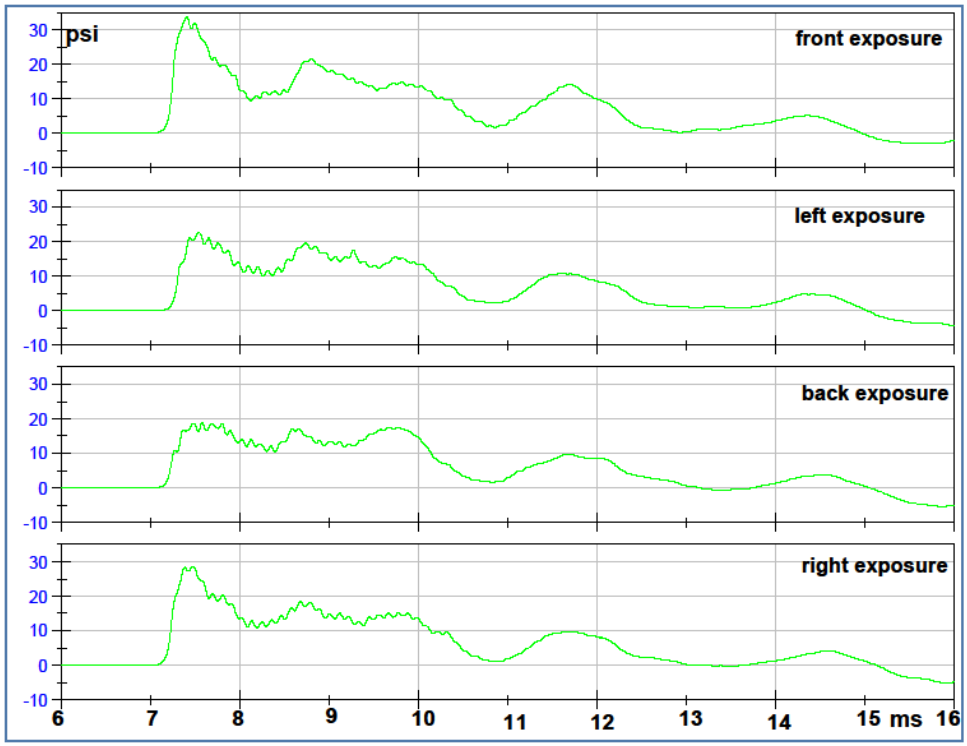

Occipital Sensor, 4 Orientations, Filtered Data, 5mm Intact Sphere

10 PSI

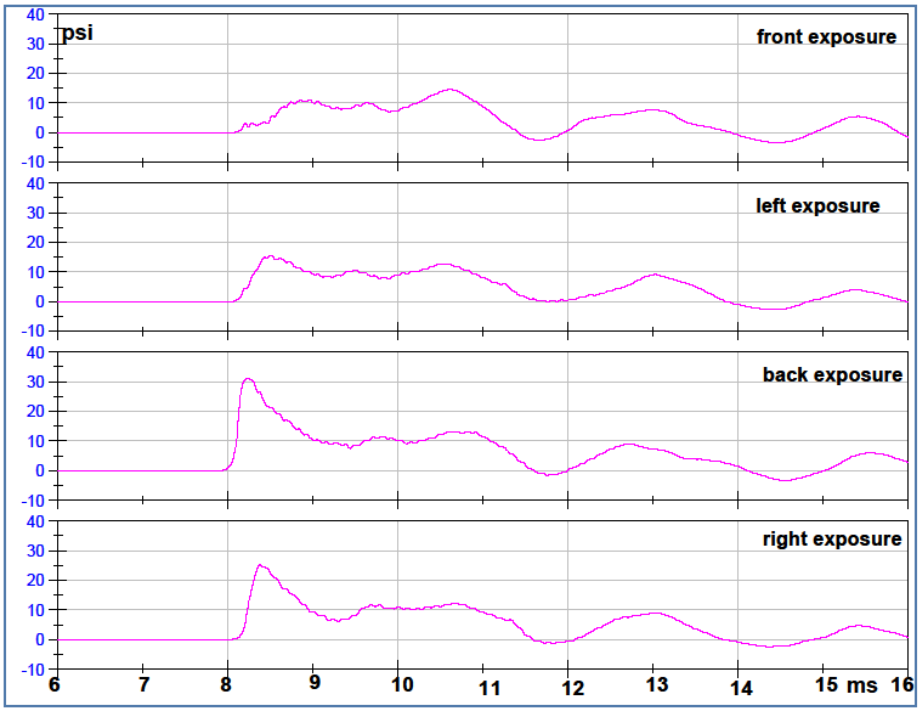

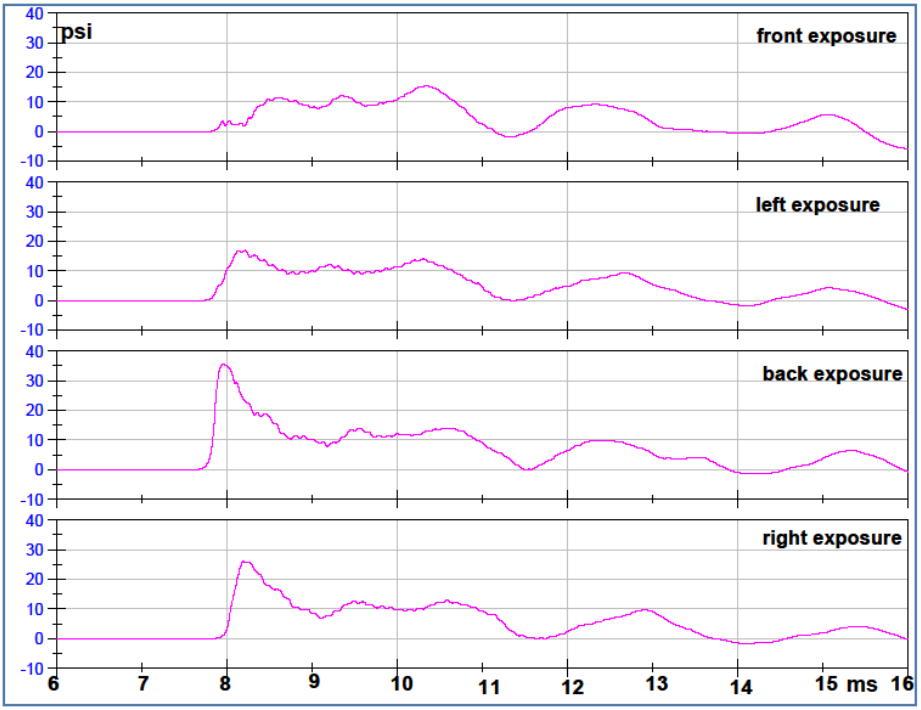

12 PSI

Occipital Sensor, 4 Orientations, Filtered Data, 5mm Intact Sphere

15 PSI

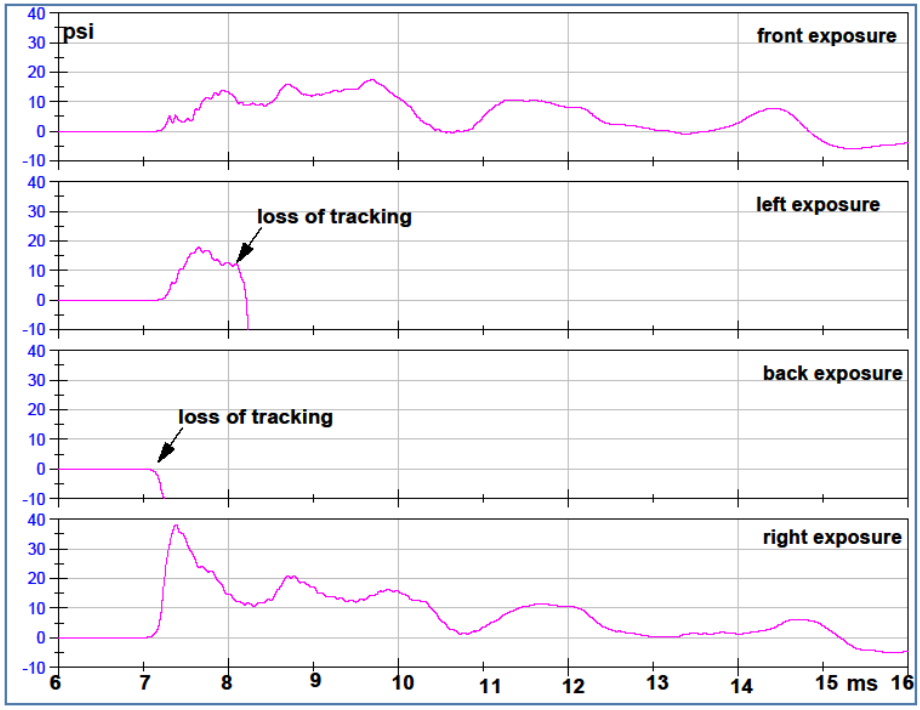

Pressure extreme for intact sphere 5mm.

Pressure Extremes for sphere 5mm										
	Maximun Pressure					Minimum Pressure				
ventricle	front 1	right	back	left	front 2	front 1	right	back	left	front 2
10 psi air	**23.29**	**20.44**	**14.08**	**16.7**	**22.78**	**-1.8**	**-1.86**	**-2.35**	**-1.84**	**-1.3**
12 psi air	**25.55**	**21.88**	**15.43**	**18.4**	**25.74**	**-0.228**	**-0.96**	**-1.02**	**-1.26**	**-0.03**
15 psi air	**33.56**	**28.62**	**18.85**	**22.57**	**NA**	**0.206**	**-0.363**	**-0.787**	**0.187**	**NA**
frontal	front 1	right	back	left	front 2	front 1	right	back	left	front 2
10 psi air	**30.68**	**28.42**	**15.93**	**14.81**	**30.23**	**-1.62**	**-1.8**	**-3.07**	**-2.84**	**-1.15**
12 psi air	**32.92**	**29.69**	**16.73**	**17.5**	**33.59**	**-1.06**	**-1.02**	**-1.74**	**-2.35**	**-0.76**
15 psi air	**42.23**	**39.04**	**20.68**	**20.82**	**NA**	**-1.04**	**-0.737**	**-2.09**	**-0.372**	**NA**
occipital	front 1	right	back	left	front 2	front 1	right	back	left	front 2
10 psi air	**14.73**	**25.17**	**31.21**	**15.55**	**14.18**	**-3.26**	**-2.53**	**-3.22**	**-2.77**	**-2.41**
12 psi air	**15.75**	**26.06**	**35.68**	**16.99**	**14.95**	**-1.92**	**-1.74**	**-1.42**	**-1.73**	**-1.57**
15 psi air	**17.64**	**38.19**	**NA**	**NA**	**18.17**	**-0.882**	**0.135**	**NA**	**NA**	**-2.28**

Percentages of peak internal pressure changes in 5 mm sphere intact and with holes, based on the cell value at the 10 psi overpressure for each orientation.

		PERCENTAGES for sphere 5mm					PERCENTAGES for sphere 5mm with holes				
AIR		Percentage Increase in Maximun Peak Pressure					Percentage Increase in Maximun Peak Pressure				
Overpressure		front 1	right	back	left	front 2	front 1	right	back	left	front 2
ventricle	20%	10%	7%	10%	10%	13%	15%	13%	16%	17%	9%
ventricle	50%	44%	40%	34%	35%	NA	NA	52%	46%	46%	44%
frontal	20%	7%	4%	5%	18%	11%	16%	14%	15%	12%	7%
frontal	50%	38%	37%	30%	41%	NA	45%	49%	41%	36%	39%
occipital	20%	7%	4%	14%	9%	5%	3%	12%	NA	20%	6%
occipital	50%	20%	52%	NA	NA	28%	32%	48%	NA	51%	28%

Maximum peak pressure increase in the 5mm-thick sphere with holes relative to the intact sphere. The number is expressed in percentage of the intact sphere results for each test. Positive numbers mean higher pressure in the intact sphere.

Percentage of Relative Maximum Peak Pressure Increase					
5mm-sphere with holes in respect to 5mm-sphere					
ventricle	front 1	right	back	left	front 2
10 psi air	**1%**	**5%**	**2%**	**1%**	**-5%**
12 psi air	**-3%**	**-1%**	**-4%**	**-5%**	**-2%**
15 psi air	**NA**	**-4%**	**-7%**	**-7%**	**NA**
frontal	front 1	right	back	left	front 2
10 psi air	**-1%**	**6%**	**11%**	**-7%**	**-7%**
12 psi air	**-9%**	**-2%**	**3%**	**-1%**	**-3%**
15 psi air	**-6%**	**-2%**	**3%**	**-3%**	**NA**
occipital	front 1	right	back	left	front 2
10 psi air	**7%**	**0%**	**3%**	**12%**	**8%**
12 psi air	**10%**	**-8%**	**NA**	**3%**	**7%**
15 psi air	**-3%**	**2%**	**NA**	**NA**	**8%**

1st rate of change of pressure for 5mm-Intact Sphere.

1st rate (psi/ms)					
ventricle	front 1	right	back	left	front 2
10 psi air	**76.76**	**62.59**	**37.28**	**44.96**	**69.02**
12 psi air	**83.39**	**63.03**	**47.58**	**53.45**	**84.9**
15 psi air	**110.85**	**94.59**	**48.17**	**73.01**	**NA**
frontal	front 1	right	back	left	front 2
10 psi air	**97.81**	**89.52**	**29.17**	**33.94**	**100.1**
12 psi air	**107.4**	**90.06**	**37.76**	**37.59**	**117.07**
15 psi air	**140.1**	**124.2**	**44.14**	**46.9**	**NA**
occipital	front 1	right	back	left	front 2
10 psi air	**22.28**	**79.27**	**109.4**	**40.91**	**26.91**
12 psi air	**27.65**	**83.12**	**127.9**	**43.06**	**27.44**
15 psi air	**39.08**	**121.7**	**NA**	**NA**	**33.61**

Comparisons of the 1st rate of change of pressure in the 5mm-thick sphere with holes relative to the intact sphere. The number is expressed in percentage of the intact sphere results for each test. Positive numbers mean higher rates in the intact sphere.

Percentages of 1st Rate of Change of Pressure for 5mm-thick sphere with holes relative to intact sphere					
ventricle	front 1	right	back	left	front 2
10 psi air	**5%**	**6%**	**6%**	**-2%**	**-5%**
12 psi air	**2%**	**1%**	**8%**	**-6%**	**4%**
15 psi air	**NA**	**5%**	**-27%**	**2%**	**NA**
frontal	front 1	right	back	left	front 2
10 psi air	**8%**	**13%**	**26%**	**-2%**	**3%**
12 psi air	**-8%**	**-4%**	**9%**	**-9%**	**10%**
15 psi air	**3%**	**4%**	**8%**	**-7%**	**NA**
occipital	front 1	right	back	left	front 2
10 psi air	**7%**	**-5%**	**3%**	**29%**	**13%**
12 psi air	**9%**	**-8%**	**NA**	**20%**	**11%**
15 psi air	**19%**	**7%**	**NA**	**NA**	**-9%**

Comparisons of 1st rate of change of pressure using spheres of different shell thickness.

The data is expressed in percentage of the thinner shell results. Positive numbers indicate higher pressure values in the thinner shell (5mm-thick sphere).

Percentages of Rate of Change of Pressure for 7mm-thick sphere relative to 5mm-thick sphere					
ventricle	front 1	right	back	left	front 2
10 psi air	**13%**	**-41%**	**-61%**	**18%**	**14%**
12 psi air	**17%**	**-2%**	**-25%**	**24%**	**20%**
15 psi air	**26%**	**0%**	**-70%**	**9%**	**NA**
frontal	front 1	right	back	left	front 2
10 psi air	**-30%**	**28%**	**65%**	**-3%**	**2%**
12 psi air	**-14%**	**21%**	**46%**	**16%**	**6%**
15 psi air	**-9%**	**19%**	**14%**	**NA**	**NA**
occipital	front 1	right	back	left	front 2
10 psi air	**52%**	**26%**	**8%**	**72%**	**62%**
12 psi air	**40%**	**20%**	**-2%**	**50%**	**36%**
15 psi air	**32%**	**NA**	**NA**	**NA**	**21%**

Table of Differential Pressure Results for 5mm Intact Sphere

Differential for sphere 5mm										
	peak differential pressure (psi)					time elapsed between peaks (ms)				
ventricle	front 1	right	back	left	front 2	front 1	right	back	left	front 2
10 psi air	**25.1**	**22.31**	**16.43**	**18.54**	**24.08**	**6.1**	**5.884**	**5.9**	**6.096**	**6.024**
12 psi air	**25.78**	**22.84**	**16.44**	**19.67**	**25.77**	**5.572**	**5.872**	**6.08**	**6.036**	**5.544**
15 psi air	**33.36**	**28.98**	**19.64**	**22.38**	**NA**	**5.538**	**6.08**	**5.784**	**0.396**	**NA**
frontal	front 1	right	back	left	front 2	front 1	right	back	left	front 2
10 psi air	**32.3**	**30.22**	**19**	**17.64**	**31.38**	**6.16**	**5.884**	**3.948**	**3.92**	**3.484**
12 psi air	**34.02**	**30.71**	**18.46**	**19.85**	**34.35**	**5.408**	**3.564**	**5.992**	**3.844**	**5.544**
15 psi air	**43.28**	**39.77**	**22.77**	**21.19**	**NA**	**5.516**	**5.812**	**3.8**	**4.98**	**NA**
occipital	front 1	right	back	left	front 2	front 1	right	back	left	front 2
10 psi air	**17.99**	**27.7**	**34.42**	**18.32**	**16.59**	**3.812**	**6.004**	**6.32**	**5.9**	**3.92**
12 psi air	**17.68**	**27.8**	**37.09**	**18.72**	**16.52**	**0.984**	**5.994**	**6.184**	**5.856**	**0.994**
15 psi air	**18.52**	**38.06**	**NA**	**NA**	**20.45**	**3.696**	**5.708**	**NA**	**NA**	**3.964**

Percentages of 1st rate of internal pressure changes in 5 mm intact sphere based on the cell value at the 10 psi overpressure for each orientation.

AIR		Percentage 1st Rate Pressure Change				
Overpressure		front 1	right	back	left	front 2
ventricle	20%	9%	1%	28%	19%	23%
ventricle	50%	44%	51%	29%	62%	NA
frontal	20%	10%	1%	29%	11%	17%
frontal	50%	43%	39%	51%	38%	NA
occipital	20%	24%	5%	17%	5%	2%
occipital	50%	75%	54%	NA	NA	25%

State of Gages during Testing of the 5mm Intact Sphere

	Strain status for sphere 5mm				
Frontal	front 1	right	back	left	front 2
10 psi air					
12 psi air					
15 psi air					
Left	front 1	right	back	left	front 2
10 psi air					
12 psi air					
15 psi air					
Right	front 1	right	back	left	front 2
10 psi air					
12 psi air					
15 psi air					
Occipital	front 1	right	back	left	front 2
10 psi air					
12 psi air					
15 psi air					

	working
	signal problems
	not working

Strain Data

Test 1 Front 1 Orientation 5mm Intact Sphere

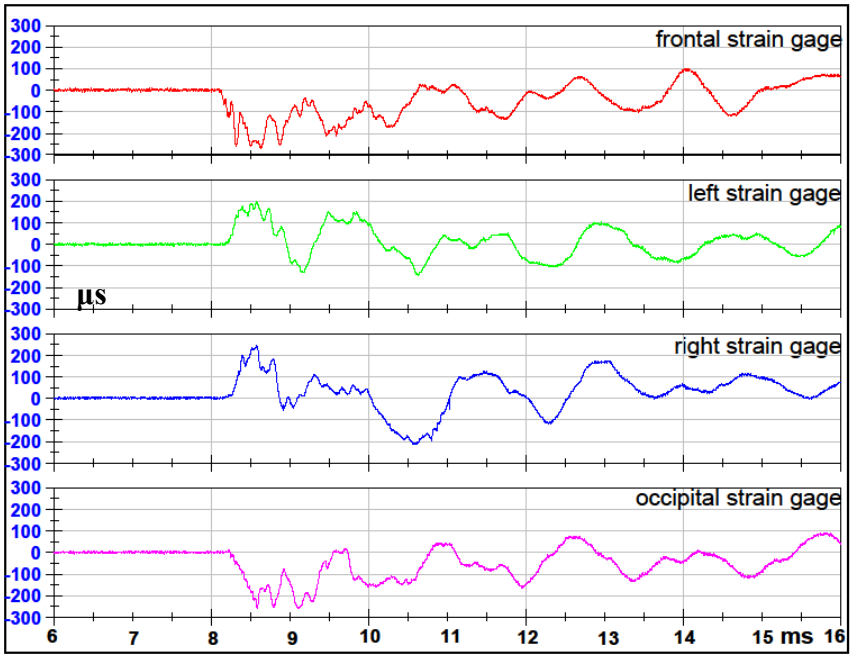

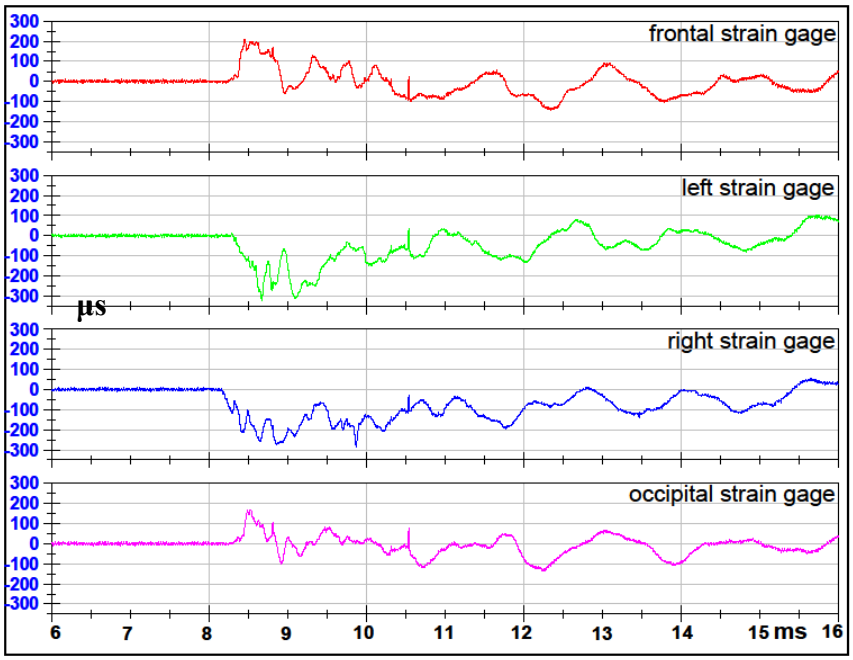

Test 2 Right Orientation 5mm Intact Sphere

Test 3 Back Orientation 5mm Intact Sphere

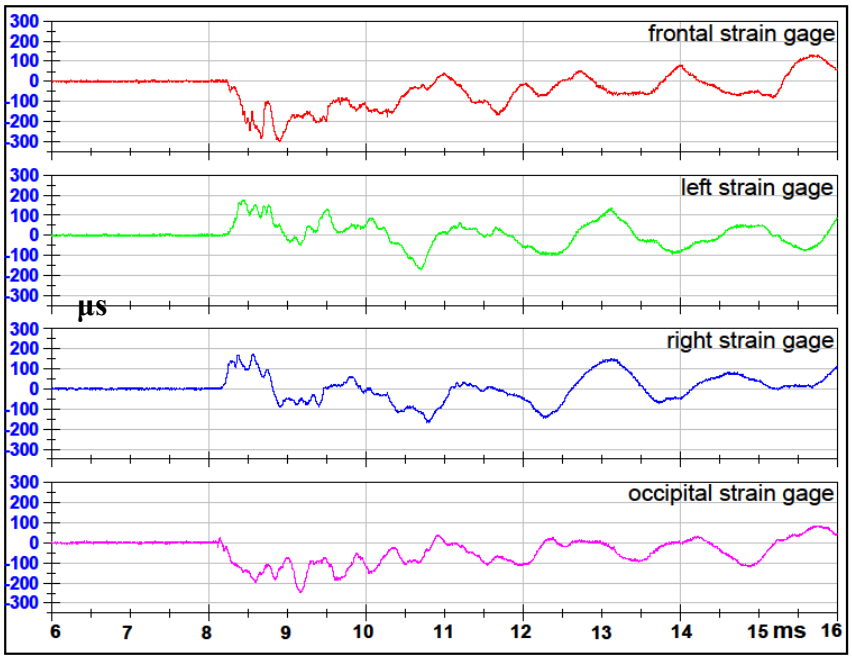

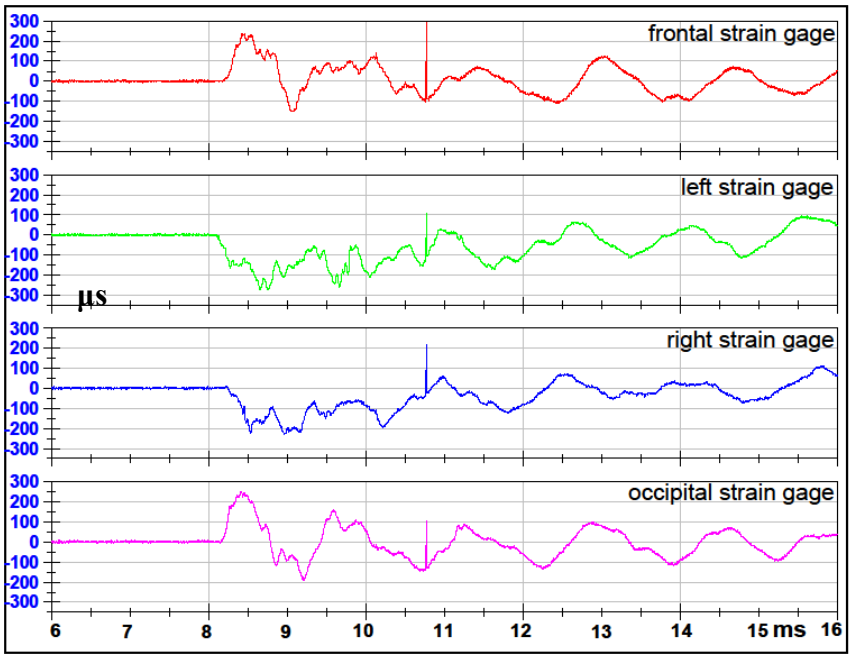

Test 4 Left Orientation 5mm Intact Sphere

Test 5 Front 2 Orientation 5mm Intact Sphere

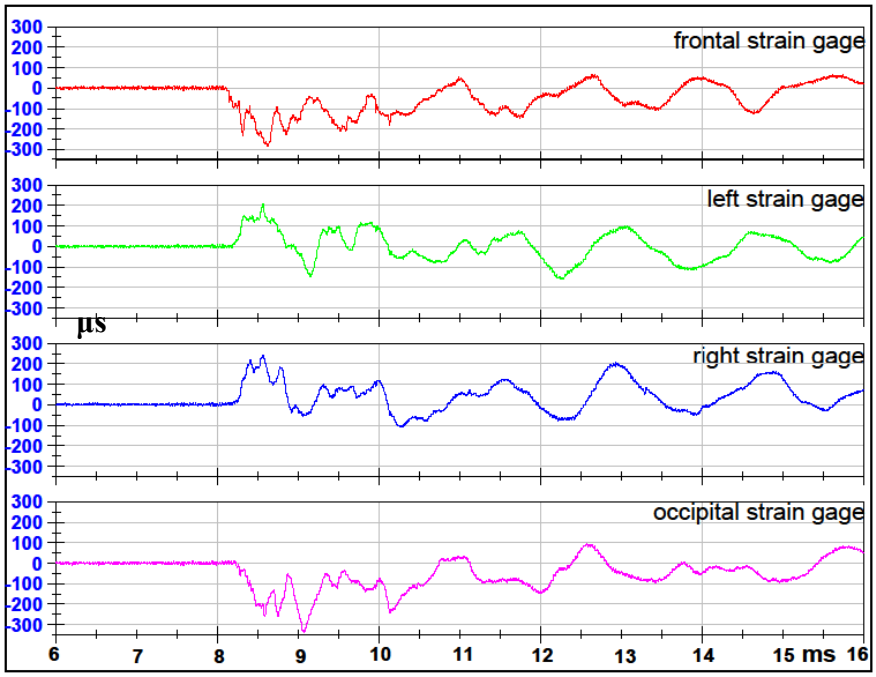

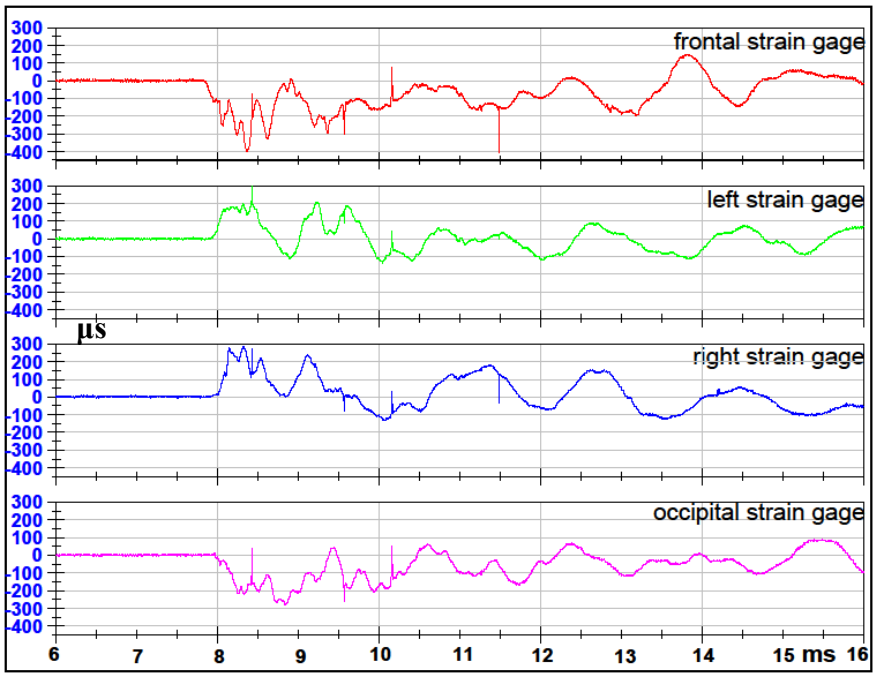

Test 6 Front 1 Orientation 5mm Intact Sphere

Test 7 Left Orientation 5mm Intact Sphere

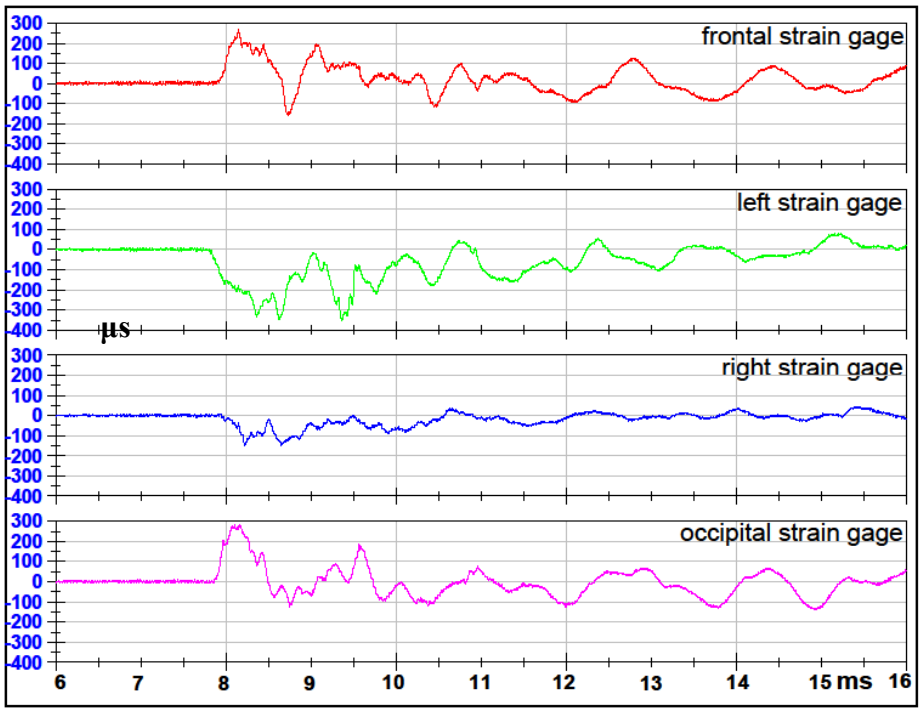

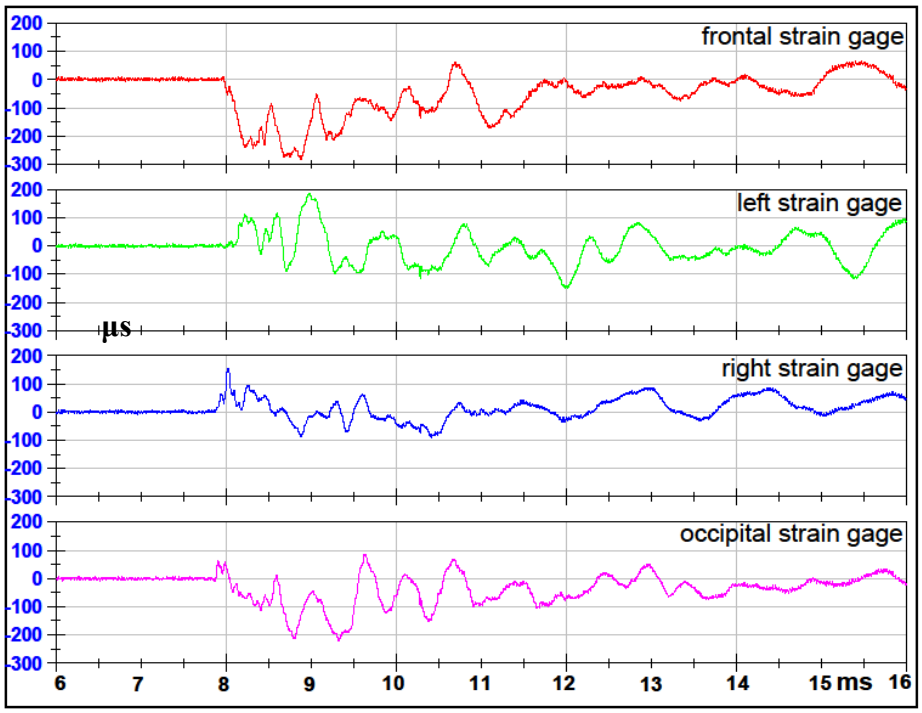

Test 8 Back Orientation 5mm Intact Sphere

Test 9 Right Orientation 5mm Intact Sphere

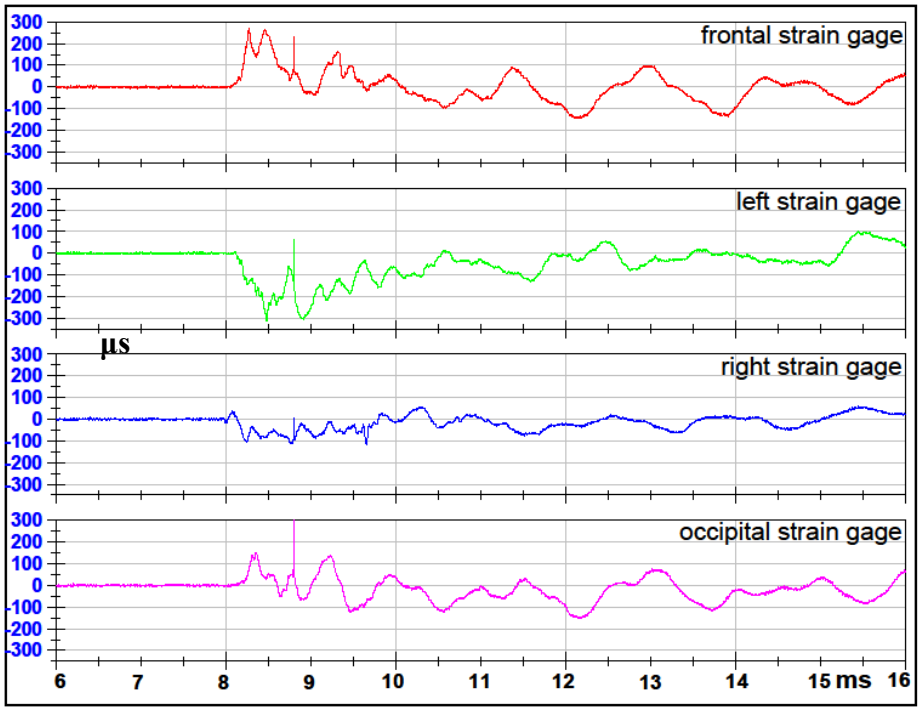

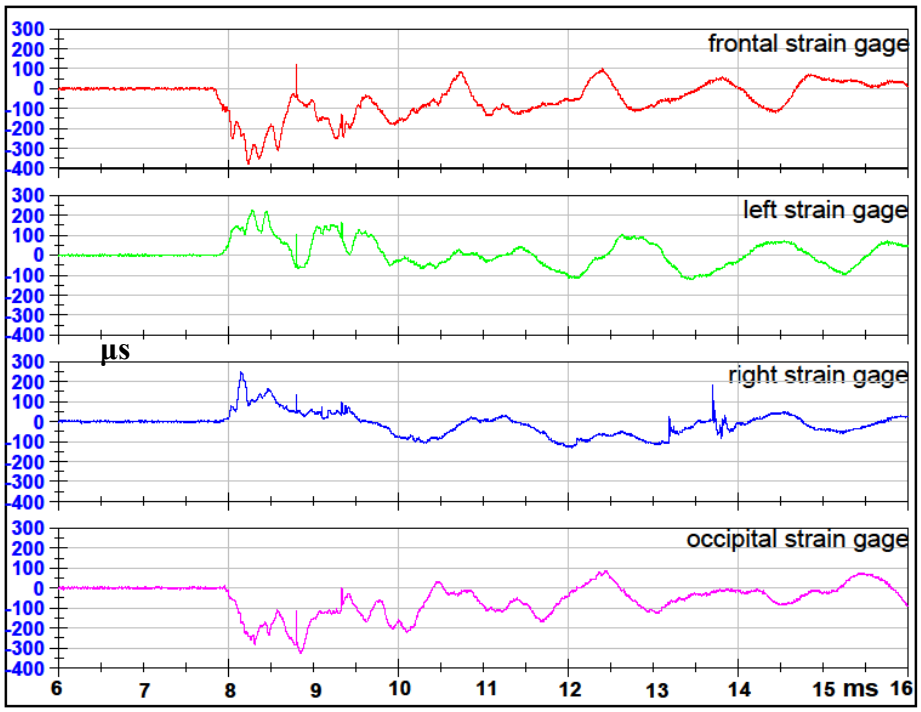

Test 10 Front 2 Orientation 5mm Intact Sphere

Test 11 Front 1 Orientation 5mm Intact Sphere

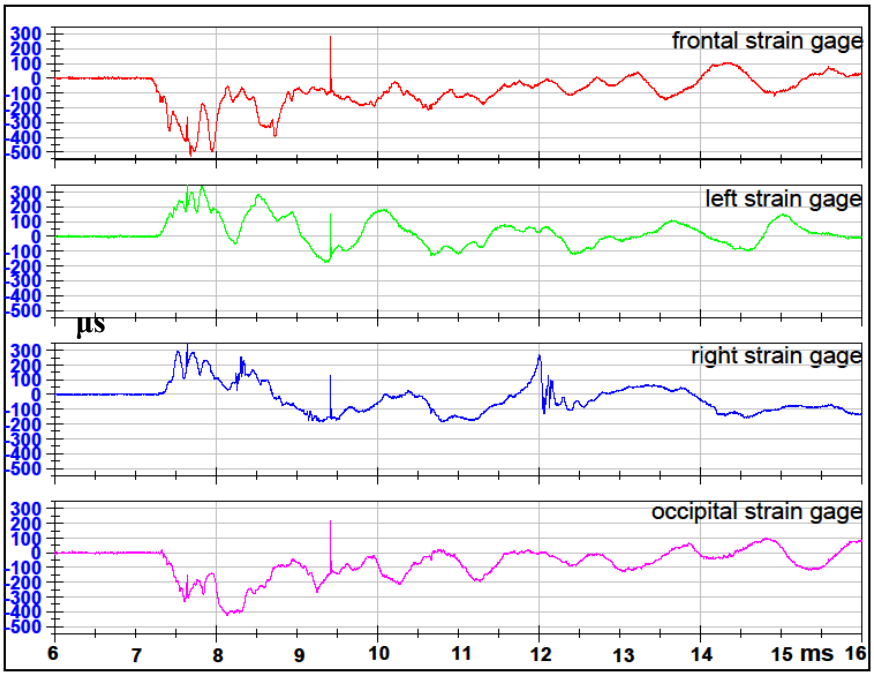

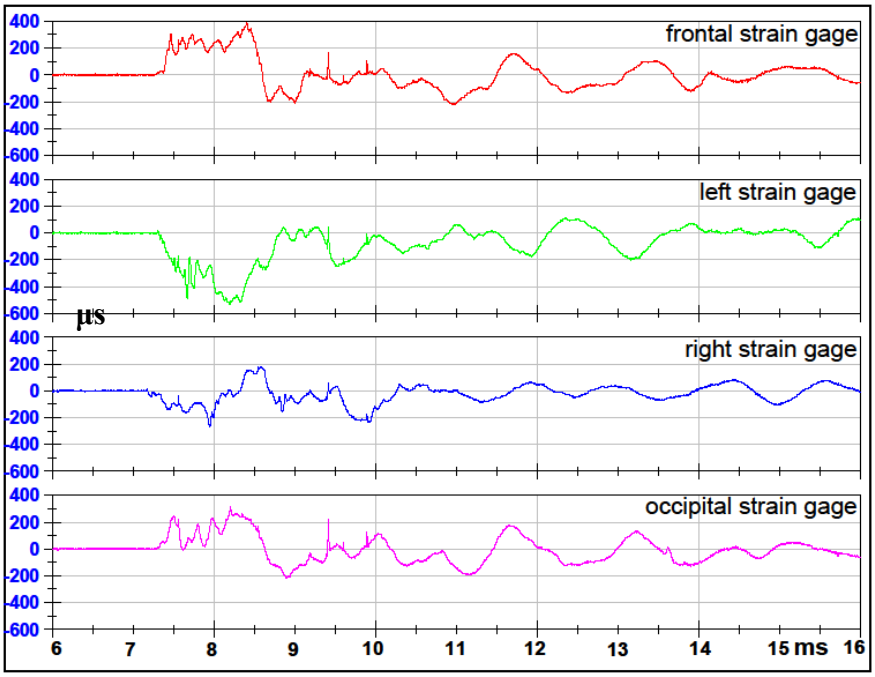

Test 12 Right Orientation 5mm Intact Sphere

Test 13 Back Orientation 5mm Intact Sphere

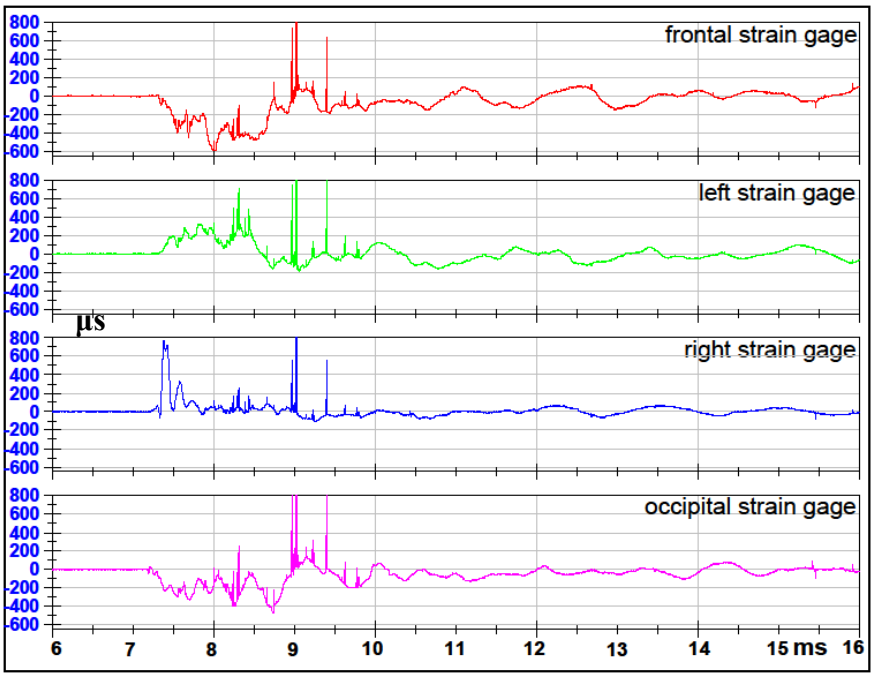

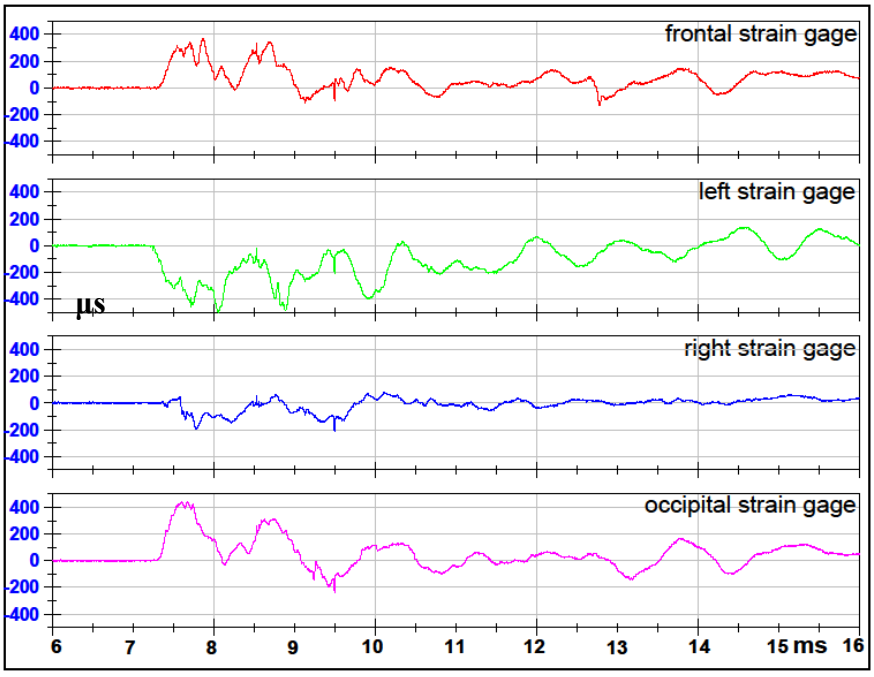

Test 14 Left Orientation 5mm Intact Sphere

Test 15 Front 2 Orientation 5mm Intact Sphere

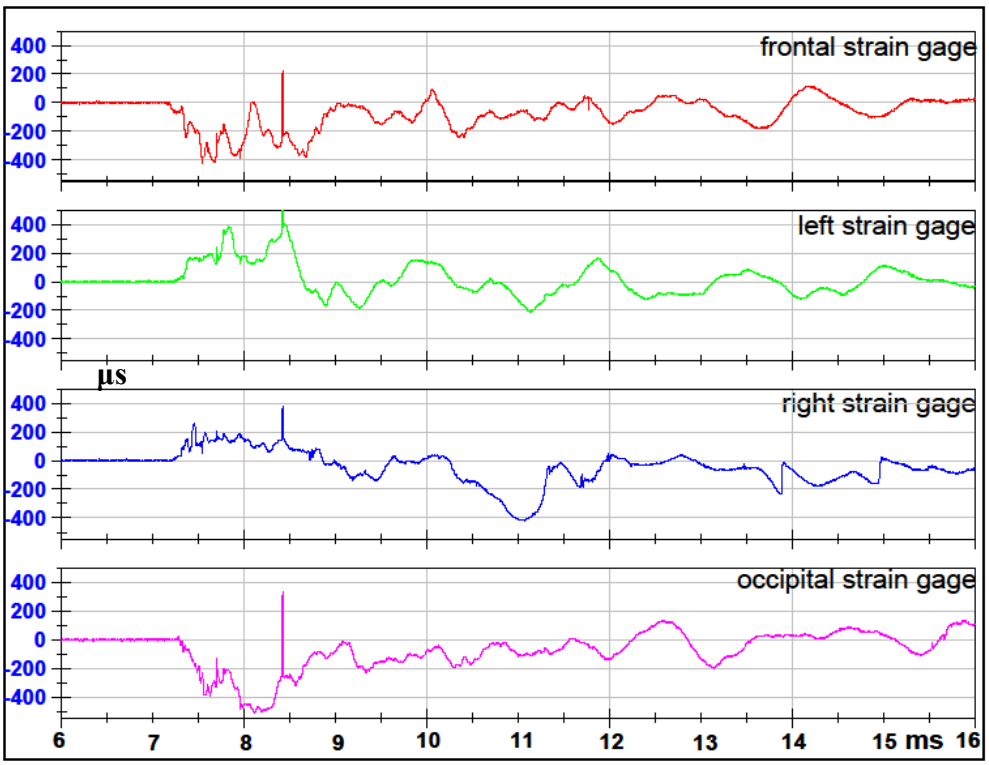

Results after the Introduction of Apertures

Test 1 Front 1 Orientation 5mm Sphere with Holes

FILTERED DATA

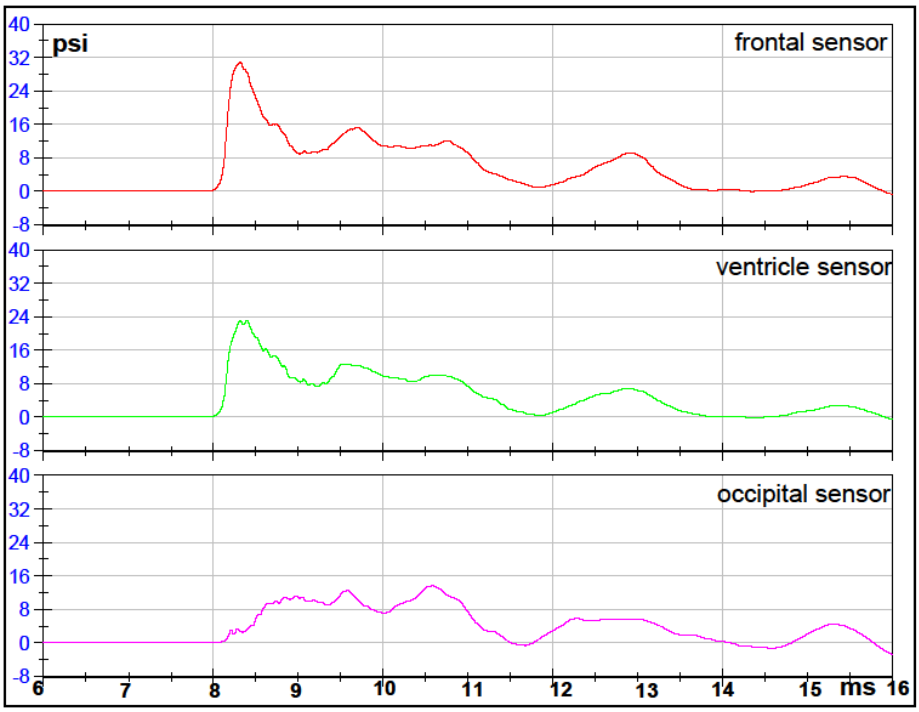

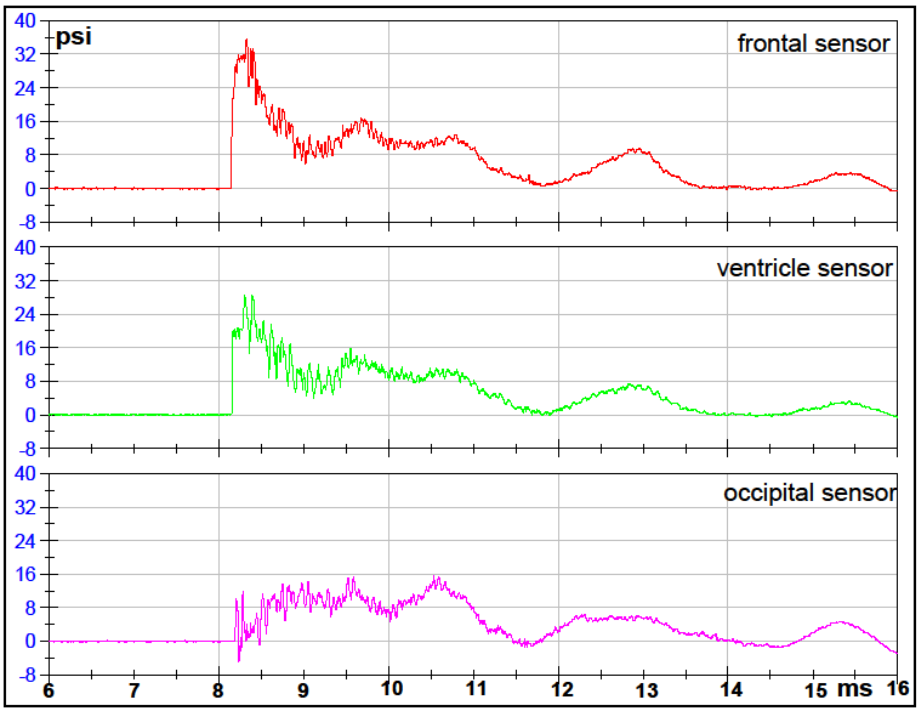

RAW DATA

Test 2 Right Orientation 5mm Sphere with Holes

FILTERED DATA

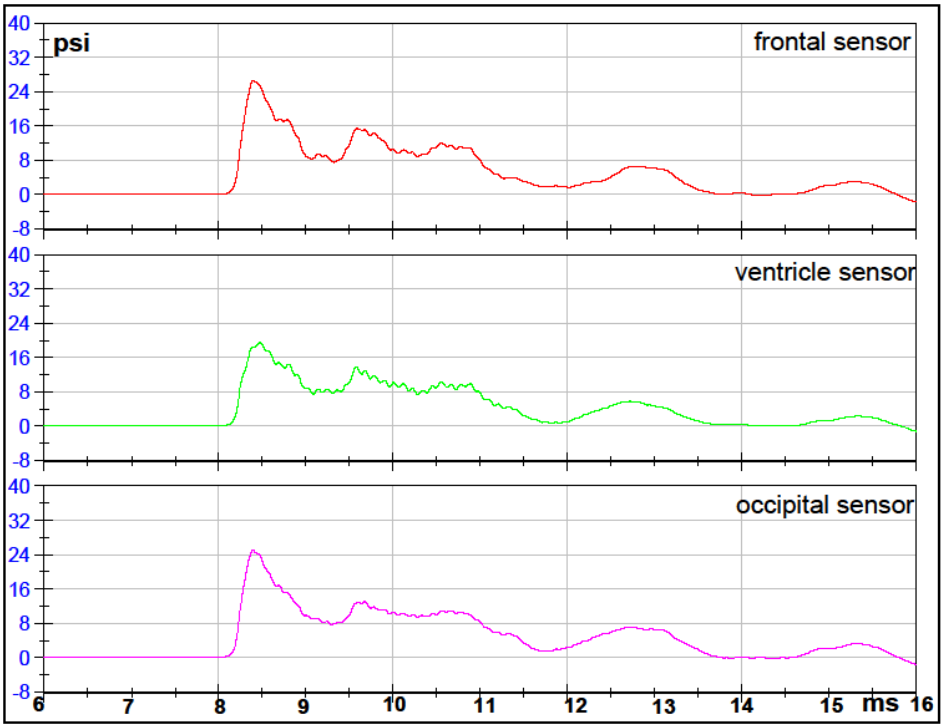

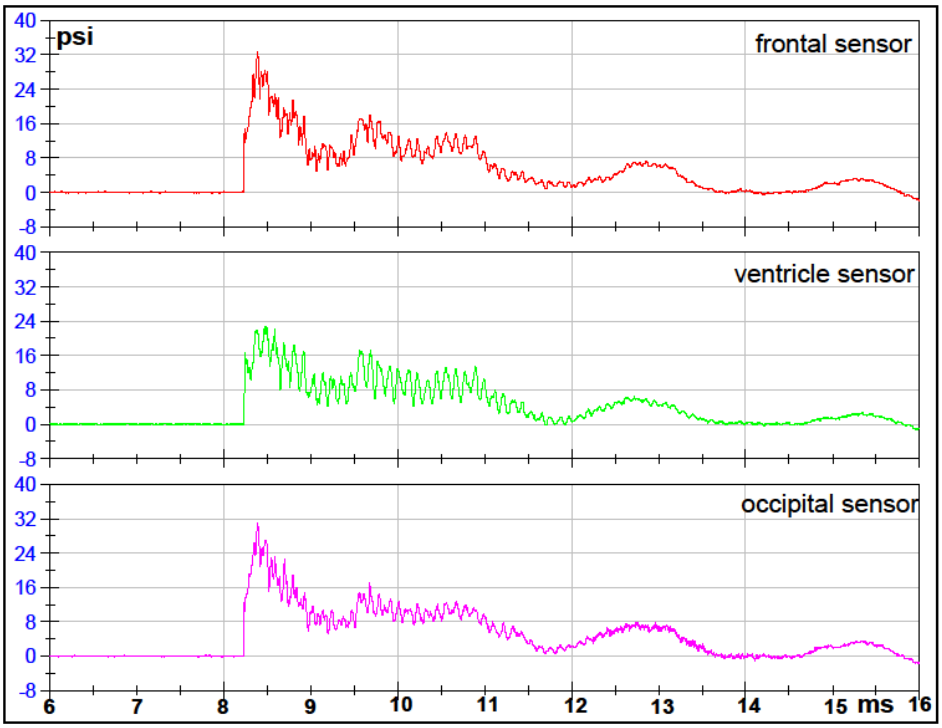

RAW DATA

Test 3 Back Orientation 5mm Sphere with Holes

FILTERED DATA

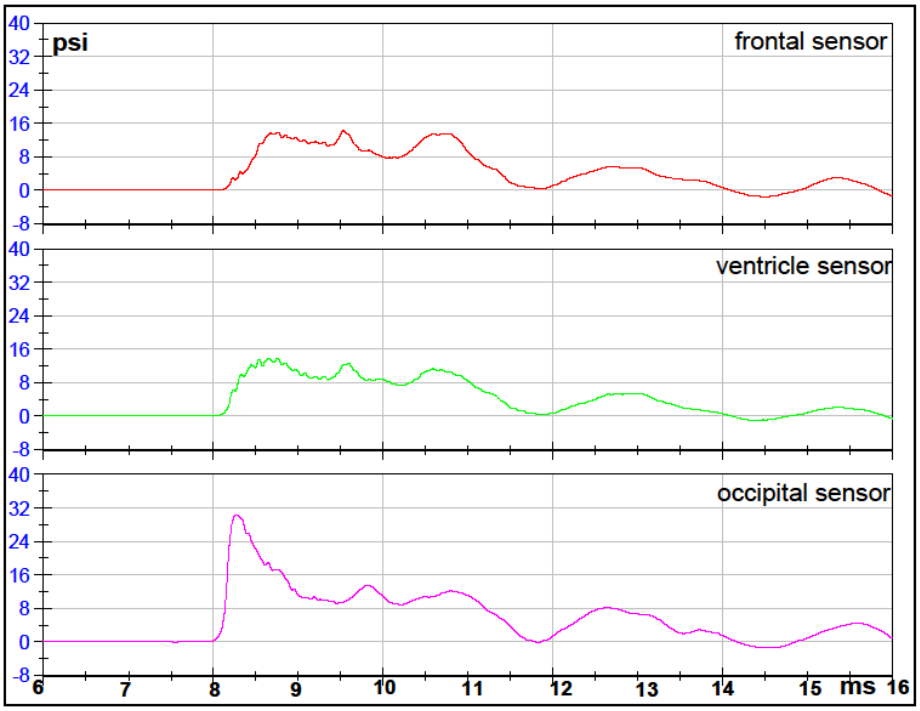

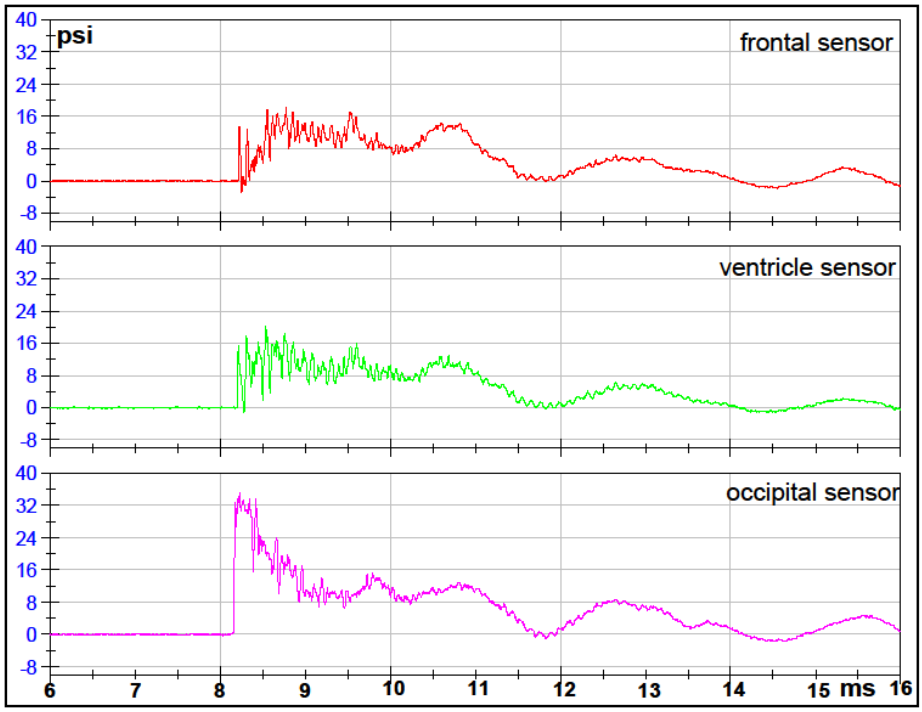

RAW DATA

Test 4 Left Orientation 5mm Sphere with Holes

FILTERED DATA

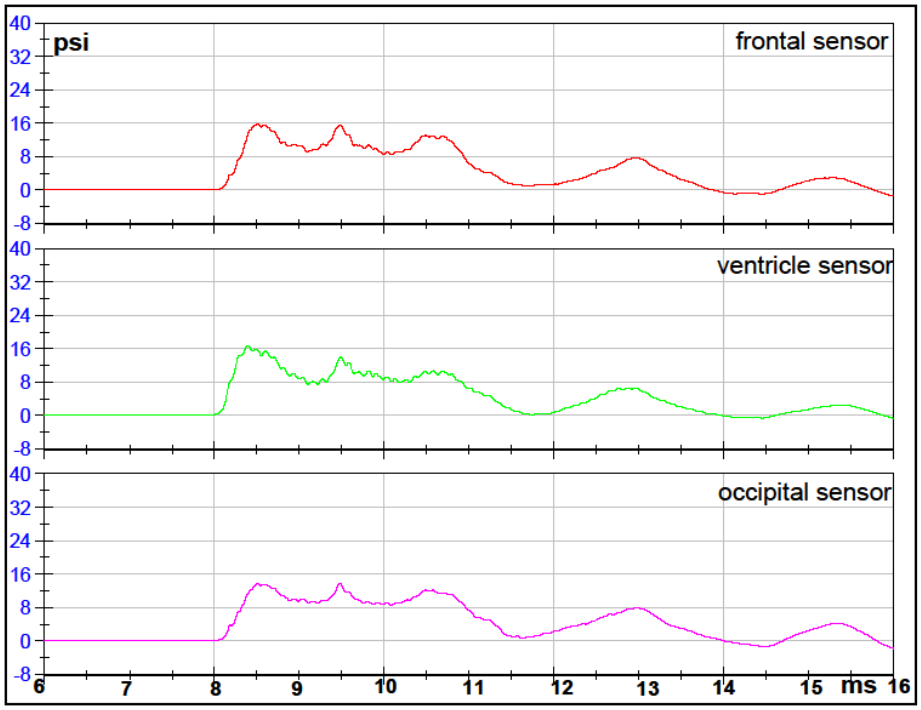

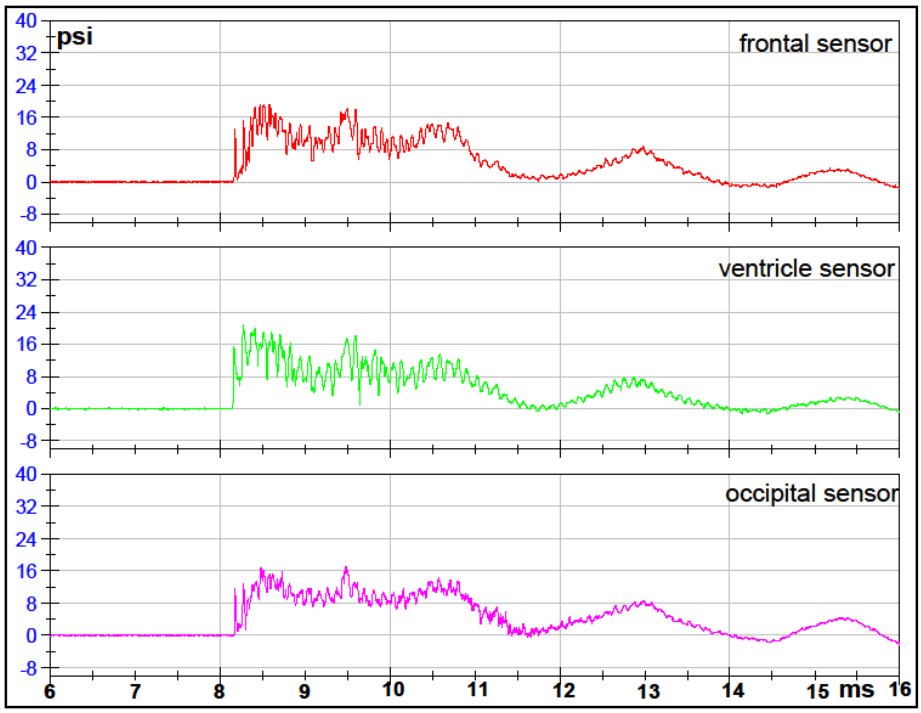

RAW DATA

Test 5 Front 2 Orientation 5mm Sphere with Holes

FILTERED DATA

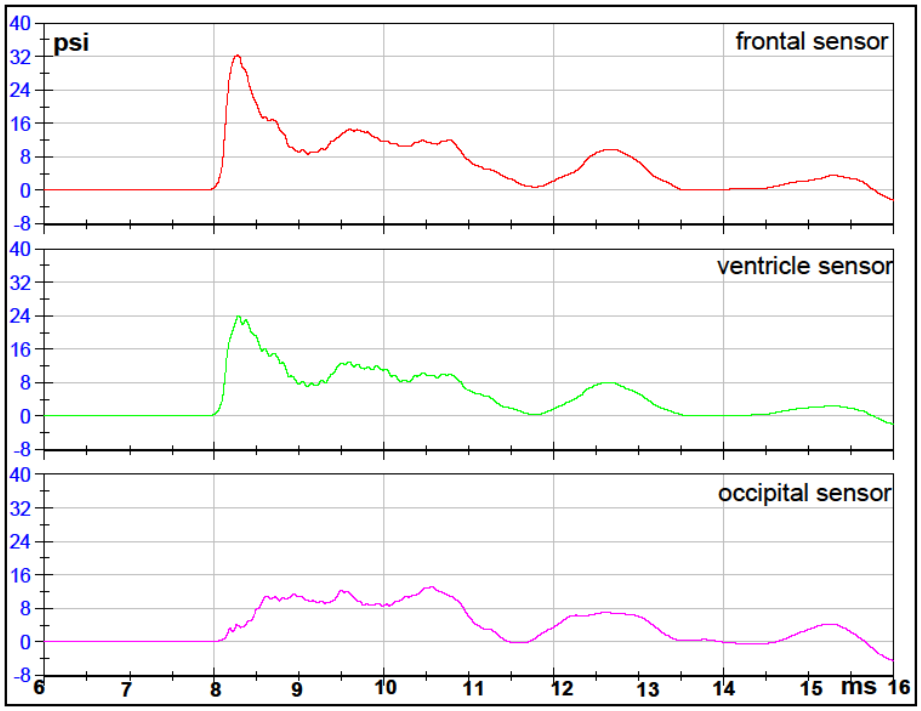

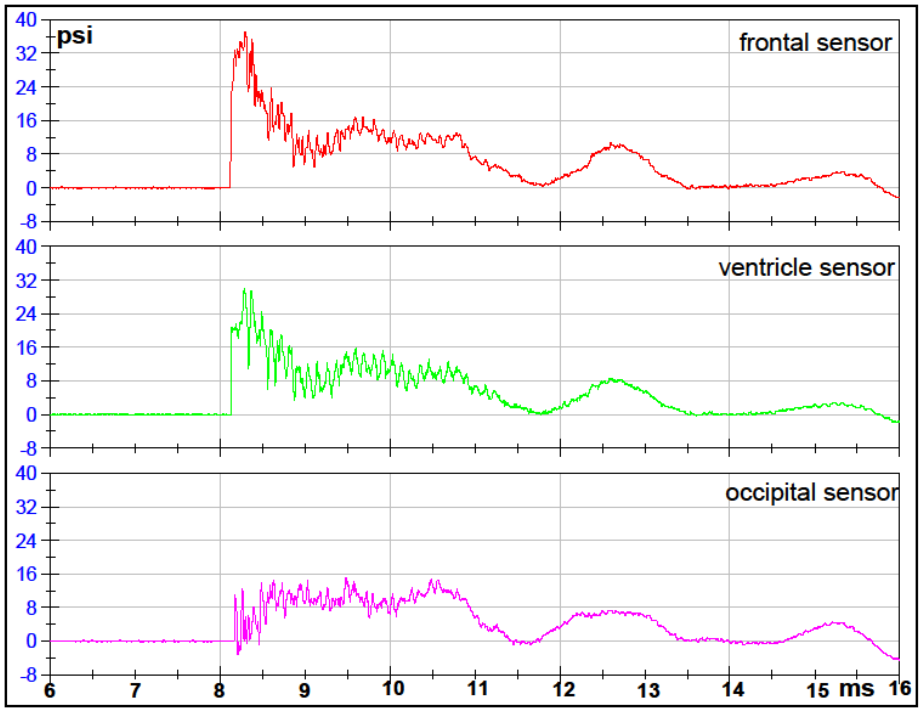

RAW DATA

Test 6 Front 1 Orientation 5mm Sphere with Holes

FILTERED DATA

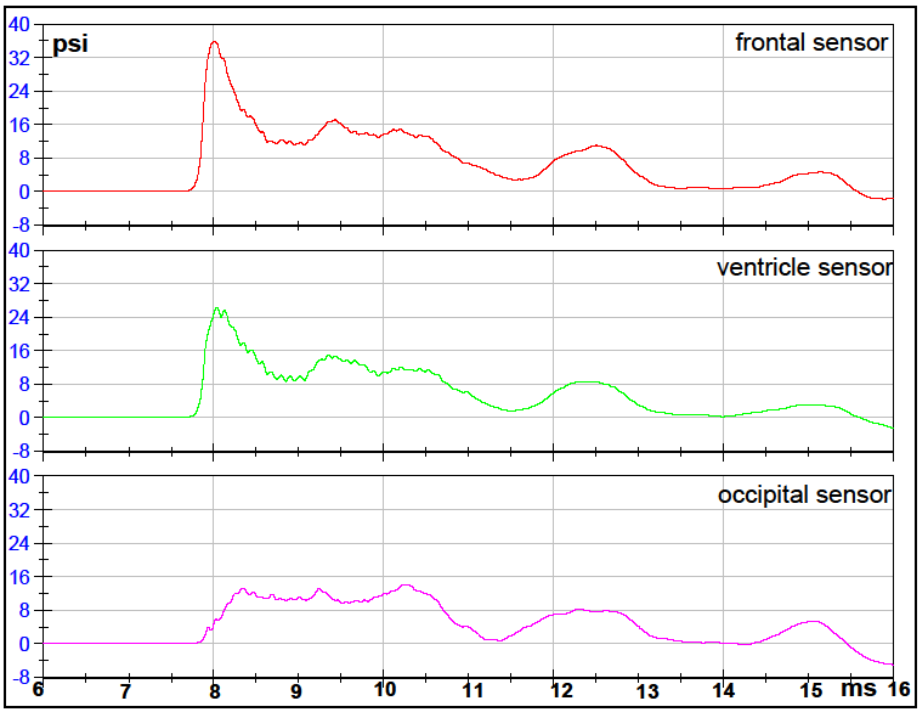

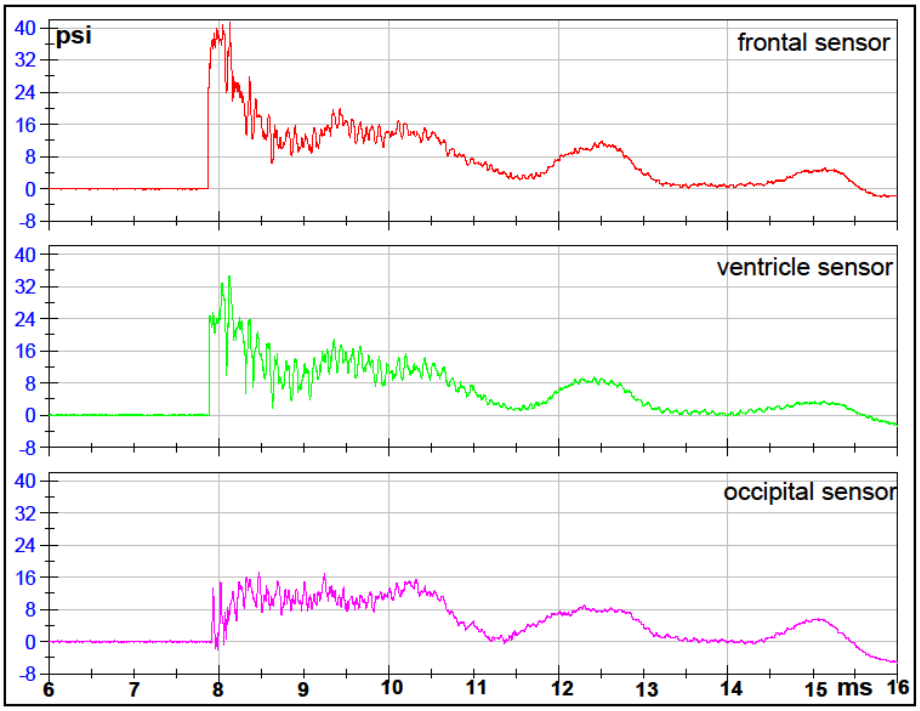

RAW DATA

Test 7 Left Orientation 5mm Sphere with Holes

FILTERED DATA

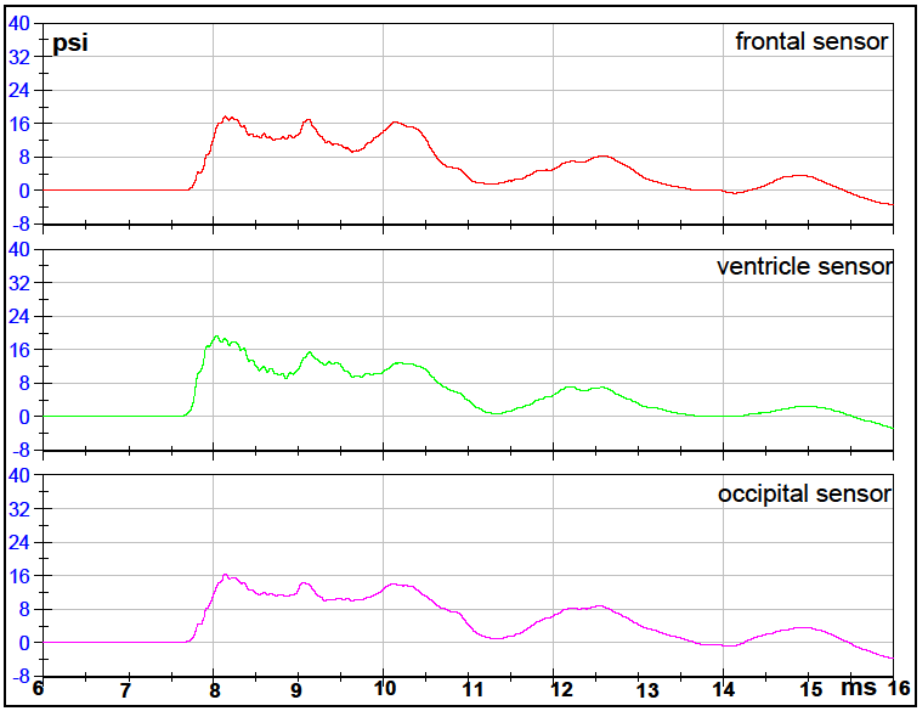

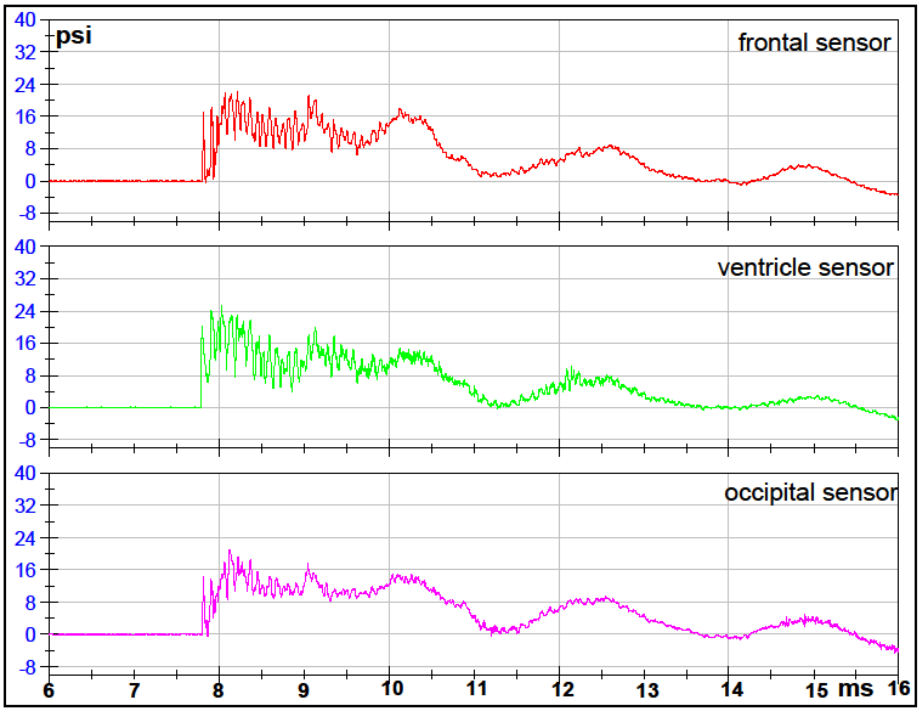

RAW DATA

Test 8 Back Orientation 5mm Sphere with Holes

FILTERED DATA

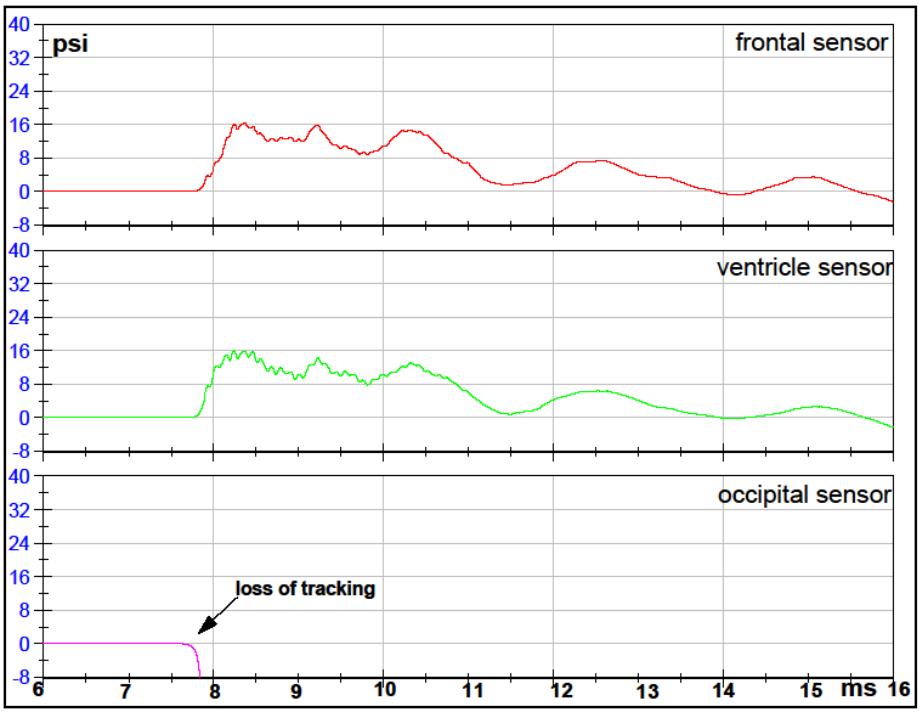

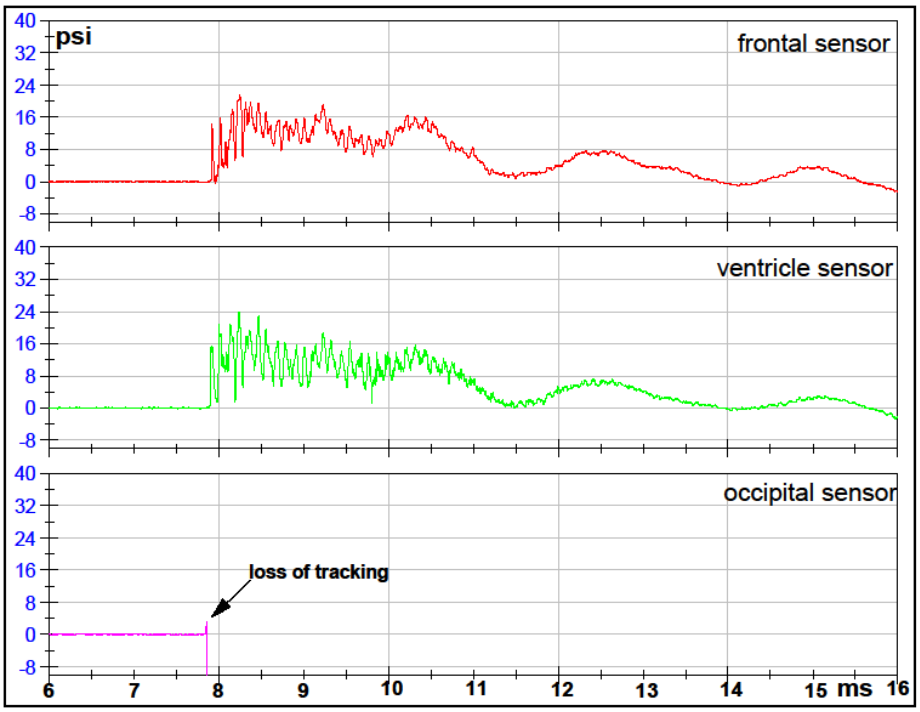

RAW DATA

Test 9 Right Orientation 5mm Sphere with Holes

FILTERED DATA

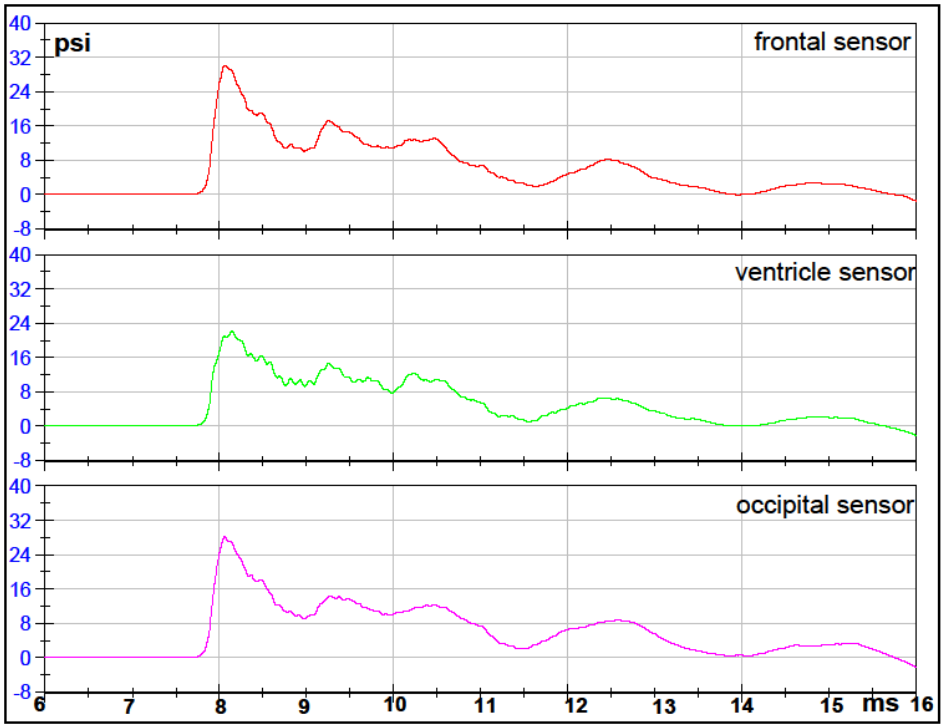

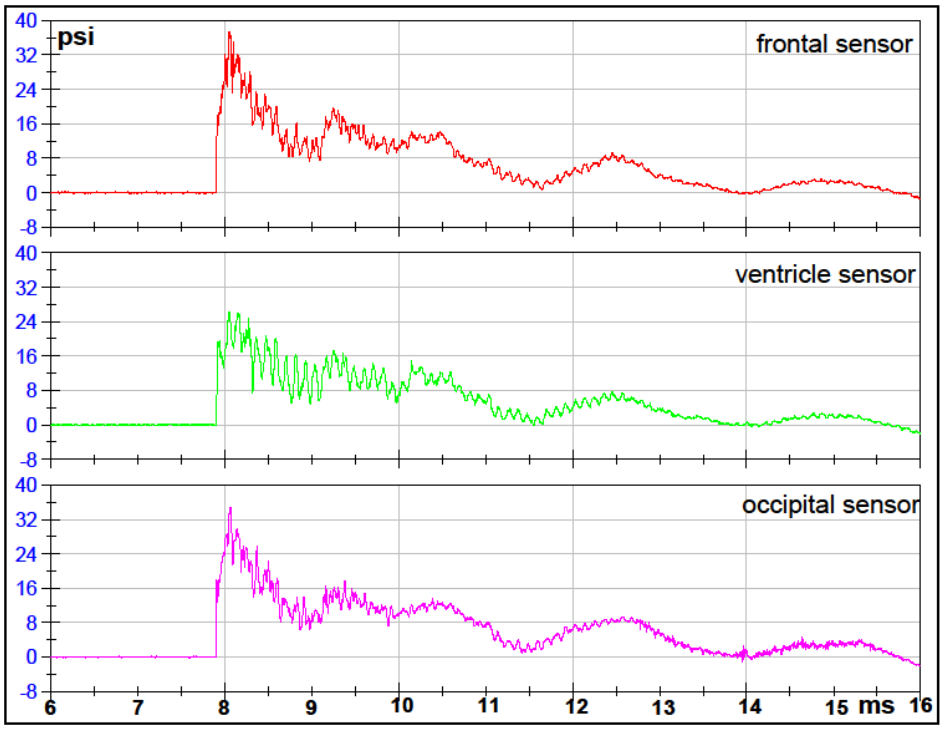

RAW DATA

Test 10 Front 2 Orientation 5mm Sphere with Holes

FILTERED DATA

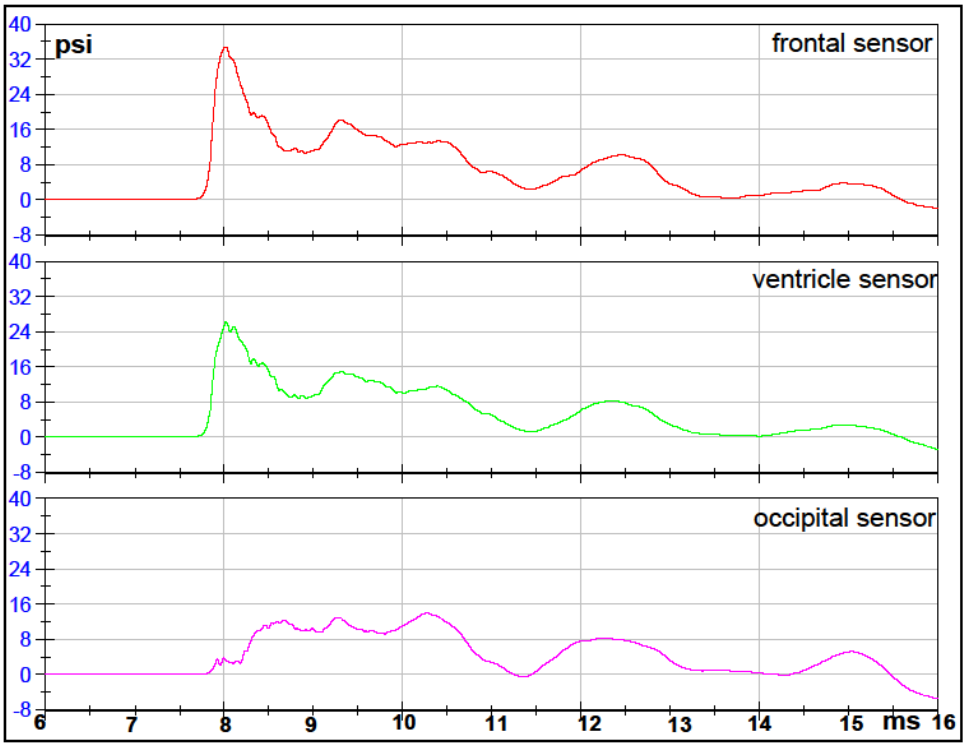

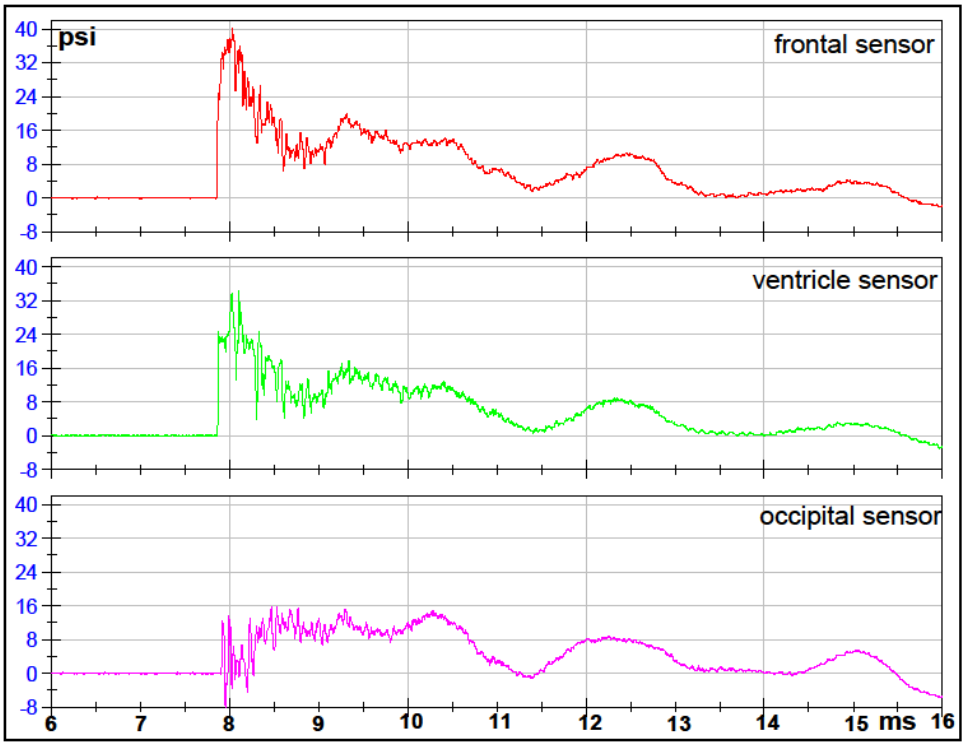

RAW DATA

Test 11 Front 1 Orientation 5mm Sphere with Holes

FILTERED DATA

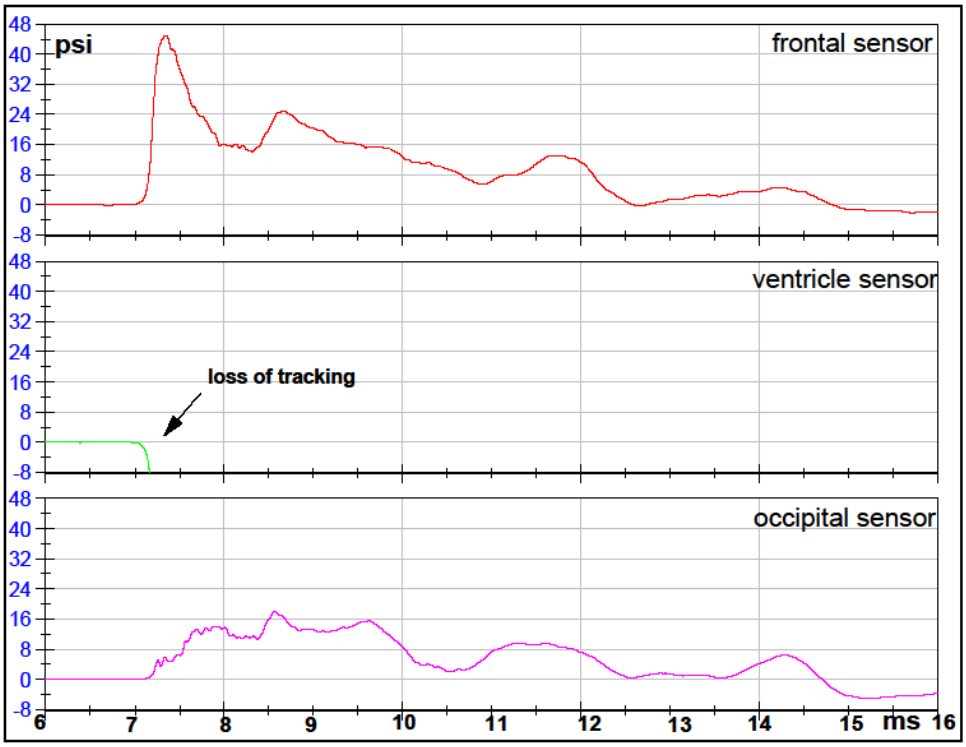

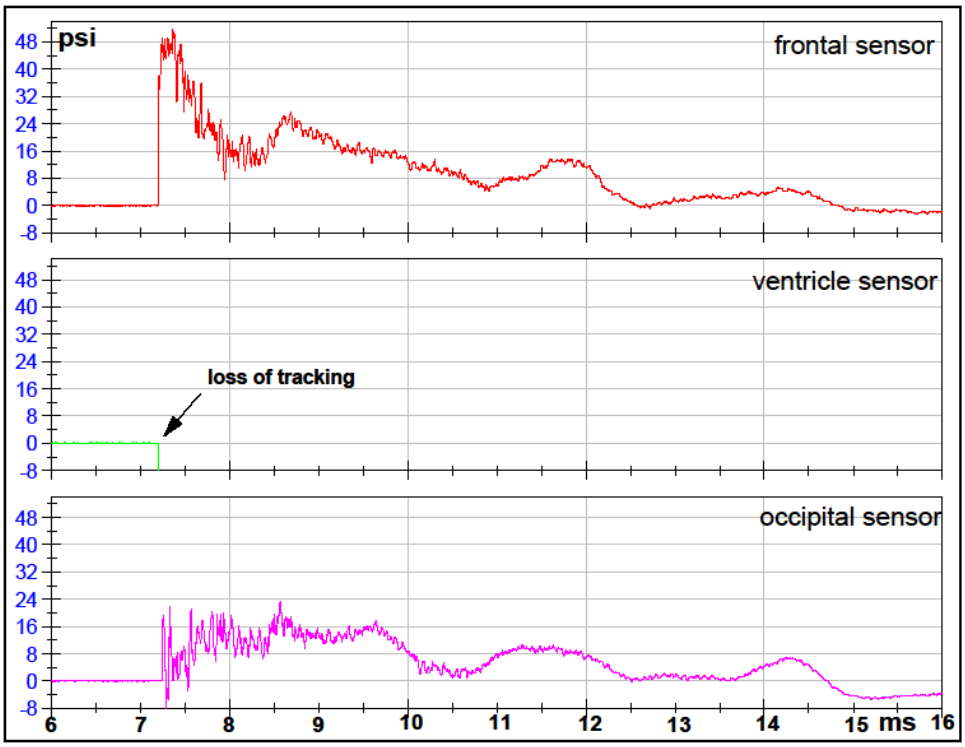

RAW DATA

Test 12 Right Orientation 5mm Sphere with Holes

FILTERED DATA

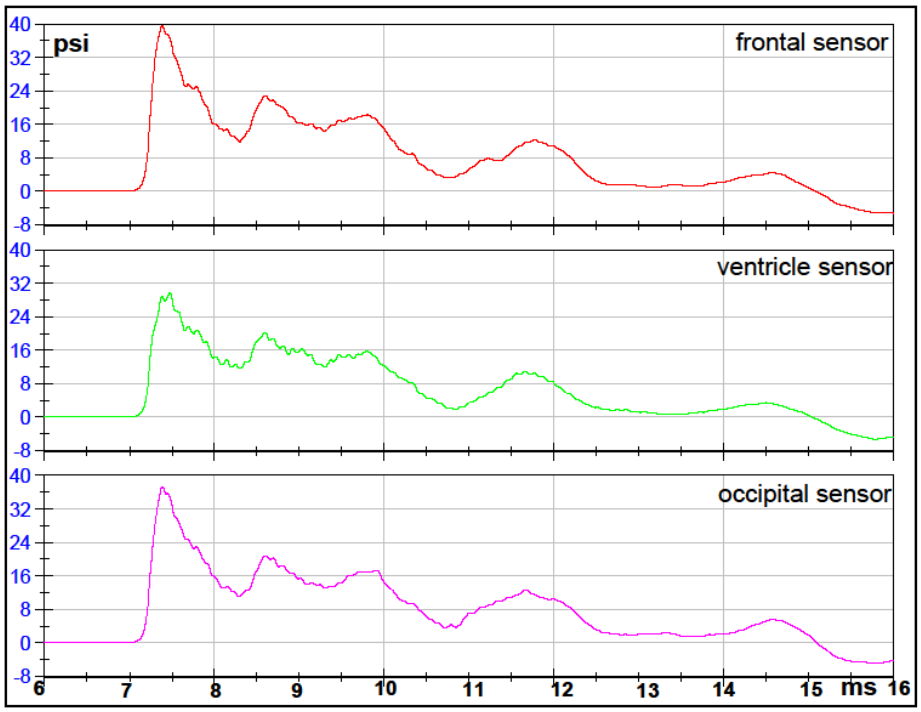

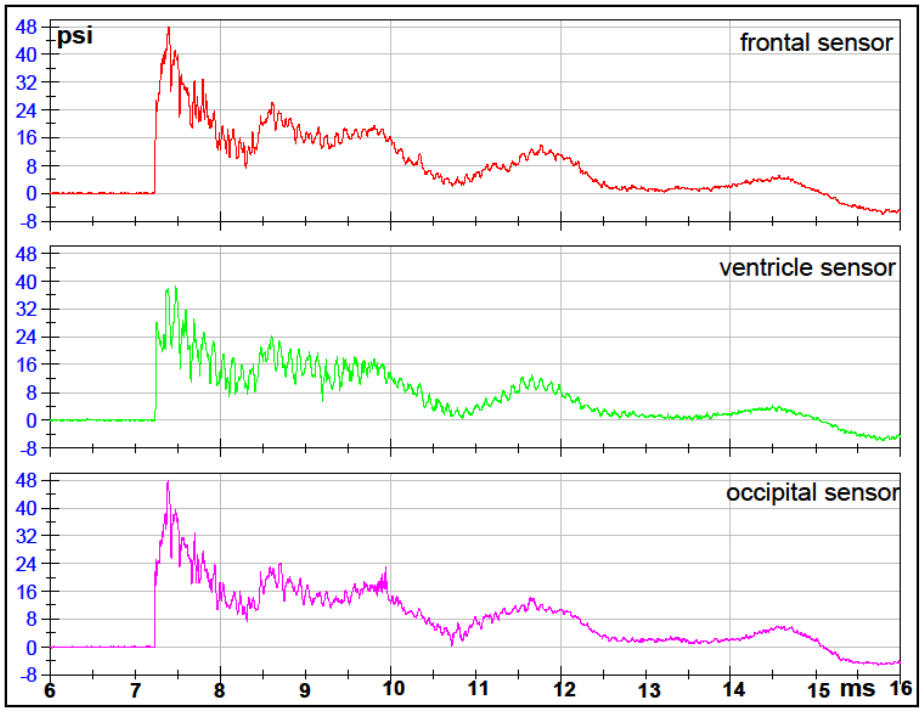

RAW DATA

Test 13 Back Orientation 5mm Sphere with Holes

FILTERED DATA

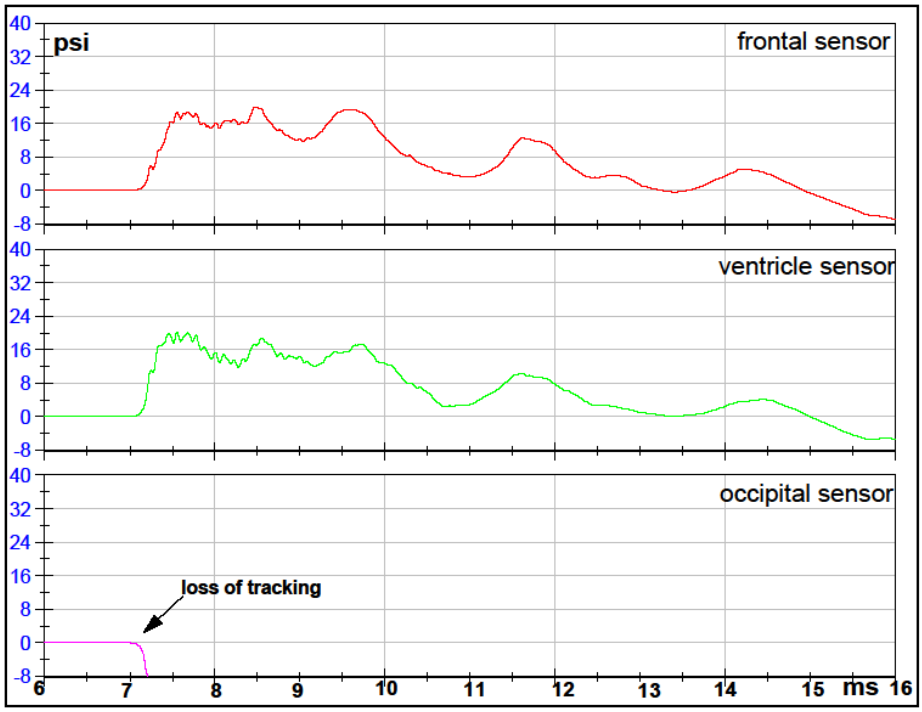

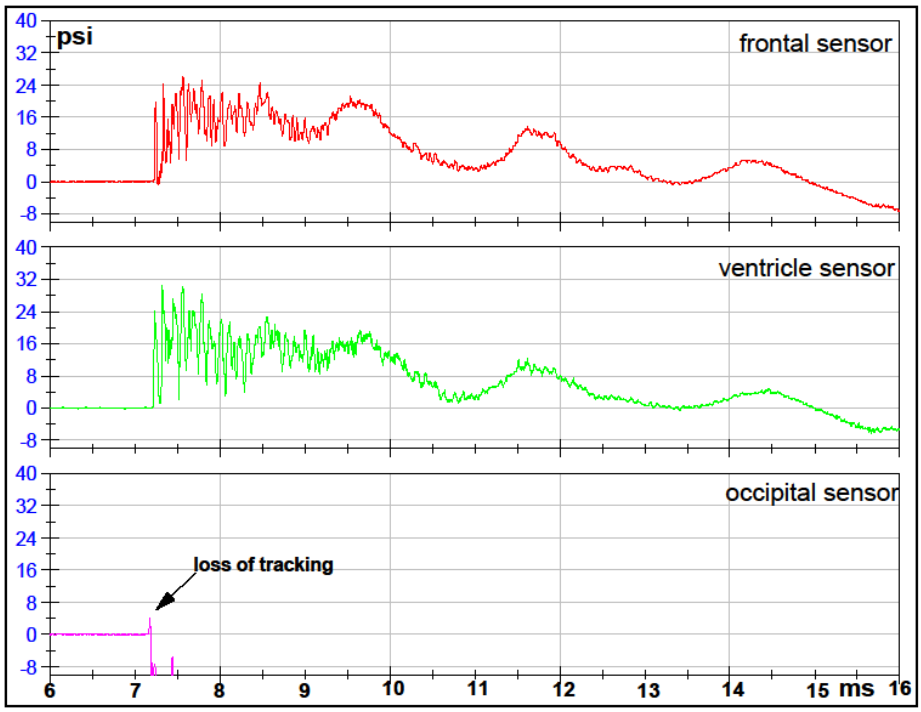

RAW DATA

Test 14 Left Orientation 5mm Sphere with Holes

FILTERED DATA

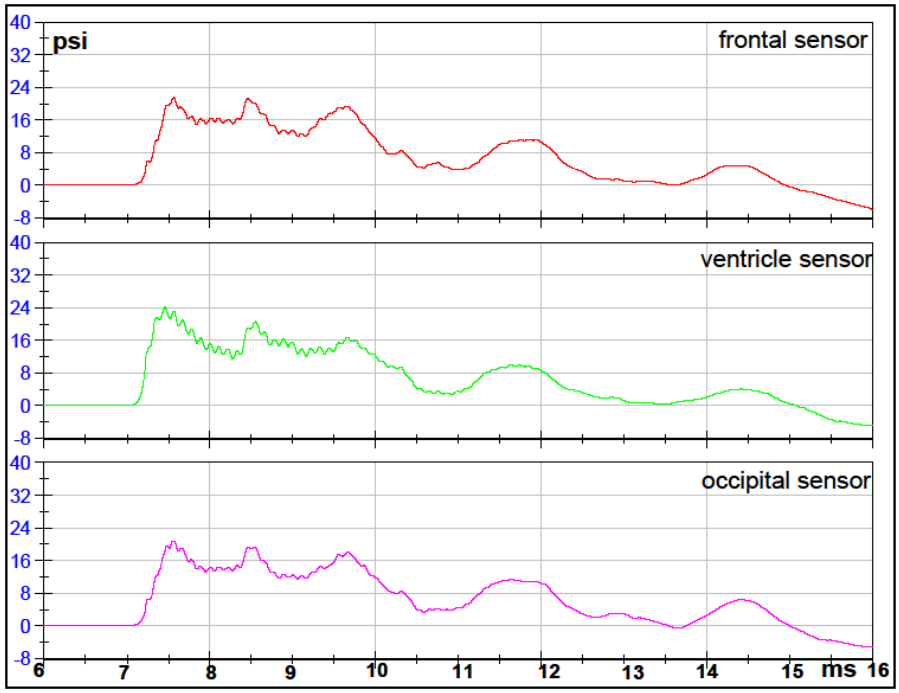

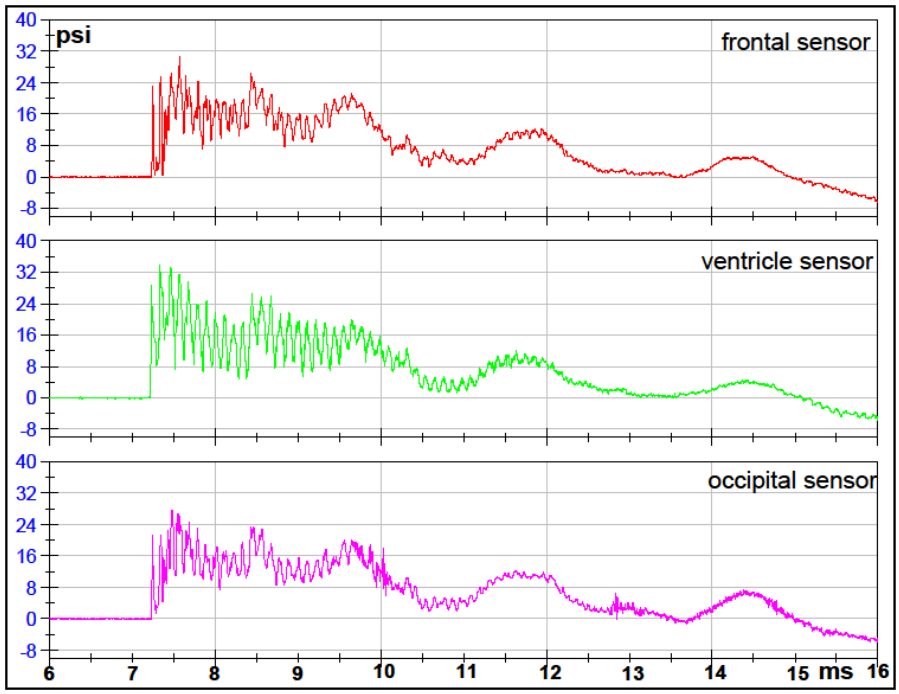

RAW DATA

Test 15 Front 2 Orientation 5mm Sphere with Holes

FILTERED DATA

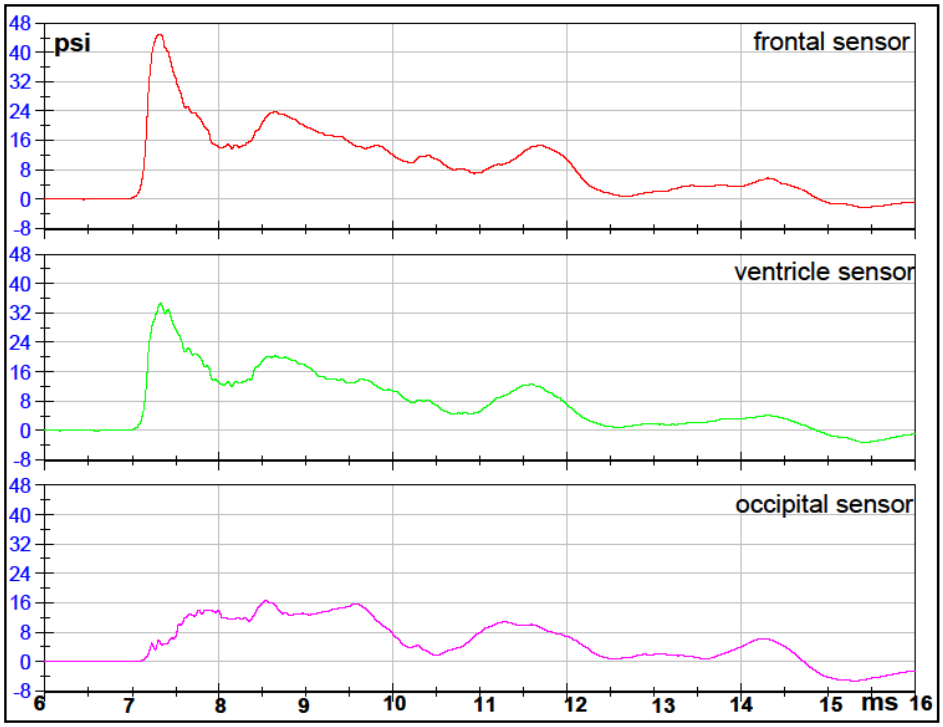

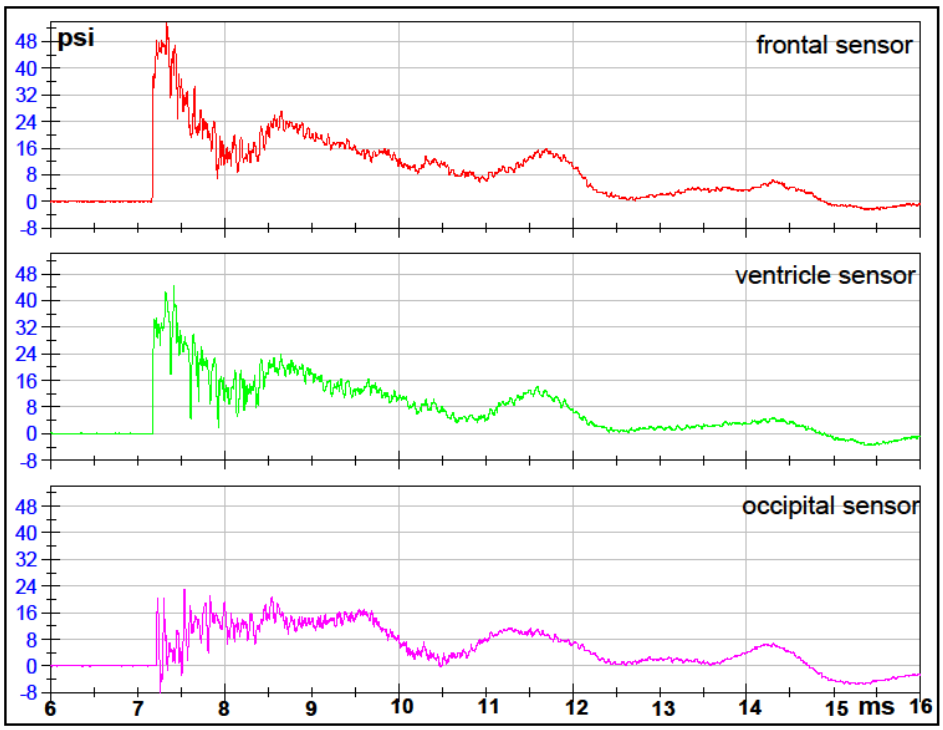

RAW DATA

Comparison for reproducibility of each pressure sensor in Front Orientation at 10psi 5mm Sphere with Holes

VENTRICLE FILTERED DATA

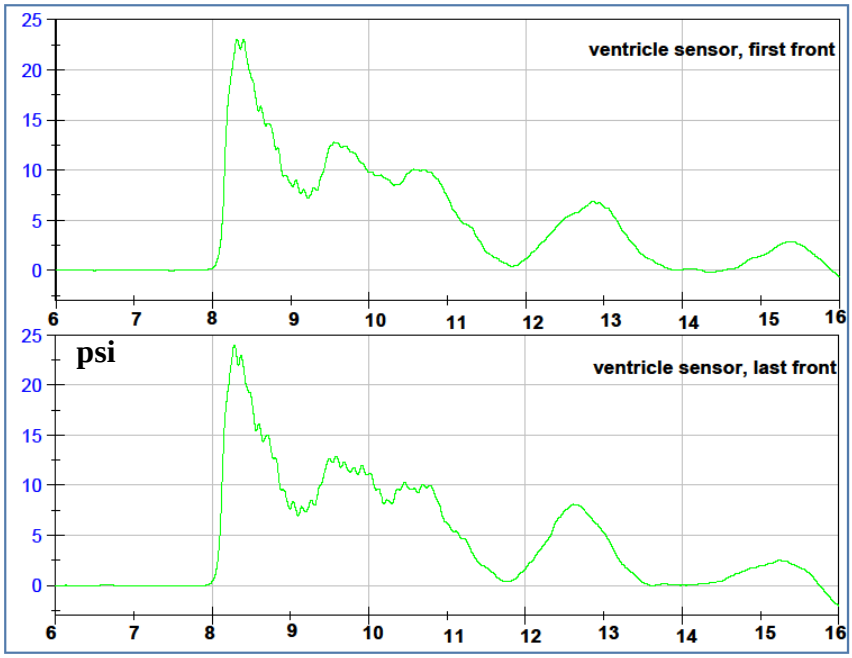

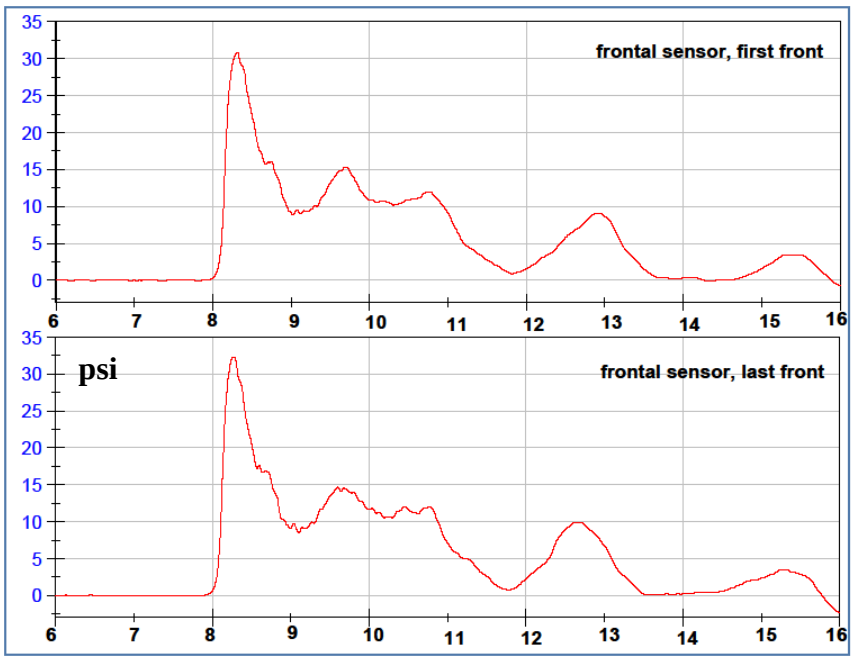

FRONTAL FILTERED DATA

Comparison for reproducibility of each pressure sensor in Front Orientation at 10psi 5mm Sphere with Holes

OCCIPITAL FILTERED DATA

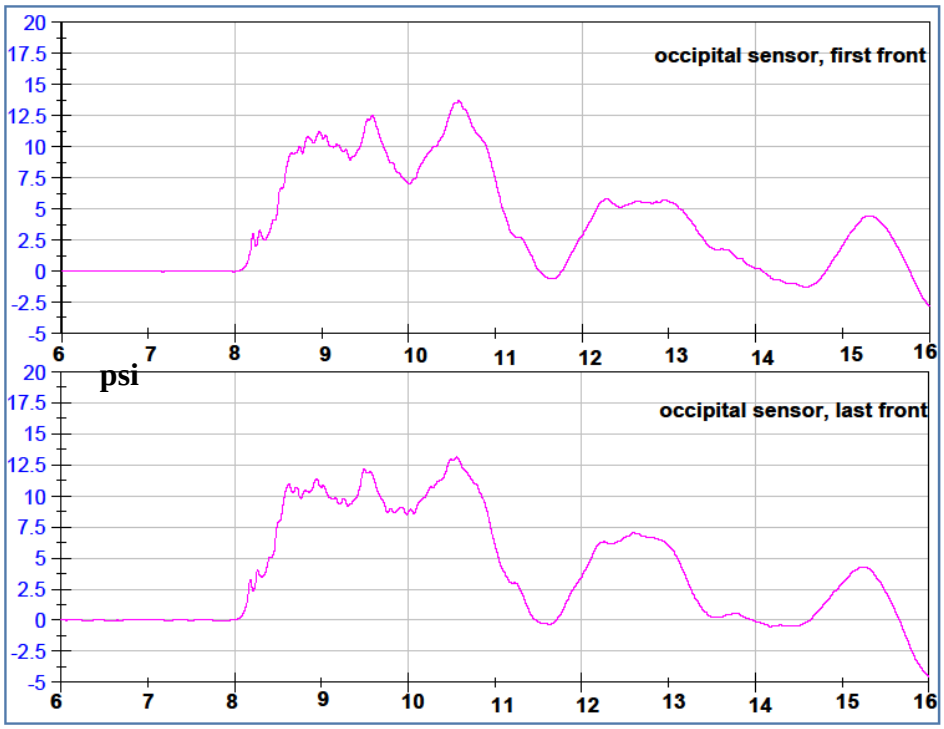

Comparison for reproducibility of each pressure sensor in Front Orientation at 12psi 5mm Sphere with Holes

VENTRICLE FILTERED DATA

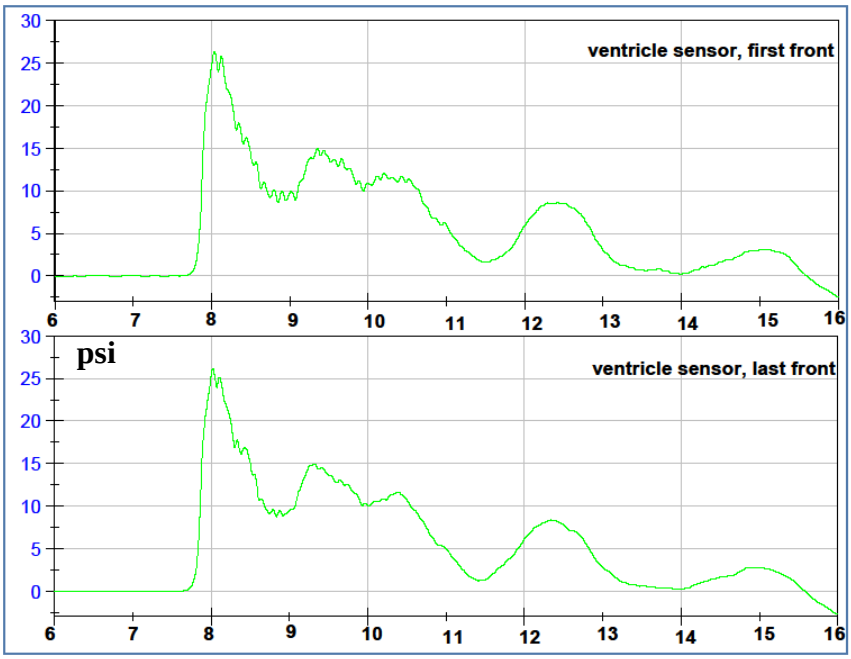

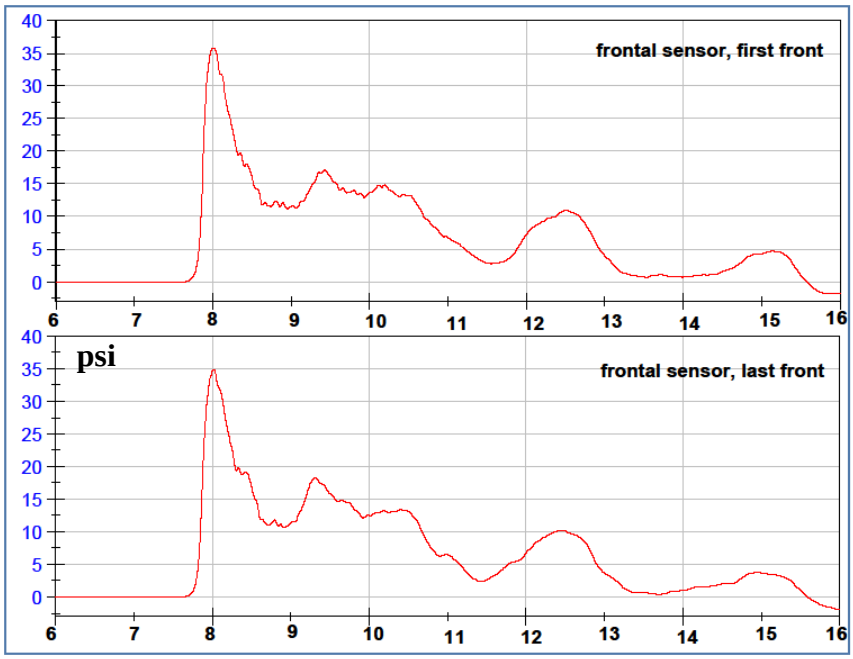

FRONTAL FILTERED DATA

Comparison for reproducibility of each pressure sensor in Front Orientation at 12psi 5mm Sphere with Holes

OCCIPITAL FILTERED DATA

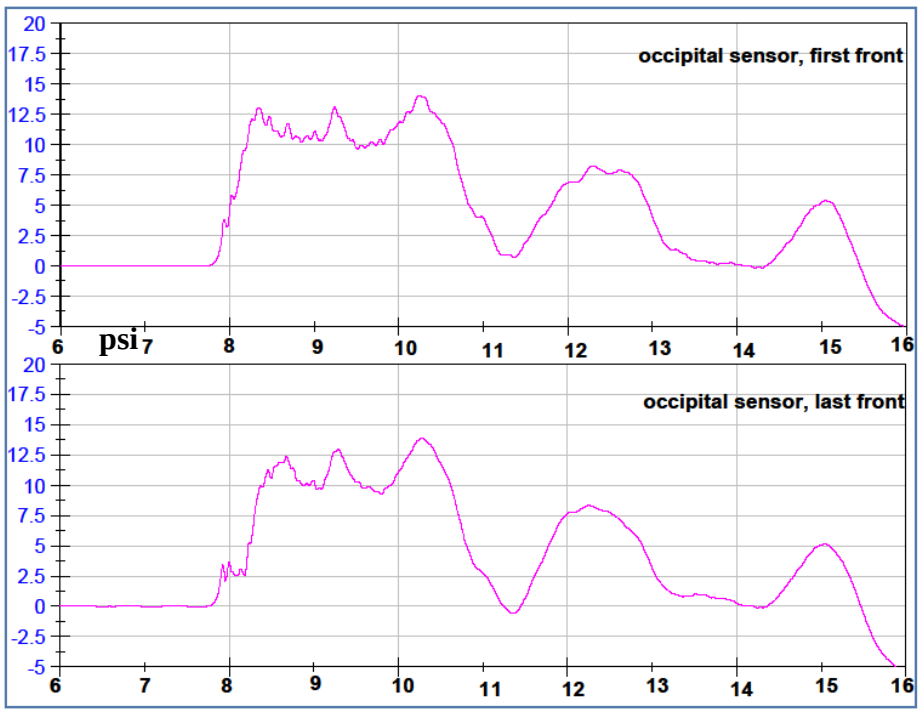

Comparison for reproducibility of each pressure sensor in Front Orientation at 15psi 5mm Sphere with Holes

VENTRICLE FILTERED DATA

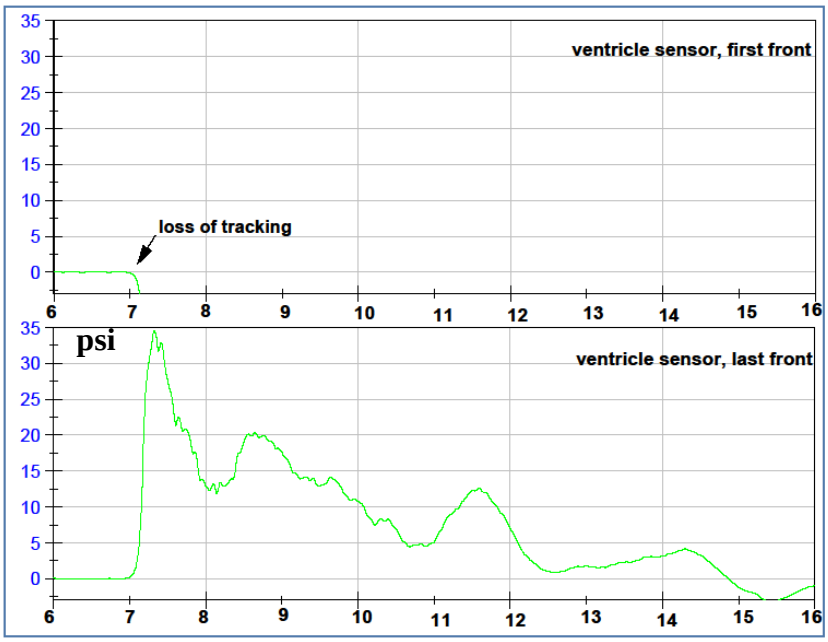

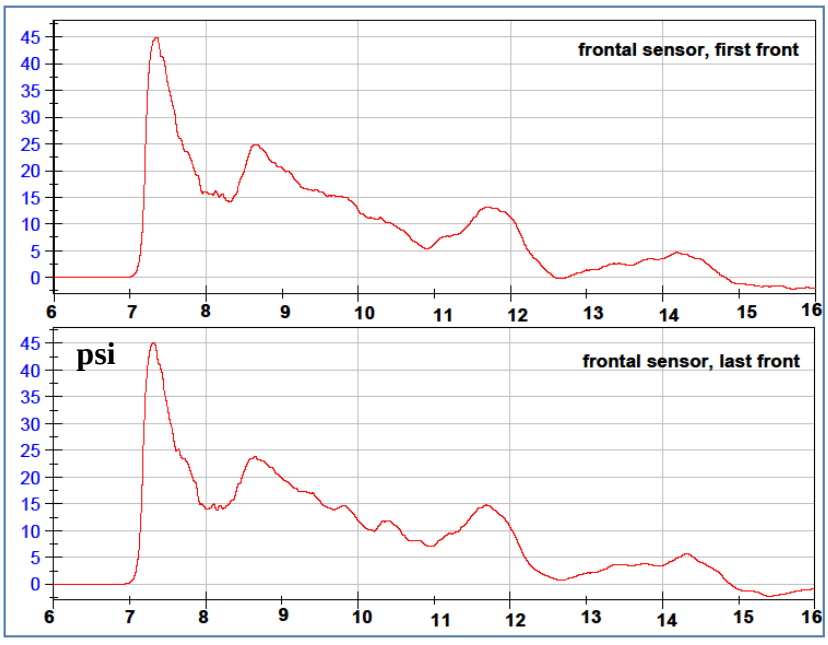

FRONTAL FILTERED DATA

Comparison for reproducibility of each pressure sensor in Front Orientation at 15psi 5mm Sphere with Holes

OCCIPITAL FILTERED DATA

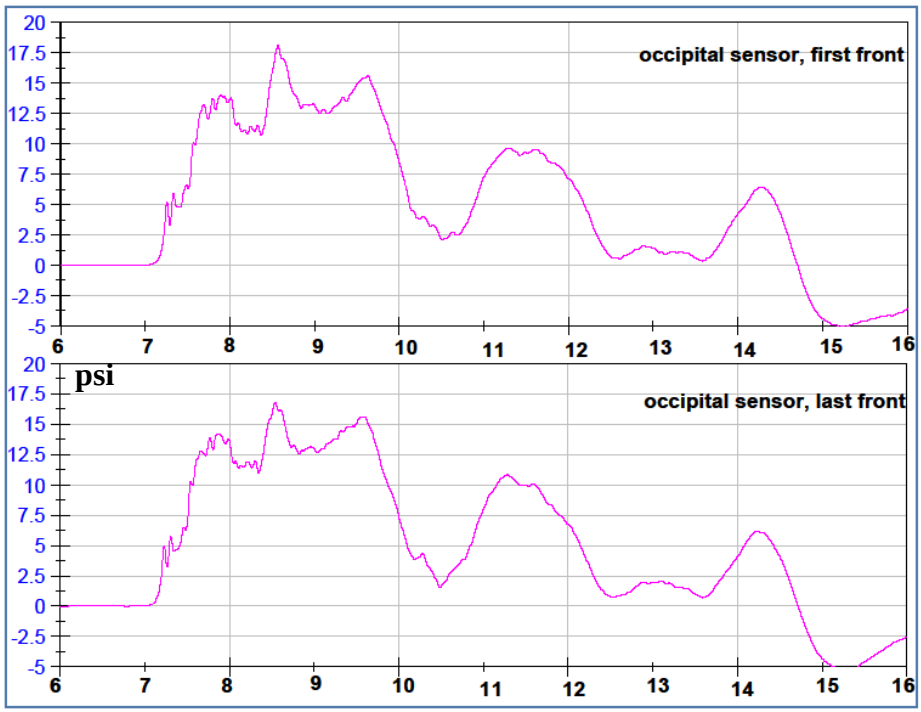

Frontal Sensor, 4 Orientations, Filtered Data, 5mm Sphere with Holes

10 PSI

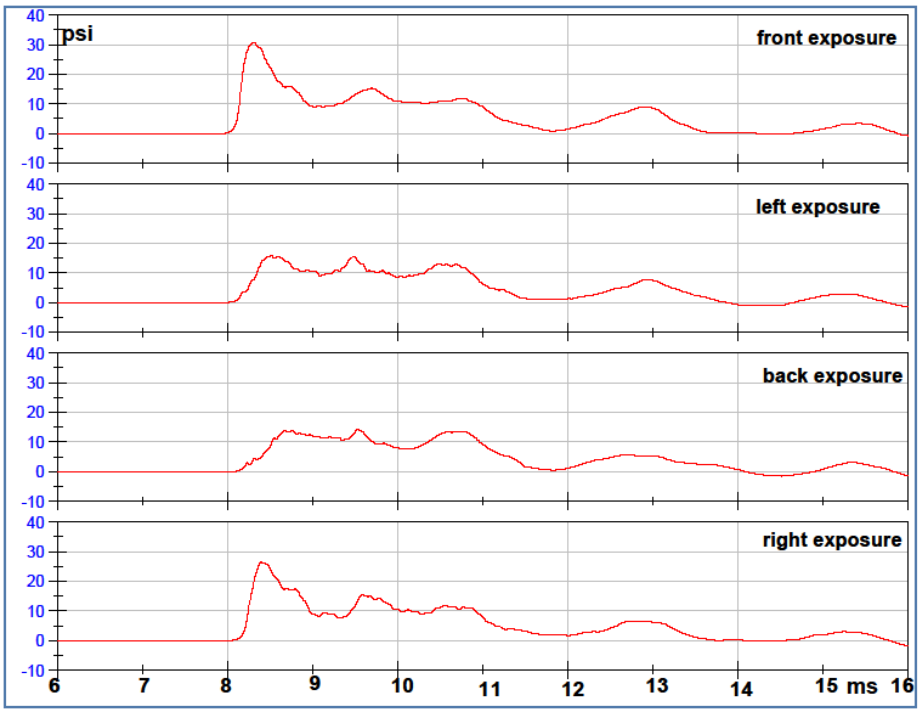

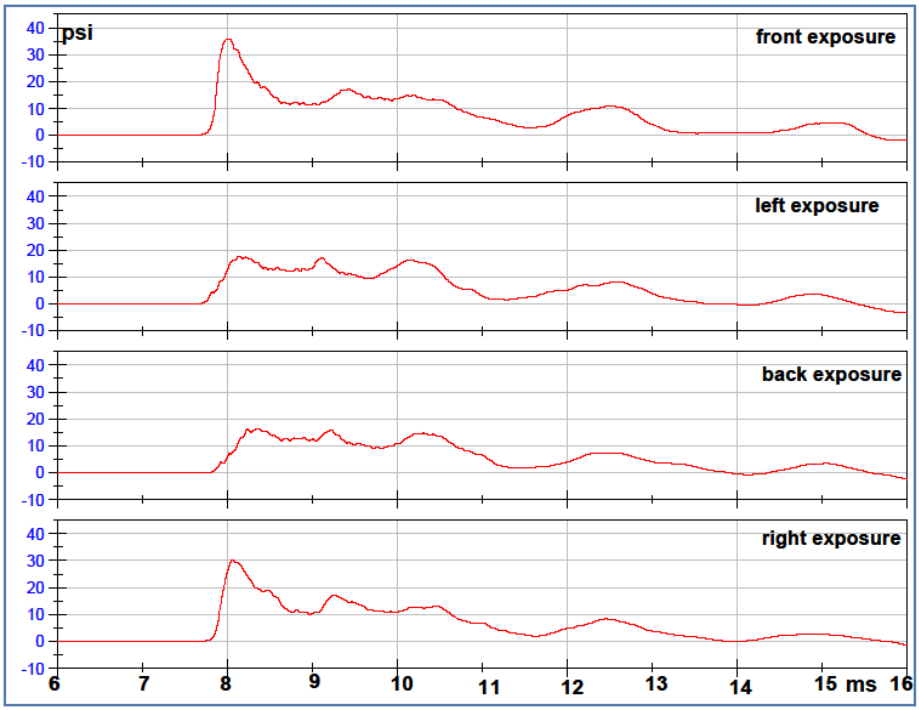

12 PSI

Frontal Sensor, 4 Orientations, Filtered Data, 5mm Sphere with Holes

15 PSI

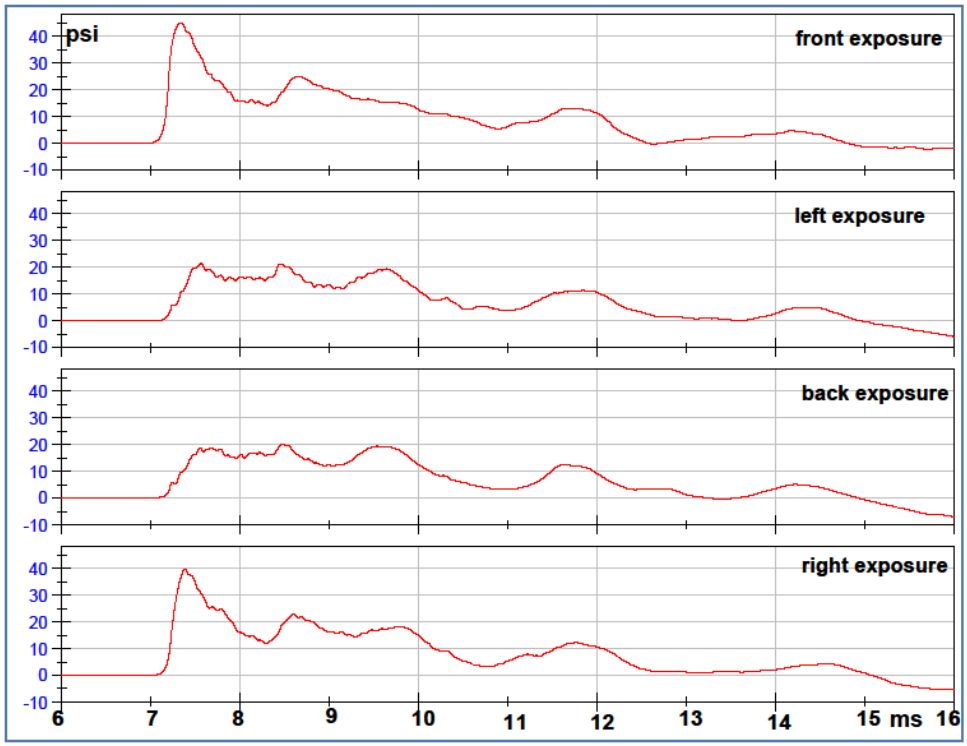

Ventricle Sensor, 4 Orientations, Filtered Data, 5mm Sphere with Holes

10 PSI

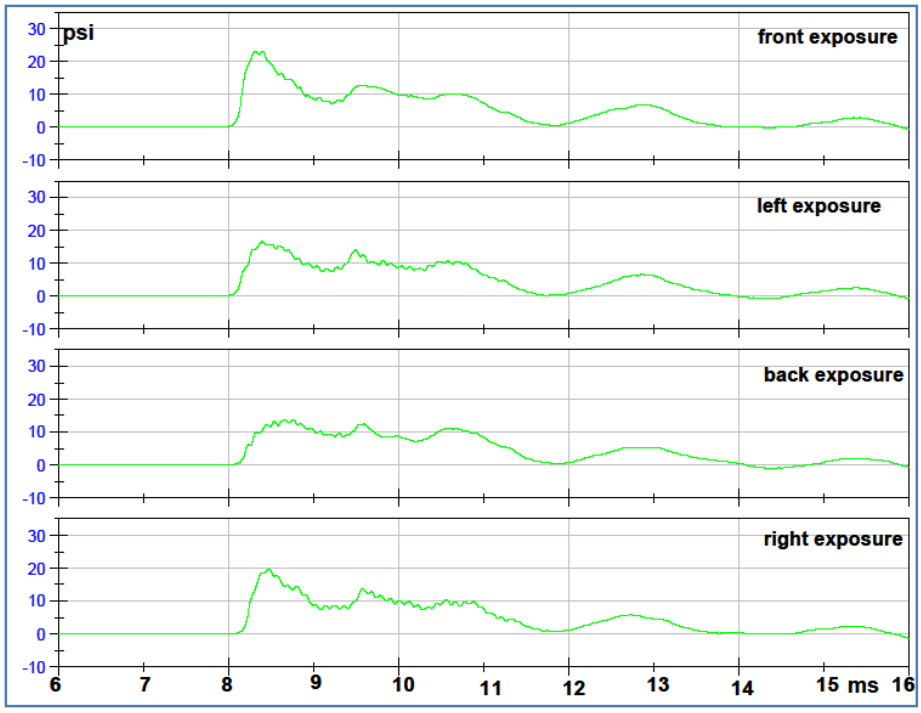

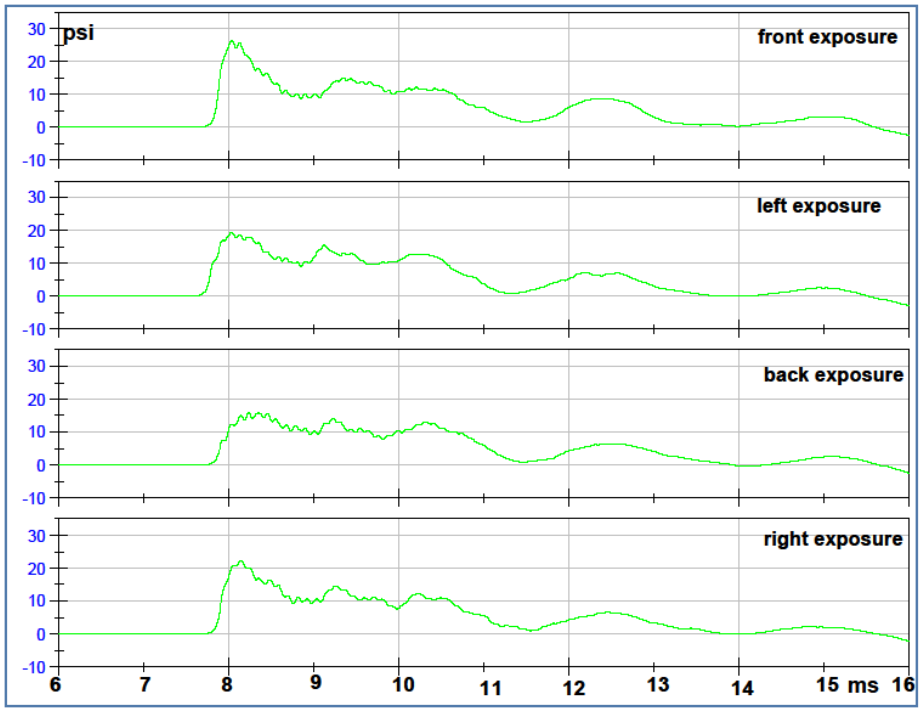

12 PSI

Ventricle Sensor, 4 Orientations, Filtered Data, 5mm Sphere with Holes

15 PSI

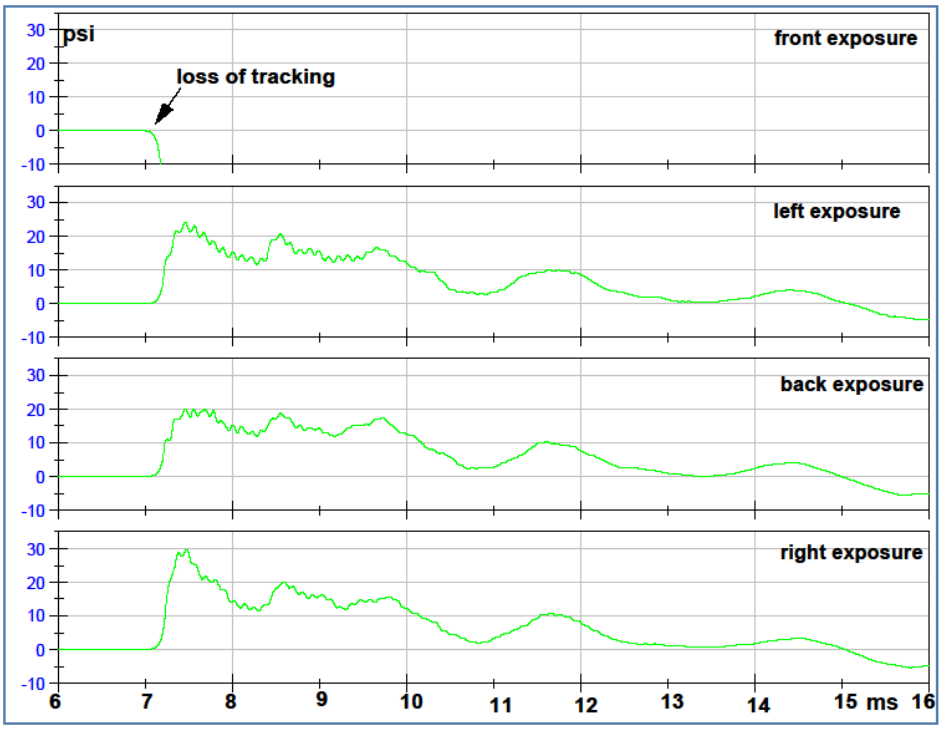

Occipital Sensor, 4 Orientations, Filtered Data, 5mm Sphere with Holes

10 PSI

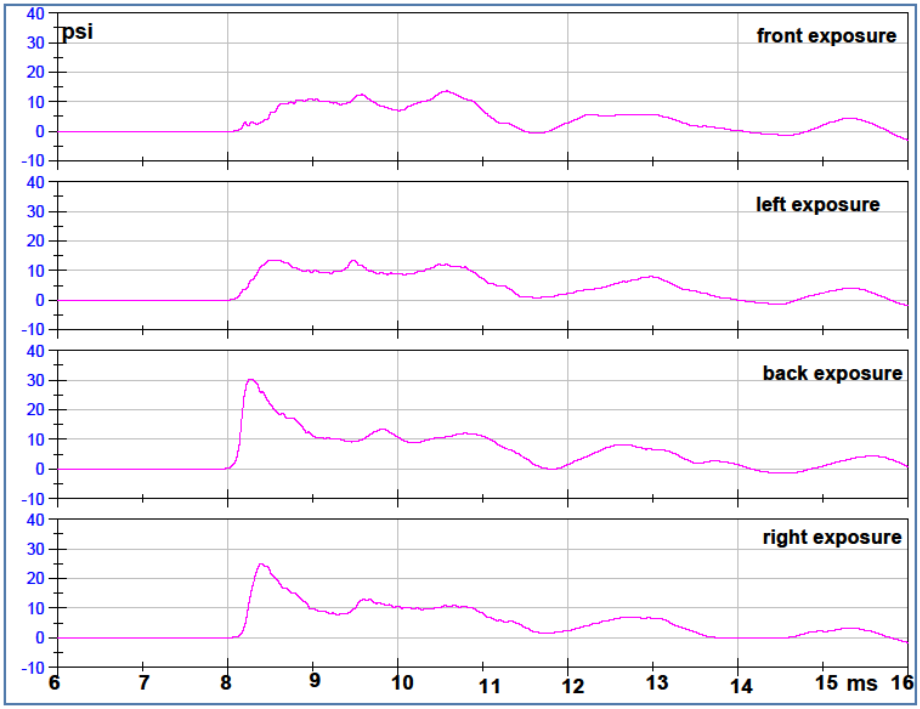

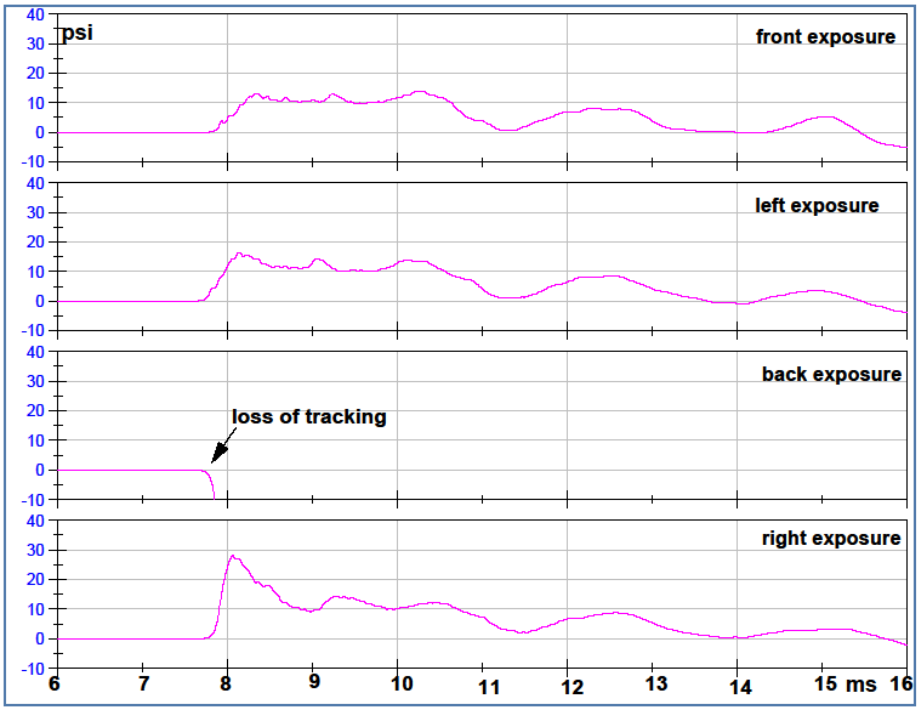

12 PSI

Occipital Sensor, 4 Orientations, Filtered Data, 5mm Sphere with Holes

15 PSI

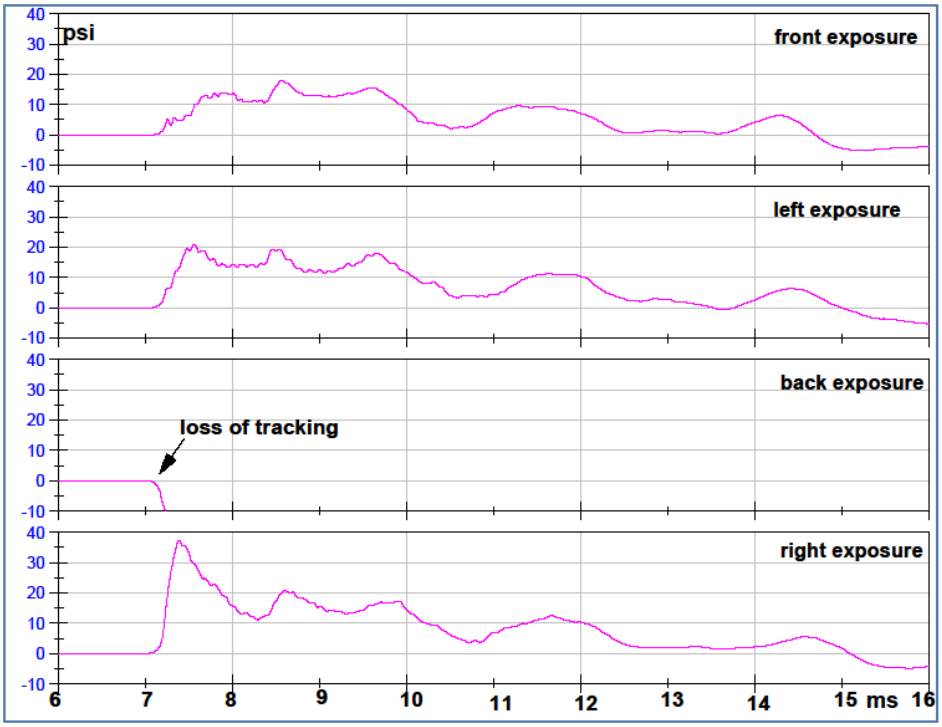

Pressure extremes for 5mm sphere with holes

Pressure Extremes for 5mm Sphere with Holes										
	Maximun Pressure					Minimum Pressure				
ventricle	front 1	right	back	left	front 2	front 1	right	back	left	front 2
10 psi air	**23**	**19.5**	**13.8**	**16.6**	**24**	**-0.18**	**0.14**	**0.11**	**0.1**	**-0.02**
12 psi air	**26.4**	**22.1**	**16**	**19.4**	**26.2**	**0.18**	**0.1**	**0.12**	**0.12**	**0.19**
15 psi air	**NA**	**29.7**	**20.1**	**24.23**	**34.5**	**NA**	**0.17**	**0.16**	**0.11**	**0.14**
frontal	front 1	right	back	left	front 2	front 1	right	back	left	front 2
10 psi air	**30.9**	**26.6**	**14.2**	**15.8**	**32.3**	**-0.08**	**-0.22**	**0.1**	**0.14**	**0.08**
12 psi air	**35.8**	**30.2**	**16.3**	**17.7**	**34.7**	**0.19**	**0.14**	**0.08**	**-0.67**	**0.15**
15 psi air	**44.9**	**39.7**	**20**	**21.5**	**45**	**-0.21**	**0.2**	**-0.32**	**0.14**	**0.24**
occipital	front 1	right	back	left	front 2	front 1	right	back	left	front 2
10 psi air	**13.7**	**25.2**	**30.4**	**13.7**	**13.1**	**-1.26**	**-0.18**	**-1.49**	**-1.36**	**-0.51**
12 psi air	**14.1**	**28.1**	**NA**	**16.4**	**13.9**	**-0.16**	**0.19**	**NA**	**-0.74**	**-0.55**
15 psi air	**18.1**	**37.3**	**NA**	**20.7**	**16.8**	**0.13**	**0.2**	**NA**	**-0.56**	**0.13**

1st rate of change of pressure for 5mm-thick sphere with holes.

1st rate (psi/ms)					
ventricle	front 1	right	back	left	front 2
10 psi air	**73**	**58.8**	**34.9**	**45.8**	**72.8**
12 psi air	**81.9**	**62.7**	**43.9**	**56.6**	**81.1**
15 psi air	**NA**	**90**	**61.2**	**71.5**	**99.9**
frontal	front 1	right	back	left	front 2
10 psi air	**89.5**	**77.7**	**21.5**	**34.7**	**96.8**
12 psi air	**115.6**	**94**	**34.4**	**41**	**105.4**
15 psi air	**136.1**	**118.8**	**40.6**	**50.3**	**139.9**
occipital	front 1	right	back	left	front 2
10 psi air	**20.8**	**83.1**	**106.6**	**29.2**	**23.5**
12 psi air	**25.1**	**89.6**	**NA**	**34.3**	**24.5**
15 psi air	**31.7**	**113.1**	**NA**	**50.7**	**36.7**

Comparisons of 1st rate of change of pressure using spheres of different shell thickness after the introduction of apertures.

The data is expressed in percentage of the thinner shell results. Positive numbers indicate higher pressure values in the thinner shell (5mm-thick sphere).

Percentages of Rate of Change of Pressure for 7mm-thick sphere with holes relative to 5mm-thick sphere with holes					
ventricle	front 1	right	back	left	front 2
10 psi air	**20%**	**-15%**	**-57%**	**20%**	**36%**
12 psi air	**33%**	**-14%**	**-31%**	**22%**	**37%**
15 psi air	**NA**	**-25%**	**-37%**	**24%**	**11%**
frontal	front 1	right	back	left	front 2
10 psi air	**-2%**	**6%**	**-42%**	**1%**	**17%**
12 psi air	**14%**	**7%**	**9%**	**13%**	**12%**
15 psi air	**NA**	**8%**	**-5%**	**-6%**	**2%**
occipital	front 1	right	back	left	front 2
10 psi air	**17%**	**23%**	**0%**	**32%**	**30%**
12 psi air	**8%**	**5%**	**NA**	**-13%**	**15%**
15 psi air	**-8%**	**3%**	**NA**	**18%**	**18%**

Table of Differential Pressure Results for 5mm Sphere with Holes

Differential for sphere with holes 5mm										
	peak differential pressure (psi)					time elapsed between peaks (ms)				
ventricle	front 1	right	back	left	front 2	front 1	right	back	left	front 2
10 psi air	**23.2**	**19.4**	**13.7**	**16.5**	**24.0**	**5.99**	**0.4**	**0.71**	**0.42**	**5.34**
12 psi air	**26.2**	**22.0**	**15.8**	**19.2**	**26.0**	**5.96**	**0.42**	**0.49**	**0.4**	**5.97**
15 psi air	**NA**	**29.6**	**20.0**	**24.1**	**34.4**	**NA**	**0.41**	**0.49**	**0.41**	**0.34**
frontal	front 1	right	back	left	front 2	front 1	right	back	left	front 2
10 psi air	**31**	**26.8**	**14.1**	**15.7**	**32.2**	**6.03**	**5.82**	**1.45**	**0.48**	**5.36**
12 psi air	**35.6**	**30.1**	**16.2**	**18.3**	**34.6**	**0.31**	**0.32**	**0.6**	**6.01**	**0.33**
15 psi air	**45.1**	**39.5**	**20.4**	**21.4**	**44.8**	**5.28**	**0.33**	**4.94**	**0.47**	**0.32**
occipital	front 1	right	back	left	front 2	front 1	right	back	left	front 2
10 psi air	**15**	**25.3**	**31.9**	**15**	**13.6**	**3.96**	**5.72**	**6.23**	**5.97**	**3.61**
12 psi air	**14.2**	**28**	**NA**	**17.2**	**14.5**	**3.96**	**0.31**	**NA**	**5.96**	**1.09**
15 psi air	**18**	**37.1**	**NA**	**21.2**	**16.6**	**1.47**	**0.33**	**NA**	**6.08**	**1.44**

Percentages of 1st rate of internal pressure changes in 5 mm sphere with holes based on the cell value at the 10 psi air overpressure for each orientation.

	AIR	Percentage 1st Rate Pressure Change				
	Overpressure	front 1	right	back	left	front 2
ventricle	20%	12%	7%	26%	24%	11%
ventricle	50%	NA	53%	75%	56%	37%
frontal	20%	29%	21%	60%	18%	9%
frontal	50%	52%	53%	89%	45%	45%
occipital	20%	21%	8%	NA	17%	4%
occipital	50%	52%	36%	NA	74%	56%

State of Gages during Testing of the 5mm Sphere with Holes

	Strain status for sphere 5mm				
Frontal	front 1	right	back	left	front 2
10 psi air					
12 psi air					
15 psi air					
Left	front 1	right	back	left	front 2
10 psi air					
12 psi air					
15 psi air					
Right	front 1	right	back	left	front 2
10 psi air					
12 psi air					
15 psi air					
Occipital	front 1	right	back	left	front 2
10 psi air					
12 psi air					
15 psi air					

	working
	signal problems
	not working

Strain Data Sphere with Holes

Test 1 Front 1 Orientation 5mm Sphere with Holes

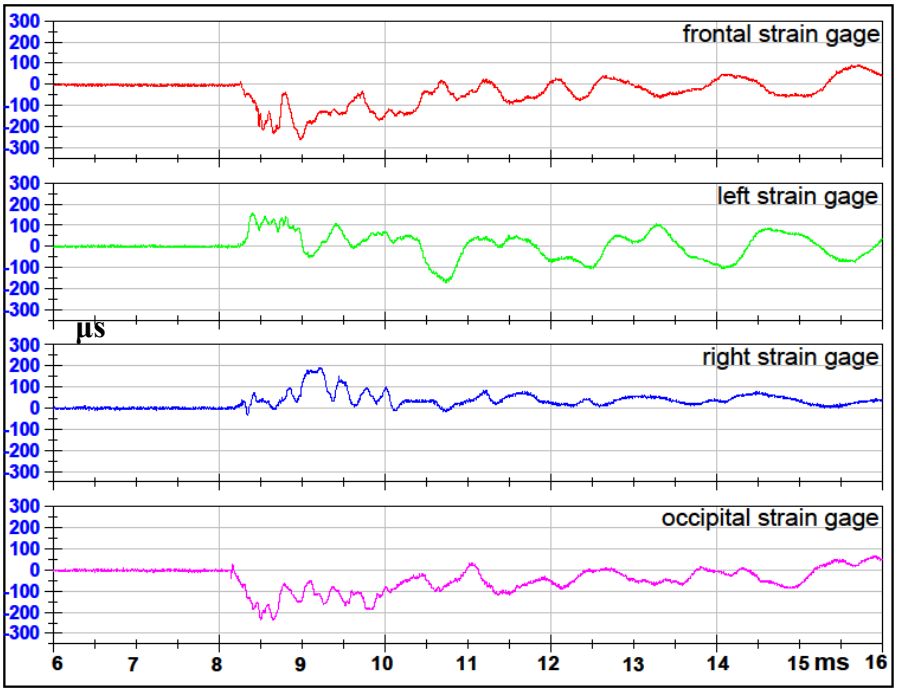

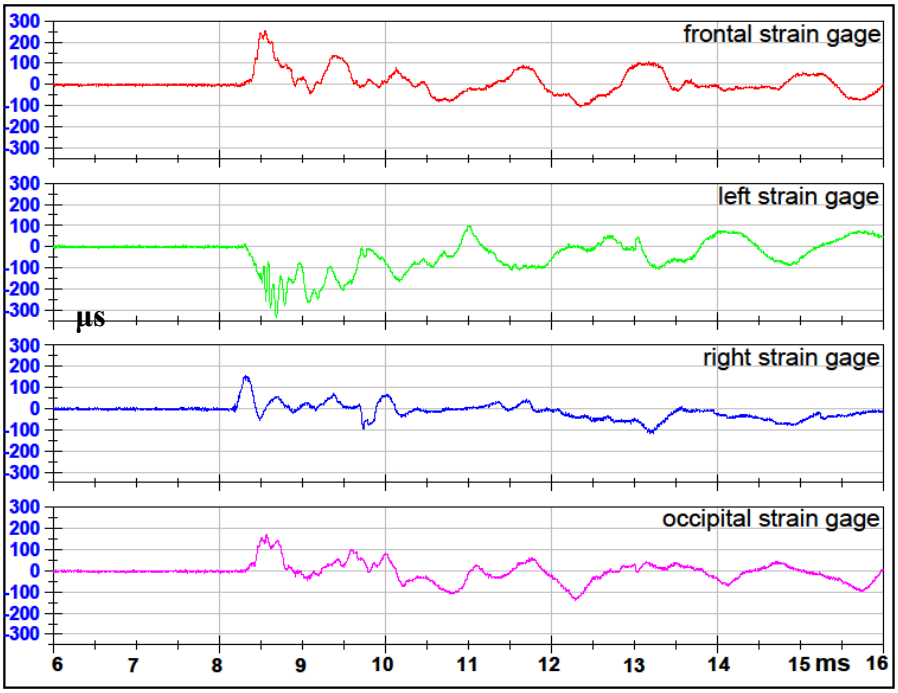

Test 2 Right Orientation 5mm Sphere with Holes

Test 3 Back Orientation 5mm Sphere with Holes

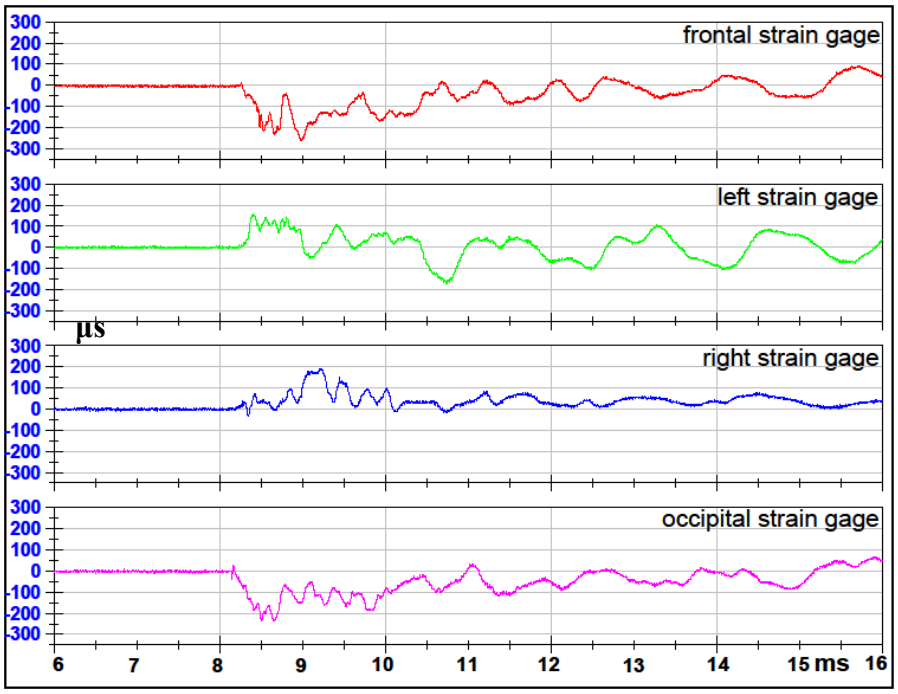

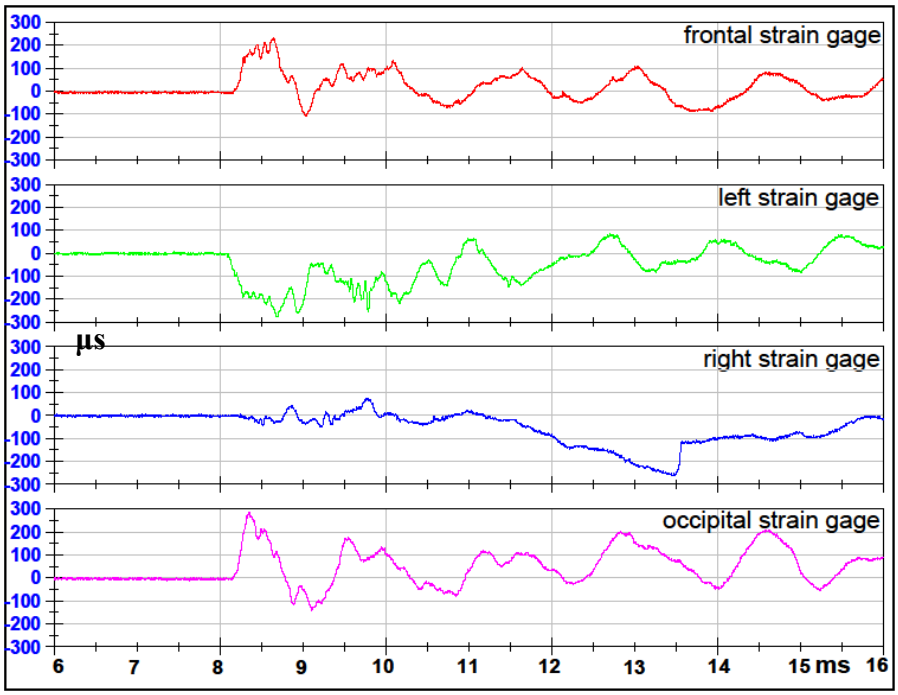

Test 4 Left Orientation 5mm Sphere with Holes

Test 5 Front 2 Orientation 5mm Sphere with Holes

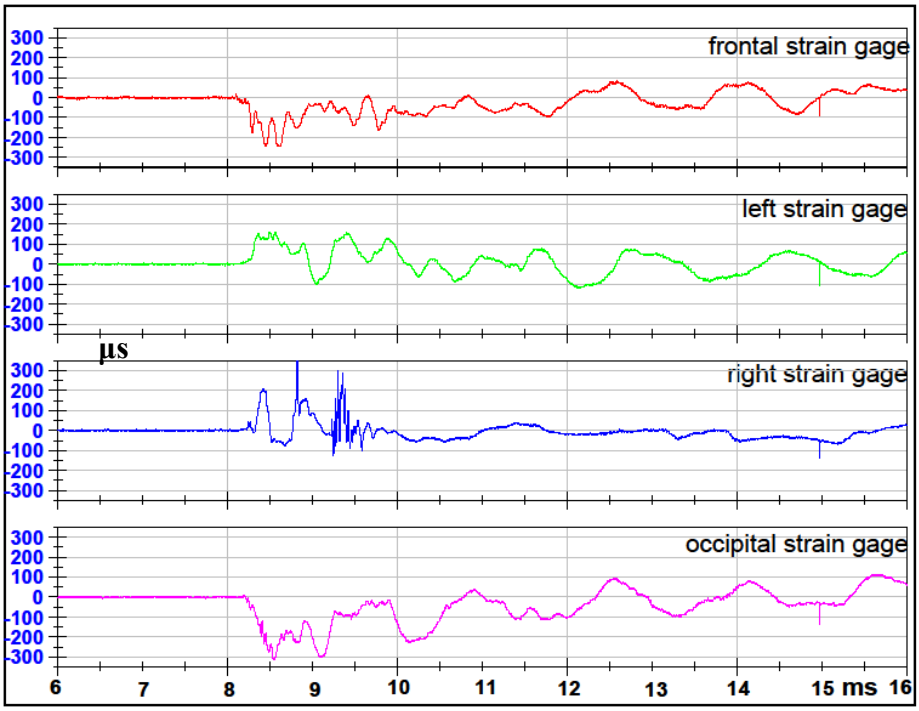

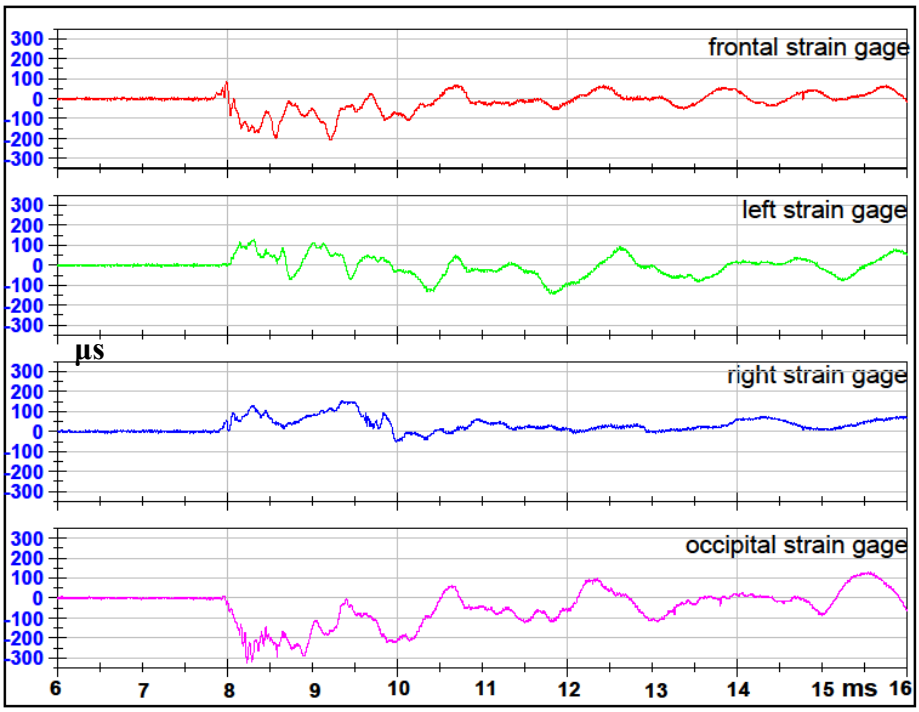

Test 6 Front 1 Orientation 5mm Sphere with Holes

Test 7 Left Orientation 5mm Sphere with Holes

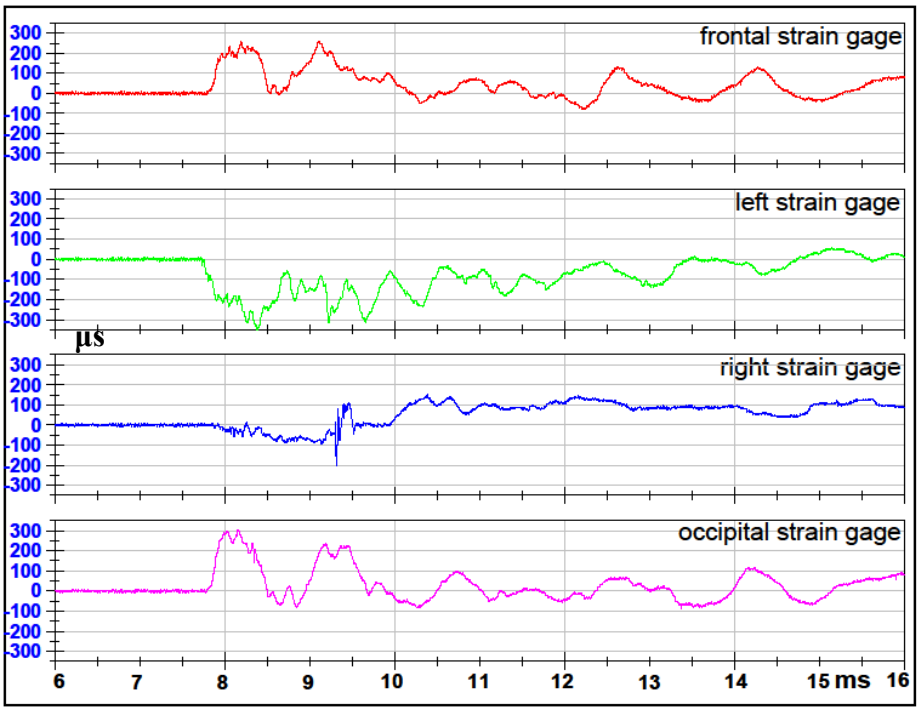

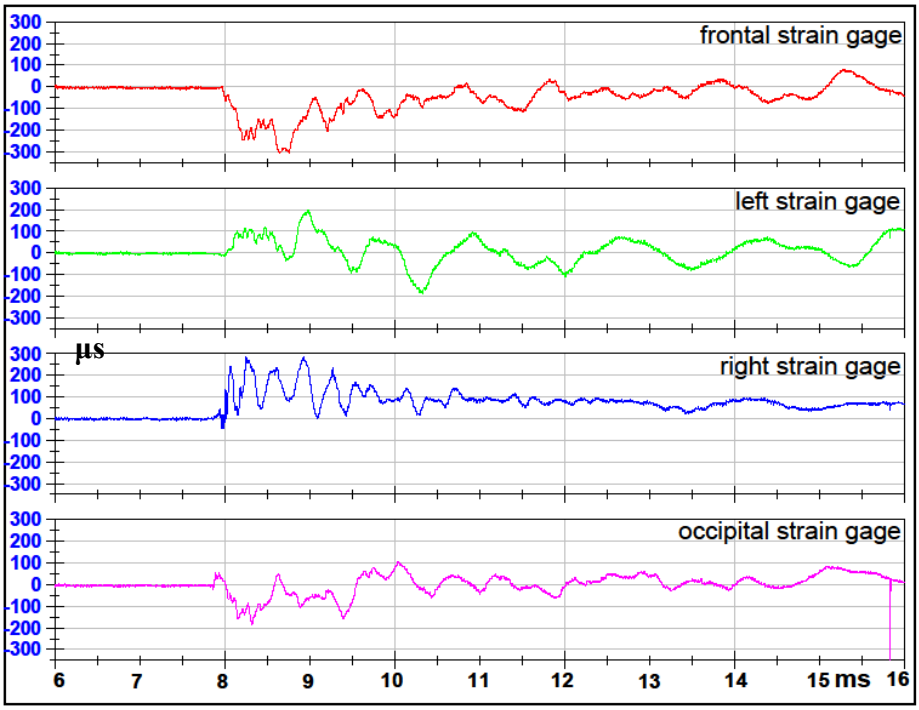

Test 8 Back Orientation 5mm Sphere with Holes

Test 9 Right Orientation 5mm Sphere with Holes

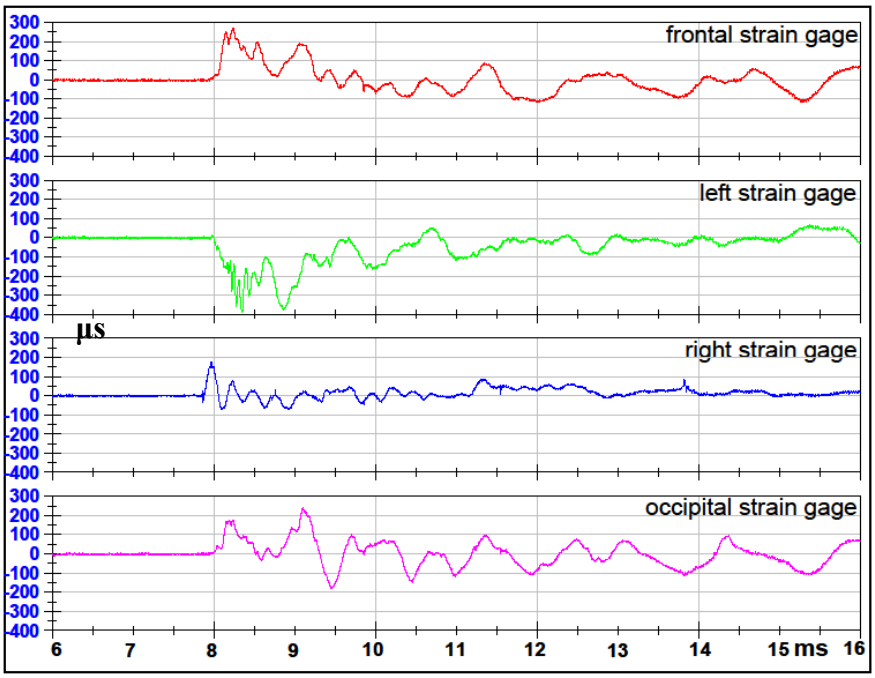

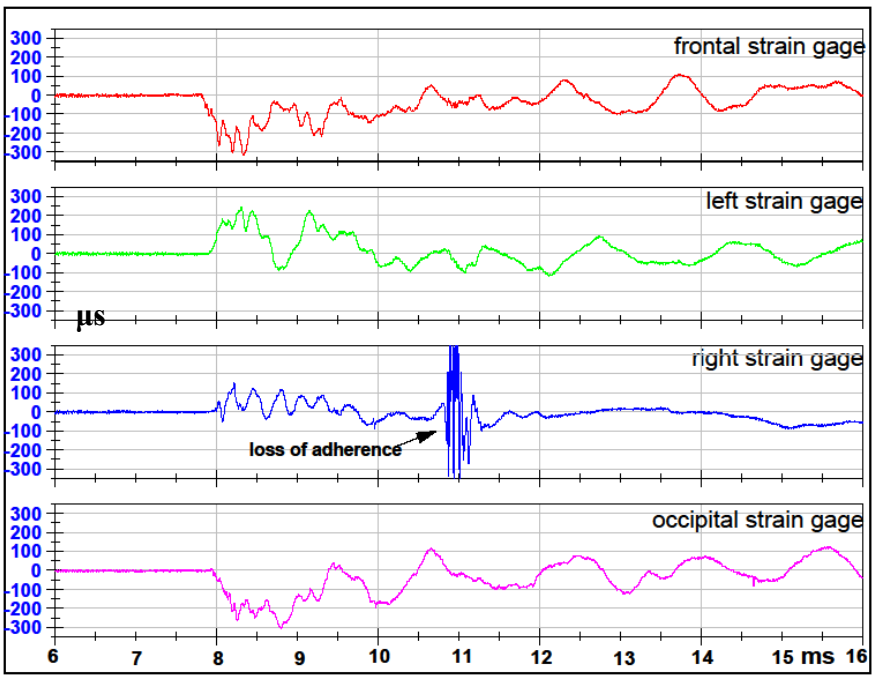

Test 10 Front 2 Orientation 5mm Sphere with Holes

Test 11 Front 1 Orientation 5mm Sphere with Holes

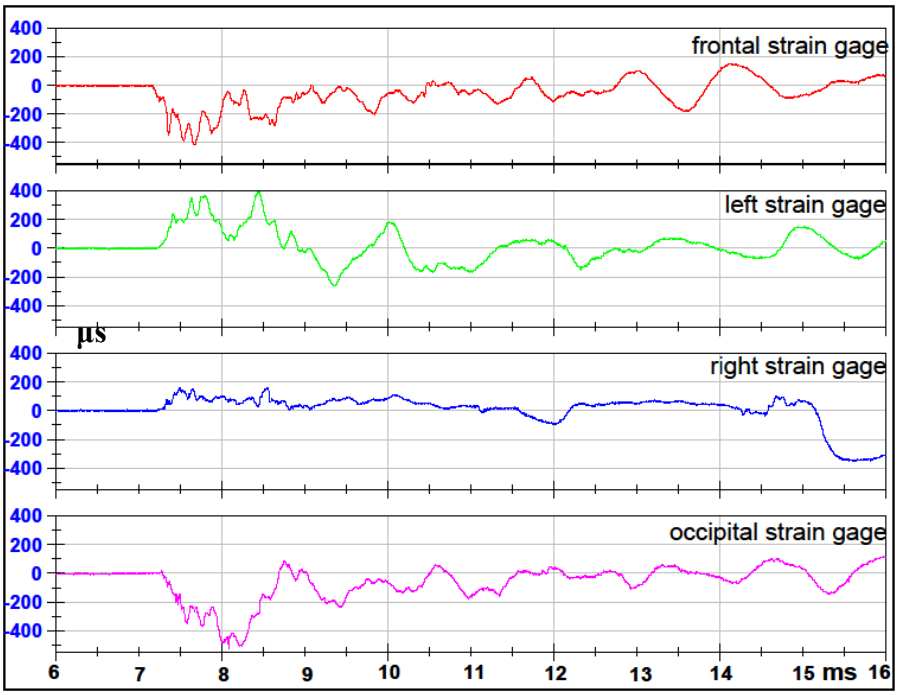

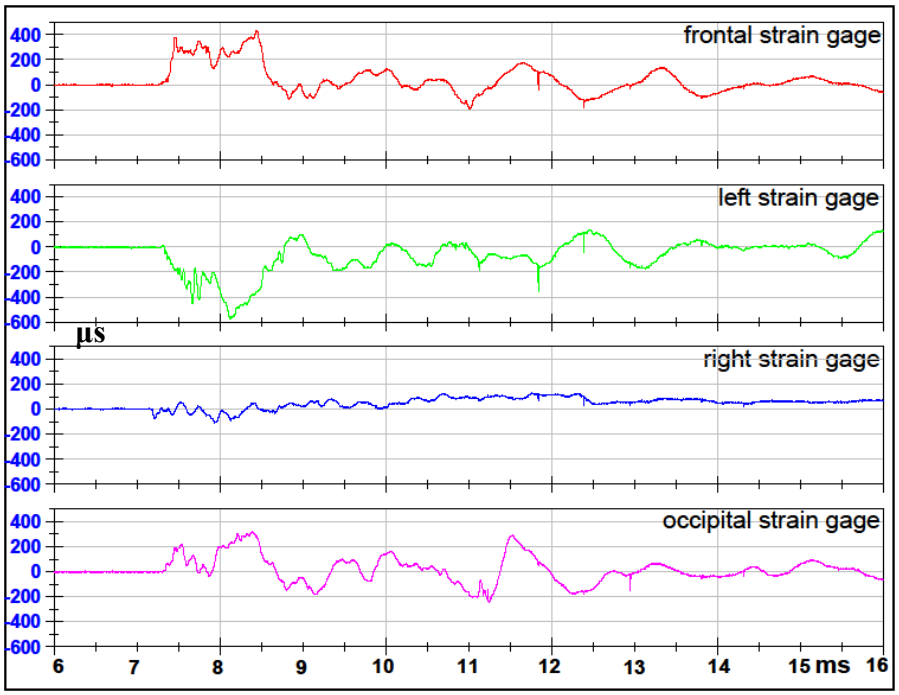

Test 12 Right Orientation 5mm Sphere with Holes

Test 13 Back Orientation 5mm Sphere with Holes

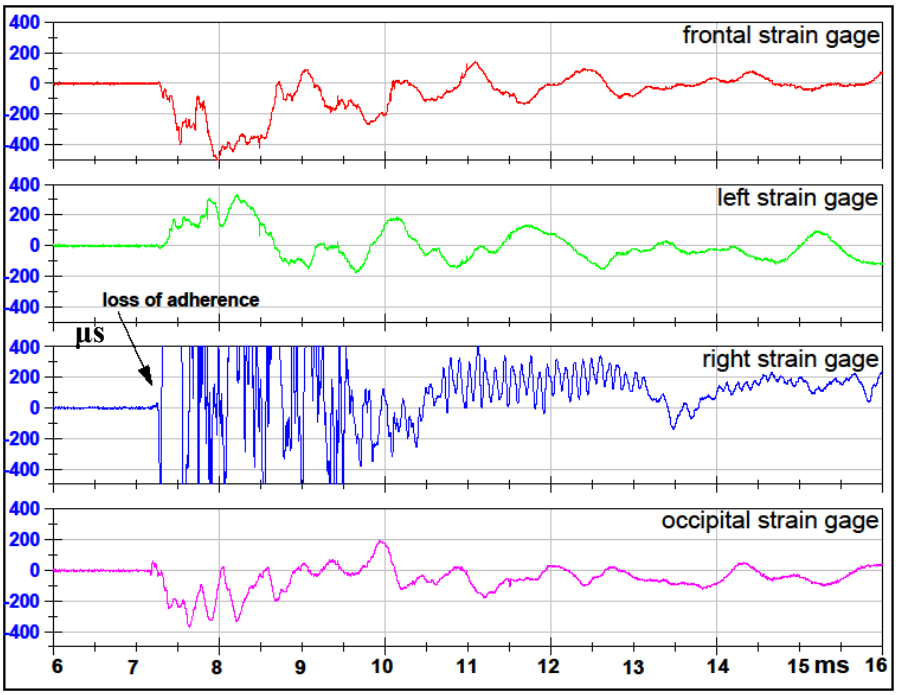

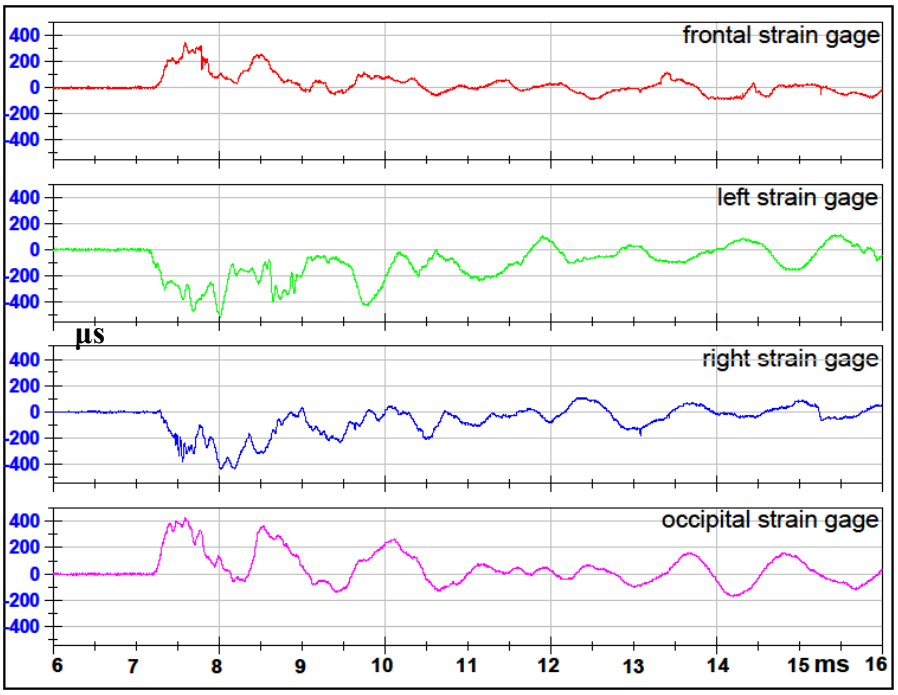

Test 14 Left Orientation 5mm Sphere with Holes

Test 15 Front 2 Orientation 5mm Sphere with Holes

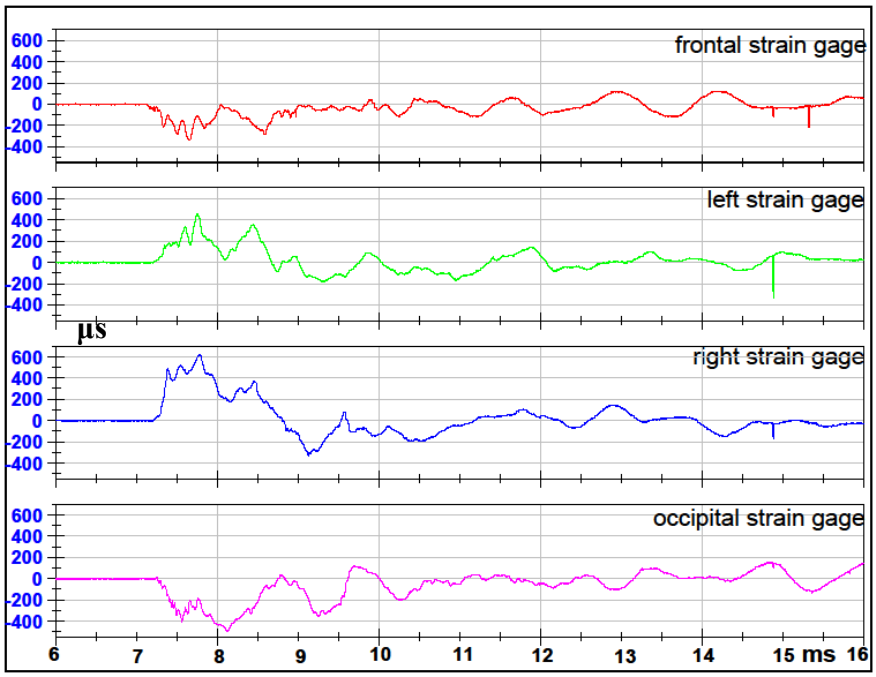

APPENDIX C

SPHERE 6 MM THICK DATA

Test 1 Front 1 Orientation 6mm Intact Sphere

FILTERED DATA

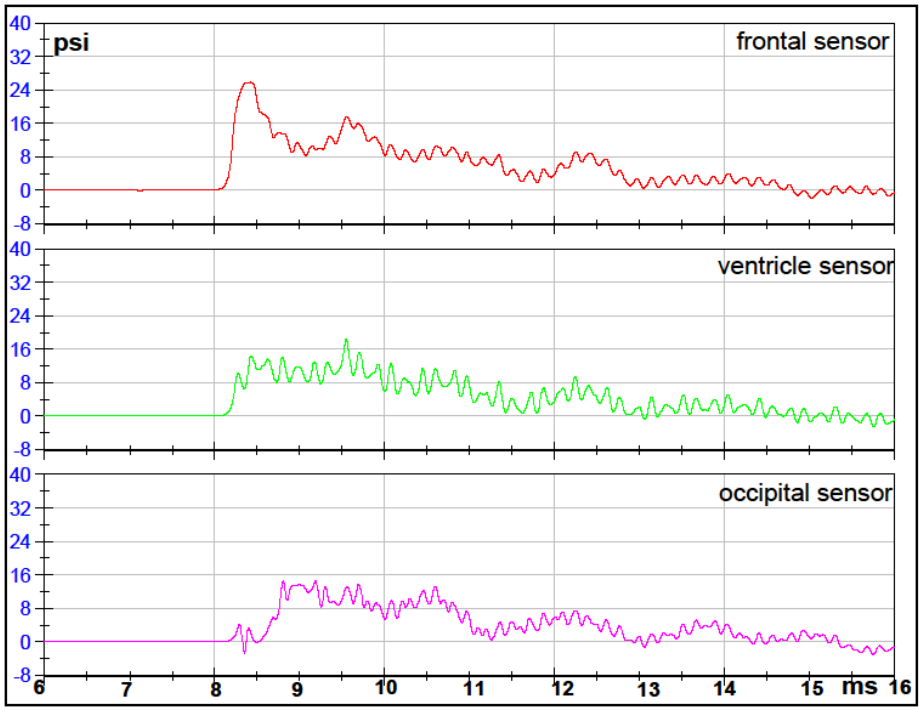

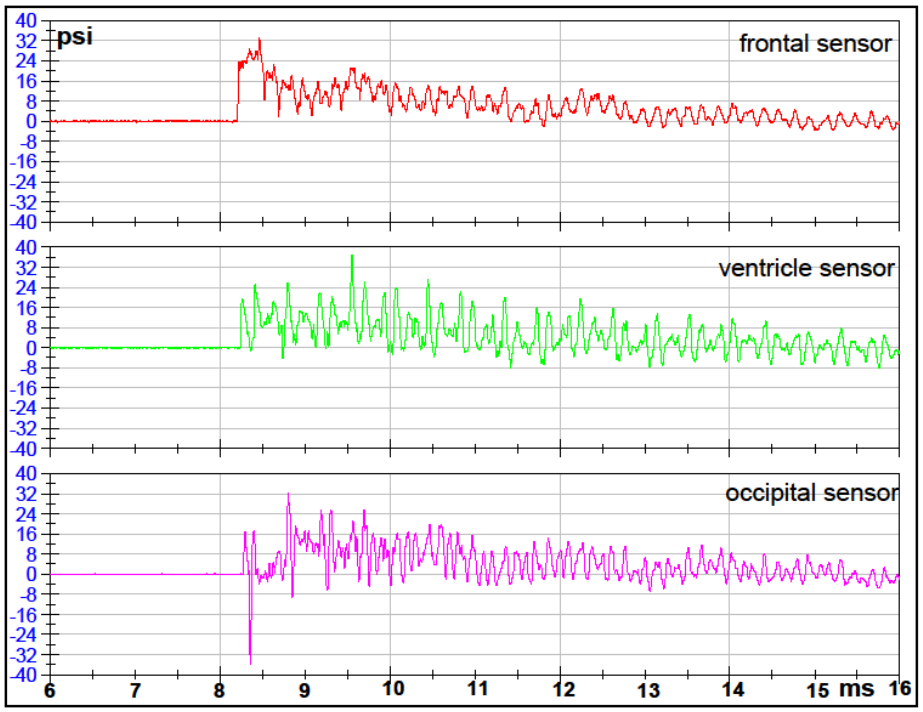

RAW DATA

Test 2 Front 2 Orientation 6mm Intact Sphere

FILTERED DATA

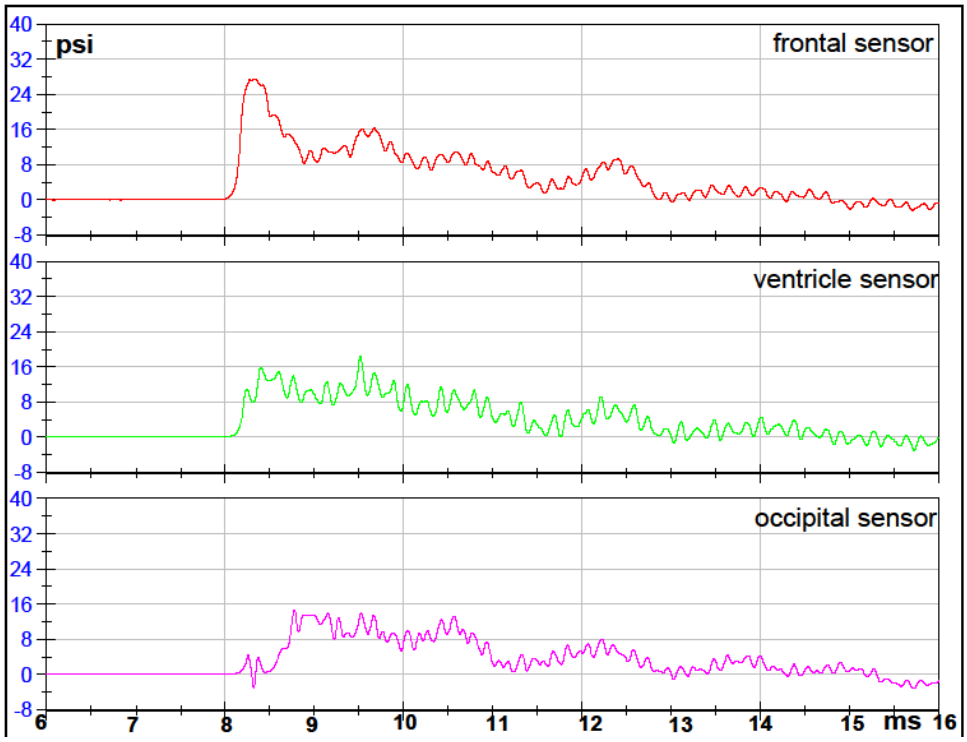

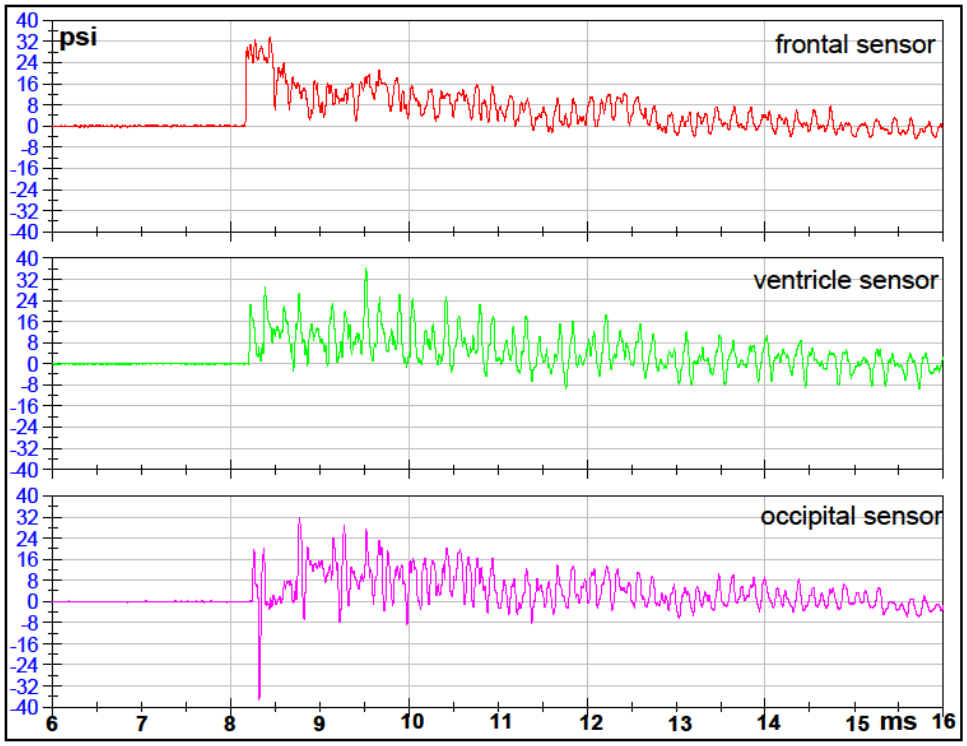

RAW DATA

Test 3 Right Orientation 6mm Intact Sphere

FILTERED DATA

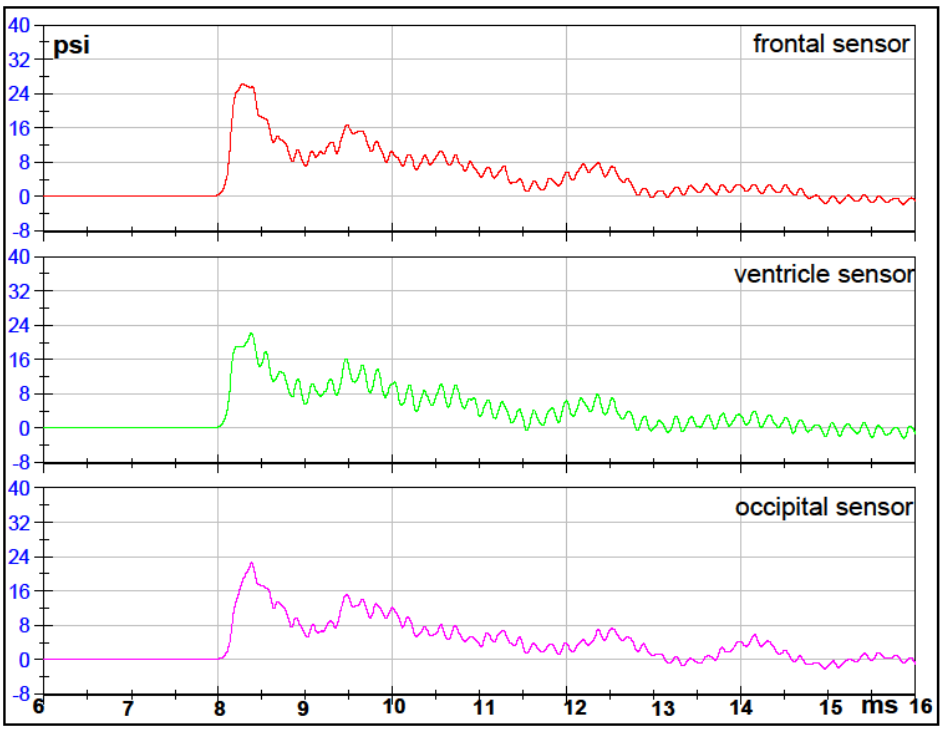

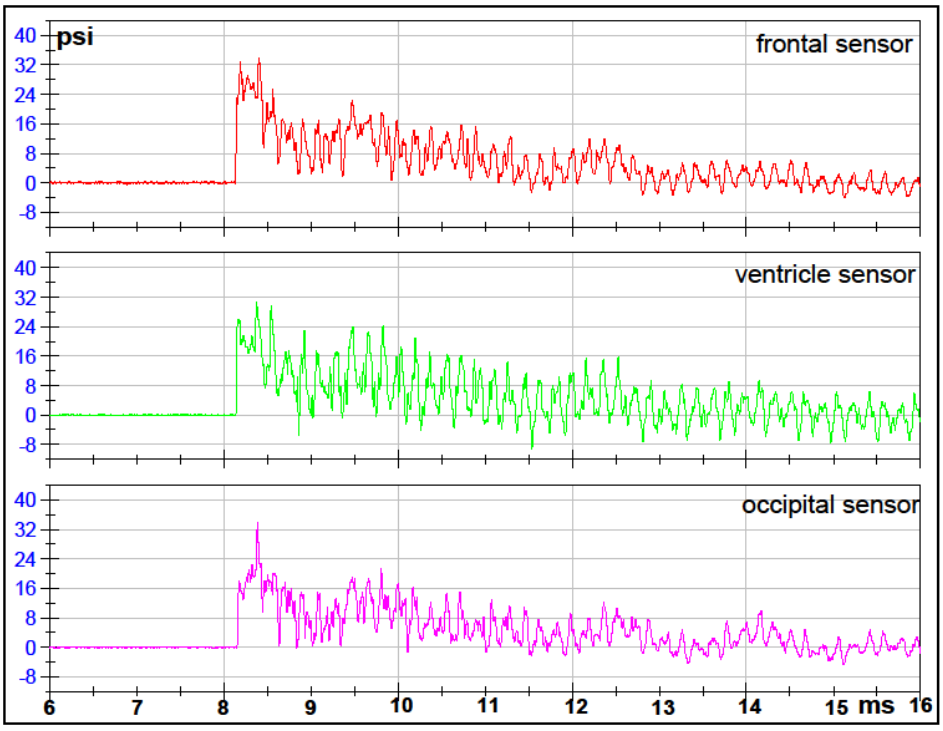

RAW DATA

Test 4 Back Orientation 6mm Intact Sphere

FILTERED DATA

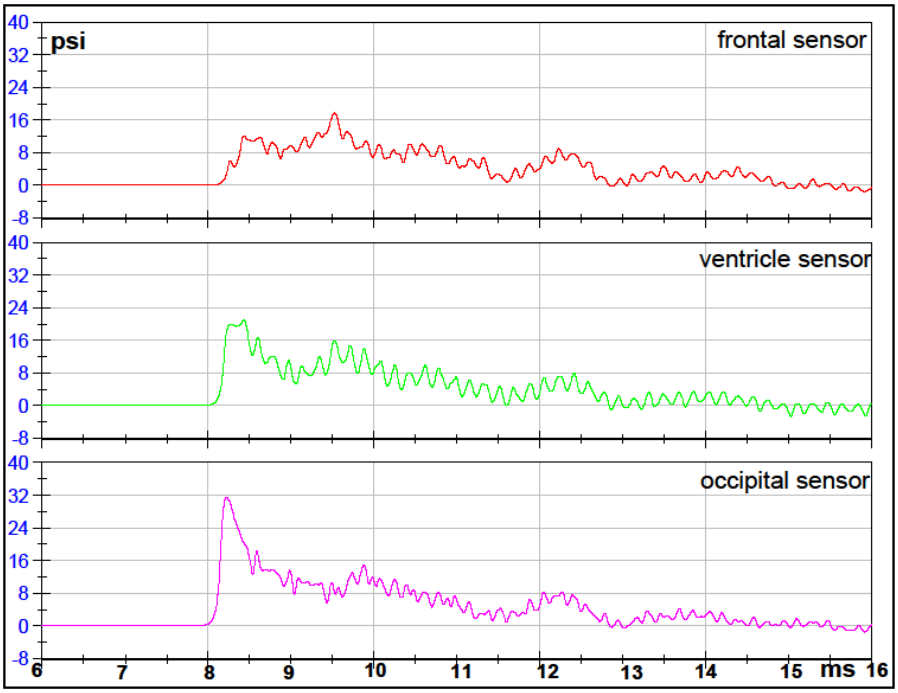

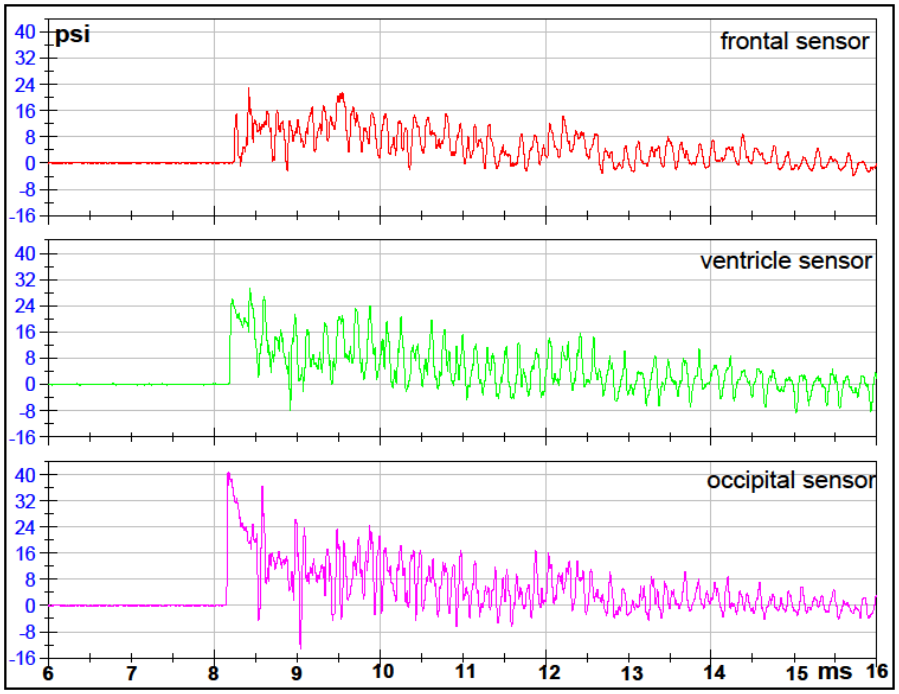

RAW DATA

Test 5 Left Orientation 6mm Intact Sphere

FILTERED DATA

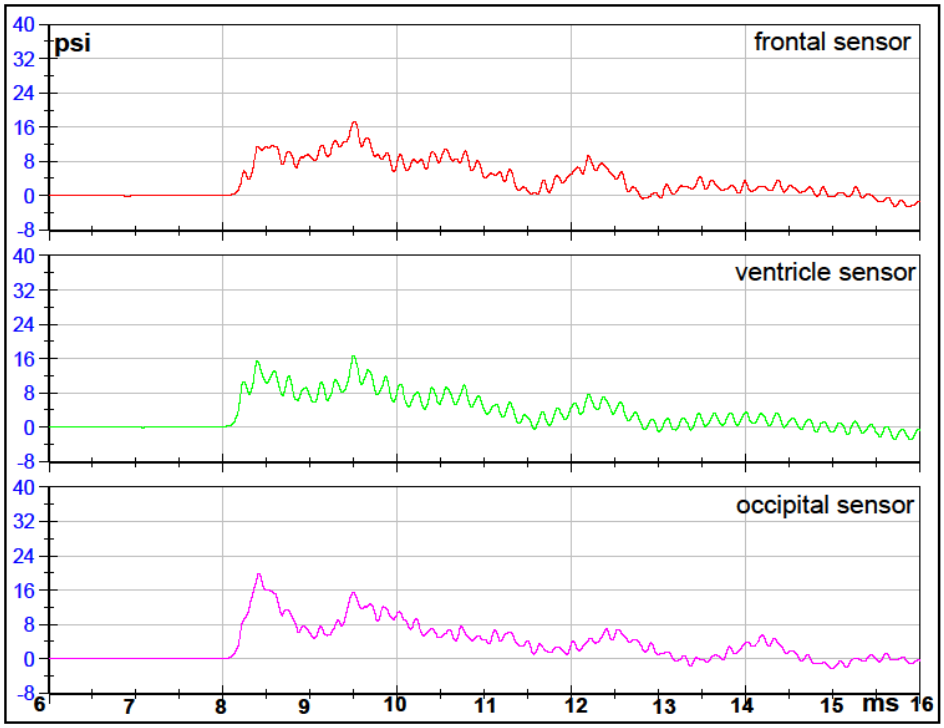

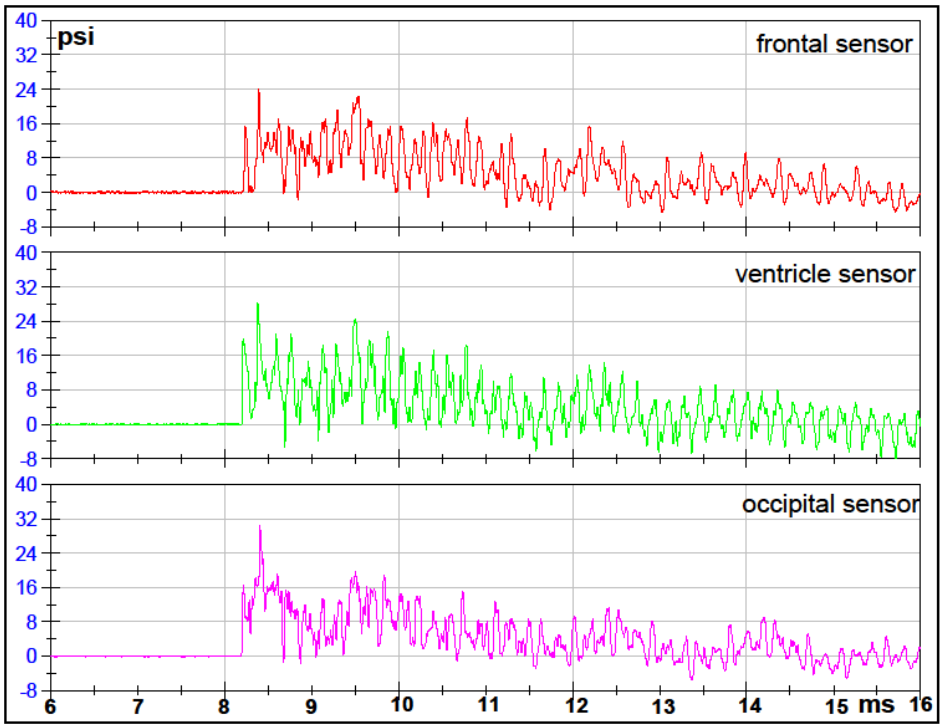

RAW DATA

Test 6 Front 1 Orientation 6mm Intact Sphere

FILTERED DATA

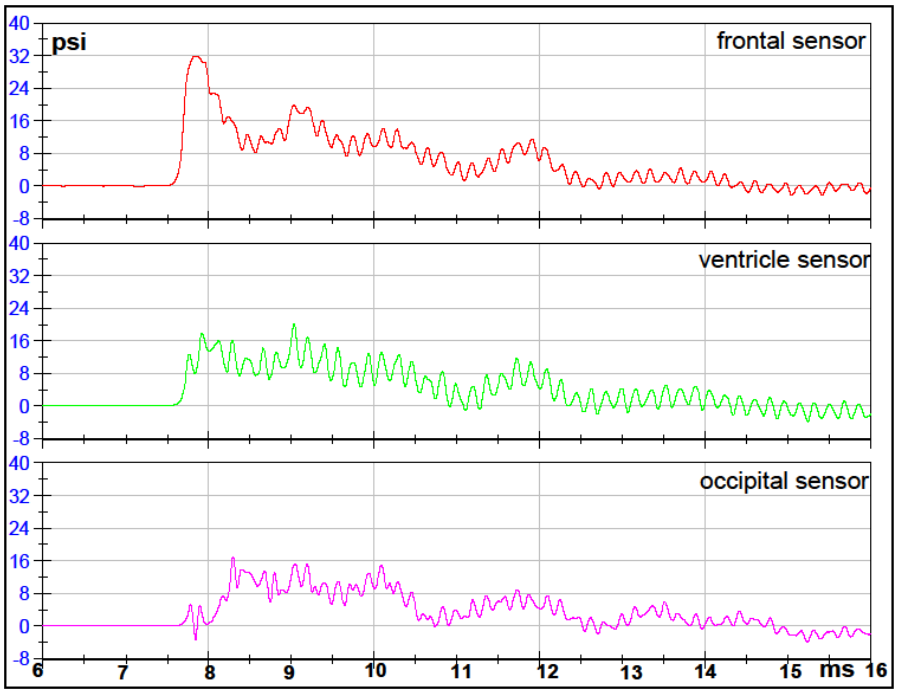

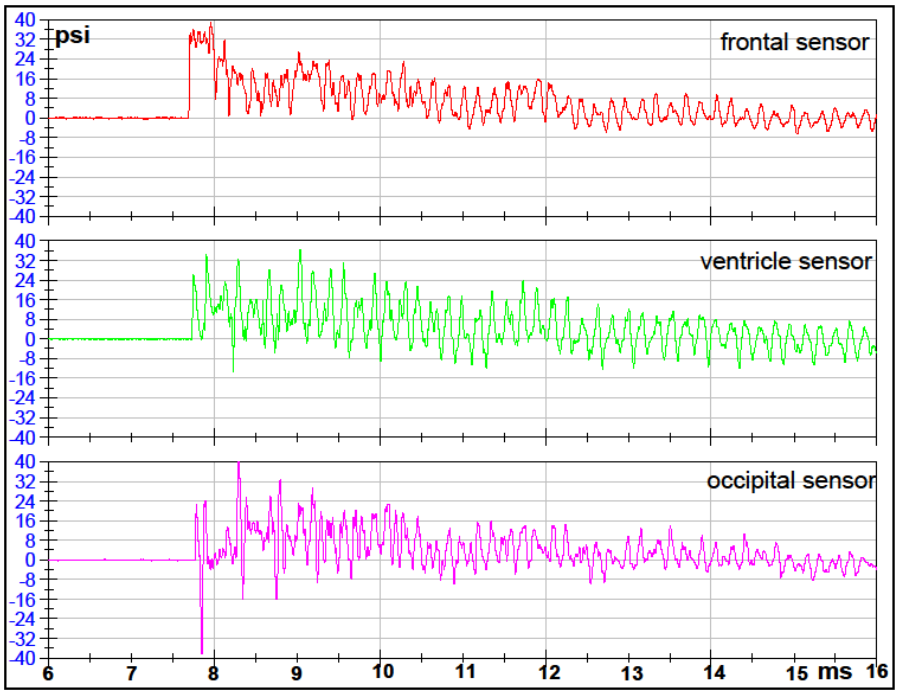

RAW DATA

Test 7 Left Orientation 6mm Intact Sphere

FILTERED DATA

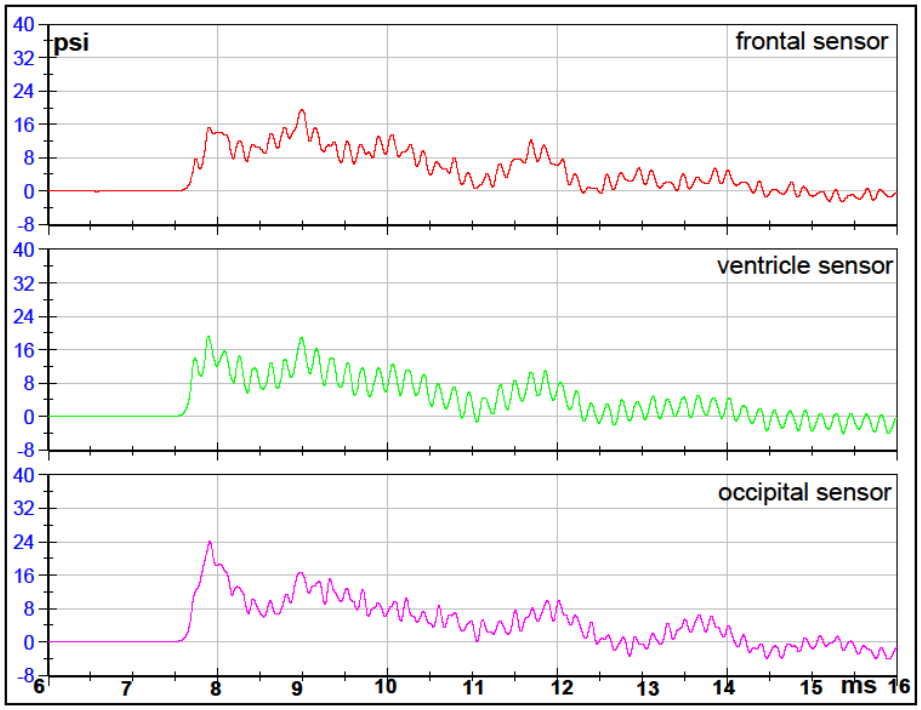

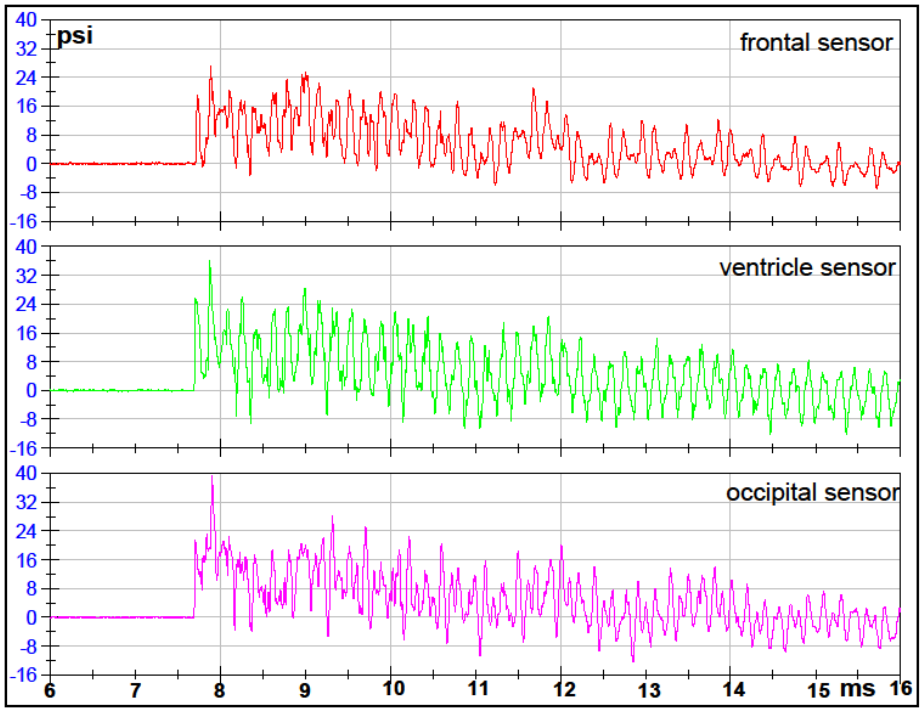

RAW DATA

Test 8 Back Orientation 6mm Intact Sphere

FILTERED DATA

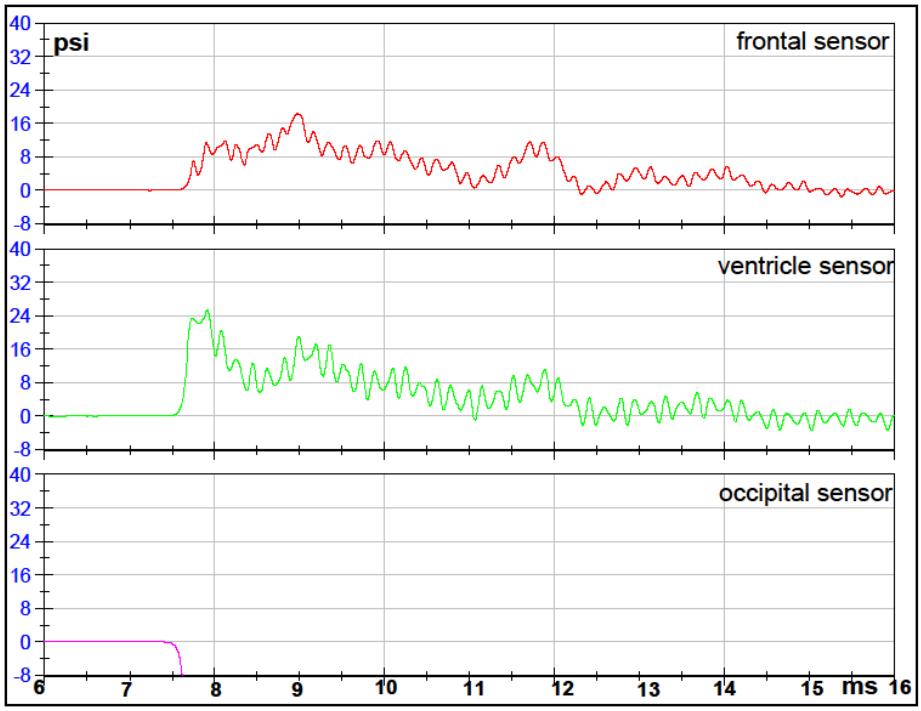

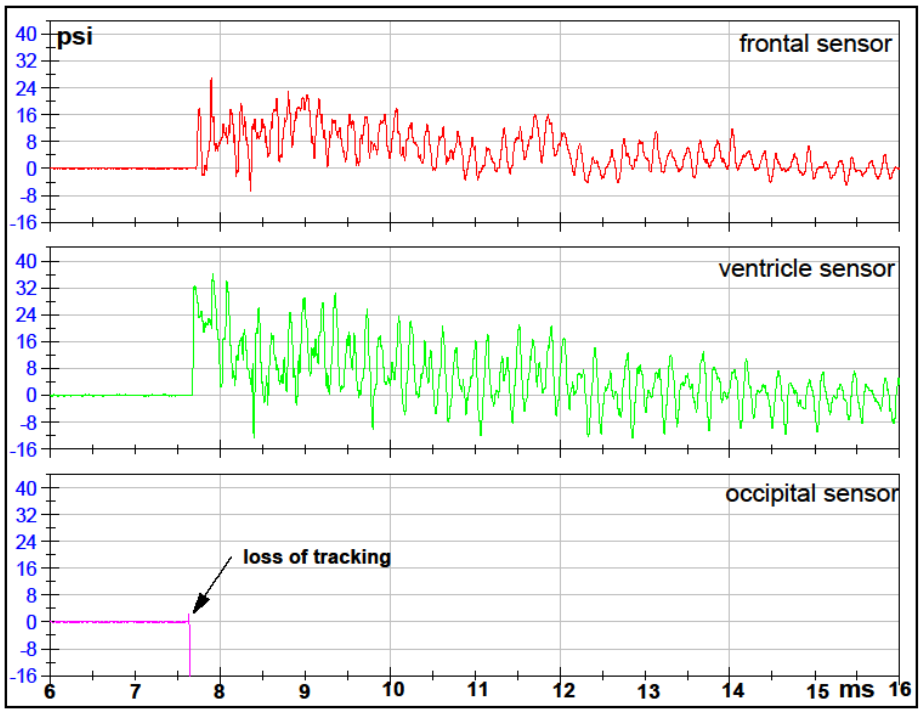

RAW DATA

Test 9 Right Orientation 6mm Intact Sphere

FILTERED DATA

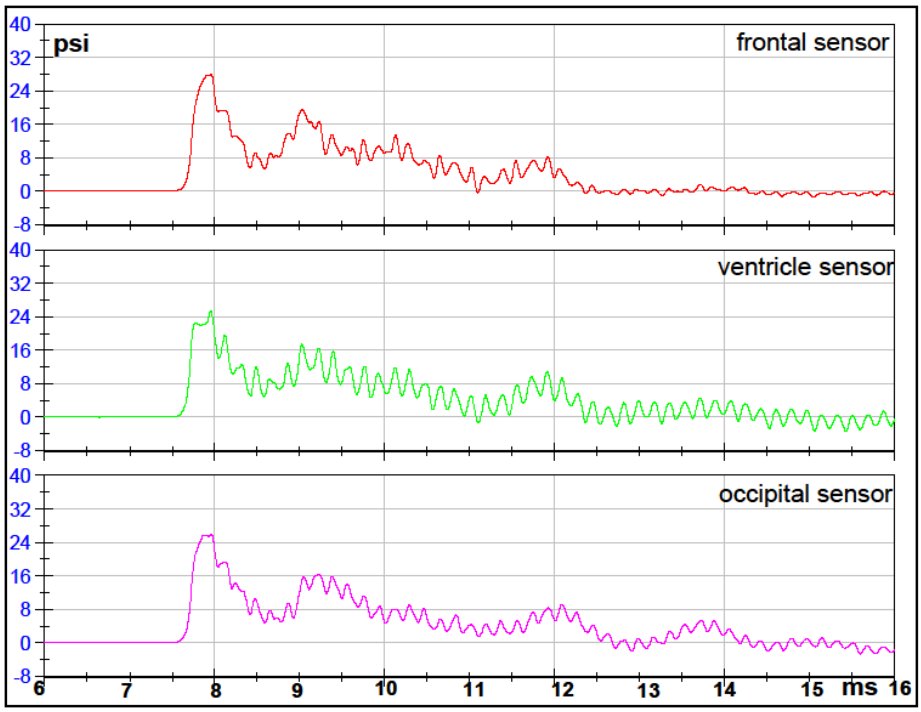

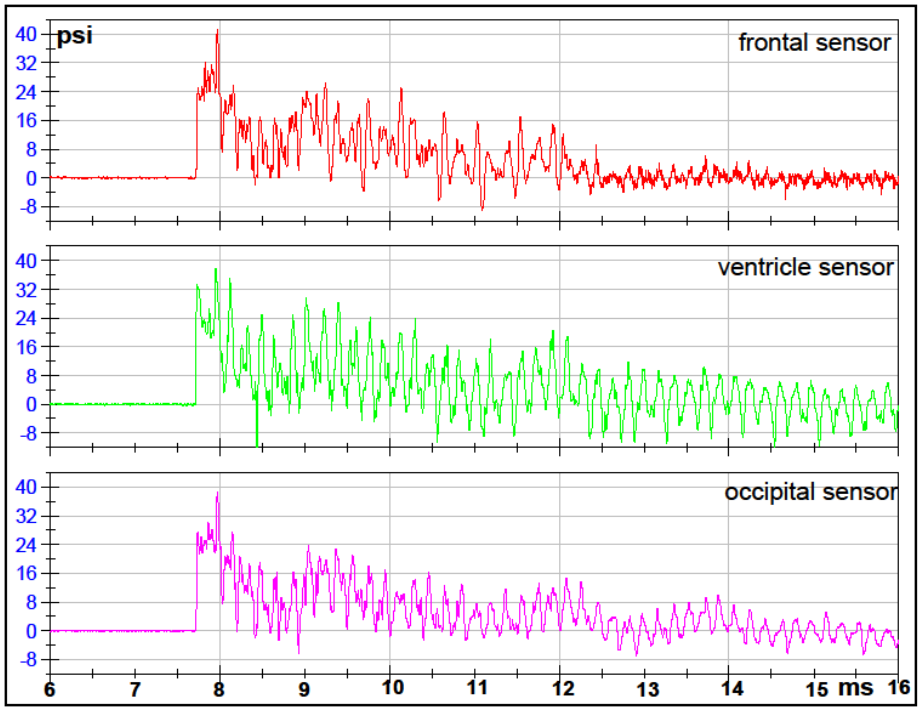

RAW DATA

Test 10 Front 2 Orientation 6mm Intact Sphere

FILTERED DATA

NA

NA

RAW DATA

Test 11 Front 1 Orientation 6mm Intact Sphere

FILTERED DATA

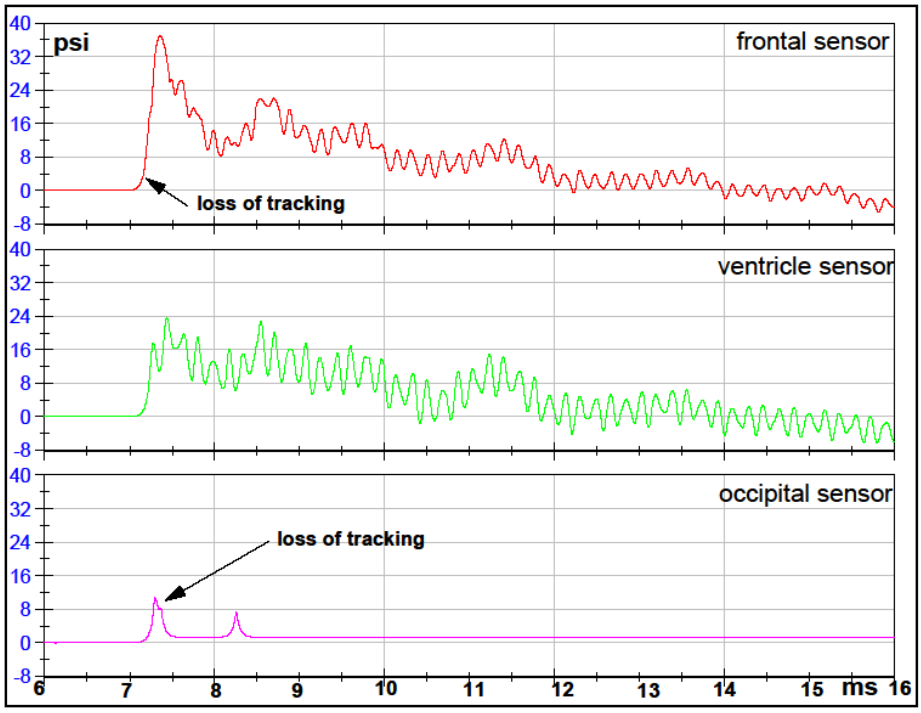

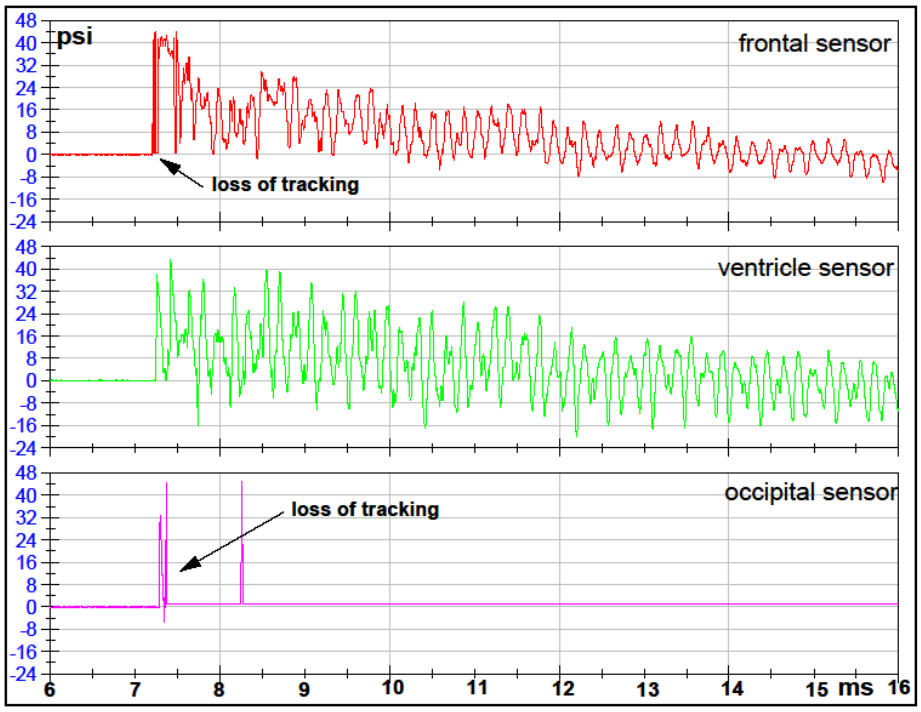

RAW DATA

Test 12 Left Orientation 6mm Intact Sphere

FILTERED DATA

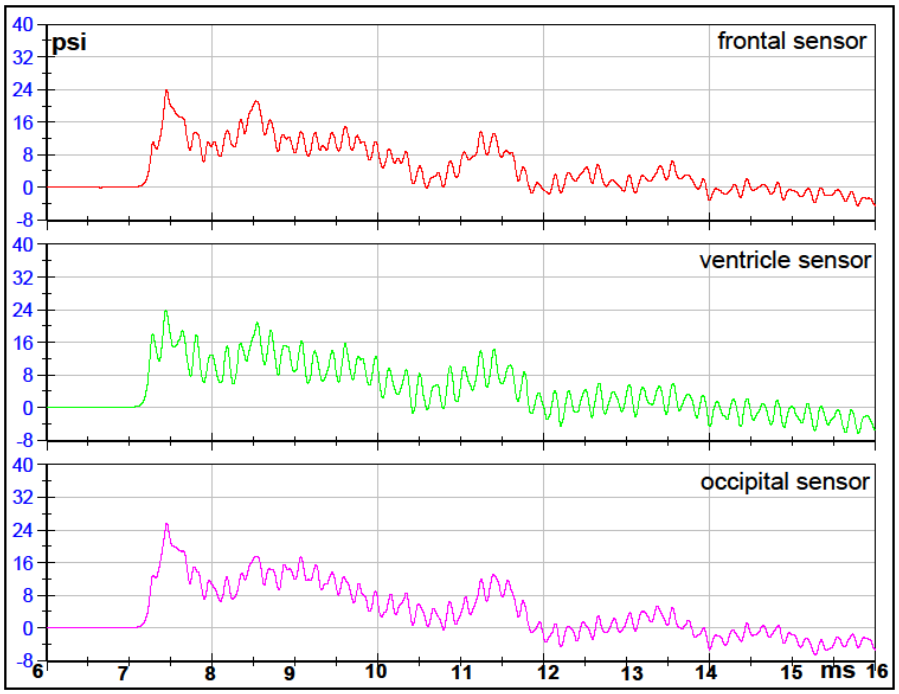

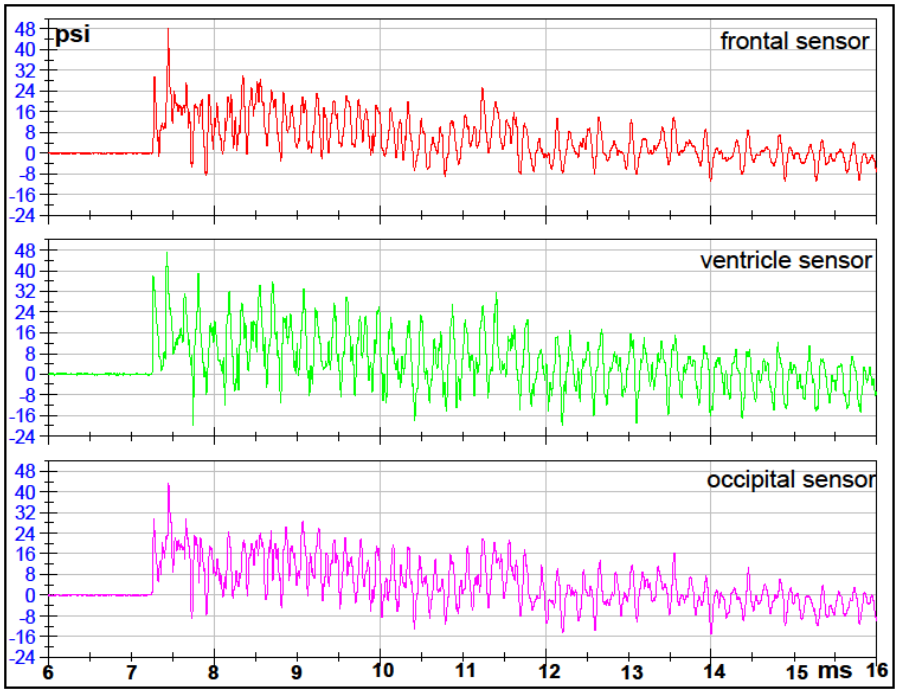

RAW DATA

Test 13 Back Orientation 6mm Intact Sphere

FILTERED DATA

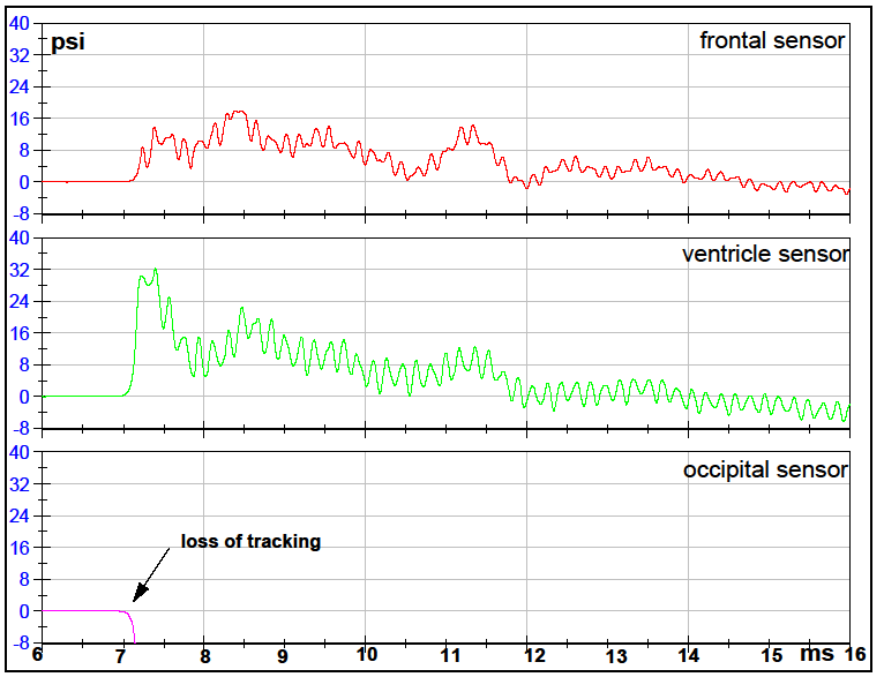

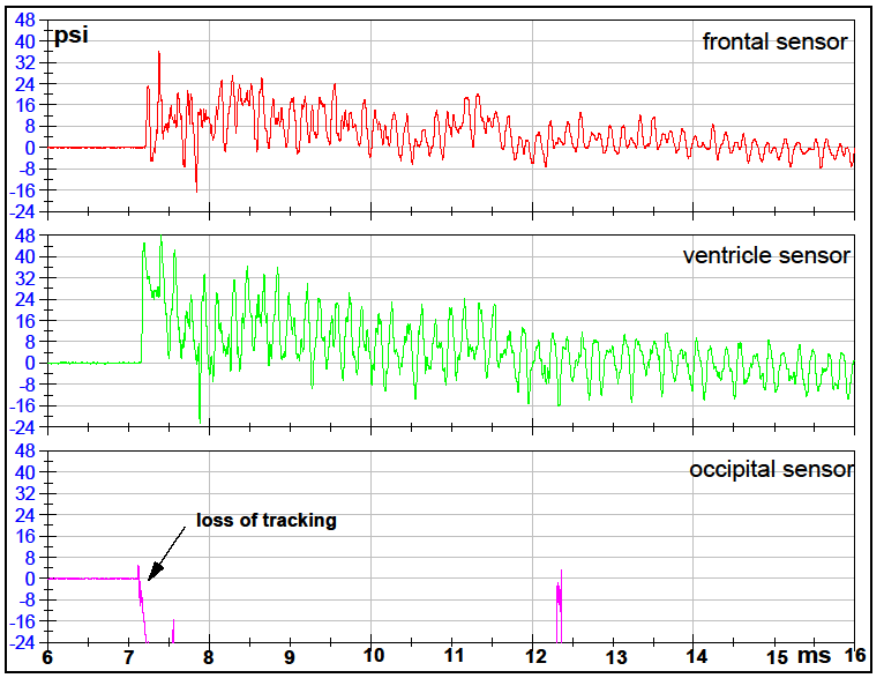

RAW DATA

Test 14 Right Orientation 6mm Intact Sphere

FILTERED DATA

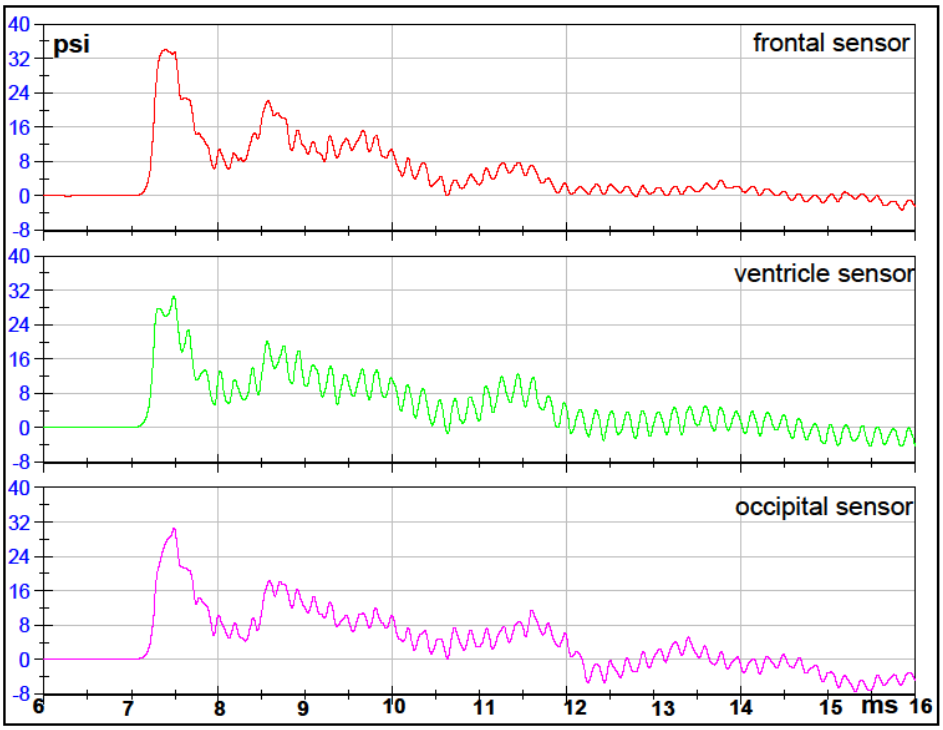

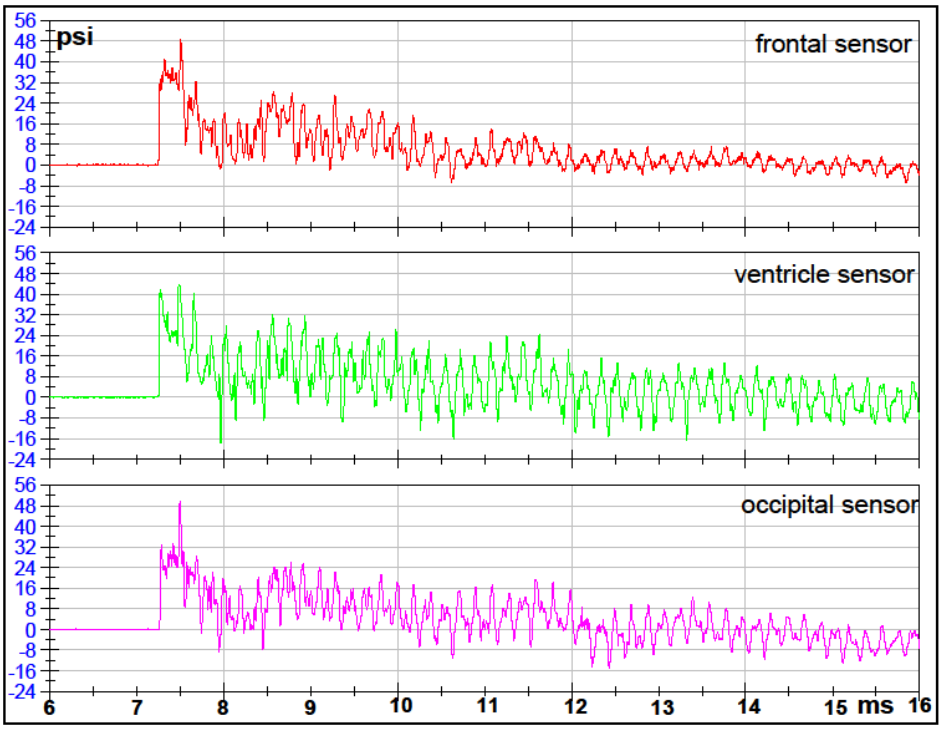

RAW DATA

Test 15 Front 2 Orientation 6mm Intact Sphere

FILTERED DATA

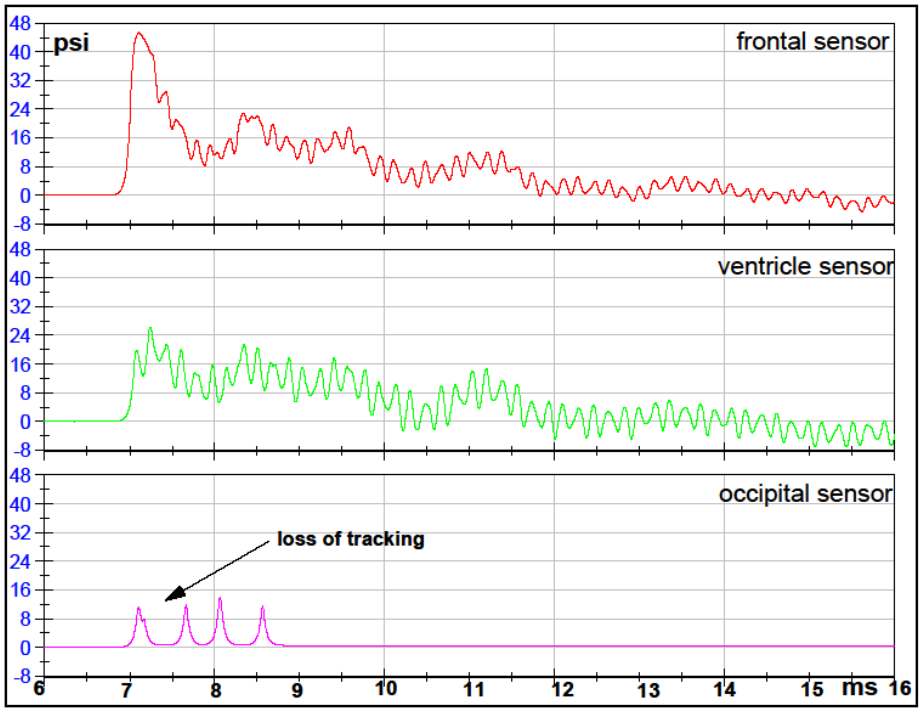

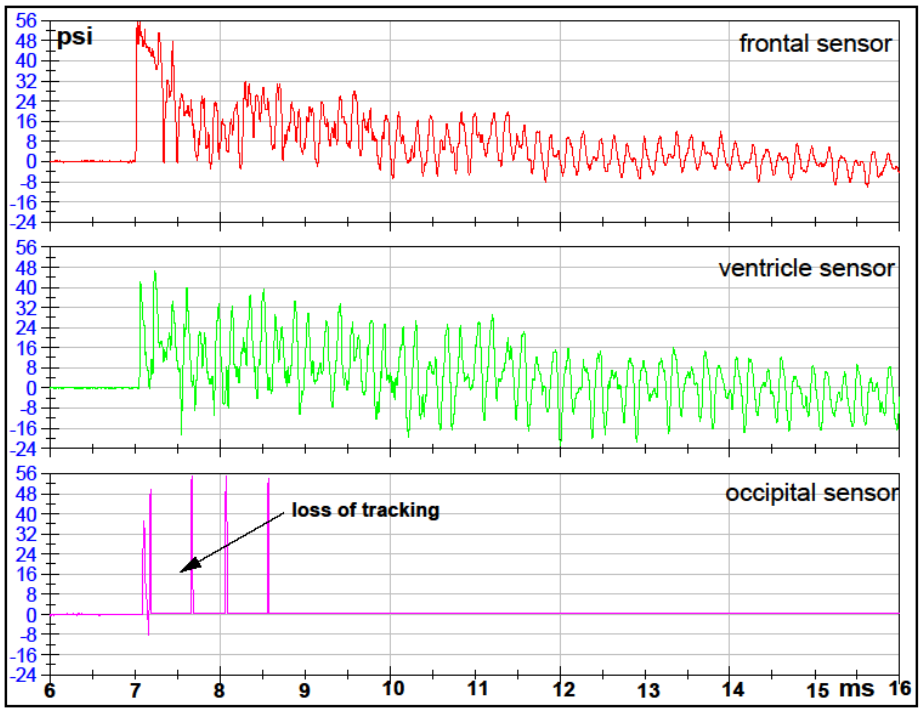

RAW DATA

Comparison for reproducibility of each pressure sensor in Front Orientation at 10psi 6mm Intact Sphere

VENTRICLE FILTERED DATA

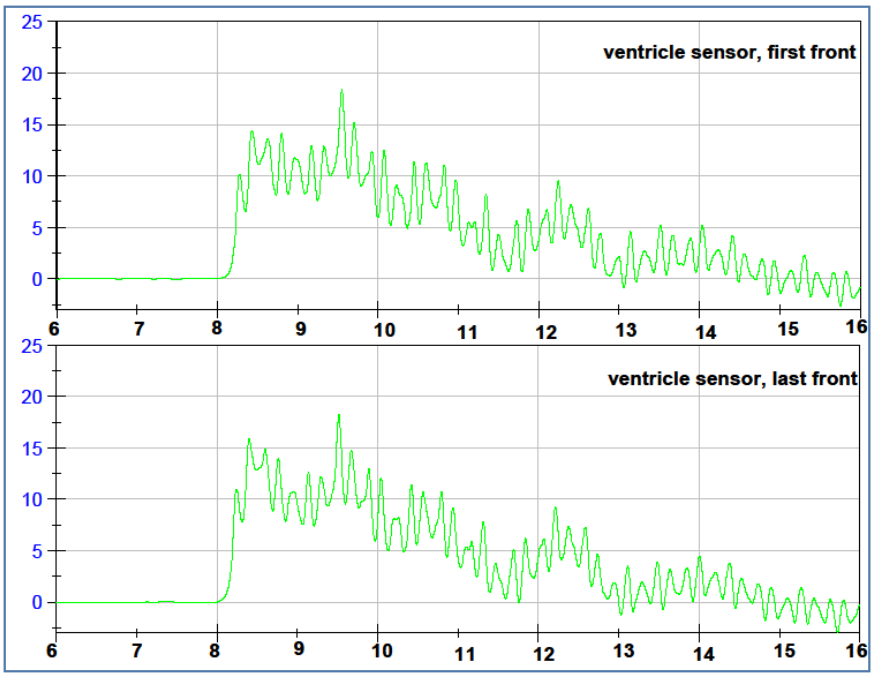

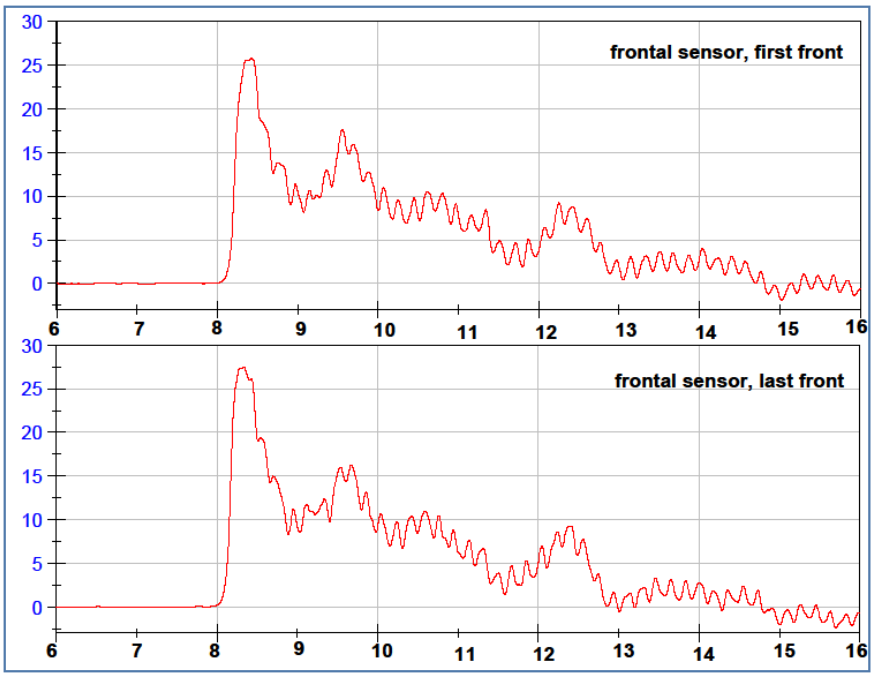

FRONTAL FILTERED DATA

Comparison for reproducibility of each pressure sensor in Front Orientation at 10psi 6mm Intact Sphere

OCCIPITAL FILTERED DATA

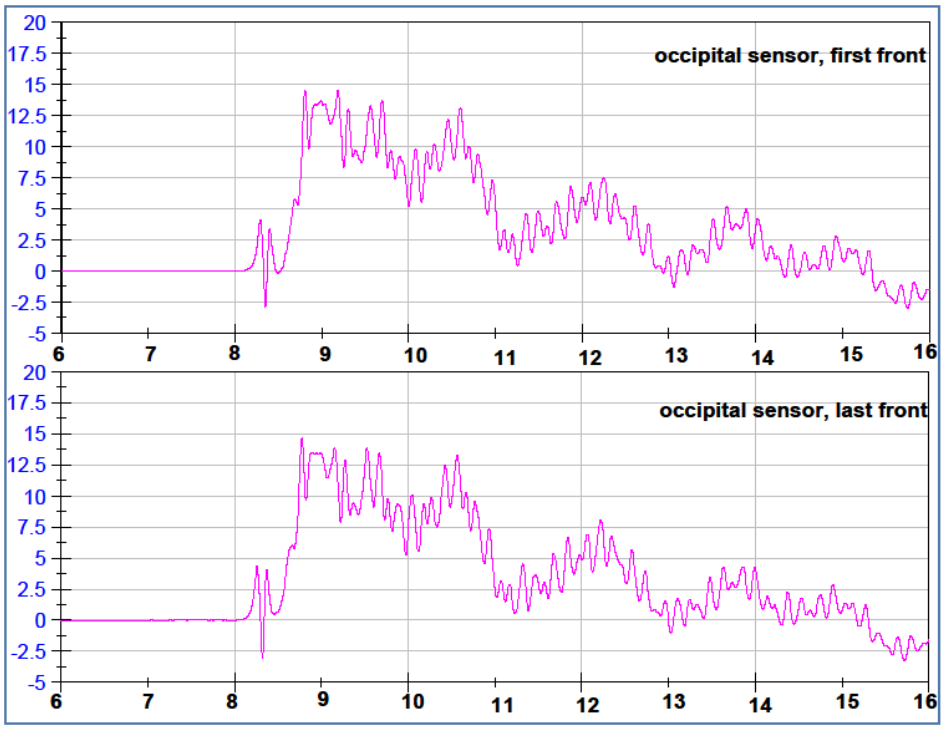

Comparison for reproducibility of each pressure sensor in Front Orientation at 12psi 6mm Intact Sphere

VENTRICLE FILTERED DATA

NA

NA

FRONTAL FILTERED DATA

Comparison for reproducibility of each pressure sensor in Front Orientation at 12psi 6mm Intact Sphere

OCCIPITAL FILTERED DATA

NA

Comparison for reproducibility of each pressure sensor in Front Orientation at 15psi 6mm Intact Sphere

VENTRICLE FILTERED DATA

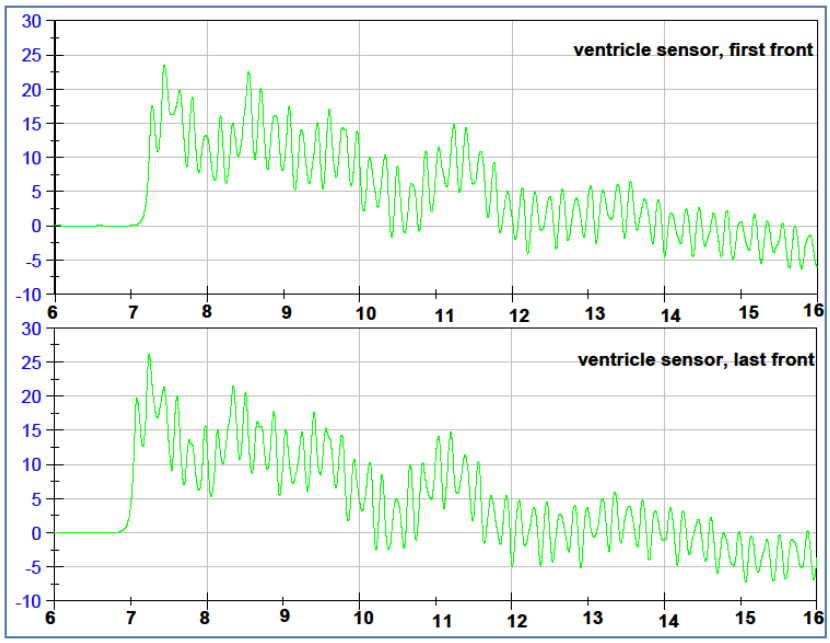

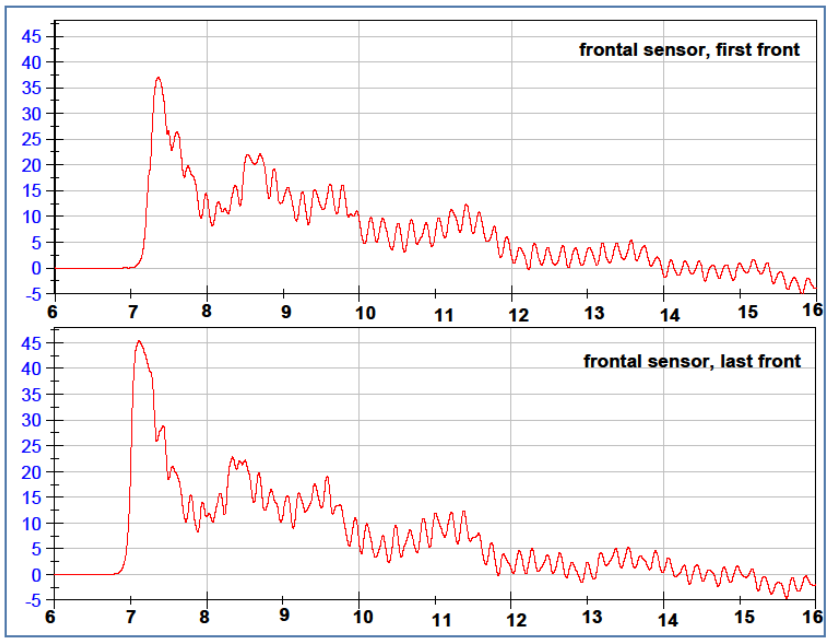

FRONTAL FILTERED DATA

Comparison for reproducibility of each pressure sensor in Front Orientation at 15psi 6mm Intact Sphere

OCCIPITAL FILTERED DATA

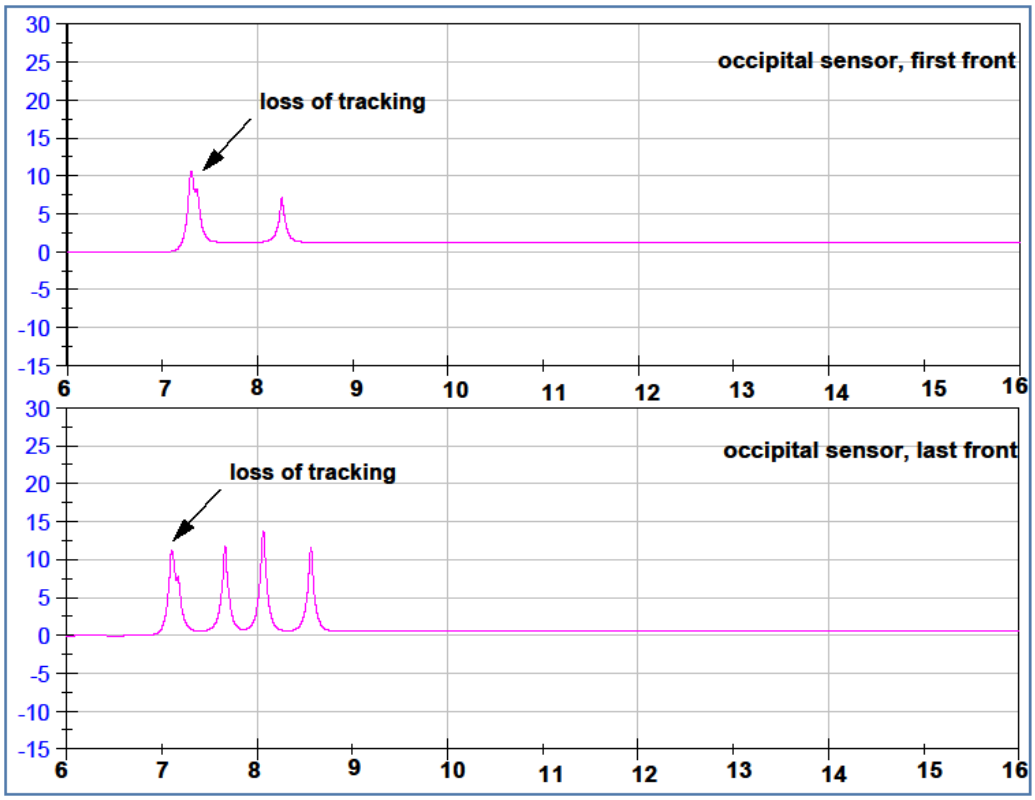

Frontal Sensor, 4 Orientations, Filtered Data, 6mm Intact Sphere

10 PSI

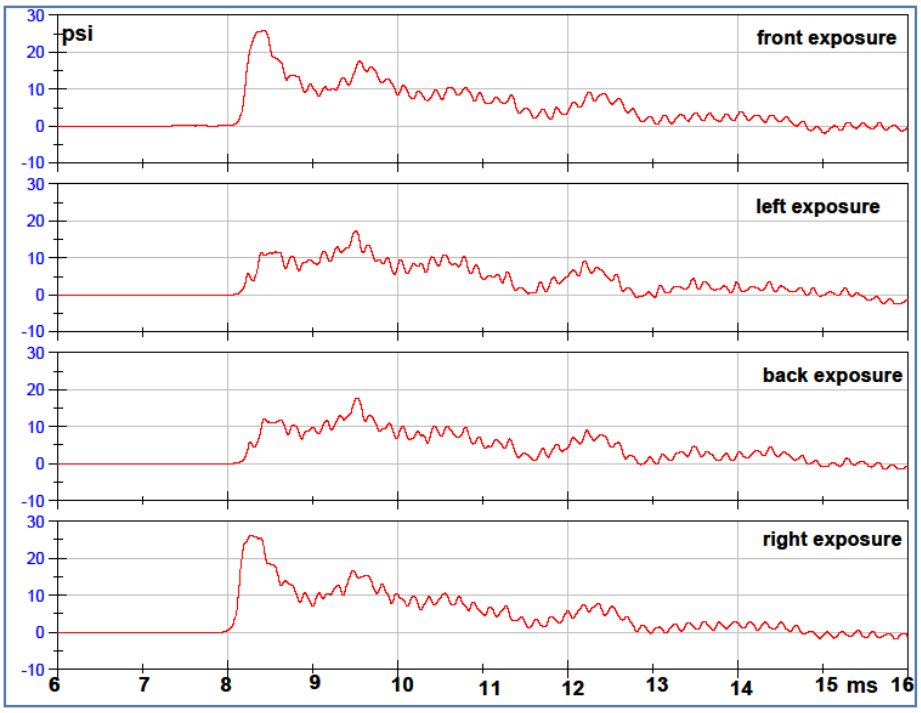

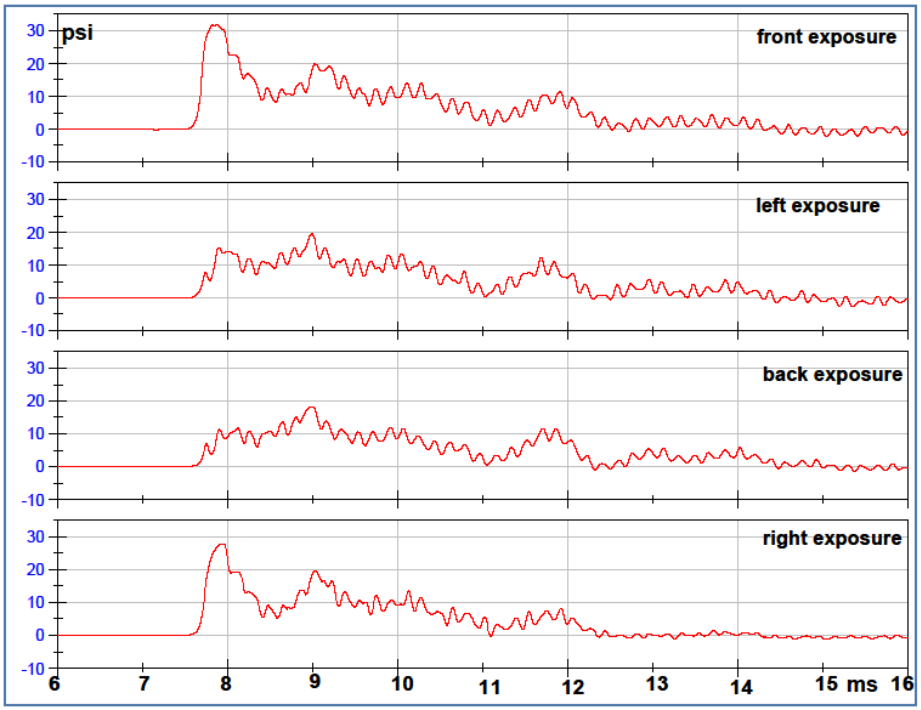

12 PSI

Frontal Sensor, 4 Orientations, Filtered Data, 6mm Intact Sphere

15 PSI

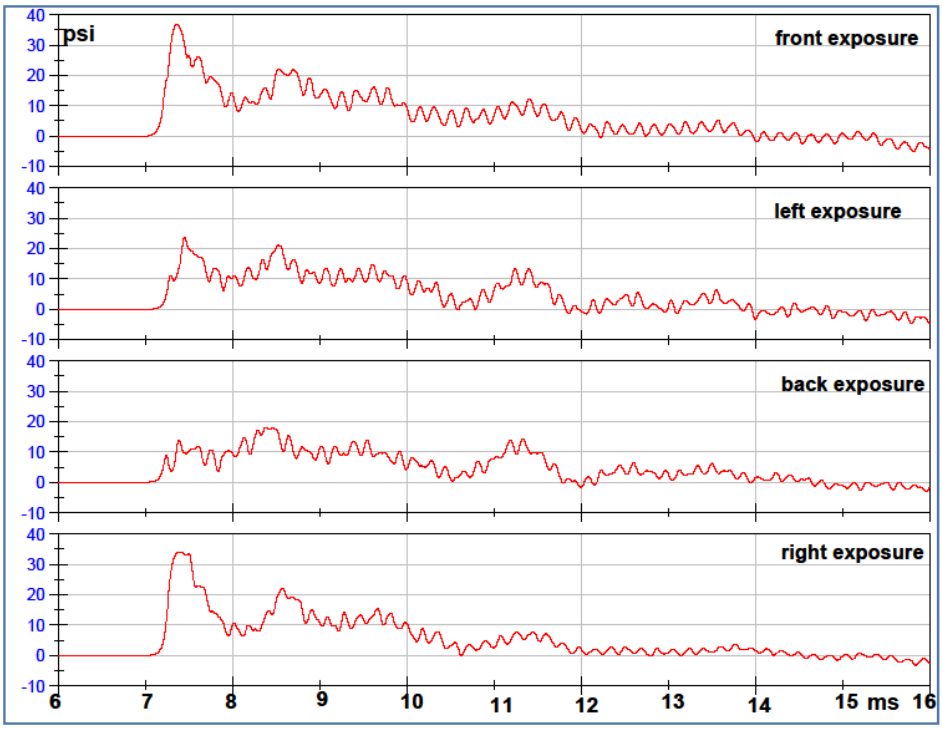

Ventricle Sensor, 4 Orientations, Filtered Data, 6mm Intact Sphere

10 PSI

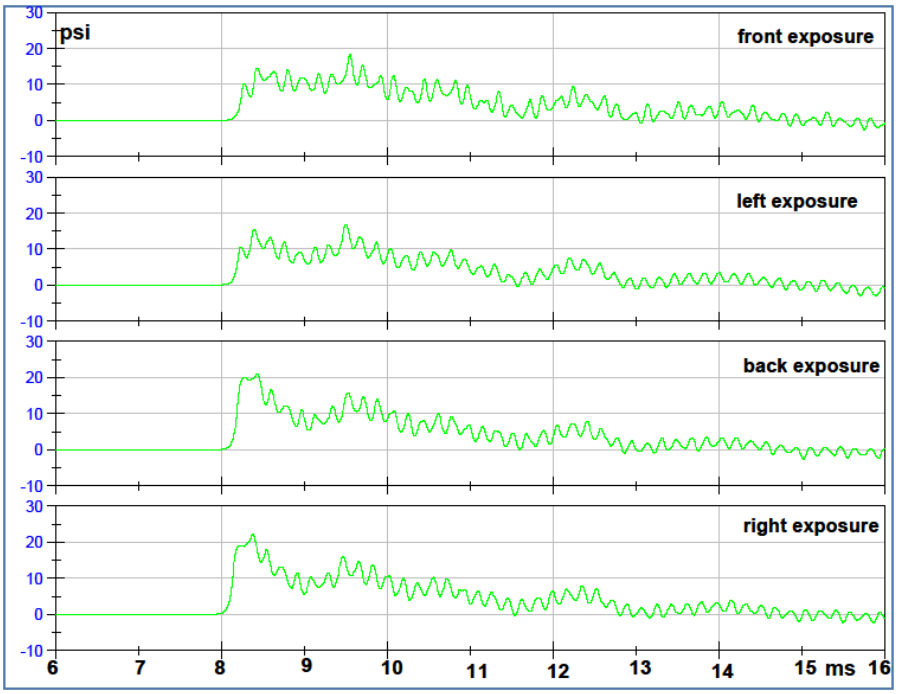

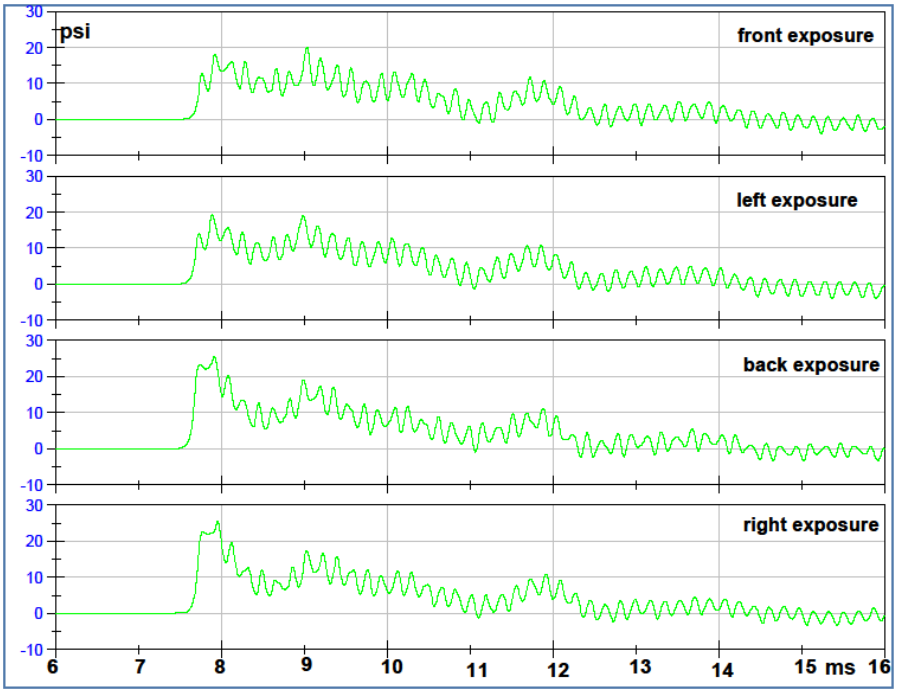

12 PSI

Ventricle Sensor, 4 Orientations, Filtered Data, 6mm Intact Sphere
15 PSI

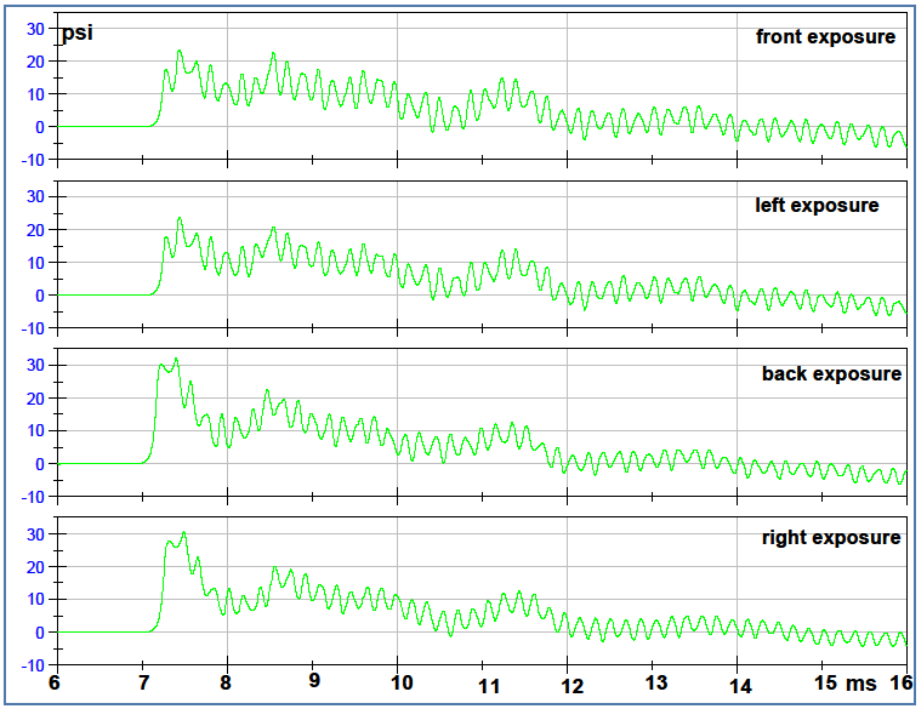

Occipital Sensor, 4 Orientations, Filtered Data, 6mm Intact Sphere

10 PSI

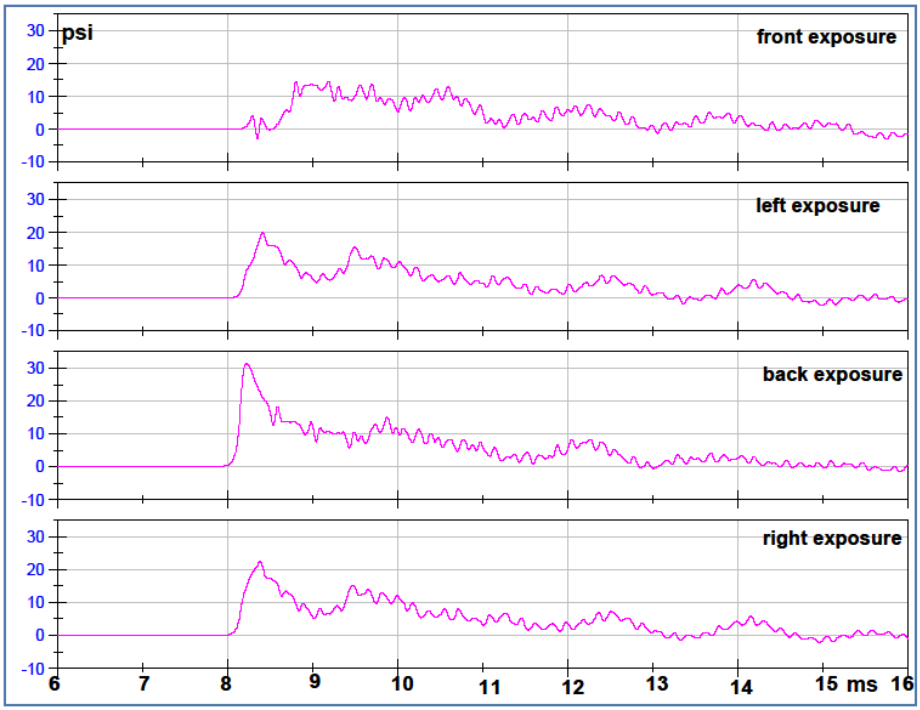

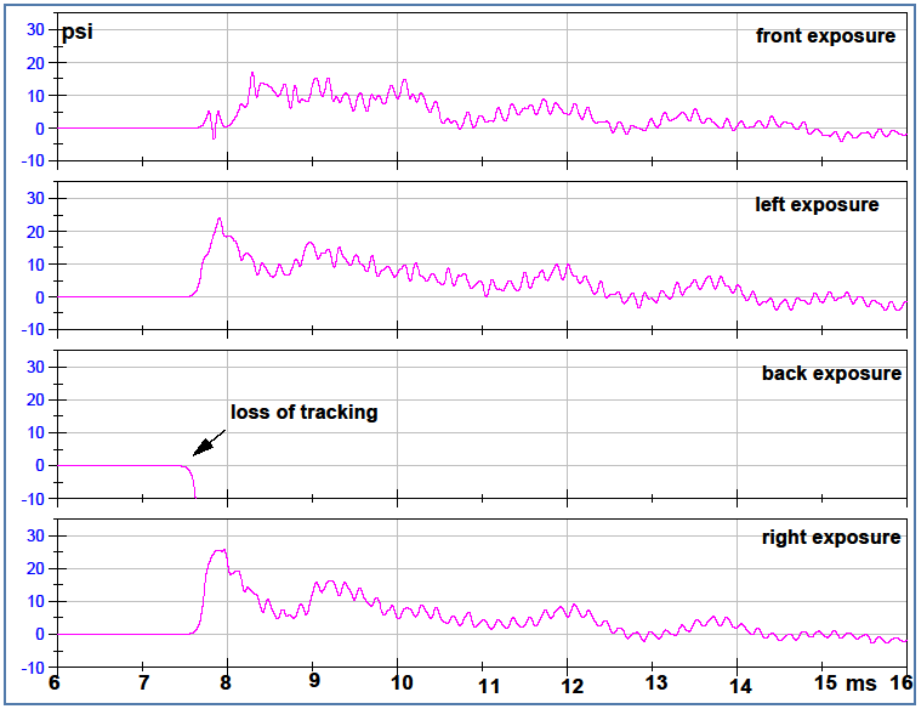

12 PSI

Occipital Sensor, 4 Orientations, Filtered Data, 6mm Intact Sphere

15 PSI

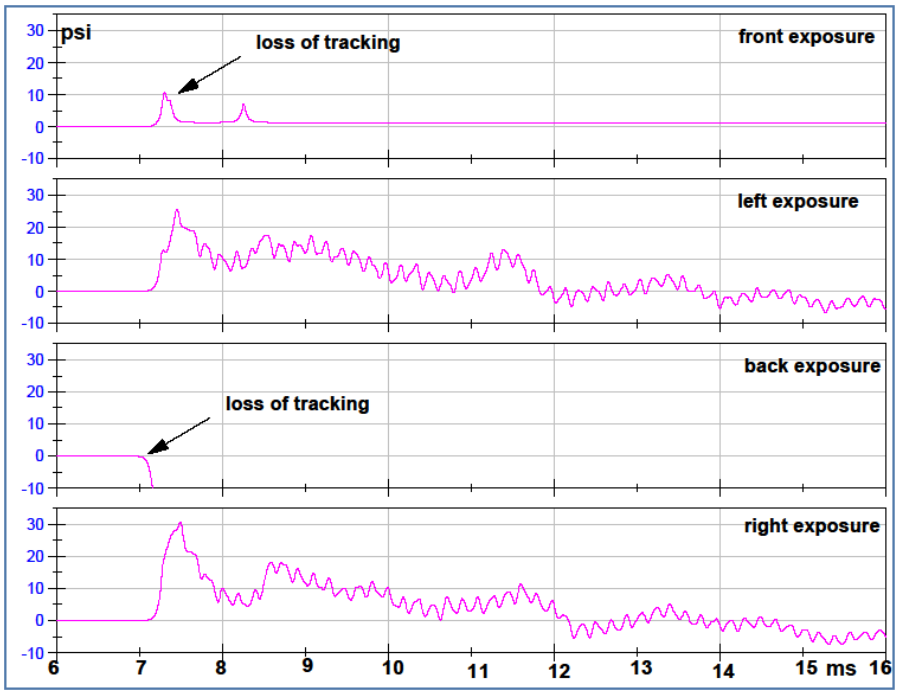

Pressure extremes for intact sphere 6mm

Pressure Extremes for Intact Sphere 6mm										
	Maximun Pressure					Minimum Pressure				
ventricle	front 1	right	back	left	front 2	front 1	right	back	left	front 2
10 psi air	**18.4**	**22.2**	**21**	**16.7**	**18.3**	**-0.85**	**-0.92**	**-0.99**	**-1.04**	**-1.23**
12 psi air	**20.1**	**25.5**	**25.4**	**19.1**	**NA**	**-2.01**	**-2.24**	**-2.35**	**-2.13**	**NA**
15 psi air	**23.5**	**30.5**	**32.2**	**23.9**	**26**	**-4.18**	**-2.94**	**-3.52**	**-4.54**	**-4.94**
frontal	front 1	right	back	left	front 2	front 1	right	back	left	front 2
10 psi air	**25.8**	**26.2**	**17.7**	**17.3**	**27.5**	**0.17**	**-0.24**	**0.2**	**-0.68**	**-0.5**
12 psi air	**31.7**	**27.9**	**18.2**	**19.5**	**NA**	**-0.76**	**-0.55**	**-0.96**	**-0.53**	**NA**
15 psi air	**37**	**34.1**	**18**	**23.8**	**45.4**	**-0.37**	**0.18**	**-1.73**	**-1.48**	**-1.52**
occipital	front 1	right	back	left	front 2	front 1	right	back	left	front 2
10 psi air	**14.5**	**22.6**	**31.3**	**19.9**	**14.5**	**-2.87**	**-0.76**	**-0.6**	**-1.76**	**-3.05**
12 psi air	**16.9**	**26**	**NA**	**24.1**	**NA**	**-3.48**	**-2.05**	**NA**	**-3.47**	**NA**
15 psi air	**NA**	**30.6**	**NA**	**25.7**	**NA**	**NA**	**-5.46**	**NA**	**-4.78**	**NA**

1st rate of change of pressure for 6mm-thick sphere.

1st rate (psi/ms)					
ventricle	front 1	right	back	left	front 2
10 psi air	**56.4**	**76.3**	**84.8**	**59**	**52**
12 psi air	**69**	**105**	**101.2**	**75.9**	**NA**
15 psi air	**92.6**	**120.5**	**132.3**	**92**	**93.6**
frontal	front 1	right	back	left	front 2
10 psi air	**81.5**	**91.6**	**37**	**39.6**	**96.9**
12 psi air	**106.5**	**77.5**	**44.2**	**48.1**	**NA**
15 psi air	**118.1**	**116.8**	**52.9**	**69.4**	**152.3**
occipital	front 1	right	back	left	front 2
10 psi air	**30.1**	**61.6**	**129.7**	**56**	**33.4**
12 psi air	**39.6**	**81.6**	**NA**	**67.2**	**NA**
15 psi air	**NA**	**84.2**	**NA**	**73.2**	**NA**

Comparisons of 1st rate of change of pressure in the 6mm-thick sphere with holes relative to the intact sphere.

The number is expressed in percentage of the intact sphere results for each test. Positive numbers mean higher rates in the intact sphere.

Percentages of Rate of Change of Pressure for 6mm-thick sphere with holes relative to intact sphere					
ventricle	front 1	right	back	left	front 2
10 psi air	**44%**	**37%**	**24%**	**27%**	**24%**
12 psi air	**41%**	**37%**	**25%**	**48%**	**NA**
15 psi air	**20%**	**27%**	**12%**	**16%**	**28%**
frontal	front 1	right	back	left	front 2
10 psi air	**10%**	**42%**	**25%**	**-23%**	**11%**
12 psi air	**0%**	**-2%**	**20%**	**-19%**	**NA**
15 psi air	**-5%**	**7%**	**7%**	**0%**	**20%**
occipital	front 1	right	back	left	front 2
10 psi air	**48%**	**10%**	**12%**	**39%**	**50%**
12 psi air	**49%**	**21%**	**NA**	**69%**	**NA**
15 psi air	**NA**	**11%**	**NA**	**20%**	**NA**

Percentages of peak internal pressure changes in 6 mm sphere intact and with apertures, based on the cell value at the 10 psi air overpressure for each orientation.

		PERCENTAGES for sphere 6mm					PERCENTAGES for sphere 6mm with holes				
AIR		Percentage Increase in Maximun Peak Pressure					Percentage Increase in Maximun Peak Pressure				
Overpressure		front 1	right	back	left	front 2	front 1	right	back	left	front 2
ventricle	20%	9%	15%	21%	14%	NA	57%	31%	23%	24%	7%
ventricle	50%	28%	37%	53%	43%	42%	106%	88%	65%	82%	78%
frontal	20%	23%	6%	3%	13%	NA	33%	30%	31%	34%	24%
frontal	50%	43%	30%	2%	38%	65%	64%	85%	59%	50%	73%
occipital	20%	17%	15%	NA	21%	NA	32%	14%	NA	21%	10%
occipital	50%	NA	35%	NA	29%	NA	67%	44%	NA	55%	NA

Maximum peak pressure increase in the 6mm-thick sphere with holes relative to the intact sphere.

The number is expressed in percentage of the intact sphere results for each test. Positive numbers mean higher pressure in the intact sphere.

Percentage of Relative Maximum Peak Pressure Increase					
6mm-sphere with holes in respect to 6mm-sphere					
ventricle	front 1	right	back	left	front 2
10 psi air	**33%**	**47%**	**28%**	**38%**	**13%**
12 psi air	**4%**	**40%**	**27%**	**33%**	**NA**
15 psi air	**-8%**	**27%**	**23%**	**21%**	**-9%**
frontal	front 1	right	back	left	front 2
10 psi air	**19%**	**32%**	**3%**	**9%**	**20%**
12 psi air	**12%**	**17%**	**-23%**	**-8%**	**NA**
15 psi air	**7%**	**3%**	**-51%**	**0%**	**17%**
occipital	front 1	right	back	left	front 2
10 psi air	**-10%**	**21%**	**9%**	**35%**	**-21%**
12 psi air	**-25%**	**22%**	**NA**	**35%**	**NA**
15 psi air	**NA**	**16%**	**NA**	**21%**	**NA**

Table of Differential Pressure Results for 6mm Intact Sphere

Differential for sphere 6mm										
	peak differential pressure (psi)					time elapsed between peaks (ms)				
ventricle	front 1	right	back	left	front 2	front 1	right	back	left	front 2
10 psi air	**19.3**	**23.1**	**22**	**17.7**	**19.5**	**3.5**	**4.78**	**4.43**	**3.51**	**3.51**
12 psi air	**22.1**	**27.7**	**27.7**	**21.2**	**NA**	**3.66**	**4.78**	**4.42**	**4.79**	**NA**
15 psi air	**27.7**	**33.4**	**35.7**	**28.4**	**31**	**4.77**	**4.93**	**4.93**	**4.77**	**4.77**
frontal	front 1	right	back	left	front 2	front 1	right	back	left	front 2
10 psi air	**25.6**	**26.4**	**17.5**	**18**	**28**	**0.38**	**4.7**	**1.41**	**3.31**	**4.67**
12 psi air	**32.4**	**28.5**	**19.2**	**20**	**NA**	**4.86**	**4.41**	**3.33**	**3.31**	**NA**
15 psi air	**37.4**	**33.9**	**19.7**	**25.3**	**46.9**	**4.86**	**0.32**	**3.62**	**4.4**	**5.81**
occipital	front 1	right	back	left	front 2	front 1	right	back	left	front 2
10 psi air	**17.4**	**23.4**	**31.9**	**21.7**	**17.6**	**0.45**	**4.78**	**4.8**	**4.95**	**0.46**
12 psi air	**20.4**	**28.1**	**NA**	**27.6**	**NA**	**0.45**	**4.94**	**NA**	**4.95**	**NA**
15 psi air	**NA**	**36.1**	**NA**	**30.5**	**NA**	**NA**	**4.74**	**NA**	**4.76**	**NA**

Percentages of 1st rate of internal pressure changes in 6mm intact sphere based on the cell value at the 10 psi air overpressure for each orientation.

AIR		Percentage 1st Rate Pressure Change				
Overpressure		front 1	right	back	left	front 2
ventricle	**20%**	**22%**	**38%**	**19%**	**29%**	**NA**
ventricle	**50%**	**64%**	**58%**	**56%**	**56%**	**80%**
frontal	**20%**	**31%**	**-15%**	**19%**	**21%**	**NA**
frontal	**50%**	**45%**	**28%**	**43%**	**75%**	**57%**
occipital	**20%**	**32%**	**32%**	**NA**	**20%**	**NA**
occipital	**50%**	**NA**	**37%**	**NA**	**31%**	**NA**

State of Gages during Testing of the 6mm Intact Sphere

	Strain status for intact sphere 6mm				
Frontal	front 1	right	back	left	front 2
10 psi air					
12 psi air					
15 psi air					
Left	front 1	right	back	left	front 2
10 psi air					
12 psi air					
15 psi air					
Right	front 1	right	back	left	front 2
10 psi air					
12 psi air					
15 psi air					
Occipital	front 1	right	back	left	front 2
10 psi air					
12 psi air					
15 psi air					

	working
	signal problems
	not working

Strain Data

Test 1 Front 1 Orientation 6mm Intact Sphere

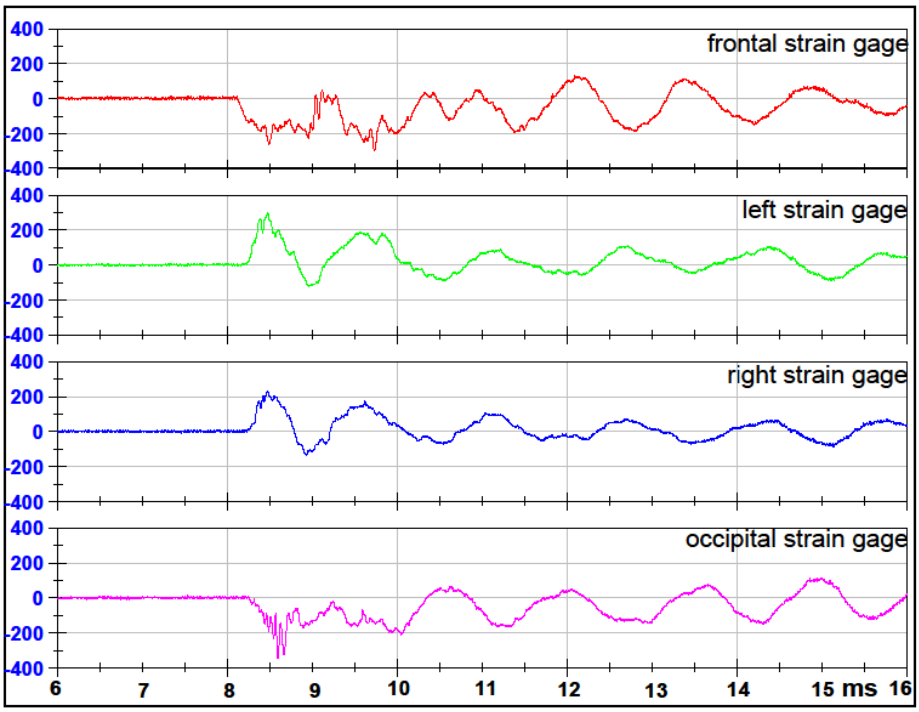

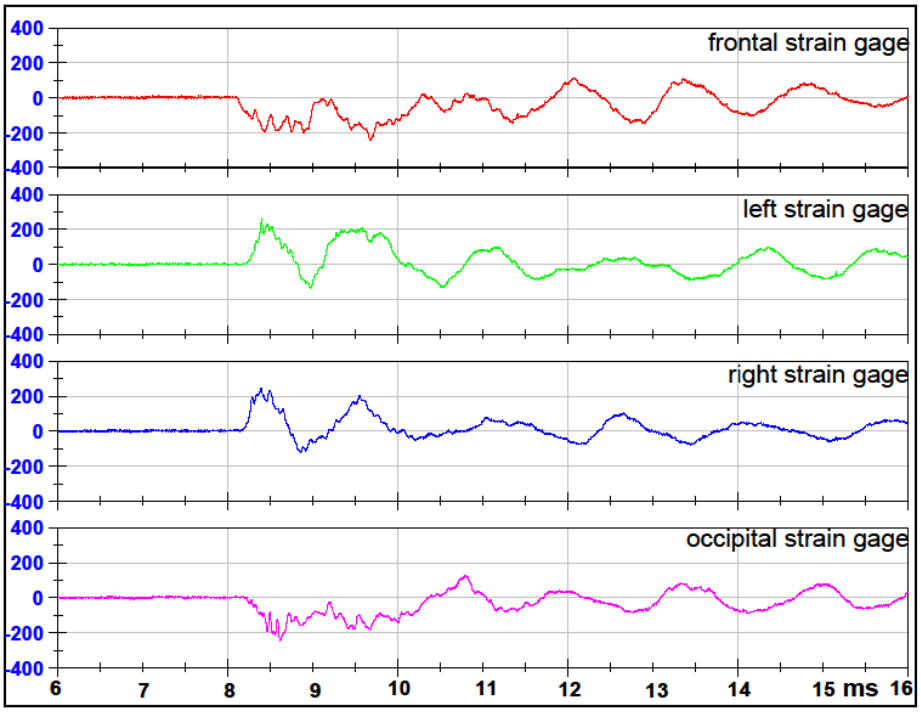

Test 2 Front 2 Orientation 6mm Intact Sphere

Test 3 Right Orientation 6mm Intact Sphere

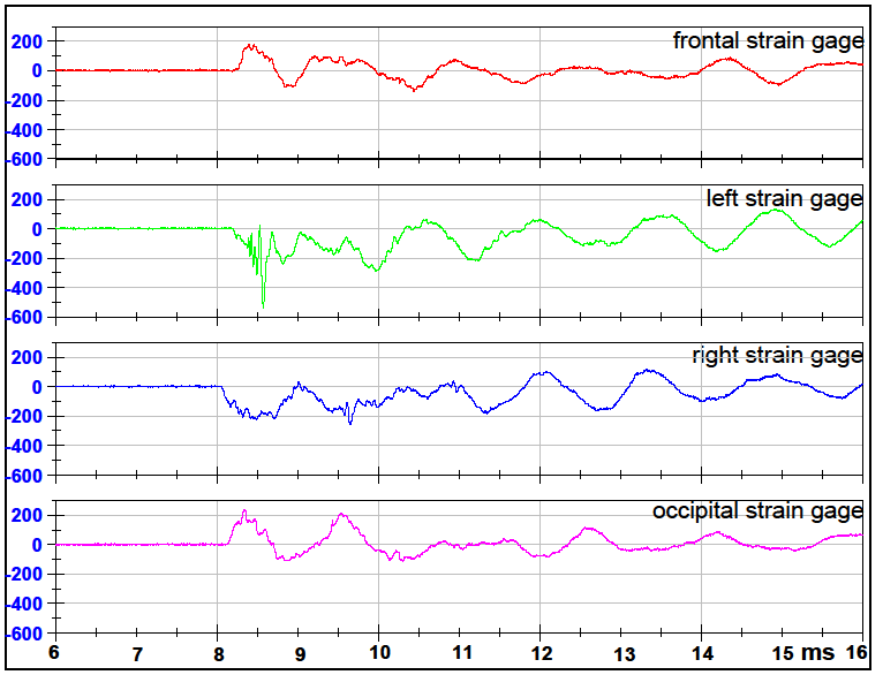

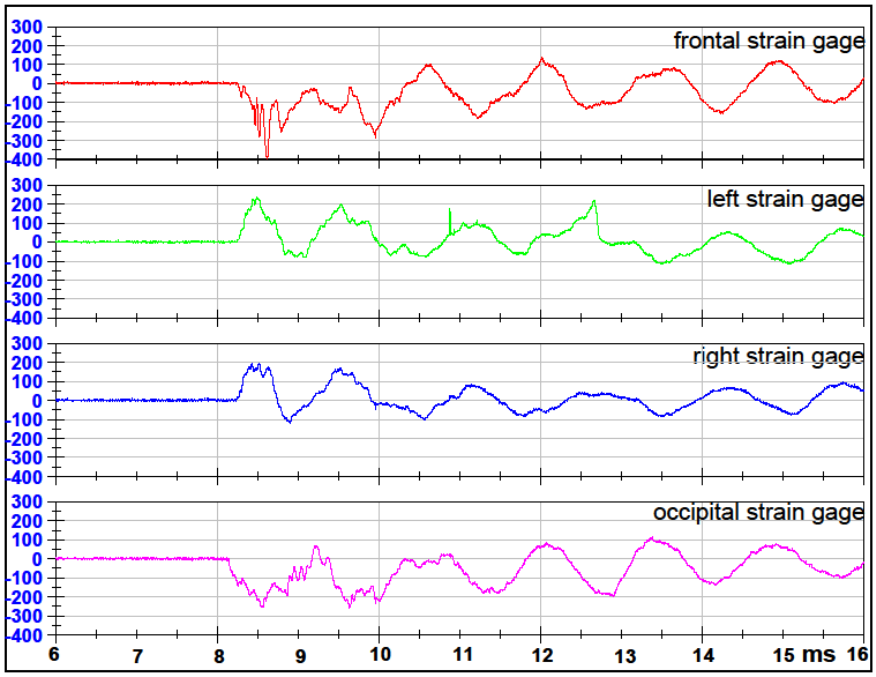

Test 4 Back Orientation 6mm Intact Sphere

Test 5 Left Orientation 6mm Intact Sphere

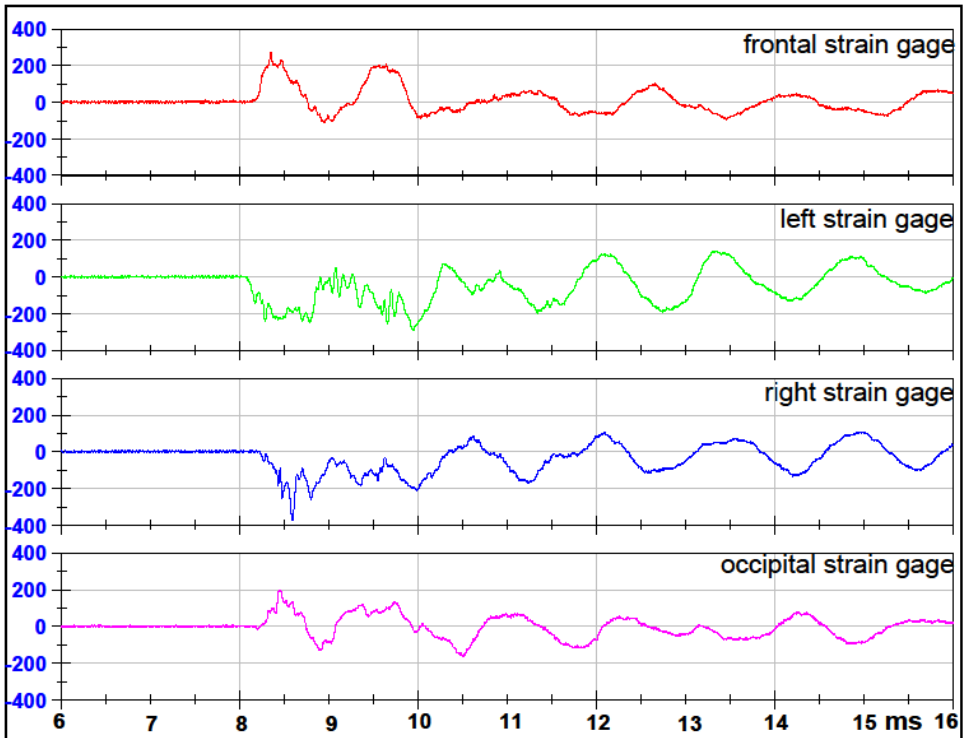

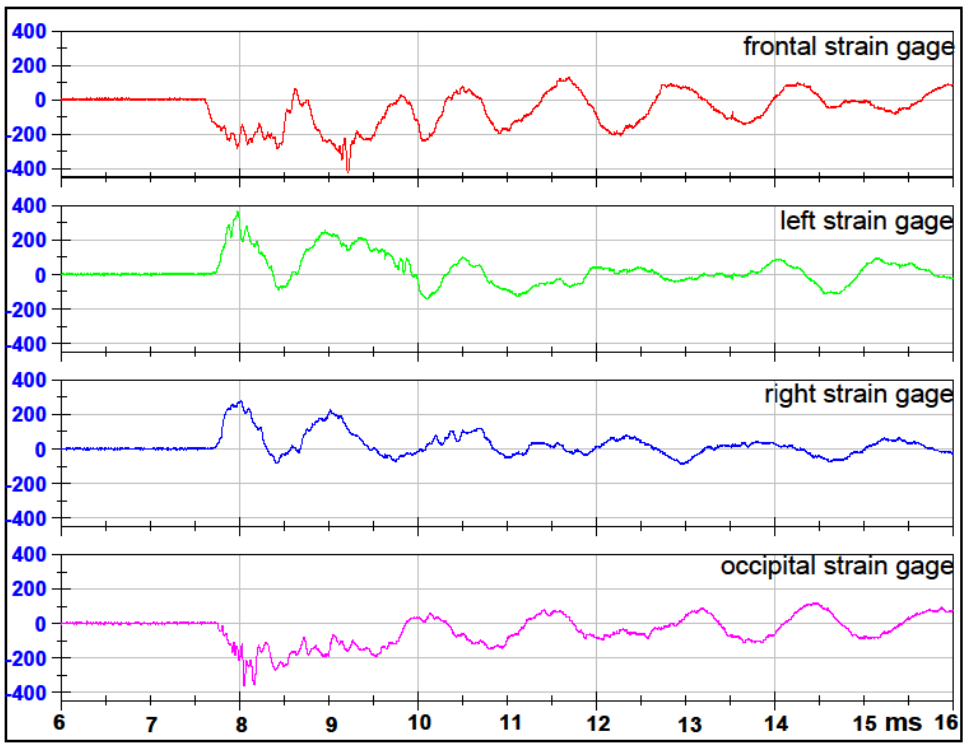

Test 6 Front 1 Orientation 6mm Intact Sphere

Test 7 Left Orientation 6mm Intact Sphere

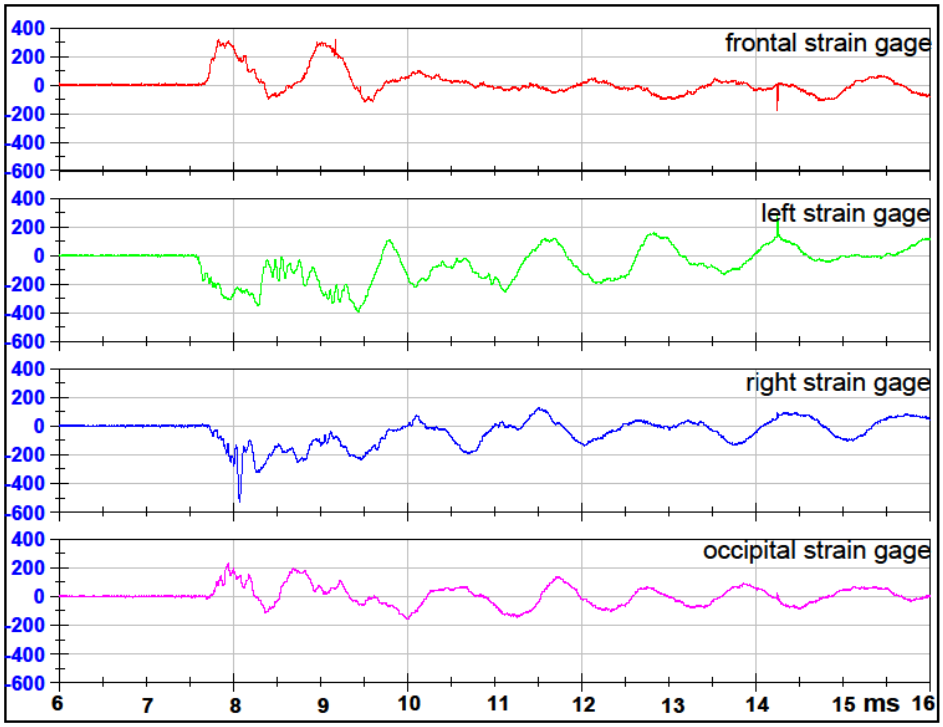

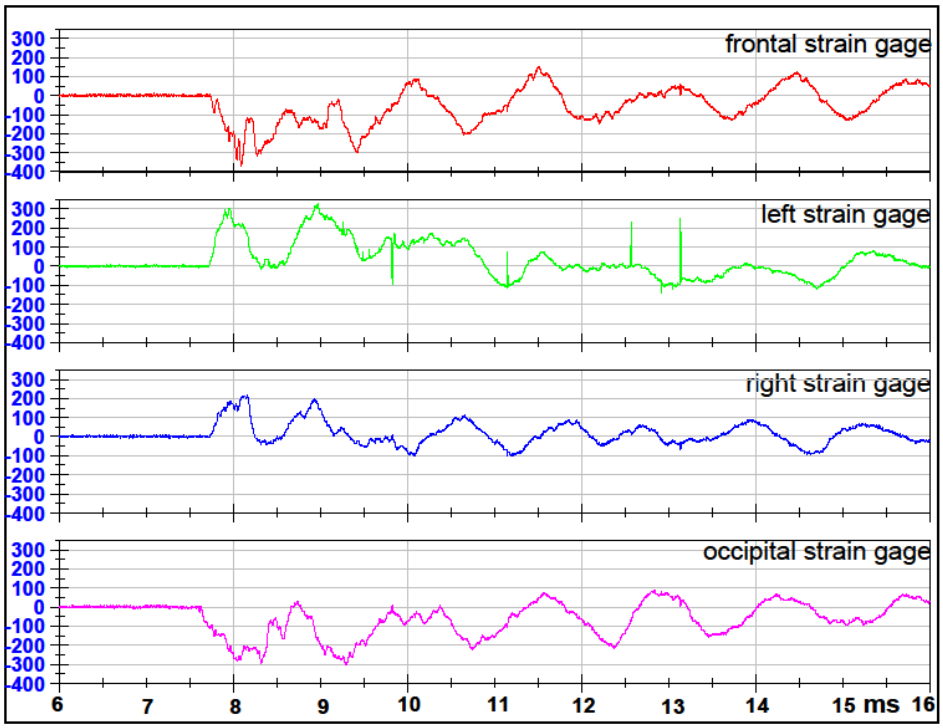

Test 8 Back Orientation 6mm Intact Sphere

Test 9 Right Orientation 6mm Intact Sphere

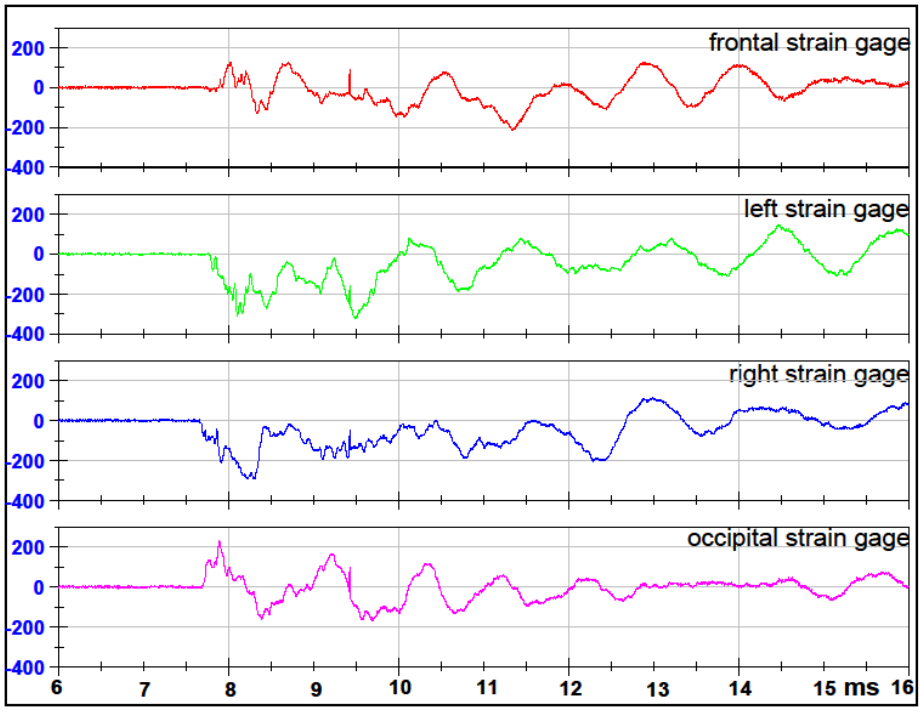

NA

Test 10 Front 2 Orientation 6mm Intact Sphere

Test 11 Front 1 Orientation 6mm Intact Sphere

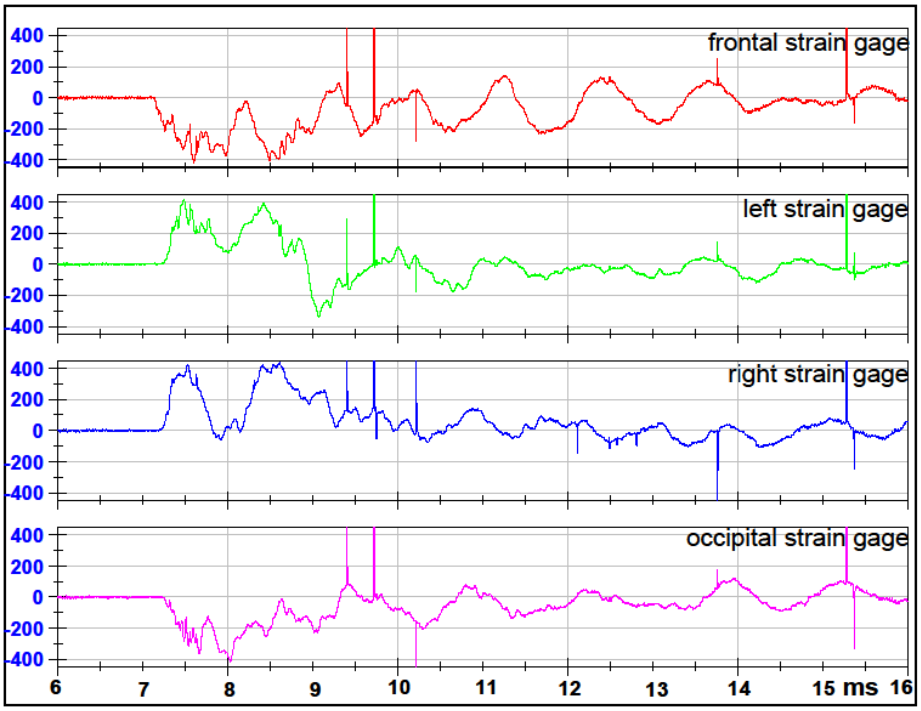

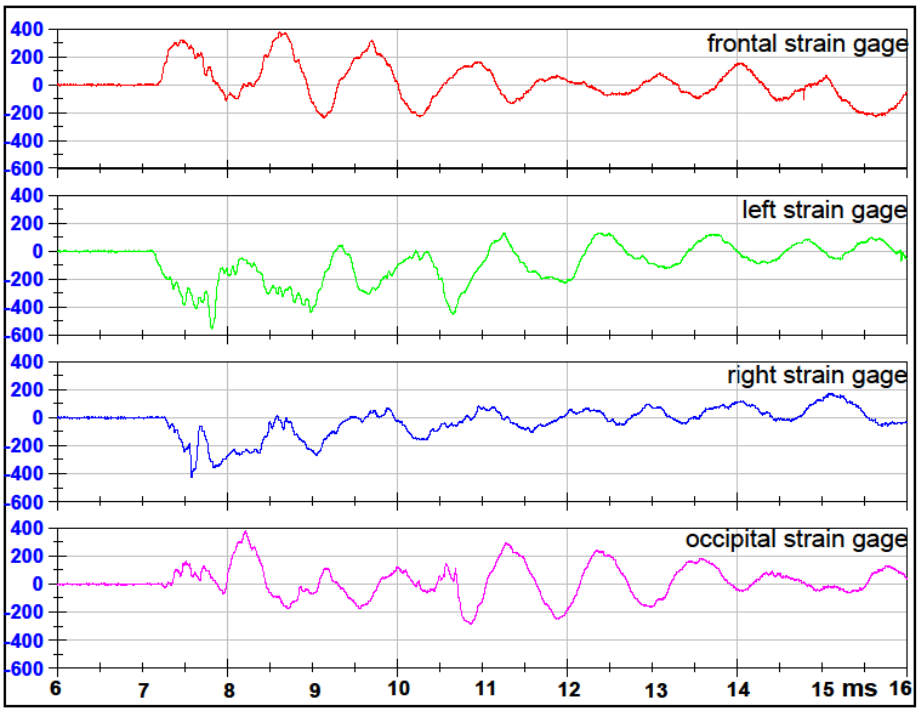

Test 12 Left Orientation 6mm Intact Sphere

Test 13 Back Orientation 6mm Intact Sphere

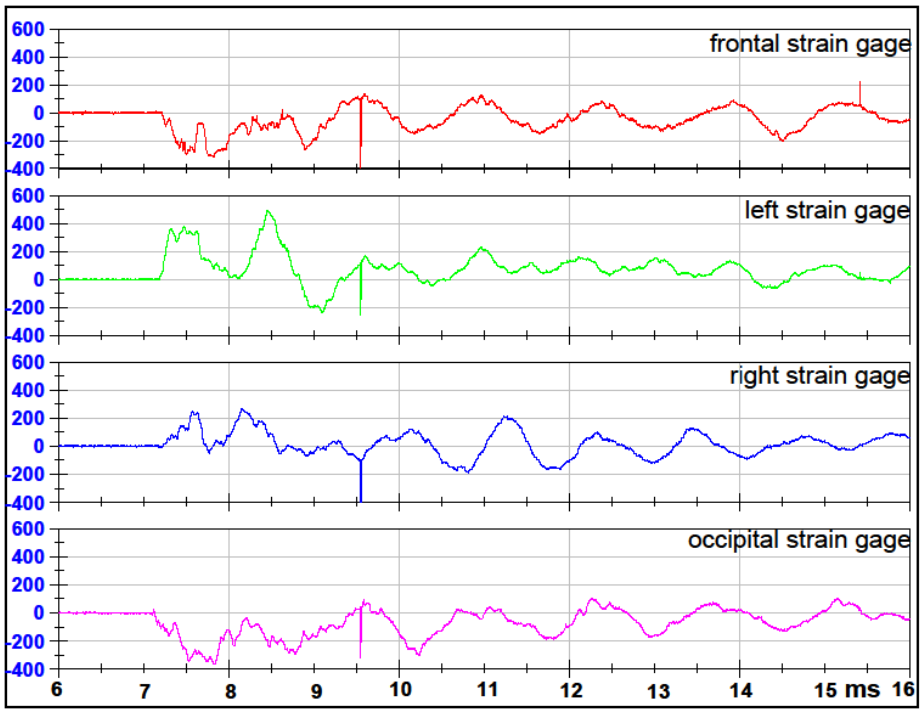

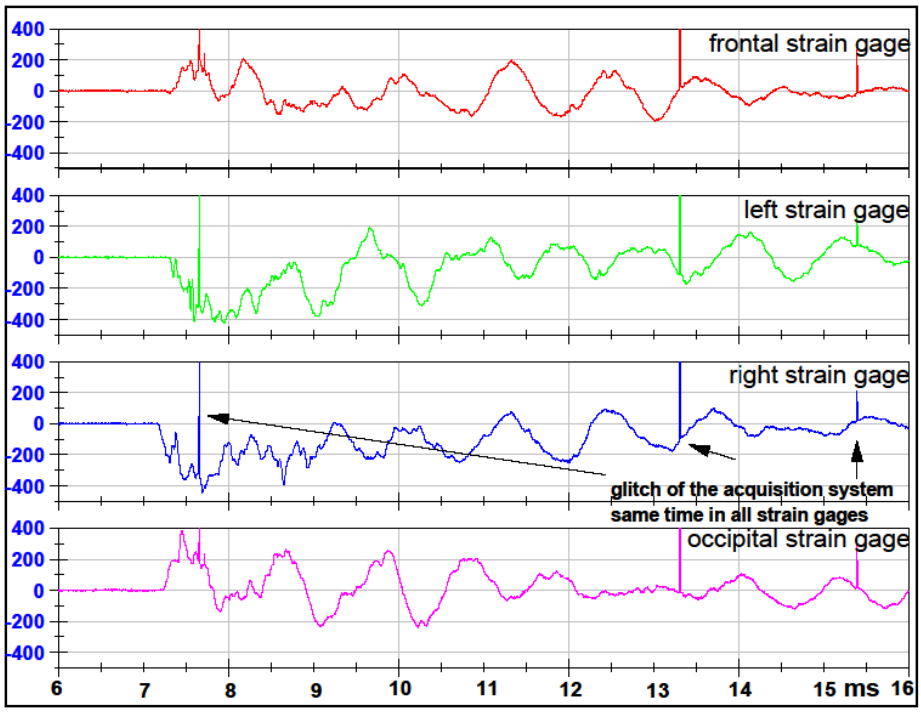

Test 14 Right Orientation 6mm Intact Sphere

Test 15 Front 2 Orientation 6mm Intact Sphere

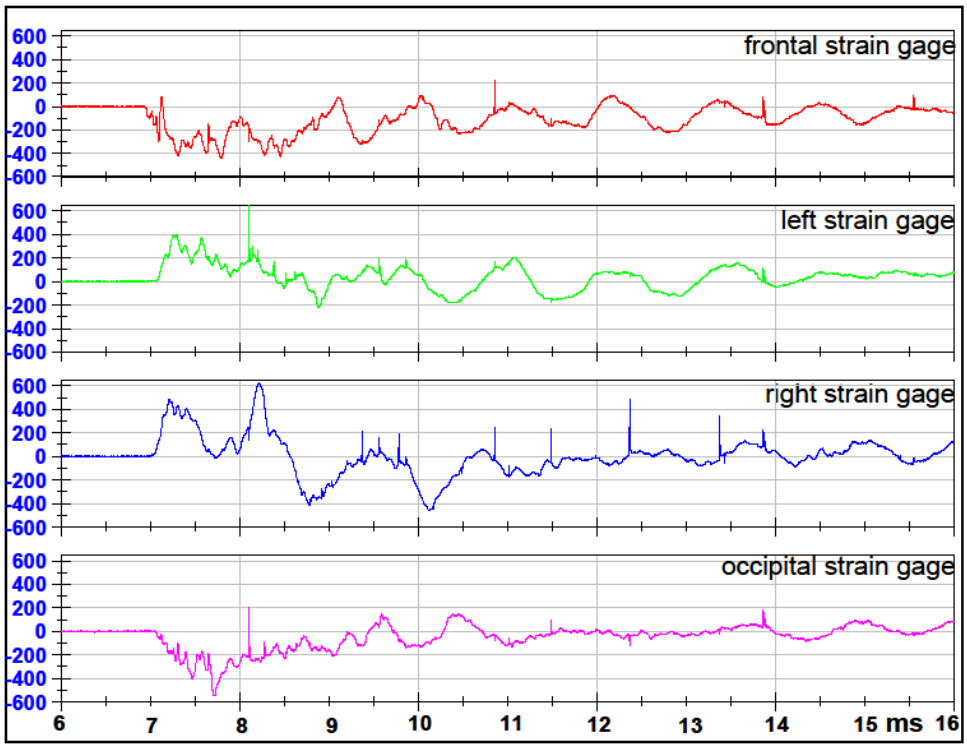

Results after the introduction of Apertures

Test 1 Front 1 Orientation 6mm Sphere with Holes

FILTERED DATA

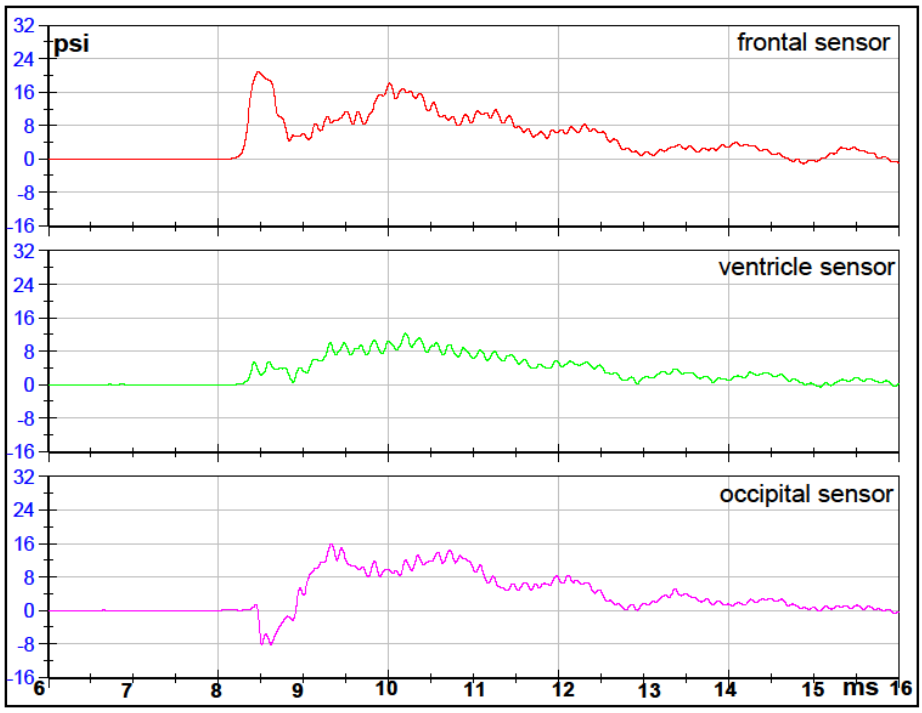

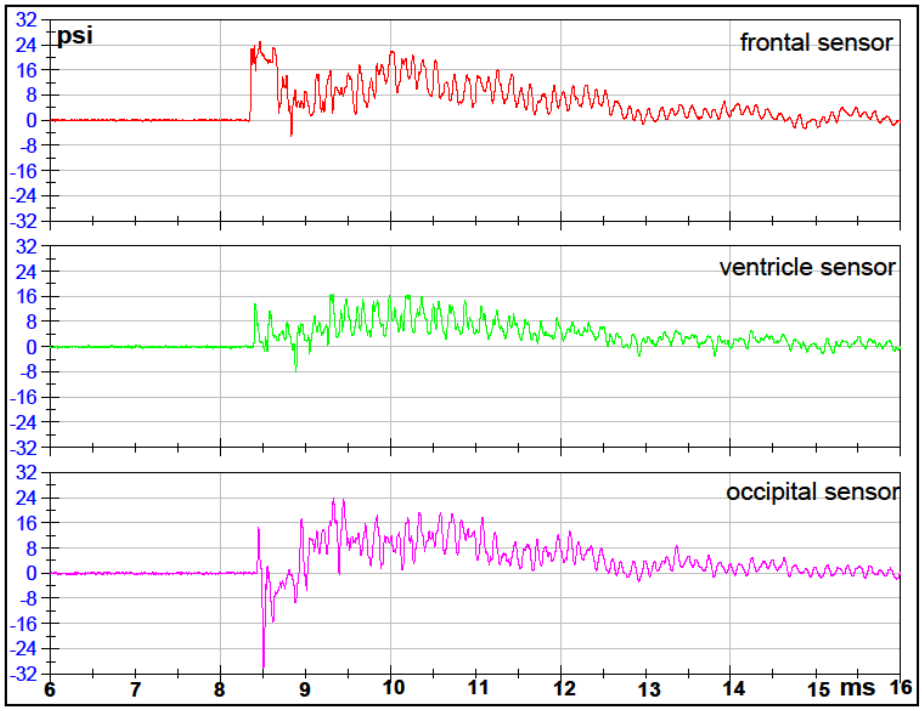

RAW DATA

Test 2 Right Orientation 6mm Sphere with Holes

FILTERED DATA

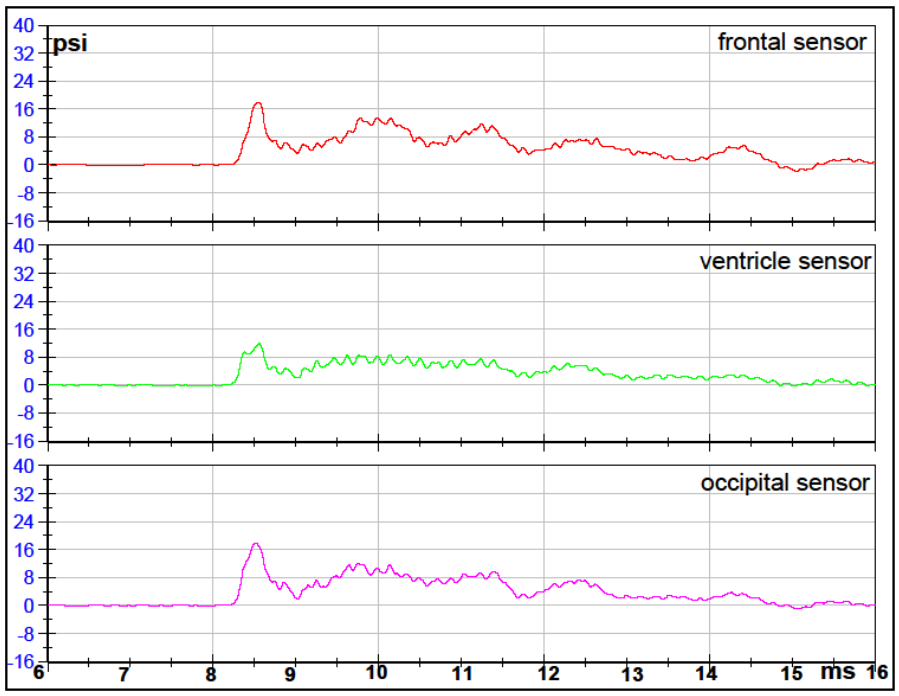

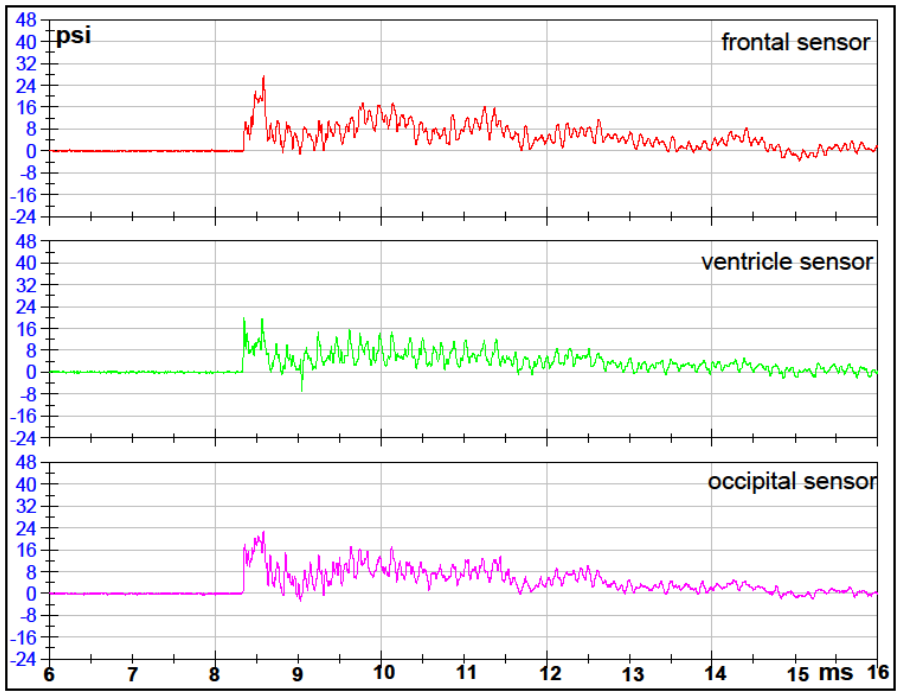

RAW DATA

Test 3 Back Orientation 6mm Sphere with Holes

FILTERED DATA

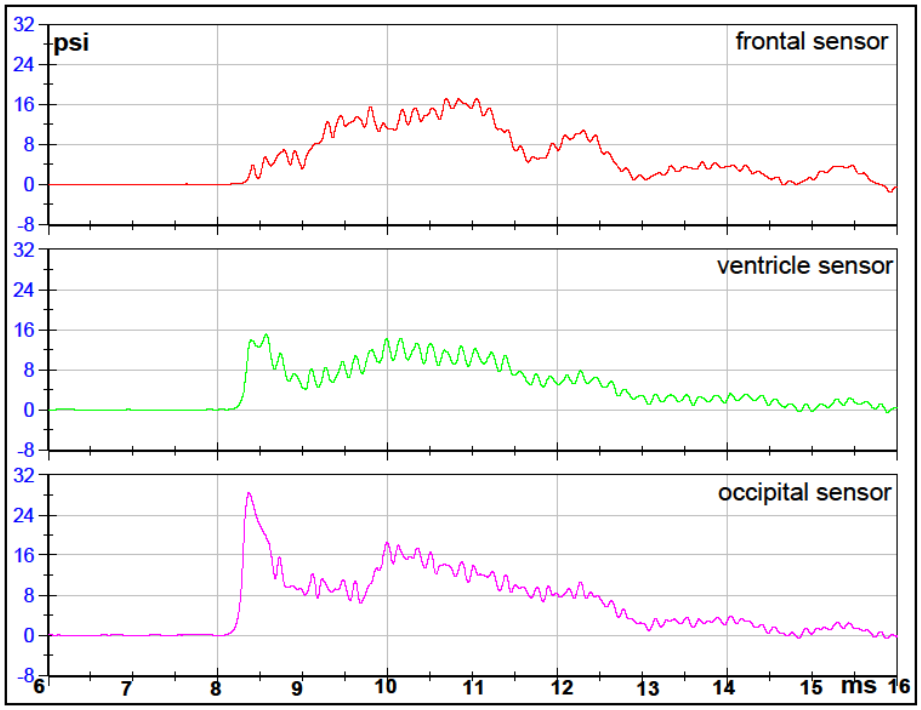

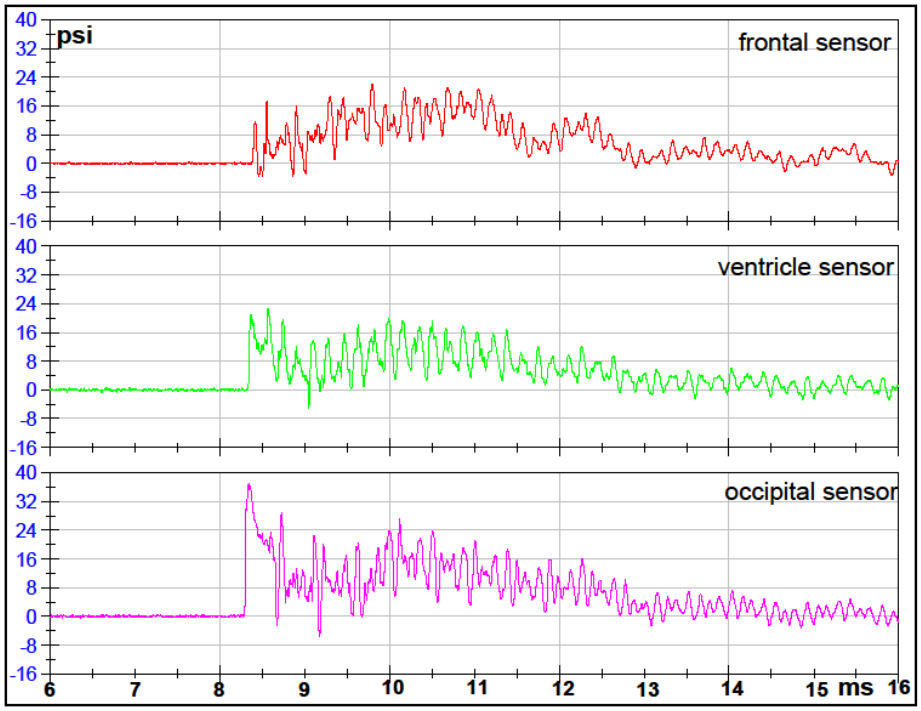

RAW DATA

Test 4 Left Orientation 6mm Sphere with Holes

FILTERED DATA

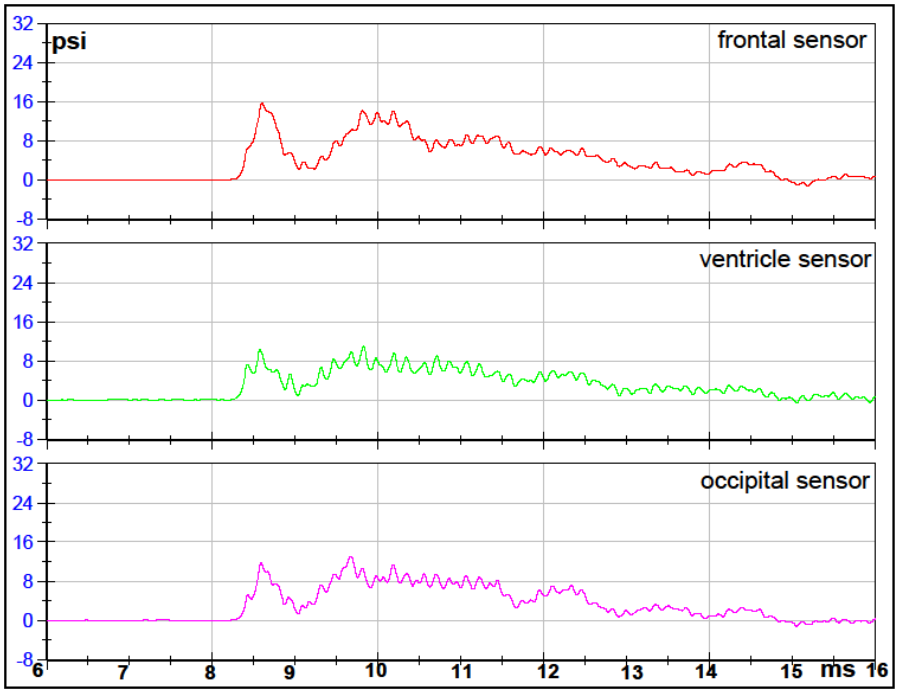

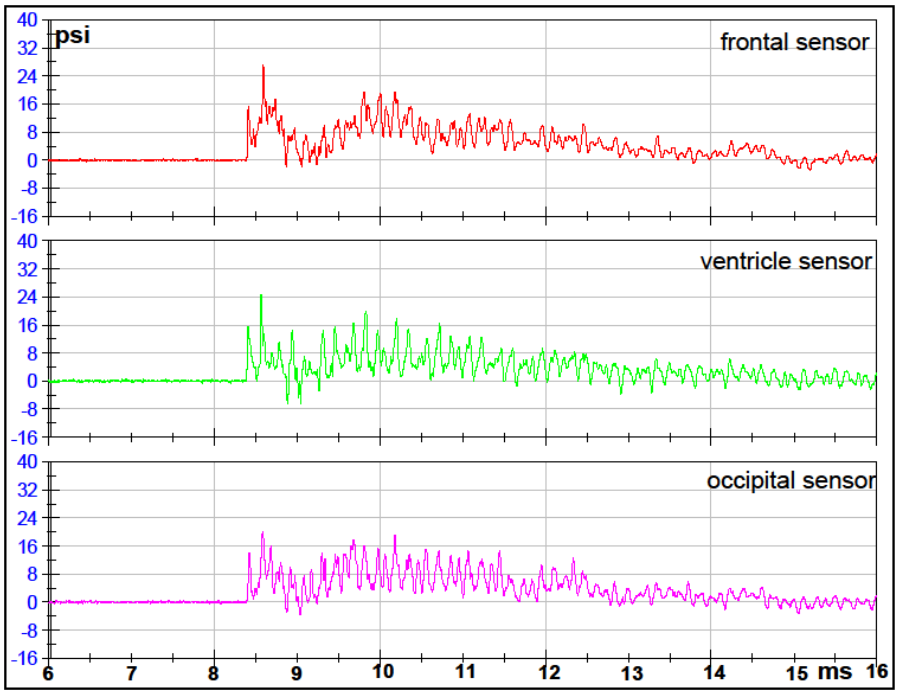

RAW DATA

Test 5 Front 2 Orientation 6mm Sphere with Holes

FILTERED DATA

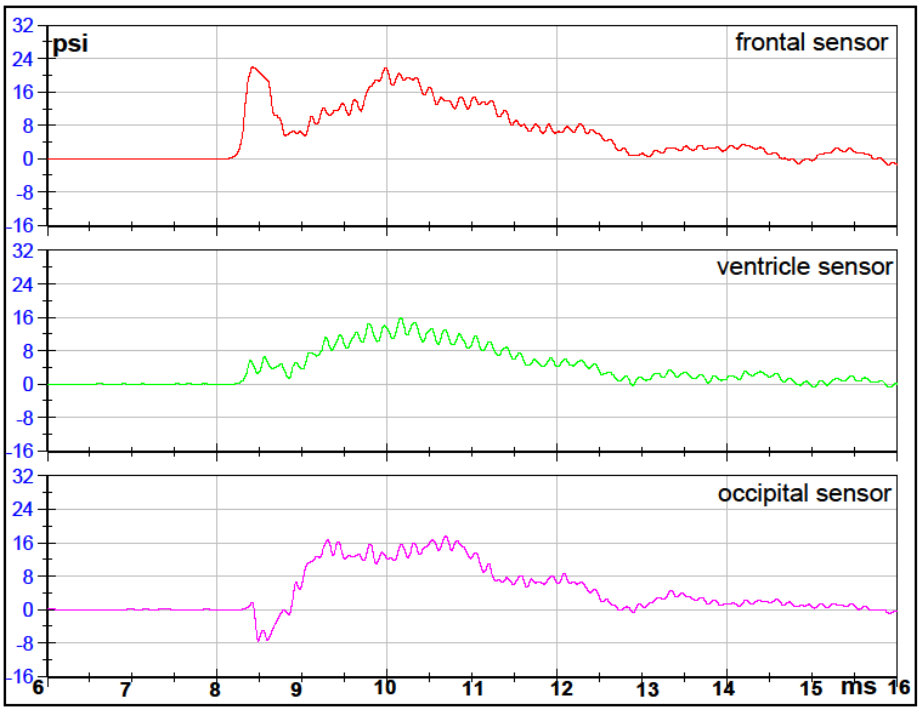

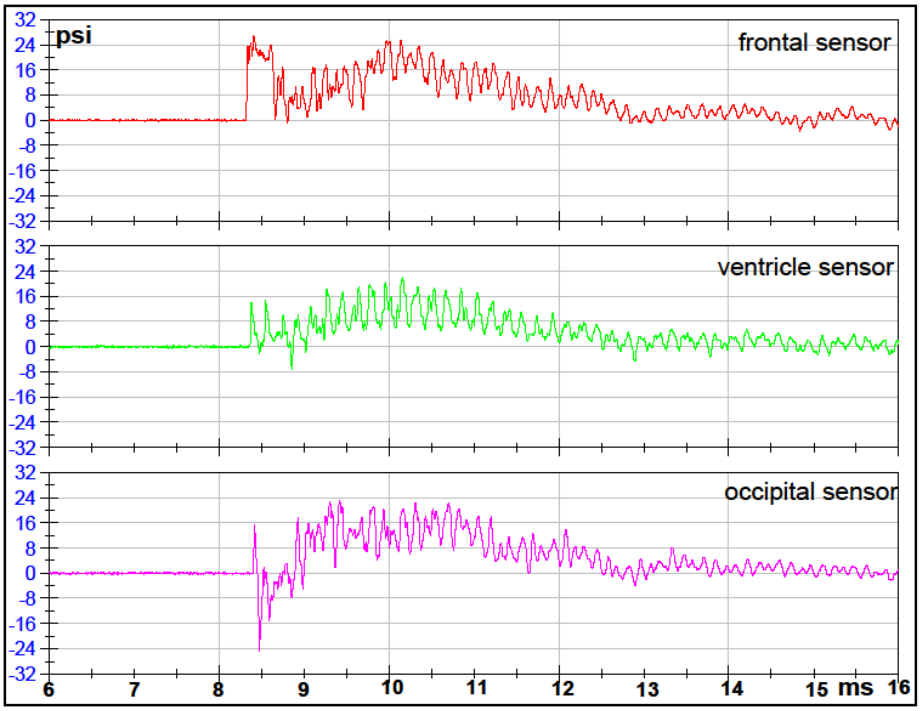

RAW DATA

Test 6 Front 1 Orientation 6mm Sphere with Holes

FILTERED DATA

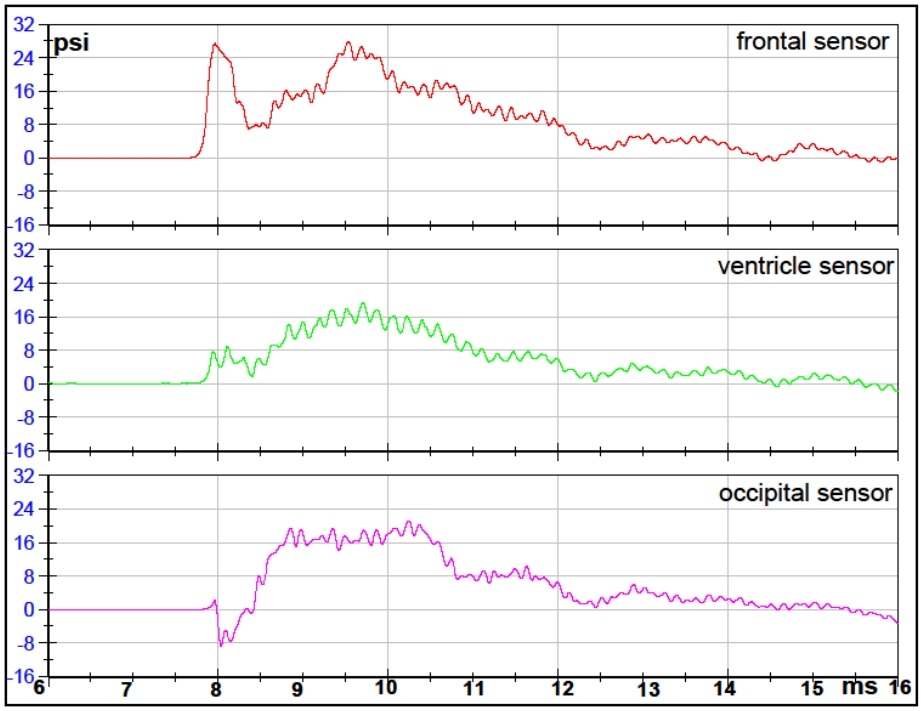

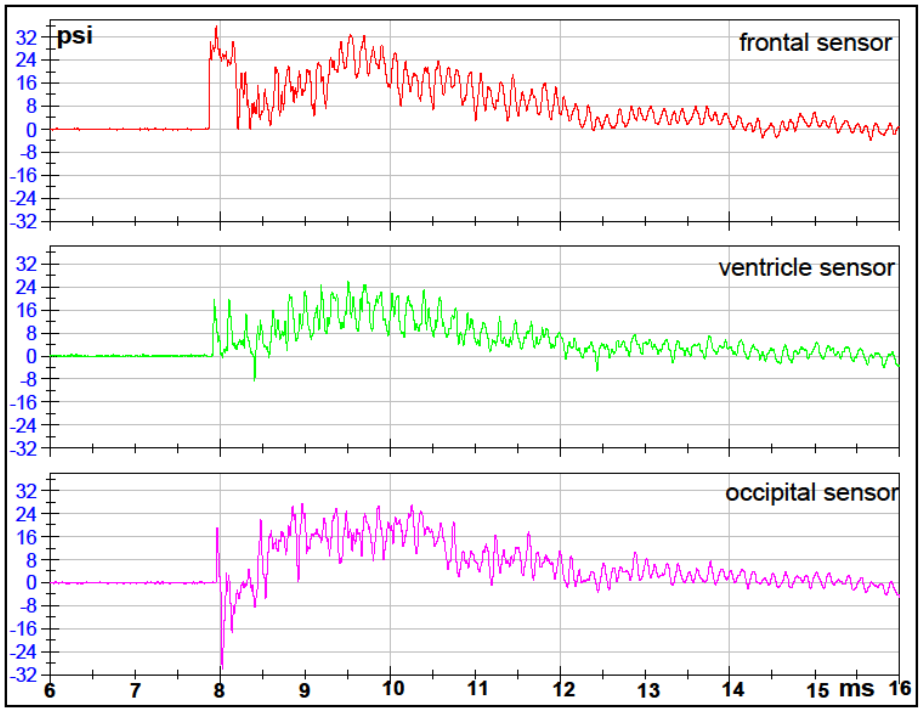

RAW DATA

Test 7 Left Orientation 6mm Sphere with Holes

FILTERED DATA

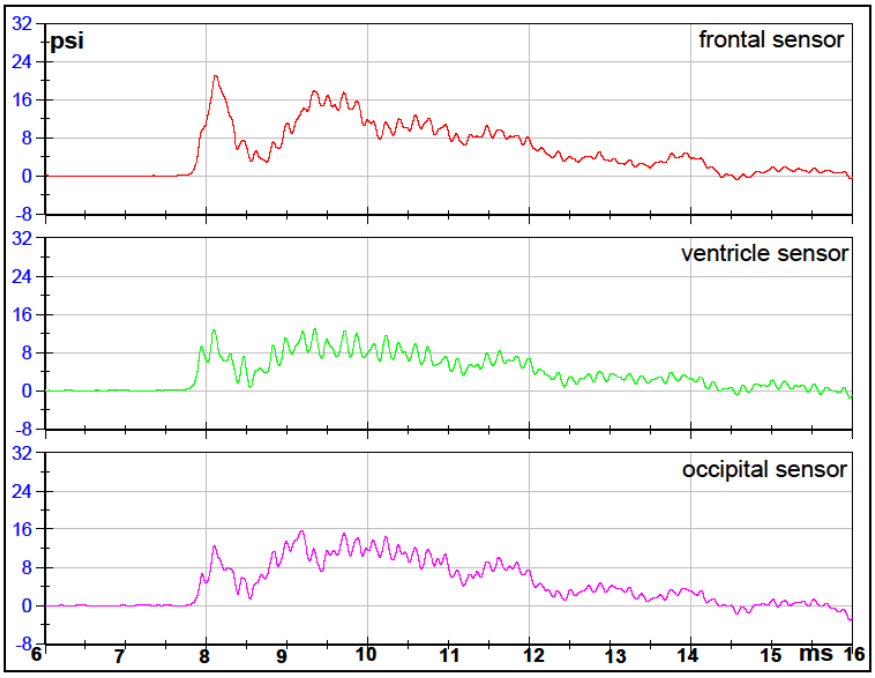

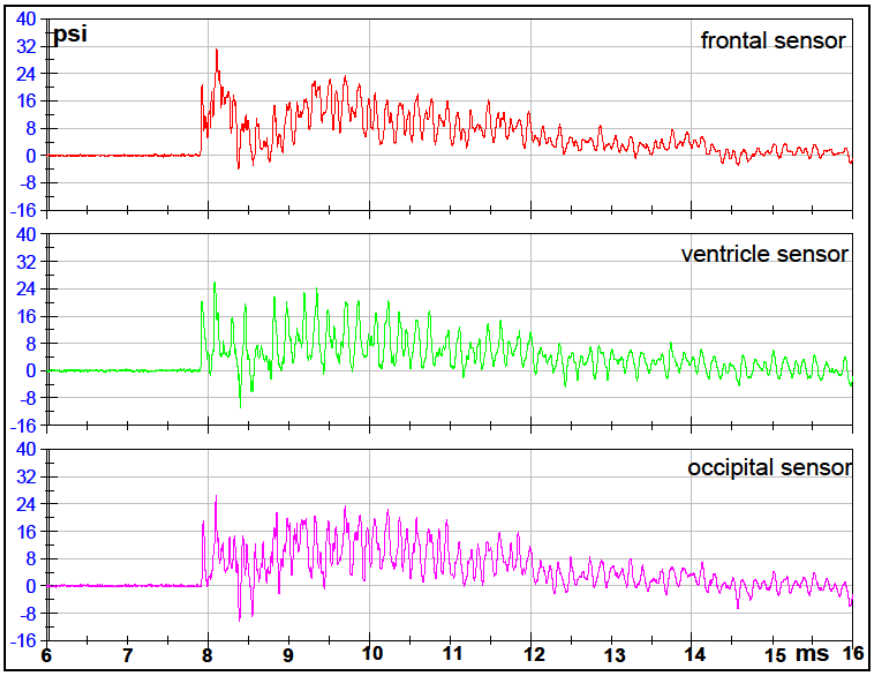

RAW DATA

Test 8 Back Orientation 6mm Sphere with Holes

FILTERED DATA

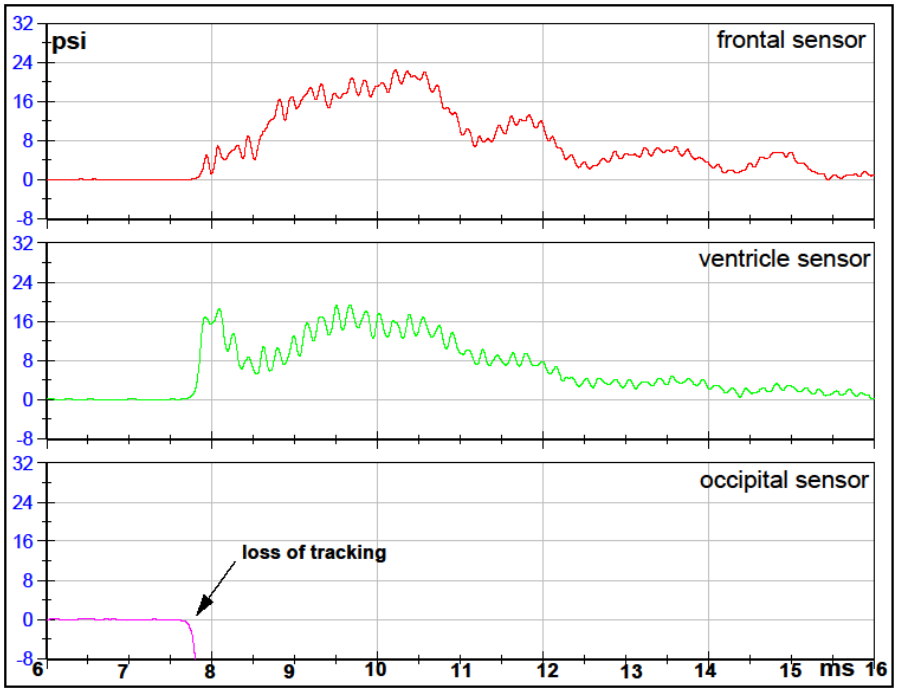

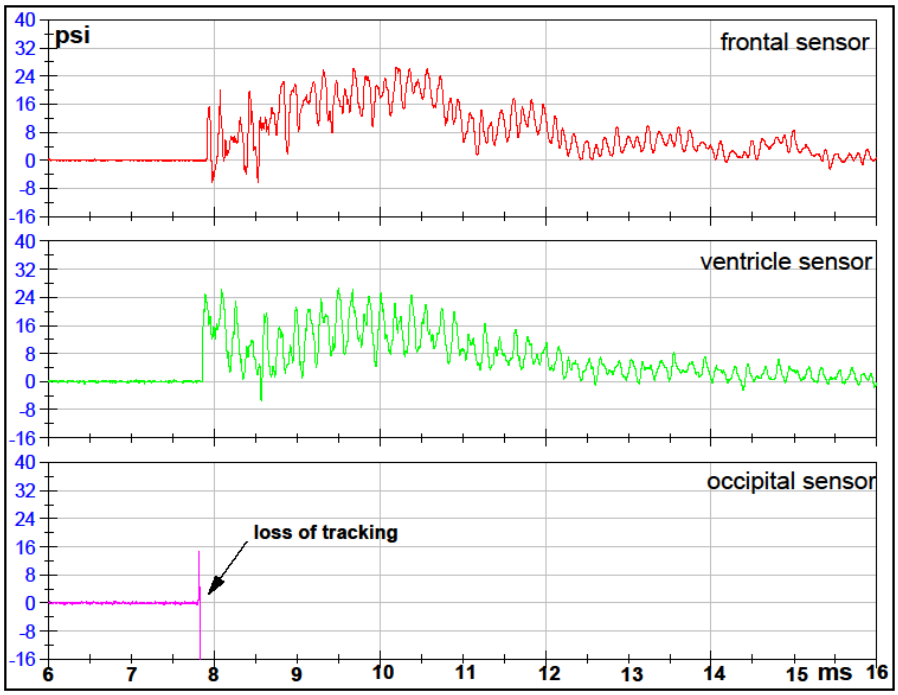

RAW DATA

Test 9 Right Orientation 6mm Sphere with Holes

FILTERED DATA

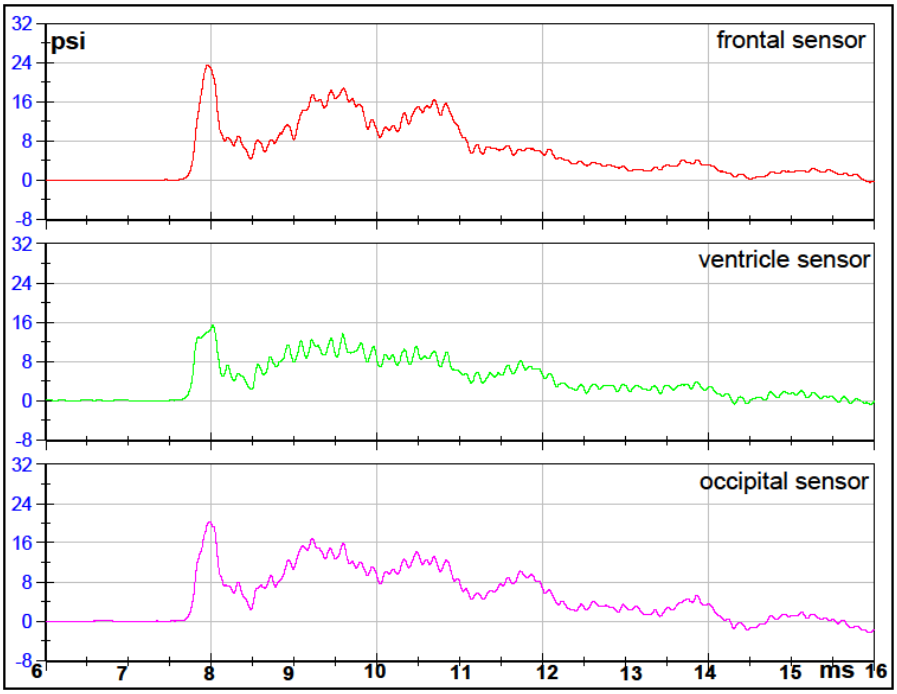

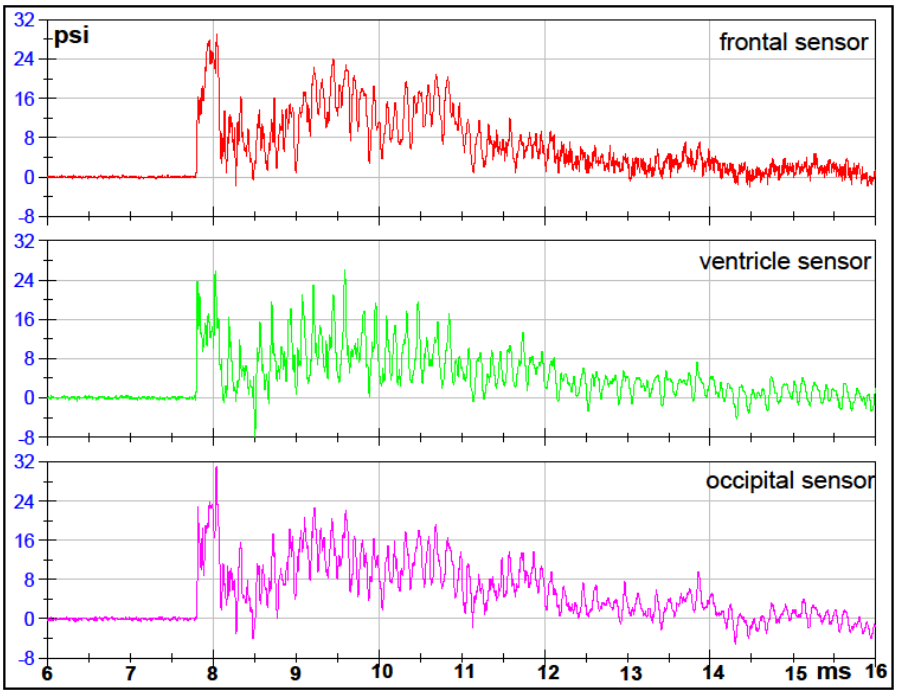

RAW DATA

Test 10 Front 2 Orientation 6mm Sphere with Holes

FILTERED DATA

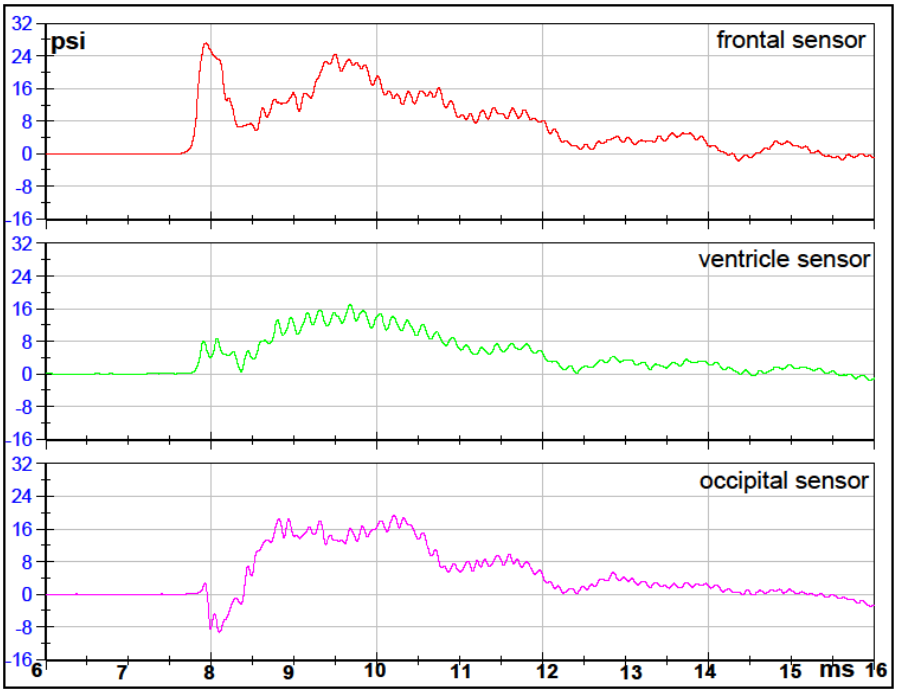

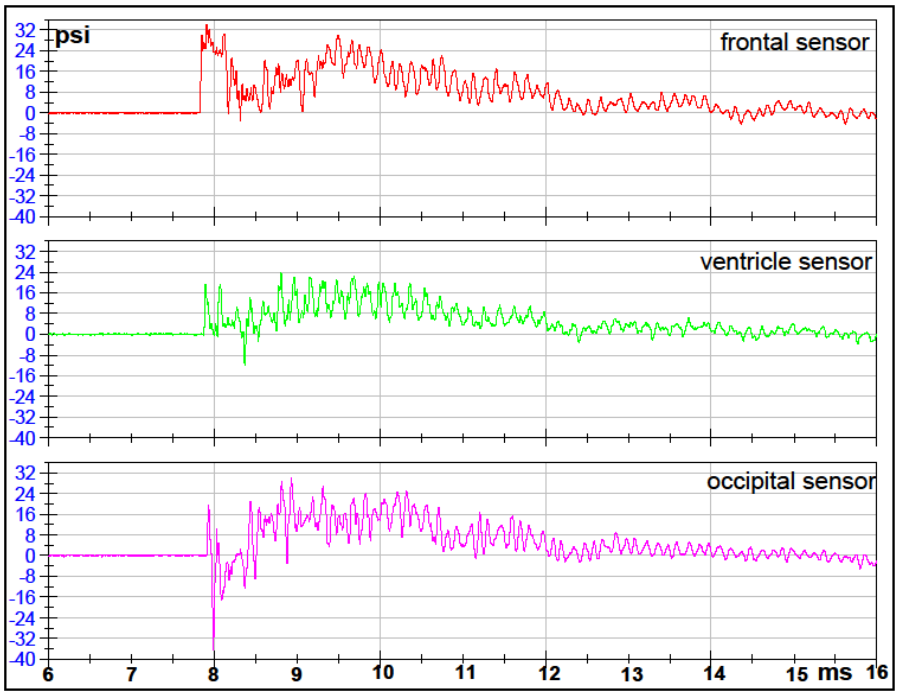

RAW DATA

Test 11 Front 1 Orientation 6mm Sphere with Holes

FILTERED DATA

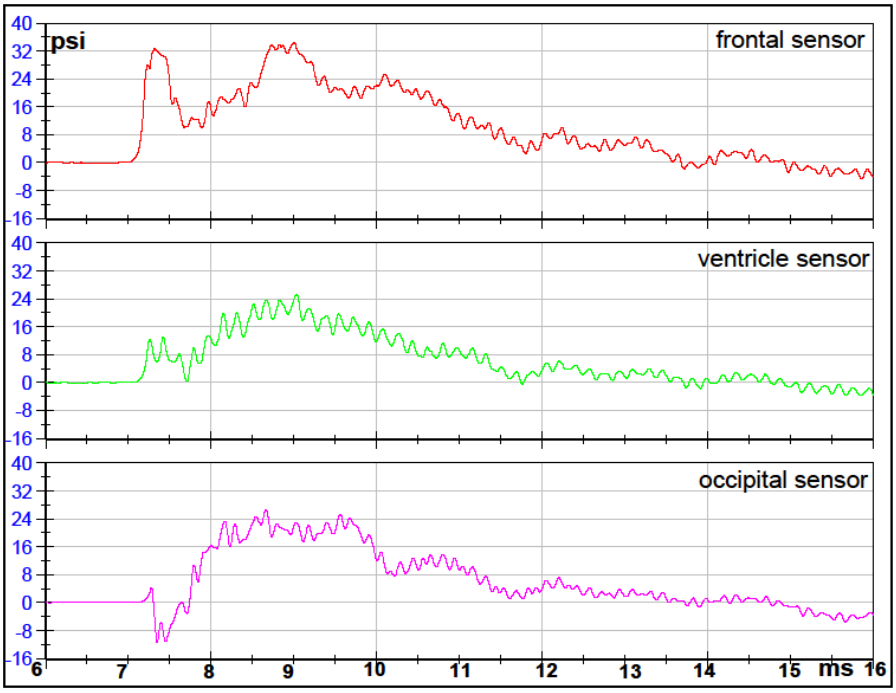

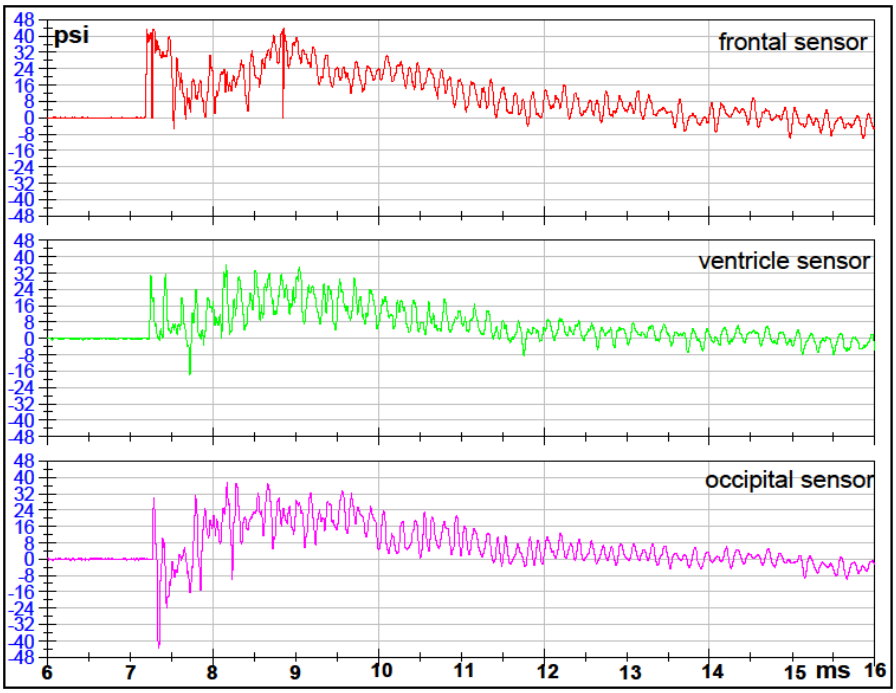

RAW DATA

Test 12 Right Orientation 6mm Sphere with Holes

FILTERED DATA

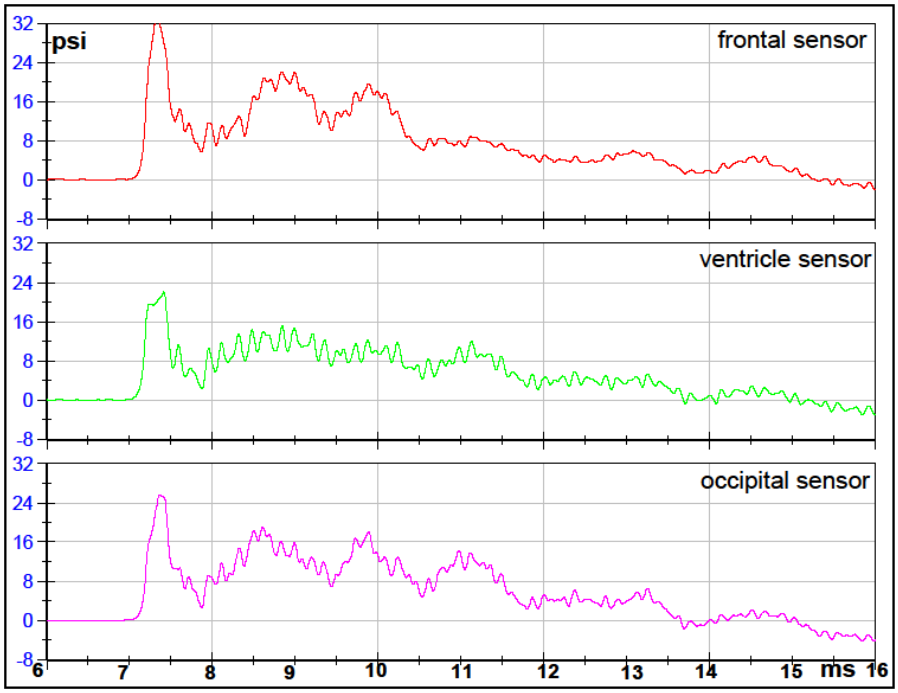

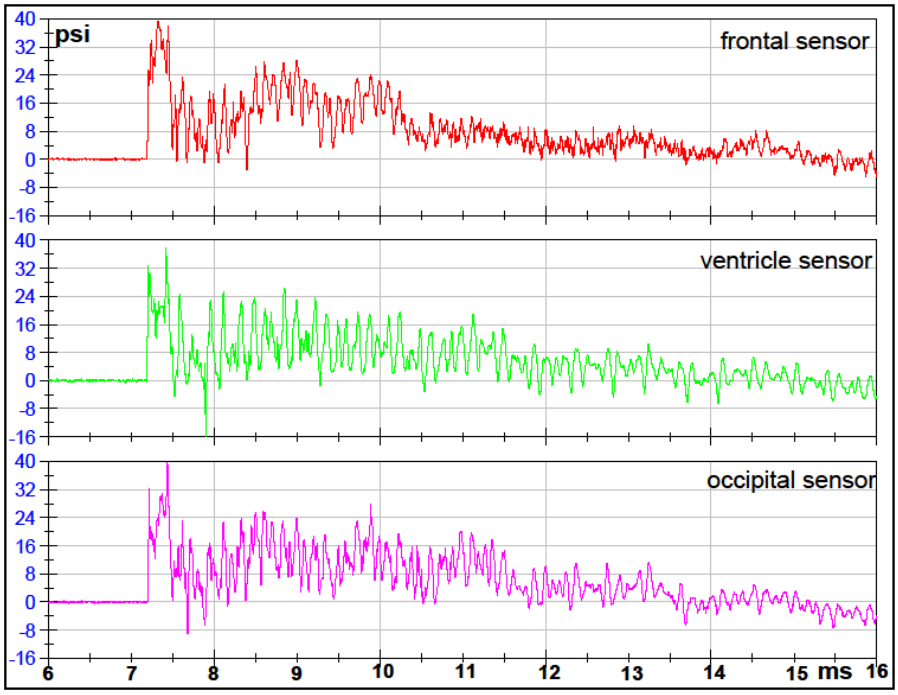

RAW DATA

Test 13 Back Orientation 6mm Sphere with Holes

FILTERED DATA

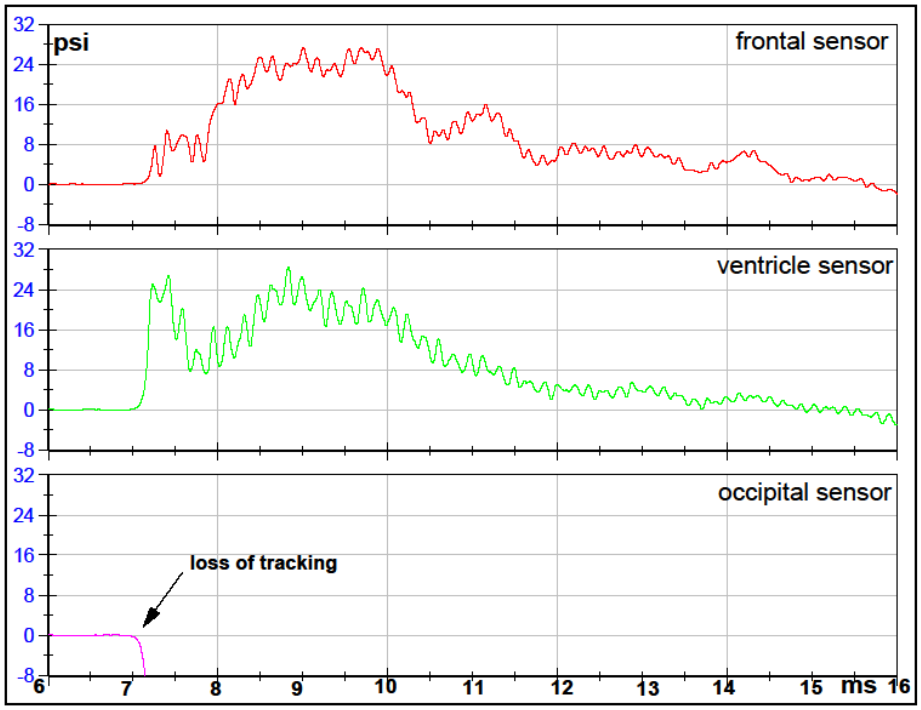

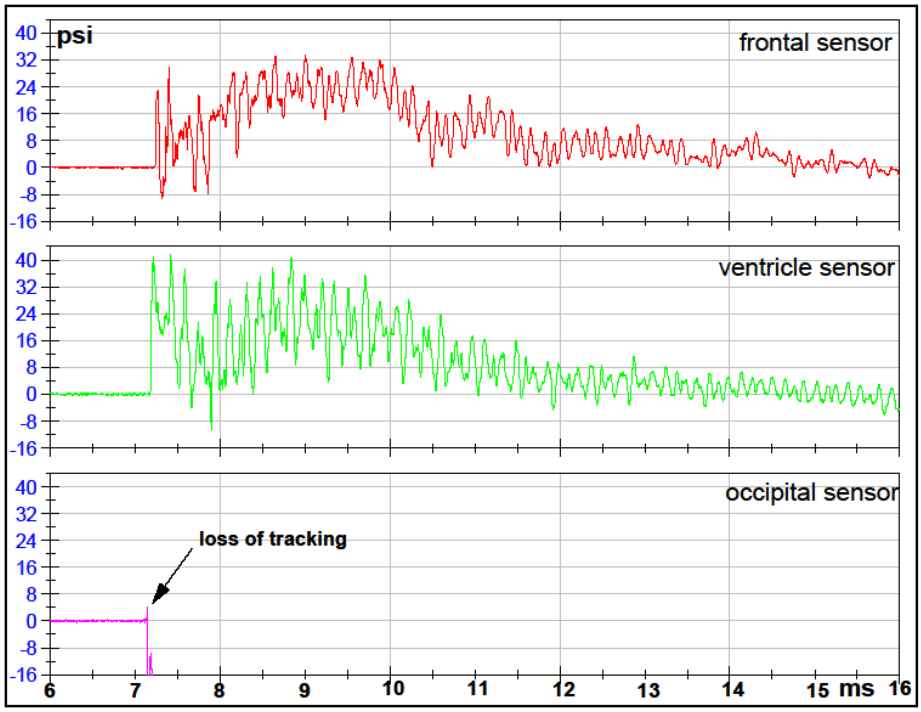

RAW DATA

Test 14 Left Orientation 6mm Sphere with Holes

FILTERED DATA

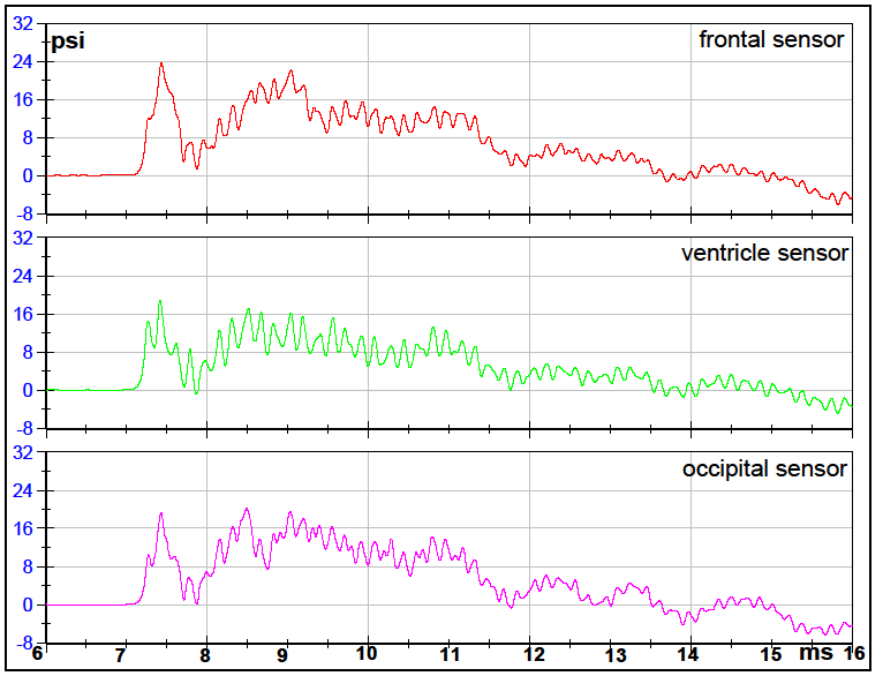

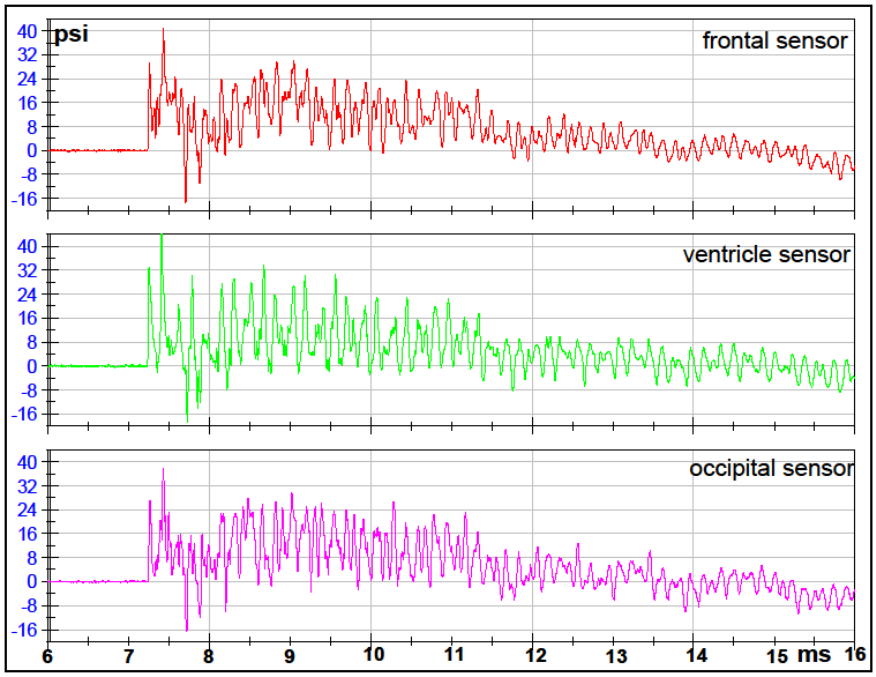

RAW DATA

Test 15 Front 2 Orientation 6mm Sphere with Holes

FILTERED DATA

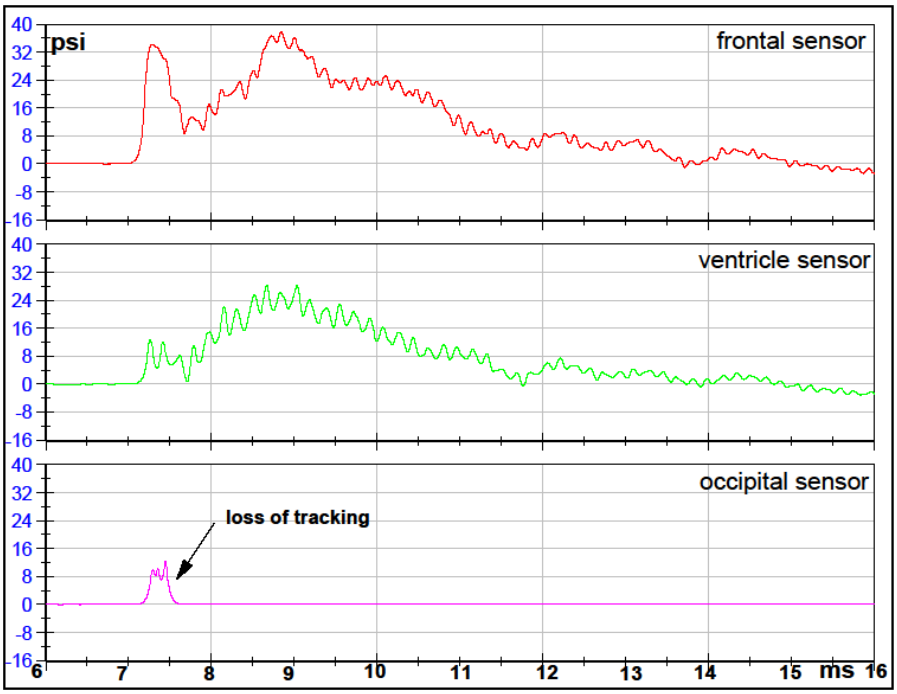

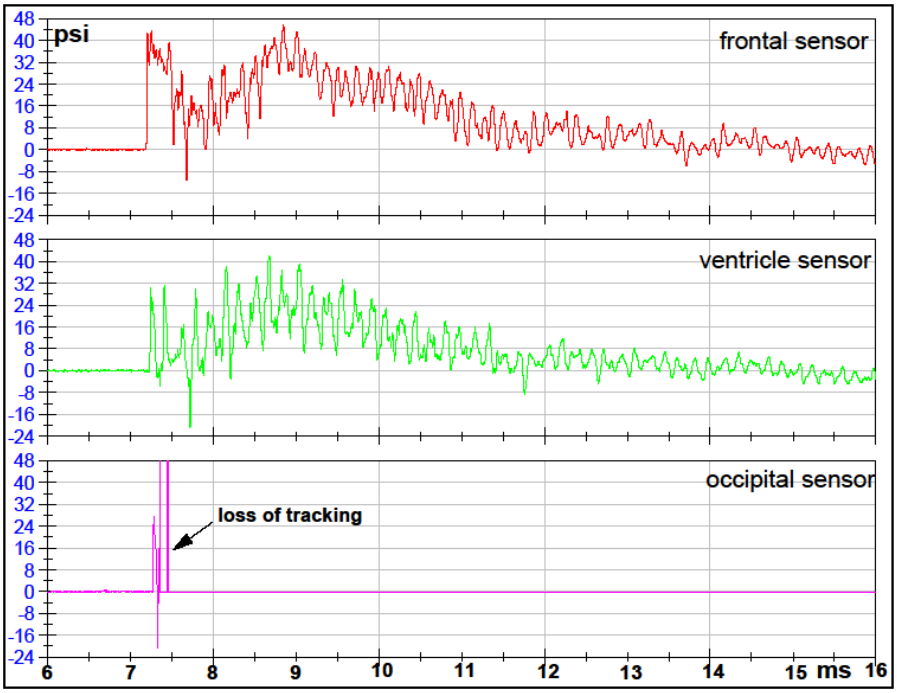

RAW DATA

Comparison for reproducibility of each pressure sensor in Front Orientation at 10psi 6mm Sphere with Holes

VENTRICLE FILTERED DATA

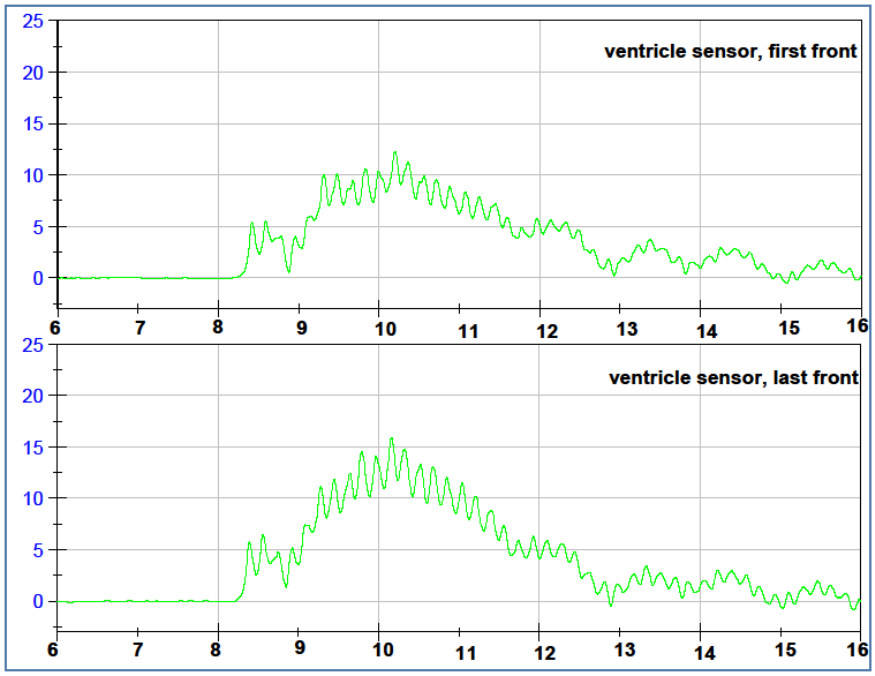

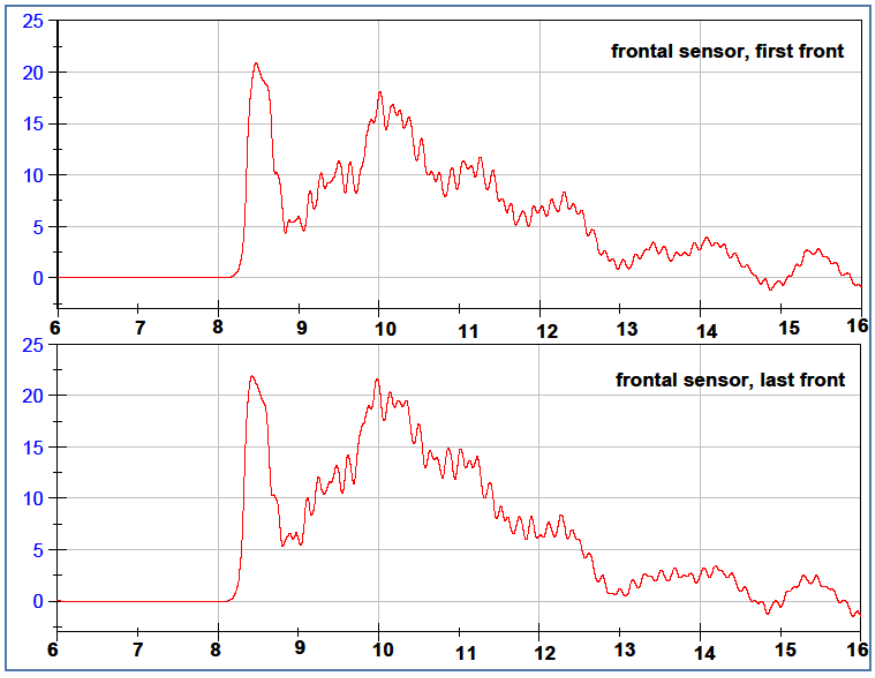

FRONTAL FILTERED DATA

Comparison for reproducibility of each pressure sensor in Front Orientation at 10psi 6mm Sphere with Holes

OCCIPITAL FILTERED DATA

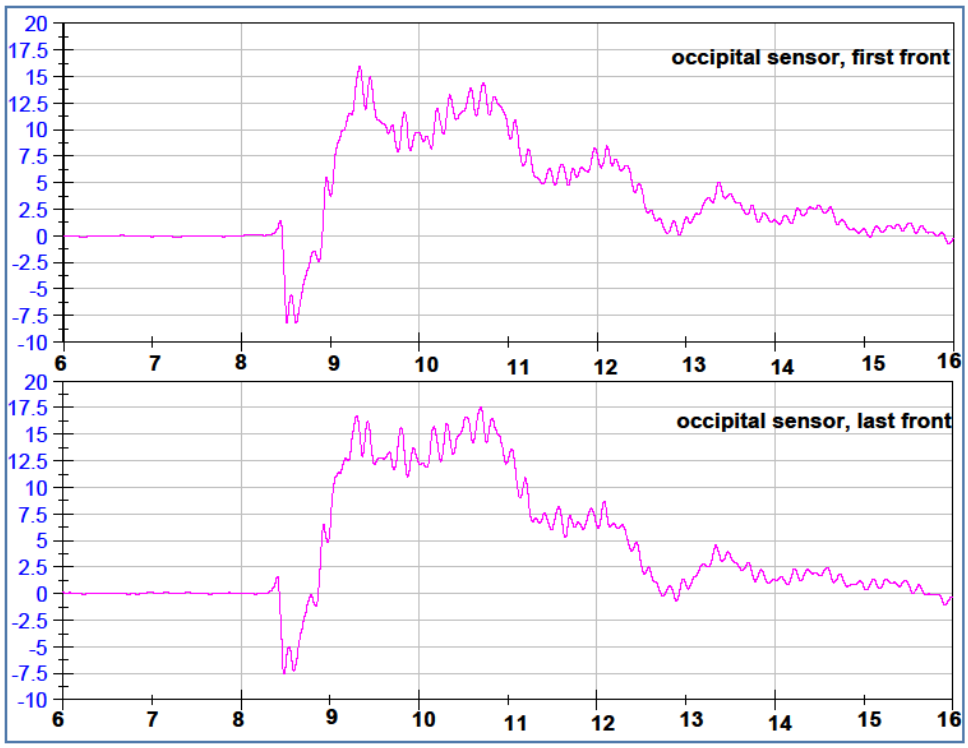

Comparison for reproducibility of each pressure sensor in Front Orientation at 12psi 6mm Sphere with Holes

VENTRICLE FILTERED DATA

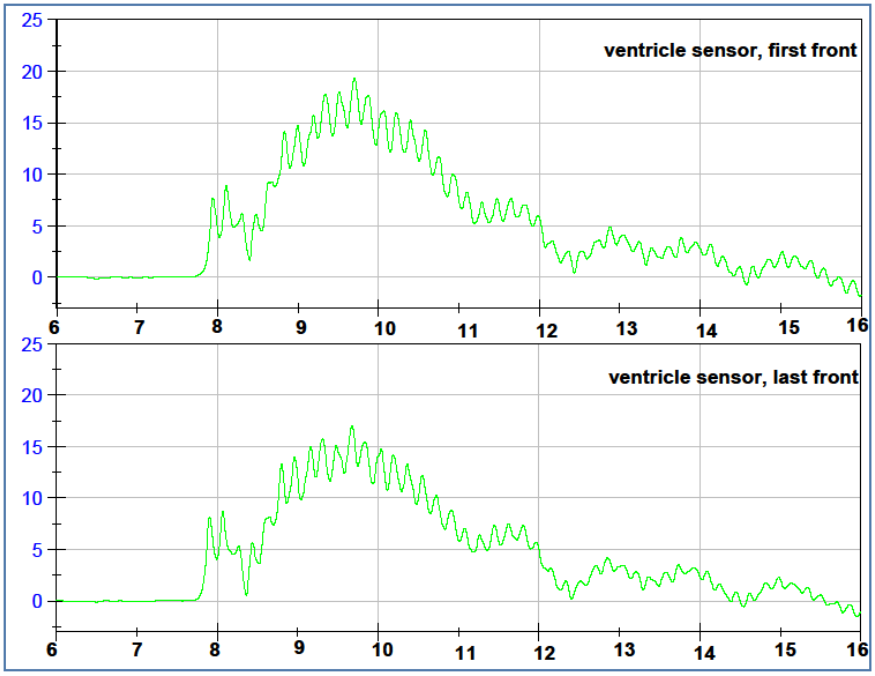

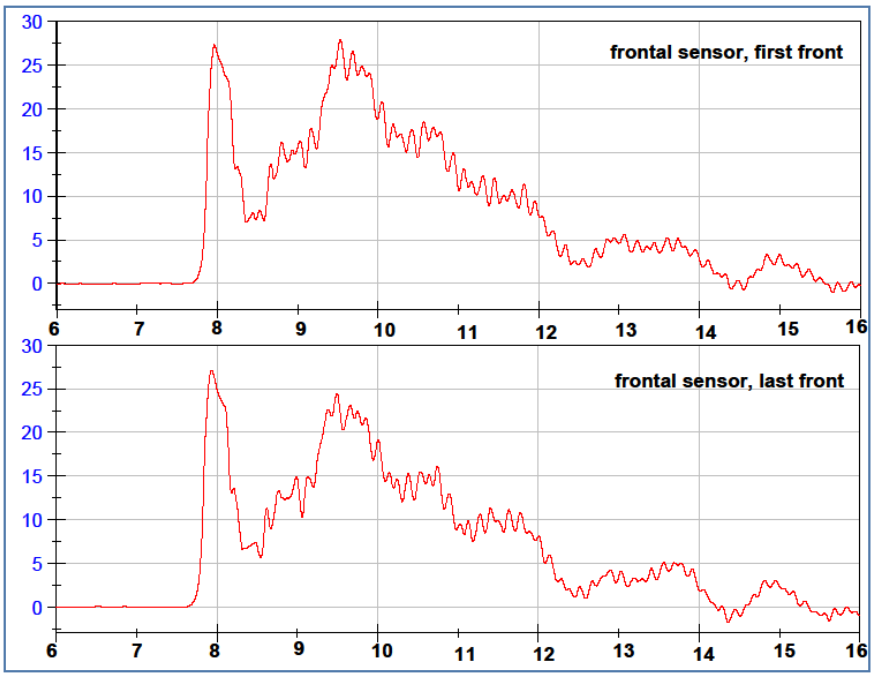

FRONTAL FILTERED DATA

Comparison for reproducibility of each pressure sensor in Front Orientation at 12psi 6mm Sphere with Holes

OCCIPITAL FILTERED DATA

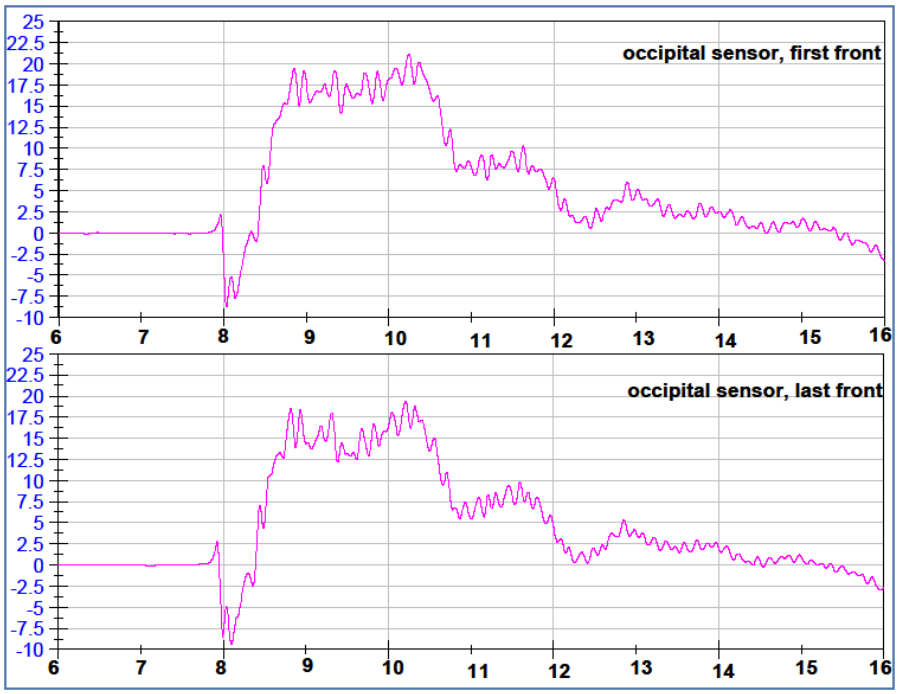

Comparison for reproducibility of each pressure sensor in Front Orientation at 15psi 6mm Sphere with Holes

VENTRICLE FILTERED DATA

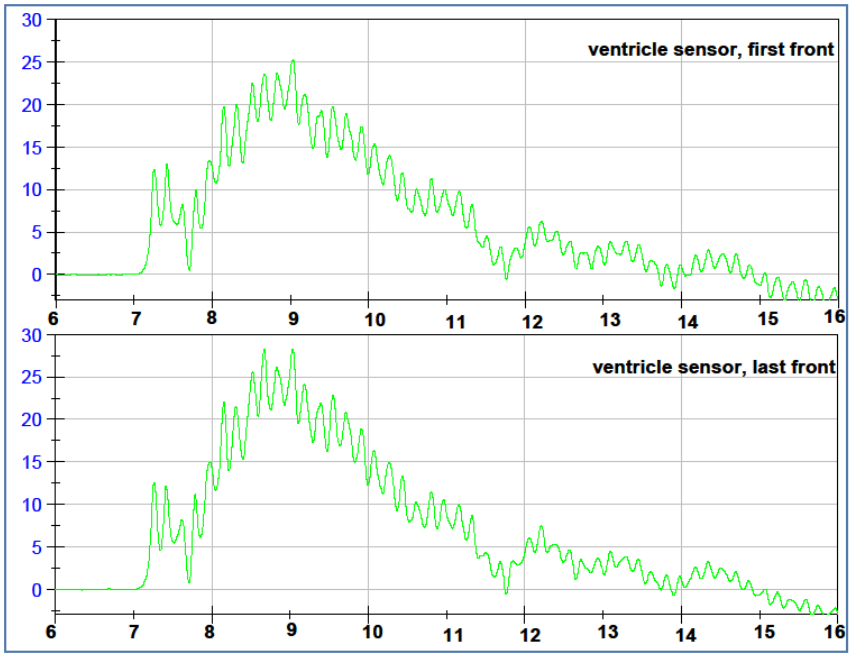

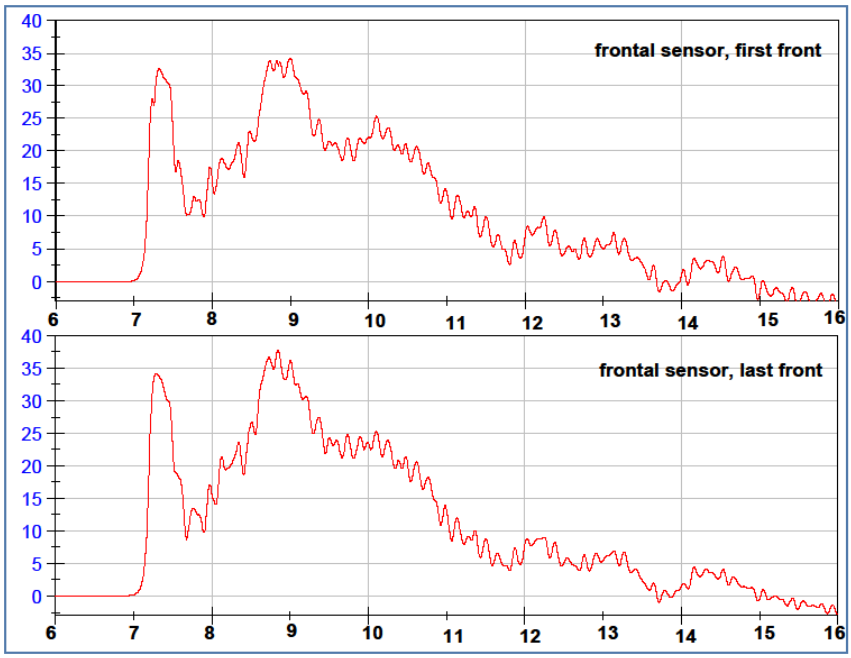

FRONTAL FILTERED DATA

Comparison for reproducibility of each pressure sensor in Front Orientation at 15psi 6mm Sphere with Holes

OCCIPITAL FILTERED DATA

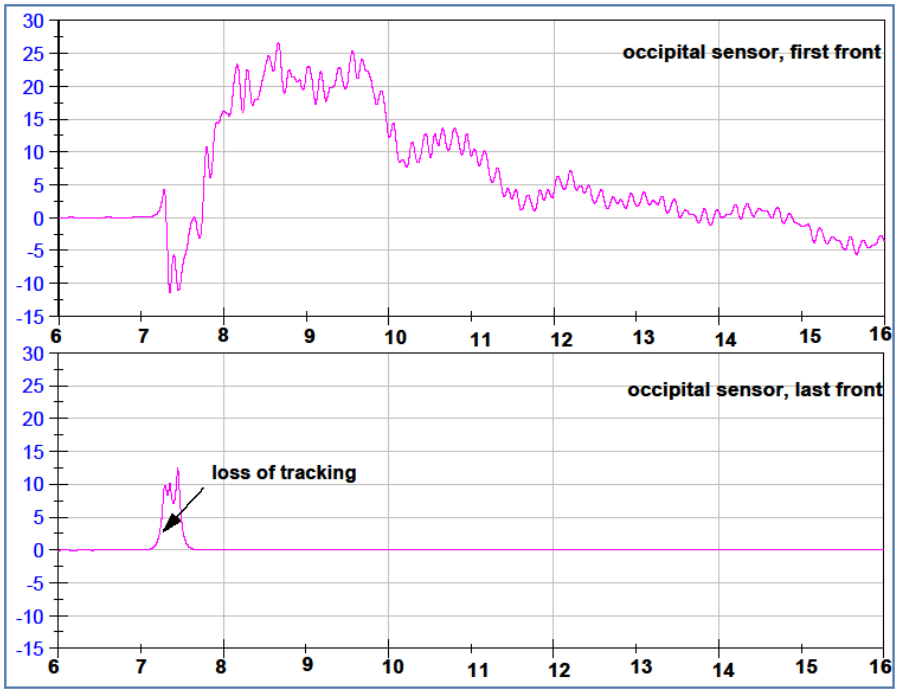

Frontal Sensor, 4 Orientations, Filtered Data, 6mm Sphere with Holes

10 PSI

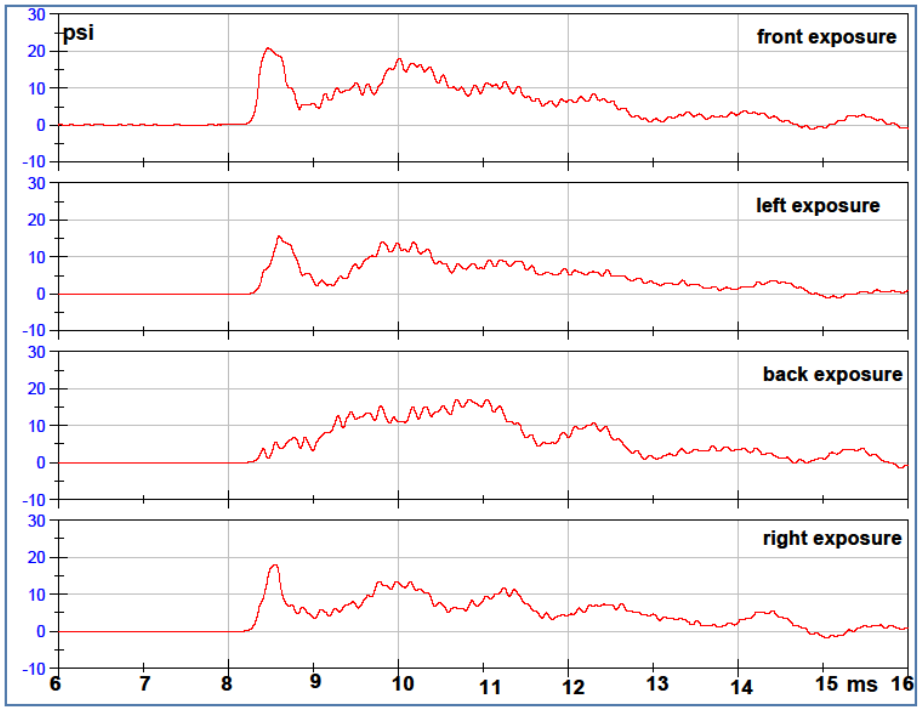

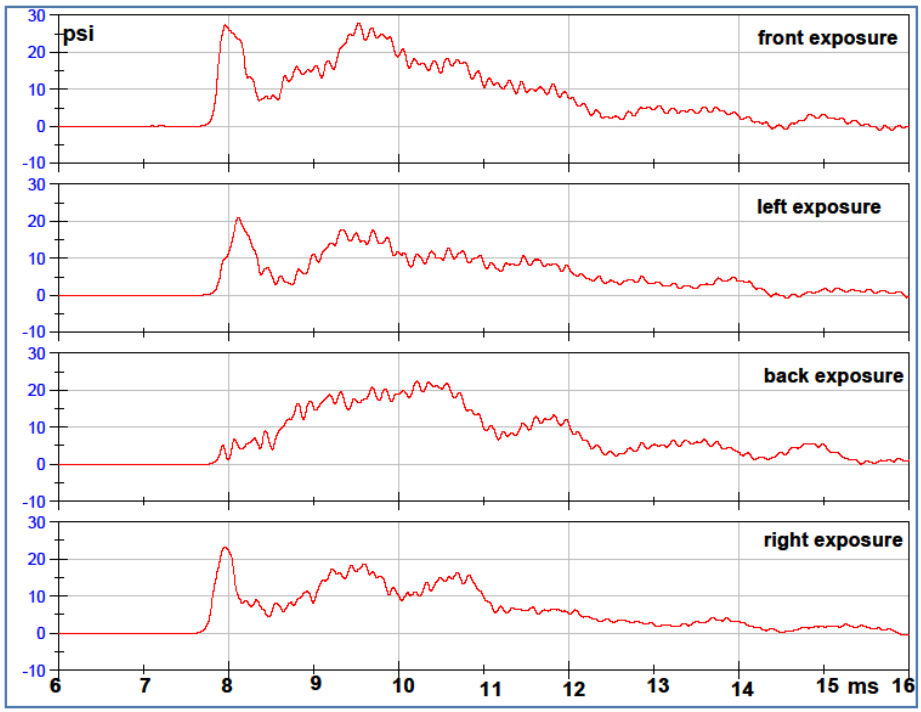

12 PSI

Frontal Sensor, 4 Orientations, Filtered Data, 6mm Sphere with Holes

15 PSI

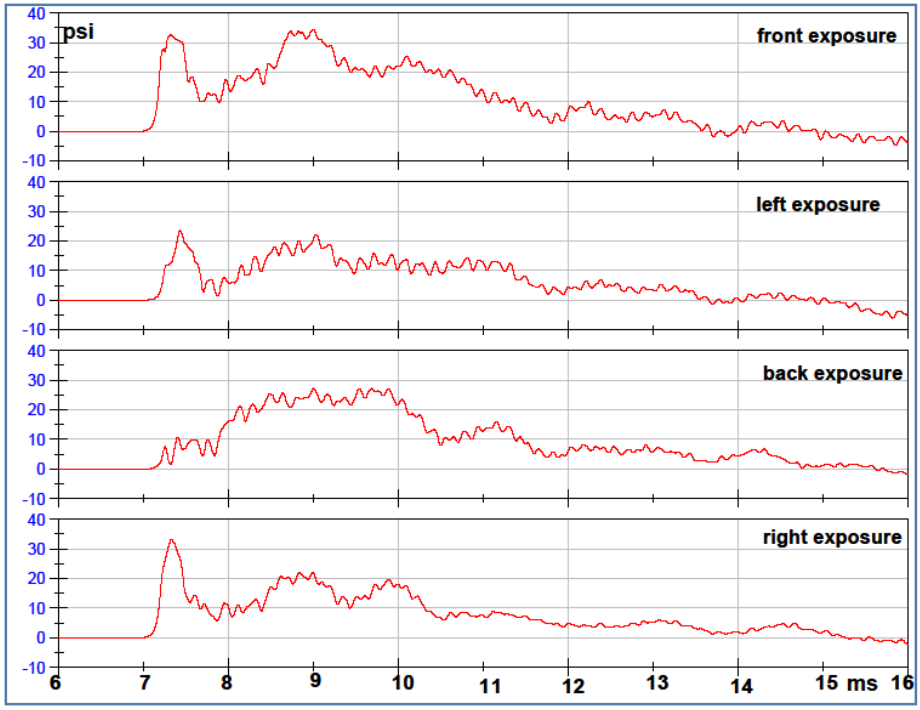

Ventricle Sensor, 4 Orientations, Filtered Data, 6mm Sphere with Holes

10 PSI

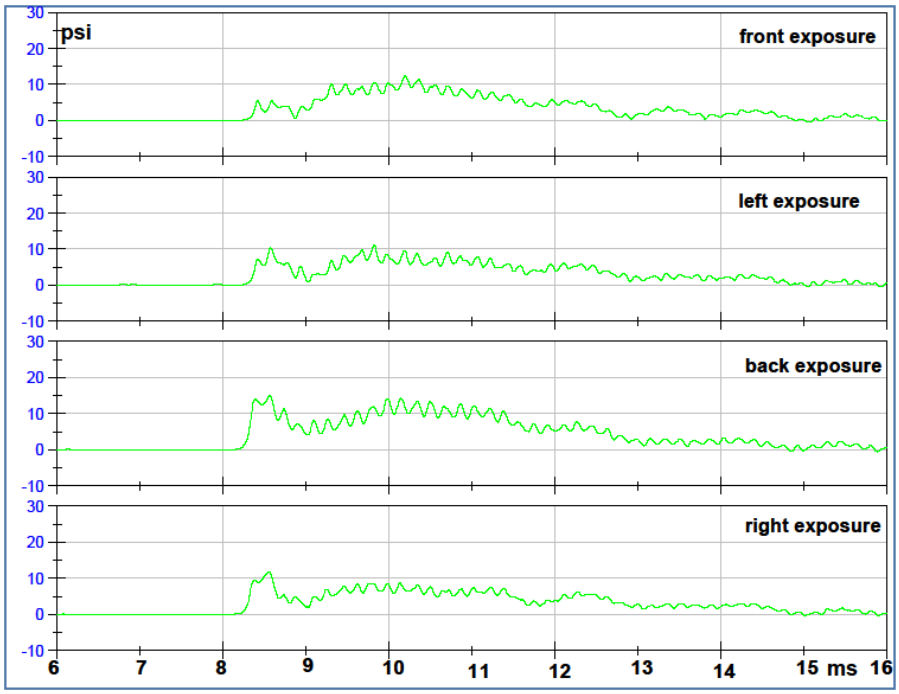

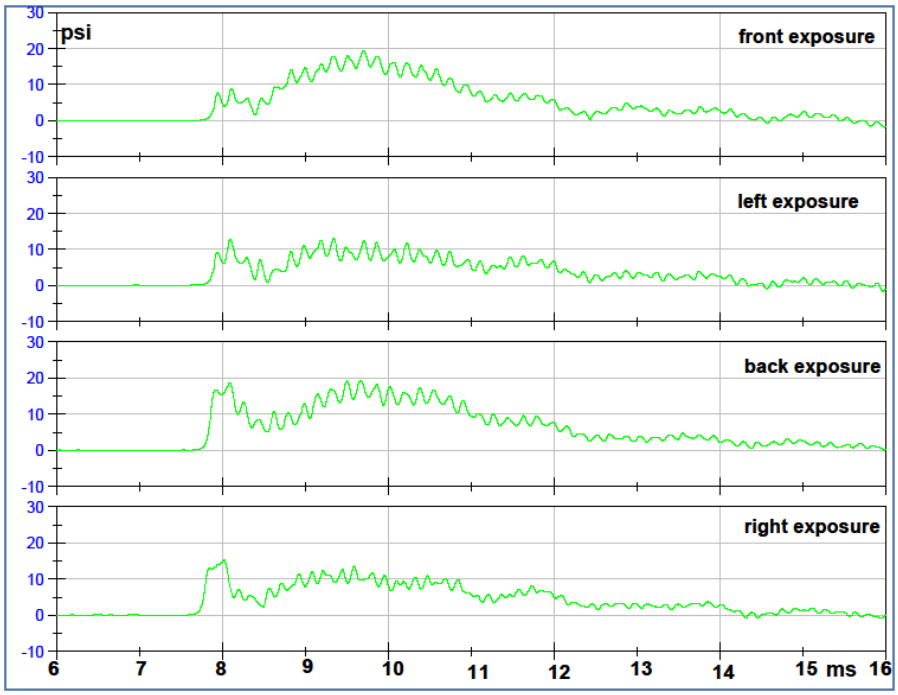

12 PSI

Ventricle Sensor, 4 Orientations, Filtered Data, 6mm Sphere with Holes

15 PSI

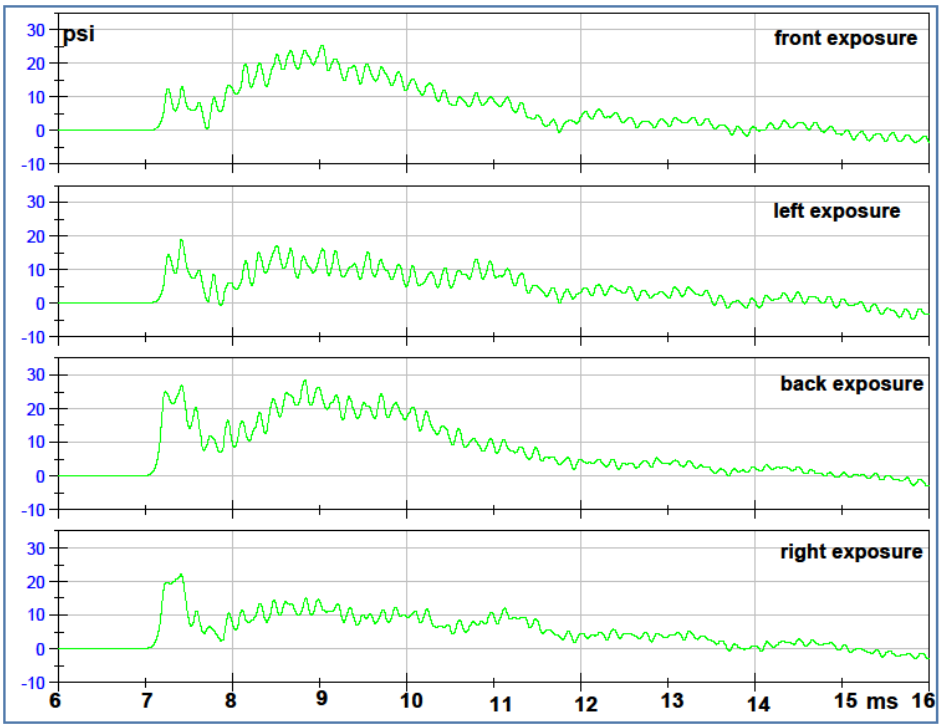

Occipital Sensor, 4 Orientations, Filtered Data, 6mm Sphere with Holes

10 PSI

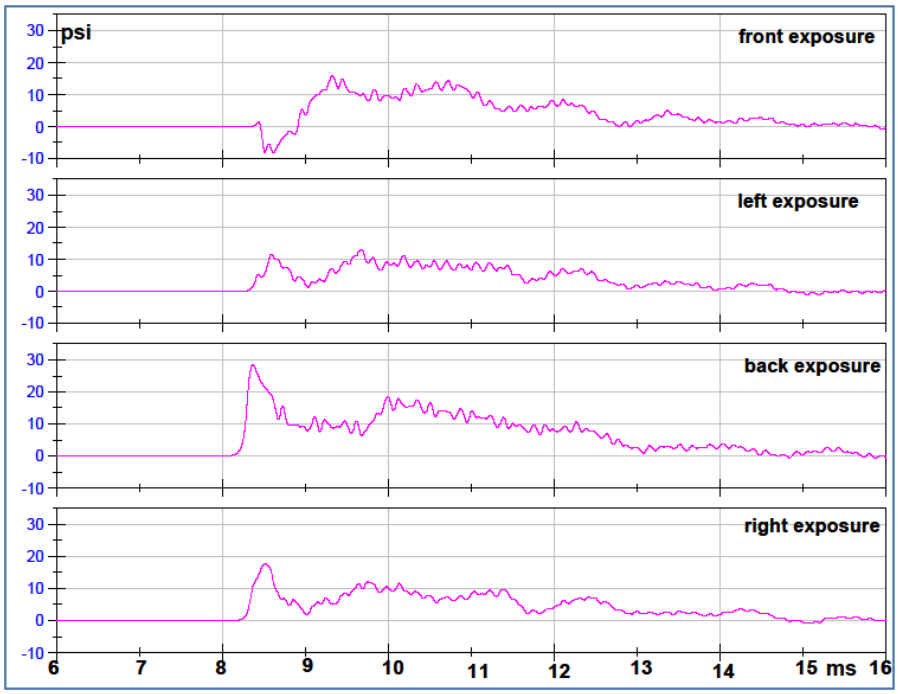

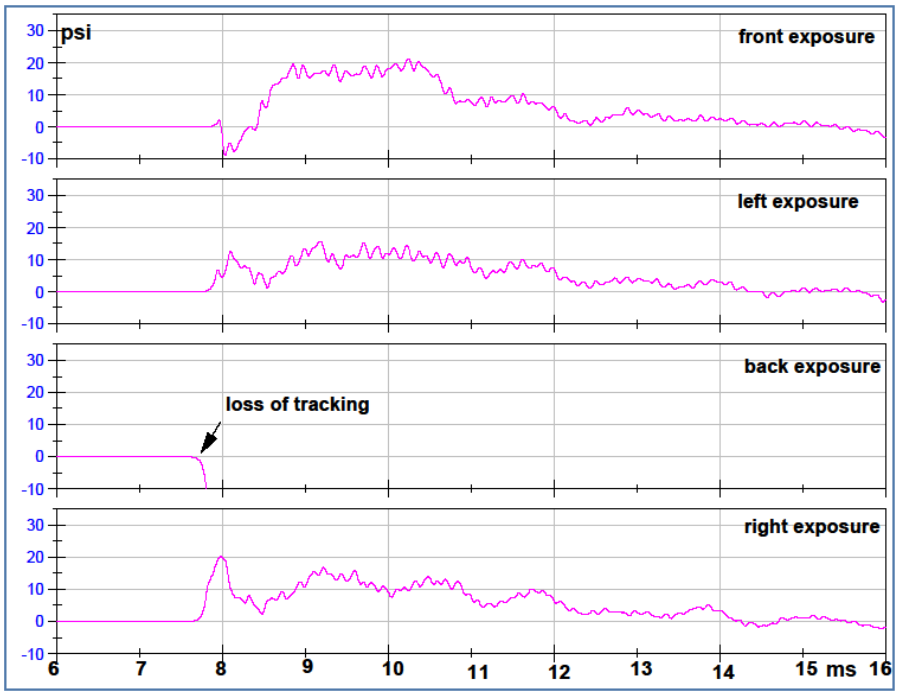

12 PSI

Occipital Sensor, 4 Orientations, Filtered Data, 6mm Sphere with Holes

15 PSI

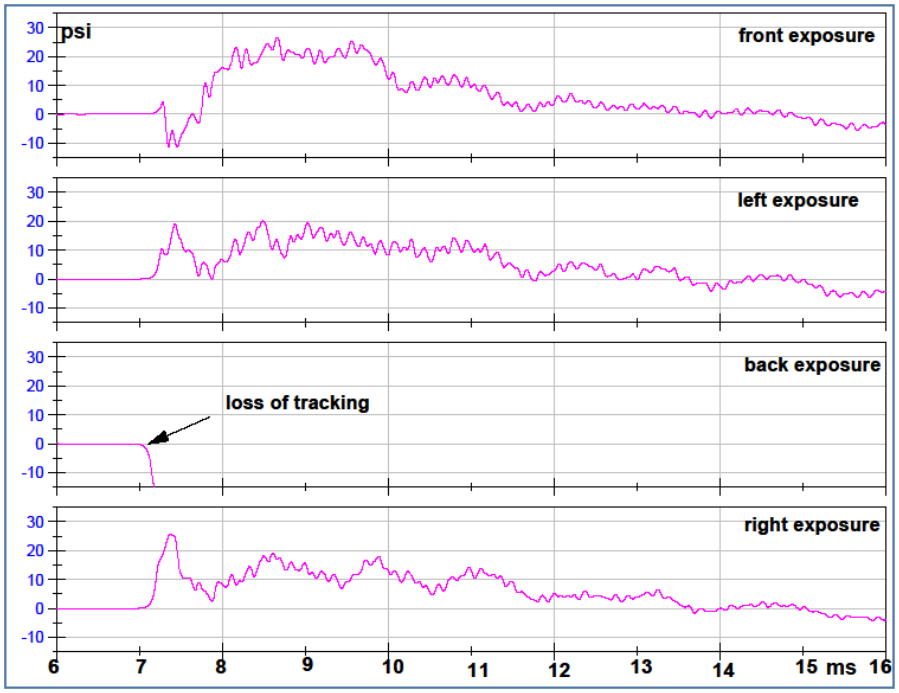

Pressure Extremes for 6mm sphere with holes

Pressure Extremes for 6mm Sphere with Holes										
	Maximun Pressure					Minimum Pressure				
ventricle	front 1	right	back	left	front 2	front 1	right	back	left	front 2
10 psi air	**12.3**	**11.8**	**15.1**	**10.3**	**15.9**	**0.10**	**0.16**	**0.17**	**0.16**	**-0.43**
12 psi air	**19.3**	**15.4**	**18.6**	**12.8**	**17.0**	**0.15**	**0.19**	**0.18**	**0.17**	**0.17**
15 psi air	**25.3**	**22.1**	**24.9**	**18.8**	**28.3**	**-0.59**	**0.69**	**0.16**	**-0.70**	**-0.59**
frontal	front 1	right	back	left	front 2	front 1	right	back	left	front 2
10 psi air	**20.9**	**17.9**	**17.1**	**15.8**	**21.9**	**0.16**	**0.18**	**0.20**	**0.15**	**0.18**
12 psi air	**27.9**	**23.3**	**22.4**	**21.1**	**27.1**	**0.16**	**0.19**	**0.18**	**0.16**	**0.20**
15 psi air	**34.3**	**33.1**	**27.2**	**23.7**	**37.8**	**0.17**	**0.17**	**0.20**	**0.20**	**0.16**
occipital	front 1	right	back	left	front 2	front 1	right	back	left	front 2
10 psi air	**16.0**	**17.8**	**28.5**	**13.0**	**17.5**	**-8.06**	**0.17**	**0.21**	**0.16**	**-7.54**
12 psi air	**21.1**	**20.3**	**NA**	**15.7**	**19.3**	**-8.77**	**0.20**	**NA**	**0.12**	**-9.34**
15 psi air	**26.6**	**25.6**	**NA**	**20.2**	**NA**	**-11.07**	**0.16**	**NA**	**0.17**	**NA**

1st rate of change of pressure for 6mm-thick sphere with holes.

1st rate (psi/ms)					
ventricle	front 1	right	back	left	front 2
10 psi air	**31.4**	**48.2**	**64.7**	**43.1**	**39.5**
12 psi air	**40.5**	**66.7**	**75.5**	**39.7**	**48.4**
15 psi air	**73.6**	**88.0**	**116.6**	**77.4**	**67.4**
frontal	front 1	right	back	left	front 2
10 psi air	**73.1**	**53.4**	**27.7**	**48.9**	**86.2**
12 psi air	**106.2**	**79.0**	**35.4**	**57.0**	**104.9**
15 psi air	**124.4**	**108.4**	**49.4**	**69.1**	**122.5**
occipital	front 1	right	back	left	front 2
10 psi air	**15.7**	**55.7**	**113.9**	**34.3**	**16.7**
12 psi air	**20.1**	**64.3**	**NA**	**20.7**	**22.9**
15 psi air	**28.2**	**74.9**	**NA**	**58.3**	**NA**

Table of Differential Pressure Results for 6mm Sphere with Holes

Differential for sphere with holes 6mm										
	peak differential pressure (psi)					time elapsed between peaks (ms)				
ventricle	front 1	right	back	left	front 2	front 1	right	back	left	front 2
10 psi air	**12.2**	**11.6**	**14.9**	**10.2**	**16.3**	**1.95**	**0.38**	**0.38**	**0.31**	**2.73**
12 psi air	**19.2**	**15.2**	**18.4**	**12.7**	**16.8**	**1.95**	**0.38**	**0.40**	**0.38**	**1.94**
15 psi air	**25.9**	**22.8**	**24.7**	**19.5**	**28.8**	**2.73**	**6.29**	**0.21**	**0.45**	**3.09**
frontal	front 1	right	back	left	front 2	front 1	right	back	left	front 2
10 psi air	**20.8**	**17.7**	**16.9**	**15.6**	**21.7**	**0.28**	**0.33**	**2.77**	**0.32**	**0.25**
12 psi air	**27.8**	**23.1**	**22.2**	**21.0**	**26.9**	**1.82**	**0.29**	**2.41**	**0.37**	**0.26**
15 psi air	**34.1**	**33.0**	**27.0**	**23.5**	**37.7**	**1.99**	**0.30**	**2.59**	**0.34**	**1.85**
occipital	front 1	right	back	left	front 2	front 1	right	back	left	front 2
10 psi air	**24.0**	**17.6**	**28.2**	**12.8**	**25.1**	**0.82**	**0.32**	**0.25**	**1.40**	**2.21**
12 psi air	**29.9**	**20.1**	**NA**	**15.6**	**28.6**	**2.21**	**0.31**	**NA**	**1.40**	**2.10**
15 psi air	**37.7**	**25.5**	**NA**	**20.0**	**NA**	**1.21**	**0.34**	**NA**	**1.40**	**NA**

Percentages of 1st rate of internal pressure changes in 6 mm sphere with holes based on the cell value at the 10 psi air overpressure for each orientation.

AIR		Percentage 1st Rate Pressure Change				
Overpressure		front 1	right	back	left	front 2
ventricle	**20%**	**29%**	**38%**	**17%**	**-8%**	**23%**
ventricle	**50%**	**135%**	**83%**	**80%**	**80%**	**70%**
frontal	**20%**	**45%**	**48%**	**28%**	**17%**	**22%**
frontal	**50%**	**70%**	**103%**	**78%**	**41%**	**42%**
occipital	**20%**	**28%**	**15%**	**NA**	**-40%**	**37%**
occipital	**50%**	**80%**	**34%**	**NA**	**70%**	**NA**

State of Gages during Testing of the 6mm Sphere with Holes

	Strain status for sphere 6mm				
Frontal	front 1	right	back	left	front 2
10 psi air					
12 psi air					
15 psi air					
Left	front 1	right	back	left	front 2
10 psi air					
12 psi air					
15 psi air					
Right	front 1	right	back	left	front 2
10 psi air					
12 psi air					
15 psi air					
Occipital	front 1	right	back	left	front 2
10 psi air					
12 psi air					
15 psi air					

	working
	signal problems
	not working

Strain Data Sphere with Holes

Test 1 Front 1 Orientation 6mm Sphere with Holes

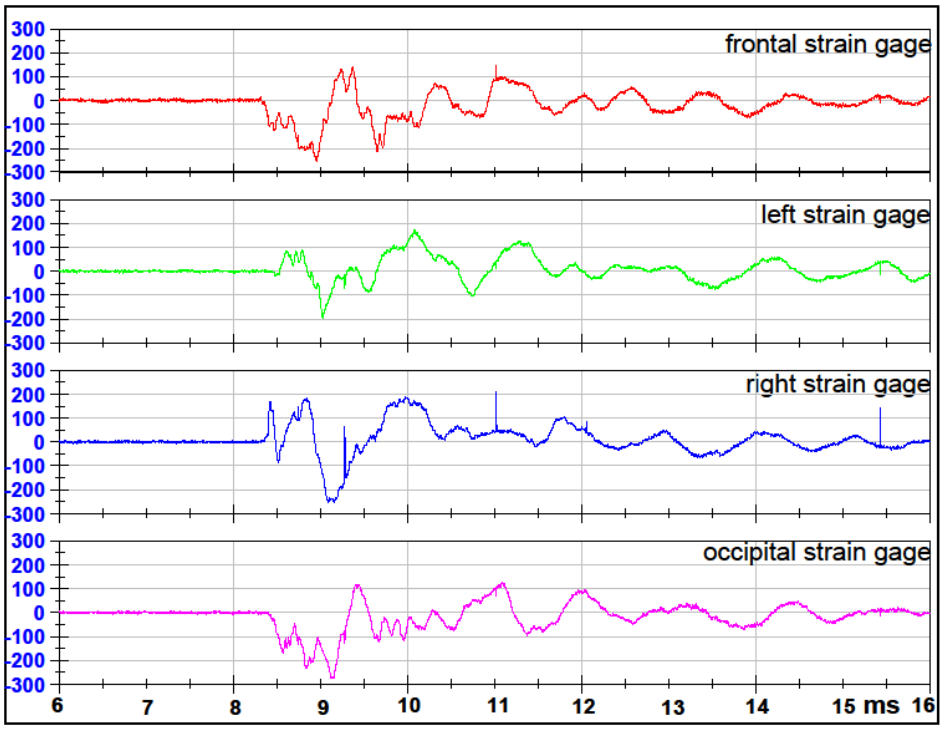

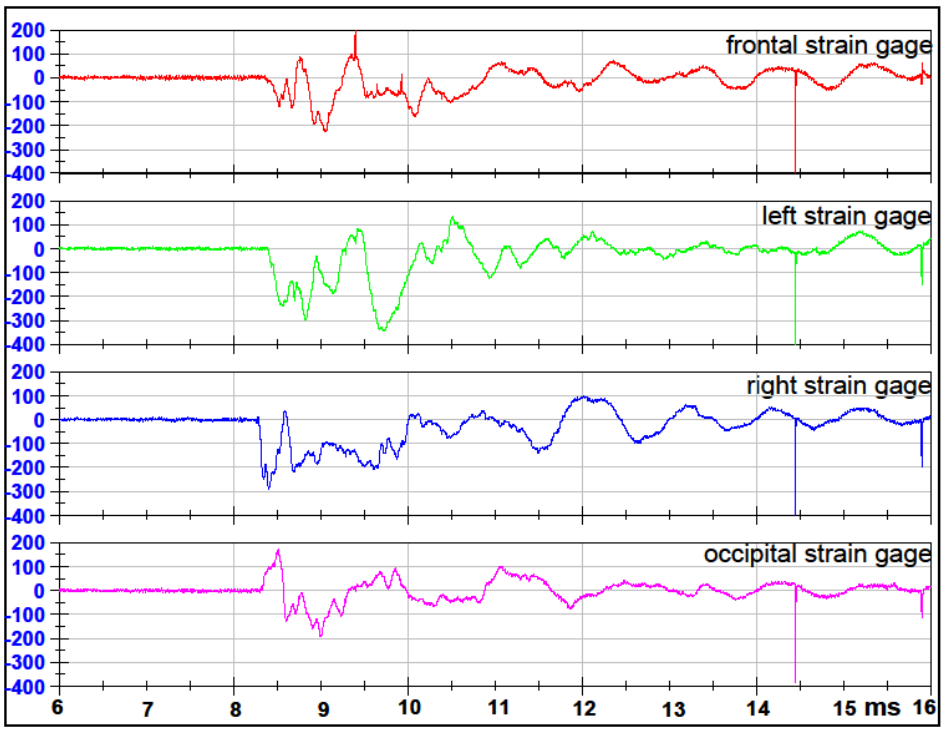

Test 2 Right Orientation 6mm Sphere with Holes

Test 3 Back Orientation 6mm Sphere with Holes

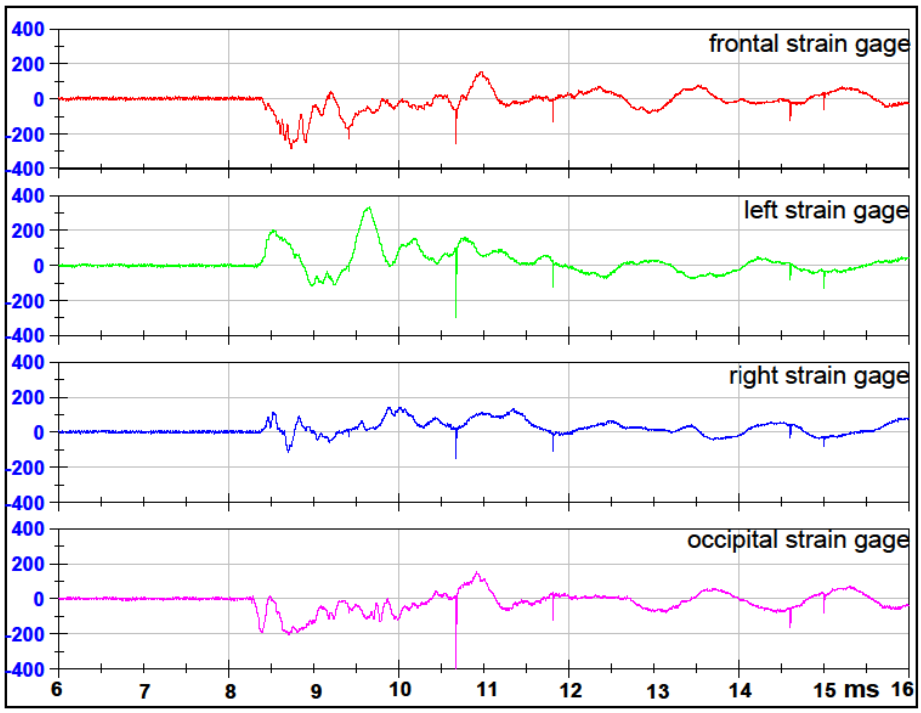

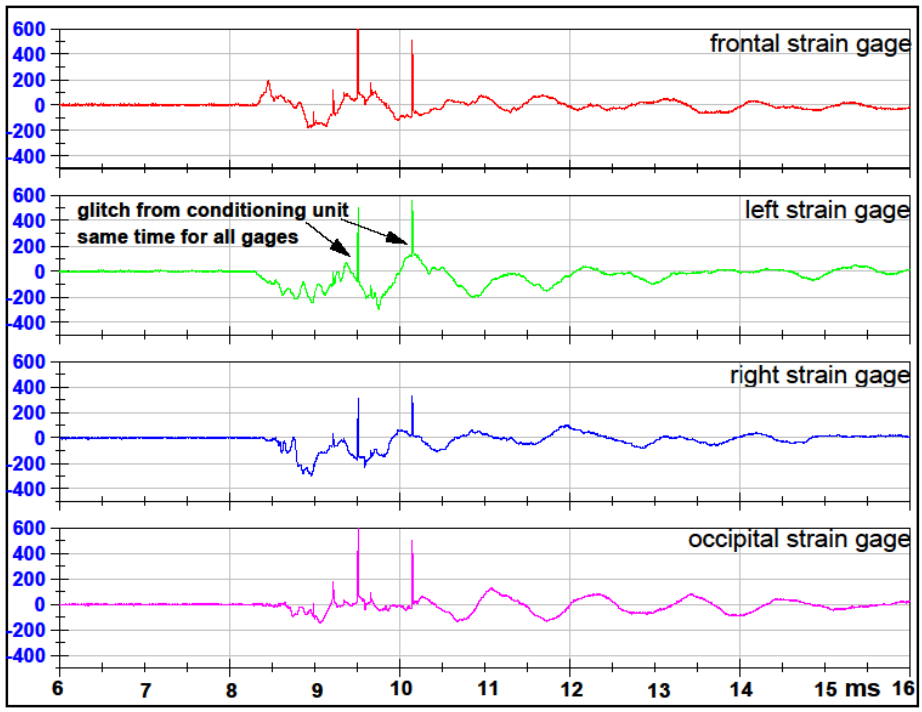

Test 4 Left Orientation 6mm Sphere with Holes

Test 5 Front 2 Orientation 6mm Sphere with Holes

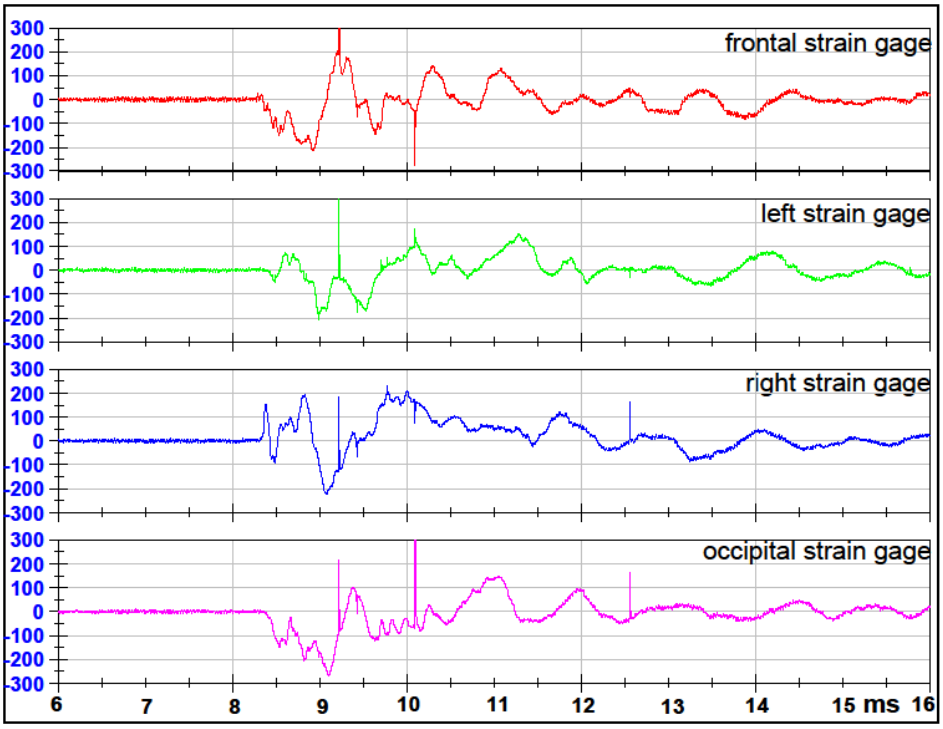

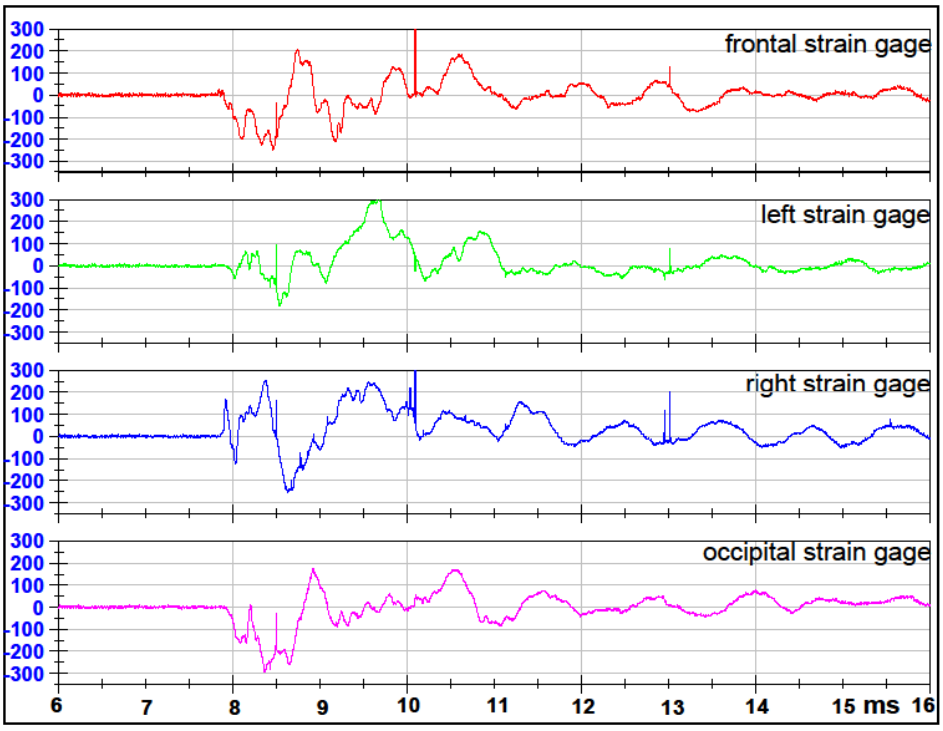

Test 6 Front 1 Orientation 6mm Sphere with Holes

Test 7 Left Orientation 6mm Sphere with Holes

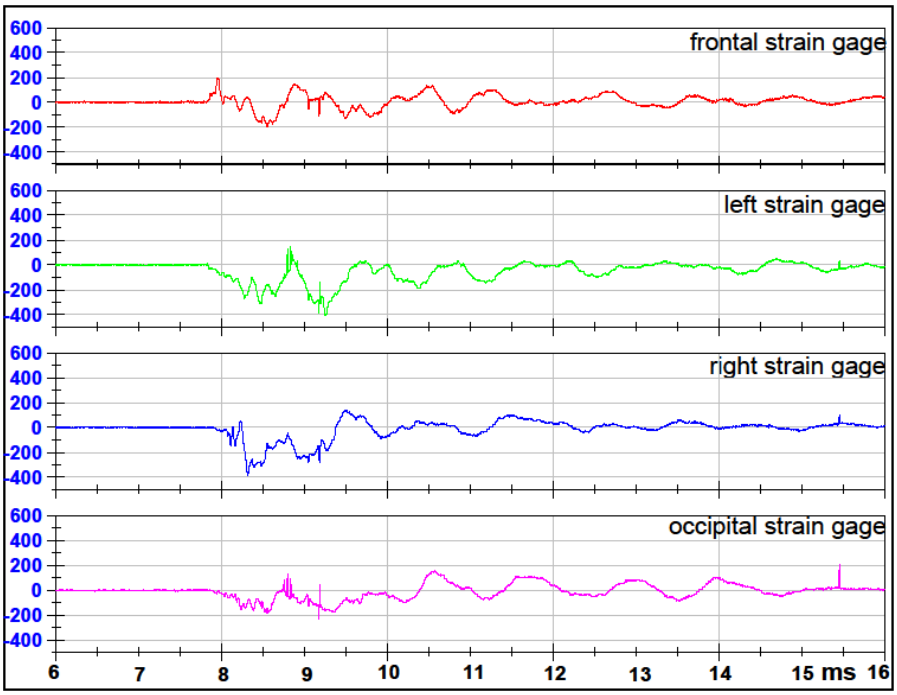

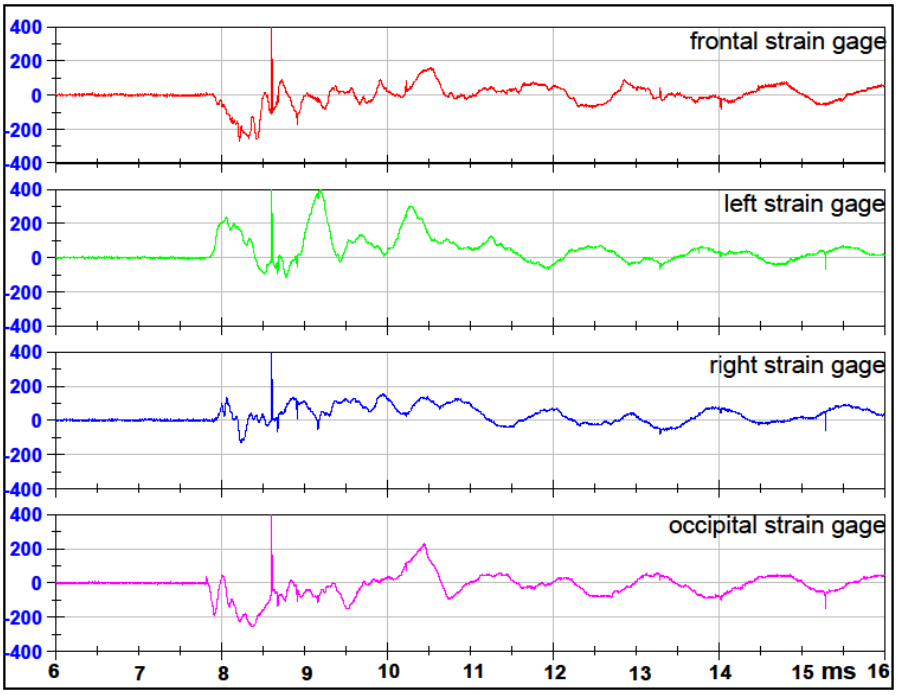

Test 8 Back Orientation 6mm Sphere with Holes

Test 9 Right Orientation 6mm Sphere with Holes

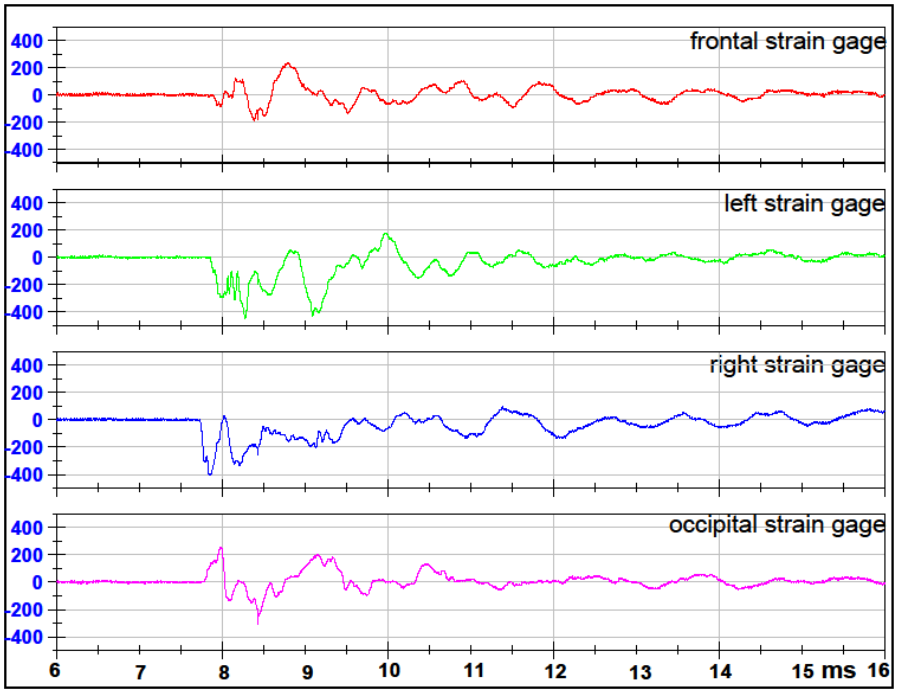

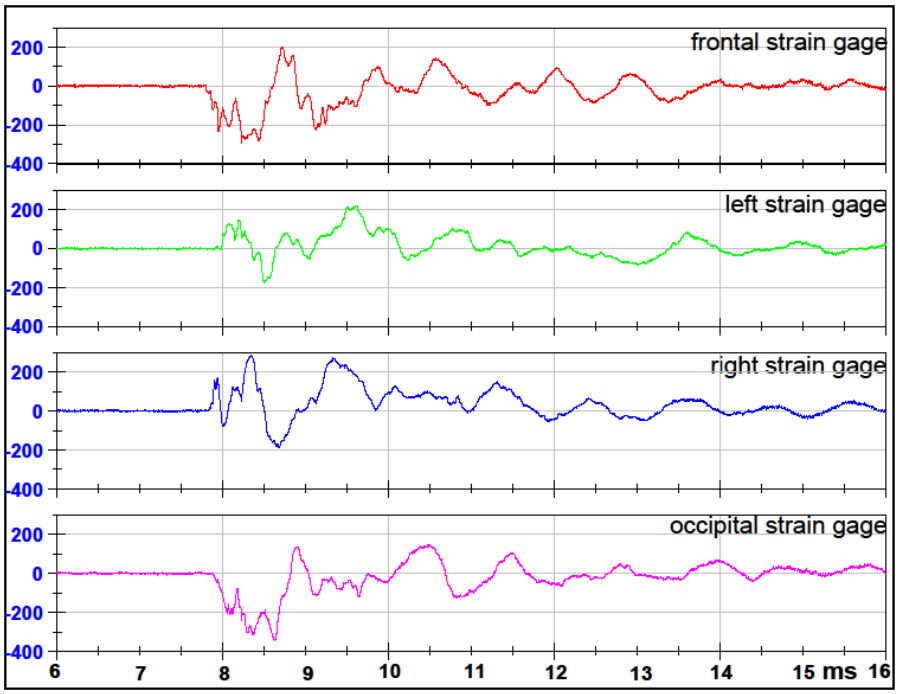

Test 10 Front 2 Orientation 6mm Sphere with Holes

Test 11 Front 1 Orientation 6mm Sphere with Holes

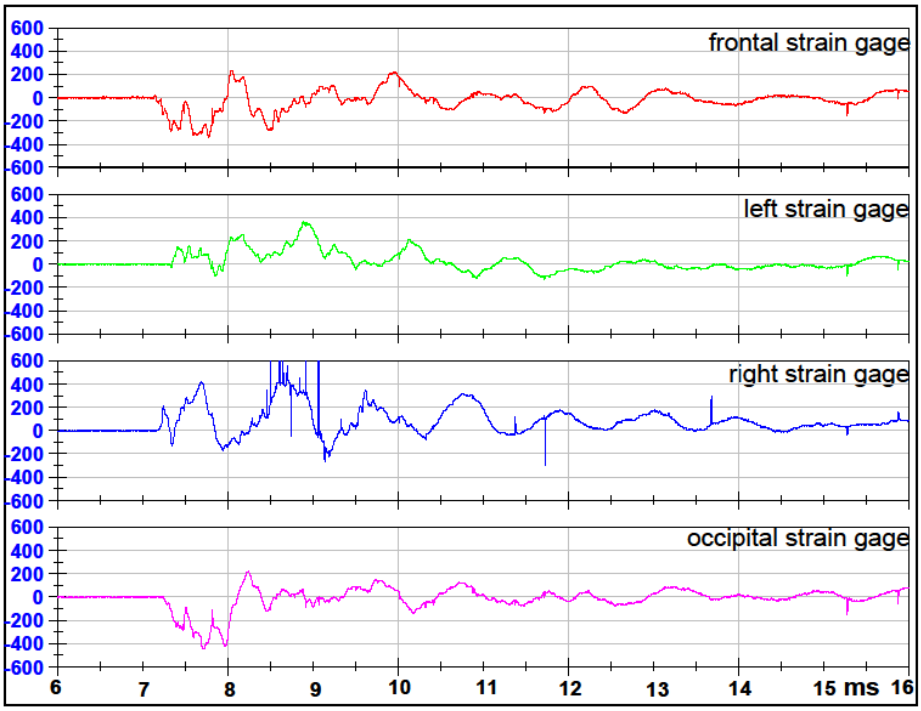

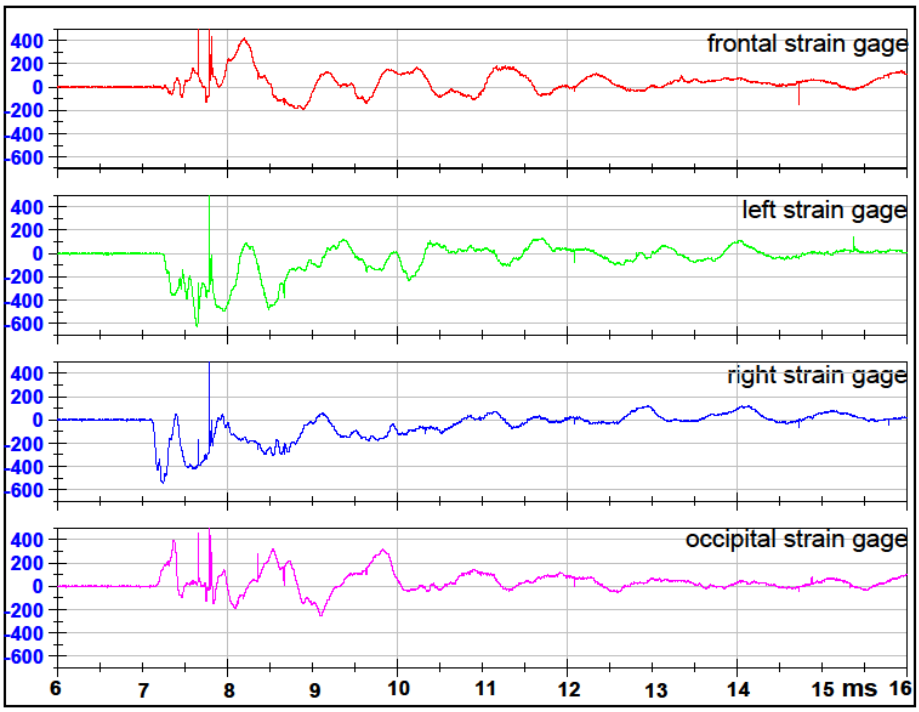

Test 12 Right Orientation 6mm Sphere with Holes

Test 13 Back Orientation 6mm Sphere with Holes

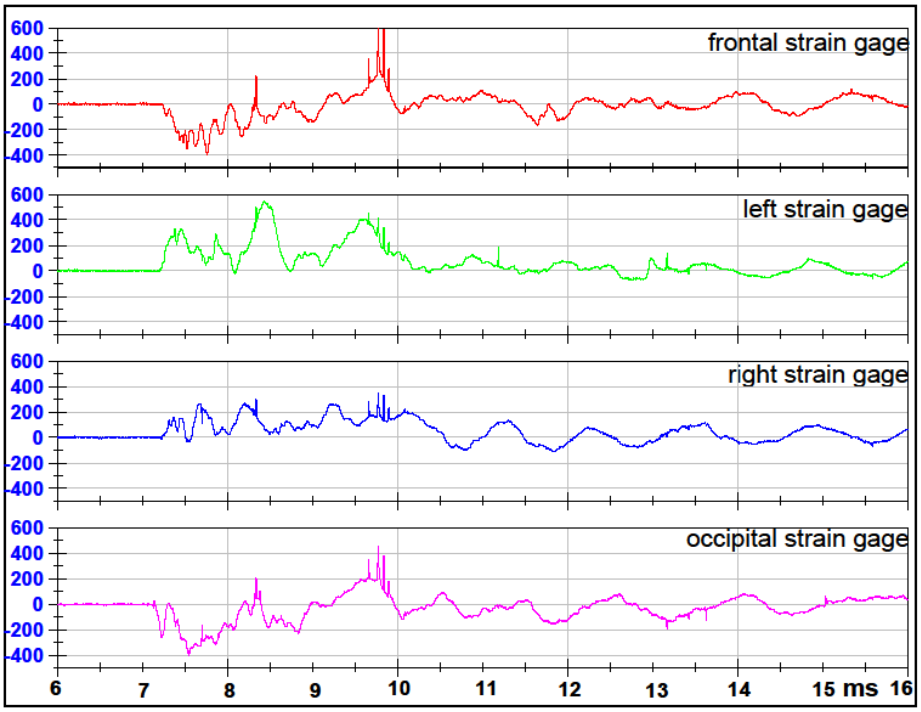

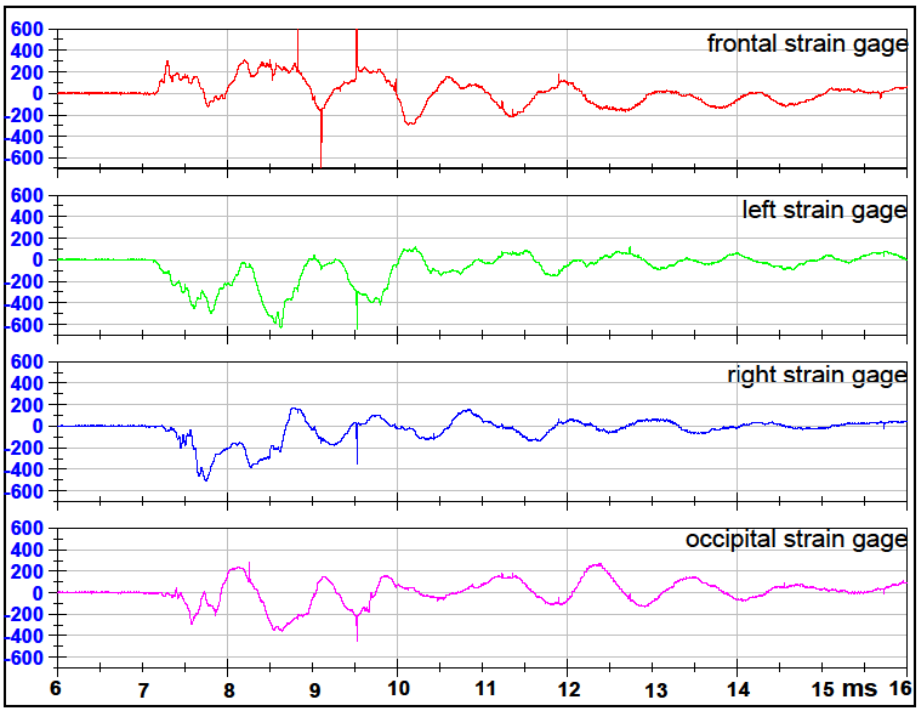

Test 14 Left Orientation 6mm Sphere with Holes

Test 15 Front 2 Orientation 6mm Sphere with Holes

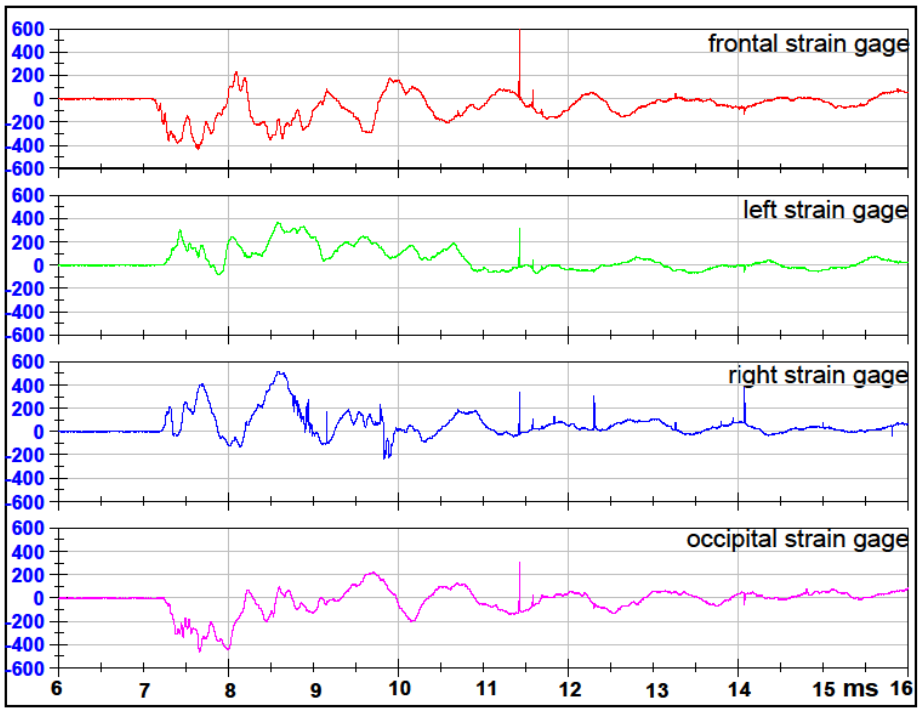

APPENDIX D

SPHERE 7 MM THICK DATA

Test 1 Front 1 Orientation 7mm Intact Sphere

FILTERED DATA

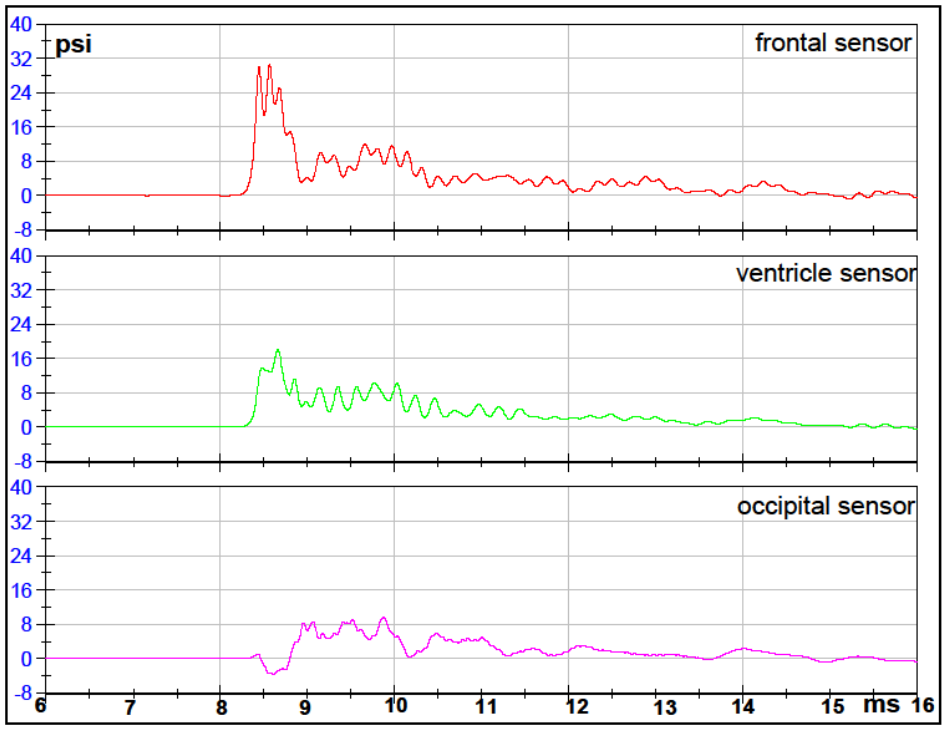

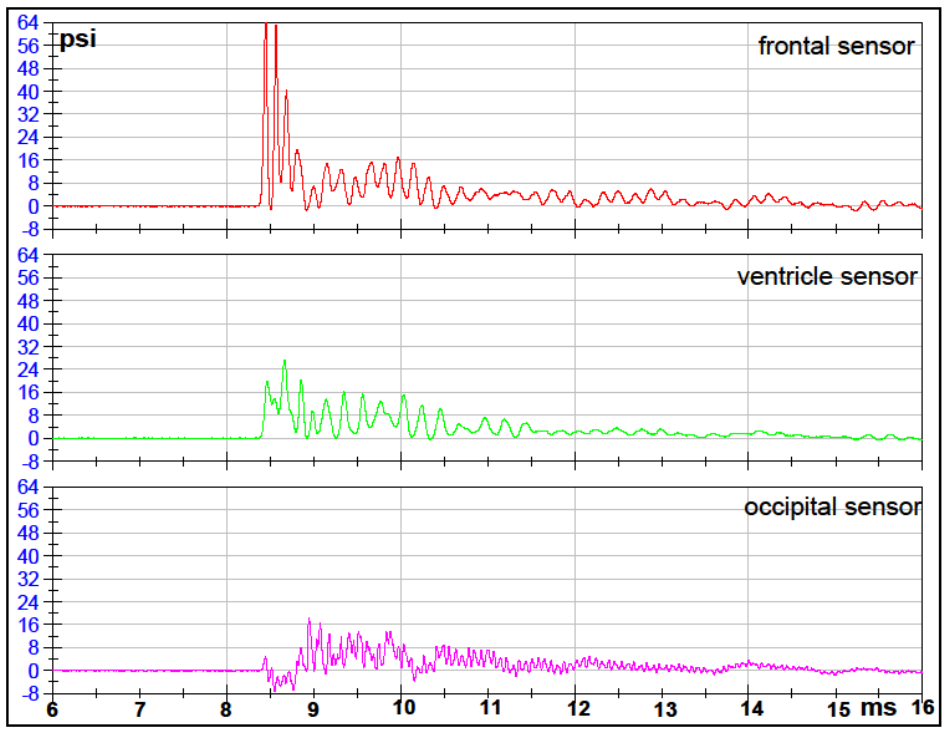

RAW DATA

Test 2 Right Orientation 7mm Intact Sphere

FILTERED DATA

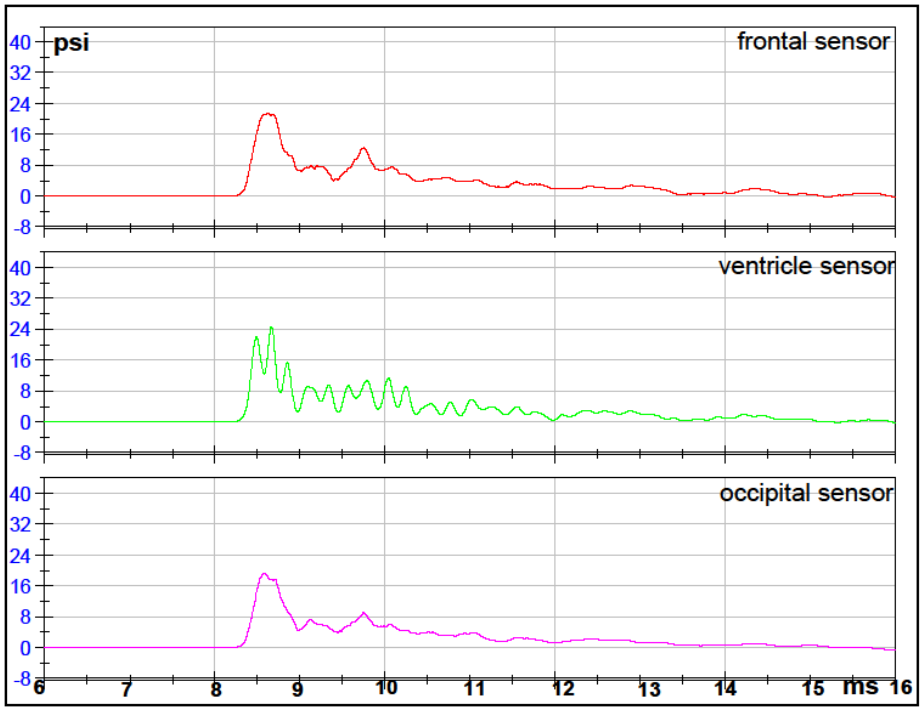

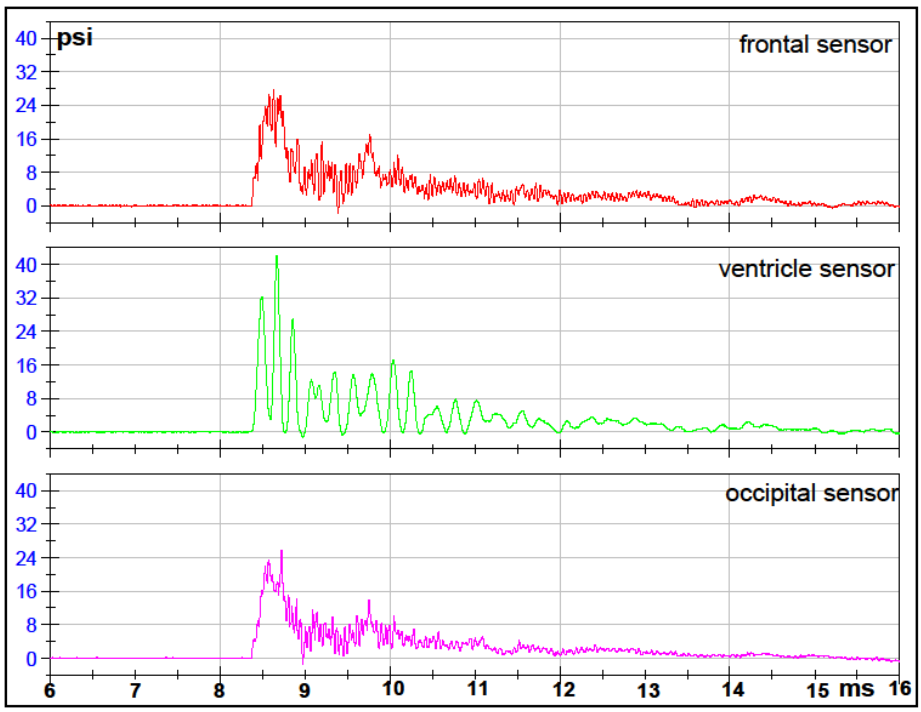

RAW DATA

Test 3 Back Orientation 7mm Intact Sphere

FILTERED DATA

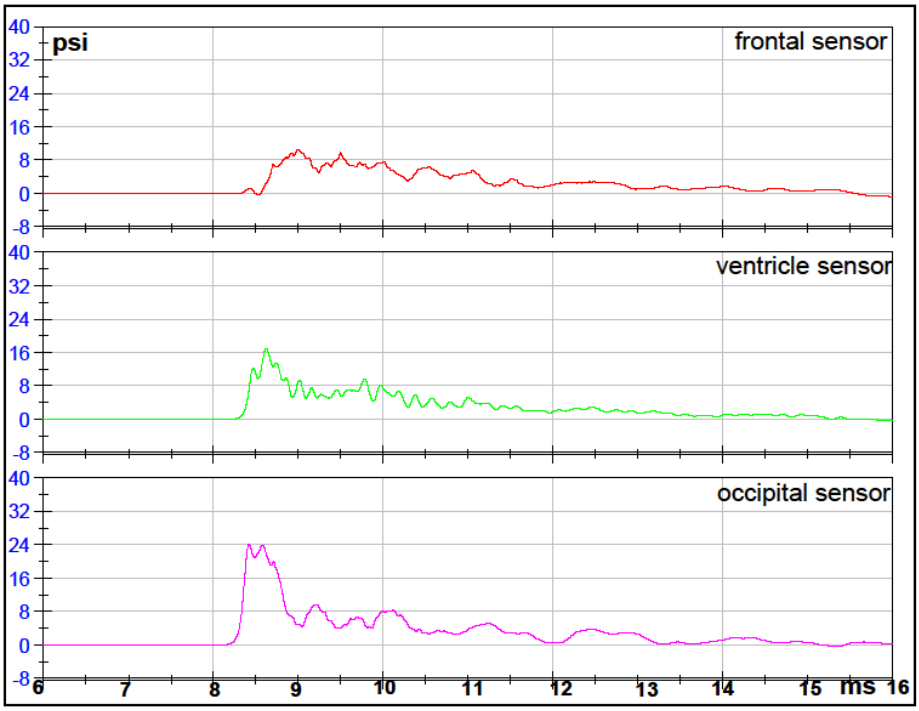

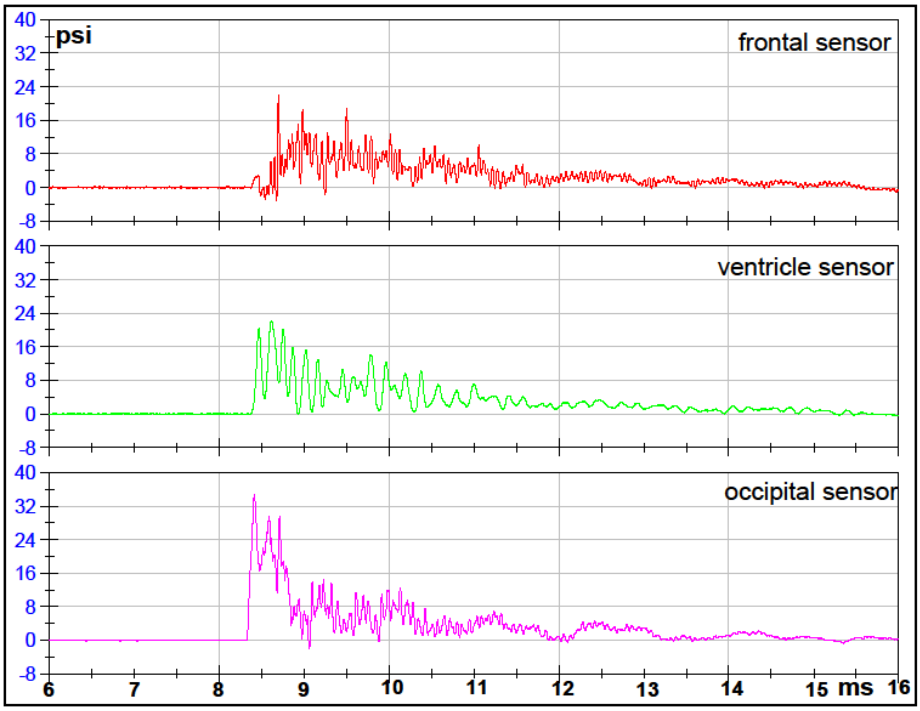

RAW DATA

Test 4 Left Orientation 7mm Intact Sphere

FILTERED DATA

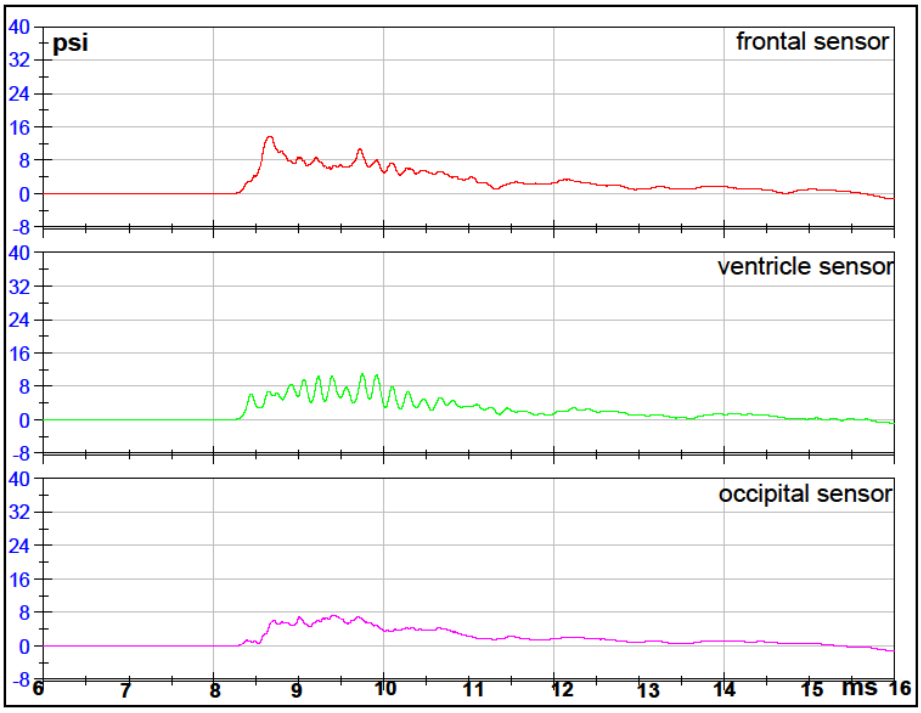

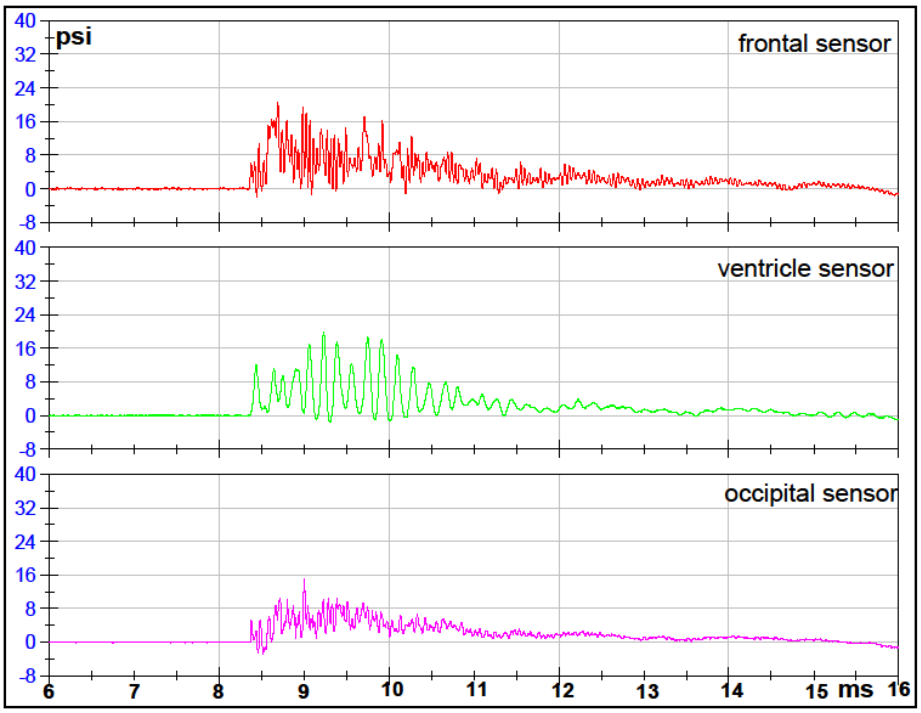

RAW DATA

Test 5 Front 2 Orientation 7mm Intact Sphere

FILTERED DATA

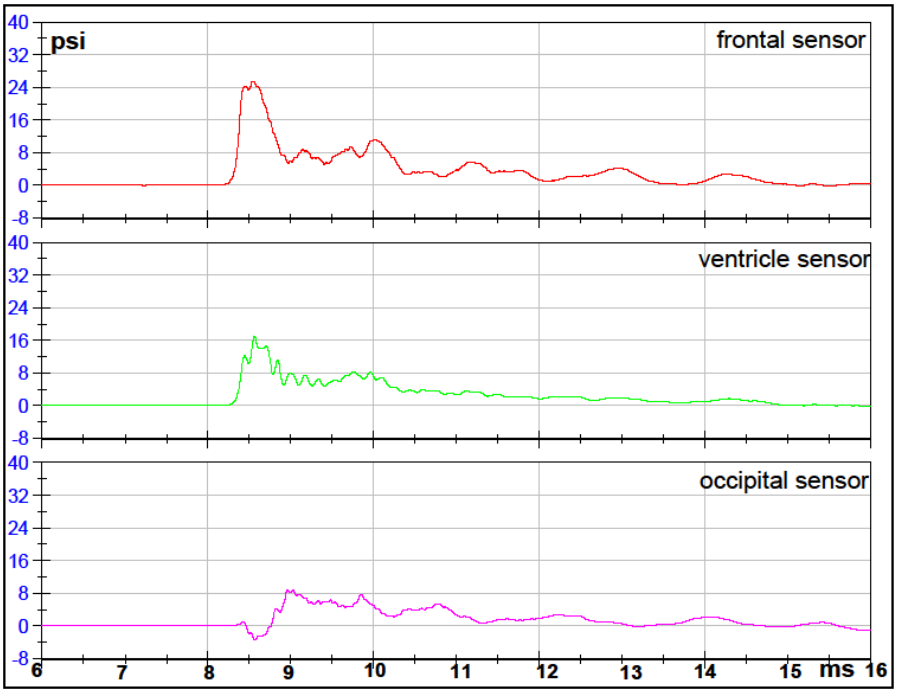

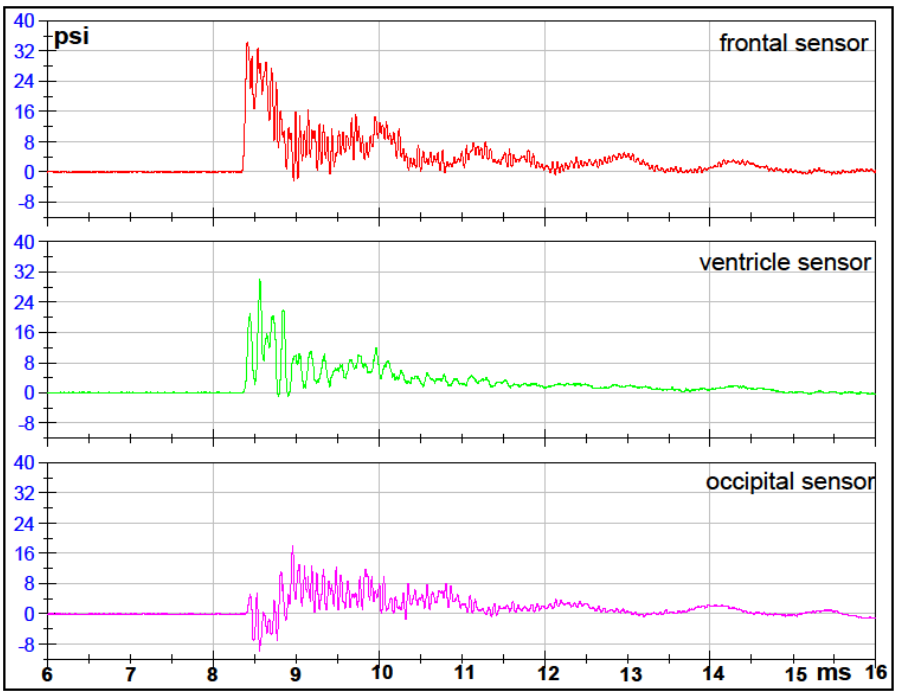

RAW DATA

Test 6 Front 1 Orientation 7mm Intact Sphere

FILTERED DATA

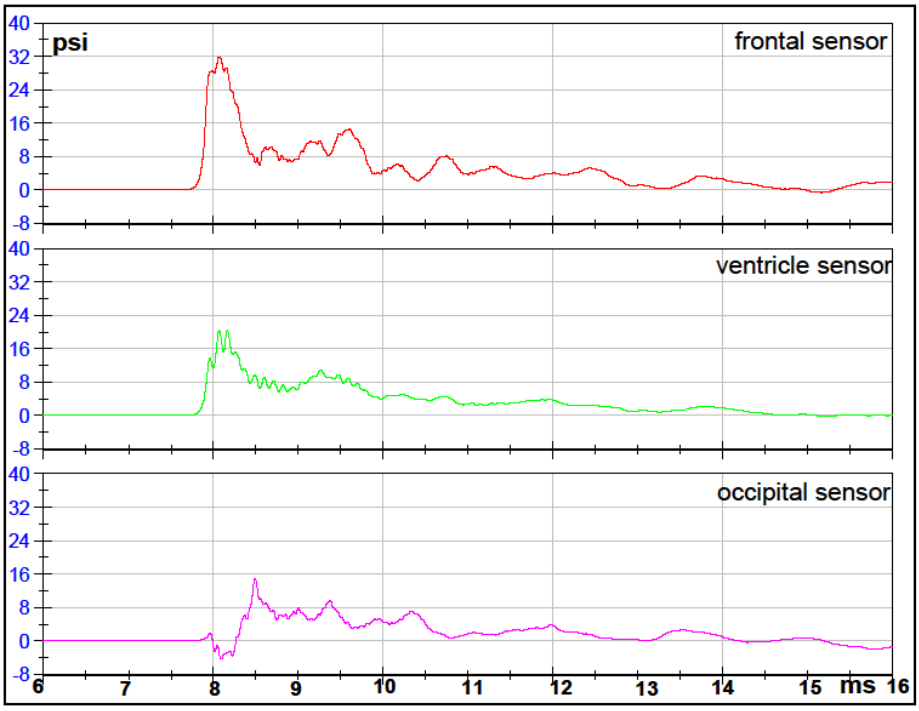

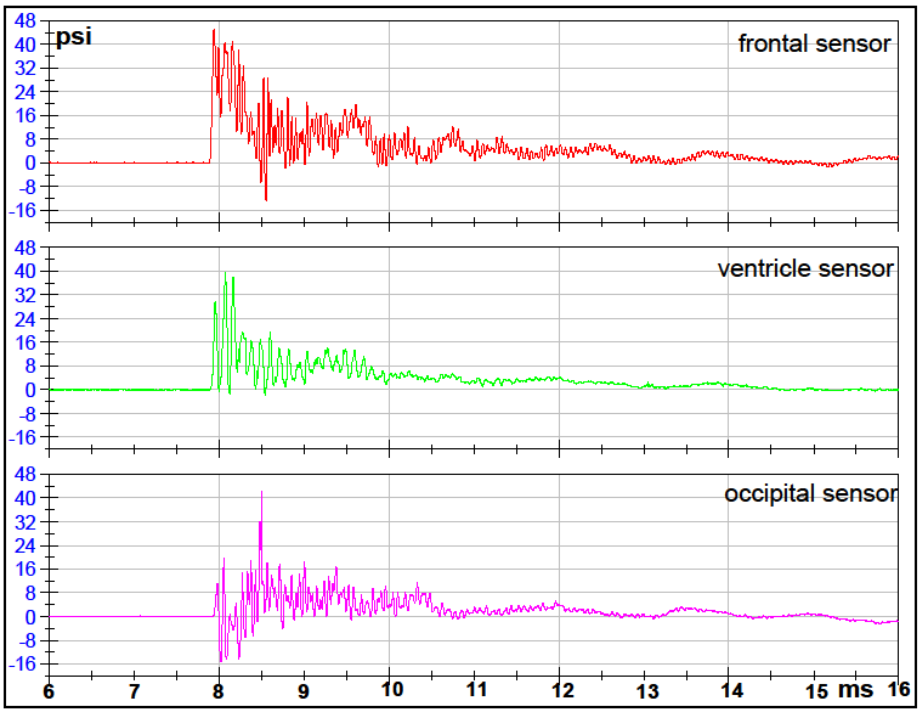

RAW DATA

Test 7 Left Orientation 7mm Intact Sphere

FILTERED DATA

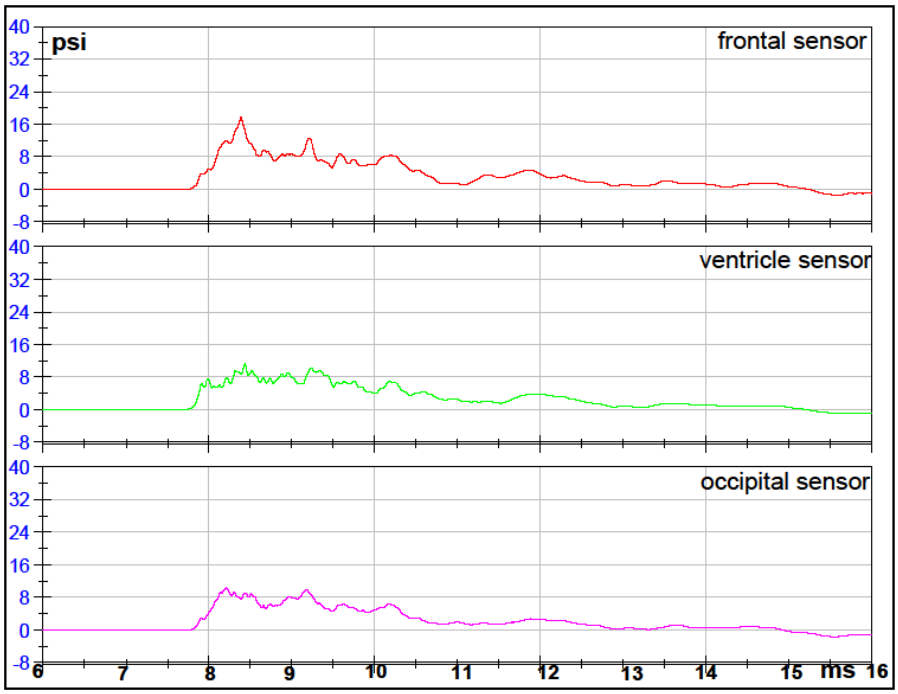

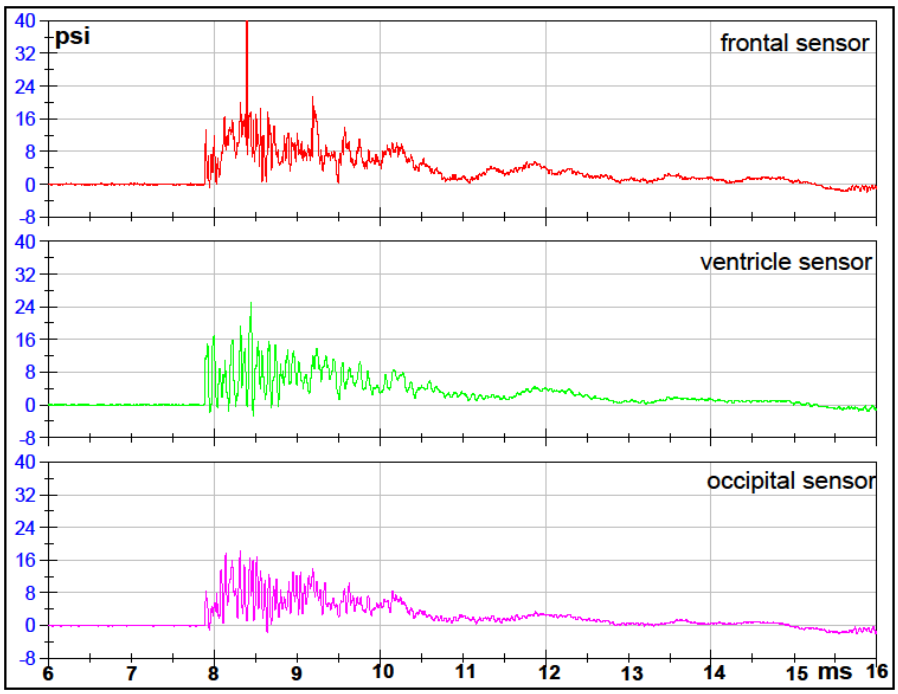

RAW DATA

Test 8 Back Orientation 7mm Intact Sphere

FILTERED DATA

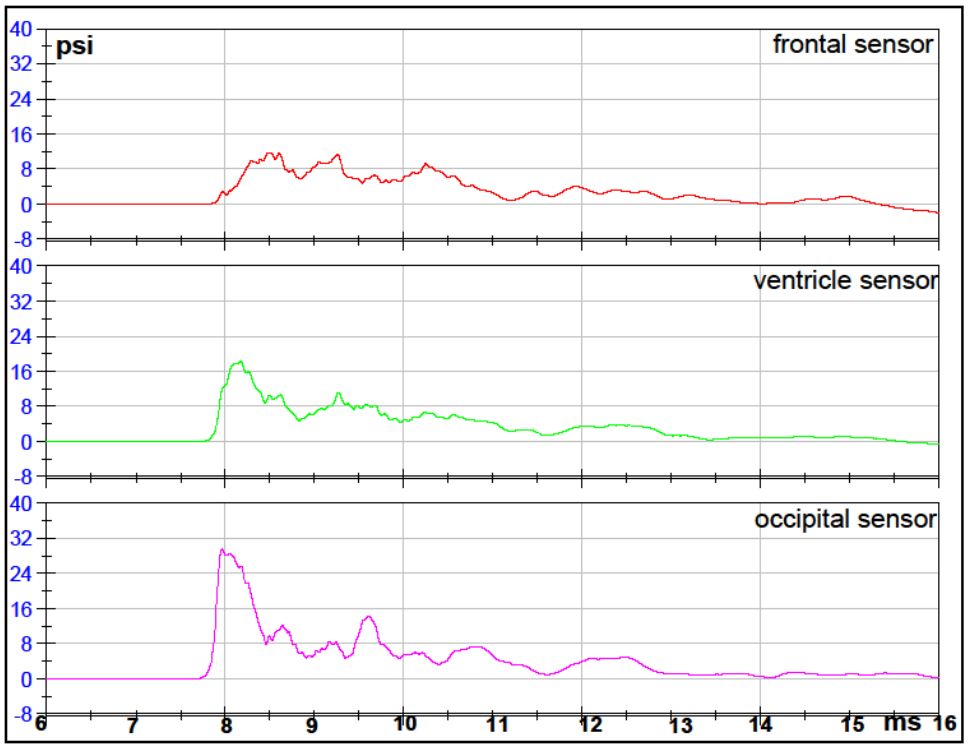

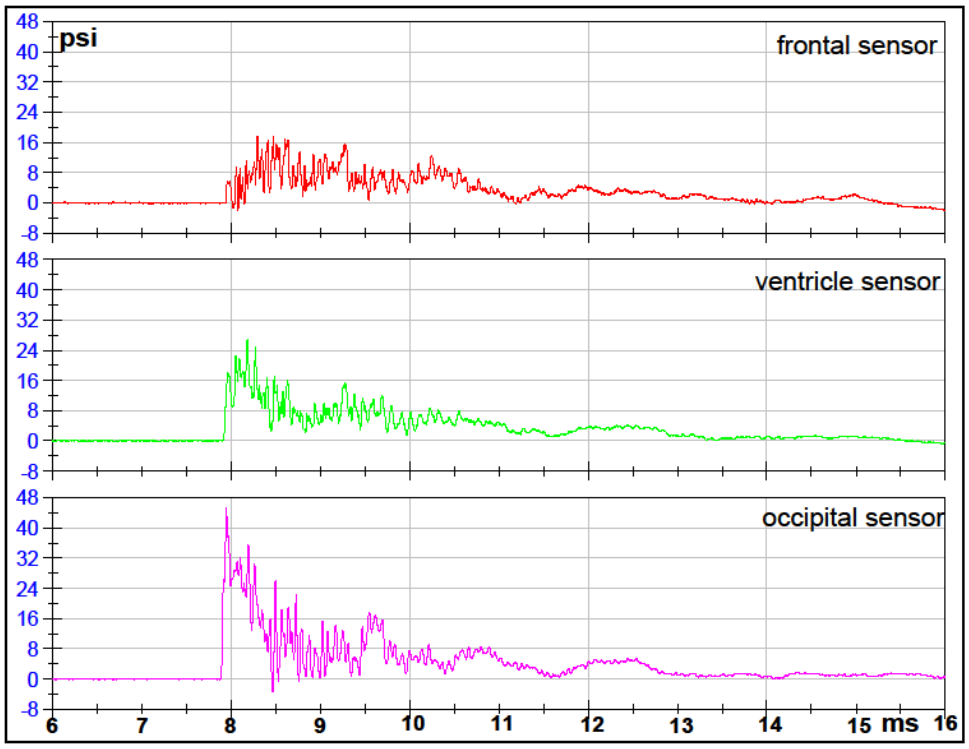

RAW DATA

Test 9 Right Orientation 7mm Intact Sphere

FILTERED DATA

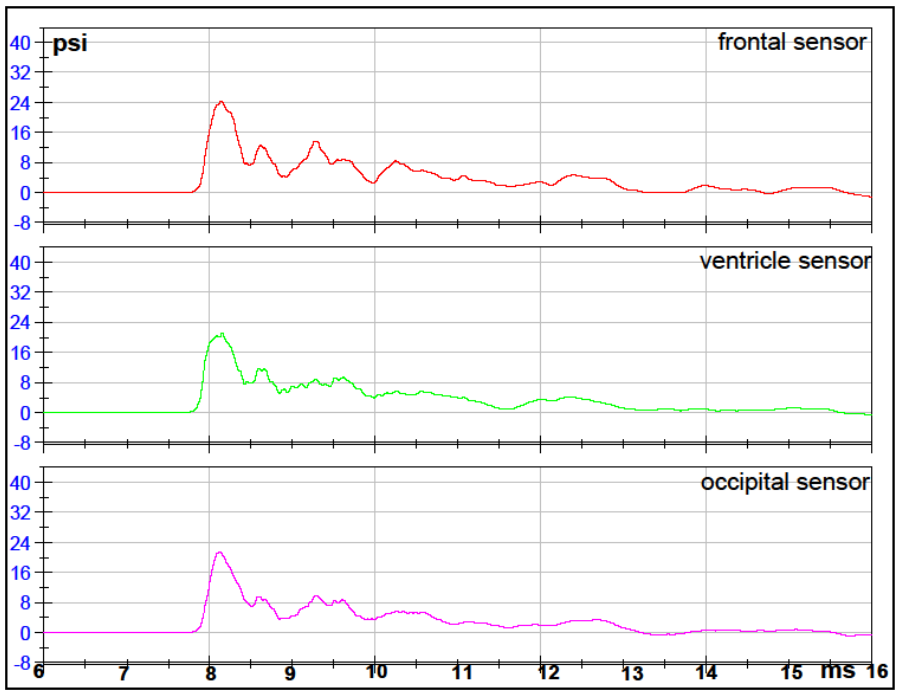

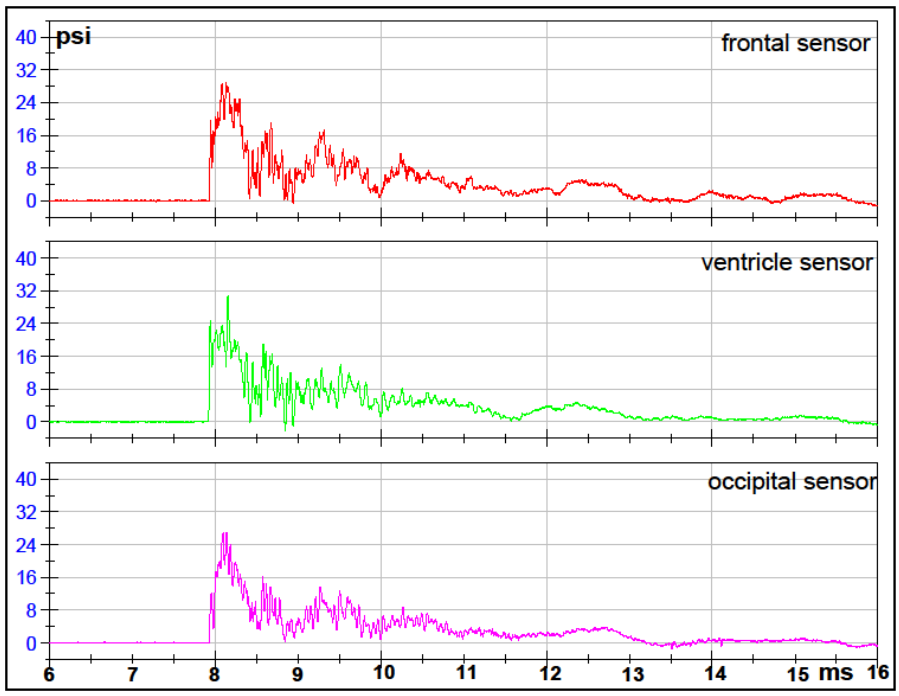

RAW DATA

Test 10 Front 2 Orientation 7mm Intact Sphere

FILTERED DATA

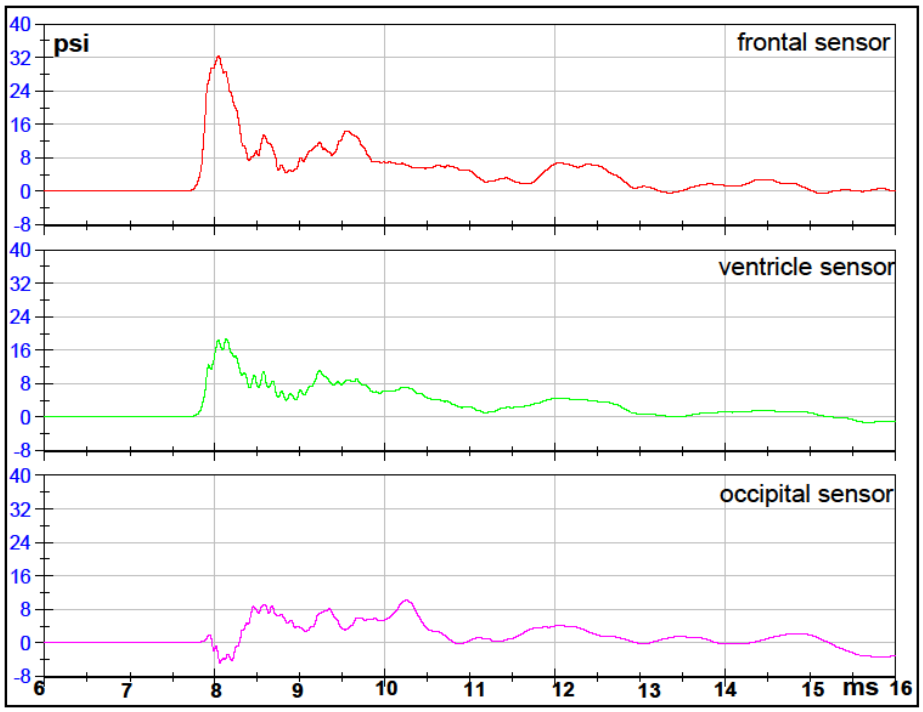

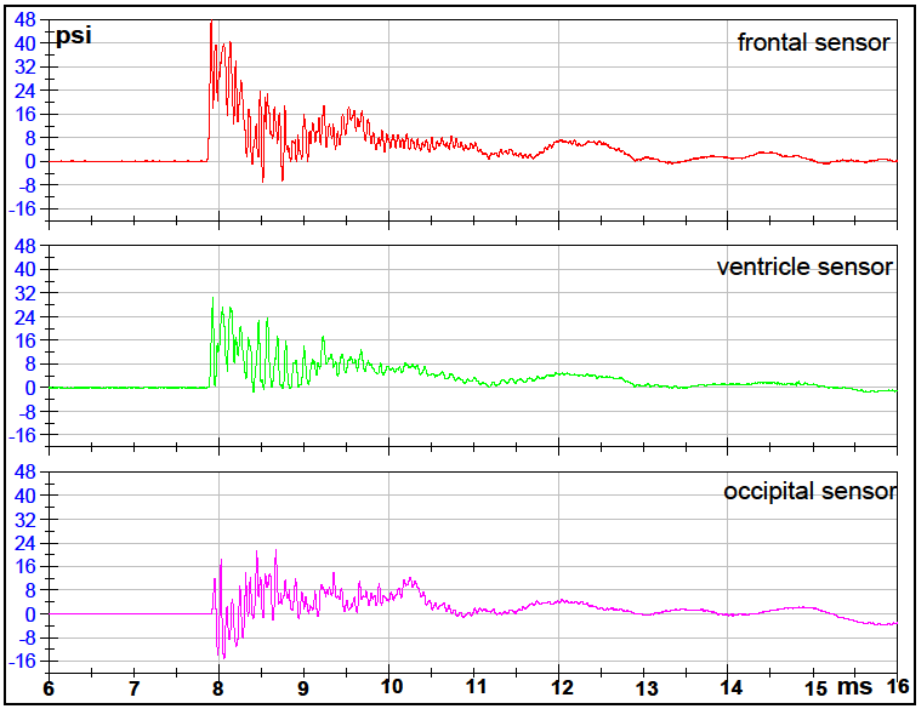

RAW DATA

Test 11 Front 1 Orientation 7mm Intact Sphere

FILTERED DATA

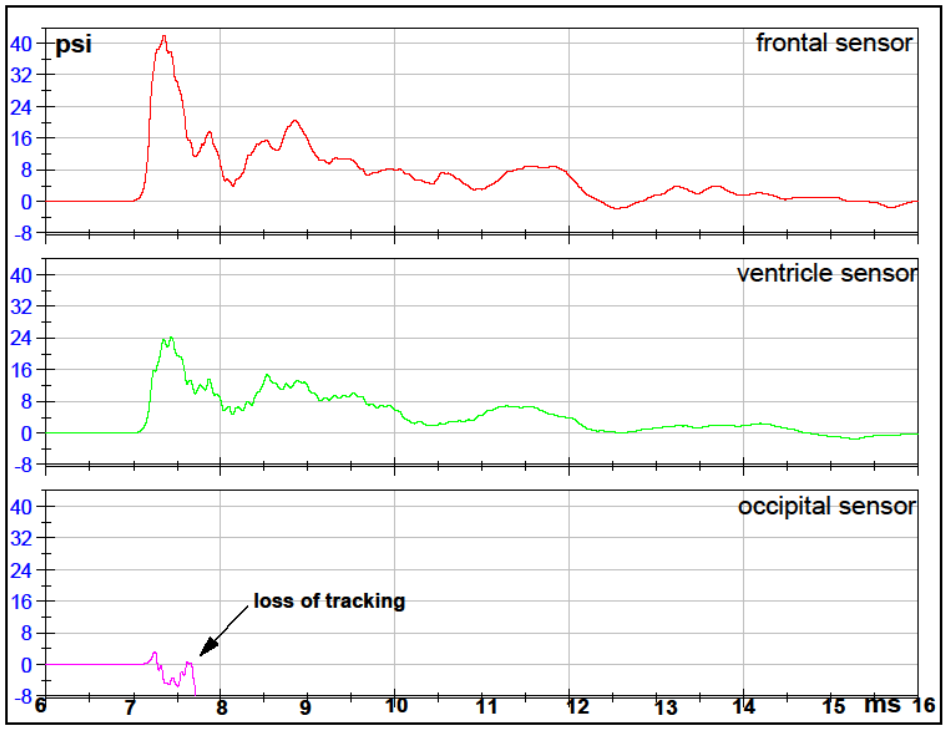

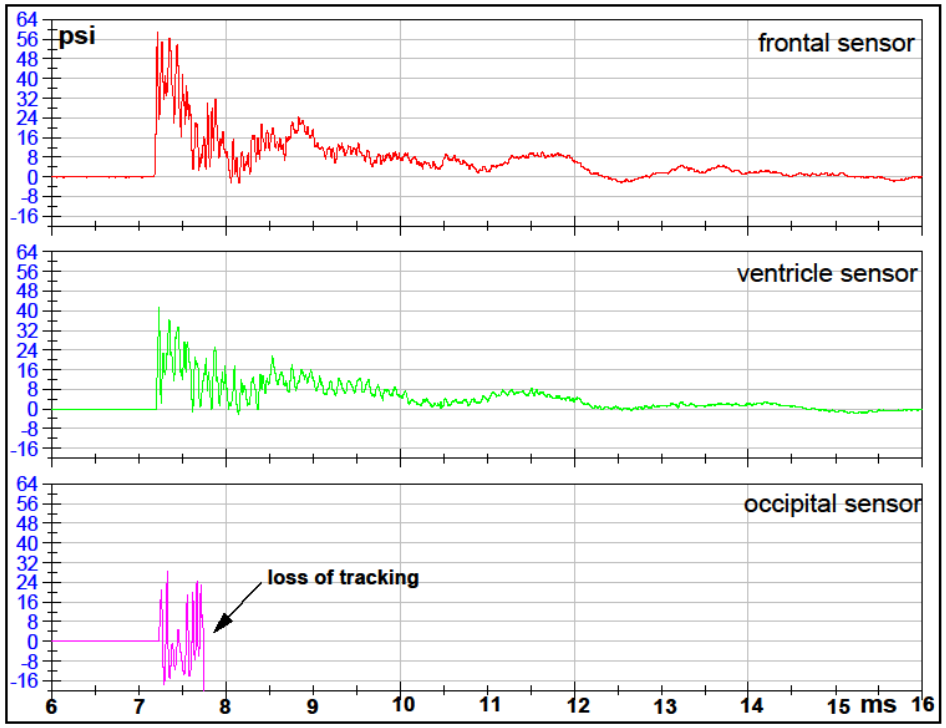

RAW DATA

Test 12 Right Orientation 7mm Intact Sphere

FILTERED DATA

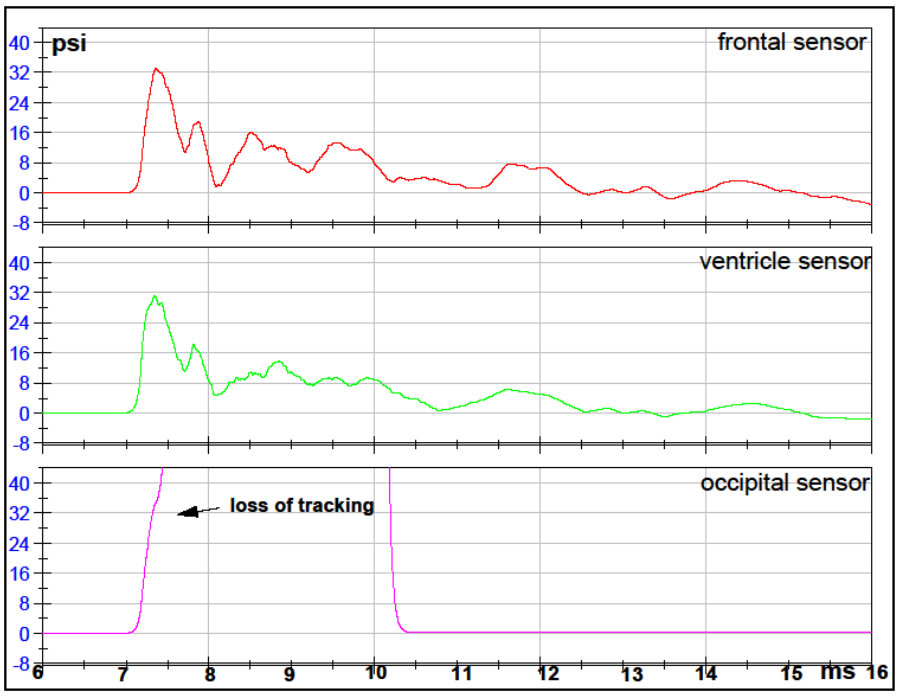

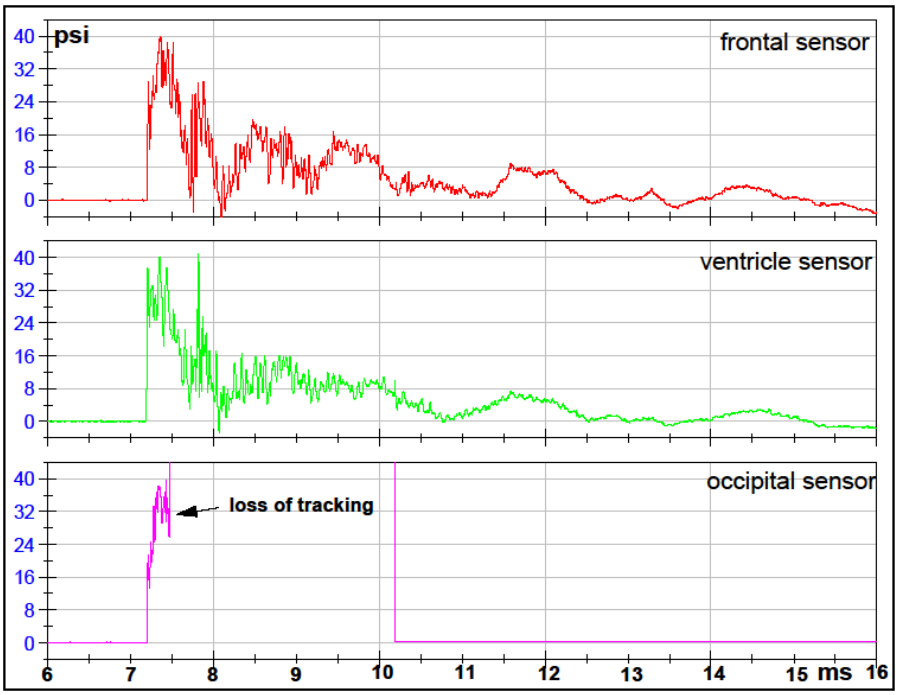

RAW DATA

Test 13 Back Orientation 7mm Intact Sphere

FILTERED DATA

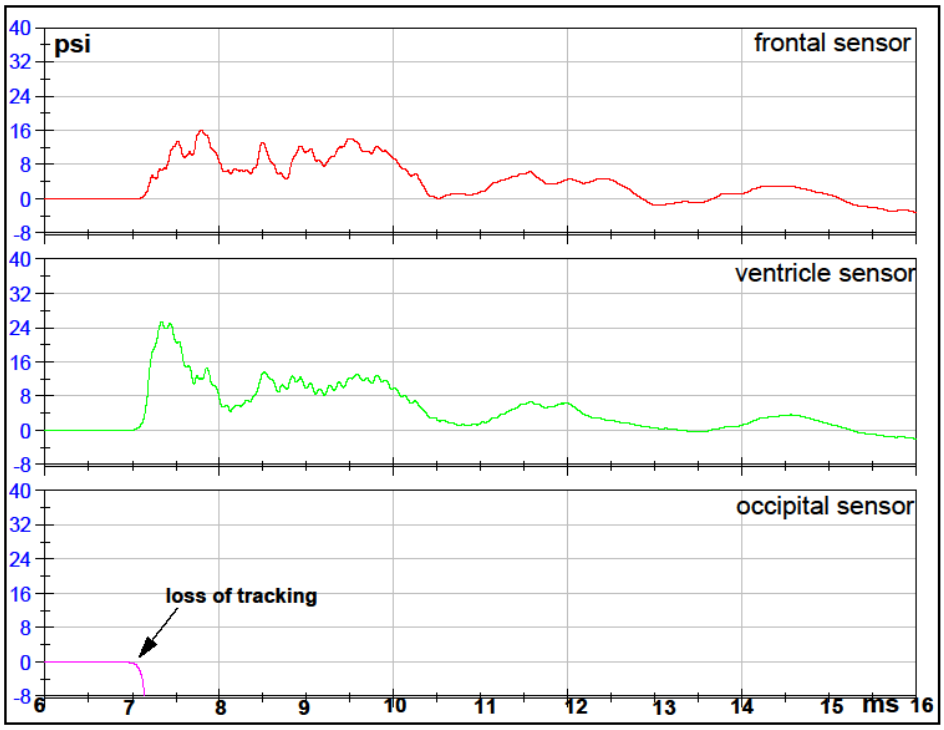

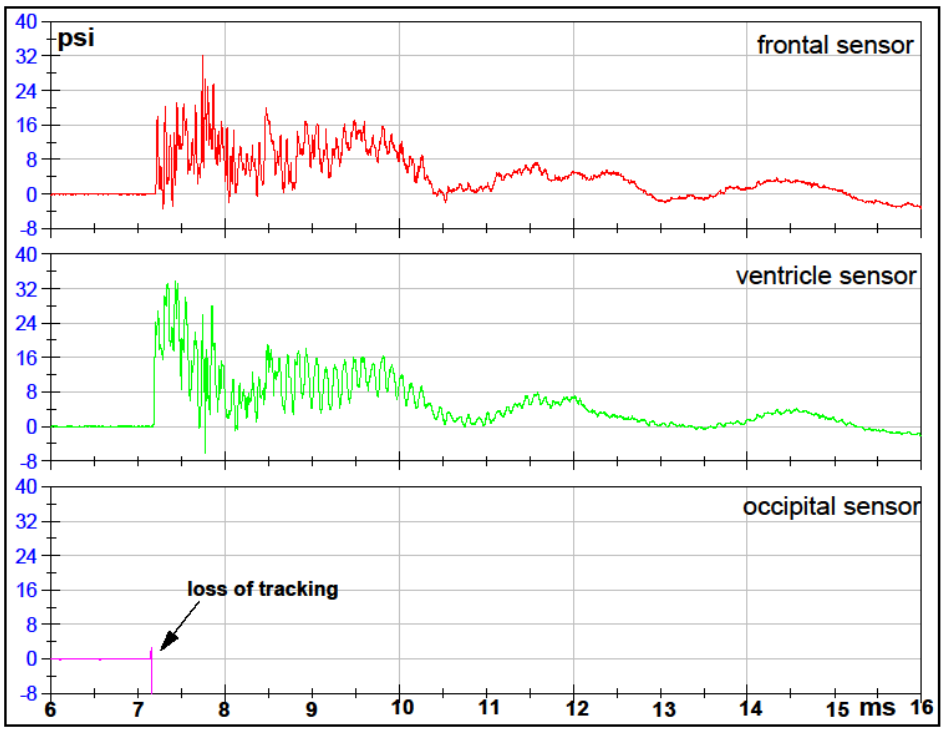

RAW DATA

Test 14 Left Orientation 7mm Intact Sphere

FILTERED DATA

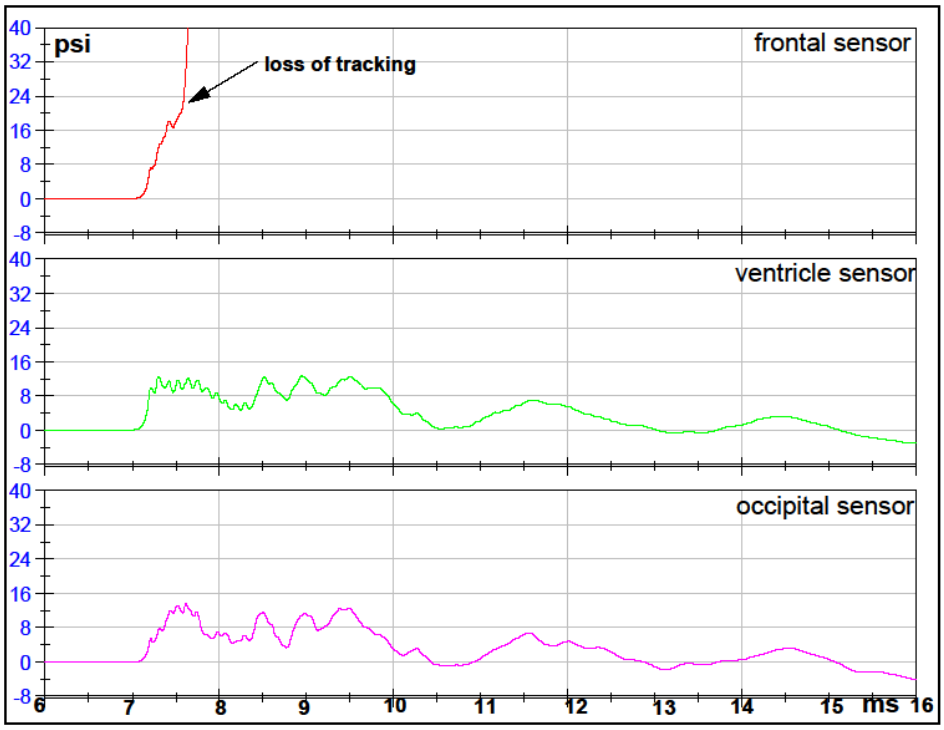

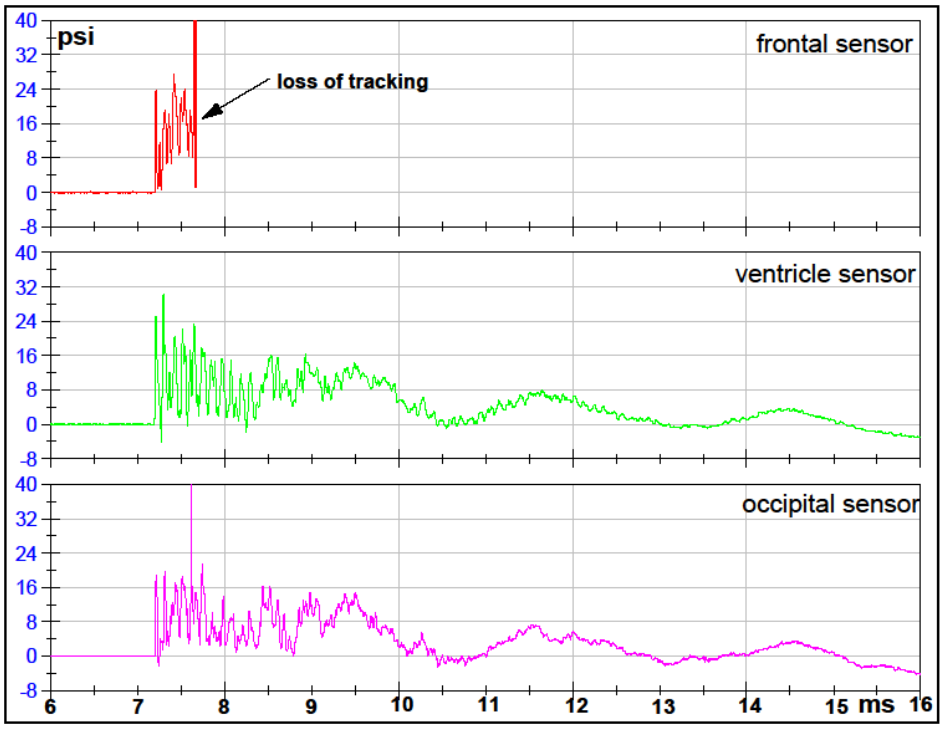

RAW DATA

Test 15 Front 2 Orientation 7mm Intact Sphere

FILTERED DATA

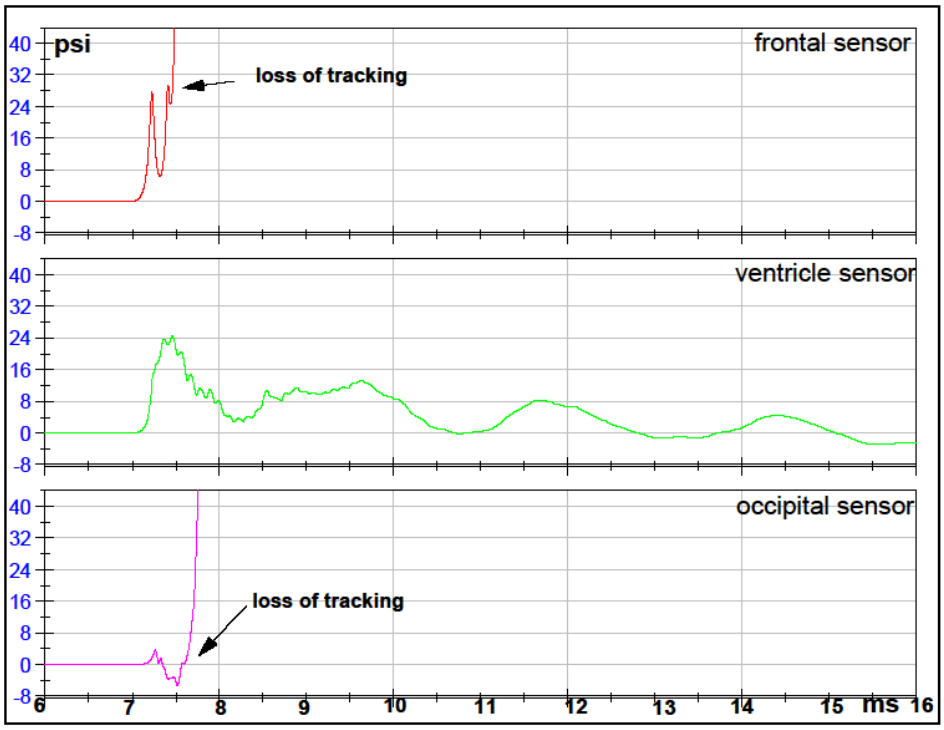

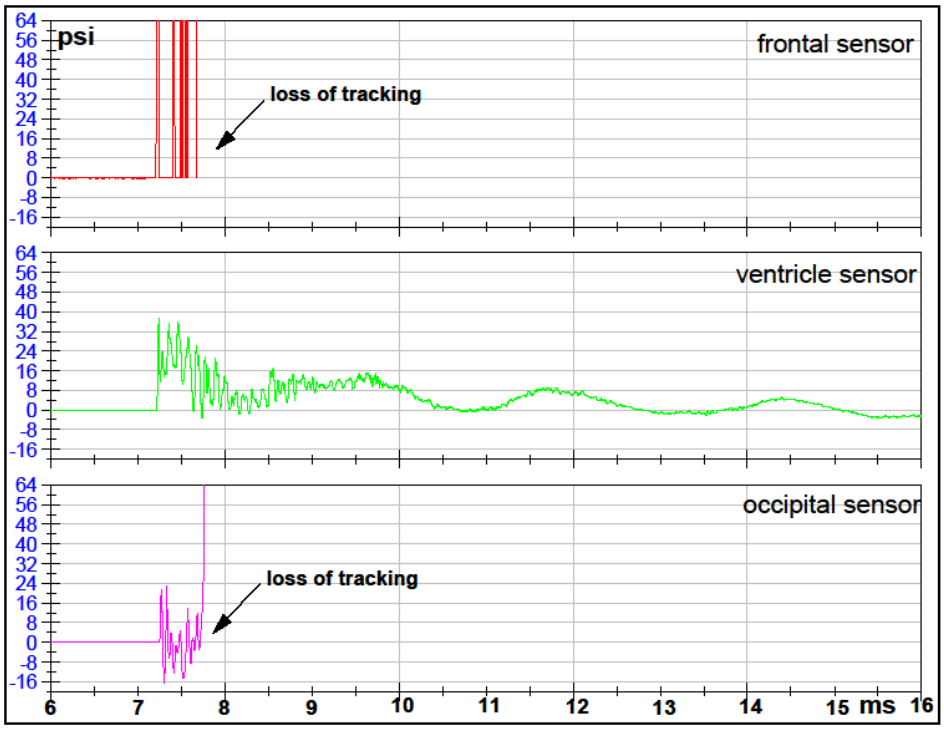

RAW DATA

Comparison for reproducibility of each pressure sensor in Front Orientation at 10psi 7mm Intact Sphere

VENTRICLE FILTERED DATA

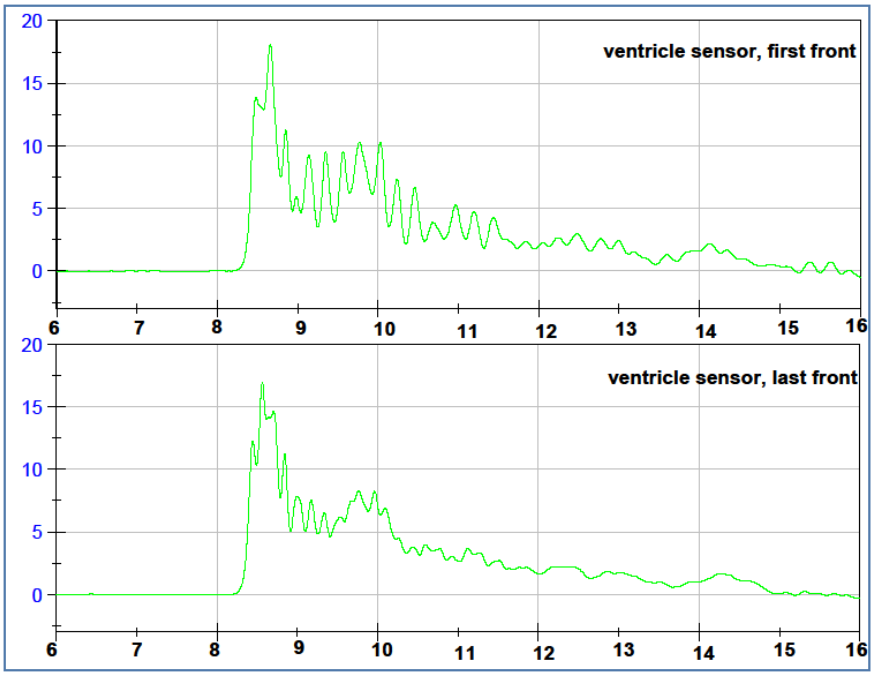

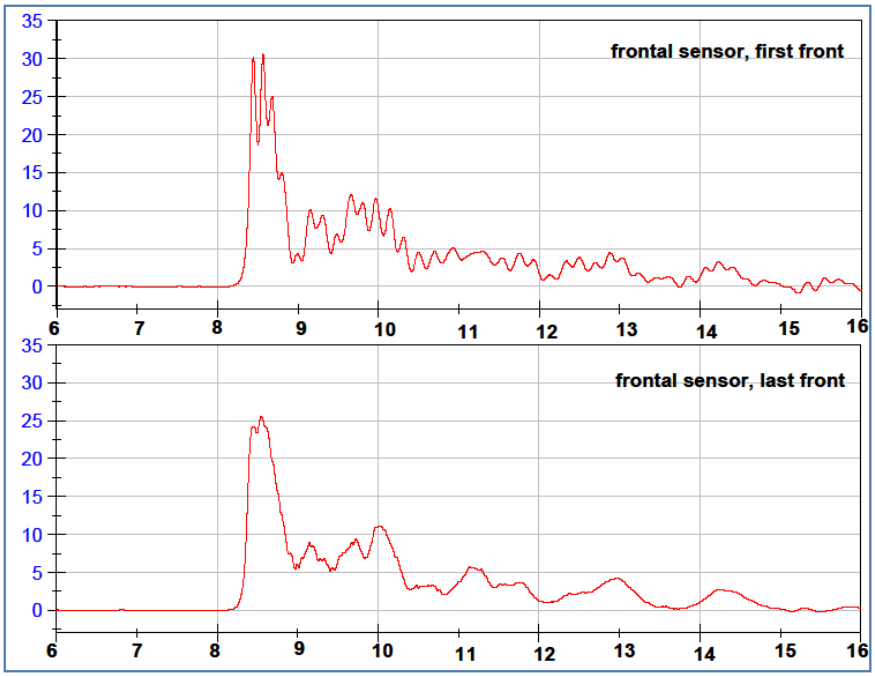

FRONTAL FILTERED DATA

Comparison for reproducibility of each pressure sensor in Front Orientation at 10psi 7mm Intact Sphere

OCCIPITAL FILTERED DATA

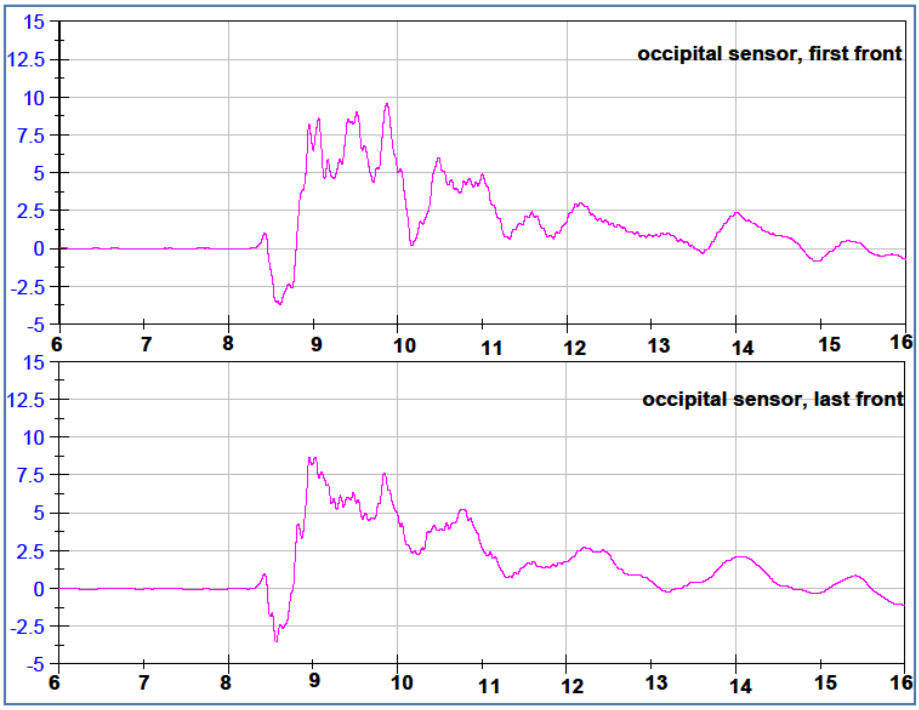

Comparison for reproducibility of each pressure sensor in Front Orientation at 12psi
7mm Intact Sphere

VENTRICLE FILTERED DATA

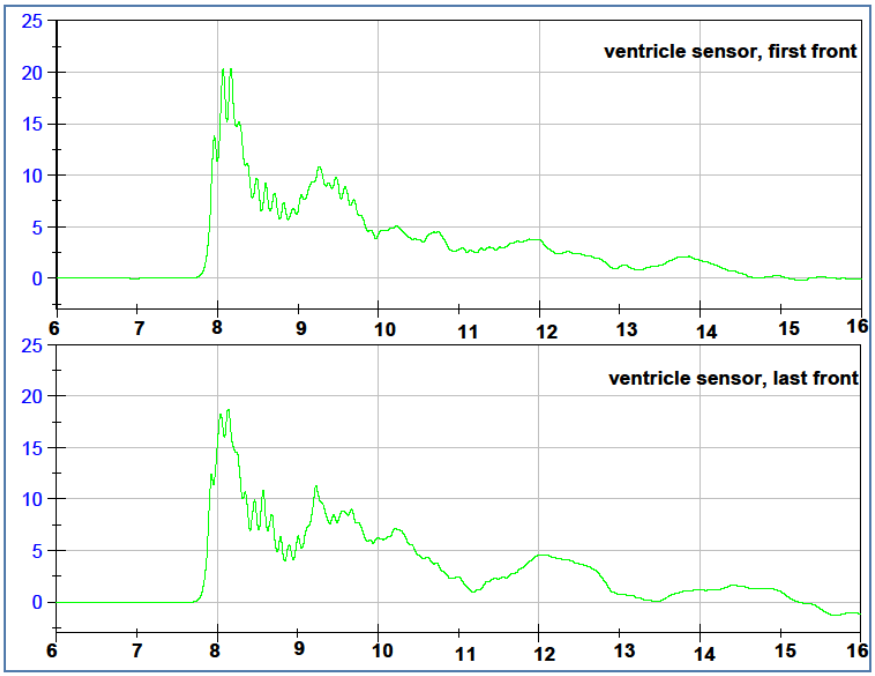

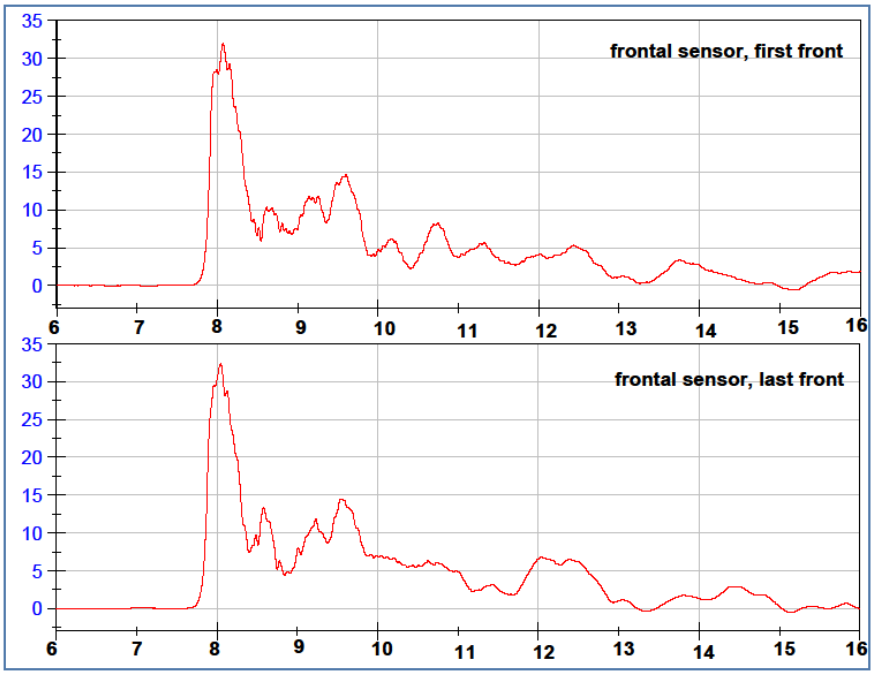

FRONTAL FILTERED DATA

Comparison for reproducibility of each pressure sensor in Front Orientation at 12psi 7mm Intact Sphere

OCCIPITAL FILTERED DATA

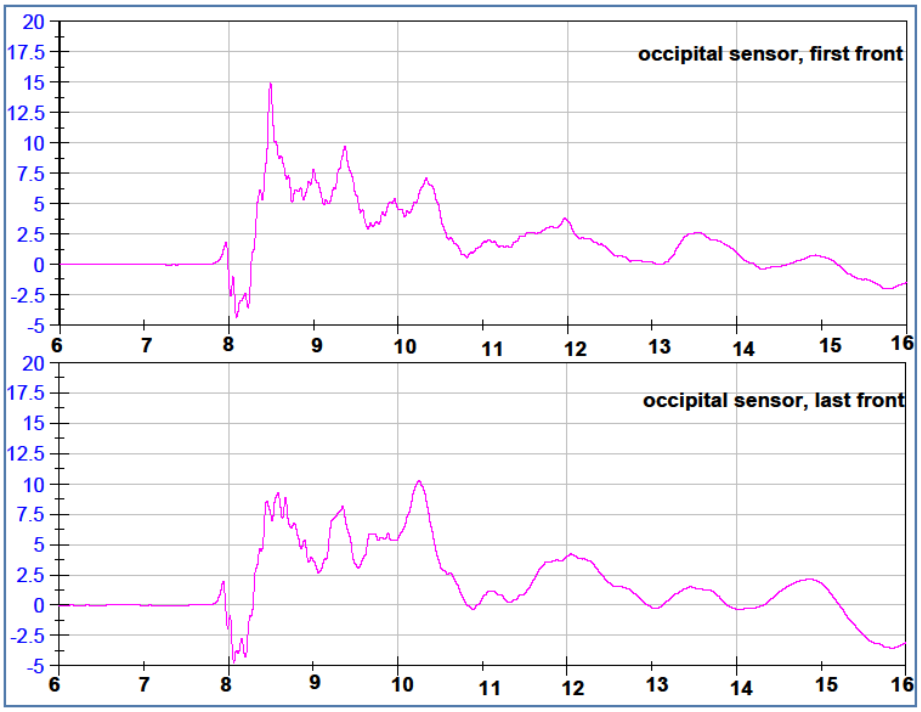

Comparison for reproducibility of each pressure sensor in Front Orientation at 15psi 7mm Intact Sphere

VENTRICLE FILTERED DATA

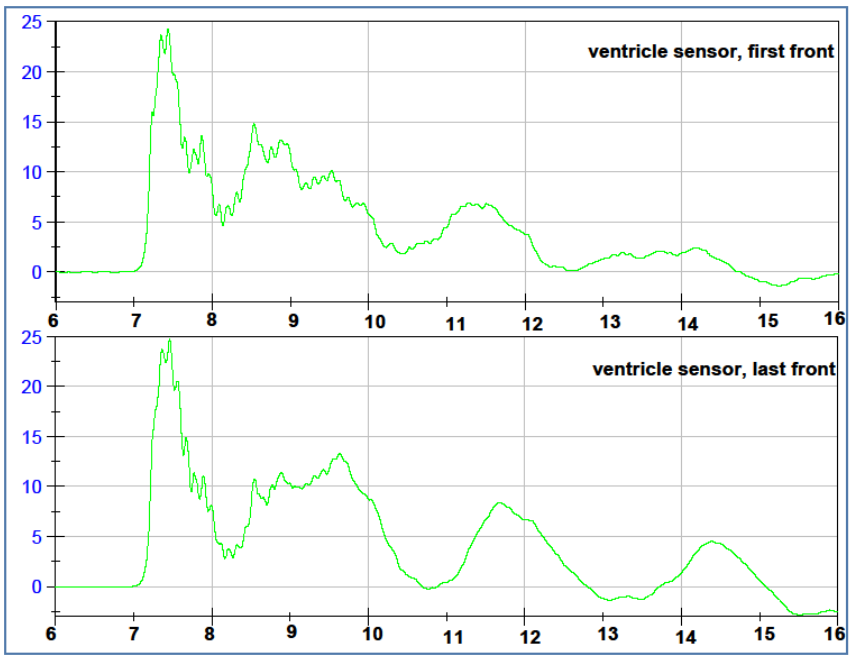

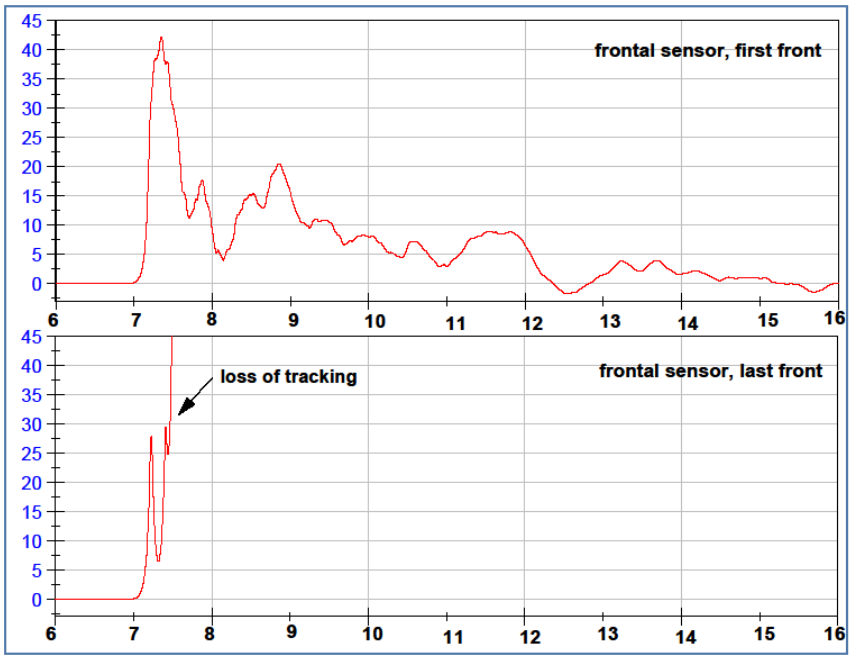

FRONTAL FILTERED DATA

Comparison for reproducibility of each pressure sensor in Front Orientation at 15psi 7mm Intact Sphere

OCCIPITAL FILTERED DATA

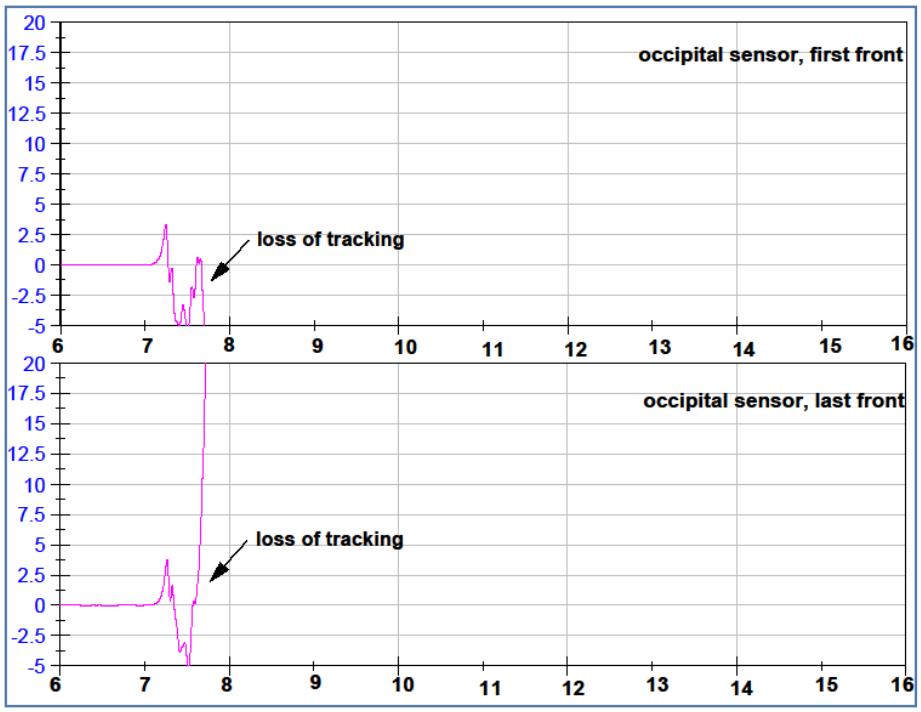

Frontal Sensor, 4 Orientations, Filtered Data, 7mm Intact Sphere

10 PSI

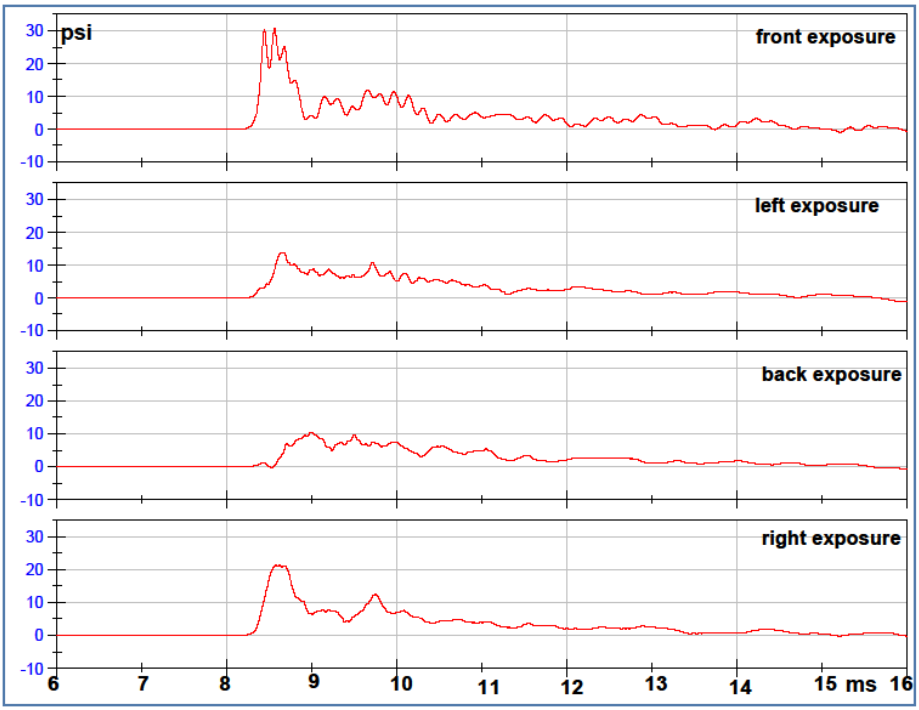

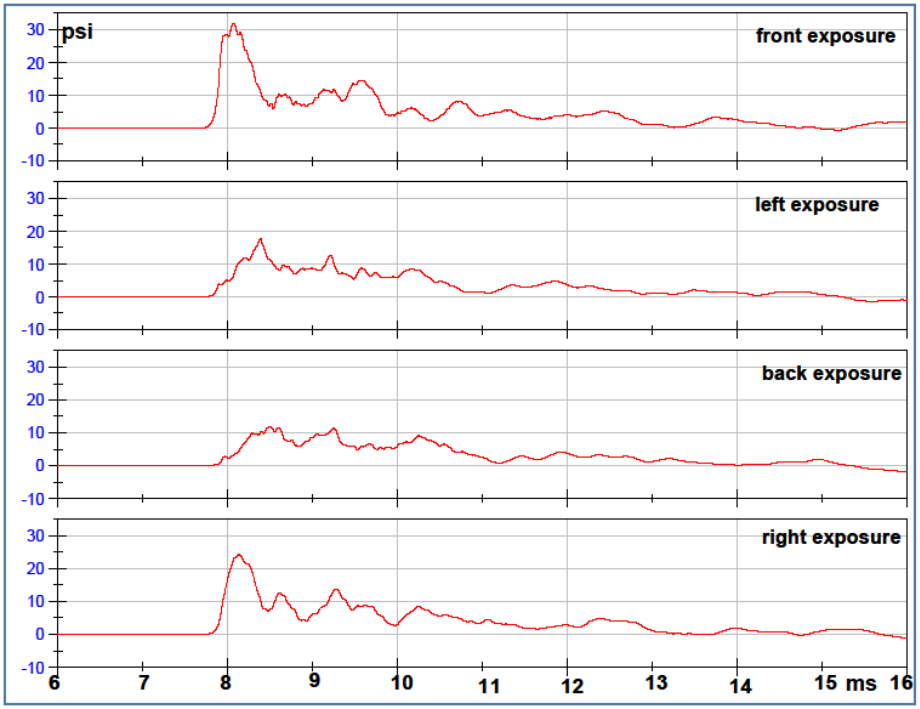

12 PSI

Frontal Sensor, 4 Orientations, Filtered Data, 7mm Intact Sphere

15 PSI

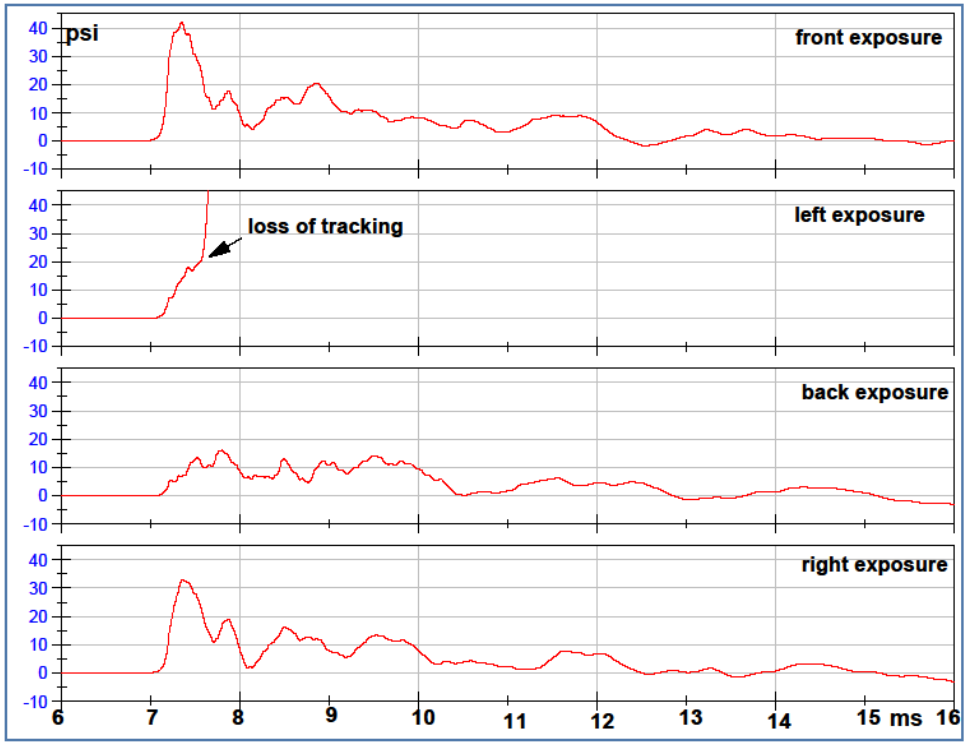

Ventricle Sensor, 4 Orientations, Filtered Data, 7mm Intact Sphere

10 PSI

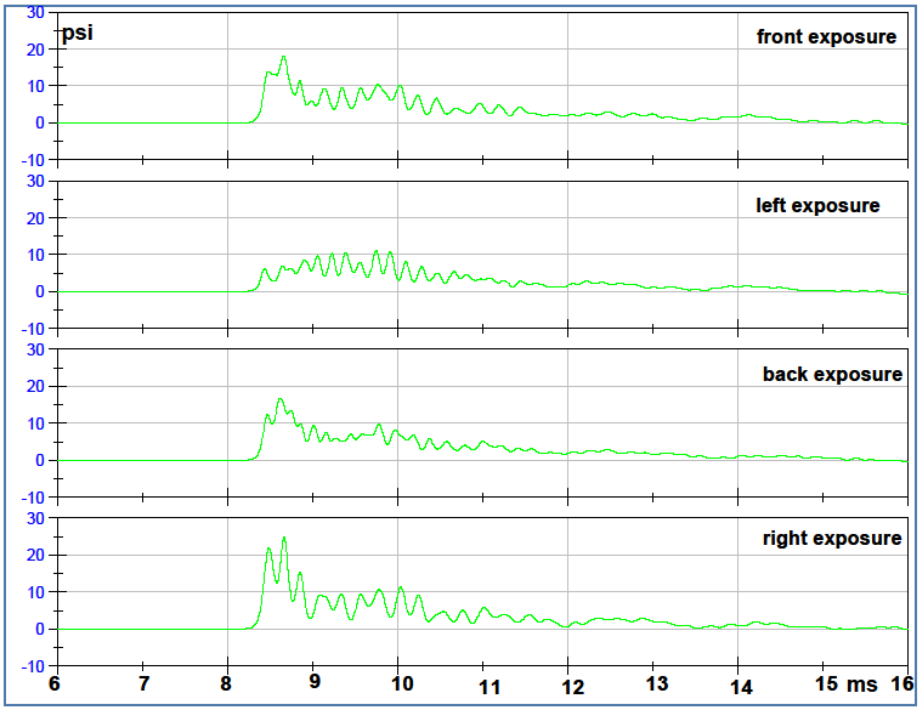

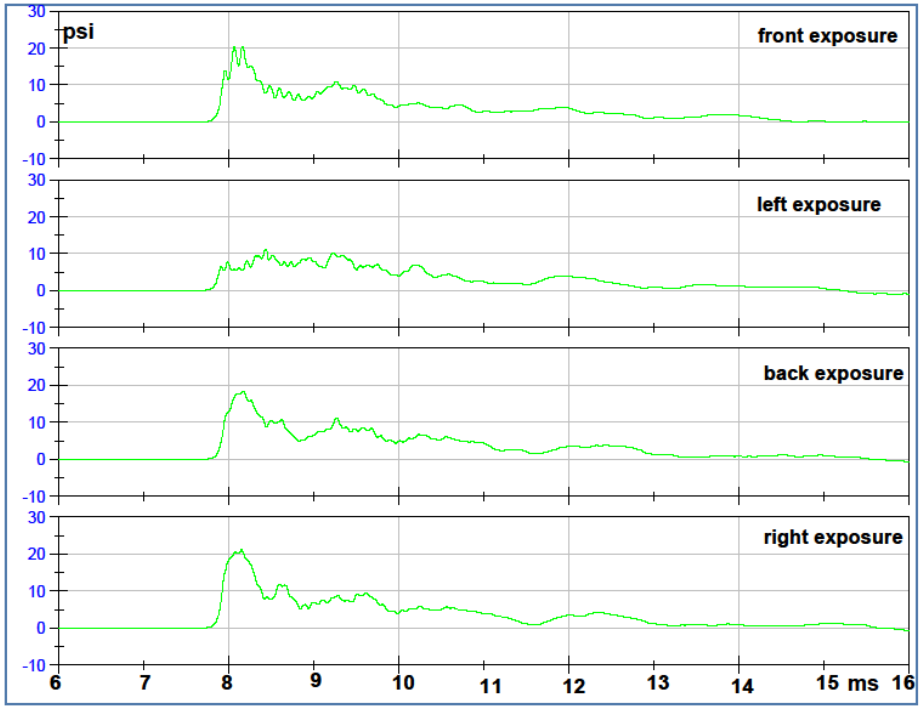

12 PSI

Ventricle Sensor, 4 Orientations, Filtered Data, 7mm Intact Sphere

15 PSI

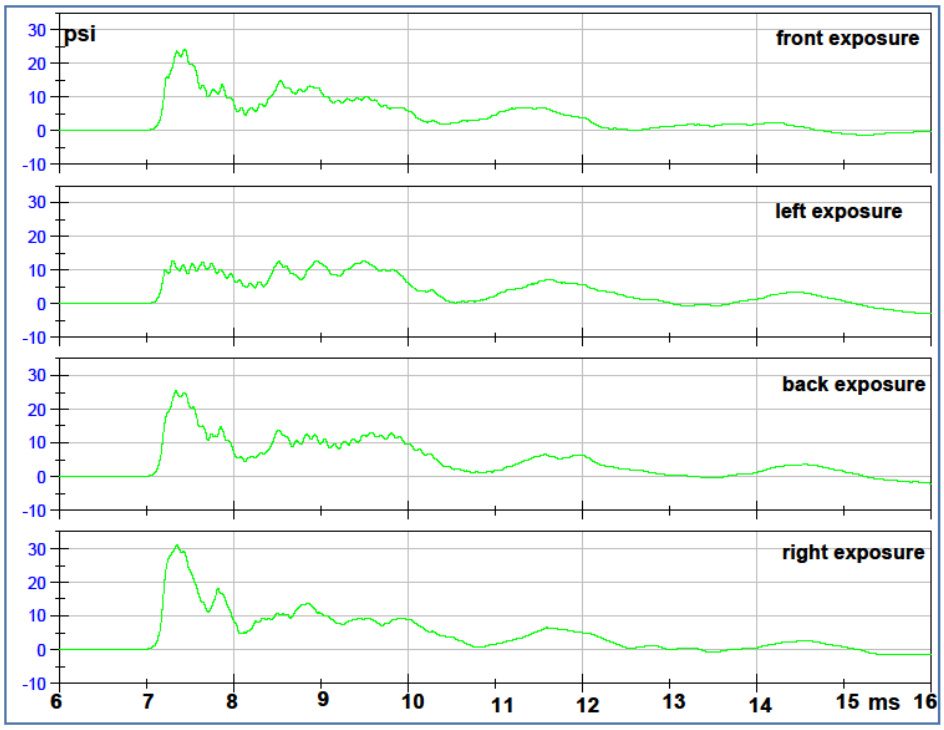

Occipital Sensor, 4 Orientations, Filtered Data, 7mm Intact Sphere

10 PSI

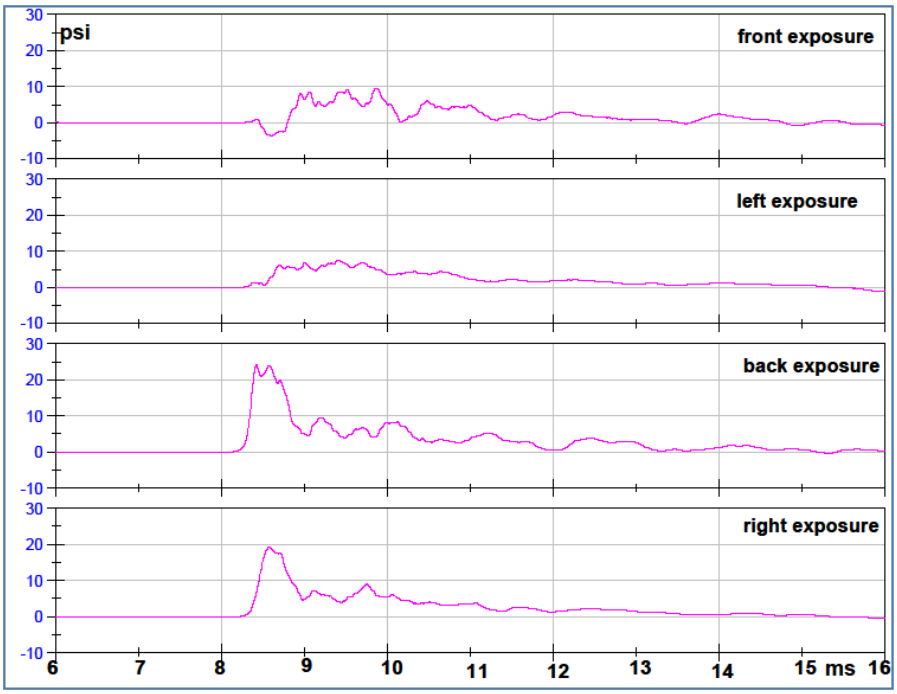

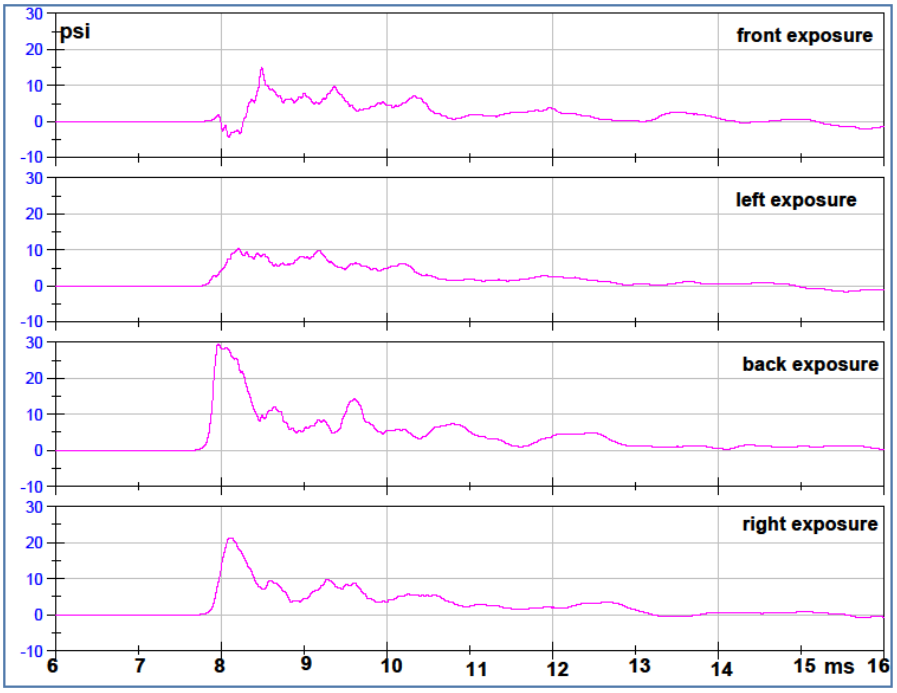

12 PSI

Occipital Sensor, 4 Orientations, Filtered Data, 7mm Intact Sphere

15 PSI

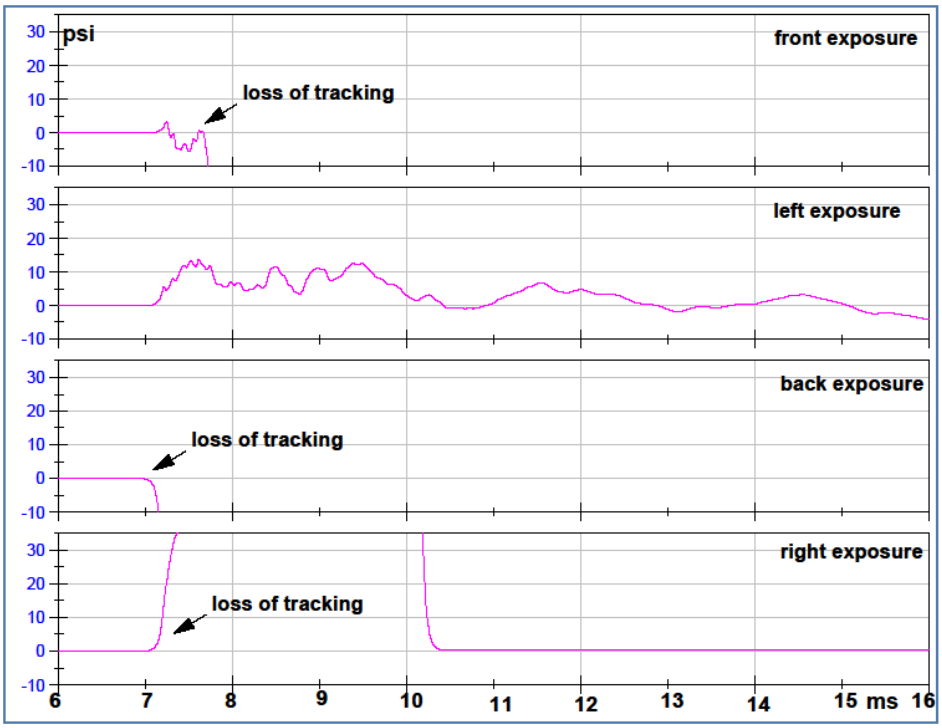

Pressure extremes for intact sphere 7mm

Pressure Extremes for Intact Sphere 7mm										
	Maximun Pressure					Minimum Pressure				
ventricle	front 1	right	back	left	front 2	front 1	right	back	left	front 2
10 psi air	**18.2**	**24.8**	**16.9**	**11.0**	**16.9**	**0.18**	**0.13**	**0.19**	**0.16**	**0.10**
12 psi air	**20.3**	**21.2**	**18.3**	**11.1**	**18.7**	**0.12**	**0.20**	**0.25**	**0.19**	**0.08**
15 psi air	**24.3**	**31.1**	**25.3**	**12.7**	**24.7**	**0.19**	**-0.79**	**-0.38**	**-0.65**	**-1.33**
frontal	front 1	right	back	left	front 2	front 1	right	back	left	front 2
10 psi air	**30.7**	**21.5**	**10.5**	**13.7**	**25.5**	**0.13**	**0.19**	**-0.28**	**0.20**	**0.10**
12 psi air	**31.9**	**24.4**	**11.8**	**17.9**	**32.3**	**0.11**	**-0.23**	**0.19**	**0.21**	**-0.39**
15 psi air	**42.0**	**33.1**	**16.0**	**NA**	**NA**	**-1.74**	**-1.50**	**-1.49**	**NA**	**NA**
occipital	front 1	right	back	left	front 2	front 1	right	back	left	front 2
10 psi air	**9.6**	**19.3**	**24.0**	**7.4**	**8.7**	**-3.68**	**0.15**	**0.21**	**0.12**	**-3.50**
12 psi air	**14.9**	**29.4**	**29.5**	**10.3**	**10.3**	**-4.36**	**-0.54**	**0.24**	**0.12**	**-4.63**
15 psi air	**NA**	**NA**	**NA**	**13.4**	**NA**	**NA**	**NA**	**NA**	**-1.69**	**NA**

1st rate of change of pressure for 7mm-thick sphere.

1st rate (psi/ms)					
ventricle	front 1	right	back	left	front 2
10 psi air	**66.8**	**88.1**	**60.2**	**36.8**	**59.6**
12 psi air	**69.1**	**64.1**	**59.3**	**40.9**	**68.3**
15 psi air	**82.2**	**94.2**	**81.7**	**66.4**	**81.5**
frontal	front 1	right	back	left	front 2
10 psi air	**127.0**	**64.3**	**10.2**	**34.9**	**98.3**
12 psi air	**122.7**	**71.0**	**20.5**	**31.6**	**109.8**
15 psi air	**152.6**	**100.2**	**37.9**	**NA**	**NA**
occipital	front 1	right	back	left	front 2
10 psi air	**10.7**	**58.3**	**100.8**	**11.5**	**10.2**
12 psi air	**16.6**	**66.8**	**130.4**	**21.5**	**17.5**
15 psi air	**26.4**	**NA**	**NA**	**34.1**	**26.7**

Comparisons of 1st rate of change of pressure in the 7mm-thick sphere with holes relative to the intact sphere.

The number is expressed in percentage of the intact sphere results for each test. Positive numbers mean higher rates in the intact sphere.

Percentages of Rate of Change of Pressure for 7mm-thick sphere with holes relative to intact sphere					
ventricle	front 1	right	back	left	front 2
10 psi air	**12%**	**23%**	**9%**	**0%**	**22%**
12 psi air	**20%**	**-12%**	**3%**	**-8%**	**26%**
15 psi air	**-15%**	**-19%**	**-3%**	**18%**	**-9%**
frontal	front 1	right	back	left	front 2
10 psi air	**28%**	**-13%**	**-201%**	**2%**	**18%**
12 psi air	**19%**	**-23%**	**-53%**	**-13%**	**16%**
15 psi air	**NA**	**-9%**	**-12%**	**NA**	**NA**
occipital	front 1	right	back	left	front 2
10 psi air	**-61%**	**-9%**	**-5%**	**-73%**	**-60%**
12 psi air	**-40%**	**-27%**	**4%**	**-79%**	**-19%**
15 psi air	**-29%**	**NA**	**NA**	**-22%**	**-13%**

Percentages of peak internal pressure changes in 7 mm sphere intact and with apertures, based on the cell value at the 10 psi air overpressure for each orientation.

		PERCENTAGES for sphere 7mm					PERCENTAGES for sphere 7mm with holes				
AIR		Percentage Increase in Maximun Peak Pressure					Percentage Increase in Maximun Peak Pressure				
Overpressure		front 1	right	back	left	front 2	front 1	right	back	left	front 2
ventricle	20%	12%	-14%	9%	2%	10%	3%	17%	12%	12%	23%
ventricle	50%	34%	26%	50%	15%	46%	59%	64%	56%	43%	77%
frontal	20%	4%	13%	12%	30%	27%	7%	14%	13%	12%	24%
frontal	50%	37%	54%	52%	NA	NA	NA	53%	38%	45%	67%
occipital	20%	55%	53%	23%	40%	19%	10%	20%	21%	30%	4%
occipital	50%	NA	NA	NA	82%	NA	21%	67%	NA	69%	21%

Maximum peak pressure increase in the 7mm-thick sphere with holes relative to the intact sphere.

The number is expressed in percentage of the intact sphere results for each test. Positive numbers mean higher pressure in the intact sphere.

Percentage of Relative Maximum Peak Pressure Increase					
7mm-sphere with holes in respect to 7mm-sphere					
ventricle	front 1	right	back	left	front 2
10 psi air	**-4%**	**15%**	**-8%**	**-28%**	**7%**
12 psi air	**5%**	**-15%**	**-11%**	**-42%**	**-3%**
15 psi air	**-23%**	**-10%**	**-12%**	**-59%**	**-12%**
frontal	front 1	right	back	left	front 2
10 psi air	**3%**	**-13%**	**-43%**	**-15%**	**-2%**
12 psi air	**0%**	**-14%**	**-45%**	**1%**	**0%**
15 psi air	**NA**	**-13%**	**-30%**	**NA**	**NA**
occipital	front 1	right	back	left	front 2
10 psi air	**-57%**	**-8%**	**-11%**	**-71%**	**-72%**
12 psi air	**-11%**	**15%**	**-9%**	**-59%**	**-51%**
15 psi air	**NA**	**NA**	**NA**	**-58%**	**NA**

Table of Differential Pressure Results for 7mm Intact Sphere

Differential for sphere 7mm										
	peak differential pressure (psi)					time elapsed between peaks (ms)				
ventricle	front 1	right	back	left	front 2	front 1	right	back	left	front 2
10 psi air	**18.0**	**24.6**	**16.6**	**10.8**	**16.8**	**0.39**	**0.42**	**0.34**	**1.48**	**0.32**
12 psi air	**20.2**	**21.0**	**18.1**	**11.0**	**18.6**	**0.31**	**0.38**	**0.38**	**0.68**	**0.40**
15 psi air	**24.1**	**31.9**	**25.7**	**13.3**	**26.0**	**0.40**	**6.13**	**6.16**	**4.23**	**5.61**
frontal	front 1	right	back	left	front 2	front 1	right	back	left	front 2
10 psi air	**30.5**	**21.3**	**10.8**	**13.5**	**25.4**	**0.35**	**0.38**	**0.46**	**0.39**	**0.36**
12 psi air	**31.8**	**24.6**	**11.6**	**17.7**	**32.7**	**0.35**	**6.59**	**0.64**	**0.61**	**5.29**
15 psi air	**43.8**	**34.6**	**17.5**	**NA**	**NA**	**5.19**	**6.22**	**5.22**	**NA**	**NA**
occipital	front 1	right	back	left	NA	front 1	right	back	left	front 2
10 psi air	**13.3**	**19.1**	**23.8**	**7.3**	**12.2**	**1.26**	**0.33**	**0.24**	**1.12**	**0.40**
12 psi air	**19.2**	**22.0**	**29.2**	**10.2**	**14.9**	**0.40**	**5.24**	**0.22**	**0.42**	**2.18**
15 psi air	**NA**	**NA**	**NA**	**15.1**	**NA**	**NA**	**NA**	**NA**	**5.47**	**NA**

Percentages of 1st rate of internal pressure changes in 7mm intact sphere based on the cell value at the 10 psi air overpressure for each orientation.

AIR		Percentage 1st Rate Pressure Change				
Overpressure		front 1	right	back	left	front 2
ventricle	20%	3%	-27%	-2%	11%	15%
ventricle	50%	23%	7%	36%	80%	37%
frontal	20%	-3%	10%	101%	-10%	12%
frontal	50%	20%	56%	272%	NA	NA
occipital	20%	56%	14%	29%	87%	71%
occipital	50%	148%	NA	NA	196%	161%

State of Gages during Testing of the 7mm Intact Sphere

	Strain status for sphere 5mm				
Frontal	front 1	right	back	left	front 2
10 psi air					
12 psi air					
15 psi air					
Left	front 1	right	back	left	front 2
10 psi air					
12 psi air					
15 psi air					
Right	front 1	right	back	left	front 2
10 psi air					
12 psi air					
15 psi air					
Occipital	front 1	right	back	left	front 2
10 psi air					
12 psi air					
15 psi air					

	working
	signal problems
	not working

Strain Data

Test 1 Front 1 Orientation 7mm Intact Sphere

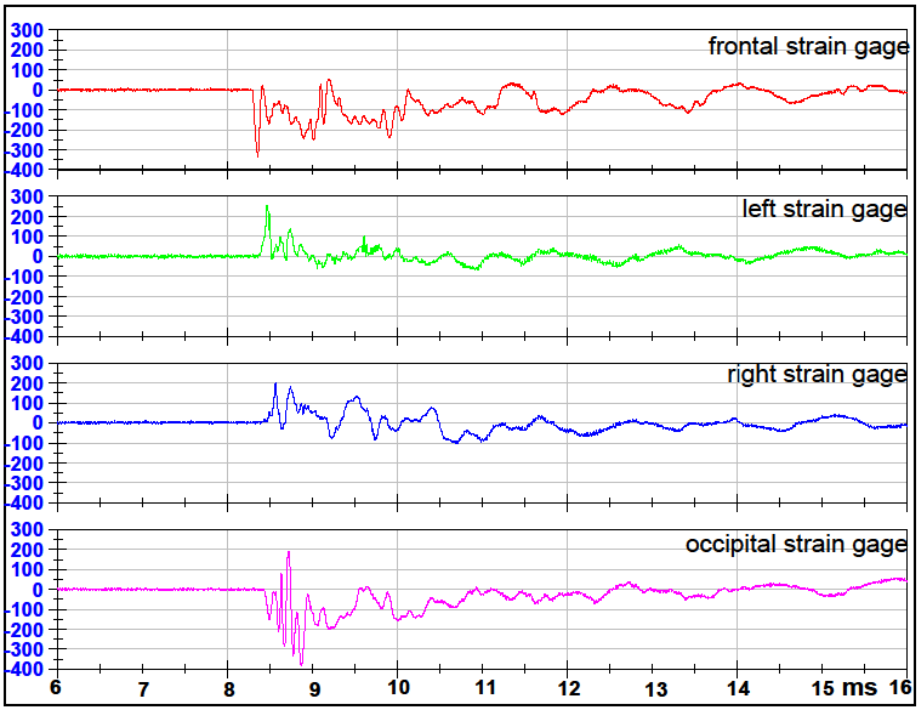

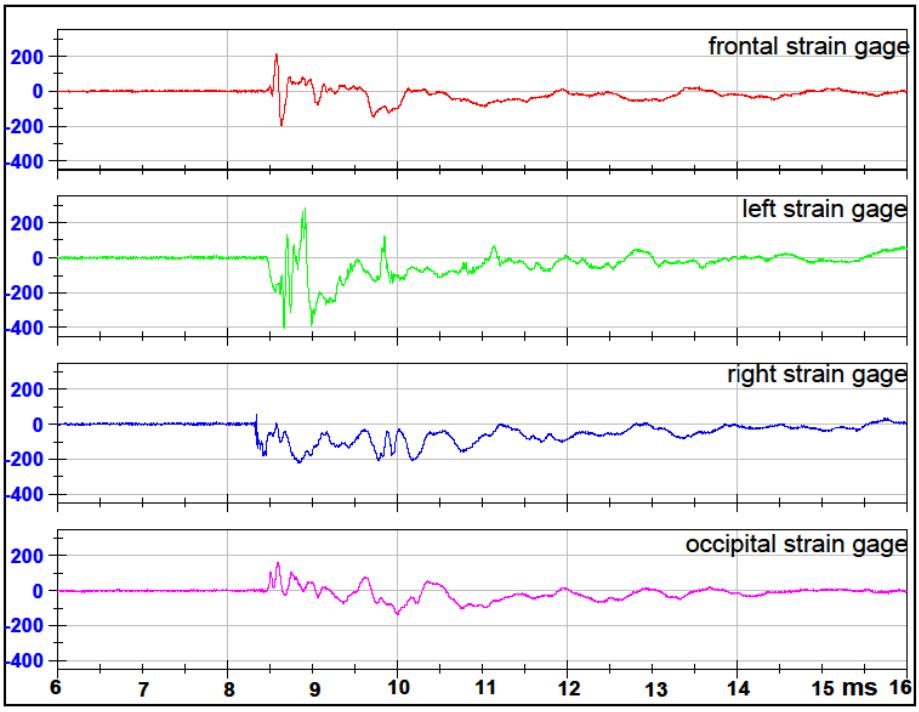

Test 2 Right Orientation 7mm Intact Sphere

Test 3 Back Orientation 7mm Intact Sphere

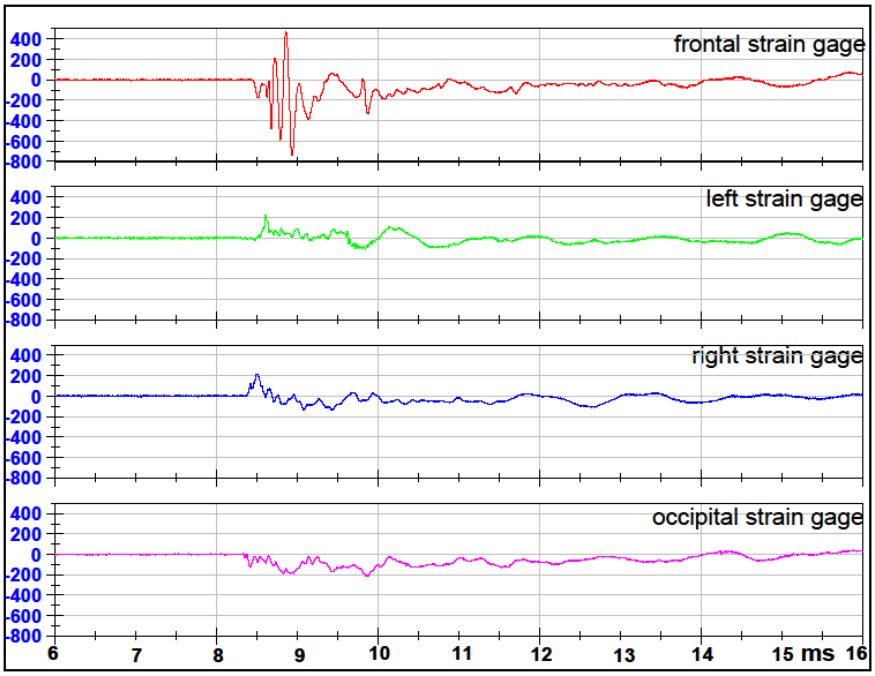

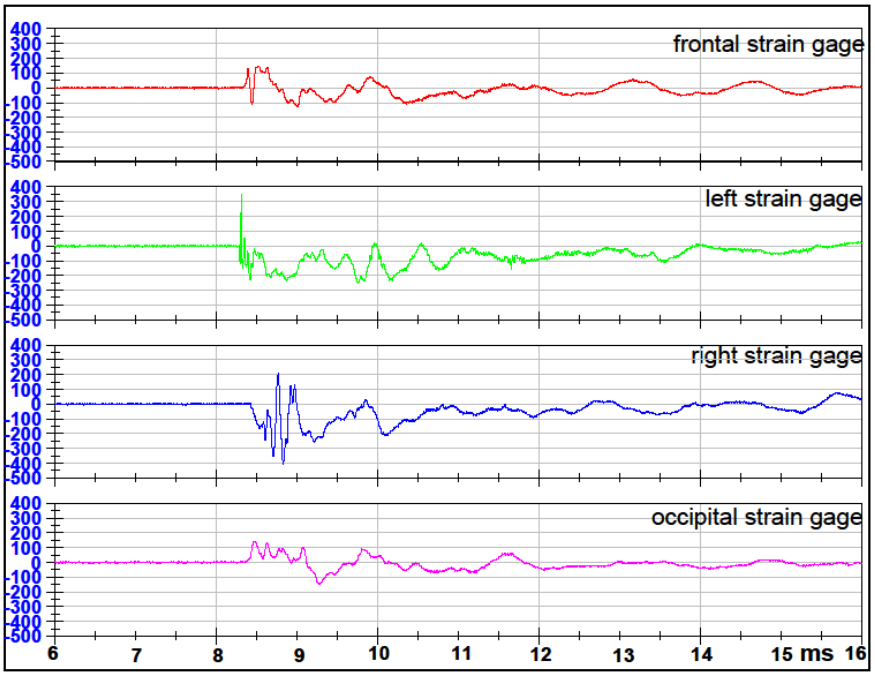

Test 4 Left Orientation 7mm Intact Sphere

Test 5 Front 2 Orientation 7mm Intact Sphere

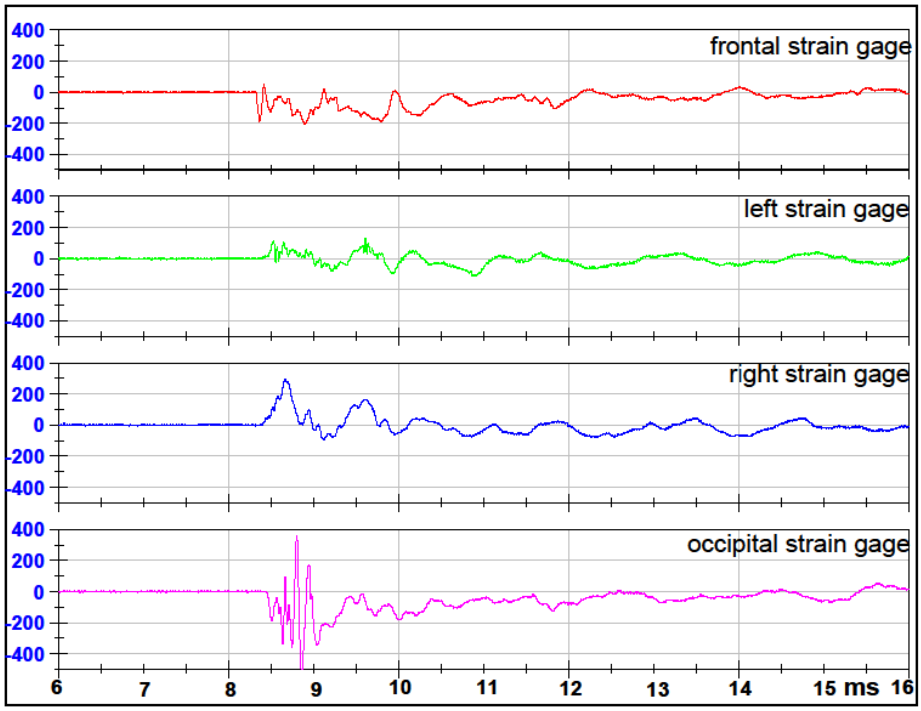

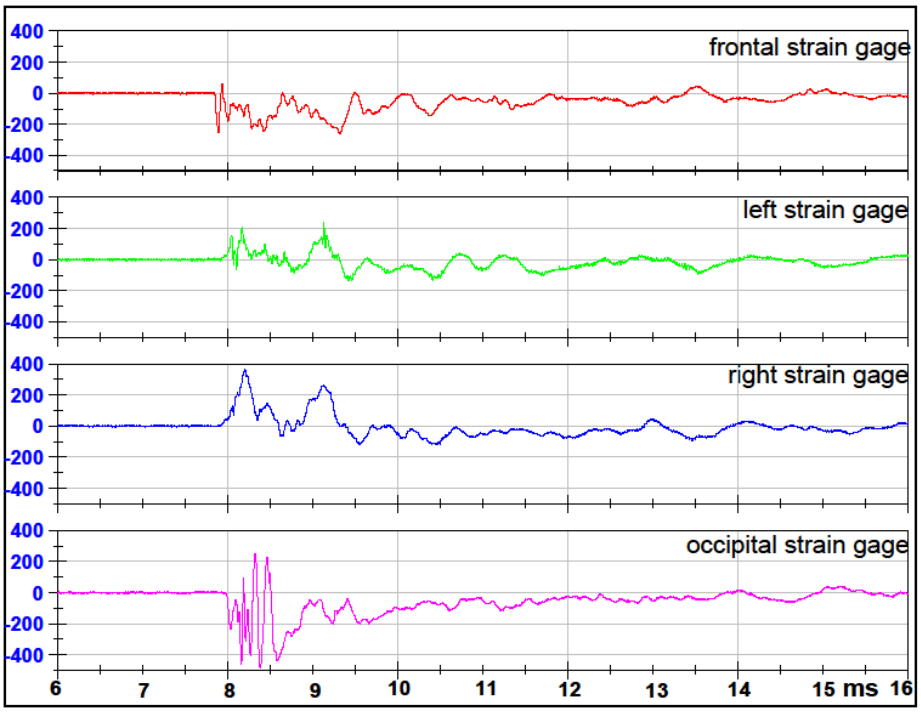

Test 6 Front 1 Orientation 7mm Intact Sphere

Test 7 Left Orientation 7mm Intact Sphere

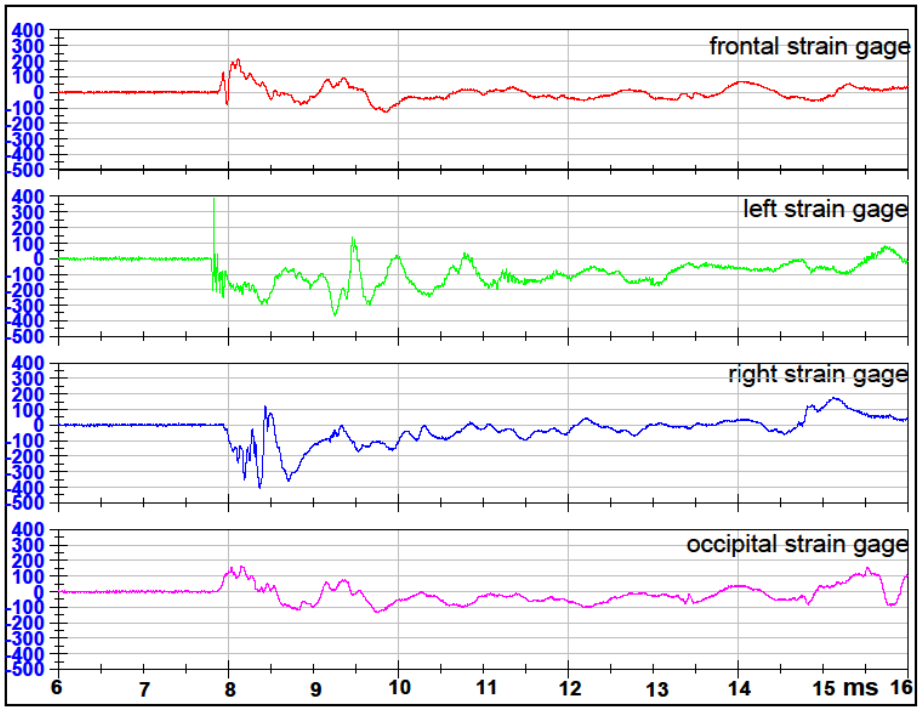

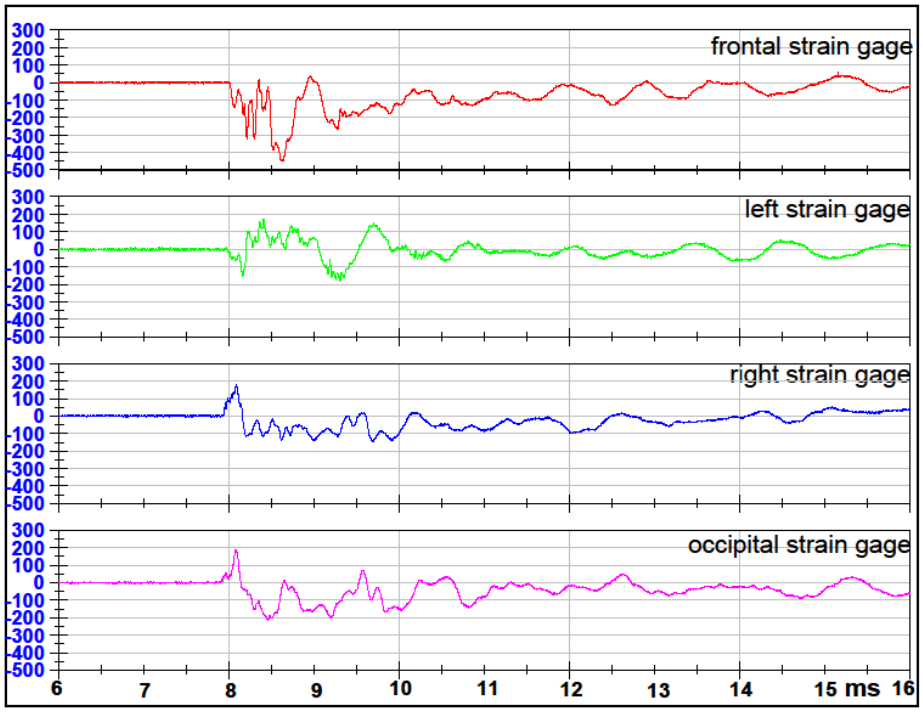

Test 8 Back Orientation 7mm Intact Sphere

Test 9 Right Orientation 7mm Intact Sphere

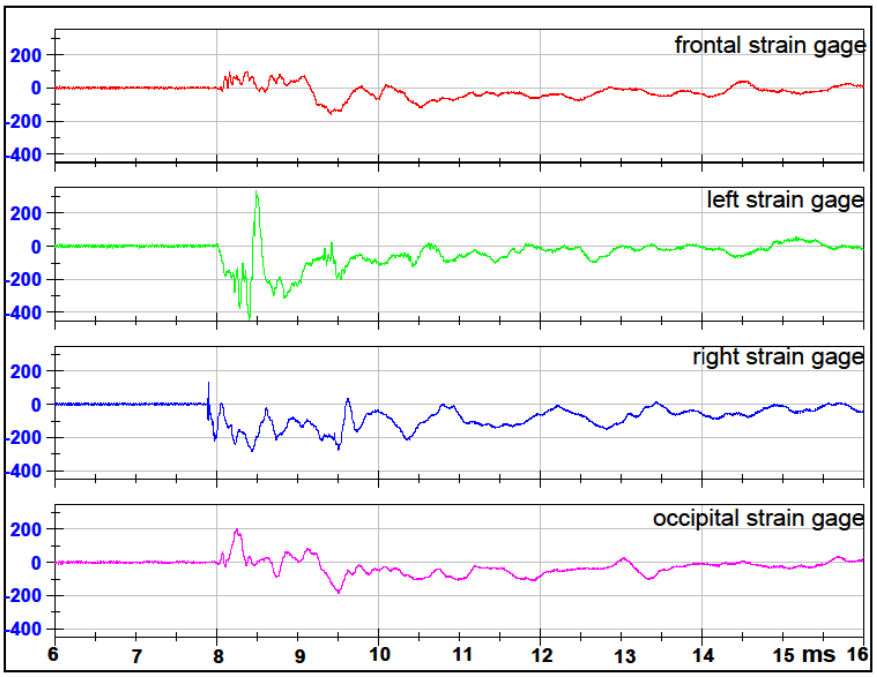

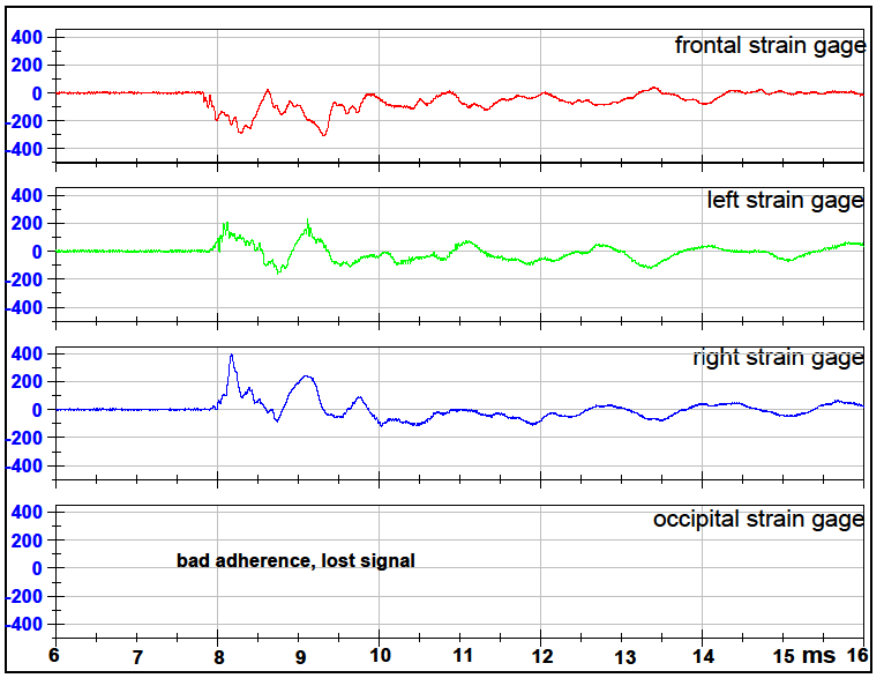

Test 10 Front 2 Orientation 7mm Intact Sphere

Test 11 Front 1 Orientation 7mm Intact Sphere

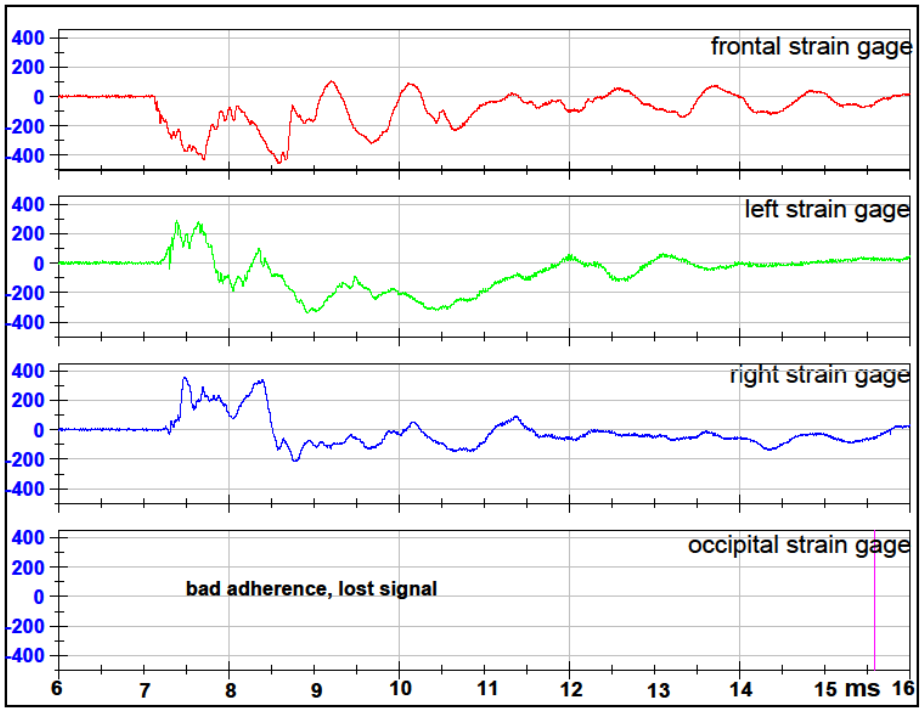

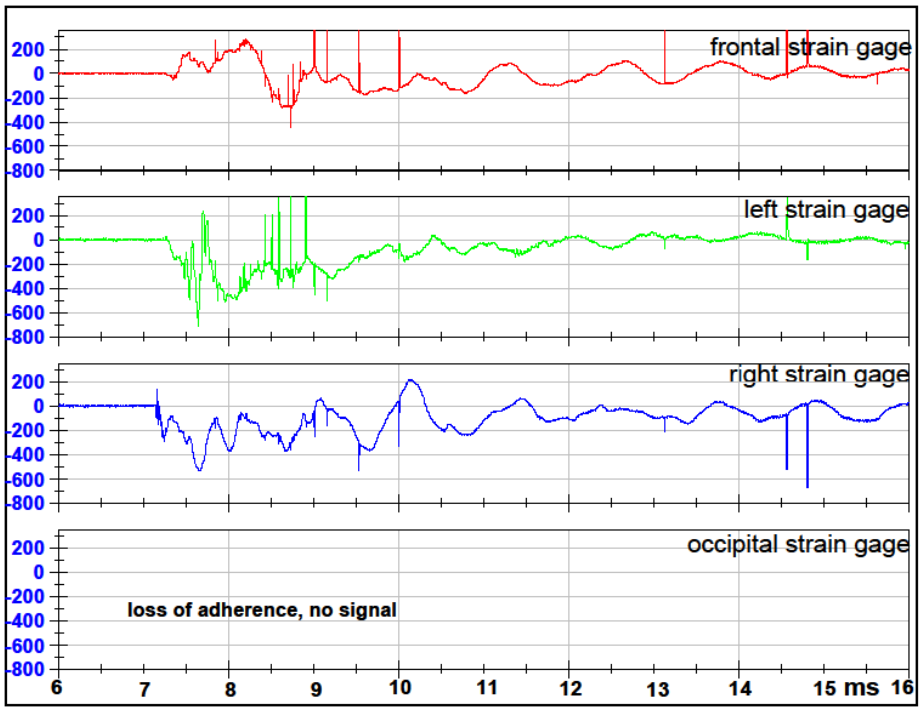

Test 12 Right Orientation 7mm Intact Sphere

Test 13 Back Orientation 7mm Intact Sphere

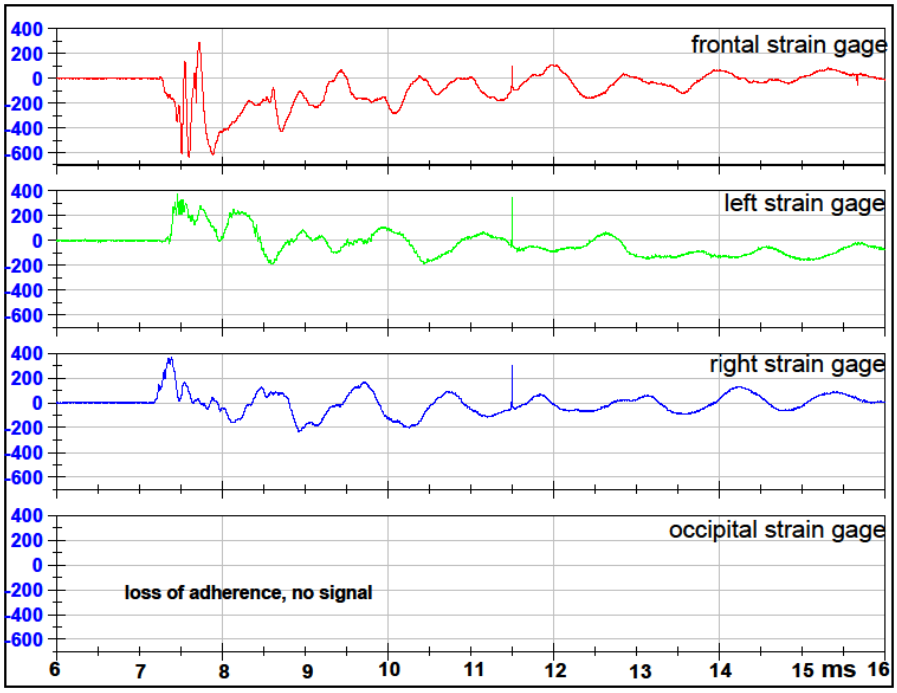

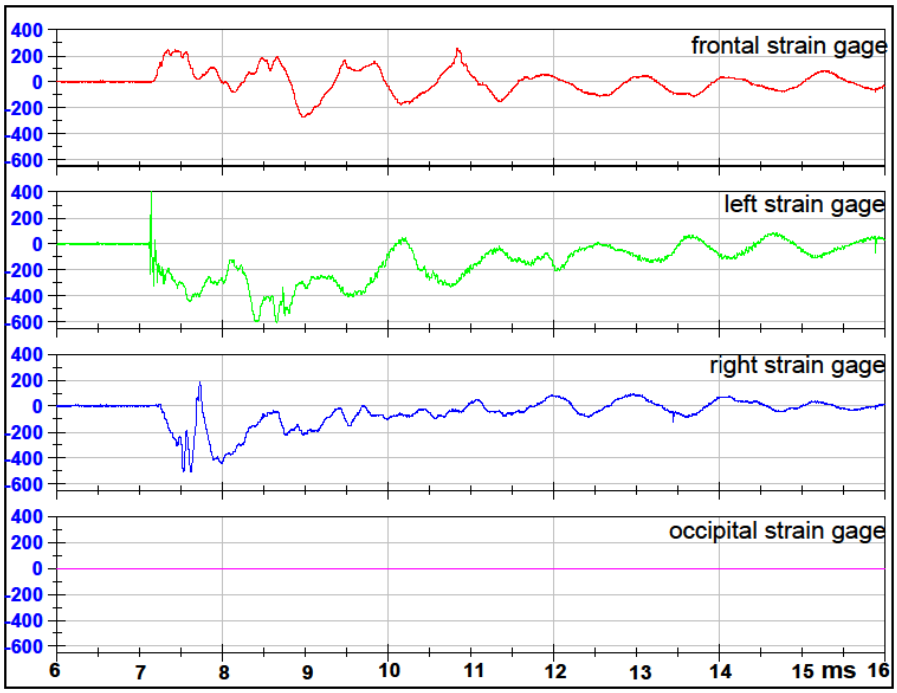

Test 14 Left Orientation 7mm Intact Sphere

Test 15 Front 2 Orientation 7mm Intact Sphere

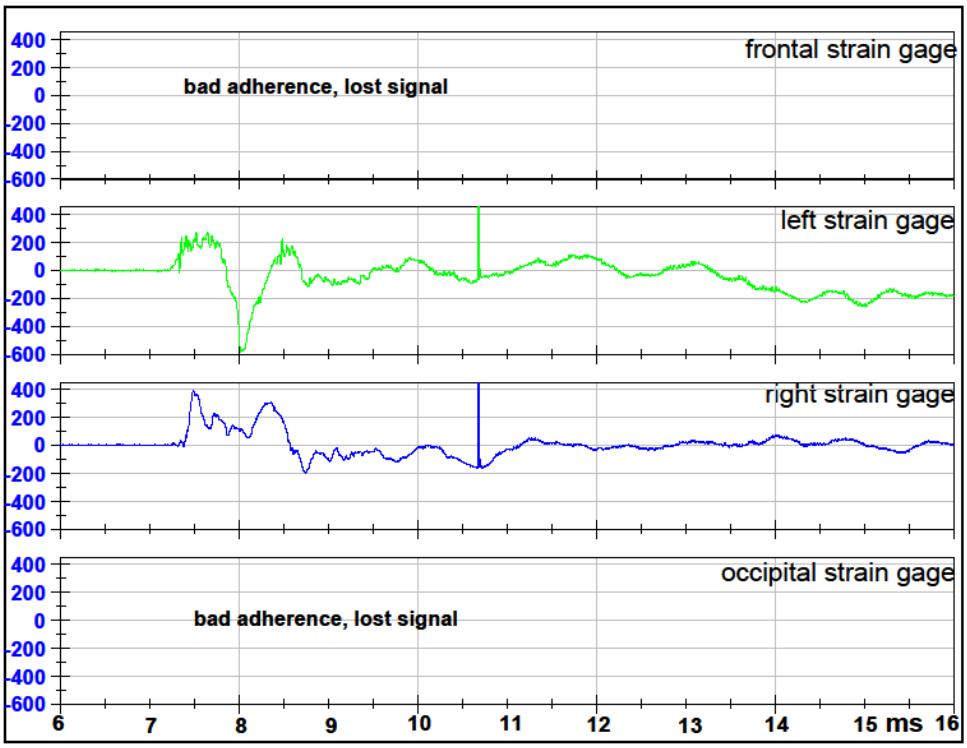

Results after the introduction of Apertures

Test 1 Front 1 Orientation 7mm Sphere with Holes

FILTERED DATA

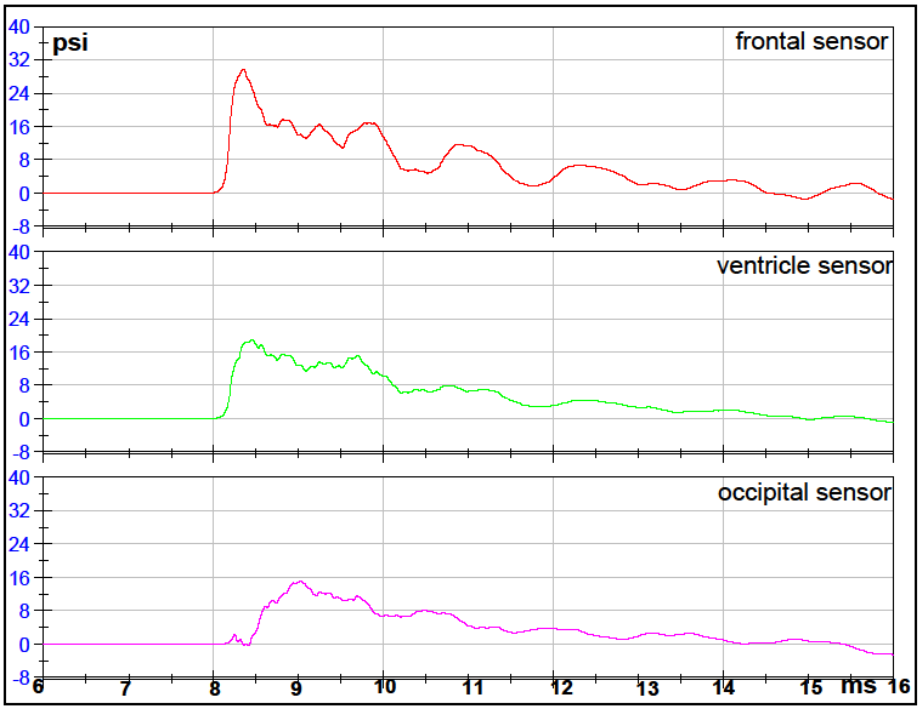

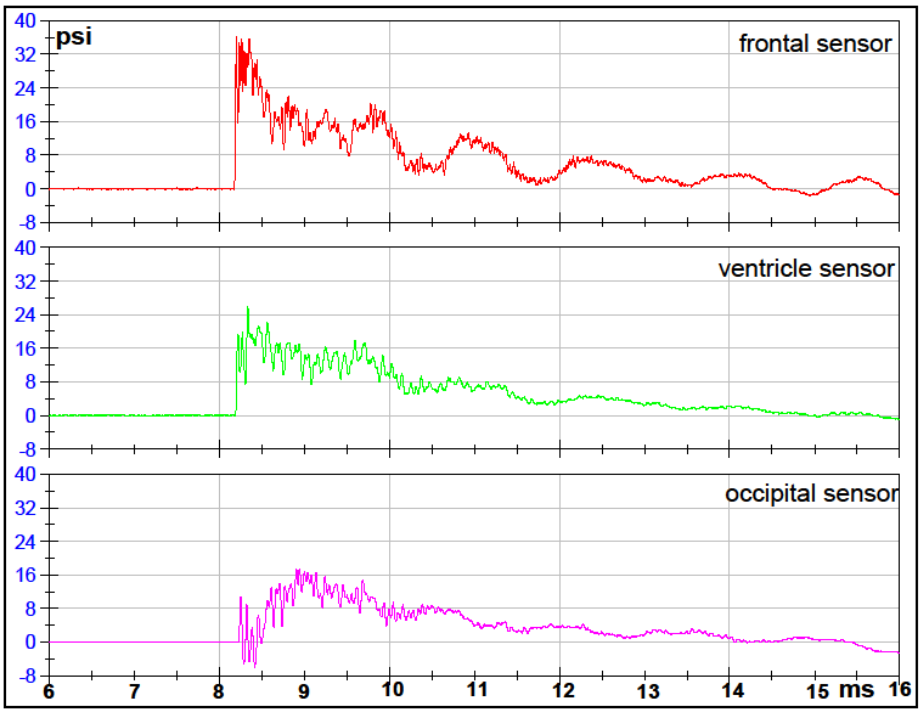

RAW DATA

Test 2 Right Orientation 7mm Sphere with Holes

FILTERED DATA

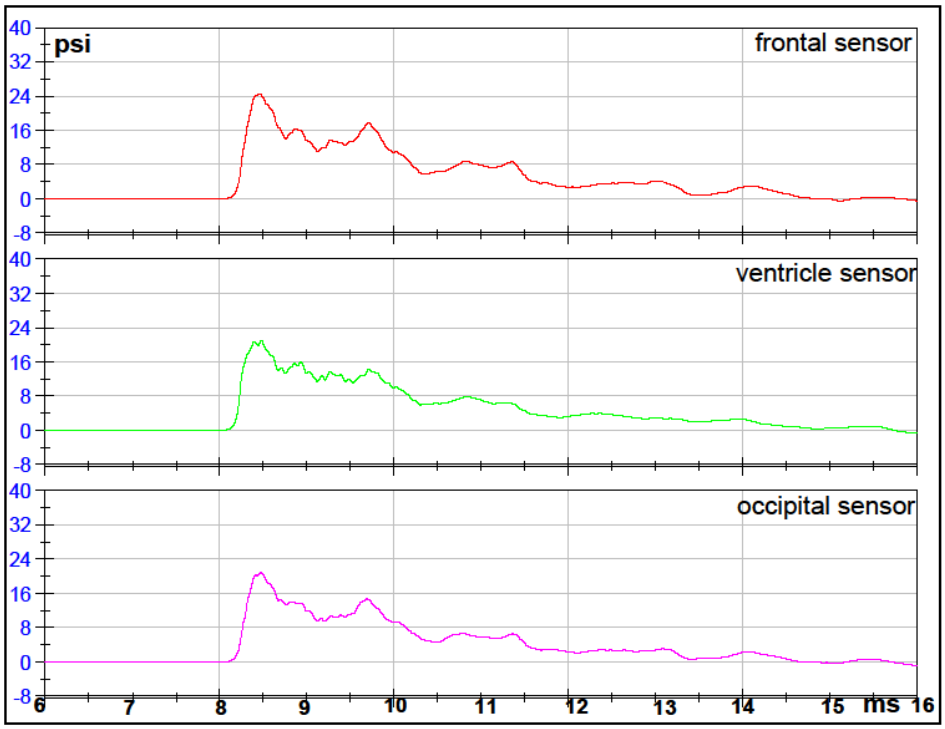

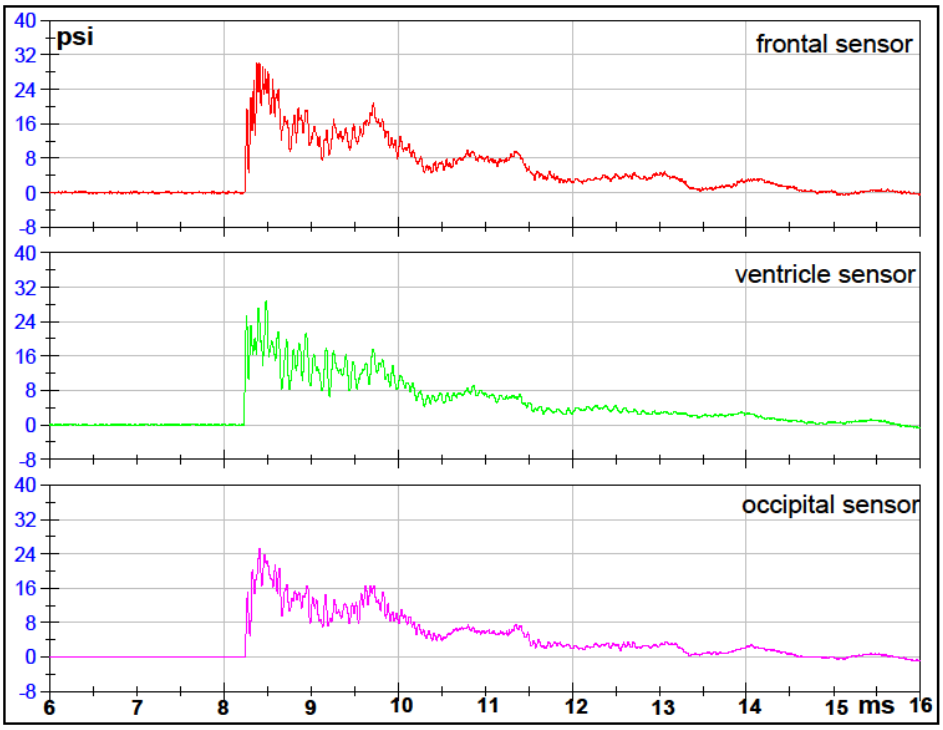

RAW DATA

Test 3 Back Orientation 7mm Sphere with Holes

FILTERED DATA

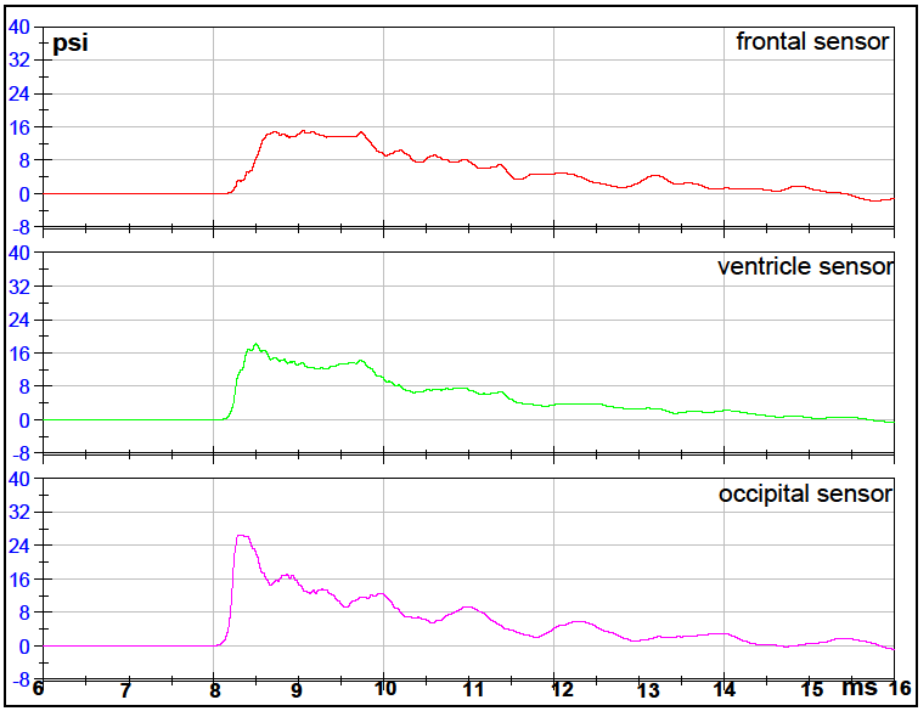

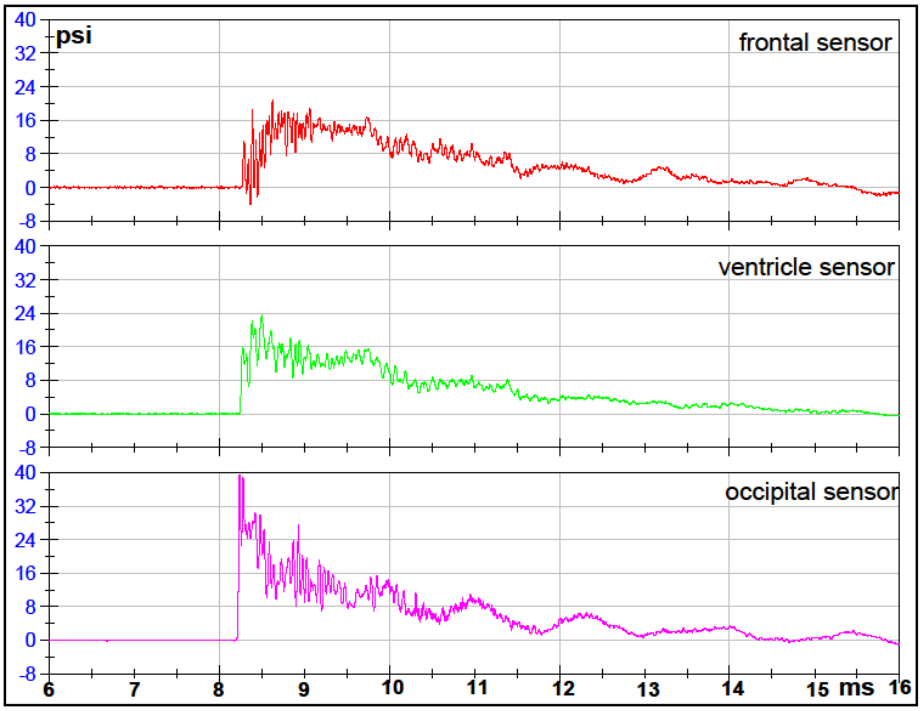

RAW DATA

Test 4 Left Orientation 7mm Sphere with Holes

FILTERED DATA

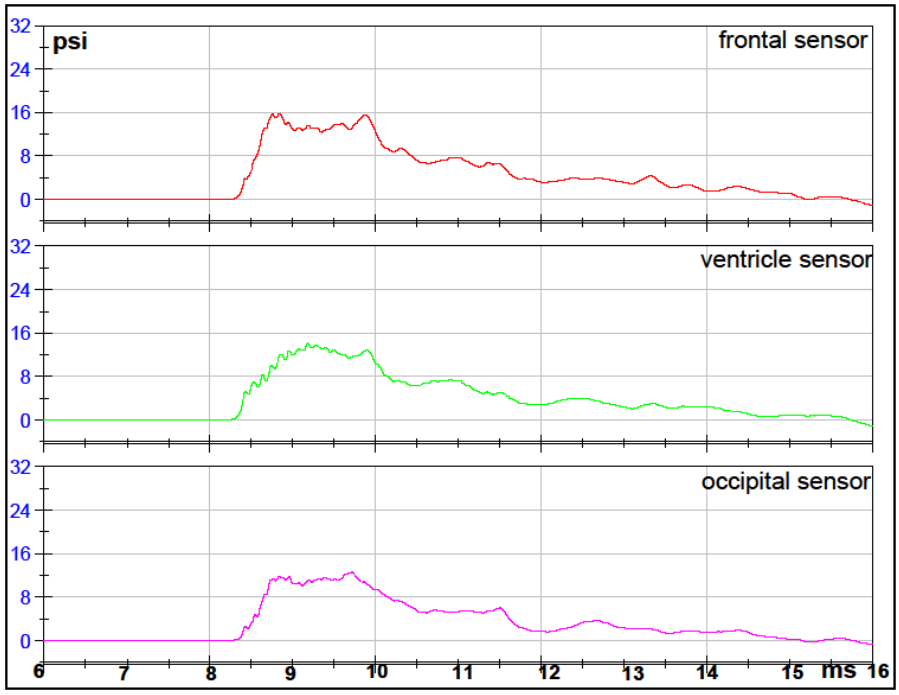

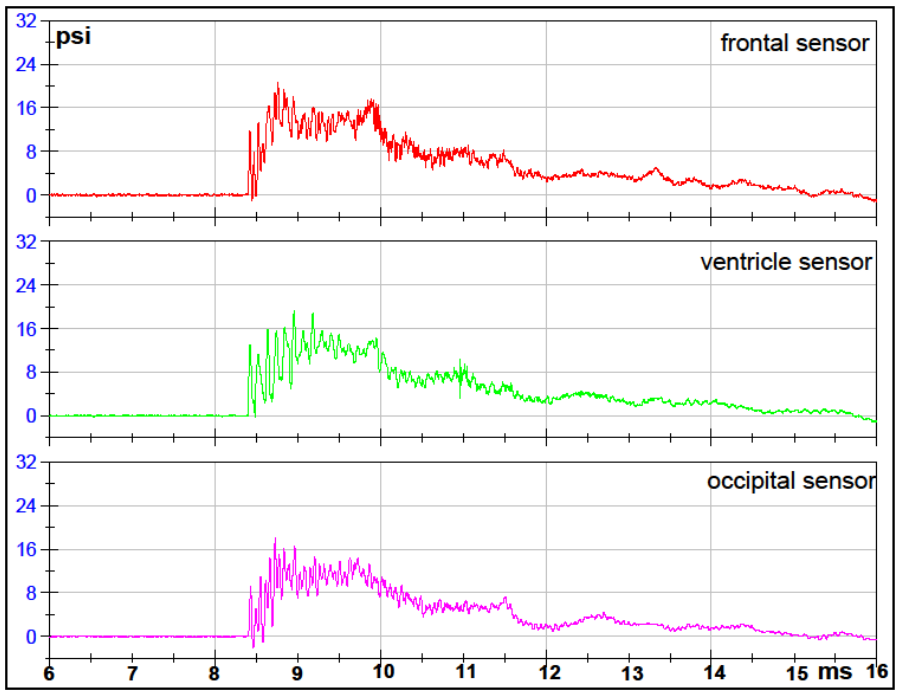

RAW DATA

Test 5 Front 2 Orientation 7mm Sphere with Holes

FILTERED DATA

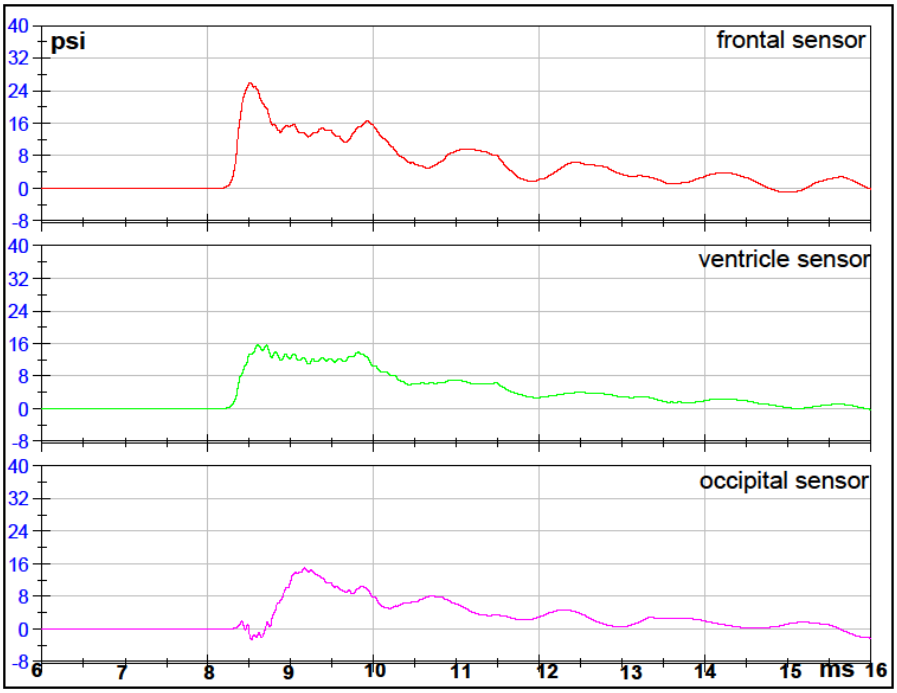

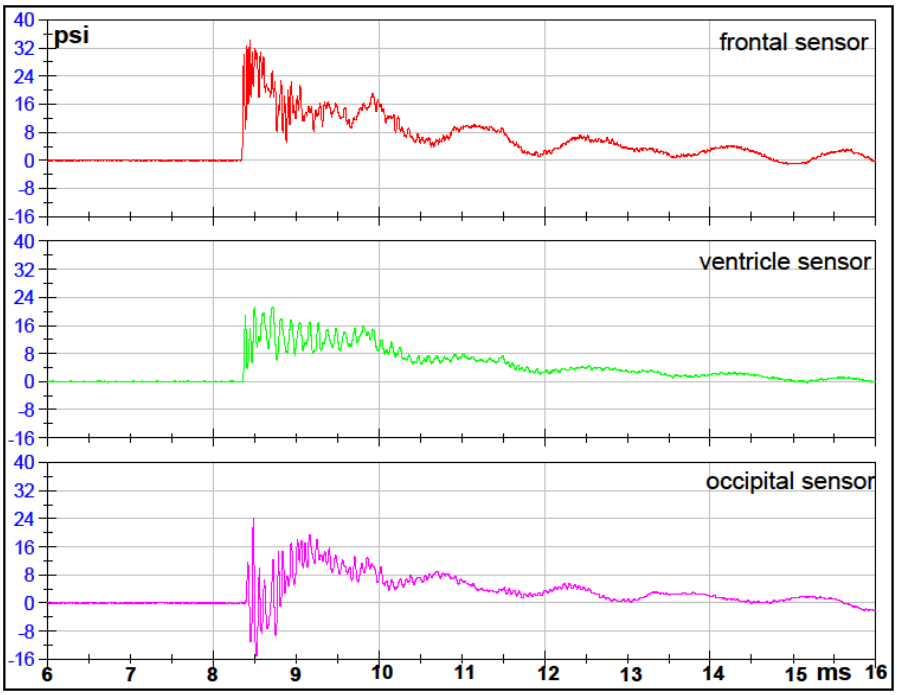

RAW DATA

Test 6 Front 1 Orientation 7mm Sphere with Holes

FILTERED DATA

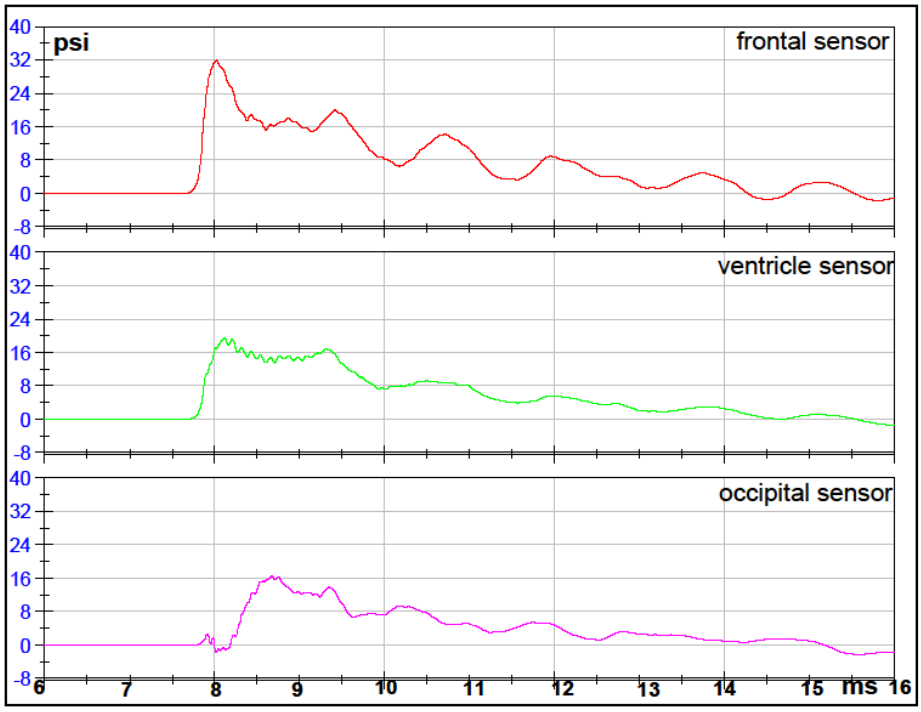

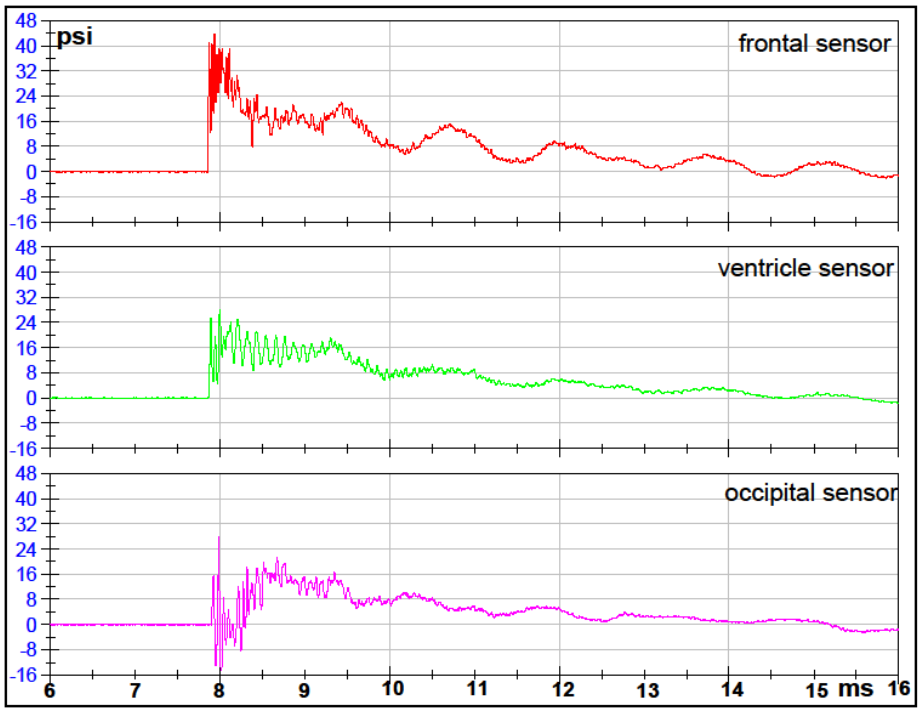

RAW DATA

Test 7 Left Orientation 7mm Sphere with Holes

FILTERED DATA

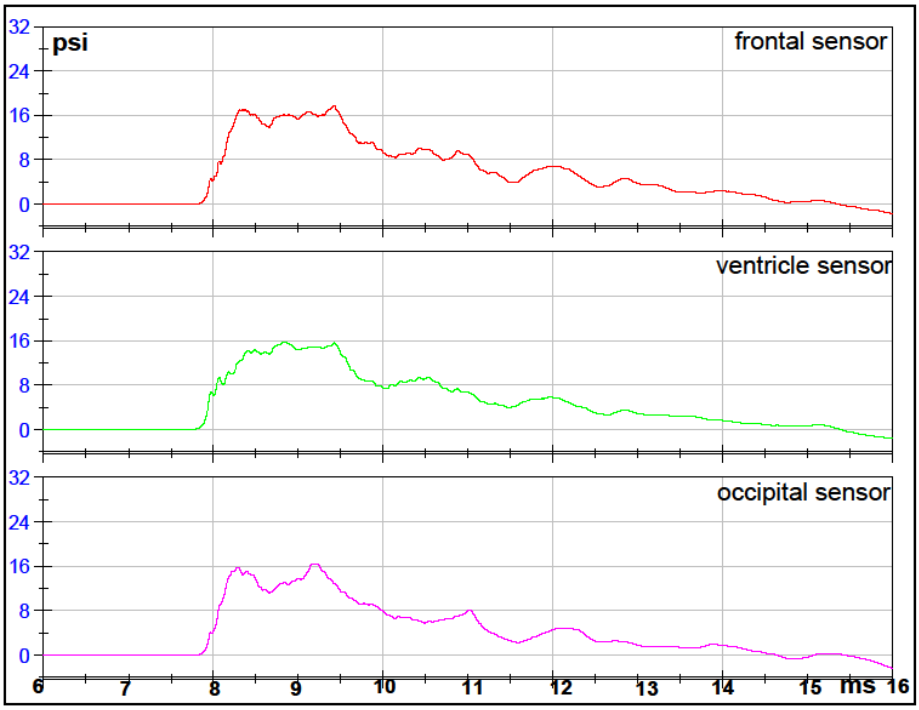

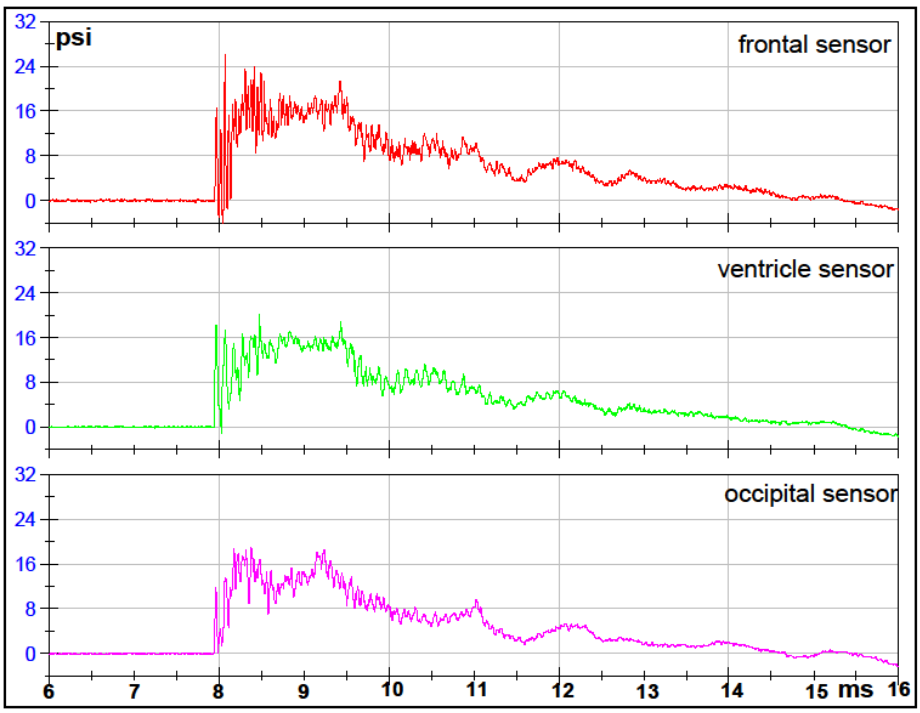

RAW DATA

Test 8 Back Orientation 7mm Sphere with Holes

FILTERED DATA

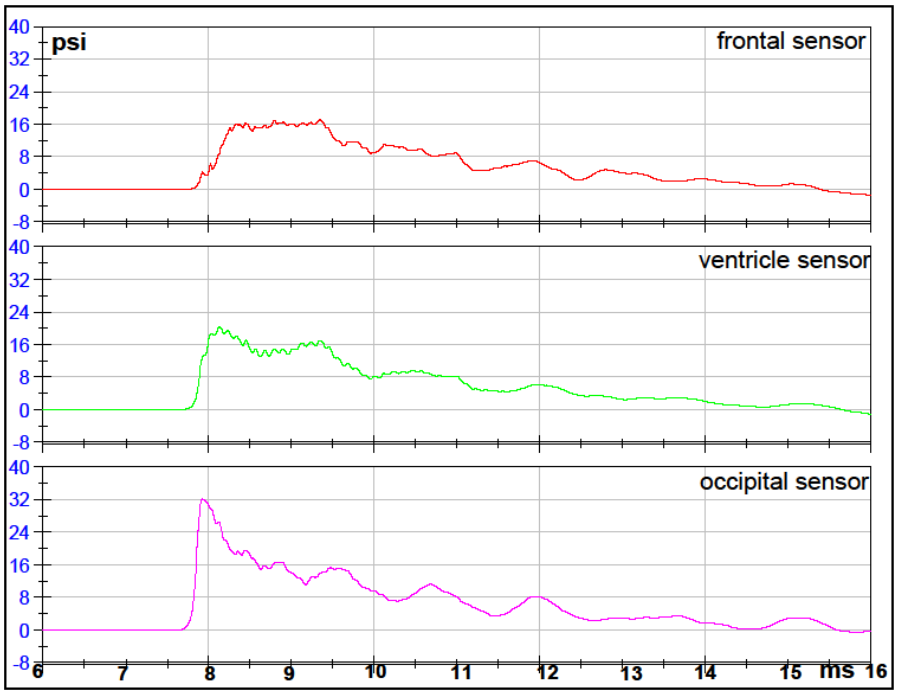

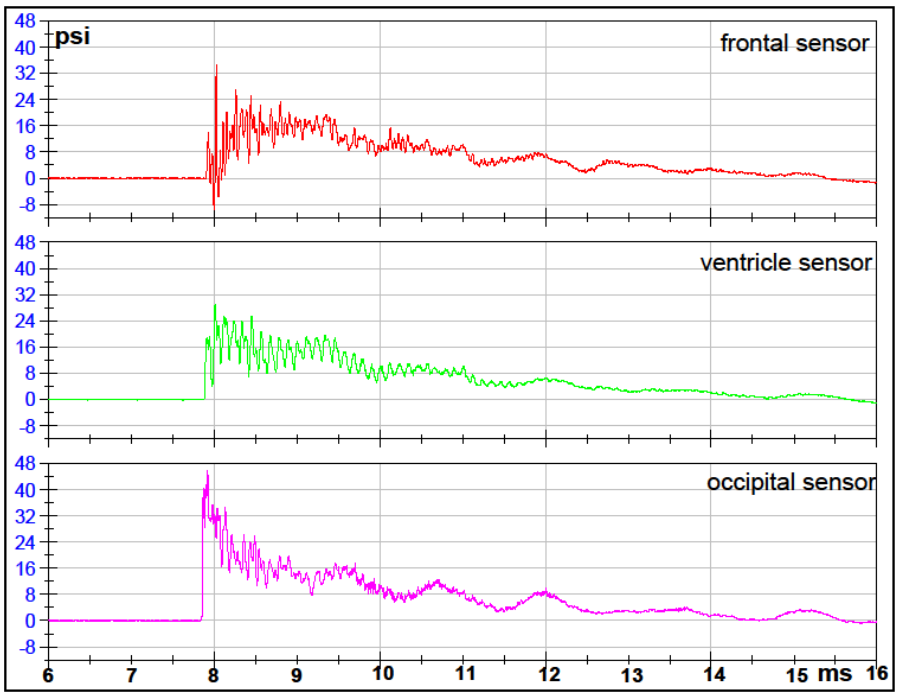

RAW DATA

Test 9 Right Orientation 7mm Sphere with Holes

FILTERED DATA

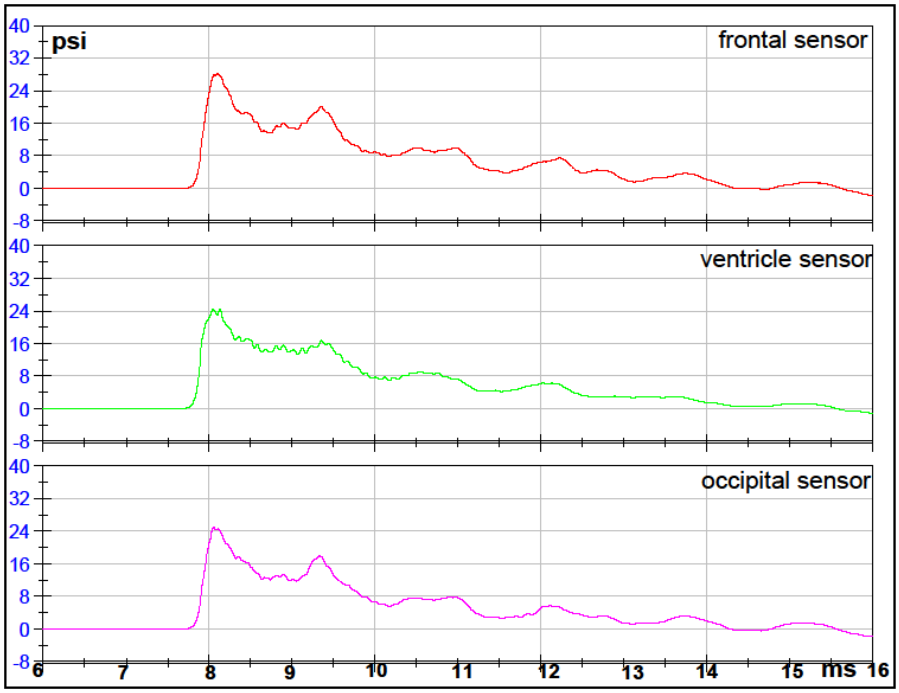

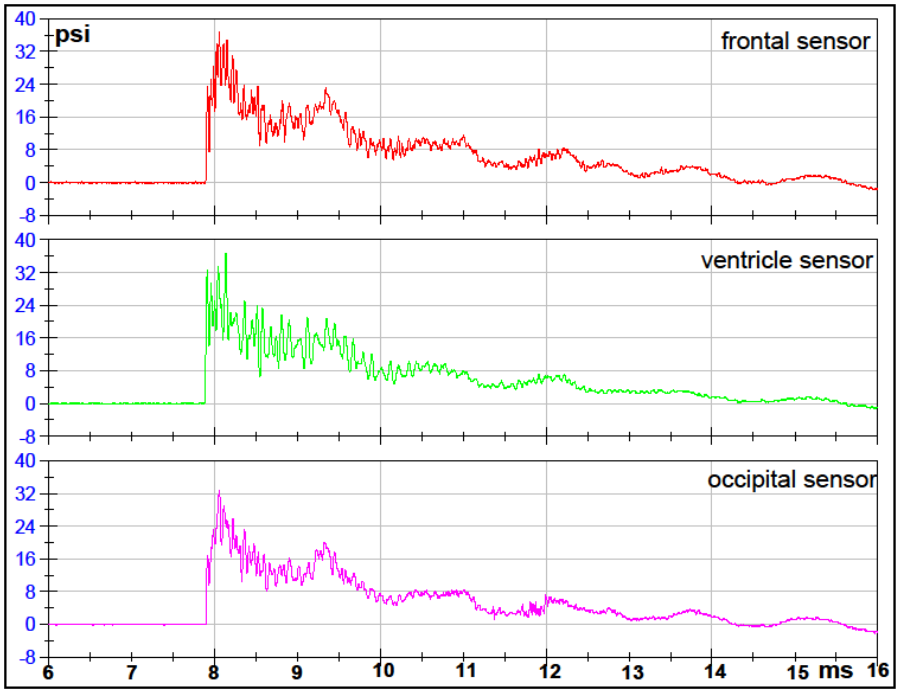

RAW DATA

Test 10 Front 2 Orientation 7mm Sphere with Holes

FILTERED DATA

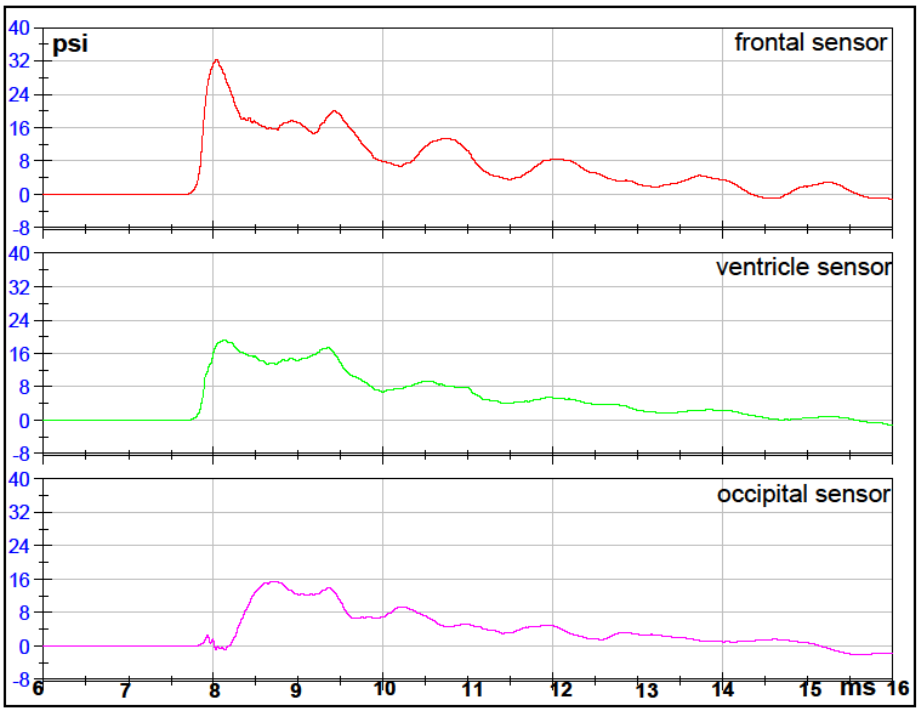

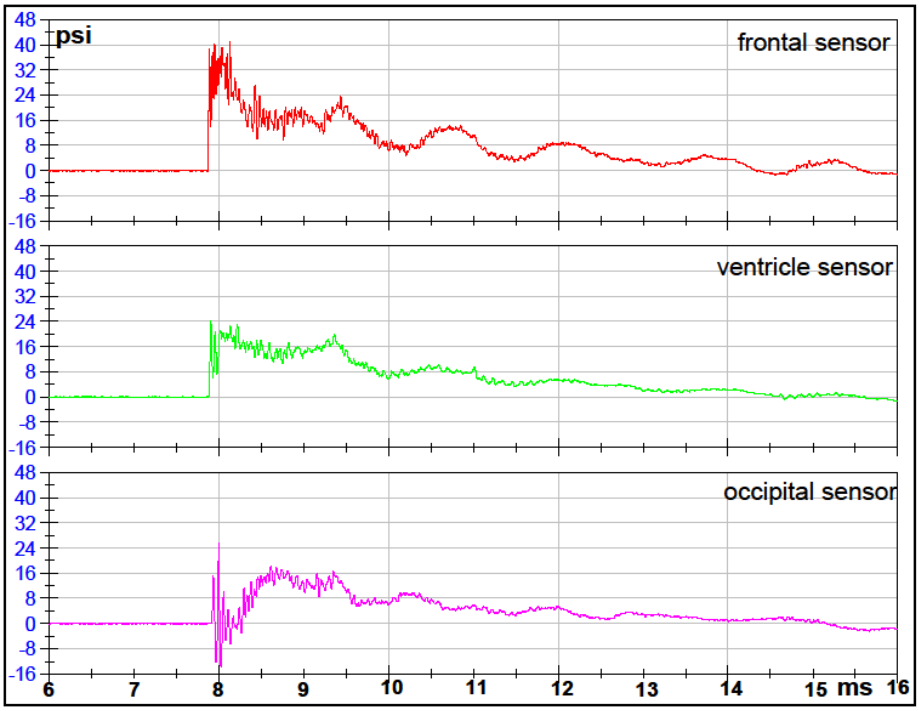

RAW DATA

Test 11 Front 1 Orientation 7mm Sphere with Holes

FILTERED DATA

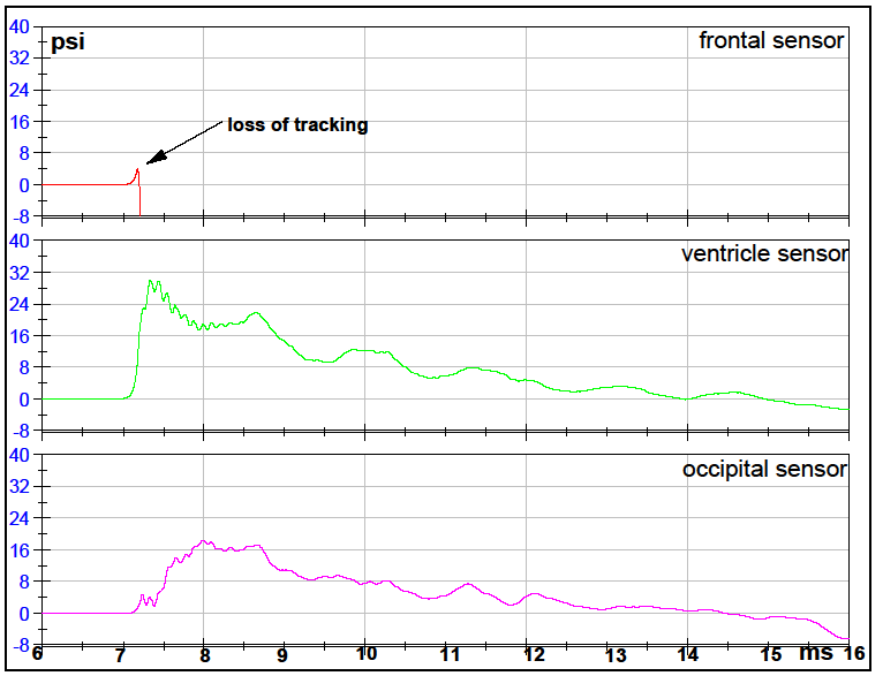

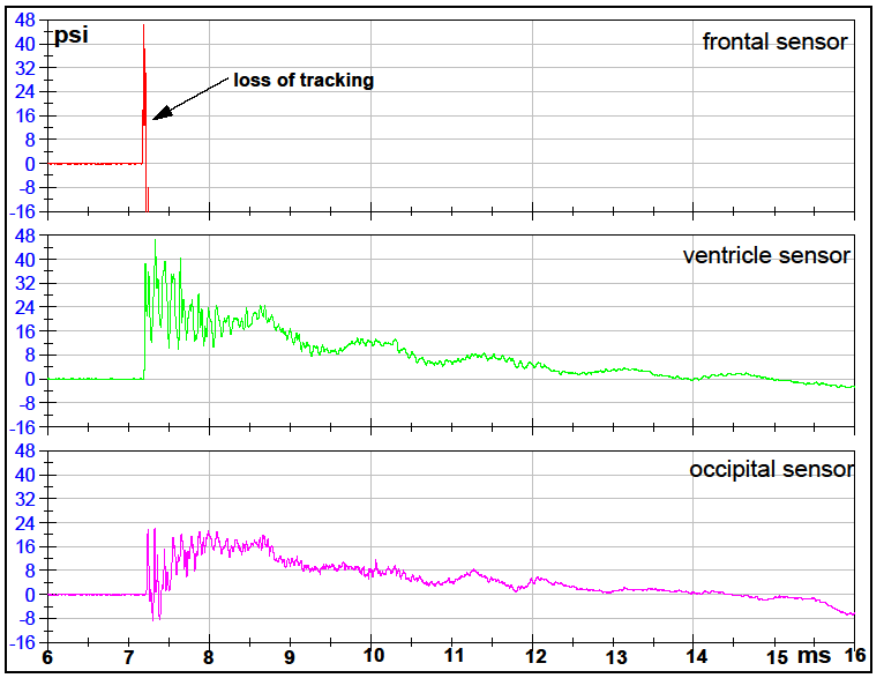

RAW DATA

Test 12 Right Orientation 7mm Sphere with Holes

FILTERED DATA

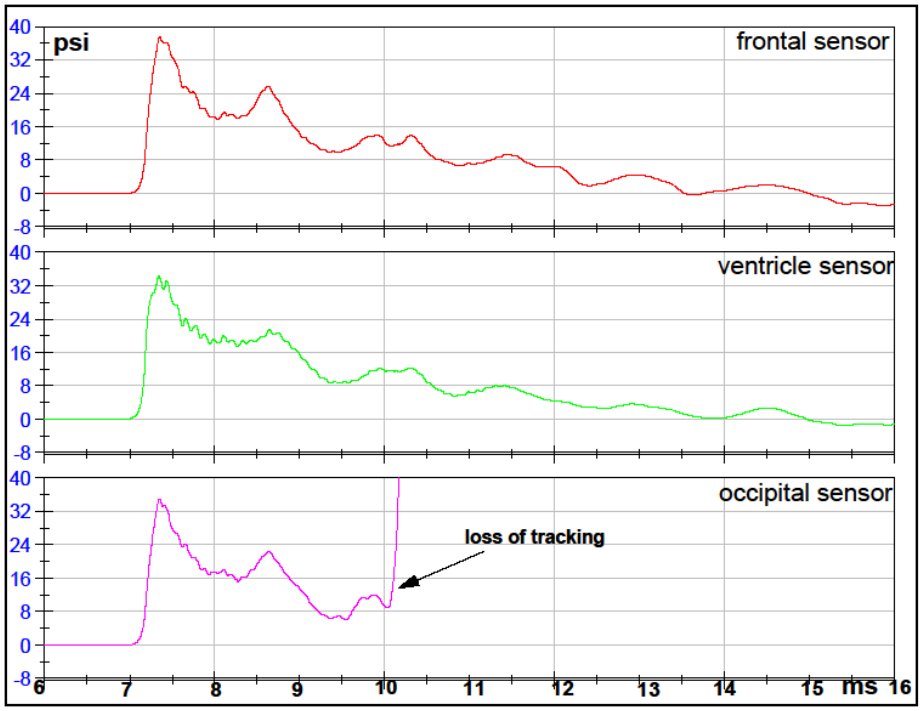

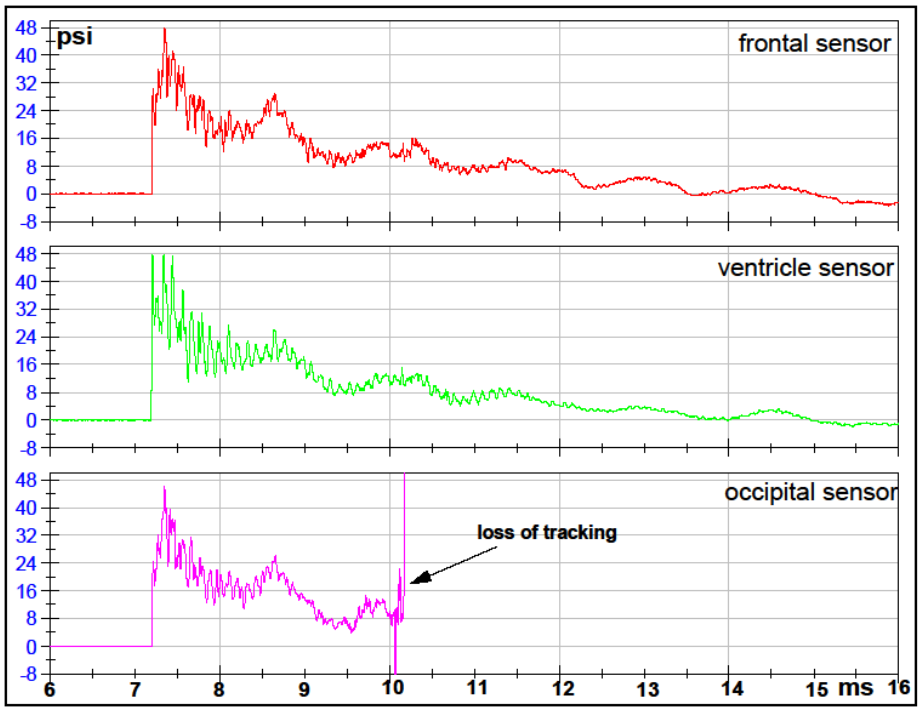

RAW DATA

Test 13 Back Orientation 7mm Sphere with Holes

FILTERED DATA

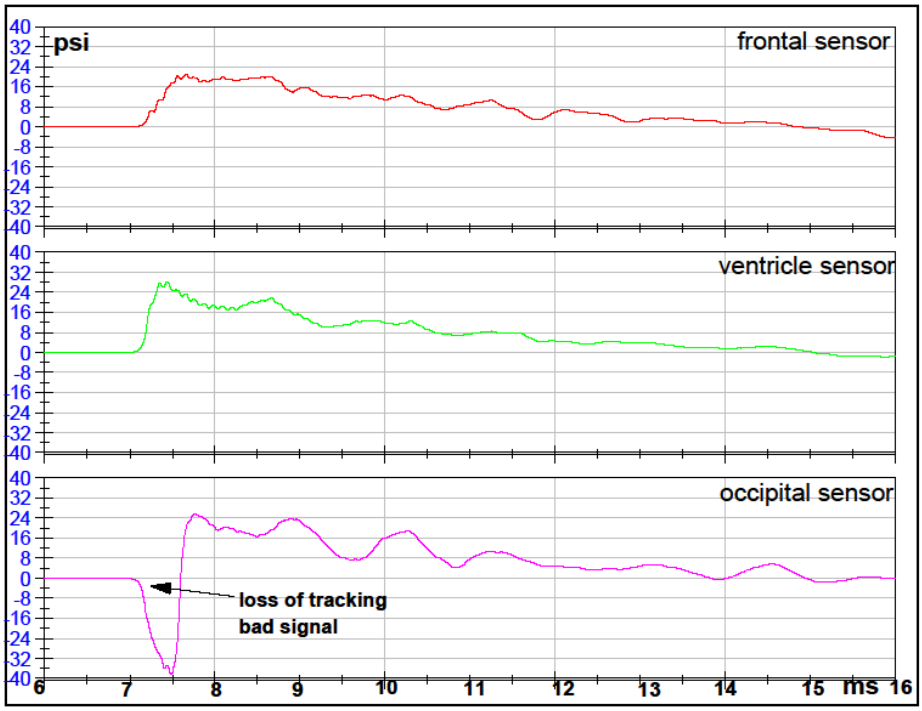

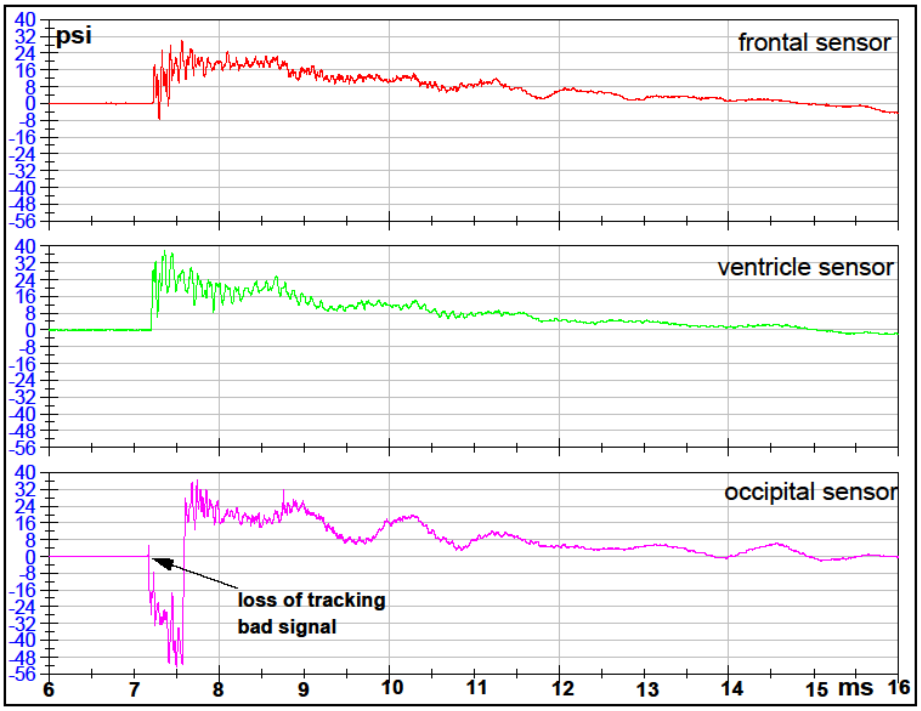

RAW DATA

Test 14 Left Orientation 7mm Sphere with Holes

FILTERED DATA

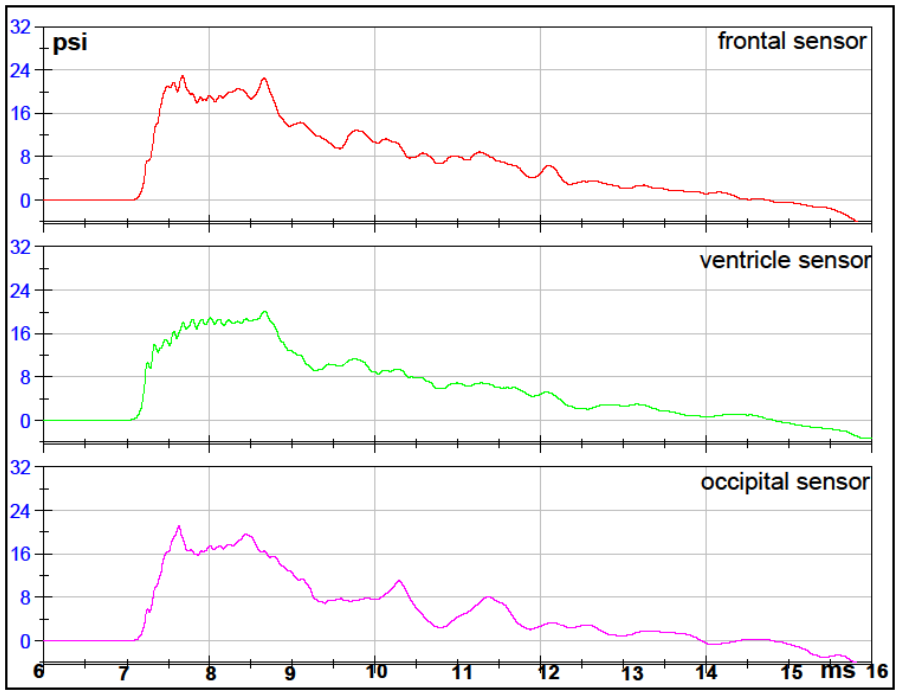

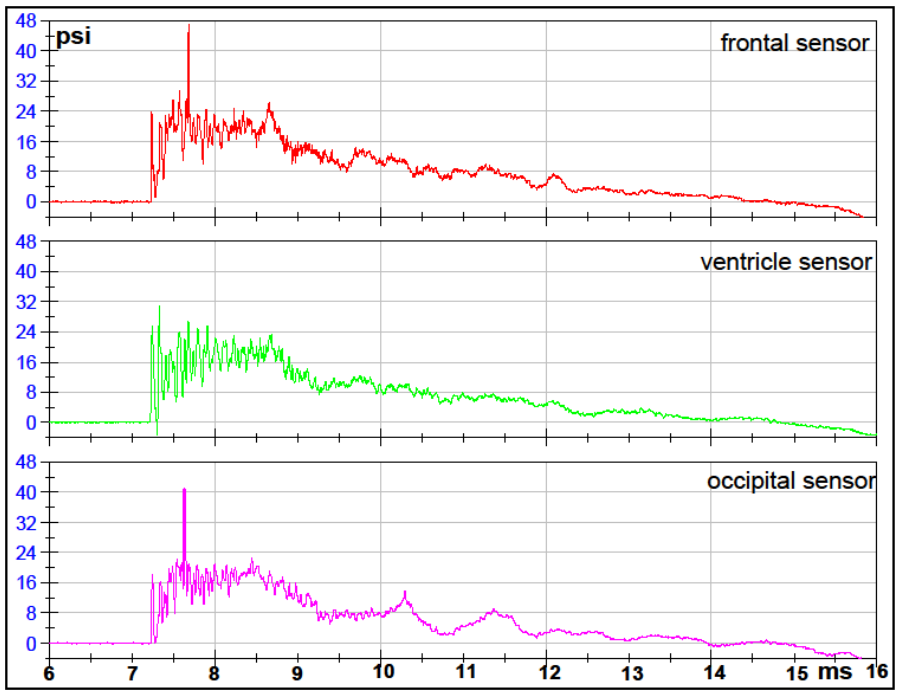

RAW DATA

Test 15 Front 2 Orientation 7mm Sphere with Holes

FILTERED DATA

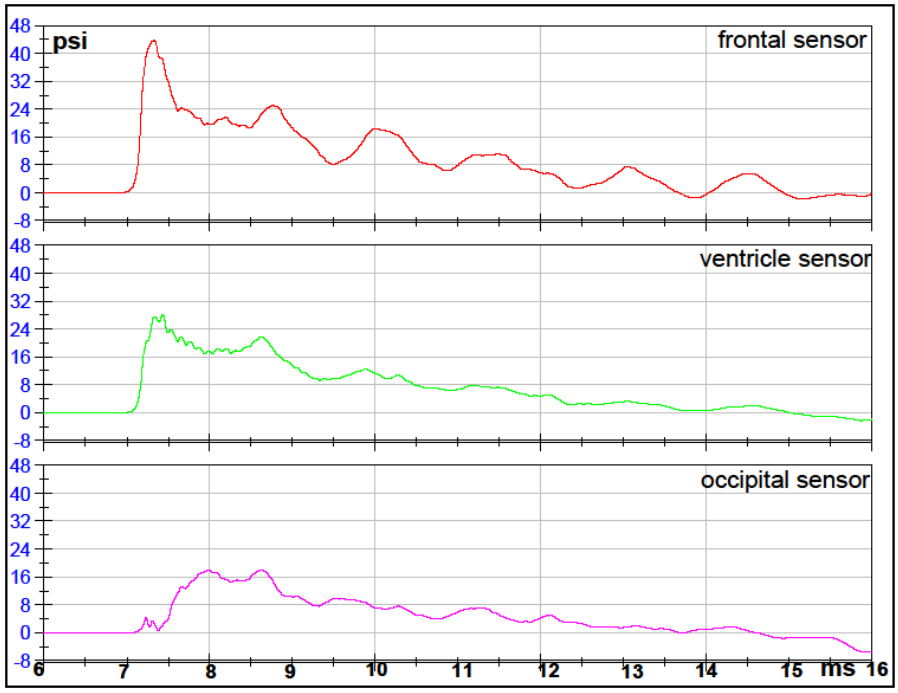

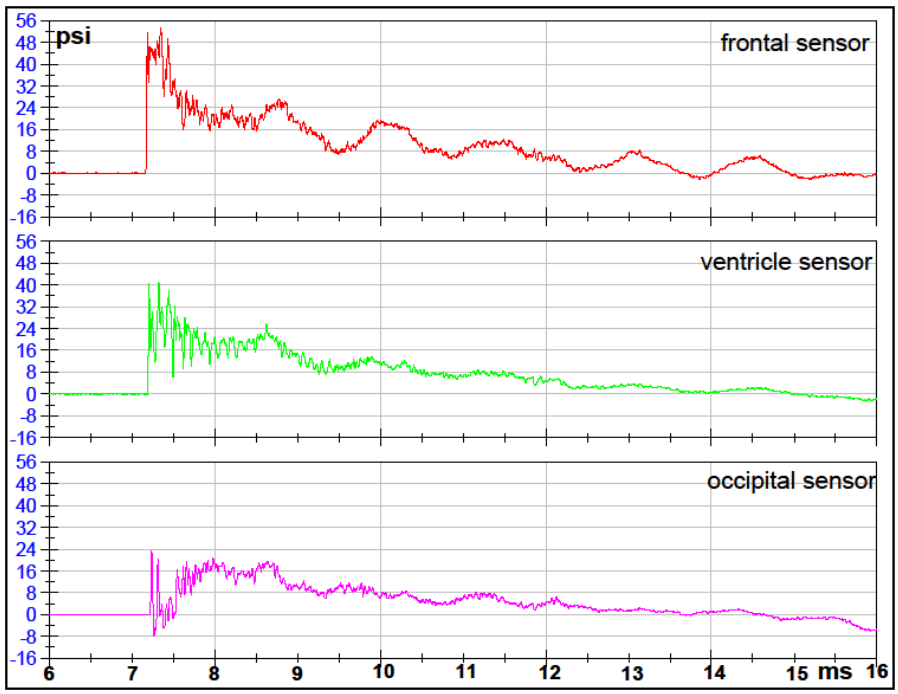

RAW DATA

Comparison for reproducibility of each pressure sensor in Front Orientation at 10psi 7mm Sphere with Holes

VENTRICLE FILTERED DATA

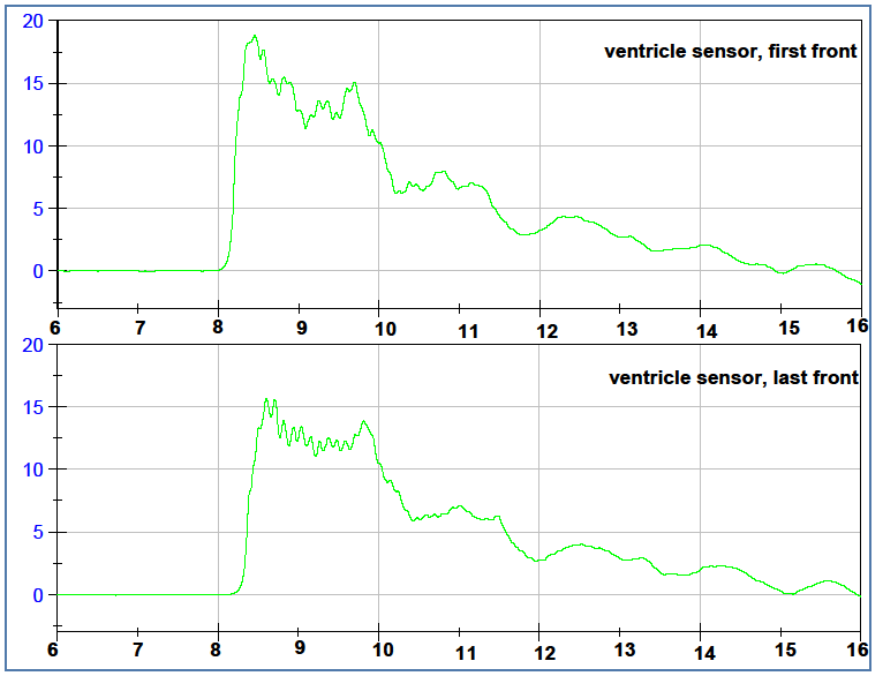

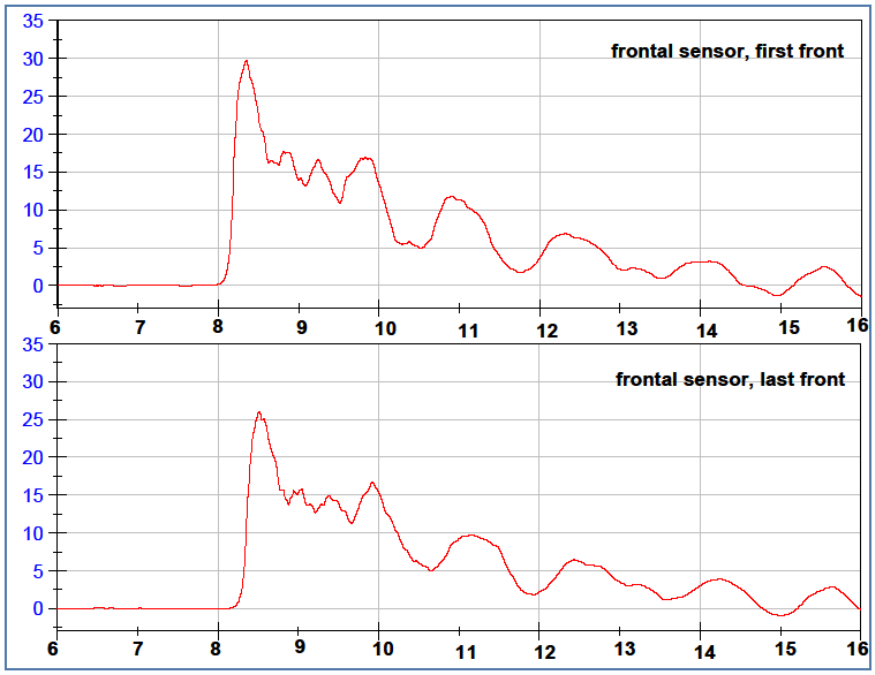

FRONTAL FILTERED DATA

Comparison for reproducibility of each pressure sensor in Front Orientation at 10psi 7mm Sphere with Holes

OCCIPITAL FILTERED DATA

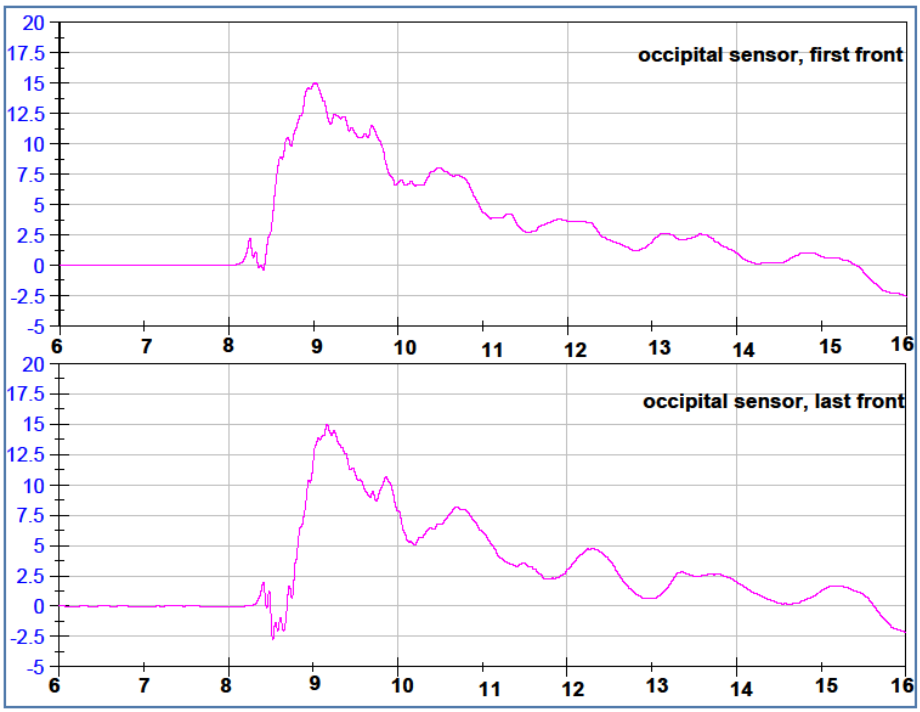

Comparison for reproducibility of each pressure sensor in Front Orientation at 12psi 7mm Sphere with Holes

VENTRICLE FILTERED DATA

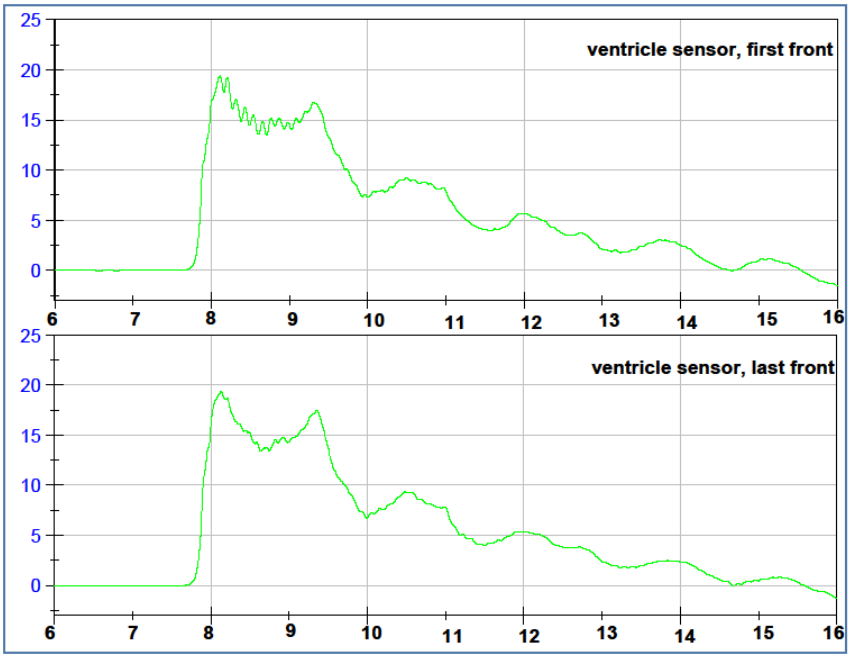

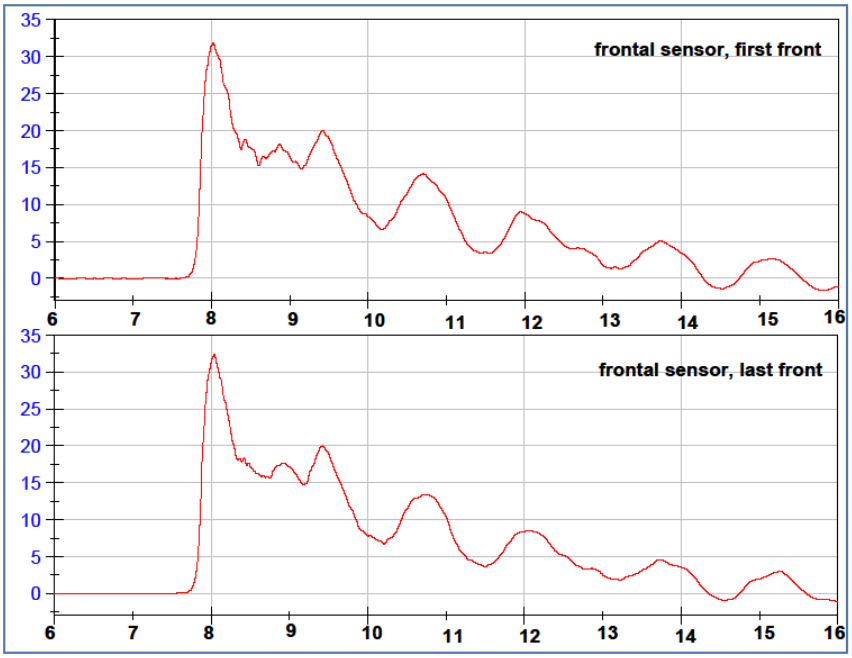

FRONTAL FILTERED DATA

Comparison for reproducibility of each pressure sensor in Front Orientation at 12psi 7mm Sphere with Holes

OCCIPITAL FILTERED DATA

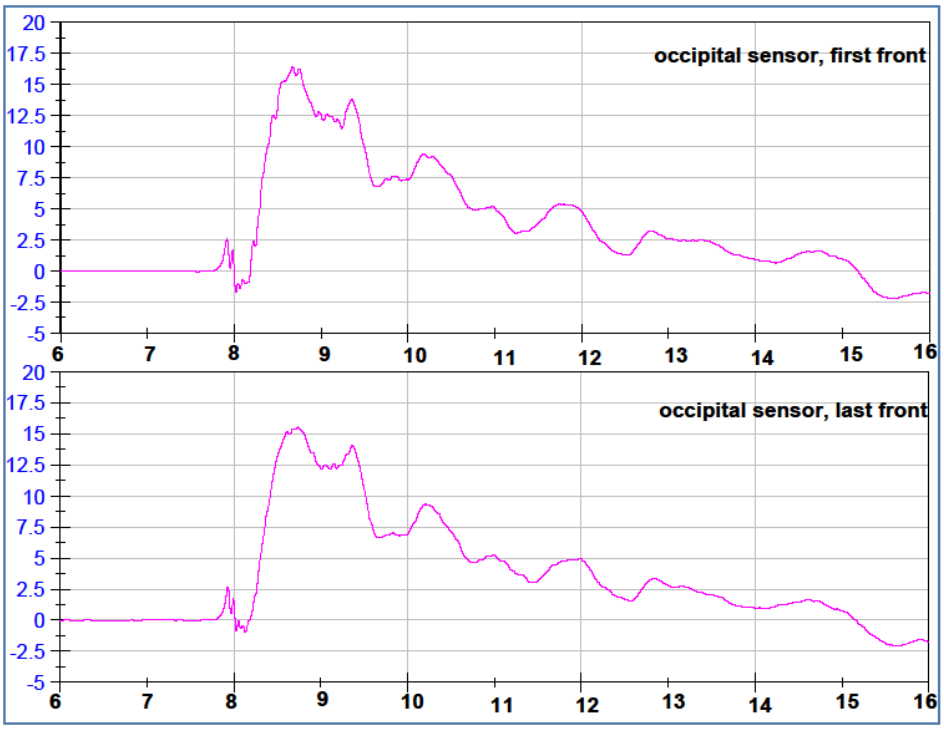

Comparison for reproducibility of each pressure sensor in Front Orientation at 15psi 7mm Sphere with Holes

VENTRICLE FILTERED DATA

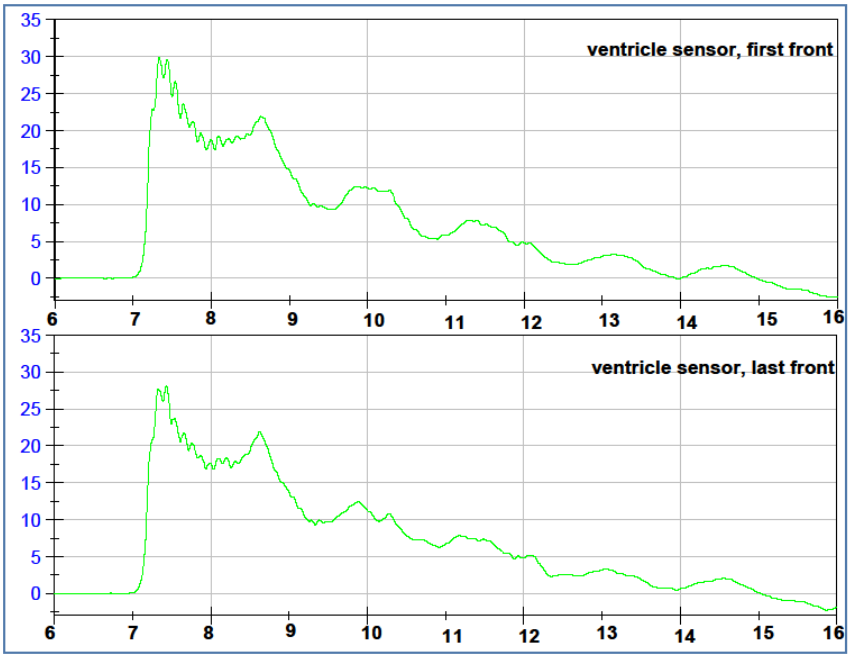

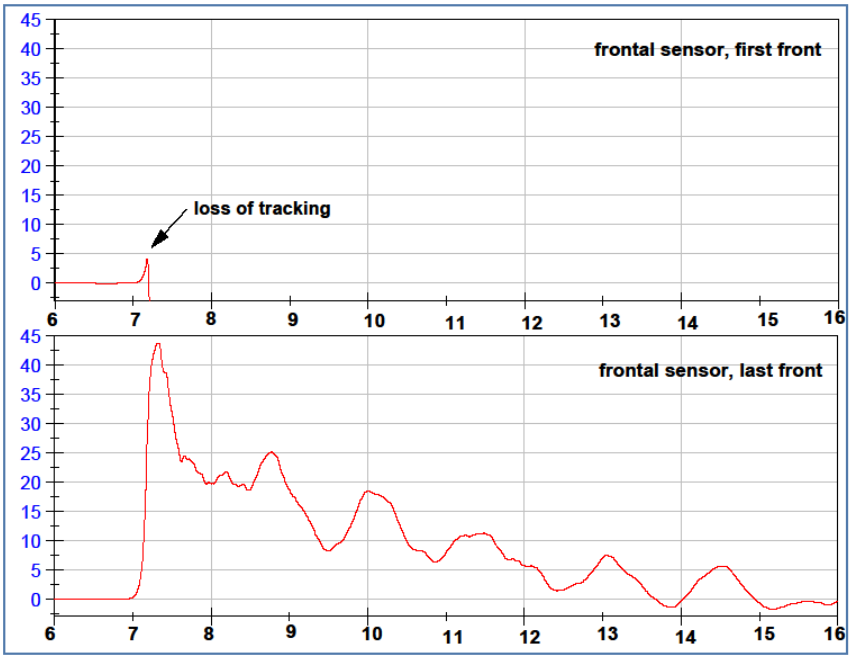

FRONTAL FILTERED DATA

Comparison for reproducibility of each pressure sensor in Front Orientation at 15psi 7mm Sphere with Holes

OCCIPITAL FILTERED DATA

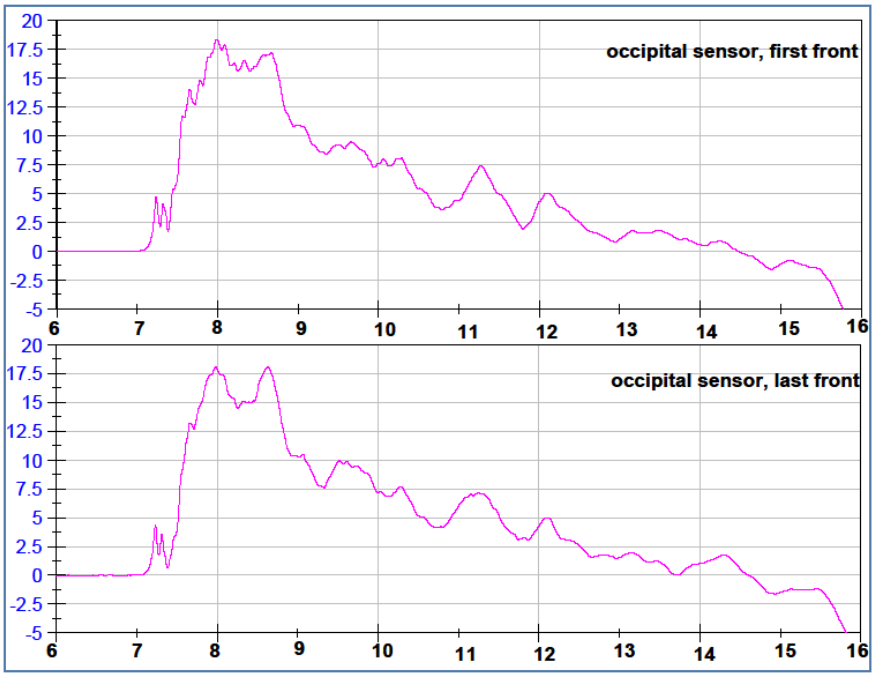

Frontal Sensor, 4 Orientations, Filtered Data, 7mm Sphere with Holes

10 PSI

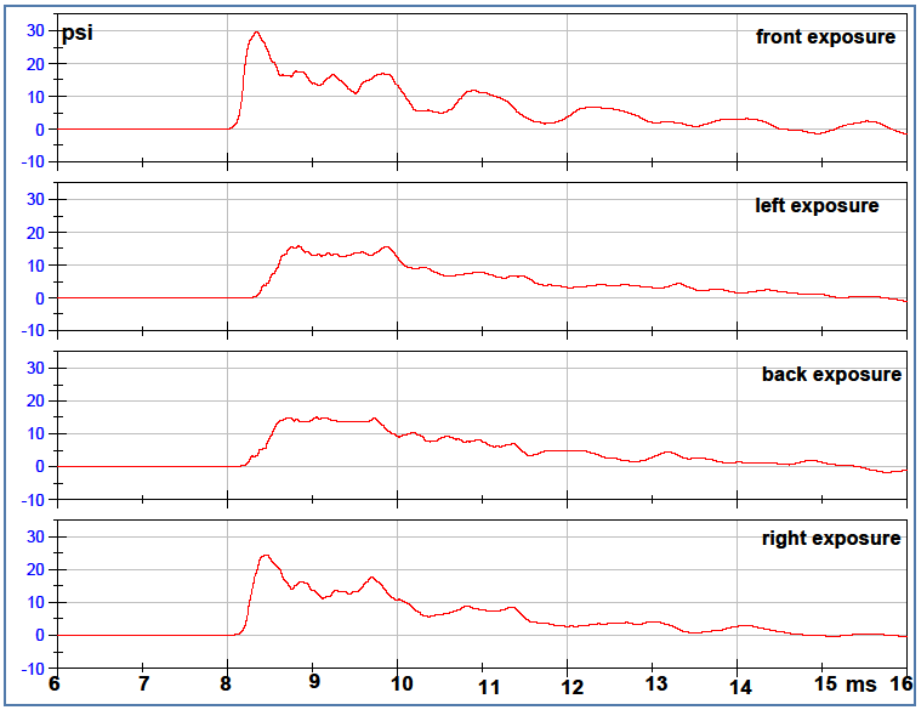

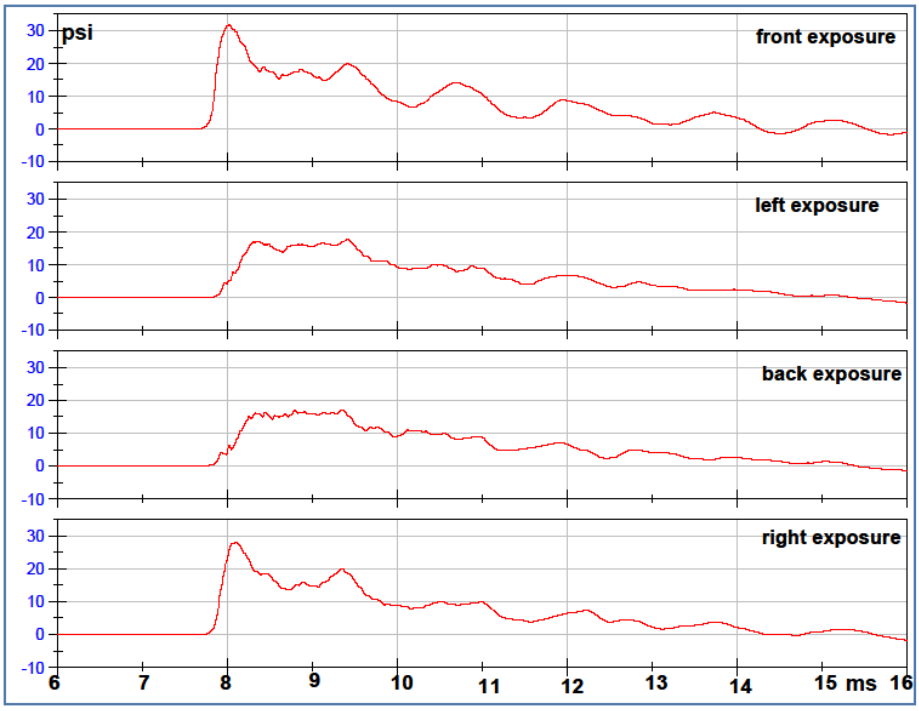

12 PSI

Frontal Sensor, 4 Orientations, Filtered Data, 7mm Sphere with Holes

15 PSI

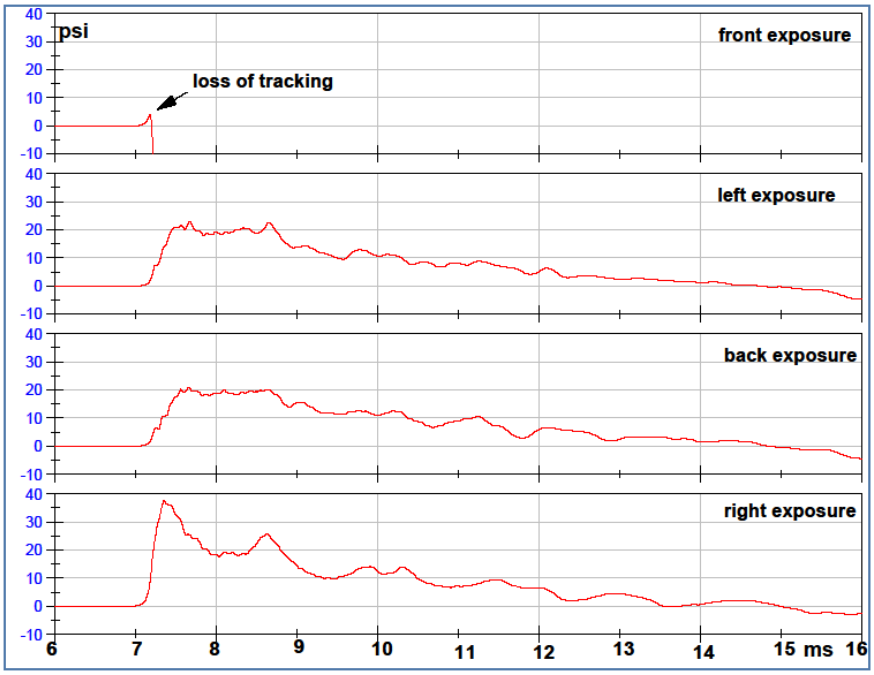

Ventricle Sensor, 4 Orientations, Filtered Data, 7mm Sphere with Holes

10 PSI

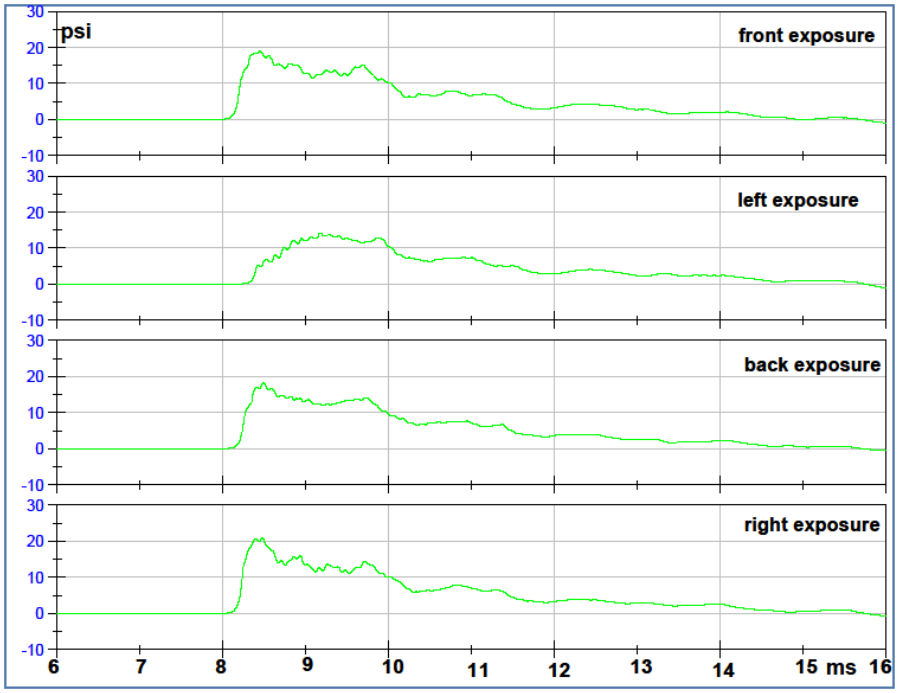

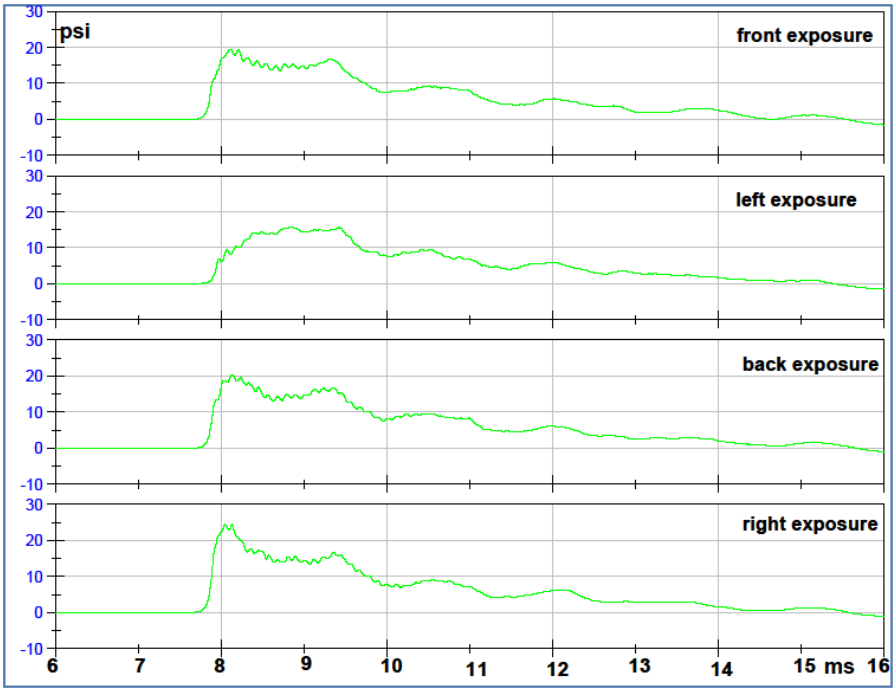

12 PSI

Ventricle Sensor, 4 Orientations, Filtered Data, 7mm Sphere with Holes
15 PSI

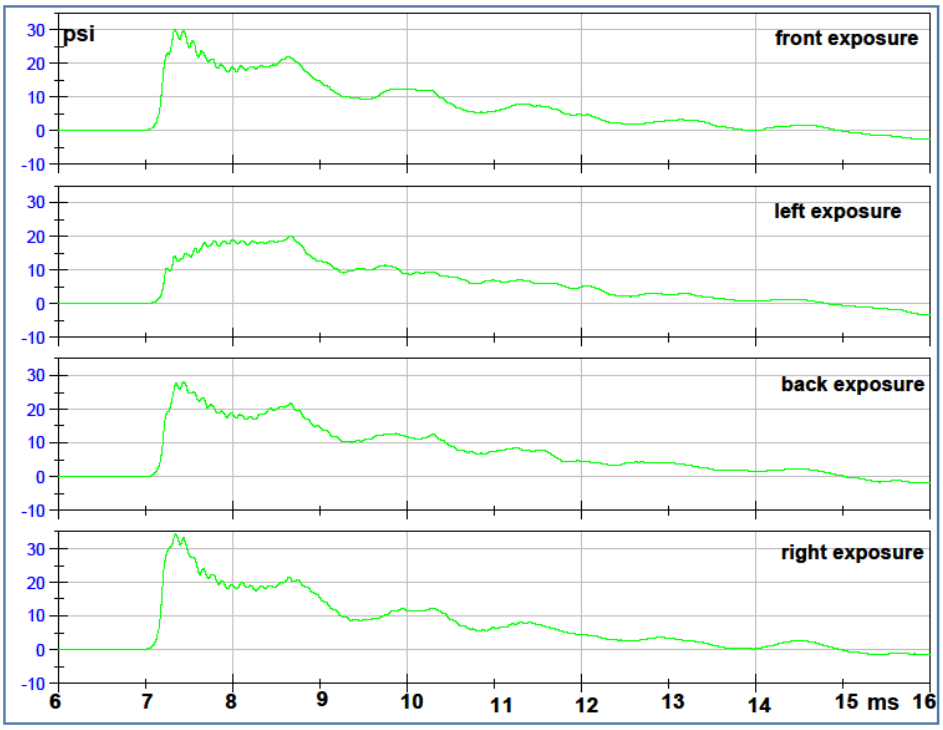

Occipital Sensor, 4 Orientations, Filtered Data, 7mm Sphere with Holes

10 PSI

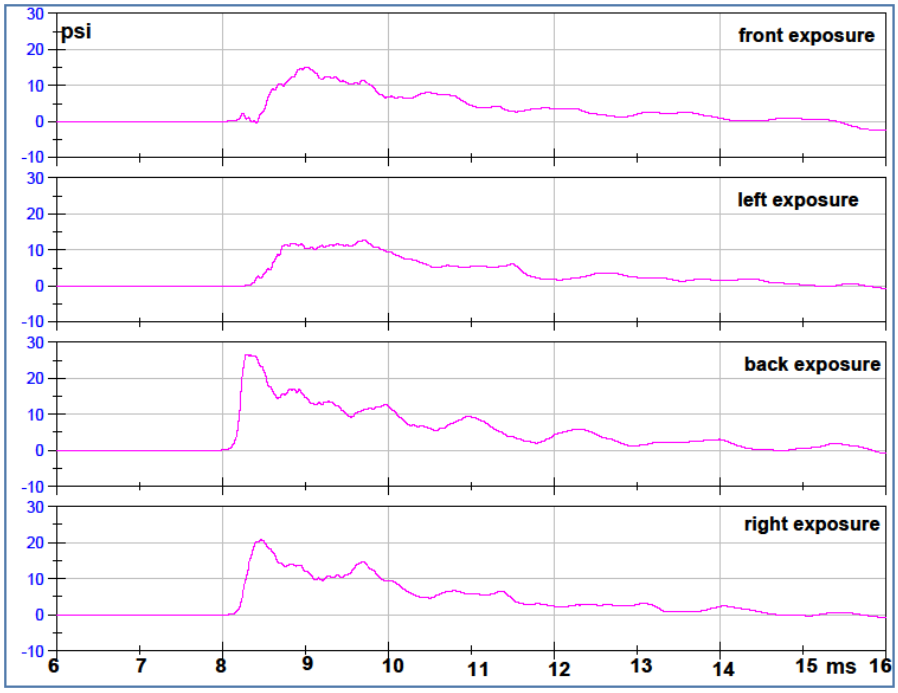

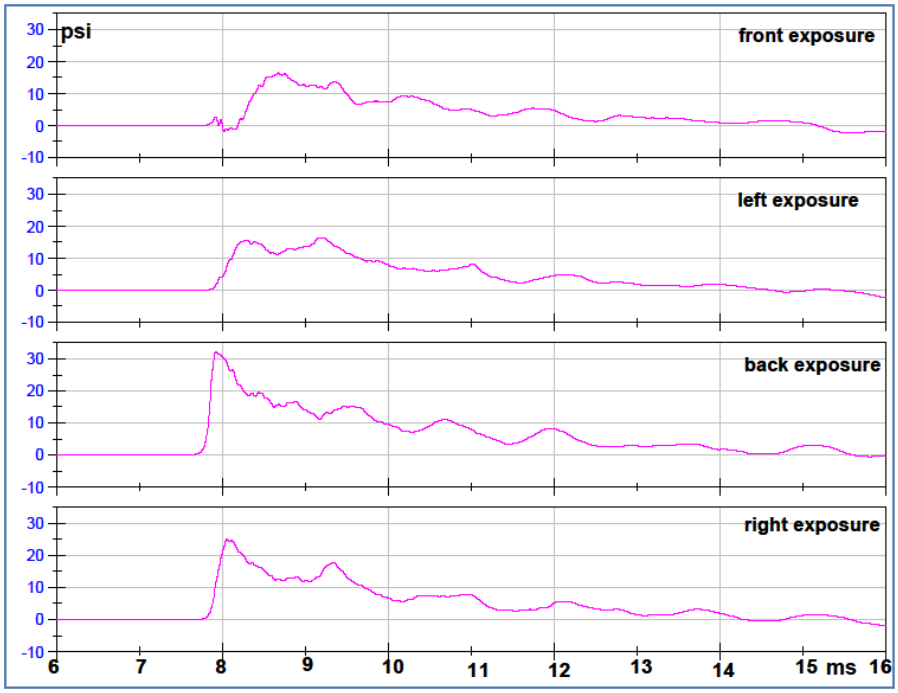

12 PSI

Occipital Sensor, 4 Orientations, Filtered Data, 7mm Sphere with Holes

15 PSI

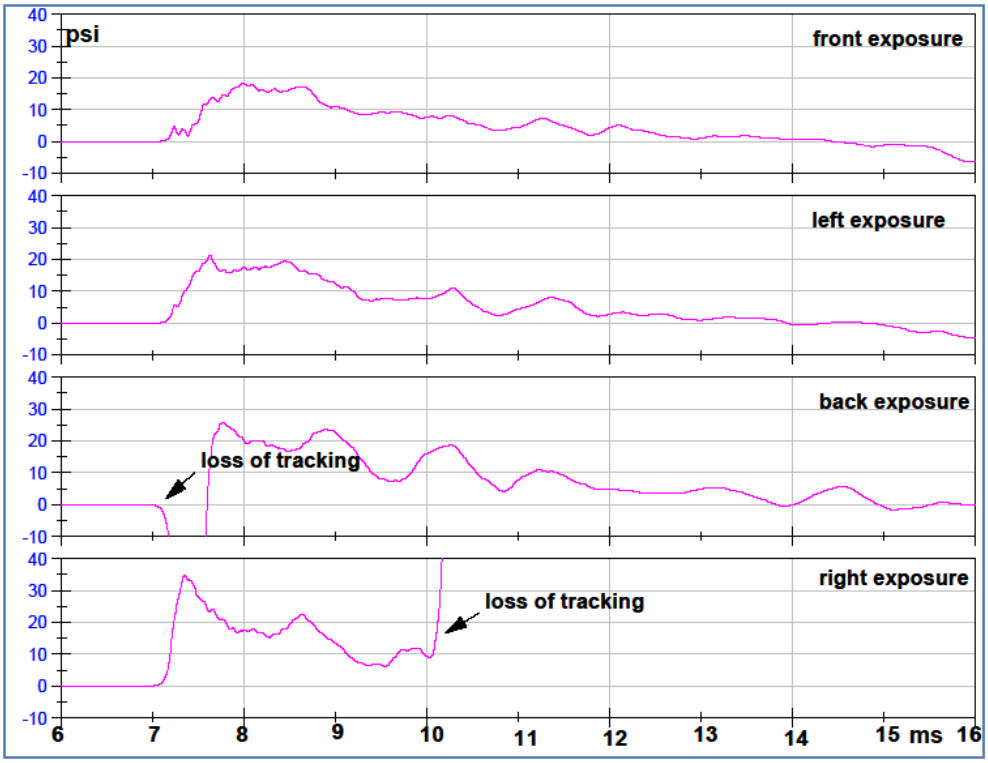

Pressure extremes for 7mm sphere with holes

Pressure Extremes for sphere with holes 7mm										
	Maximun Pressure					Minimum Pressure				
ventricle	front 1	right	back	left	front 2	front 1	right	back	left	front 2
10 psi air	**18.8**	**20.9**	**18.2**	**14.1**	**15.7**	**0.20**	**0.19**	**0.14**	**0.18**	**0.18**
12 psi air	**19.4**	**24.4**	**20.4**	**15.8**	**19.3**	**0.12**	**0.13**	**0.17**	**0.17**	**0.21**
15 psi air	**29.9**	**34.3**	**28.3**	**20.2**	**27.7**	**0.14**	**0.19**	**0.13**	**0.20**	**0.17**
frontal	front 1	right	back	left	front 2	front 1	right	back	left	front 2
10 psi air	**29.7**	**24.3**	**15.0**	**15.8**	**26.0**	**0.21**	**0.17**	**0.17**	**0.21**	**0.18**
12 psi air	**31.9**	**27.8**	**17.1**	**17.7**	**32.3**	**-1.38**	**0.15**	**0.19**	**0.16**	**-0.95**
15 psi air	**NA**	**37.3**	**20.7**	**22.9**	**43.5**	**NA**	**0.18**	**0.20**	**0.19**	**-1.45**
occipital	front 1	right	back	left	front 2	front 1	right	back	left	front 2
10 psi air	**15.0**	**20.8**	**26.5**	**12.6**	**15.0**	**-0.35**	**0.13**	**0.18**	**0.14**	**-2.72**
12 psi air	**16.5**	**25.0**	**32.2**	**16.4**	**15.5**	**-1.73**	**0.22**	**0.15**	**0.13**	**-0.96**
15 psi air	**18.2**	**34.7**	**NA**	**21.3**	**18.0**	**0.21**	**0.21**	**NA**	**0.12**	**0.13**

1st rate of change of pressure for 7mm-thick sphere with holes.

1st rate (psi/ms)					
ventricle	front 1	right	back	left	front 2
10 psi air	**58.7**	**67.6**	**54.8**	**36.7**	**46.2**
12 psi air	**54.9**	**71.5**	**57.6**	**44.0**	**50.8**
15 psi air	**94.7**	**112.1**	**84.1**	**54.5**	**88.8**
frontal	front 1	right	back	left	front 2
10 psi air	**90.9**	**72.9**	**30.6**	**34.4**	**80.7**
12 psi air	**98.9**	**87.6**	**31.3**	**35.8**	**92.5**
15 psi air	**NA**	**109.2**	**42.5**	**53.3**	**137.0**
occipital	front 1	right	back	left	front 2
10 psi air	**17.2**	**63.6**	**106.3**	**19.9**	**16.4**
12 psi air	**23.2**	**84.7**	**125.3**	**38.6**	**20.7**
15 psi air	**34.1**	**109.9**	**NA**	**41.8**	**30.3**

Table of Differential Pressure Results for 7mm Sphere with Holes

Differential for sphere with holes 7mm										
	peak differential pressure (psi)					time elapsed between peaks (ms)				
ventricle	front 1	right	back	left	front 2	front 1	right	back	left	front 2
10 psi air	**18.6**	**20.8**	**18.1**	**13.9**	**15.5**	**0.40**	**0.40**	**0.40**	**0.90**	**0.38**
12 psi air	**19.3**	**24.3**	**20.2**	**15.6**	**19.1**	**0.40**	**0.34**	**0.40**	**1.03**	**0.38**
15 psi air	**29.9**	**34.1**	**28.2**	**20.0**	**27.6**	**0.32**	**0.33**	**0.40**	**1.60**	**0.42**
frontal	front 1	right	back	left	front 2	front 1	right	back	left	front 2
10 psi air	**29.5**	**24.3**	**14.9**	**15.6**	**25.8**	**0.32**	**0.38**	**0.88**	**0.54**	**0.32**
12 psi air	**33.3**	**27.7**	**16.9**	**17.6**	**33.3**	**6.47**	**0.32**	**1.56**	**1.58**	**6.50**
15 psi air	**NA**	**37.1**	**20.5**	**22.7**	**44.9**	**NA**	**0.34**	**0.58**	**0.58**	**6.57**
occipital	front 1	right	back	left	front 2	front 1	right	back	left	front 2
10 psi air	**15.3**	**20.7**	**26.4**	**12.5**	**17.7**	**0.60**	**0.38**	**0.25**	**1.42**	**0.64**
12 psi air	**18.2**	**24.7**	**32.1**	**16.3**	**16.5**	**0.66**	**0.29**	**0.26**	**1.34**	**0.61**
15 psi air	**18.4**	**34.7**	**NA**	**21.1**	**17.9**	**0.88**	**0.32**	**NA**	**0.54**	**0.89**

Percentages of 1st rate of internal pressure changes in 7mm sphere with holes based on the cell value at the 10 psi air overpressure for each orientation.

AIR		Percentage 1st Rate Pressure Change				
Overpressure		**front 1**	**right**	**back**	**left**	**front 2**
ventricle	**20%**	**-6%**	**6%**	**5%**	**20%**	**10%**
ventricle	**50%**	**61%**	**66%**	**54%**	**49%**	**92%**
frontal	**20%**	**9%**	**20%**	**2%**	**4%**	**15%**
frontal	**50%**	**NA**	**50%**	**39%**	**55%**	**70%**
occipital	**20%**	**35%**	**33%**	**18%**	**94%**	**27%**
occipital	**50%**	**98%**	**73%**	**NA**	**109%**	**85%**

State of Gages during Testing of the 7mm Sphere with Holes

	Strain status for sphere 5mm				
Frontal	front 1	right	back	left	front 2
10 psi air					
12 psi air					
15 psi air					
Left	front 1	right	back	left	front 2
10 psi air					
12 psi air					
15 psi air					
Right	front 1	right	back	left	front 2
10 psi air					
12 psi air					
15 psi air					
Occipital	front 1	right	back	left	front 2
10 psi air					
12 psi air					
15 psi air					

	working
	signal problems
	not working

Strain Data Sphere with Holes

Test 1 Front 1 Orientation 7mm Sphere with Holes

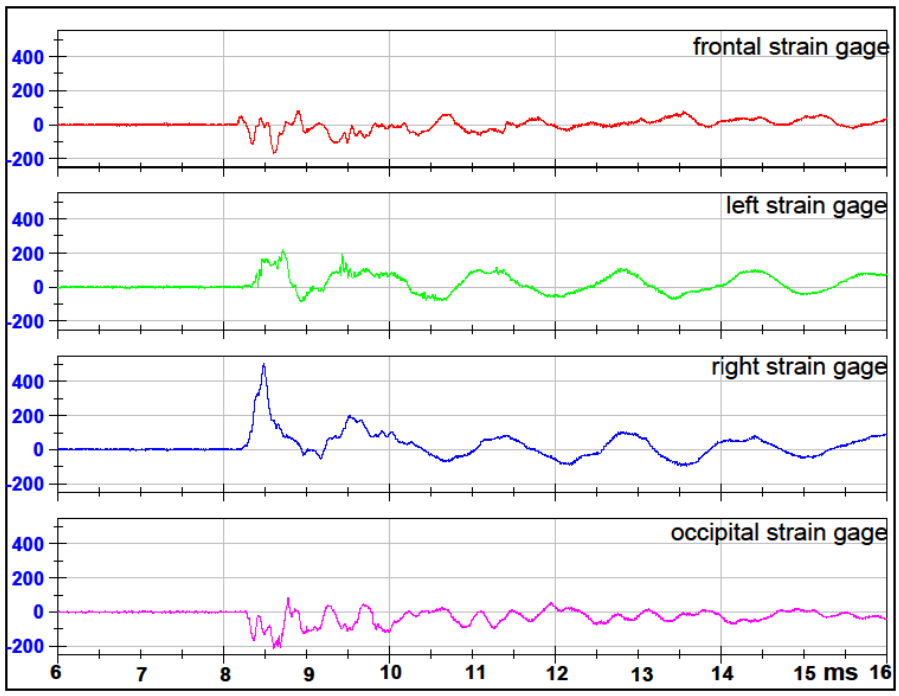

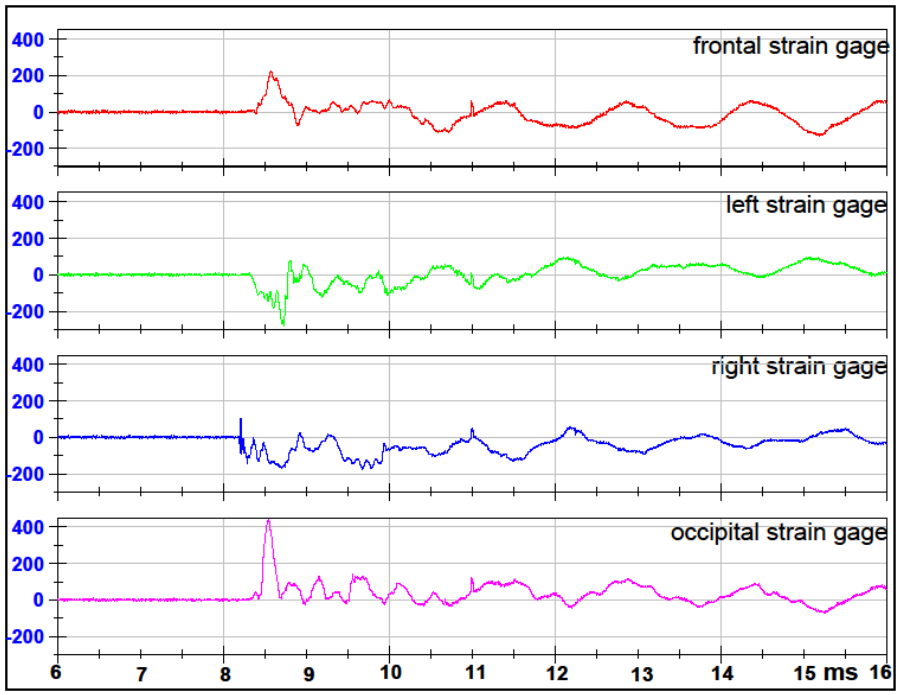

Test 2 Right Orientation 7mm Sphere with Holes

Test 3 Back Orientation 7mm Sphere with Holes

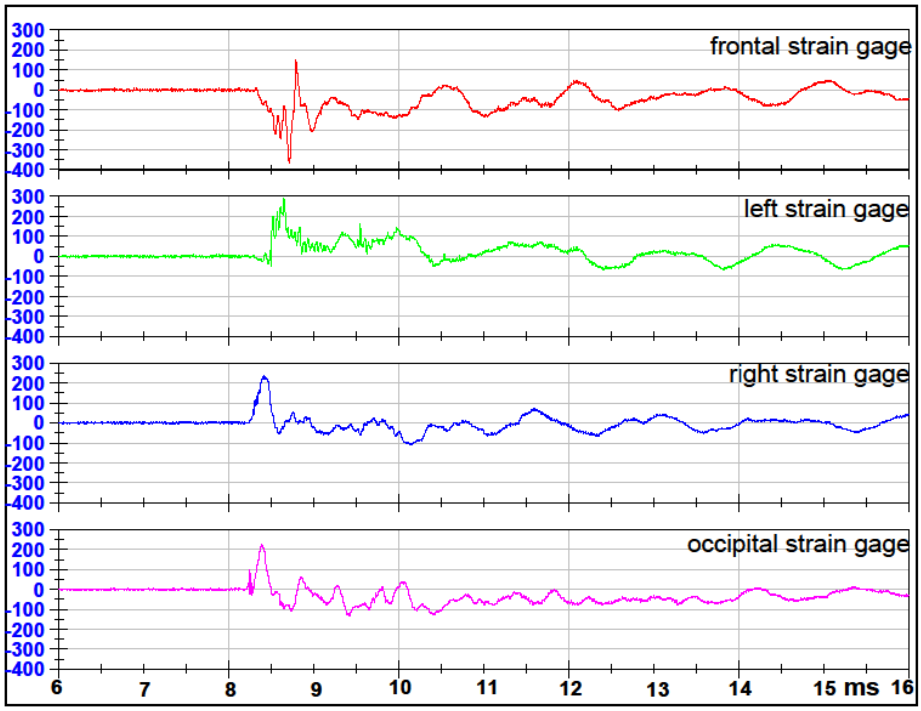

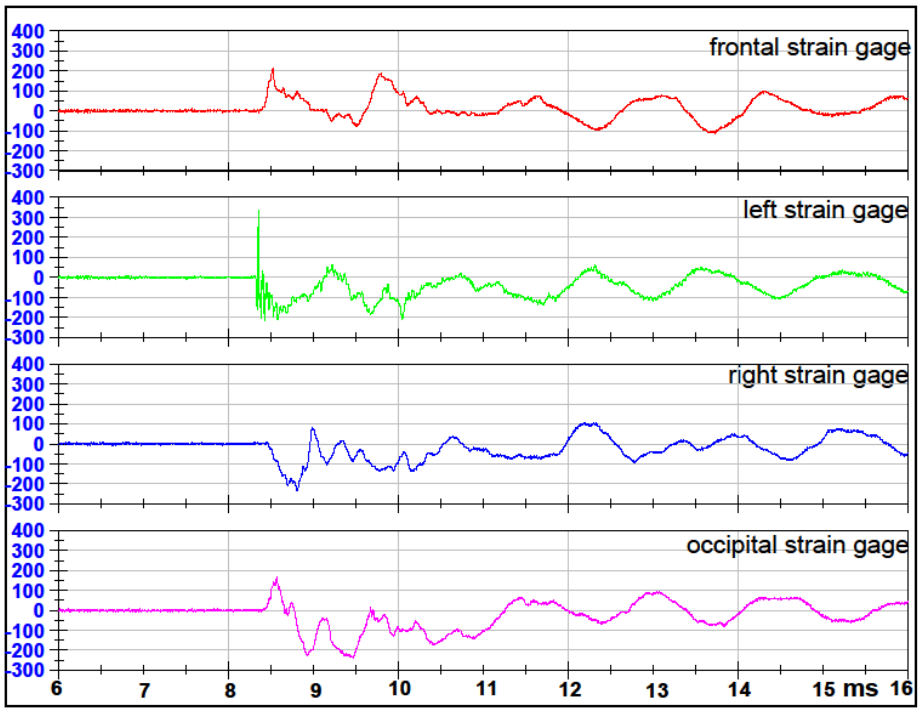

Test 4 Left Orientation 7mm Sphere with Holes

Test 5 Front 2 Orientation 7mm Sphere with Holes

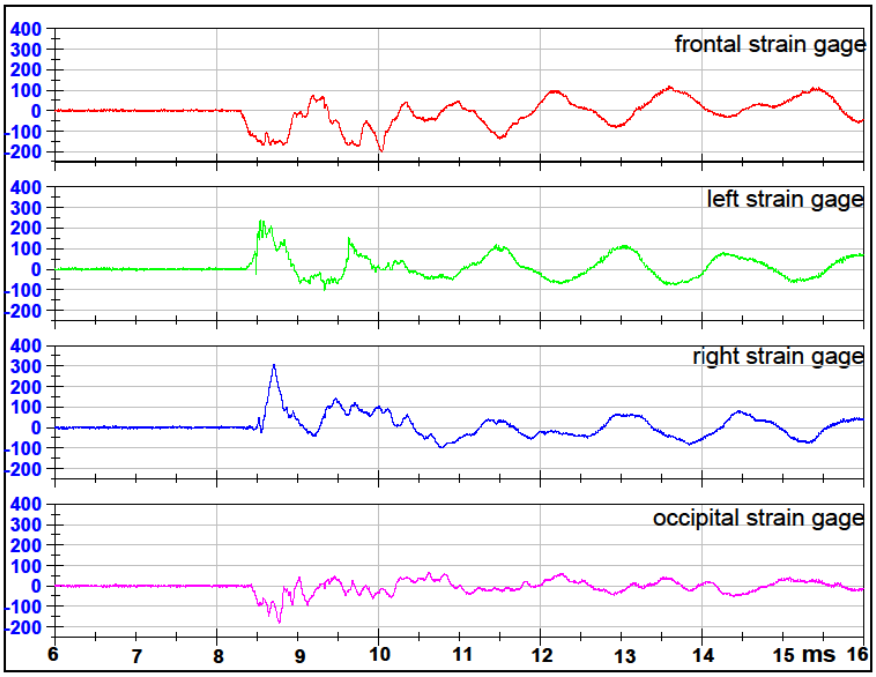

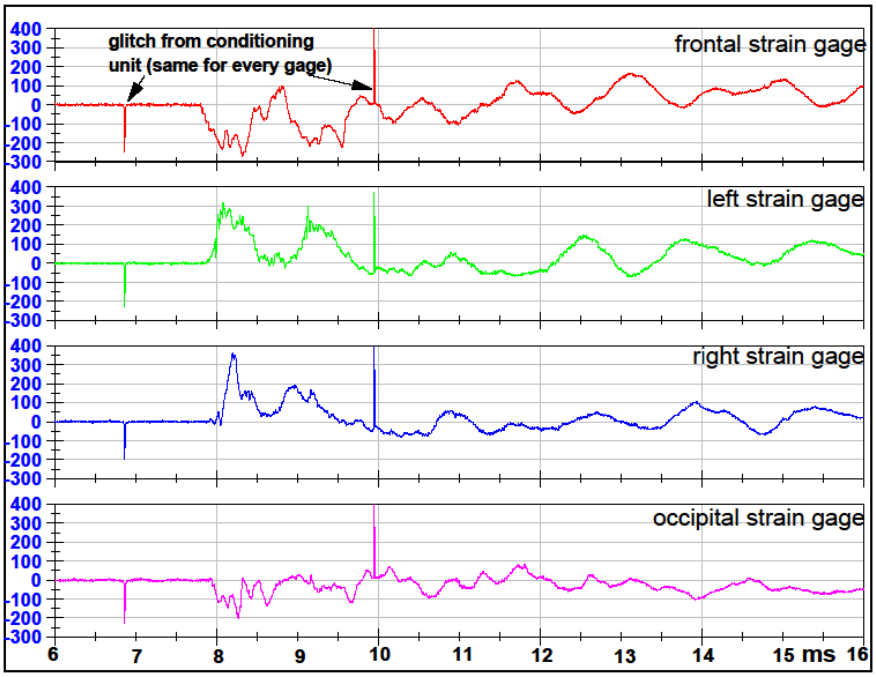

Test 6 Front 1 Orientation 7mm Sphere with Holes

Test 7 Left Orientation 7mm Sphere with Holes

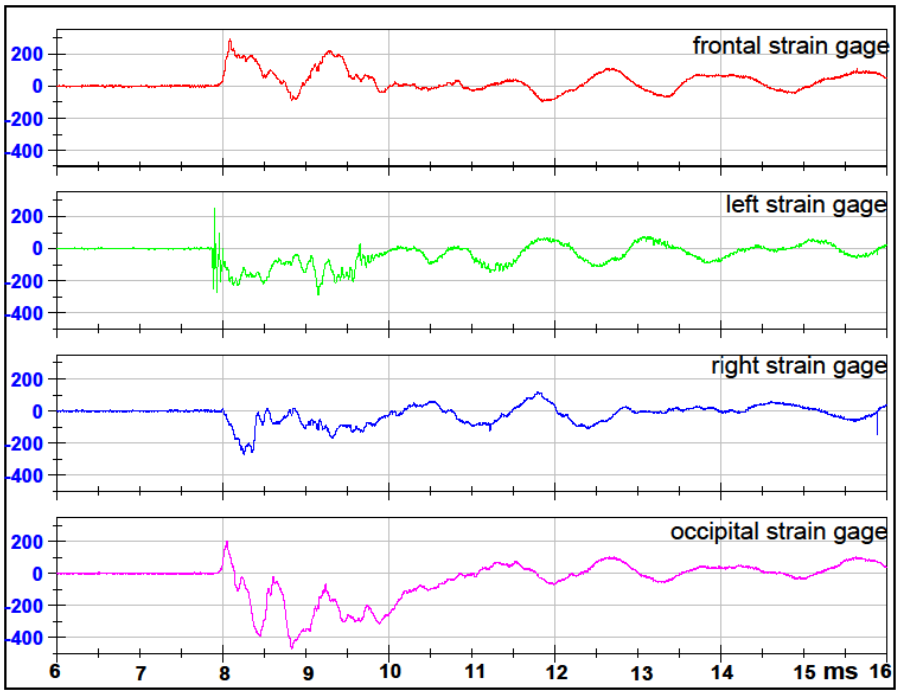

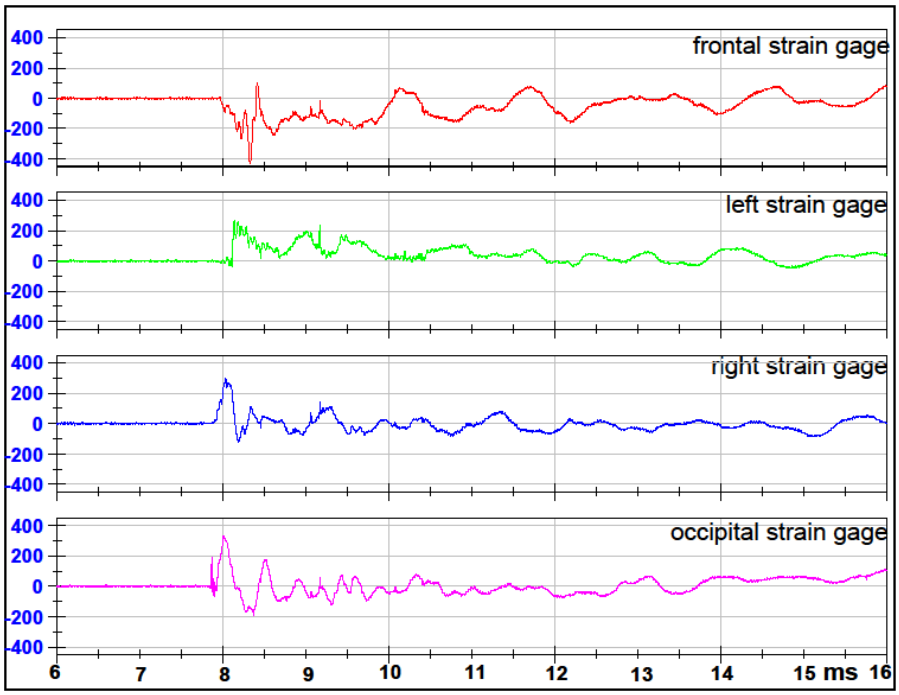

Test 8 Back Orientation 7mm Sphere with Holes

Test 9 Right Orientation 7mm Sphere with Holes

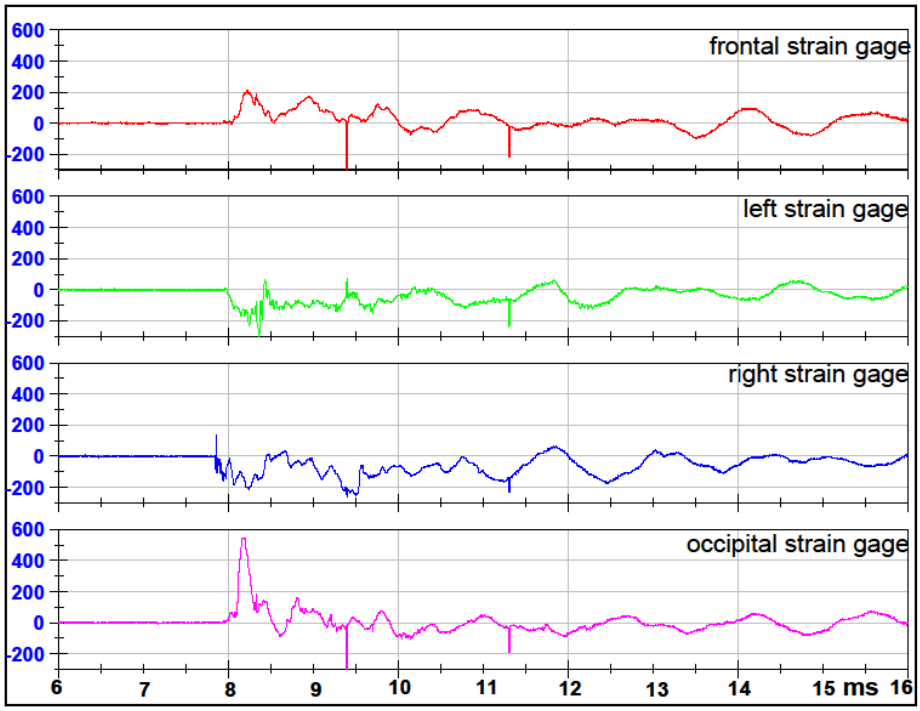

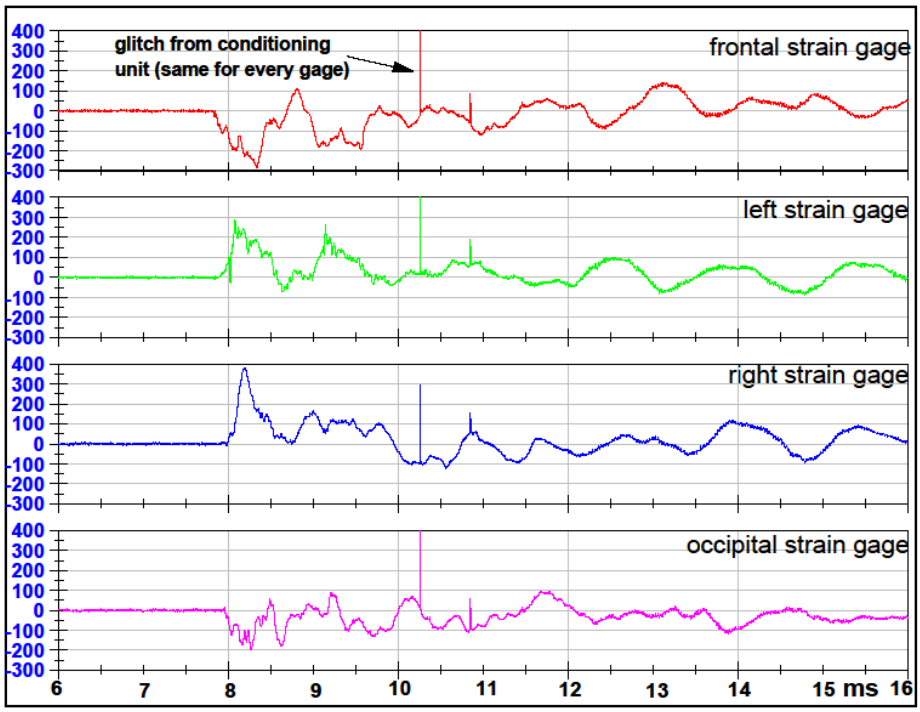

Test 10 Front 2 Orientation 7mm Sphere with Holes

Test 11 Front 1 Orientation 7mm Sphere with Holes

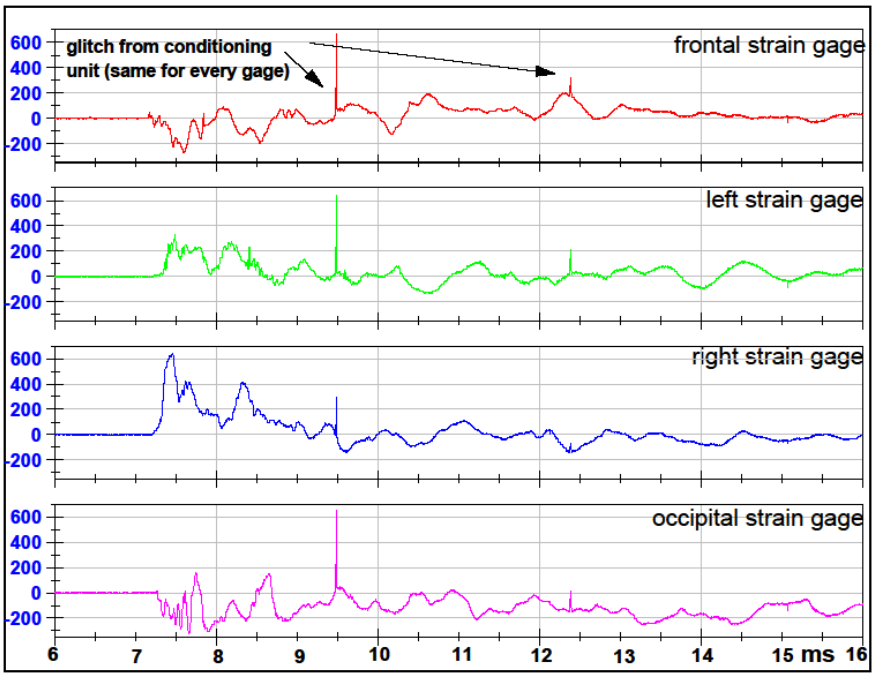

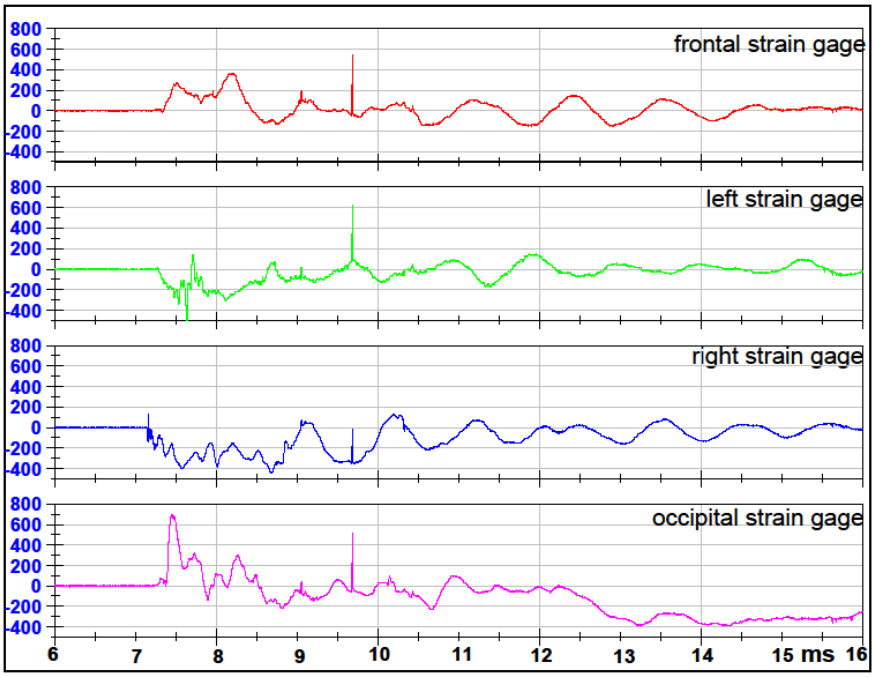

Test 12 Right Orientation 7mm Sphere with Holes

Test 13 Back Orientation 7mm Sphere with Holes

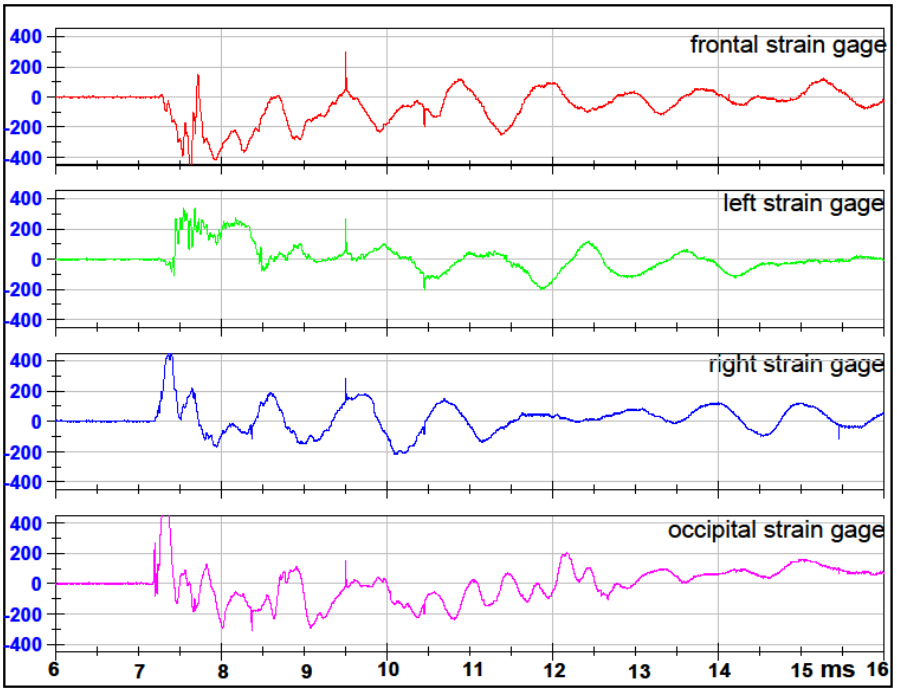

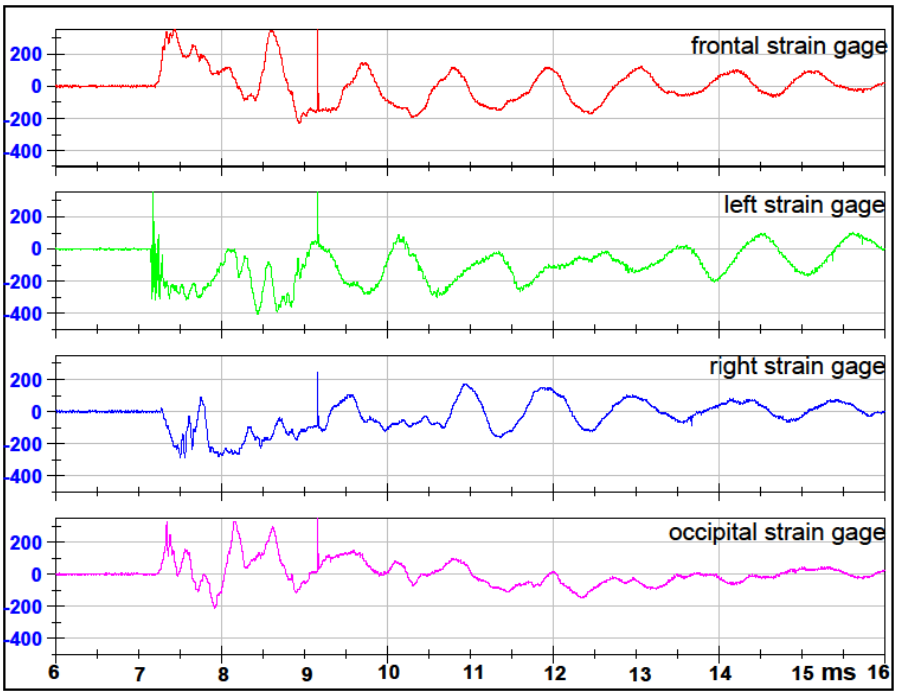

Test 14 Left Orientation 7mm Sphere with Holes

Test 15 Front 2 Orientation 7mm Sphere with Holes

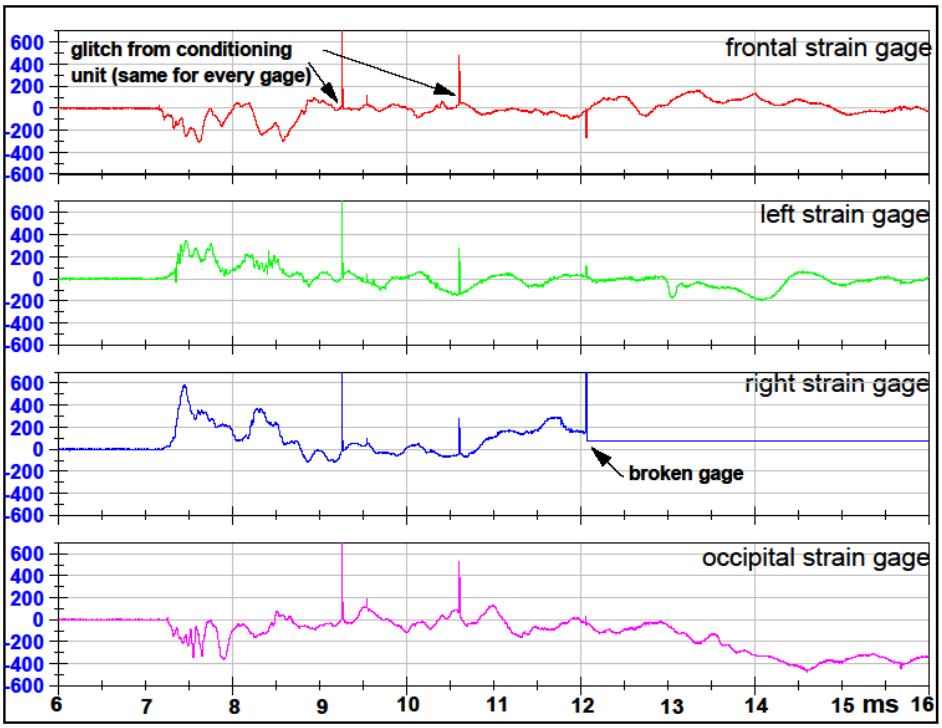

REFERENCES

Adams, T., Heisey, R.S., Smith, M.C., Briner, B.J. (1992). Parietal bone mobility in the anesthetized cat. Journal of the American Osteopathic Association 92(5): 599-622.

Axelsson, H., Hjelmqvist, H., Medin, A., Persson, J.K.E., Suneson, A. (2000). Physiological changes in pigs exposed to a blast wave from a detonating high-explosive charge. Military Medicine 165(2): 119-126.

Bhattacharjee, Y. (2008 Jan 25). Neuroscience. Shell shock revisited: solving the puzzle of blast trauma. Science, AAAS. 319: 406-8.

Blinkov, S.M., Glezer, I.I. (1968). The human brain in figures and tables. A quantitative handbook. New York, Plenum Press.

Blix, A.S., Folkow, L.P., Sorlie, D.G. (2000). Simulations of the effect of currently used grenade harpoons for the killing of whales using a pig-model. Acta Veterinaria Scandinavica 41(3): 237-42.

Brands D.W.A., Bovendeerd P.H.M., Gerrit W.M.P., Wismans J.S.H.M, Paas M.H.J.W., van Bree J.L.M.J. (1999). Comparison of the dynamic behavior of brain tissue and two model materials. Proceedings 43rd Stapp Car Conference: 313-320.

Bryant, R.A. (2008). Disentangling mild traumatic brain injury and stress reactions. New England Journal of Medicine 358(5): 525-7.

Celander, H., Clemedson, C.J., Ericsson, U.A., Hultman, H.I. (1955a). The use of a compressed air operated shock tube for physiological blast research. Acta Physiologica Scandinavica 33(1): 6-13.

Celander, H., Clemedson C.J., Ericsson, U.A., Hultman, H.I. (1955b). A study on the relation between the duration of the shock wave and the severity of the blast injury produced by it. Acta Physiologica Scandinavica 33(1): 14-18.

Cernak I., Savic J., Malicevic Z., Gordana Z., Radosevic P., Ivanovic I., Davidovic L. (1996). Involvement of the central nervous system in the general response to pulmonary blast injury. The Journal of Trauma, Injury, Infection, and Critical Care 40(3S): 100S-104S.

Cernak, I., Savic J., Ignjatovic D., Jevtic M. (1999a). Blast injury from explosive munitions. Journal of Trauma: injury, infection, and critical care 47(1): 96-104.

Cernak, I., Savic, V.J., Lazarov, A., Joksimovic, M., Markovic, S. (1999b). Neuroendocrine responses following graded traumatic brain injury in male adults. Brain Injury 13(12): 1005-1015.

Cernak, I., Wang Z., Jiang J., Bian X., Savic J. (2001). Ultrastructural and functional characteristics of blast injury-induced neurotrauma. The Journal of Trauma, Injury, Infection, and Critical Care 50(4): 695-706.

Chafi, M.S., Karami, G., Ziejewsky, M. (2010). Biomechanical assessment of brain dynamic responses due to blast pressure waves. Annals of Biomedical Engineering 38(2): 490-504.

Chavko, M., Koller W.A., Pruzaczyk W.K., McCarron R.M. (2007). Measurement of blast wave by a miniature fiber optic pressure transducer in the rat brain. Journal of Neuroscience Methods 159(2): 277-81.

Chavko, M., Watanabe, T., Adeeb, S., Lankasky, J., Ahlers, S.T., McCarron, R.M. (2011) Relationship between orientation to a blast and pressure wave propagation inside the rat brain. Journal of Neuroscience Methods 195(1): 61-6.

Clemedson, C.J., Criborn, C.O. (1955). Mechanical response of different parts of a living body to a high explosive shock wave impact. The American Journal of Physiology 181(3): 471-6.

Clemedson, C.J. (1956a). Shockwave transmission to the central nervous system. Acta Physiologica Scandinavica 37(2-3): 204-14.

Clemedson, C.J. (1956b). Blast Injury. Physiological Reviews 36(3): 336-54.

Clemedson, C.J., Pettersson, H. (1956). Propagation of a high explosive air shock wave through different parts of an animal body. American Journal of Physiology 184(1): 119-126.

Clemedson, C.J., Jonsson, A. (1961a). Transmission and reflection of high explosive shock waves in bone. Acta Physiologica Scandinavica 51: 47-61.

Clemedson, C.J., Jonsson, A. (1961b). Transmission of elastic disturbances caused by air shock waves in a living body. Journal of Applied Physiology 16(3): 426-430.

Courtney, A.C., Courtney M.W. (2009). A thoracic mechanism of mild traumatic brain injury due to blast pressure waves Medical Hypotheses 72: 76-83.

Dal Cengio Leonardi A., Bir C.A., Ritzel D.V., VandeVord P.J. (2009). The effects of intracranial pressure sensor location and skull apertures during exposure of a rat model to an air shock wave. The Second Joint Symposium of the International and National Neurotrauma Societies, Santa Barbara, CA, Poster Presentation, September 2009.

Dal Cengio Leonardi, A., Ritzel, D.V., VandeVord P.J. (2010). Cranial flexure as a primary mechanism of blast-TBI, Neurotrauma 2010 Symposium in Las Vegas, Nevada, Poster Presentation.

Dal Cengio Leonardi A., Bir C.A., Ritzel D.V., VandeVord P.J. (2011). Intracranial pressure increases during exposure to a shock wave. Journal of Neurotrauma 28: 1-10.

Dionne, J.P., Jette', F.X., Makris, A. (2004). Injury criteria for blast-induced head acceleration. Personal Armour System Symposium (PASS 2004): 1-10.

Dionne, J.P., Makris, A., El Maach, I. (2006). Blast-induced traumatic brain injury: an engineering approach. Personal Armour System Symposium (PASS 2006): 1-7.

Engin, A.E. (1969). The axisymmetric response of a fluid-filled spherical shell to a local radial impulse- a model for head injury. Journal of Biomechanics 2: 325-341.

Franke, K.E. (1956). Response of the human skull to mechanical vibrations. Journal of the Acoustical Society of America 28: 1277-1284.

Fournier, E., Sullivan, D., Bayne, T., Shewchenko, N., Martineau, L. (2007). Blast Headform Development. Literature Review. Defense Research and Development Canada -Valcartier. Quebec,: 31.

Glasstone, S., Dolan, P.J. (1977). The effects of nuclear weapons Prepared and published by the UNITED STATES DEPARTMENT OF DEFENSE and the ENERGY RESEARCH AND DEVELOPMENT ADMINISTRATION, Third Edition

Gondusky, J.S., Reiter, M.P. (2005). Protecting military convoys in Iraq: an examination of battle injuries sustained by mechanized battalion during Operation Iraqi Freedom II. Military Medicine 170: 546-49.

Guy, R.J., Glover, M.A., Cripps, N.P.J. (2000). Primary blast injury: pathophysiology and implications for treatment. Part III: Injury to the central nervous system and the limbs. Journal of the Royal Naval Medical Service 86(1): 27-31.

Hakansson, B., Brandt, A., Carlsson, P., Tjellstrom, A. (1994). Resonance frequencies of the human skull in vivo Journal of the Acoustical Society of America 95(3): 1474-1481.

Hardy, W.N., Mason, M.J., Foster, C.D., Shah, C.S., Kopacz, J.M., Yang, K.H., King, A.I., Bishop, J., Bey, M., Anderst, W., Tashman, S. (2007). A study of the response of the human cadaver head to impact. Stapp Car Crash Journal 51: 17-80.

Ho, J., Kleiven, S. (2007). Dynamic response of the brain with vasculature: a three-dimensional computational study. Journal of Biomechanics 40: 3006-3012.

Hoge, C.W., McGurk, D., Thomas, J.L., Cox, A.L., Engel, C.C., Castro, C.A. (2008). Mild traumatic brain injury in US soldiers returning from Iraq. New England Journal of Medicine 358(5): 453-63.

Horgan, T.J., Gilchrist, M.D. (2004). Influence of FE model variability in predicting brain motion and intracranial pressure changes in head impact simulations. International Journal of Crashworthiness 9(4): 401-418.

Iremonger, M. (1997). Physics of Detonations and Blast-waves. Scientific Foundation of Trauma. D. Cooper, Gann. Oxford, Butterworth, Heinemann. 1: 189-199.

Irwin, R., Lerner, M.R., Bealer, J.F., Brackett, D.J., Tuggle, D.W. (1997). Cardiopulmonary physiology of primary blast injury. The Journal of Trauma, Injury, Infection, and Critical Care 43(4): 650-655.

Ivarsson, J., Viano, D.C., Lovsund, P., Aldman, B. (2000). Strain relief from the cerebral ventricles during head impact: experimental studies on natural protection of the brain. Journal of Biomechanics 33: 181-189.

Khalil, T.B., Viano, D.C., Smith, D.L. (1979). Experimental analysis of the vibrational characteristics of the human skull. Journal of Sounds and Vibrations 63(3): 351-376.

Knudsen, S.K., Oen, E.O. (2003). Blast-induced neurotrauma in whales. Neuroscience Research 46: 377-386.

Livingston, W.K., Davis, E.W., Livingston, K.E. (1945). Delayed recovery in peripheral nerve lesions caused by high-velocity projectile wounding. Journal of Neurosurgery 2: 170-176.

Mayorga, M. A. (1997). The pathology of blast overpressure injury. Toxicology 121: 17-28.

Moore, K.L., Agur, A.M. (2002). Essential Clinical Anatomy. 2nd Edition. Publishers: Lippincott Williams & Wilkins.

Moss, W.C., King, M.J., Blackman, E.G. (2009). Skull flexure from blast waves: a mechanism for brain injury with implications for helmet design. Physical Review Letters 103(10), 108702_1-108702_4.

Mott, D.R., Schwer, D.A., Young, T.R. Jr., Levine, J., Dionne, J.P., Makris, A., Hubler, G. (2007). Blast-induced pressure fields beneath a military helmet. Military Aspects of Blast and Shock (MABS 20). Oslo: 1-23.

Nyein, M.K., Jason, A.M., Yu, L., Pita, C.M., Joannopoulus, J.D., Moore, D.F., Radovitzky, R.A. (2010). In silico investigation of intracranial blast mitigation

with relevance to military traumatic brain injury. Proceedings of the National Academy of Sciences of the United States of America 107(48): 20703-8.

Okie, S. (2005). Traumatic brain injury in the war zone. New England Journal of Medicine 352(20): 2043-7.

Okie, S. (2006). Reconstructing lives-- a tale of two soldiers. New England Journal of Medicine 355(25): 2609-15.

Parnaik, Y., Beillas, P., Demetropoulos, C.K., Hardy, W.N., Yang, K.H., King, A.I. (2004). The influence of surrogate blood vessels on the impact response of a physical model of the brain. Stapp Car Crash Journal 48: 259-277.

Prange, M.T., Margulies, S.S. (2002). Regional, directional, and age-dependent properties of the brain undergoing large deformation. Journal of Biomechanical Engineering 124: 244-252.

Rengachari, S.S., Ellenbogen, R.G., Editors, (2005). Principles of Neurosurgery Edinburg, Elsevier Mosby.

Romba, J.J., Martin, P. (1961). The propagation of air shock waves on a biophysical model. Armed Services Technical Information Agency, Arlington Hall Station, Arlington 12, Virginia. U.S. Army Ordnance. Technical Memorandum 17-61. Human Engineering Laboratories, Aberdeen Proving Ground, Maryland, pps 1-25.

Ruan, J., Prasad, P. (2001). The effects of skull thickness variations on human head dynamic impact responses. Stapp Car Crash Journal 45: 1-19.

Saljo, A., Arrhen, F., Bolouri, H., Mayorga, M., Hamberger, A. (2008). Neuropathology and pressure in the pig brain resulting from low-impulse noise exposure. Journal of Neurotrauma 25: 1397-1406.

Shuck, L., Advani, S. (1972). Rheological response of human brain tissue in shear. Journal of Basic Engineering 94: 905-911.

Stalnaker, R.L., Fogle, J.L., McElhaney, J.H. (1971). Driving point impedance characteristcs of the head. Journal of Biomechanics 4: 127-139.

Su, T.C. (1981). The effect of viscosity on the free oscillations of fluid filled spherical shell. Journal of Sound and Vibration 74(2): 205-220.

Suneson, A., Hansson,H.A., Seeman, T. (1990). Pressure wave injuries to the nervous system caused by high-energy missile extremity impact: part II. Distal effects on the central nervous system-A light and electron microscopic study on pigs. The Journal of Trauma: Injury, Infection, and Critical Care 30(3): 295-306.

Takhounts, E.G., Crandall, J.R., Darvish, K.K. (2003). On the importance of non-linearity of brain tissue under large deformations. Stapp Car Crash Journal 47: 107-134.

Taylor, P.A., Ford, C.C. (2009). Simulation of blast –induced early-time intracranial wave physics leading to traumatic brain injury. Journal of Biomechanical Engineering, Transactions of the ASME, 131: 1-11.

Thali, M.J., Kneubuehl, B.P., Dirnhofer, R. (2002a). A skin-skull-brain model for the biomechanical reconstruction of blunt forces to the human head. Forensic Science International 125: 195-200.

Thali, M.J., Kneubuehl, B.P., Zollinger, U., Dirnhofer, R. (2002b). The skin-skull-brain model: a new instrument for the study of gunshot effects. Forensic Science International 125: 178-189.

Trudeau, D.L., Anderson, J., Hansen, L.M., Shagalov, D.N., Schmoller, J., Nugent, S., Barton, S. (1998). Findings of mild traumatic brain injury in combat veterans with PTSD and a history of blast concussion. Journal of Neuropsychiatry 10(3): 308-13.

Warden, D. (2006). Military TBI during the Iraq and Afghanistan wars. Journal of Head Trauma Rehabilitation 21(5): 398-402.

Young, M.W. (1945). Mechanics of blast injury. War Medicine 8: 73.

Zhang, J., Yoganandan N., Pintar F.A., Gennarelli T.A. (2005). Temporal cavity and pressure distribution in a brain simulant following ballistic penetration. Journal of Neurotrauma 22(11): 1335-1347.

Zhang, J., Yoganandan N., Pintar F.A., Guan, Y., Gennarelli T.A. (2007). Experimental model for civilian ballistic brain injury biomechanics quantification. Journal of Biomechanics 40: 2341-2346.

Zhang, L., Bae, J., Hardy, W.N., Monson, K.L., Manley, G.T., Goldsmith, W., Yang, K.H., King, A.I. (2002). Computational study of the contribution of the vasculature on the dynamic response of the brain. Stapp Car Crash Journal 46: 145-163.

Zhu, D.C., Xenos, M., Linninger, A.A., Penn, R.D. (2006). Dynamics of lateral ventricle and cerebrospinal fluid in normal and hydrocephalic brains. Journal of Magnetic Resonance Imaging 24: 756-770.

Zoroya, G. (2005). Key Iraq Wound: brain trauma. USA Today, March 3rd 2005.

ABSTRACT

AN INVESTIGATION OF THE BIOMECHANICAL RESPONSE FROM SHOCK WAVE LOADING TO THE HEAD

by

ALESSANDRA DAL CENGIO LEONARDI

August 2011

Advisor: Pamela J. VandeVord

Major: Biomedical Engineering

Degree: Doctor of Philosophy

There is a pressing need for a comprehensive explanation of the mechanism of brain injury after exposure to blast and several hypotheses have been suggested. The focus of this research was to investigate one of the hypotheses for primary brain injury due to blast: multimodal skull flexure. The significance of this research is twofold. First, resolution of the mode of energy transfer and of the induced stresses within the skull-brain system will allow for creations of mitigation/protective techniques/equipment, as well as design of experiments investigating live-cell response using more reliable physical models. Second, the data obtained experimentally will be available to validate computational models already developed, as well as future blast injury models.

Initially, to examine the mechanical response to shock wave exposure, studies were conducted with three polyurethane spheres, used as simplified models of a human skull/brain system. The spheres had identical geometry, but differed in key characteristics: shell thickness and composition of the filling. The

spheres were placed in an inverted position inside a shock tube and were exposed to a first series of fifteen simulated blasts, changing pressure magnitudes and orientation of the sample. Subsequently, apertures were introduced in the spheres and a second series of fifteen simulated blasts was conducted, reproducing the same shock wave overpressure magnitudes and orientations of the sample. Internal pressures in three regions of the filling and strain values in four regions of the shell were collected.

All installation and testing details followed a scheme that was also applied to the cadaveric study conducted concurrently. This scheme was designed to allow comparison of the cadaveric data and the sphere data, as a means to help identify the primary components of the biomechanical response of the skull/brain system.

The specific aims of the sphere study were to map the internal pressures in different regions of the filling; to compare pressure distribution patterns with surface strain data recorded at the same time, for evaluation of gross deformations of the shell in relation to internal pressure profiles; to determine the relationship between magnitude levels of incident pressure and values of internal pressures in the simplified models; to investigate the effects of orientation, shell thickness, and apertures on internal pressures in the models.

Concurrently, four unembalmed cadavers heads were placed in an inverted position inside a shock tube and were exposed to fifteen simulated blasts, changing pressure magnitudes and orientation of the head. Intracranial pressures (ICP) in four regions of the brain and strain values in five regions of the

skull were collected. The strain values were analyzed to evaluate gross deformations of the skull in relation to ICP profiles. The specific aims of the cadaveric study were to ascertain the relationship between magnitude levels of incident pressure and values of ICP in different regions of the brain, to investigate the effects of orientation on ICP in the same regions, and to compare pressure distribution patterns with surface strain data recorded at the same time.

Results from both studies suggested that internal pressure values were linked to the mechanical response of the coupled skull/brain (or shell/fluid) system, and that the distribution of the internal pressures supported the multimodal skull flexure theory. Pressure and strain results suggested that a shock wave interacting with the skull/brain (shell/fluid) system produces skull deformation, surface ripples, relative motion between the skull and brain, and a global skull compression as forecasted by the multimodal skull flexure theory.

In conclusion, the presence of the spacial and temporal pressure distributions caused by the multimodal skull flexure is undoubtedly creating stresses in the brain tissue, and it is reasonable to suspect that these stresses could be a primary source of injury.

Furthermore, results showed that significant values of internal pressure were recorded even in the absence of a fully functioning vasculature and/or an intact body, refuting previous studies that uphold the thoracic mechanism as a primary mechanism of brain injury during exposure to blast.

This research project was partially supported by a Predoctoral Associated Health Research Fellowship managed by the *John D. Dingell Medical Center, Detroit MI* for the

Department of Veterans Affairs, CDMRP grant # W81XWH-09-1-0498, and by the Kales Scholarship for Biomedical Engineering students.

AUTOBIOGRAPHICAL STATEMENT

ALESSANDRA DAL CENGIO LEONARDI

EDUCATION

Ph.D. Biomedical Engineering, Wayne State University-WSU, Detroit, MI, 2011
M.S. Biomedical Engineering, Wayne State University-WSU, Detroit, MI, 2006
B.S. Electrical Engineering, Universita' degli Studi di Padova, Padova, Italy, 1992

POSITIONS

2009-2011 Predoctoral Research Fellow, John D. Dingell VA Medical Center, Detroit, MI
2007-2009 Graduate Research Assistant, Biomedical Engineering, WSU, Detroit
2005-2007 Graduate Research Assistant, Internal Medicine, WSU, Detroit

HONORS AND AWARDS

2011 Wayne State University Highest Scholastic Achievement Award
2009 Wayne State University Summer Dissertation Fellowship
2009 Wayne State University OVPR Award
2008 Wayne State University Graduate Professional Scholarship
2008 Anthony and Joyce Kales Scholarship for BME students
2007 Wayne State University Graduate Professional Scholarship
2006 Wayne State University Highest Scholastic Achievement Award
1991 Merit Travel Award, Fondazione Gini, University of Padua, Italy

PUBBLICATIONS AND PRESENTATIONS

Dal Cengio Leonardi A, Bir C, Ritzel D, VandeVord P. Intracranial pressure increases during exposure to a shock wave. Journal of Neurotrauma, January 2011; 28: 85-94.

Zhu F, Mao H, Dal Cengio Leonardi A, Wagner C, Chou C, Jin X, Bir C, VandeVord P, Yang KH, King AI. Development of an FE Model of the Rat Head Subjected to Air Shock Loading. Stapp Car Crash Journal, November 2010; 54: 211-225.

Leung LY, VandeVord PJ, Dal Cengio AL, Bir C, Yang KH, King AI. Blast Related Neurotrauma: a review of cellular injury. Molecular and Cellular Biomechanics, September 2008; 5(3): 155-68.

Zhu F, Chou C, Wagner C, Jin X, Dal Cengio Leonardi A, VandeVord P, Yang KH, King AI. Mechanical Responses of a Surrogate Head Physical Model under Air Shock Loading: a Combined Experimental and Numerical Investigation. Biomechanics and Modeling in Mechanobiology (submitted).

Dal Cengio Leonardi A, Ritzel D, VandeVord P. Cranial Flexure as a Primary Mechanism for Blast-TBI, Neurotrauma 2010 Symposium, Las Vegas, Nevada, June 15, 2010. Poster Presentation.

Dal Cengio Leonardi A, Bir C, Ritzel D, VandeVord P. The effects of intracranial pressure sensor location and skull apertures during exposure of a rat model to an air shock wave, The Second Joint Symposium of the International and National Neurotrauma Societies, Santa Barbara, CA, September 2009. Poster Presentation.

Dal Cengio Leonardi A, Ritzel D, VandeVord P. The effects of apertures on internal pressures measured during shock wave exposure. ASME 2011 Summer Bioengineering Conference, Farmington, Pennsylvania, June 22-25, 2011. Podium Session (accepted).